

**NRC HIGH-LEVEL RADIOACTIVE  
WASTE RESEARCH AT CNWRA  
JANUARY – JUNE 1993**

*Prepared for*

**Nuclear Regulatory Commission  
Contract NRC-02-88-005**

*Prepared by*

**Center for Nuclear Waste Regulatory Analyses  
San Antonio, Texas**

**August 1993**



**NRC HIGH-LEVEL RADIOACTIVE WASTE  
RESEARCH AT CNWRA  
JANUARY THROUGH JUNE 1993**

*Prepared for*

**Nuclear Regulatory Commission  
Contract NRC-02-88-005**

*Prepared by*

**M.P. Ahola, R.G. Baca, A.C. Bagtzoglou, A.H. Chowdhury,  
C.B. Connor, G. Cragolino, D. Dunn, A. Ghosh, R.T. Green,  
B. Henderson, B.H. Hill, S.M. Hsiung, B.W. Leslie,  
R.D. Manteufel, R.H. Martin, S. Mohanty, W.M. Murphy,  
R.T. Pabalan, E.C. Percy, N. Sridhar, D.R. Turner,  
G.W. Wittmeyer, S.R. Young**

*Edited by*

**Budhi Sagar**

**Center for Nuclear Waste Regulatory Analyses  
San Antonio, Texas**

**August 1993**

## PREVIOUS REPORTS IN SERIES

Number	Name	Date Issued
CNWRA 90-01Q	First Quarterly Research Report for 1990 January 1 — March 30	May 1990
CNWRA 90-02Q	Second Quarterly Research Report for 1990 April 1 — June 30	August 1990
CNWRA 90-03Q	Third Quarterly Research Report for 1990 July 1 — September 30	November 1990
NUREG/CR-5817 Volume 1 CNWRA 90-01A	Report on Research Activities for Calendar Year 1990	December 1991
CNWRA 91-01Q	First Quarterly Research Report for 1991 January 1 — March 30	May 1991
CNWRA 91-02Q	Second Quarterly Research Report for 1991 April 1 — June 30	August 1991
CNWRA 91-03Q	Third Quarterly Research Report for 1991 July 1 — September 30	November 1991
NUREG/CR-5817 Volume 2 CNWRA 91-01A	NRC High-Level Radioactive Waste Research at CNWRA Calendar Year 1991	February 1993
NUREG/CR-5817 Volume 3, No.1 CNWRA 92-01S	NRC High-Level Radioactive Waste Research at CNWRA January — June 1992	May 1993

## PREFACE

The Center for Nuclear Waste Regulatory Analyses (CNWRA), a Federally Funded Research and Development Center (FFRDC), conducts research on behalf of the U.S. Nuclear Regulatory Commission (NRC). The NRC-funded research at the CNWRA is focused on activities related to the NRC responsibilities defined under the Nuclear Waste Policy Act, as amended (NWPA). Progress for the period of January 1, 1993 to June 30, 1993 on 11 research projects that are currently active is described in this report. For a brief summary of the work in the reporting period, the reader is referred to the Executive Summary beginning on page 1-1.

In addition to disseminating research results through publications in appropriate open literature (e.g., CNWRA topical reports, NRC documents, journals, technical meetings, workshops, and symposia), the CNWRA produces these research reports twice yearly. See page ii for a list of previous reports in this series.

Each chapter in this semiannual report summarizes the progress made in a particular research project and is authored by the researchers in that project. Since readers of this report may only be interested in a particular topic, each chapter is self contained and can be read without reference to other chapters. Coverage in the semiannual reports is limited to only the key aspects of progress made; greater detail is provided in topical reports that are produced during the course of the research or at its conclusion, as necessary. The editor of this report ensures that each chapter of the report is reviewed for its technical and programmatic content and that some uniformity as to the depth of descriptions is maintained across the various chapters.

The NRC evaluates its research needs continually as the research progresses. The research needs are based on user needs identified jointly by the NRC Offices of Nuclear Material Safety and Safeguards (NMSS) and Nuclear Regulatory Research (RES). Generally, the NMSS is the user in the sense that its staff applies the research results to strengthen its reviews of the submittals by the U.S. Department of Energy (DOE), including the License Application for the first High-Level Nuclear Waste (HLW) Repository. In their turn, the user needs are based on Key Technical Uncertainties (KTUs) that are identified during the process of developing strategies and methods for determining compliance with the applicable regulations — in this case, 10 CFR Part 60. Thus, the research is directed towards resolution of the KTUs.

Three new research projects were initiated in the reporting period. These are: Tectonism in Basin and Range, Field Volcanism, and Regional Hydrology. Because of the late start of the Regional Hydrology research project, the progress on this project is not included in this volume of the semiannual report. Two of the research projects (Unsaturated Mass Transport — Chapter 2 and Stochastic Analysis of Unsaturated Flow and Transport — Chapter 6) described herein are expected to be concluded in the next six months.

(THIS PAGE INTENTIONALLY LEFT BLANK)

# CONTENTS

Section	Page
PREFACE .....	iii
FIGURES .....	x
TABLES .....	xv
ACKNOWLEDGMENTS .....	xvi
1 EXECUTIVE SUMMARY .....	1-1
1.1 INTRODUCTION .....	1-1
1.2 UNSATURATED MASS TRANSPORT (GEOCHEMISTRY) .....	1-3
1.3 THERMOHYDROLOGY .....	1-3
1.4 SEISMIC ROCK MECHANICS .....	1-5
1.5 INTEGRATED WASTE PACKAGE EXPERIMENTS .....	1-6
1.6 STOCHASTIC ANALYSIS OF UNSATURATED FLOW AND TRANSPORT .....	1-7
1.7 GEOCHEMICAL ANALOGS .....	1-8
1.8 SORPTION MODELING FOR HIGH-LEVEL WASTE PERFORMANCE ASSESSMENT .....	1-9
1.9 PERFORMANCE ASSESSMENT RESEARCH .....	1-10
1.10 VOLCANIC SYSTEMS .....	1-11
1.11 TECTONICS PROCESSES .....	1-12
1.12 FIELD VOLCANISM .....	1-12
1.13 REFERENCES .....	1-13
2 UNSATURATED MASS TRANSPORT (GEOCHEMISTRY) .....	2-1
2.1 TECHNICAL OBJECTIVES .....	2-1
2.2 EXPERIMENTAL STUDIES .....	2-2
2.2.1 Specific Technical Objectives .....	2-2
2.2.2 Analcime and Clinoptilolite Dissolution Experiments .....	2-2
2.2.3 Ion-Exchange Isotherm Experiments .....	2-3
2.3 GEOCHEMICAL MODELING OF KINETICS AND THERMODYNAMICS OF ANALCIME-CLINOPTILOLITE-WATER INTERACTIONS .....	2-4
2.3.1 Background .....	2-4
2.3.2 Analcime Growth .....	2-5
2.3.3 Clinoptilolite Dissolution .....	2-6
2.3.4 Phase Relations .....	2-10
2.3.5 Reaction Paths .....	2-13
2.3.6 Groundwater at Yucca Mountain .....	2-14
2.4 ASSESSMENT OF PROGRESS IN THE GEOCHEMISTRY RESEARCH PROJECT	2-14
2.5 PLANS FOR NEXT REPORTING PERIOD .....	2-17
2.6 REFERENCES .....	2-18
3 THERMOHYDROLOGY .....	3-1
3.1 TECHNICAL OBJECTIVES .....	3-1
3.2 LABORATORY EXPERIMENTS .....	3-2
3.3 EXPERIMENTAL APPARATUS .....	3-3

## CONTENTS (cont'd)

Section		Page
3.4	EXPERIMENTAL RESULTS .....	3-5
3.4.1	Visual Observation .....	3-6
3.4.2	Thermistors .....	3-6
3.4.3	Tensiometers .....	3-8
3.4.4	Gamma-ray Densitometer .....	3-8
3.5	ANALYSES .....	3-11
3.5.1	Capillary Diffusivity .....	3-11
3.5.2	Liquid Redistribution due to Temperature-Dependent Surface Tension .....	3-13
3.5.3	Condensation/Vaporization Source Term for Liquid Water .....	3-15
3.6	CONCLUSIONS .....	3-15
3.7	ASSESSMENT OF PROGRESS .....	3-17
3.8	FUTURE PLANS .....	3-18
3.9	NOMENCLATURE .....	3-18
3.10	REFERENCES .....	3-19
4	SEISMIC ROCK MECHANICS .....	4-1
4.1	TECHNICAL OBJECTIVES .....	4-1
4.2	SIGNIFICANT TECHNICAL ACCOMPLISHMENTS .....	4-3
4.2.1	Assessment of Analytical Models/Computer Codes .....	4-3
4.2.1.1	Model Setup .....	4-3
4.2.1.2	Modeling Results .....	4-5
4.2.2	Thermal-Mechanical-Hydrological Coupled Modeling (DECOVALEX) .....	4-7
4.2.2.1	DECOVALEX Phase II Modeling Studies .....	4-10
4.2.2.2	Near-Field Repository Model (BMT3) .....	4-10
4.3	ASSESSMENT OF PROGRESS TOWARDS MEETING PROJECT OBJECTIVES .....	4-15
4.4	PLANS FOR NEXT REPORTING PERIOD .....	4-16
4.5	REFERENCES .....	4-16
5	INTEGRATED WASTE PACKAGE EXPERIMENTS .....	5-1
5.1	TECHNICAL OBJECTIVES .....	5-1
5.2	LONG-TERM PREDICTION OF CONTAINER CORROSION .....	5-2
5.3	EXPERIMENTAL PROCEDURES .....	5-4
5.3.1	Localized Corrosion Studies .....	5-4
5.3.2	Slow Strain Rate Tests .....	5-6
5.4	RESULTS .....	5-10
5.4.1	Localized Corrosion of Cr-Depleted Surfaces .....	5-10
5.4.1.1	Cyclic Polarization Behavior .....	5-10
5.4.1.2	Constant Potential Studies .....	5-10
5.4.1.3	Corrosion Potential Measurements .....	5-13
5.4.2	Slow Strain Rate Tests of Type 316L Stainless Steel .....	5-13
5.5	DISCUSSION .....	5-22
5.5.1	Localized Corrosion of Mill-Finished Alloy 825 .....	5-22

## CONTENTS (cont'd)

Section	Page
5.5.2	Stress Corrosion Cracking of Type 316L Stainless Steel . . . . . 5-26
5.6	CONCLUSIONS AND RECOMMENDATIONS . . . . . 5-28
5.6.1	Localized Corrosion . . . . . 5-28
5.6.2	Stress Corrosion Cracking . . . . . 5-29
5.7	PROGRESS TOWARDS MEETING PROJECT OBJECTIVES . . . . . 5-29
5.8	PLANS FOR THE NEXT REPORTING PERIOD . . . . . 5-30
5.9	REFERENCES . . . . . 5-30
6	STOCHASTIC ANALYSIS OF UNSATURATED FLOW AND TRANSPORT . . . . . 6-1
6.1	TECHNICAL OBJECTIVES . . . . . 6-1
6.2	LIMITATIONS IN THE REGULATORY USE OF NUMERICAL SOLUTE TRANSPORT MODELS . . . . . 6-2
6.3	RECENT ENHANCEMENTS OF THE BIGFLOW NUMERICAL CODE . . . . . 6-4
6.4	SEMI-ANALYTICAL PREDICTION OF THE EFFECTIVE HYDRAULIC CONDUCTIVITY OF SATURATED AND UNSATURATED MEDIA . . . . . 6-7
6.4.1	Fracture Network Generator and Verification . . . . . 6-9
6.4.2	Determination of Effective Hydraulic Properties . . . . . 6-11
6.4.3	Real Space Renormalization Group Method . . . . . 6-13
6.4.4	Determining Effective Hydraulic Conductivity by the RSRG Method . . . . . 6-14
6.4.5	Results and Discussion . . . . . 6-17
6.4.6	Summary and Conclusions . . . . . 6-17
6.5	ASSESSMENT OF PROGRESS TO DATE . . . . . 6-18
6.6	PLANS FOR NEXT REPORTING PERIOD . . . . . 6-21
6.7	REFERENCES . . . . . 6-21
7	GEOCHEMICAL NATURAL ANALOG RESEARCH . . . . . 7-1
7.1	TECHNICAL OBJECTIVES . . . . . 7-1
7.2	SIGNIFICANT TECHNICAL ACCOMPLISHMENTS . . . . . 7-2
7.2.1	Sampling Uranium Distributions at Varying Scales . . . . . 7-3
7.2.1.1	Distribution of U at Meter and Centimeter Scales . . . . . 7-6
7.2.1.2	Distribution of U at $\mu\text{m}$ Scales . . . . . 7-11
7.2.2	Conclusions . . . . . 7-14
7.3	ASSESSMENT OF PROGRESS TOWARDS MEETING PROJECT OBJECTIVES . . 7-16
7.4	PLANS FOR NEXT REPORTING PERIOD . . . . . 7-16
7.5	REFERENCES . . . . . 7-17
8	SORPTION MODELING FOR HLW PERFORMANCE ASSESSMENT . . . . . 8-1
8.1	TECHNICAL OBJECTIVES . . . . . 8-1
8.2	TASK 2 — SORPTION MODELING . . . . . 8-2
8.2.1	Introduction . . . . . 8-2
8.2.2	Potentiometric Titration Data . . . . . 8-3
8.2.3	Data Interpretation . . . . . 8-4

## CONTENTS (cont'd)

Section	Page	
8.2.3.1	Fixed Model Parameters . . . . .	8-6
8.2.3.2	Parameter Estimation Using FITEQL . . . . .	8-7
8.2.4	Discussion of Results . . . . .	8-8
8.2.5	Conclusions . . . . .	8-9
8.3	SORPTION EXPERIMENTS . . . . .	8-11
8.3.1	Experimental Procedures . . . . .	8-12
8.3.2	Results and Discussion . . . . .	8-13
8.4	ASSESSMENT OF PROGRESS TOWARDS MEETING PROJECT OBJECTIVES . .	8-13
8.5	PLANS FOR NEXT REPORTING PERIOD . . . . .	8-15
8.6	REFERENCES . . . . .	8-16
9	PERFORMANCE ASSESSMENT RESEARCH . . . . .	9-1
9.1	TECHNICAL OBJECTIVES . . . . .	9-1
9.2	SIGNIFICANT TECHNICAL ACCOMPLISHMENTS . . . . .	9-2
9.2.1	Task 1 - Conceptual Model Development: Flow and Transport in Fractured Tuff . . . . .	9-3
9.2.2	Task 2 - Computational Model Development: Adaptive Mesh and Spectral Element Methods . . . . .	9-4
9.2.2.1	Adaptive Mesh Methods . . . . .	9-4
9.2.2.2	Spectral Element Method . . . . .	9-11
9.2.3	Task 3 - Model Evaluation: Yucca Mountain INTRAVAL Test Case . . . . .	9-15
9.2.3.1	Conceptual Model Development . . . . .	9-15
9.2.3.2	Numerical Methods . . . . .	9-17
9.2.3.3	Summary of Preliminary Results . . . . .	9-17
9.3	ASSESSMENT OF PROGRESS . . . . .	9-18
9.4	PLANS FOR NEXT REPORTING PERIOD . . . . .	9-21
9.5	REFERENCES . . . . .	9-22
10	VOLCANISM RESEARCH . . . . .	10-1
10.1	TECHNICAL OBJECTIVES . . . . .	10-1
10.2	SIGNIFICANT TECHNICAL ACCOMPLISHMENTS . . . . .	10-2
10.2.1	Recurrence Rates for Volcano Formation in the YMR . . . . .	10-3
10.2.2	Probability Models . . . . .	10-9
10.2.3	Summary of Probability Analysis . . . . .	10-12
10.2.4	Cluster Analysis of San Francisco Volcanic Field Vents Using Computerized Data- bases . . . . .	10-15
10.2.5	Alignment Analysis of the SP Mountain Cluster . . . . .	10-21
10.3	ASSESSMENT OF PROGRESS . . . . .	10-25
10.4	PLANNED PROGRESS IN THE NEXT SIX MONTHS . . . . .	10-25
10.5	REFERENCES . . . . .	10-26
11	TECTONIC PROCESSES IN THE CENTRAL BASIN AND RANGE REGION . . .	11-1
11.1	TECHNICAL OBJECTIVES . . . . .	11-1

## CONTENTS (cont'd)

Section	Page
11.2	SIGNIFICANT TECHNICAL ACCOMPLISHMENTS . . . . . 11-3
11.3	REVIEW OF LITERATURE AND OTHER SOURCES OF DATA ON LATE NEOGENE AND QUATERNARY TECTONISM IN THE CENTRAL BASIN AND RANGE REGION . . . . . 11-3
11.3.1	Patterns and Rates of Geodetic Strain . . . . . 11-5
11.3.2	Patterns and Rates of Quaternary Faulting and Seismic Strain Release . . . . . 11-6
11.4	REVIEW OF LITERATURE ON PALEOSEISMOLOGY AND GEOCHRONOLOGY OF FAULTING . . . . . 11-8
11.5	GEOLOGIC SETTING TECTONIC DATABASE . . . . . 11-10
11.5.1	Central Basin and Range Regional Tectonic Database . . . . . 11-11
11.5.1.1	Digital Terrain Model . . . . . 11-11
11.5.1.2	Earthquake Hypocenters . . . . . 11-15
11.5.1.3	Quaternary Faults . . . . . 11-15
11.5.1.4	Quaternary Volcanic Fields . . . . . 11-15
11.5.2	Yucca Mountain Tectonic Database . . . . . 11-21
11.5.2.1	Digital Terrain Model . . . . . 11-21
11.5.2.2	Quaternary Faults . . . . . 11-21
11.5.2.3	Topographic Contours and Borehole Locations . . . . . 11-21
11.5.2.4	Analysis of Terrain Data . . . . . 11-21
11.6	ASSESSMENT OF PROGRESS TOWARDS MEETING PROJECT OBJECTIVES . . 11-33
11.7	PLANS FOR NEXT REPORT PERIOD . . . . . 11-33
11.8	REFERENCES . . . . . 11-34
12	FIELD VOLCANISM RESEARCH . . . . . 12-1
12.1	TECHNICAL OBJECTIVES . . . . . 12-1
12.2	SIGNIFICANT TECHNICAL ACCOMPLISHMENTS . . . . . 12-2
12.2.1	Data from the April 1992 Eruption of Cerro Negro, Nicaragua . . . . . 12-4
12.2.2	Data From the 1975 Eruption of Tolbachik Cinder Cones, Kamchatka, Russia . . . . . 12-9
12.2.3	Cinder Cone Eruption Energetics . . . . . 12-10
12.2.4	Implications for Volcanism in the Yucca Mountain region . . . . . 12-13
12.3	ASSESSMENT OF PROGRESS . . . . . 12-13
12.4	PLANNED PROGRESS IN THE NEXT SIX MONTHS . . . . . 12-14
12.5	REFERENCES . . . . . 12-15

# FIGURES

Figure	Page
1-1	Relationship of NRC HLW Research Program to licensing needs . . . . . 1-2
2-1	Isotherms for ion-exchange at 25 °C between clinoptilolite and NaCl/SrCl <sub>2</sub> aqueous mixtures at total solution concentrations of 0.005, 0.05, or 0.5 N. . . . . 2-5
2-2	Moles of Si (A) and Al (B) precipitated from supersaturated solutions as a function of time in two analcime growth experiments, RACDTIA . . . . . 2-7
2-3	Moles of Al precipitated as a function of moles of Si precipitated in analcime growth experiments RACDTIA and RACDTIIIA. The slope of the line to the Al/Si . . . 2-8
2-4	Moles of Si and Al released from clinoptilolite in dissolution experiments CDVSEI and CDVSEII. The curve is a fit to the Si release data using the rate Eq. (2-3) . . . . . 2-9
2-5	Net moles of Si and Al released in ACDTB series analcime dissolution and analcime plus clinoptilolite equilibration studies. Initial analcime dissolution . . . . . 2-10
2-6	Aqueous solution properties shown as the base-ten logarithm of the product of the Na <sup>+</sup> and Al(OH) <sub>4</sub> <sup>-</sup> activities plotted as a function of the logarithm of the . . . 2-11
2-7	Aqueous solution properties represented as the logarithm of the product of the Al(OH) <sub>4</sub> <sup>-</sup> and H <sup>+</sup> ion activities plotted as a function of the logarithm of the . . . . . 2-15
3-1	Test 12 experimental setup (all dimensions in cm) . . . . . 3-4
3-2	Temperature measurements in test 12 . . . . . 3-7
3-3	Steady-state, horizontal temperature profiles . . . . . 3-7
3-4	Tensiometer measurements in test 12 (insets show measurement locations) . . . . . 3-9
3-5	Liquid saturation based on gamma-ray densitometer measurements in test 12 (insets show measurement locations) . . . . . 3-10
3-6	Horizontal liquid saturation profiles based on gamma-ray densitometer measurements in test 12 (insets show measurement locations) . . . . . 3-12
3-7	Characteristic curves for the porous medium used in: (a) test 6 and (b) test 12 . . . . . 3-14
3-8	Comparison of the temperature dependence of $P_v$ , $\eta$ , and $[293/(T+273)]^3$ . . . . . 3-16
3-9	Illustration of $Q_{V/C}$ showing the condensation, vaporization, and dryout zones . . . . . 3-16
4-1	UDEC model for simulating laboratory test on single-joint specimen . . . . . 4-4
4-2	Plot showing distorted mesh for the top block due to numerical instability resulting from large number of calculations. . . . . 4-6
4-3	Joint shear stress versus shear displacement plot using model in Figure 4-1 . . . . . 4-6
4-4	Modified UDEC model for simulating laboratory test on single-joint specimen . . . . . 4-8
4-5	Joint shear stress versus shear displacement plot using model in Figure 4-4 . . . . . 4-8
4-6	UDEC and laboratory test results of shear stress versus shear displacement plot for Test No. 11 under normal stress of 1.08 MPa . . . . . 4-9
4-7	UDEC results and laboratory measurements of joint dilation for Test No. 11 under 1.08 MPa normal stress . . . . . 4-9
4-8	Near-field repository model, BMT3 . . . . . 4-10
4-9	(a) Fracture geometry given for near field repository model, BMT3, and (b) UDEC model . . . . . 4-12

## FIGURES (cont'd)

Figure		Page
4-10	UDEEC results for the principal stresses (indicated by line segments) and displacements (indicated by arrows) after (a) tunnel excavation (b) 4 years of heating . . . . .	4-13
4-11	UDEEC results for the fracture flow rates after (1) tunnel excavation, and (b) 4 years of heating (one line thickness represents a flowrate of $5 \times 10^{-10} \text{ m}^2/\text{s}$ ) . . . . .	4-14
5-1	Schematic illustration of the approach used for long-term life prediction of container materials under localized corrosion conditions . . . . .	5-3
5-2	Successive cyclic potentiodynamic polarization scans for mill-finished alloy 825 in deaerated 1000 ppm $\text{Cl}^-$ at 95 °C. Scan Rate = 0.17 mV/s. Fresh solution was . . .	5-11
5-3	Breakdown and repassivation potentials in deaerated 1000 ppm $\text{Cl}^-$ solution at 95 °C versus surface Cr concentration on corroded and cleaned specimens . . . . .	5-11
5-4	Current density as a function of time for polished and mill-finished (Cr-depleted) specimens of alloy 825 in 1000 ppm $\text{Cl}^-$ solution at 95 °C. The solution was . . . . .	5-12
5-5	Current density as a function of time for mill-finished alloy 825 specimens at various applied potentials. The solution was purged with high-purity nitrogen. . . . .	5-12
5-6	Effect of surface condition, thermal treatment, and redox species on the corrosion potential of alloy 825 at 95 °C. Solution used contained 1000 ppm $\text{Cl}^-$ + 85 ppm . .	5-14
5-7	Effect of chloride concentration on pitting ( $E_p$ ), repassivation ( $E_{rp}$ ), and corrosion ( $E_{corr}$ ) potentials of type 316L stainless steel in chloride-containing . . . . .	5-15
5-8	Potentials and chloride concentrations selected for slow strain rate tests of type 316L stainless steel in dilute chloride solutions at 95 °C in relation to pitting . . . . .	5-17
5-9	Side surface of specimen tested under open-circuit conditions in 40% $\text{MgCl}_2$ solution at 120 °C showing the presence of many secondary cracks . . . . .	5-20
5-10	Fracture surface of specimen tested under open-circuit conditions in 40% $\text{MgCl}_2$ solution at 120 °C . . . . .	5-20
5-11	Fractograph showing the transgranular SCC area of the specimen tested under open-circuit conditions in 40% $\text{MgCl}_2$ solution at 120 °C . . . . .	5-21
5-12	Fractograph showing the intergranular SCC area of the specimen tested under open-circuit conditions in 40% $\text{MgCl}_2$ solution at 120 °C . . . . .	5-21
5-13	Stress versus elongation curves obtained in slow strain rate tests of type 316L stainless steel in concentrated LiCl solutions at temperatures ranging from 95 to 120 °C . . . . .	5-23
5-14	Schematic illustration of the formation of a corrosion potential as a result of anodic dissolution kinetics and cathodic redox reaction kinetics. A single redox . . . . .	5-24
5-15	Effect of chloride concentration on the pit initiation ( $E_p$ ) and repassivation ( $E_{rp}$ ) potentials of alloy 825 and corrosion potential ( $E_{corr}$ ) in the presence of . . . . .	5-27
5-16	Potential and chloride concentrations selected for slow strain rate tests of type 316L stainless steel in concentrated chloride solutions ( $\text{MgCl}_2$ , LiCl, and NaCl) at . . . . .	5-28
6-1	Concentrations versus $x$ for the advancing front problem obtained using several numerical methods . . . . .	6-5
6-2	Error-to-signal ratios versus $x$ for the advancing front problem obtained using several numerical methods . . . . .	6-5

## FIGURES (cont'd)

Figure		Page
6-3	Comparison of pressure head versus elevation solution for BIGFLOW and PORFLOW at a time $T=30$ million years; (a) Absolute values of . . . . .	6-8
6-4	Comparison of pressure head versus elevation solution for BIGFLOW and semi-analytical solution . . . . .	6-9
6-5	Schematic depicting the conceptual model for a fracture and its corresponding continuum approximation . . . . .	6-11
6-6	Examples of highly fractured, heterogeneous structures; (a) Binary matrix-fracture system; and (b) Stochastic matrix-fracture system . . . . .	6-12
6-7	Schematic of the RSRG transformation: cluster of cells transforms to a cell, cell transforms to a site, etc. . . . .	6-15
6-8	Schematic of a fully connected fracture network with anisotropic fracture density . . .	6-17
6-9	Comparison of effective unsaturated hydraulic conductivity between a fracture system with fully connecting fractures and a system with a random binary . . . . .	6-19
7-1	Location map of the Nopal I analog site . . . . .	7-4
7-2	Concentration of U in the fracture-filling material of a major fracture at 13.5 m North . . . . .	7-7
7-3	Selected XRD patterns of the fracture-filling material collected at varying distance from the edge of the visible U mineralization . . . . .	7-7
7-4	East/West profile of U content in bulk rock at 9.1 m North . . . . .	7-9
7-5	Centimeter-scale profiles of U content of bulk rock as a function of distance from the edge of the fracture . . . . .	7-10
7-6	Centimeter-scale profiles of U content of bulk rock as a function of distance from the edge of the fracture . . . . .	7-10
7-7	Plots of total alpha impacts per unit area, per unit time for samples NOPI-ECP-22.35/15.3-TS1 and NOPI-ECP-22.5/10.4-TS1 corrected for local background U concentration . . . . .	7-13
7-8	Plot of total alpha impacts per unit area, per unit time for sample NOPI-ECP-22.35/15.3-TS1 versus a model alpha impact intensity profile . . . . .	7-15
7-9	Plot of total alpha impacts per unit area, per unit time for sample NOPI-ECP-22.5/10.4-TS1 versus a model alpha impact intensity profile . . . . .	7-15
8-1	Data from the experiments on uranium sorption on Na-montmorillonite in terms of percent of uranium lost from solution versus equilibrium pH. Initial uranium . . . . .	8-14
8-2	Data from experiments on uranium sorption on alpha-alumina in terms of percent of uranium lost from solution versus equilibrium pH. Initial uranium concentration . . .	8-14
9-1	Moisture retention curves for low permeability sample obtained by centrifuge method . . . . .	9-5
9-2	Comparison of calculated pressure heads at $T=1$ day from UNSAT1D Code (Celia, 1991) and from the adaptive meshing code developed by the authors . . . .	9-8
9-3	Comparison of adaptive grid and fixed grid pressure head solutions . . . . .	9-9
9-4	Mass balance error caused by grid projection using linear basis functions . . . . .	9-10

## FIGURES (cont'd)

Figure		Page
9-5	Comparisons of SEM and analytic solutions for $u=1$ and $D=0.01$ . . . . .	9-13
9-6	Pressure head profiles computed using SEM . . . . .	9-16
9-7	Effect of steady-state infiltration rates (m/s) on the predicted water saturation profile at well bore UZN-54 . . . . .	9-19
9-8	Comparison between the predicted and measured water saturation profiles at well bore UZN-54 for a steady-state infiltration rate of $\sim 0.003$ mm/yr . . . . .	9-20
10-1	Post-caldera basaltic vent locations in the Yucca Mountain region. . . . .	10-5
10-2	Recurrence rate for the formation of new volcanoes in the Yucca Mountain region is estimated using a number of near-neighbor nonhomogeneous Poisson models. . . . .	10-8
10-3	Estimated probability of disruption of the high-level waste repository varies with the number of near neighbors used in nonhomogeneous Poisson models and because of uncertainty in the ages of Quaternary Yucca Mountain cinder cones . . . . .	10-10
10-4	Estimated probability of a volcano forming at the repository site increases with increasing area of the site. . . . .	10-11
10-5	Probability of a volcano forming within an 8 km <sup>2</sup> area during the next 10,000 years is contoured using 6 near-neighbor (a) and 10 near-neighbor (b) nonhomogeneous . .	10-13
10-6	Volcanic Fields currently under investigation using the GIS and volcanism database . .	10-16
10-7	Volcanoes and mapped faults of the San Francisco Volcanic Field, Arizona. . . . .	10-18
10-8	Vent clusters of the San Francisco Volcanic Field, Arizona. . . . .	10-20
10-9	Volcanoes of the San Francisco Volcanic Field, Arizona, that are located within 1 km of a mapped fault. . . . .	10-22
10-10	Vent alignments of the SP Mountain cluster . . . . .	10-23
11-1	Location maps showing geographic areas covered by the Geologic Setting Tectonic Database . . . . .	11-12
11-2	Digital Shaded-Relief Terrain Model of the area covered by the central Basin and Range Regional Tectonic Database . . . . .	11-13
11-3	Map of Quaternary fault traces and earthquake epicenters from the Regional Tectonic Database plotted onto the regional digital terrain model . . . . .	11-17
11-4	Map of Quaternary fault traces and late Neogene and Quaternary basaltic volcanic fields from the Regional Tectonic Database plotted onto the regional digital terrain model . . . . .	11-19
11-5	Digital Shaded-Relief Terrain Model of the area covered by the Yucca Mountain Tectonic Database . . . . .	11-23
11-6	Map of Neogene and Quaternary faults from the Yucca Mountain Tectonic Database plotted onto the digital terrain model . . . . .	11-25
11-7	Map of photogeologic lineaments from the Yucca Mountain Tectonic Database plotted onto the digital terrain model . . . . .	11-27
11-8	Map showing location of selected boreholes at Yucca Mountain plotted on Digital Terrain Model . . . . .	11-29
11-9	Shaded-relief digital terrain model show in Figure 5 illuminated from west, north, south, and east . . . . .	11-31

## FIGURES (cont'd)

Figure		Page
12-1	Location of Cerro Negro, Nicaragua. Late Quaternary cinder cones and maars of the El Hoyo complex are shown as solid triangles; older Quaternary(?) cones are . . . . .	12-5
12-2	Photo of typical activity during the 1971 eruption of Cerro Negro. The vulcanian-style activity results in a tight, cauliflower-shaped eruption column . . . . .	12-6
12-3	Isopach map of airfall from the April 1992 eruption of Cerro Negro. This eruption was voluminous and dispersive compared to 1968 or 1971 activity. . . . .	12-7
12-4	Real-time seismic amplitude measurements collected during the second phase of eruptive activity at Cerro Negro during the 1992 eruption. RSAM units are . . . . .	12-8
12-5	The thickness of the ash deposit varies exponentially with distance from Cerro Negro. Ash samples were collected during and immediately following the eruption at . . . . .	12-11

## TABLES

Table	Page
5-1	Chemical compositions of the heat of type 316L SS used in this study . . . . . 5-7
5-2	Experimental conditions for slow strain rate tests (extension rate = $1.3 \times 10^{-5}$ mm/s) of type 316 L stainless steel in dilute chloride solutions . . . . . 5-8
5-3	Experimental conditions for slow strain rate tests (extension rate = $1.3 \times 10^{-5}$ mm/s) of type 316 L stainless steel in concentrated chloride solutions . . . . . 5-9
5-4	Results of slow strain rate tests of type 316L stainless steel in dilute chloride solutions at 95 °C (Test conditions are given in Table 5-2.) . . . . . 5-16
5-5	Results of slow strain rate tests of type 316L stainless steel in concentrated chloride solutions (Test conditions are given in Table 5-3.) . . . . . 5-18
5-6	Effect of thermal aging on the electrochemical parameters of alloy 825 in a solution of 1000 ppm $\text{Cl}^-$ + 85 ppm $\text{HCO}_3^-$ + 20 ppm $\text{SO}_4^{2-}$ + 10 ppm $\text{NO}_3^-$ + 2 ppm $\text{F}^-$ at 95 °C . . . . . 5-26
6-1	Material hydraulic properties used in the modified COVE-2A exercise . . . . . 6-7
6-2	Execution time comparison between numerical simulation and RSRG method for the determination of effective saturated conductivity . . . . . 6-19
6-3	Execution time comparison between numerical simulation and RSRG method for the determination of effective unsaturated conductivity . . . . . 6-19
8-1	Mineral properties used in interpreting potentiometric titration (25 °C) with data sources . . . . . 8-4
8-2	Summary of surface complexation model parameters (modified from Hayes et al., 1991) . . . . . 8-5
8-3	Best estimate values for SCM constants (T = 25 °C) . . . . . 8-10
9-1	Summary of soil properties (adapted from Celia et al., 1990) . . . . . 9-14
10-1	Locations of volcanic centers and ages used for statistical models in the Yucca Mountain Region. . . . . 10-4
12-1	Leachate concentrations (ppm) in three eruptions of Cerro Negro . . . . . 12-10

## ACKNOWLEDGMENTS

This report was prepared to document work performed by the Center for Nuclear Waste Regulatory Analyses (CNWRA) for the U.S. Nuclear Regulatory Commission (NRC) under Contract No. NRC-02-88-005. The activities reported herein were performed on behalf of the NRC Office of Nuclear Regulatory Research (RES), Division of Regulatory Applications. The report is an independent product of the CNWRA and does not necessarily reflect the views or regulatory position of the NRC.

Active support from several people during the production of this report is thankfully acknowledged. First and foremost, this report is possible only because of the wholehearted cooperation from the principal investigators and researchers within each project who kept to the tight schedule of the editor. Technical reviewers — P.C. Lichtner, V. Kapoor, P.K. Nair, W.M. Murphy, G.W. Wittmeyer, D.R. Turner, E.C. Percy, J.L. Russell, G.A. Cragnolino, and M.P. Miklas provided substantive comments that materially improved the quality of the report. Programmatic reviews were performed by W. Patrick, in addition to the editor. Able secretarial support was provided by J. Bishop, E. Cantu, B. Caudle, M. Gruhlke, R. Sanchez, B. Garcia, C. Garcia, and A. Ramos. T. Fischer, D. Moore, J. Pryor, and C. Gray of the SwRI Publications Group provided editorial support.

Finally, the valued interaction with NRC project managers — J. Randall, L. Kovach, G. Birchard, T. McCartin, M. McNeil, T. Nicholson, and J. Philip — is gratefully acknowledged.

# 1 EXECUTIVE SUMMARY

## 1.1 INTRODUCTION

Progress from January 1 to June 30, 1993, on 11 research projects under way at the Center for Nuclear Waste Regulatory Analyses (CNWRA) is discussed in this report. All 11 projects are sponsored by the U.S. Nuclear Regulatory Commission (NRC) to fulfill its mandate under the Nuclear Waste Policy Act (NWPA), as amended. In this regard, it is important to recognize that the NRC's regulatory responsibilities are distinct from those of the Department of Energy (DOE), which is responsible for siting, constructing, and operating a repository for the disposal of high-level nuclear waste (HLW). The DOE has undertaken the development and implementation of a broad range of techniques and methods to obtain information and produce analyses necessary to determine site suitability, design of the engineered portions of the repository, and completion of a license application. In fulfilling its responsibilities for assuring the radiological health and safety of the public, the NRC conducts confirmatory and exploratory (also referred to as anticipatory) research to:

- Develop the licensing tools and technical bases necessary to judge the adequacy of DOE's license application
- Ensure a sufficient independent understanding of the basic physical processes taking place at the proposed geologic repository site
- Maintain an independent, but limited, confirmatory research capability to be used in evaluating DOE prelicensing and license application submittals

Figure 1-1 depicts the basic relation between NRC's research program and licensing needs. Regulations applicable to the licensing of a HLW repository (primarily 10 CFR Part 60) are translated into regulatory requirements, each one of which must be met before the NRC staff can recommend the issuance of a license. Strategies and methods for determining whether DOE's demonstration of compliance with the regulatory requirements is acceptable are currently being developed and documented in NRC's License Application Review Plan (LARP). Key technical uncertainties (KTU) are defined based on the risk to compliance determination. Resolution of the KTUs is the primary objective of the research undertaken by the NRC. Each chapter outlines the specific KTUs being addressed by the research described in that chapter.

Each of the research projects discussed herein is being conducted in accordance with approved Research Project Plans, which were developed consistent with the NRC statement-of-work. These plans are the vehicle for establishing the objectives, technical approach, justification, and funding for each of the studies. They also describe the interrelationships among the various projects, which provide a sound basis for integrating research results. Because the plans primarily address planning and management matters, they are not discussed further in this report (with the exception of stating project objectives).

This document provides, an executive summary that covers, in capsule form, the progress of each research project over the past 6 months. The executive summary is followed by Chapters 2 through 12, representing each of the 11 currently active research projects, respectively. Project objectives and a report of research activities and results (as appropriate) to date are given in each chapter. Progress toward fulfillment of identified research needs and development of particular regulatory products is



addressed in cases where such progress has been significant. In addition, commentary is provided on anticipated progress for each project in the ensuing 6-month period.

## 1.2 UNSATURATED MASS TRANSPORT (GEOCHEMISTRY)

Interactions between groundwater and zeolite minerals clinoptilolite and analcime are likely to play a major role in controlling groundwater compositions at Yucca Mountain, Nevada, and are significant for assessments of waste package and waste form performance and radionuclide migration in a proposed repository at Yucca Mountain. Nevertheless, the basic kinetic and thermodynamic properties of these minerals required for evaluations of repository performance are sparse, uncertain, or absent. The objective of this research project is to obtain new data on the fundamental properties of these minerals and their interactions with aqueous solutions in experimental studies and to apply these and other data to the interpretation and modeling of the Yucca Mountain geochemical system and to repository-induced geochemical perturbations. This report presents new experimental data on  $\text{Na}^+/\text{Sr}^{2+}$  ion-exchange studies and analcime and clinoptilolite dissolution, growth, and equilibration studies. Interpretation of the analcime data provides a determination of the analcime solubility bracketed by dissolution and precipitation measurements. The solubility measurement permits determination of the equilibrium constant for analcime dissolution and the standard-state Gibbs free energy of formation of analcime. Interpretation of clinoptilolite dissolution data shows the reaction to be incongruent. Silica release from clinoptilolite can be interpreted according to a general dissolution rate law. Thermodynamic data derived for analcime and equilibrium interpretations of groundwater data from saturated zone tuffaceous aquifers at Yucca Mountain and Oasis Valley strongly indicate that analcime solubility controls the groundwater chemistry. Evaluation of the new experimental data on  $\text{Na}^+/\text{Sr}^{2+}$  ion-exchange using a Margules thermodynamic formulation for excess Gibbs energy of mixtures reinforces the CNWRA previous finding, which is based on ion-exchange experiments involving  $\text{Na}^+/\text{K}^+$  and  $\text{Na}^+/\text{Ca}^{2+}$ , that a Margules model for zeolite solid solutions allows prediction of ion-exchange equilibria over a wide range of solution composition and concentration and provides a basis for understanding rock-groundwater interactions in multicomponent systems such as that found at Yucca Mountain, Nevada.

## 1.3 THERMOHYDROLOGY

The significance of thermohydrologic phenomena in the performance of a geologic repository has been widely recognized. Accordingly, the NRC has specified in 10 CFR Part 60 the necessity of understanding thermohydrologic mechanisms as they affect the repository overall system performance (10 CFR 60.112) and the components to the multiple barrier system: waste package [10 CFR 60.113(a)(1)(ii)(A)]; controlled release [10 CFR 60.113(a)(1)(ii)(B)]; and the disturbed zone as part of the geologic setting [10 CFR 60.113(a)(2)].

A thorough understanding of the thermohydrologic mechanisms present at a HLW repository located in unsaturated fractured rock is imperative in order to conduct a performance assessment (PA) of the repository. The movement of water in the far field, although not directly affected by repository-induced changes in temperature, may be influenced by thermal and hydrologic changes that occur proximal to the repository. In particular, specific PAs cannot be properly completed without a sufficient understanding of the temperature and liquid saturation regimes to which the repository will be subjected. For example, assessment of the design of the waste package and the engineered barrier system (EBS) can be significantly affected by the thermal and flow regimes primarily through either the presence or absence of water. Likewise, assessment of the geochemistry and the transport phenomena (e.g., sorption

mechanisms, solubility, precipitation) is also highly dependent upon the thermal and hydrologic regime at the repository. In summary, the performance of essentially all of the components of the repository will be affected by the heat-generating nature of the waste and its effect on the redistribution of subsurface water.

The research needs of the NRC/HLW have been identified in an unpublished NRC memorandum. Particular research needs addressed, at least in part by these investigations, include: (i) determination of flow paths and fluxes in unsaturated rock; (ii) characterization of matrix/fracture flow in unsaturated fractured rocks; (iii) applicability of existing flow and transport codes; and (iv) effects of drying and wetting in the repository environment. A discussion of the efforts to address drying/wetting phenomena, flow paths and flux using numerical results from a flow and transport code, and preliminary analysis using the principles of similitude is contained in this chapter.

A laboratory experimental study of thermally driven liquid redistribution in partially saturated porous medium, has been conducted and reported herein. The experimental setup consisted of a sealed rectangular enclosure subject to a steady-state temperature profile across the largest enclosure dimension.

The experimental results indicate that:

- Vaporization, vapor flow, condensation, and liquid advection are important mass transfer mechanisms for water in a nonisothermal porous medium.
- A relatively small dryout zone developed near the hot side in both tests.
- The local liquid saturation increased throughout the majority of the porous volume of the experiment due to the displacement of liquid in the dryout zone.
- The liquid saturation profile was predominately one-dimensional (1D) (due to the imposed temperature profile being predominately 1D).
- The largest gradients in liquid saturation occurred near the dryout zone.
- A wet band developed in front of the dryout zone and was more pronounced in test 6, which used glass beads (instead of alumina powder in test 12) for the porous medium and was subjected to a smaller temperature gradient.

A simplified mathematical model has been developed and used to assess the capillary diffusivity, the temperature-dependent surface tension, and condensation/vaporization source term. Conclusions from the theoretical analyses include:

- The capillary diffusivity and time scale have been identified and found to be in qualitative agreement with the experimental observation that test 12 responded more quickly than test 6.
- A model for liquid redistribution due to temperature-dependent surface tension has been developed and found to be in qualitative agreement with experimental observations.

- A model for condensation/vaporization source term for liquid water has been developed and found to be in qualitative agreement with the experimental observation of the development of a wet band.

## 1.4 SEISMIC ROCK MECHANICS

Long-term deterioration of vertical emplacement boreholes and emplacement drifts (if in-drift emplacement is considered) and potential near-field fluid flow resulting from the coupled effects are among the important concerns for safe, HLW disposal. A number of factors have been identified that could potentially cause the degradation problem or change near-field flow patterns. Two of the factors are the potential for repetitive seismic loads (including earthquakes and nuclear explosions at the Nevada Test Site) and thermal loads generated by the decay of the emplaced waste. A KTU that has been identified, which could pose high risk of noncompliance with the performance objectives of 10 CFR Part 60, is the ability to predict the long-term effects of repetitive seismic and thermal conditions on the degradation of emplacement drifts and emplacement boreholes that may have implications on the performance of the EBSs, retrievability of waste, and long-term waste isolation, especially if some of these openings are left "unfilled" at closure. Regulatory requirement 10 CFR 60.133(f) calls for careful consideration of excavation methods for the construction of the underground facility so that the potential for creating preferential pathways for groundwater to contact the waste packages or radionuclides migration to the accessible environment will be minimized. Long-term deterioration of underground openings through the effects of repetitive seismicity may have a potentially much greater effect than that attributable to different excavation methods. Consequently, including such adverse effects of repetitive seismic loads in the design consideration for the underground facility is apparently warranted. The objective of the Seismic Rock Mechanics Research Project is to conduct laboratory and field studies, and theoretical analyses to develop techniques that could be used to predict the response of near-field rock mass at the proposed repository at the Yucca Mountain site when it is subjected to repetitive seismic and long-term temperature conditions. The techniques developed and the knowledge gained in this project will be used to support the development and implementation of portions of the LARP and precicensing activities. The results of ongoing activities in Tasks 3 and 9 are reported herein.

Task 3 includes two types of qualification studies on computer codes. Among the six computer codes evaluated, only the UDEC and 3DEC codes reproduced the analytical solutions of four benchmark problems selected for the first-phase qualifications studies. The related results have been reported previously. During this reporting period, the UDEC code has been selected for the second phase of qualification studies, to compare with the results of laboratory tests of a single joint using Apache Leap tuff specimens. At this stage, only pseudostatic tests have been modeled, and the Continuously Yielding rock joint model has been evaluated. The limited study with UDEC identified a minor problem in the logic used for joint shear stress calculation at contact points. It was determined that the joint shear stress at a contact point may be in error if the assigned joint length for the shear stress calculation decreases with the joint shear displacement. This problem could be eliminated by designing the UDEC model in such a way as to maintain a constant joint length. The second phase study also identified some deficiencies of the existing rock joint model for the prediction of joint behavior. These deficiencies include that the rock joint models under evaluation may not be able to predict sufficiently the joint shear and dilation behavior during reverse joint shearing. Both joint forward and reverse shearing are important phenomena of a rock joint when it is subjected to an earthquake load contrary to conduct of a static analysis, where the forward shearing is the only concern. These deficiencies could result in an

overestimation of the stability of emplacement drifts and emplacement boreholes and prediction of an incorrect pattern of near-field fluid flow (including preferential pathways for water and gas).

Task 9, DECOVALEX Modeling, is currently at its second phase. The Near-Field Repository Model (BMT3), one of two problems for the Phase, has been analyzed by the NRC-CNWRA team during this period. It was found that for a given geometric configuration and a given initial volumetric heat flux,  $470 \text{ W/m}^3$ , the maximum temperature, about  $172 \text{ }^\circ\text{C}$  at the center of the heat source, is reached at a time of 4 years. At this temperature, the flow rate through the upper portion of the tunnel wall has decreased as a result of the thermal expansion of the rock mass, pinching off the fractures in this region, resulting in a significant reduction of 60 percent in the total flow rate into the tunnel at this time period as compared to when no heat is applied. This result tends to support the concept that, during the period of high thermal output from the waste canisters, the overall permeability through the disturbed zone around the emplacement boreholes and drifts could be substantially reduced. This would lead to better isolation of the canisters from inflowing groundwater, as well as protection from release of radionuclides from a breached container.

## 1.5 INTEGRATED WASTE PACKAGE EXPERIMENTS

The NRC regulation 10 CFR 60.113 requires waste packages to provide substantially complete containment of radionuclides for a minimum period of 300 to 1000 years. As stated in the High-Level Waste Management (HLWM) user needs and the LARP Section 5.4, two KTUs related to the assessment of EBS compliance with performance objectives are: (i) the extrapolation of short-term laboratory and prototype test results to predict long-term performance, and (ii) the effects of environmental factors on the EBS performance. The goal of the Integrated Waste Package Experiments (IWPE) program is to provide a critical evaluation of the information available for long-term performance prediction by a suitable combination of literature surveys and critical experiments. Because the current waste package concept relies on a thin-walled metal container, most of the current effort in the IWPE program is focused on the degradation modes of candidate container materials. To achieve its objectives, the IWPE program is divided into six tasks: Task 1-Corrosion, Task 2-Stress Corrosion Cracking, Task 3-Materials Thermal Stability, Task 4-Microbiologically Influenced Corrosion, Task 5-Other Degradation Modes, and Task 6-General Reporting. The results of ongoing activities in Tasks 1 and 2 are reported here.

The general approach to long-term life prediction of container materials under a variety of failure modes with a focus on localized corrosion is pointed out, along with the role of experimental investigations. Three important parameters in this approach are the corrosion, initiation, and repassivation potentials. Experimental investigations of the effect of surface condition on initiation and repassivation potentials are reported in Section 5. It is shown that the surface chromium depletion found on the mill-finished plates of alloy 825 has a detrimental effect on localized corrosion by lowering the pit initiation potential. However, the repassivation potential measured on nonchromium-depleted specimens can still serve as conservative, lower-bound parameters for long-term prediction of localized corrosion. The corrosion potential of alloy 825 under three different redox conditions is measured as a function of surface changes induced by thermal oxidation. Prior thermal oxidation increased the corrosion potential of the nonchromium-depleted specimens by decreasing the anodic passive current density. The effect of thermal oxidation on chromium-depleted specimens was not as significant. The corrosion potential of alloy 825 in the hydrogen peroxide-containing solution was higher than in the oxygenated environment. The corrosion potential of the chromium-depleted specimen in the oxygenated environments was lower than the pit initiation and repassivation potentials in the 1000 ppm  $\text{Cl}^-$  environment, and, hence, no

pitting corrosion is likely to occur in this environment. However, if hydrogen peroxide due to radiolysis is present, then pitting and crevice corrosion may be possibilities. Long-term tests (e.g., ranging from a few months to 5 years) under controlled potential conditions are recommended to establish the validity of using repassivation potential for long-term prediction of localized corrosion. Additional long-term tests under repository relevant redox conditions, where the corrosion potential of the specimens will be monitored, are also recommended. The need for experimental data on the fundamental parameters affecting the kinetics of redox processes on candidate container alloys, such as alloy 825, is pointed out.

The applicability of critical potentials for localized corrosion for predicting stress corrosion cracking is explored by the use of slow strain rate tests on type 316L stainless steel. It is shown that stress corrosion cracking of type 316L stainless steel in concentrated chloride solutions, such as  $MgCl_2$  and  $LiCl$ , can be promoted by using the slow strain rate technique. These environments are well-established test environments for inducing stress corrosion cracking in this type of alloy. However, no stress corrosion cracking was observed by this test technique in  $NaCl$  or  $LiCl$  solutions containing less than about 6 moles chloride/kg water at 95 °C and over a wide range of potentials. On the other hand, field experience with type 316L stainless steel suggests that stress corrosion cracking occurs at very low chloride concentrations at these temperatures. Hence, alternate test techniques, such as constant deflection tests, must be used to explore the range of environmental conditions that can cause stress corrosion cracking of these alloys.

The results to date can be used for PA calculations and for providing guidance to the DOE in its evaluation of candidate container materials.

## 1.6 STOCHASTIC ANALYSIS OF UNSATURATED FLOW AND TRANSPORT

Surface complexation models have been recently developed to describe the chemically complex adsorption of metals at an electrostatically charged mineral/water interface. Before applying surface complexation models to radionuclide sorption data, it is necessary to determine the model-specific equilibrium constants that describe the acid-base chemistry for each mineral of interest. Potentiometric titration data available in the peer-reviewed literature for a number of different minerals have been gathered and interpreted for the Constant Capacitance, Diffuse-Layer, and Triple-Layer surface complexation models. To avoid the problem of simultaneously adjusting multiple parameters to obtain a non-unique, best fit to one data set, the uniform approach recommended by Dzombak and Morel (1990) and Hayes et al. (1990) has been adopted. This involved fixing a set of consistent model parameters and using the parameter optimization code FITEQL (Westall, 1982) to solve the mass balance/mass action constraints and obtain a unique set of necessary equilibrium constants. A single set of statistically weighted equilibrium constants has been developed for each mineral and model based on the standard deviations associated with each data set. The results of the analysis are reported in Section 8.2. With these parameters in place, it is now possible to interpret existing radionuclide sorption data using surface complexation models. Because a consistent approach has been used to derive these parameters, it will be possible to compare model results and evaluate model performance.

Experimental results were reported previously (Pabalan and Turner, 1993; Pabalan et al., 1993) that indicate that uranium sorption on clinoptilolite, which is the predominant zeolite mineral underneath Yucca Mountain, Nevada, is strongly dependent on solution pH and, to some extent, on the total concentration of uranium. Uranium sorption on clinoptilolite is important at near-neutral solution pH, but steeply decreases at pH values away from neutral. To complement these sorption studies on clinoptilolite,

new experiments were initiated during this report period using the clay mineral montmorillonite, which is another important mineral present underneath Yucca Mountain, as the sorbing phase. These experiments were designed to evaluate the effects of pH, aqueous uranium speciation, and aqueous uranium concentration on uranium sorption on clays. Additional experiments were also initiated using alpha-alumina as the sorbent phase in order to evaluate the effect of sorbent-surface-area/solution-volume ratio. Experimental data on these three minerals, which have very distinct crystal structure and surface properties, will help determine which parameters are critical in controlling the sorption of uranium on geologic materials and may help identify simplified approaches to modeling radionuclide sorption for use in PA calculations.

Preliminary results of the experiments on Na-montmorillonite and alpha-alumina are presented in Section 8.3. The results are complicated by significant losses of uranium either to the container walls or to the syringe filters. Control experiments indicated that the relative amount of uranium lost to containers and filters can be substantial, particularly at low initial solution concentrations (5 ppb U), and that these losses show a strong dependence on the equilibrium pH of the solution. New experiments were subsequently initiated. These were designed to minimize the extraneous losses of uranium and included a greater number of control solutions. A more detailed study of uranium losses as a function of pH and container type was also initiated. Results of these experiments will be reported in the next semi-annual research report.

## 1.7 GEOCHEMICAL ANALOGS

The Geochemical Natural Analog Research Project was created to develop a better understanding of the usefulness and limitations of natural analog studies when employed to support a license application for a HLW repository and to provide fundamental data on the long-term behavior of HLW within a repository environment. Field and literature data were used to select two sites for analog research: (i) the Nopal I uranium deposit in the Peña Blanca district, Chihuahua, Mexico; and (ii) the Akrotiri archaeological site on Thera (Santorini), Greece. This report describes recent results from the Nopal I site.

Uranium transport at the Nopal I site has been strongly influenced by fractures, but it is clear that U-bearing solutions have not been restricted to fractures. Preliminary measurements of U transport at a wide range of distance scales have been completed along a major, continuous fracture, through heavily fractured tuff, through relatively unfractured tuff, and through mineralogically and texturally homogeneous, unfractured tuff. These measurements establish that, at Nopal I, transport of U through a major fracture has achieved greater distances than U transport through tuff heavily fractured at a centimeter scale or U transport through homogeneous, unfractured tuff. Uranium transport distances along a major fracture are at least 25 times larger than U transport distances through generally fractured tuff. This disparity may reflect different durations and conditions of transport.

Some U concentration profiles at Nopal I have relatively simple forms, whereas others do not. Uranium concentration profiles across a 2-m transect through generally fractured tuff and those away from microfractures through otherwise unfractured tuff can be fit closely by a simple model assuming pure diffusion in a semi-infinite medium with a constant concentration boundary condition. This model could strictly be correct only if the U mobility occurred without effects on U transport by chemical reactions or variations in hydrologic properties within the domain. This relationship could be explained by a linear  $K_d$  sorption model. Alternatively, profiles measured away from a large fracture, through tuff with limited very fine fracturing, do not have a simple form and cannot be fit by the simple diffusion

model used to fit the other transects. This difference may be caused by mineralogic or textural heterogeneities in the sample domain, by chemical reactions between the U-bearing fluids and the tuff, by formation of the extant U profiles by advection rather than diffusion, or by combinations of these or other processes.

These measurements and interpretations are an initial attempt to define conceptual models for mechanisms of U transport at Nopal I. The significance of these measurements for PA modeling remains uncertain and requires definition of the conditions under which the U transport occurred.

## **1.8 SORPTION MODELING FOR HIGH-LEVEL WASTE PERFORMANCE ASSESSMENT**

Surface complexation models have been recently developed to describe the chemically complex adsorption of metals at an electrostatically charged mineral/water interface. Before applying surface complexation models to radionuclide sorption data, it is necessary to determine the model-specific equilibrium constants that describe the acid-base chemistry for each mineral of interest. Potentiometric titration data available in the peer-reviewed literature for a number of different minerals have been gathered and interpreted for the Constant Capacitance, Diffuse-Layer, and Triple-Layer surface complexation models. To avoid the problem of simultaneously adjusting multiple parameters to obtain a non-unique, best fit to one data set, the uniform approach recommended by Dzombak and Morel (1990) and Hayes et al. (1990) has been adopted. This involved fixing a set of consistent model parameters and using the parameter optimization code FITEQL (Westall, 1982) to solve the mass balance/mass action constraints and obtain a unique set of necessary equilibrium constants. A single set of statistically weighted equilibrium constants has been developed for each mineral and model based on the standard deviations associated with each data set. The results of the analysis are reported in Section 8.2. With these parameters in place, it is now possible to interpret existing radionuclide sorption data using surface complexation models. Because a consistent approach has been used to derive these parameters, it will be possible to compare model results and evaluate model performance.

Experimental results were reported previously (Pabalan and Turner, 1993; Pabalan et al., 1993) that indicate that uranium sorption on clinoptilolite, which is the predominant zeolite mineral underneath Yucca Mountain, Nevada, is strongly dependent on solution pH and, to some extent, on the total concentration of uranium. Uranium sorption on clinoptilolite is important at near-neutral solution pH, but steeply decreases at pH values away from neutral. To complement these sorption studies on clinoptilolite, new experiments were initiated during this report period using the clay mineral montmorillonite, which is another important mineral present underneath Yucca Mountain, as the sorbing phase. These experiments were designed to evaluate the effects of pH, aqueous uranium speciation, and aqueous uranium concentration on uranium sorption on clays. Additional experiments were also initiated using alpha-alumina as the sorbent phase in order to evaluate the effect of sorbent-surface-area/solution-volume ratio. Experimental data on these three minerals, which have very distinct crystal structure and surface properties, will help determine which parameters are critical in controlling the sorption of uranium on geologic materials and may help identify simplified approaches to modeling radionuclide sorption for use in PA calculations.

Preliminary results of the experiments on Na-montmorillonite and alpha-alumina are presented in Section 8.3. The results are complicated by significant losses of uranium either to the container walls or to the syringe filters. Control experiments indicated that the relative amount of uranium lost to

containers and filters can be substantial, particularly at low initial solution concentrations (5 ppb U), and that these losses show a strong dependence on the equilibrium pH of the solution. New experiments were subsequently initiated. These were designed to minimize the extraneous losses of uranium and included a greater number of control solutions. A more detailed study of uranium losses as a function of pH and container type was also initiated. Results of these experiments will be reported in the next semi-annual research report.

## 1.9 PERFORMANCE ASSESSMENT RESEARCH

The primary programmatic objectives of this project are three-fold. The first objective is to provide modeling technology that will benefit the NRC Iterative Performance Assessment (IPA) activity and the development of methodologies that will be used in compliance determination methods. The second, and equally important, objective is to address KTUs associated with: (i) conceptual models; (ii) mathematical models; (iii) model parameters; (iv) future system states (i.e., disruptive scenarios); and (v) model validation. These KTUs are defined in Compliance Determination Strategy (CDS) 6.1 Assessment of Compliance with the Requirement for Cumulative Releases of Radioactive Materials. In this reporting period, priority attention was focused on: (i) the INTRAVAL model validation exercise; (ii) development of conceptual models of flow and transport in fractured-porous tuff; and (iii) development of efficient and robust computational techniques for flow and transport modeling. The third objective is to provide the technical basis for formulating guidance to the DOE in the specific areas of PA modeling approaches and validation strategies for hydrologic models.

Prior research conducted at the CNWRA (Wittmeyer and Sagar, 1992), in conjunction with the international model validation project INTRAVAL, focused on the evaluation of flow and transport models using field data from the Las Cruces Trench site in New Mexico. Recently, the INTRAVAL group elected to pursue the Yucca Mountain test case proposed by Alan Flint of the U.S. Geological Survey (USGS). The validation exercise, as posed to the INTRAVAL modelers, was to use rock-hydraulic property data, detailed micro-stratigraphic data, and measured saturation profiles in near-surface boreholes and then to predict the saturation profile at a yet-to-be-drilled borehole. For this exercise, a conceptual model of the hydrostratigraphic setting was formulated. Initially, general finite difference and finite element computer codes were applied to model the unsaturated flow in a 1D column. Because of numerical problems encountered (i.e., long computer execution times and nonconvergent results), a simple 1D, steady-state flow code was developed. The code was applied using a composite fracture-matrix formulation for the unsaturated hydraulic conductivity function. On a qualitative basis, the comparison between the preliminary numerical simulation and observed saturation profile showed reasonable agreement, except in the upper 10 meters of the column.

Understanding solute transport through fractured-porous media is of fundamental importance to predicting the isolation performance of the proposed repository at Yucca Mountain. Natural analog field sites where transport has occurred over many thousands of years can provide a setting where such processes can be investigated. A reconnaissance level effort was initiated, in this reporting period, to study the hydraulic properties of the matrix of volcanic tuff at a natural analog field site in an attempt to relate those properties to its geochemical and transport characteristics. This activity is integrated with the Geochemical Natural Analogs Research Project and Sorption Research Project and is primarily focused on analysis of experiment data from these projects. The aim of this project is to formulate conceptual models of flow and transport in the fractured-porous tuff.

The mathematical models describing flow and transport in an unsaturated medium, such as welded tuff at Yucca Mountain, are extremely difficult to solve numerically. In many cases, PA codes using conventional finite difference and finite element techniques produce numerical results that exhibit spurious oscillations and/or are nonconvergent. This numerical difficulty poses a serious problem to development of reliable predictive tools that will be used to assess compliance with the performance objectives specified in 10 CFR 60.112 and 60.113. Studies were performed of advanced numerical methods used in computational fluid dynamics (CFD). In particular, evaluations were made of adaptive meshing techniques and the spectral element method. These advanced techniques were applied to solve the convection-dispersion equation and Richards' equation for unsaturated flow. Results of simple computational test cases indicate that adaptive meshing has a great potential for providing accurate numerical solutions for steady-state, unsaturated flow problems. The Spectral Element Method was found to provide highly accurate numerical solutions for the transport equation.

## 1.10 VOLCANIC SYSTEMS

Characterization of the frequency and nature of past volcanic events in the Yucca Mountain region (YMR), and assessment of the probability and consequences of future volcanism, are critical aspects of pre-licensing scientific investigations. The technical objectives of the Volcanic Systems of the Basin and Range research project are to (i) assess the probability of continued magmatic activity in the YMR, (ii) develop models that better predict the interaction between structure and volcanism in this tectonic setting, and (iii) develop scenarios for the impact of volcanism on the candidate Yucca Mountain repository. These studies will provide pre-licensing guidance to the DOE and are critical to license application review, as evinced in specific section of the LARP (Section 3.2.1.9, evidence of igneous activity as a potentially adverse condition, Section 3.2.27, impact of volcanism on groundwater movement, and Section 6.1, assessment of compliance with the requirement for cumulative releases of radioactive materials). The Volcanic System of the Basin and Range research project has been designed to assess the probability of future volcanism in the YMR, taking into account the range of activity and structural controls on activity that are an inherent part of western Great Basin volcanism.

During the last 6 months, near-neighbor nonhomogeneous Poisson probability models have been substantially refined to estimate the probability of volcanic disruption of the candidate HLW repository. Assuming a late Quaternary recurrence rate of  $7 \pm 2$  volcanoes/million years, these models estimate a probability of disruption of between  $8.0 \times 10^{-5}$  and  $3.4 \times 10^{-4}$  in 10,000 years, with most estimates between  $1 \times 10^{-4}$  and  $3 \times 10^{-4}$ . Estimates based on a lower, post-caldera basalt recurrence rate of approximately 3 volcanoes/million years are between  $6.9 \times 10^{-5}$  and  $9.2 \times 10^{-5}$  in 10,000 years. The probability of volcanism within the next 10,000 years decreases east of the candidate repository site, and increases west of the site in the Crater Flat area. Further refinement of probability models will likely alter these estimates, and they are not intended to represent a complete analysis of the probability of repository disruption by igneous activity. The nonhomogeneous models takes into account one important geological feature of volcanic fields: centers tend to cluster within these fields through time. Additional geological information, such as the impact of pre-existing structure or strain rate on volcanism, will need to be taken fully into account before a more refined assessment of the probability of future volcanic activity in the YMR can be made with confidence.

Insight into the relationships between crustal stress, magma ascent, and fault geometries can be gained through the study of analogous volcanic fields using an ARC/Info-based geographical information system (GIS). GIS study of the San Francisco volcanic field, coupled with vent alignment analyses,

indicates that structural control and vent clustering strongly influence cinder cone distribution in this area. Vent alignments in this area are closely linked to NE-trending reactivated Precambrian faults and joint sets. During the next 6 months, additional study will be made of the geology of cinder cone alignments in order to assess the reasons for their development and longevity of their activity. This has important implications for probability studies of the volcanism in the YMR because probability calculations may change dramatically as structural controls are incorporated into models.

## **1.11 TECTONICS PROCESSES**

The objectives of the Tectonics Research Project are: (i) to compile and integrate tectonic data for the central Basin and Range and Yucca Mountain regions; and (ii) to develop and assess models of tectonic processes. The purpose of the project is to determine the adequacy of existing data, methods, and models for demonstrating and determining compliance with regulatory requirements. Of particular concern is the adequacy of existing, and anticipated data, for meeting quantitative waste-isolation performance objectives. Current activities consist of literature review and data compilation tasks. A GIS is being used to compile data from disparate sources into an integrated management and display environment. Significant technical accomplishments to date consist of: (i) development of digital terrain models of the Yucca Mountain and central Basin and Range regions; (ii) production of integrated maps of Quaternary faults, Quaternary basaltic volcanic fields, and historic earthquake seismicity; and (iii) compilation of an initial database of geodetically measured regional strain and slip-rates determined for individual fault systems. Scoping review of the Geologic Setting Tectonic Database has produced two preliminary technical findings. First, historic fault slip in the Mojave Desert region of southeastern California is generally restricted to Quaternary faults with Holocene slip. Quaternary faults that have not experienced slip during the Holocene have not generally been historically active. This preliminary observation suggests that a time frame of 10,000–100,000 years (rather than the 1.6–2.0 million years of the Quaternary Period) may be an appropriate age range for definition of an active fault in this region. Second, analyses of extent, interconnectivity, and patterns of faulting may be significantly improved using synthetic low-angle illumination of digital terrain models of the Yucca Mountain area. Illumination of a terrain model of Yucca Mountain from north and south strongly enhances a marked, near-linear trend of fault-controlled topography that is not apparent with normal illumination. Data and references compiled by Tectonics Research have been used to develop CDSs on Structural Deformation (LARP No. 3.2.1.5) and Structural Deformation and Groundwater (LARP No. 3.2.2.8).

## **1.12 FIELD VOLCANISM**

The Field Volcanism project began in mid-April 1993. The technical objectives of the project are to better characterize the effect of volcanic activity on repository performance and, as a result, better constrain probability models of disruption of the repository. This characterization will be possible through: investigation of the (i) mechanics of mafic cinder cone eruptions, (ii) extent and characteristics of shallow hydrothermal systems and diffuse degassing associated with small volume mafic eruptions, and (iii) nature of mafic intrusive geometries at repository depths. These studies are critical to provide precensing guidance to the DOE and in license application review, as evinced in specific sections of the LARP (Section 3.2.1.9, evidence of igneous activity as a potentially adverse condition; Section 3.2.2.7, impact of volcanism on groundwater movement; and Section 6.1, assessment of compliance with the requirement for cumulative releases of radioactive materials). Defensible promulgation of conclusions about the probability and consequences of potential volcanic activity in the YMR will require study of

Plio-Quaternary cinder cones in the western Great Basin and comparison with modern, recently active cinder cones located elsewhere.

Bounding the ranges of eruption style and energetics that occur at active cinder cones is an important aspect of consequence studies. Thermal energy release is calculated for eruptions at two recently active cinder cones: Tolbachik, Kamchatka, Russia, 1975, and Cerro Negro, Nicaragua, 1992. Total thermal energy release during formation of Cone I at Tolbachik was approximately  $2.7 \times 10^{18}$  J, and the rate of energy release during the most explosive phase of activity was on the order of  $2.2 \times 10^{12}$  W. This amount is about one-third the total thermal energy release due to the 1883 eruption of Krakatau. The average rate of thermal energy release during the most explosive phase of the 1992 eruption of Cerro Negro was  $6.7 \times 10^{11}$  to  $1.6 \times 10^{12}$  W and the total energy release was between  $4.3 \times 10^{16}$  and  $1.0 \times 10^{17}$  J. These eruptions were more energetic than anticipated based on traditional models of cinder cone volcanism. Review of the literature indicates that many cinder cone eruptions have been more nearly Plinian, with sustained explosive eruption columns, than strombolian or vulcanian, styles of eruption characterized by instantaneous explosions. Differences in eruptive style have important implications for how magma could interact with the HLW package in the repository environment.

Studies of the deposits of western Great Basin volcanoes have been initiated, with particular attention being paid to near-vent facies. Aspects of these deposits that will be studied in detail include: vesiculation of the juvenile clasts, concentration of crustal xenoliths, and distribution of ballistic fragments. Research into the nature of potential field anomalies resulting from igneous intrusions and the geology of mafic dikes at repository depths also has been initiated. During the next 6 months, these studies will provide results relevant to site characterization and compliance.

### 1.13 REFERENCES

- Dzombak, D.A., and F.M.M. Morel. 1990. *Surface Complexation Modeling: Hydrous Ferric Oxide*. New York: John Wiley and Sons.
- Hayes, K.F., G. Redden, W. Ela, and J.O. Leckie. 1990. *Application of Surface Complexation Models for Radionuclide Adsorption: Sensitivity Analysis of Model Input Parameters*. NUREG/CR-5547. Washington, DC: U.S. Nuclear Regulatory Commission.
- Pabalan, R.T. and D.R. Turner. 1993. *Sorption Modeling for HLW Performance Assessment. NRC High-Level Radioactive Waste Research at CNWRA July 1 Through December 31, 1992*. W.C. Patrick, ed. CNWRA 92-02S. San Antonio, TX: Center for Nuclear Waste Regulatory Analyses: 8-1 to 8-18.
- Westall, J.C. 1982. *FITEQL: A Computer Program for Determination of Chemical Equilibrium Constants From Experimental Data, Version 2.0*. Rpt. 82-02. Corvallis, OR: Oregon State University.
- Wittmeyer, G. and B. Sagar 1992. *Performance Assessment Research Report on Research Activities for Calendar Year 1991*. W.C. Patrick, ed. NUREG/CR5817. Washington, DC: U.S. Nuclear Regulatory Commission: 9-12 to 9-28.

## 2 UNSATURATED MASS TRANSPORT (GEOCHEMISTRY)

*by William M. Murphy and Roberto T. Pabalan*

*Investigators: William M. Murphy, Roberto T. Pabalan, James D. Prikryl, Bret W. Leslie, F. Paul Bertetti, and Christopher J. Goulet (CNWRA)*

*NRC Project Officer: George F. Birchard*

### 2.1 TECHNICAL OBJECTIVES

To support the U.S. Nuclear Regulatory Commission (NRC) high-level nuclear waste (HLW) program, the Center for Nuclear Waste Regulatory Analyses (CNWRA) is conducting research activities under the Geochemistry Research Project, which comprises modeling and experimental tasks. The technical objective of the modeling task is to provide thermodynamic, kinetic, and mass transfer analyses of natural and experimental systems in order to develop an understanding of ambient and repository geochemical conditions at Yucca Mountain and to enable predictions of the evolution of these systems. The objective of the experimental task is to provide data that are important to understanding and predicting rock-groundwater interactions (e.g., dissolution/precipitation, ion-exchange) and data that were obtained independently of the U.S. Department of Energy (DOE) research activities.

Groundwater and mineral chemistry affect repository performance through their influence on HLW container and waste form alteration processes and by their effects on the retardation of radionuclide transport in the geosphere. Information developed by thermodynamic and kinetic analysis of experimental data for gas-water-rock interactions in this project addresses a variety of needs identified by the NRC Office of Nuclear Material Safety and Safeguards (NMSS). These needs include characterization of the waste package environment, dissolution of minerals, stability of zeolites and relations between zeolite chemistry and water chemistry, evolution of groundwater chemistry, gas phase control on groundwater chemistry, and movement of carbon-14. General user needs applicable to all these aspects of the repository system addressed by this project include nonequilibrium conditions, thermodynamic uncertainties, and extrapolation of field and laboratory data.

Information developed in the Geochemistry Research Project will be used to support specific sections of the License Application Review Plan (LARP), particularly regulatory requirement topics — Description of Individual Systems and Characteristics of the Site: Geochemical System (3.1.3), Assessment of Compliance with Siting Criteria; Geochemical System: Individual Favorable Conditions; Nature and Rates of Geochemical Processes (3.2.3.1), Assessment of Compliance with Siting Criteria; Geochemical System: Individual Favorable Conditions; Geochemical Conditions (3.2.3.2.), Assessment of Compliance with Siting Criteria; Geochemical System: Individual Favorable Conditions; Mineral Assemblages (3.2.3.3), Assessment of Compliance with Siting Criteria; Geochemical System: Potentially Adverse Conditions: Groundwater Conditions and the Engineered Barrier System (3.2.3.4), Assessment of Compliance with Siting Criteria; Geochemical System: Potentially Adverse Conditions; Geochemical Processes (3.2.3.5), Assessment of Compliance with Siting Criteria; Geochemical System: Potentially Adverse Conditions; Not Reducing Groundwater Conditions (3.2.3.6), and Assessment of Compliance with Siting Criteria; Geochemical System: Potentially Adverse Conditions; and Gaseous Radionuclide Movement (3.2.3.7).

Although Compliance Determination Strategies (CDS) for the individual LARP sections are currently under development, preliminary typing has indicated the existence of Key Technical Uncertainties (KTU) with regard to compliance determination for several of the LARP sections listed earlier. These uncertainties relate to fundamental geochemical problems associated with gas-water-rock interactions and their effects on containment, waste form behavior, and radionuclide transport. Notably, LARP Sections 3.2.3.1, 3.2.3.2, 3.2.3.3, 3.2.3.4, 3.2.3.5, and 3.2.3.7 have been identified to pose KTUs associated with the geochemical system.

The focus of the Geochemistry Research Project on the specific geochemical conditions at Yucca Mountain and those anticipated for the potential repository therefore provides information useful to numerous other research and technical assistance activities of the NRC and the CNWRA. Information and understanding developed in this project have been used (and will continue to be used) in support of several other research projects, notably Integrated Waste Package Experiments (IWPE), Geochemical Natural Analogs, and Sorption Modeling for HLW Performance Assessment (PA). This information and its understanding have also been used to provide technical assistance in PA auxiliary analyses relating to radionuclide solubilities and gaseous transport of carbon-14. In addition, these studies have contributed to the conduct of independent reviews of site characterization activities and reports, and they foster the capability for reviews of the license application provided by the DOE.

## **2.2 EXPERIMENTAL STUDIES** **by Roberto T. Pabalan**

### **2.2.1 Specific Technical Objectives**

A major geologic feature potentially affecting the suitability of Yucca Mountain, Nevada, as a repository site for HLW is the presence of thick, laterally extensive zones of zeolitic tuff. Because of their sorptive properties, zeolites could provide important geologic barriers to migration of radionuclides from the repository to the accessible environment. An evaluation of the relative importance of zeolites as retardation agents requires a knowledge of their thermodynamic stabilities and ion-exchange properties under geochemical conditions relevant to the Yucca Mountain system. These properties may vary with groundwater chemistry, zeolite composition, and temperature. In addition, uncertainties exist in determining groundwater chemistries in the vadose zone at Yucca Mountain. It may be possible to reduce these uncertainties by investigating groundwater/zeolite equilibria through ion-exchange and phase-equilibrium experiments, coupled with thermodynamic modeling. Therefore, experimental studies on the thermodynamic and ion-exchange properties of zeolites are being conducted under Task 3 of the Geochemistry Research Project.

### **2.2.2 Analcime and Clinoptilolite Dissolution Experiments**

Experiments are continuing on phase equilibria between aqueous solutions and homoionic Na-forms of the zeolite minerals analcime and clinoptilolite [ideal formulas  $\text{NaAlSi}_2\text{O}_6 \cdot \text{H}_2\text{O}$  and  $\text{NaAlSi}_5\text{O}_{12} \cdot 4\text{H}_2\text{O}$ , respectively (Flanigen, 1986)]. The objective of the experiments is to resolve uncertainties in the standard-state thermodynamic properties of clinoptilolite and analcime. These experiments essentially involve reacting weighed amounts of analcime and/or clinoptilolite powder with known weights of 0.1 M NaCl-0.01 M  $\text{NaHCO}_3$  solution. For those experiments designed to study analcime growth kinetics and reversibility of analcime dissolution reactions, the NaCl- $\text{NaHCO}_3$  solutions were spiked with  $\text{SiO}_2$  and Al to raise the initial  $\text{SiO}_2$  and Al concentrations above saturation levels. The

mixtures were kept agitated at  $25 \pm 0.2$  °C using a constant temperature water bath and were allowed to maintain equilibrium with atmospheric  $\text{CO}_2(\text{g})$ . In these experiments, the pH of the solutions remained very close to 9.0 due to carbonate equilibrium reactions. Aqueous samples (50-mL volume) were taken periodically and were analyzed for  $\text{SiO}_2$  and Al concentrations using a Milton Roy 1201 UV-Vis spectrophotometer. The use of glassware in the analysis of  $\text{SiO}_2$  was avoided because of potential silica contamination. The pH and  $\text{Na}^+$  concentrations were also analyzed using ion-selective electrodes. The 50-mL aliquots were not replaced with fresh solutions because replacement would cause a discontinuity in the evolution of the solution composition and complicate data interpretation. Therefore, each bottle was carefully weighed before and after a sample was taken to account for evaporation losses and changes in the volume of the solutions.

Preliminary data and interpretation have been presented in previous CNWRA research progress reports (Pabalan, 1992; 1993, and Murphy et al., 1992). A more recent and detailed interpretation of experimental data available up to this point is presented in Section 2.3.

### 2.2.3 Ion-Exchange Isotherm Experiments

Ion-exchange behavior of zeolites depends on several factors, including solid and aqueous phase compositions as well as aqueous concentrations (Barrer, 1978). Results of ion-exchange isotherm experiments between well-characterized specimens of Na-clinoptilolite and aqueous solutions of  $\text{Na}^+$ ,  $\text{K}^+$ , and  $\text{Ca}^{2+}$  at total solution concentrations of 0.005, 0.05, and 0.5 N were reported in previous CNWRA research progress reports (Pabalan, 1991a) and in Pabalan and Griffin (1993). These experiments were designed to investigate the effects on the exchange equilibrium of changes in total aqueous solution concentration and the relative concentrations of the different exchangeable cations initially found in solution. The results of these experiments were interpreted using excess Gibbs energy models for the aqueous and zeolite phases to account for nonideality in the system. The data were also used to test model predictions of isotherm shapes and selectivities at some value of total solution concentration based on a single isotherm measured at another solution concentration. The results indicated that thermodynamic models for nonideal behavior in aqueous solutions and zeolite phases are useful in describing and predicting solid solution and ion-exchange properties of clinoptilolite.

To further test the applicability of these thermodynamic models, a new set of ion-exchange experiments was conducted during this report period involving clinoptilolite and aqueous solutions of  $\text{Na}^+/\text{Sr}^{2+}$ . The procedures used were similar to those of previous experiments. The points on the isotherm were obtained by equilibrating weighed amounts of Na-clinoptilolite with a series of solutions of known volumes containing the two competing cations in different concentration ratios, but at constant total normalities of 0.005, 0.05 and 0.50 N. The 0.50 N aqueous mixtures were prepared by weight from reagent grade chloride salts of the respective cations. The 0.05 N solutions were prepared by a factor of ten dilutions of the 0.50 N mixtures. An appropriate amount of  $^{90}\text{Sr}$  spike was added to each mixture to allow analysis of Sr concentration in solution by liquid scintillation counting. The clinoptilolite + solution mixtures were contained in 15- to 250-mL polypropylene bottles, which were kept agitated and thermostated at 25 °C in a shaker water bath for at least 1 week.

After equilibrium was established, aliquots of the reference and experimental solutions were taken for analysis of both  $\text{Na}^+$  and  $\text{Sr}^{2+}$ . Na concentrations were analyzed either by Na-selective electrodes or by atomic absorption spectrometry.  $\text{Sr}^{2+}$  concentrations were determined by measuring  $^{90}\text{Sr}$  activities using a Packard Tri-Carb Model 1900TR liquid scintillation analyzer.

Results of the  $\text{Na}^+/\text{Sr}^{2+}$  experiments are plotted in Figure 2-1 in terms of the equivalent cationic mole fractions of  $\text{Sr}^{2+}$  in solution and in the zeolite phase. The solid symbols in the figure are isotherm points calculated from the measured  $\text{Sr}^{2+}$  concentrations, whereas the open symbols are isotherm points calculated from the  $\text{Na}^+$  analytical data. The isotherm data at 0.05 N were used to fit a Margules solid solution model described previously (Pabalan, 1991a; 1991b) and derive values of the equilibrium constant,  $K$ , and the Margules parameters,  $W_{\text{Na}}$  and  $W_{\text{Sr}}$ . The values derived for  $\ln K$ ,  $W_{\text{Na}}$ , and  $W_{\text{Sr}}$  are equal to  $-1.1539$ ,  $-2.682$ , and  $-3.2656$ , respectively. The isotherms for the 0.005 and the 0.5 N solutions were predicted using the parameters derived from the 0.05 N data. As shown in Figure 2-1, the agreement between predicted and experimental values is very good. There is some scatter in the experimental data for the 0.5 N isotherm. An evaluation of the experimental design indicated that the solution-volume to zeolite-mass ratio was not properly optimized for the 0.5 N isotherm experiment, resulting in large uncertainties associated with the isotherm points. A new set of isotherm experiments at 0.5 N is ongoing, with the experimental parameters optimized to reduce the scatter in the data points and minimize the uncertainties in the calculated isotherm data.

## **2.3 GEOCHEMICAL MODELING OF KINETICS AND THERMODYNAMICS OF ANALCIME-CLINOPTILOLITE-WATER INTERACTIONS**

by William M. Murphy

### **2.3.1 Background**

The technical objective of the modeling task of the Geochemistry Research Project is to provide thermodynamic, kinetic, and mass transfer analyses of natural and experimental systems to develop an understanding of ambient and repository geochemical conditions at Yucca Mountain and to enable predictions of the evolution of these systems. Common zeolite minerals, notably analcime and clinoptilolite, provide a key indication of past and present geochemical conditions at Yucca Mountain, and would serve as retardation agents for radioelement migration. Despite the general geochemical importance of natural zeolites and their particular significance for the performance of the proposed repository, basic thermodynamic and kinetic properties of zeolite-water interactions are poorly known. This lack of fundamental data severely restricts the confidence with which models can be developed to interpret and predict the evolution of the geochemical environment at Yucca Mountain. One major focus of the Geochemistry Research Project has been development of new thermodynamic and kinetic data for zeolite-water reactions through experimental studies and theoretical data interpretation.

Analcime and clinoptilolite dissolution, growth, and solubility experiments provide information on mineral-solution reaction rates, reaction mechanisms, and equilibria. Data on and interpretations of the analcime dissolution rate and mechanism and limits on analcime solubility and the standard Gibbs free energy of formation for analcime have been reported in previous quarterly, annual, and semi-annual reports in this series (e.g., Pabalan and Murphy, 1992a, 1992b) and in Murphy et al. (1992). This report extends these results to provide an interpretation of new data for analcime growth kinetics, analcime solubility reversal, equilibration of analcime and clinoptilolite, and clinoptilolite dissolution. In addition, groundwater data from the saturated zone in the vicinity of Yucca Mountain are interpreted in the context of the experimental data.

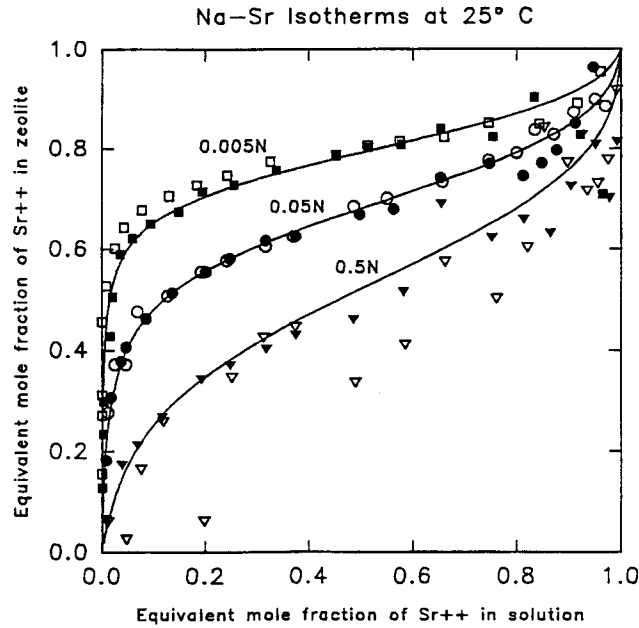


Figure 2-1. Isotherms for ion-exchange at 25 °C between clinoptilolite and NaCl/SrCl<sub>2</sub> aqueous mixtures at total solution concentrations of 0.005, 0.05, or 0.5 N. Solid symbols are isotherm points calculated from analytical data on Sr<sup>2+</sup>, whereas open symbols are isotherm points calculated from Na<sup>+</sup> analysis. The curves represent values calculated using a Margules model for zeolite solid solutions with parameters derived by fitting only the 0.05 N isotherm data.

### 2.3.2 Analcime Growth

Definitive solubility measurements require demonstration of the approach to equilibrium from both undersaturation and supersaturation (reversal). Experiments to precipitate (grow) analcime from synthetic supersaturated solutions were designed and conducted to provide a reverse (maximum) limit to the solubility. A minimum solubility limit was reported previously, which was based on dissolution studies (Pabalan and Murphy, 1992b). Analytical data for aluminum and silicon concentrations obtained in the analcime growth experiment were corrected for water evaporation and the mass of solutes removed during sampling to obtain the moles of precipitated species. Mass transfer from solution to the growing analcime crystal was calculated according to:

$$n_{I,P}(t_s) = m_I(t_0)W(t_0) - m_I(t_s)W(t_s) - n_{I,E}(t_s) \quad (2-1)$$

where variables are defined as follows:

- $n_{I,P}(t_s)$  = moles of species, I, precipitated at sampling time,  $t_s$
- $m_I(t_0), m_I(t_s)$  = molality of species, I, in the initial unreacted solution at time,  $t_0$ , and time,  $t_s$ , respectively
- $W(t_0), W(t_s)$  = mass of water at time,  $t_0$ , and time,  $t_s$ , respectively
- $n_{I,E}(t_s)$  = moles of species, I, extracted in samples taken prior to time,  $t_s$

Calculations of the moles of Si and Al precipitated using Eq. (2-1) indicate that the rate of the growth reaction, corresponding to the slope of the trend of the data in Figure 2-2, decreased with time. These data are consistent with the approach to equilibrium from a supersaturated state. Data for the relative number of moles of Al and Si removed from solution show that, within analytical uncertainty, the precipitating analcime has an Al/Si ratio equal to that inferred for the primary material. The analcime stoichiometry is interpreted to be  $Na_{1.02}Al_{1.02}Si_{1.98}O_6 \cdot H_2O$  (Pabalan and Murphy, 1992a), and the slope of the line in Figure 2-3 corresponds to the Al/Si ratio for this stoichiometry. Equilibration of analcime structural water with the dilute aqueous solutions of the experiments is likely, but as yet undetermined. Provisionally, the nominal stoichiometric value of 1.0  $H_2O$  per formula unit has been adopted.

### 2.3.3 Clinoptilolite Dissolution

Elemental release in clinoptilolite dissolution experiments can be calculated by

$$n_{I,R}(t_s) = m_I(t_s)W(t_s) + n_{I,E}(t_s) \quad (2-2)$$

where  $n_{I,R}(t_s)$  stands for the number of moles of species, I, released at sampling time,  $t_s$ , and the other variables are defined after Eq. (2-1).

Release of Si in clinoptilolite dissolution experiments calculated with Eq. (2-2) followed a trend of decreasing rate of reaction, corresponding to the variation in the slope of the curve in Figure 2-4. This result is consistent with the approach to equilibrium. Values for the moles of release of Al based on aqueous solution data are somewhat erratic, but generally Al release increased with time. Release of Si was approximately 1000 times greater than release of Al (scales for the two species in Figure 2-4 differ by this factor), although their atomic ratio in the primary clinoptilolite is approximately 5. Incongruent elemental release may be due to selective leaching of Si or reprecipitation of Al [e.g., as  $Al(OH)_3$ ]; or the clinoptilolite may be contaminated with silica (e.g., amorphous silica), which is preferentially released.

Although the data for release rate of Si from clinoptilolite (Figure 2-4) are not definitive with respect to reaction mechanism, the systematic Si release rate suggests general rate equations are appropriate. A speculative surface reaction rate equation can be written

$$\frac{d\xi}{dt} = k^*s \left[ 1 - \left( \frac{Q}{K} \right)^{(1/\sigma)} \right] \quad (2-3)$$

for the reaction



where the variables are defined as:

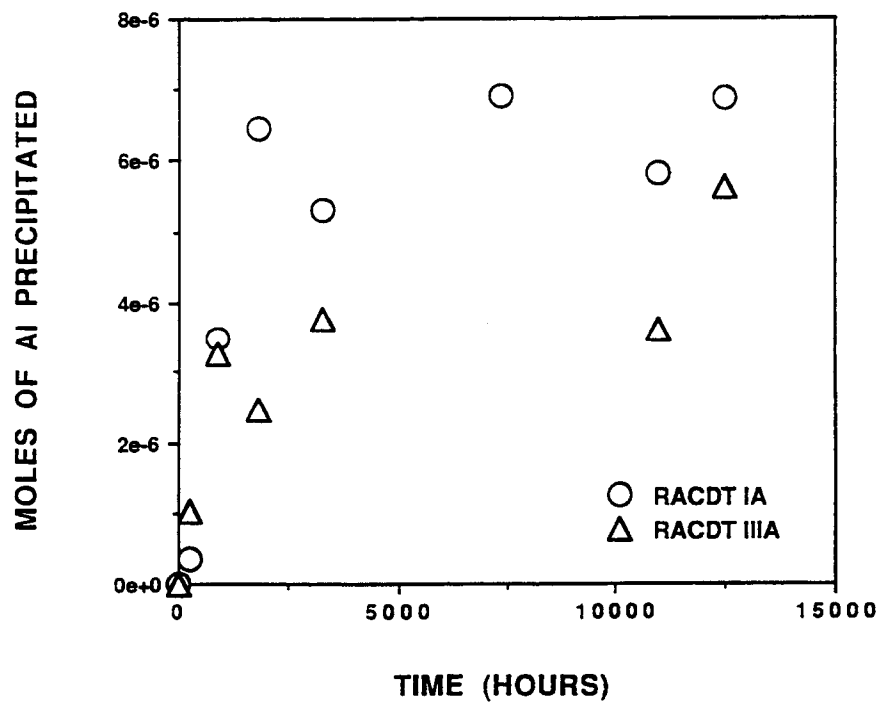
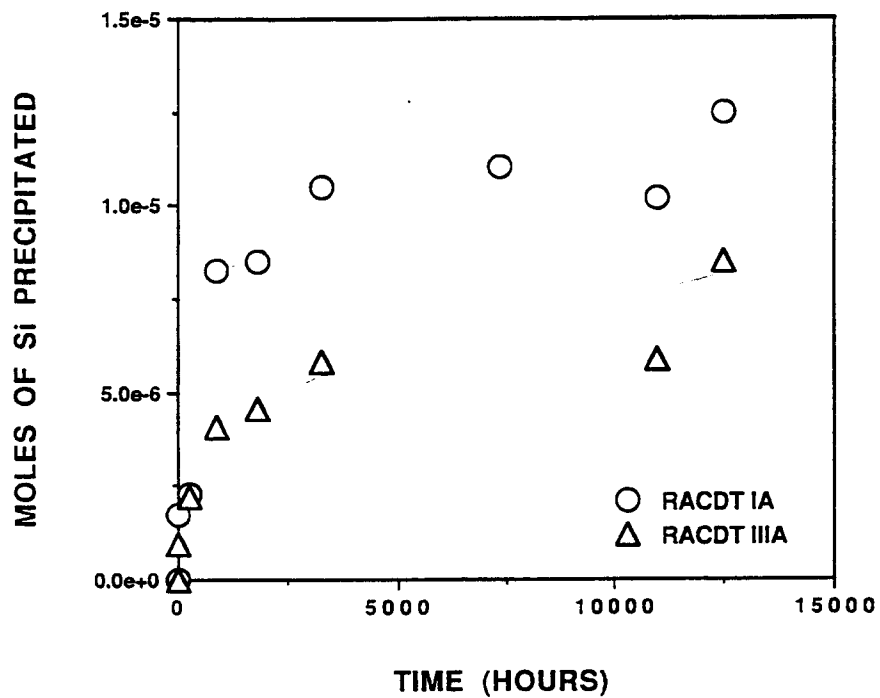


Figure 2-2. Moles of Si (A) and Al (B) precipitated from supersaturated solutions as a function of time in two analcime growth experiments, RACDTIA and RACDTIIIA.

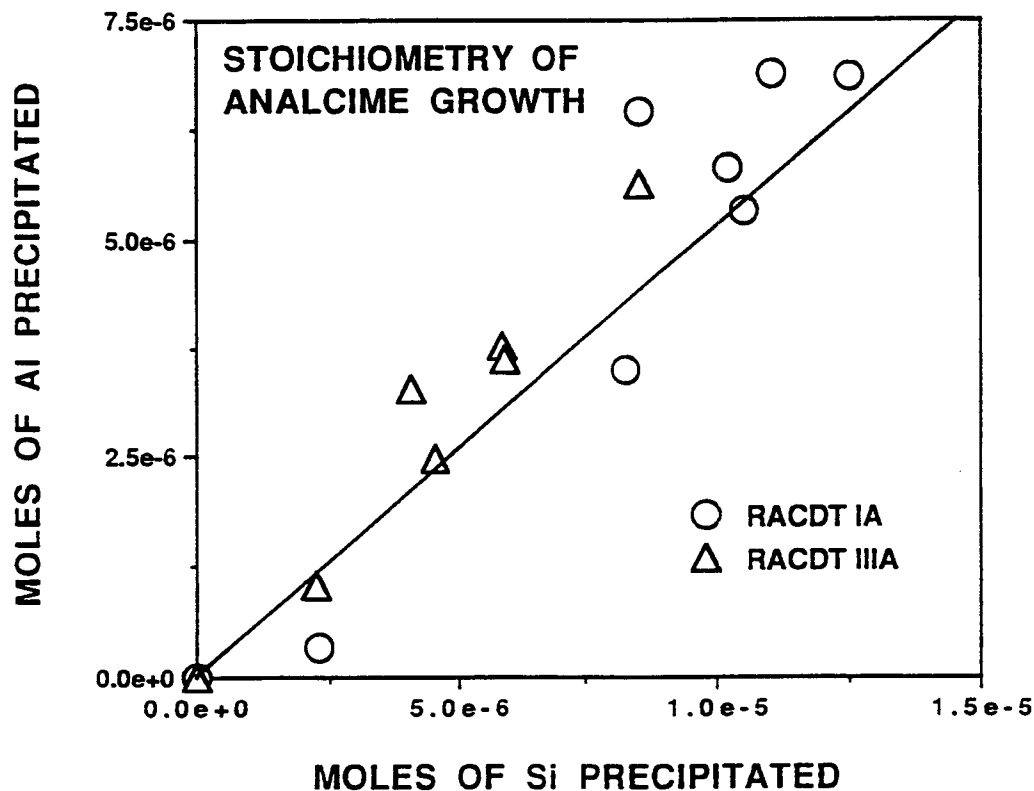


Figure 2-3. Moles of Al precipitated as a function of moles of Si precipitated in analcime growth experiments RACDTIA and RACDTIIIA. The slope of the line corresponds to the Al/Si ratio of the primary analcime determined by bulk analysis (0.515).

- $\xi$  = number of moles of clinoptilolite dissolved
- $k^*s$  = product of apparent rate constant and surface area
- $Q$  = reaction quotient for reaction 2-4
- $K$  = equilibrium constant for reaction 2-4
- $\sigma$  = stoichiometric number

The reaction quotient is given by

$$Q = a_{\text{Na}^+}^2 \cdot a_{\text{Al(OH)}_4^-}^2 \cdot a_{\text{SiO}_2}^{10} \quad (2-5)$$

where  $a_i$  stands for the thermodynamic activity of the subscripted aqueous species, and  $\text{H}_2\text{O}$  and clinoptilolite are assumed to be in their standard states with activities equal to one. The equilibrium constant,  $K$ , equals  $Q$  under conditions of equilibrium. The clinoptilolite stoichiometry adopted here facilitates description of solid solution of  $\text{Ca}^{2+}$  for  $2 \text{Na}^+$  preserving unit stoichiometric coefficients.

The curve in Figure 2-4 was generated by a regression of the Si release data using a numerical integration of Eq. (2-3). For the regression, the values for the  $\text{Al(OH)}_4^-$  molality were interpolated between analytical points, and aqueous,  $\text{Na}^+$  molality was calculated by mass balance accounting for

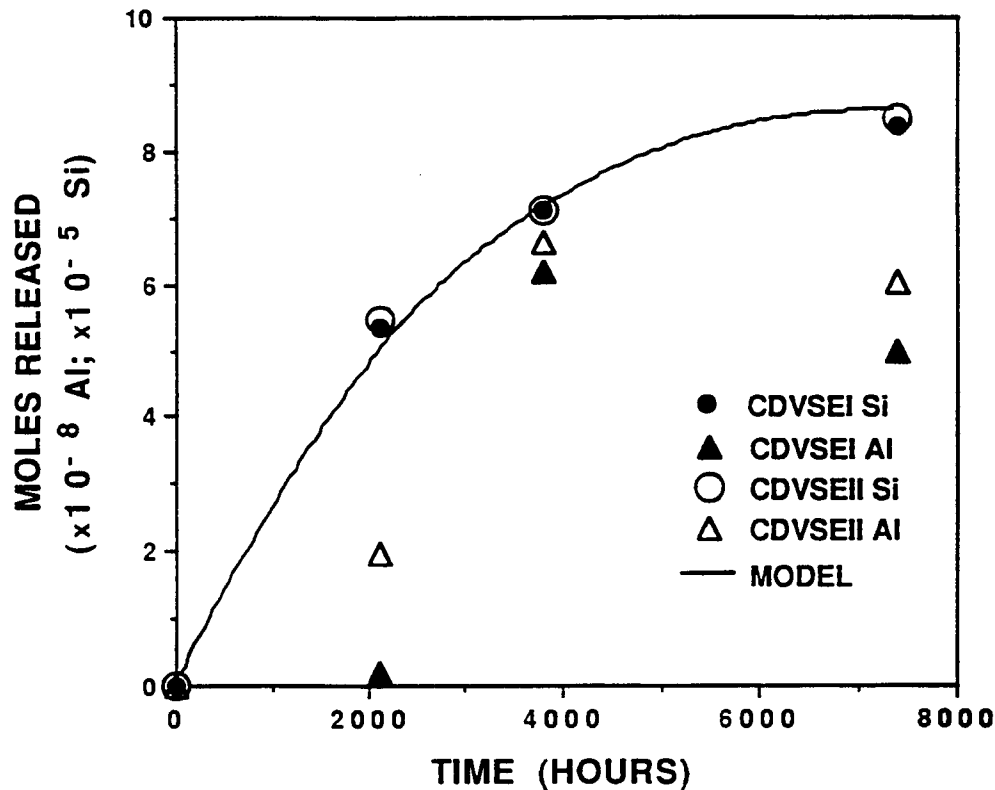


Figure 2-4. Moles of Si and Al released from clinoptilolite in dissolution experiments CDVSEI and CDVSEII. The curve is a fit to the Si release data using the rate Eq. (2-3).

initial conditions in the experiments, evaporation, solute extraction due to sampling, and  $\text{Na}^+$  release from clinoptilolite (which was negligible relative to the initial concentration). Activity coefficients (which remained constant) were based on an extended Debye-Huckel algorithm and calculated in EQ3 speciations for the aqueous solutions. The value of  $K = 10^{-50}$  used in the regression is consistent with the limiting clinoptilolite solubility measurement described below. Values of  $k^*s = 8.7 \times 10^{-13}$  moles/sec and  $\sigma = 20$  in Eq. (2-3) yield the good fit to the data shown in Figure 2-4. The net release of Al does not correspond to the same expression.

Incongruent clinoptilolite dissolution suggests an interpretation of results of the mixed analcime plus clinoptilolite system evolution (Figure 2-5). Net moles released were calculated using Eq. (2-2). Abundant Si release followed the addition of clinoptilolite to the solutions that were partially equilibrated with analcime. Si release was accompanied by Al decrease in solution and a decrease of the net moles of Al release, that is, Al precipitation. This effect was previously attributed to simultaneous clinoptilolite dissolution and analcime growth. However, growth of analcime under these conditions appears to conflict with the measurement of analcime solubility (see Section 2.3.4). The Si release and Al precipitation data are also consistent with clinoptilolite dissolution and precipitation of a secondary Al-bearing product other than analcime. Aqueous solutions evolved to states of metastable supersaturation with respect to Al phases during initial analcime dissolution. On addition of clinoptilolite to the system, the clinoptilolite crystals, or a silica-depleted residual clinoptilolite substrate, may have provided for nucleation of the secondary

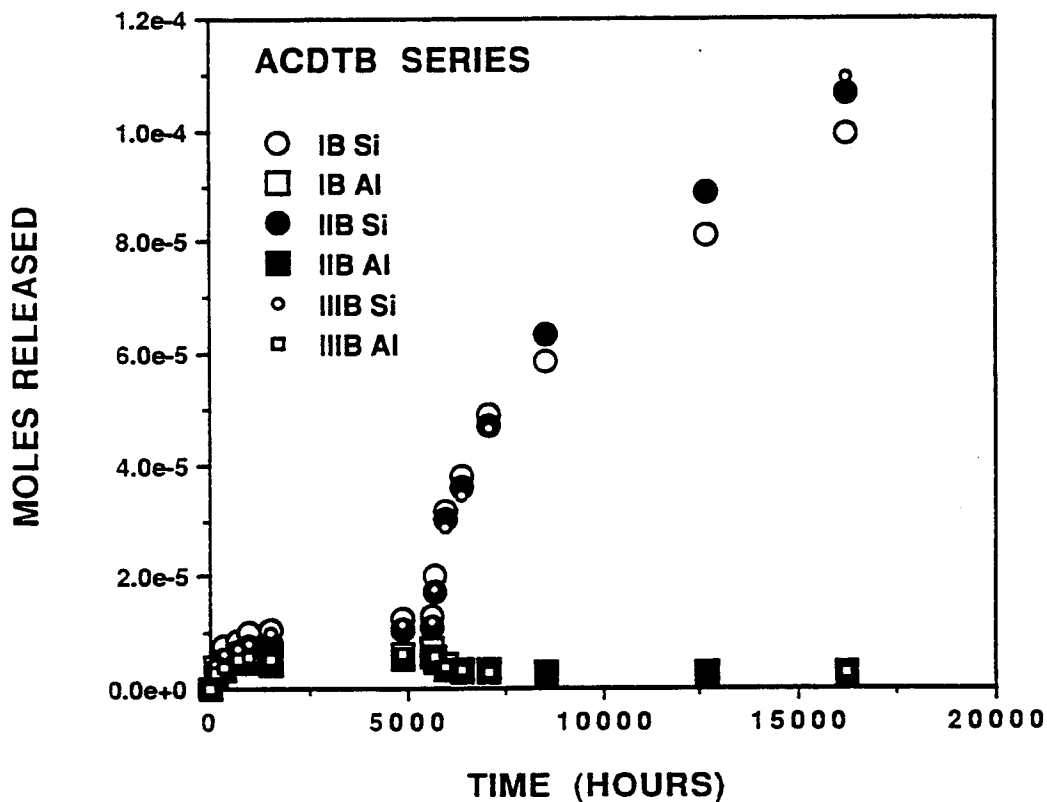


Figure 2-5. Net moles of Si and Al released in ACDTB series analcime dissolution and analcime plus clinoptilolite equilibration studies. Initial analcime dissolution released both Si and Al. Addition of clinoptilolite to the system at 5,639 hours led to additional Si release and Al precipitation.

product. Microscopic and x-ray observations of the solids will perhaps clarify these issues when the analcime plus clinoptilolite experiments are terminated.

### 2.3.4 Phase Relations

Equilibrium distributions of aqueous species for all experimental aqueous solution analyses have been computed with EQ3NR version 7.1 using the database data0.com.R16 (Wolery, 1992). Analytical measurements were used to constrain total Si and Al concentrations and pH. Total Na concentrations were calculated based on initial solution compositions corrected for concentration of Na due to evaporation (dissolution and precipitation of minerals had negligible effects on the Na concentration). Calculated Na values correspond closely to analytical measurements. The bicarbonate content of the solutions was calculated by adjusting its value to achieve electroneutrality in the speciated solutions. Calculated equilibrium fugacities of CO<sub>2</sub> were close to atmospheric values, which provides a check of the accuracy of the data and interpretation.

Thermodynamic activities of aqueous species obtained in the speciation computations illustrate reaction paths taken by the solid-solution mixtures when plotted on an appropriate activity diagram (Figure 2-6). Data defining the analcime solubility reversal are displayed in the expanded-scale inset figure. Small circles represent water chemistry in analcime dissolution experiments, and small rectangles are based on data from analcime growth experiments corresponding to the data in Figures 2-2 and 2-3.

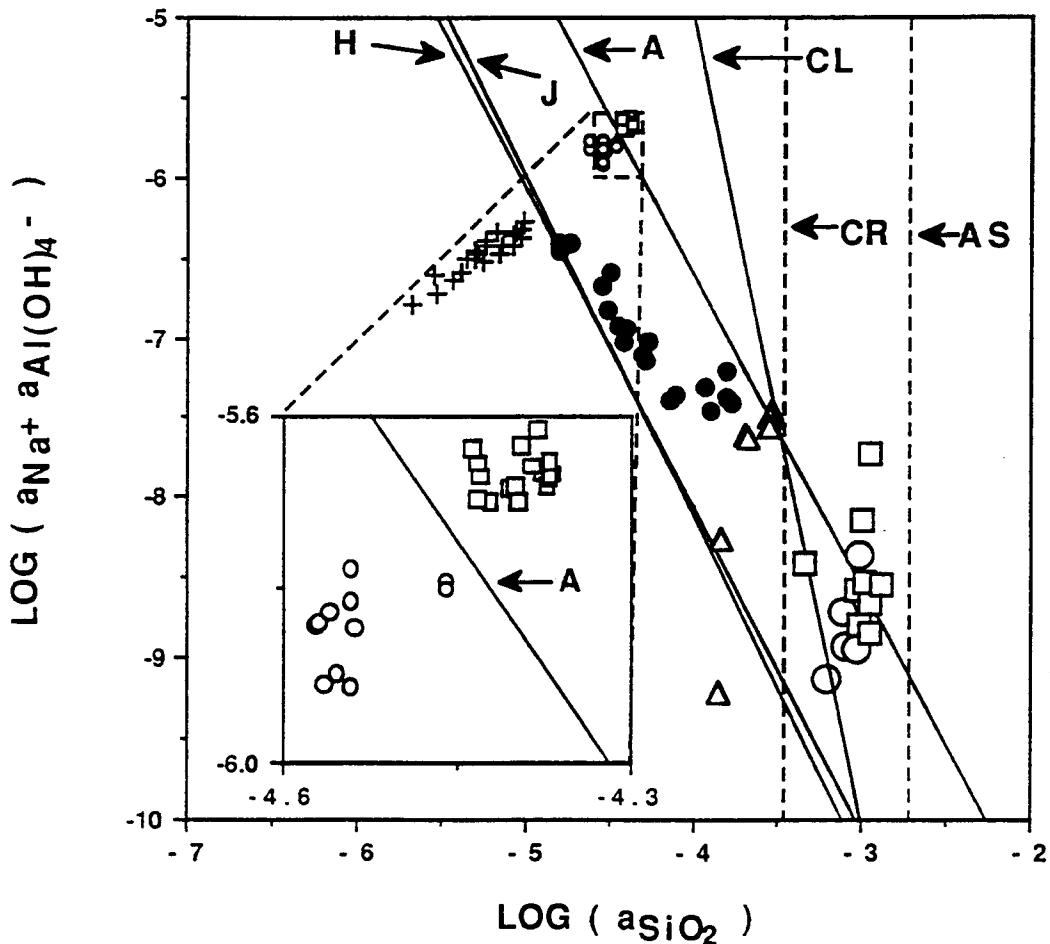
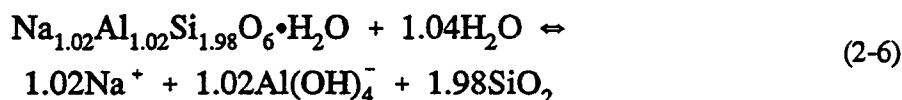


Figure 2-6. Aqueous solution properties shown as the base-ten logarithm of the product of the  $\text{Na}^+$  and  $\text{Al(OH)}_4^-$  activities plotted as a function of the logarithm of the aqueous  $\text{SiO}_2$  activity. Experimental data and solubility curves are for 25 °C. Small circles are data from analcime dissolution solubility experiments ASE. Small squares are data from analcime precipitation solubility experiments RACDT. A subset of these data is shown at an expanded scale in the inset figure. Line A is the analcime solubility defined by these data. Lines H and J are analcime solubilities based on thermodynamic data determined by Helgeson et al. (1978) and Johnson et al. (1982), respectively. Crosses are data from analcime dissolution experiments ACDTB. Solid circles are data from the analcime plus clinoptilolite equilibration study ACDTB. Open triangles are data from clinoptilolite dissolution study CDVSE. Line CL bounds the clinoptilolite dissolution data and represents a lower limit of the clinoptilolite solubility. Open squares and open circles are based on chemical analyses and equilibrium aqueous speciations of groundwaters from the saturated zone tuffaceous aquifer near Yucca Mountain and Oasis Valley, respectively. Lines CR and AS represent the solubilities of cristobalite and amorphous silica, respectively.

Equilibrium between analcime and aqueous species according to the reaction



is described by the law of mass action, which can be written as

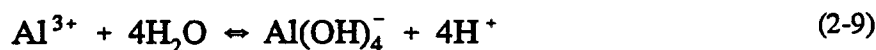
$$K = (a_{\text{Na}^+})^{1.02} (a_{\text{Al}(\text{OH})_4^-})^{1.02} (a_{\text{SiO}_2})^{1.98} \quad (2-7)$$

where  $K$  denotes the equilibrium constant for the reaction, and  $\text{H}_2\text{O}$  and the nonstoichiometric analcime are assumed to be in standard-states with unit activities. Eq. (2-7) can be rewritten as

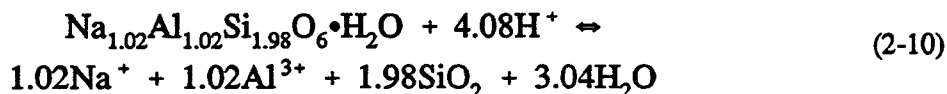
$$\log[(a_{\text{Na}^+})(a_{\text{Al}(\text{OH})_4^-})] = -\frac{1.98}{1.02} \log(a_{\text{SiO}_2}) + \frac{1}{1.02} \log K \quad (2-8)$$

which is the equation for analcime solubility in the coordinates of Figure 2-6. Line A in Figure 2-6 has been drawn between the data derived from analcime dissolution and precipitation experiments, and corresponds to Eq. (2-8). The value of  $\log K$  for reaction (2-6) consistent with line A is  $-14.67$ .

Aluminum hydrolysis can be expressed as



The equilibrium constant for this reaction at  $25^\circ\text{C}$  is  $10^{-22.1477}$  according to the data0.com.R16 database associated with EQ3/6. Subtracting reaction Eq. (2-9) (multiplied by 1.02) from reaction Eq. (2-6) yields



The base ten logarithm of the equilibrium constant for reaction (2-10) ( $\log K_{R10}$ ) is given by  $-14.67 + (1.02) \times (22.1477) = 7.92$ . Standard-state Gibbs free energies of formation in kilojoules per mole for the aqueous species in reaction Eq. (2-10) at  $25^\circ\text{C}$  taken from SUPCRT92 (Johnson et al., 1992) are  $-261.876$ ,  $-482.728$ ,  $-833.395$ ,  $-237.178$ , and  $0.0$  for  $\text{Na}^+$ ,  $\text{Al}^{3+}$ ,  $\text{SiO}_2$ ,  $\text{H}_2\text{O}$ , and  $\text{H}^+$ , respectively. Standard-state free energies are related to the equilibrium constant for reaction Eq. (2-10) by

$$\begin{aligned} -RT \ln K_{R10} = \Delta G_{R10}^\circ = & 1.02 \Delta G_{\text{Na}^+}^\circ + 1.02 \Delta G_{\text{Al}^{3+}}^\circ \\ & + 1.98 \Delta G_{\text{SiO}_2}^\circ + 3.04 \Delta G_{\text{H}_2\text{O}}^\circ - 4.08 \Delta G_{\text{H}^+}^\circ - \Delta G_{\text{Analcime}}^\circ \end{aligned} \quad (2-11)$$

where  $R$  and  $T$  stand for the gas constant and absolute temperature,  $\Delta G_{R10}^\circ$  stands for the standard Gibbs free energy for reaction (2-10), and  $\Delta G_i^\circ$  denotes standard Gibbs free energies of formation for the subscripted species. Using the data given above, Eq. (2-11) can be solved for the standard Gibbs free energy of formation for analcime, which is  $-3085.4$  kJ/mole.

Standard Gibbs free energies of formation of analcime in the literature are  $-3091.73 \pm 3.682$  kJ/mole,  $-3088.2$  kJ/mole, and  $-3077.2 \pm 3.3$  kJ/mole (Robie et al., 1978; Helgeson et al.,

1978; and Johnson et al., 1982, respectively). Lines H and J are analcime solubility limits calculated using the thermodynamic data and mineral stoichiometries adopted by Helgeson et al. (1978) and Johnson et al. (1982), respectively. These limits are significantly smaller than those based on the present study, as is evident on the background scale of Figure 2-6. The solubility limits depend strongly on the mineral stoichiometries as well as the standard Gibbs free energies of formation. Helgeson et al. (1978) adopted the nominal analcime stoichiometry  $\text{NaAlSi}_2\text{O}_6 \cdot \text{H}_2\text{O}$ , and Johnson et al. (1982) adopted a silica rich stoichiometry based on analytical data:  $\text{Na}_{0.96}\text{Al}_{0.96}\text{Si}_{2.04}\text{O}_6 \cdot \text{H}_2\text{O}$ .

### 2.3.5 Reaction Paths

Data from the clinoptilolite dissolution study corresponding to the data in Figure 2-4 are plotted as triangles in Figure 2-6. Solutions evolved from lower to higher silica activities in these experiments. The maximum values place a lower limit on the clinoptilolite solubility. Although incongruent dissolution of clinoptilolite affects the reaction path for irreversible dissolution, it does not alter its thermodynamic solubility limit in the phase diagram. Line CL is drawn to approximate a minimum limit on the clinoptilolite solubility based on the experimental data and interpretation. Its slope equals  $-5$ , the negative of the Si/Al and Si/Na ratio in idealized clinoptilolite.

The EQ3/6 database data0.com.R16 contains a value for the equilibrium constant for Na-clinoptilolite dissolution. This value is based on calorimetric data from Johnson et al. (1991) and ion-exchange data from the literature interpreted by Viani and Bruton (1992). The Na-exchanged clinoptilolite has a formula,  $\text{Na}_{3.467}\text{Al}_{3.45}\text{Fe}_{0.017}\text{Si}_{4.533}\text{O}_{36} \cdot 10.922\text{H}_2\text{O}$ . Because the clinoptilolite contains iron and does not have equal stoichiometric numbers of Na and Al, its solubility cannot be represented on Figure 2-6. Nevertheless, comparison of the Viani and Bruton (1992) data with results from the experimental clinoptilolite dissolution study can provide an evaluation of the data. Equilibrium with hematite provides a reasonable lower limit for the total iron concentration. Assuming equilibrium with hematite, EQ3/6 computations indicate that the final solutions in the clinoptilolite dissolution study would contain iron at  $1.3 \times 10^{-12}$  molal and would be supersaturated with respect to the Na-(Fe)-clinoptilolite by approximately 50 kJ/mole. Higher iron concentrations would lead to even greater supersaturations. This inconsistency between the experimental clinoptilolite dissolution data and the Viani and Bruton (1992) Na-clinoptilolite thermodynamic properties reveals significant uncertainty in the appropriate properties for clinoptilolite to be used in modeling water-rock interactions at Yucca Mountain.

Reaction paths for the analcime dissolution and subsequent analcime-plus-clinoptilolite reaction, corresponding to the data in Figure 2-5, are shown in Figure 2-6 as series of crosses and solid circles, respectively. Activities of the aqueous species increased in the solutions during the initial dissolution of analcime (crosses). The sharp increase in silica and decrease in Al that commenced with the introduction of clinoptilolite into the system is responsible for the negative slope of the subsequent trend of the reaction path (solid circles). Solutions along this path are undersaturated with respect to analcime as determined in the analcime solubility studies represented by line A. Consequently, analcime precipitation is unlikely to be the sink for Al. Incongruent clinoptilolite dissolution is indicated, as it is in the clinoptilolite dissolution study. The most evolved solutions in the analcime-plus-clinoptilolite reaction series lie below the projected analcime solubility limit (line A) and provide an additional constraint on this limit. These solution compositions are also close to the speculative equilibrium point between analcime and clinoptilolite, which is represented by the intersection of lines A and CL.

### 2.3.6 Groundwater at Yucca Mountain

Equilibrium aqueous speciation computations were performed with EQ3/6 using chemical analyses for a variety of water samples taken from the saturated-zone tuffaceous aquifer in the vicinity of Yucca Mountain and from Oasis Valley, south of Yucca Mountain. Water analyses were reported by Young (1972) for wells J-11, J-12, and J-13; by Daniels et al. (1982) for wells UE25b-1, UE29a-2, H1-4000, and J-13; and by White (1979) for the Oasis Valley area. The bicarbonate concentrations for the aqueous speciation calculations were based on charge balance in the solutions, and analytical data were used to constrain total concentrations of other species and pH. Calculated bicarbonate values are reasonably consistent with analytical data (e.g., for alkalinity). Results of these speciation calculations are plotted as open squares (Yucca Mountain data) and open circles (Oasis Valley data) in Figure 2-6.

Data for waters from Yucca Mountain and Oasis Valley show small variations in the aqueous silica activity. Silica activities are near  $10^{-3}$ , and generally lie between the cristobalite and amorphous silica solubilities at 25 °C (lines CR and AS, respectively, in Figure 2-6), based on data from data0.com.R16. This trend suggests silica activities buffered naturally by metastable equilibrium with a silica phase (e.g., leached volcanic glass). Values for the product of the  $\text{Na}^+$  and  $\text{Al}(\text{OH})_4^-$  ion activities in the Yucca Mountain and Oasis Valley waters are mainly between  $10^{-8}$  and  $10^{-9}$ , which is a fairly restricted relative and absolute variation. In the coordinates of Figure 2-6, the groundwater data center near the intersection of the natural silica buffer concentration and the experimental analcime solubility limit (line A). This result is a strong indication of the role of analcime in controlling water compositions in the tuffaceous aquifers.

An additional test of analcime equilibrium control of groundwater compositions is provided in an activity diagram showing relations between  $\text{Na}^+$  and  $\text{Al}(\text{OH})_4^-$  activities at 25 °C (Figure 2-7). To plot analcime solubility limits in the coordinates of Figure 2-7, the aqueous silica activity was fixed at  $10^{-3}$ , which corresponds to the apparent natural buffer in the Yucca Mountain area tuffaceous aquifer system (see Yucca Mountain and Oasis Valley data in Figure 2-6). Analcime solubility based on the equilibrium constant adduced above is plotted in this figure as line A. Analcime solubilities based on thermodynamic data from Helgeson et al. (1978) and Johnson et al. (1982) are indicated by lines H and J, respectively. Other minerals that could play a role in control of groundwater chemistry include low albite and gibbsite whose solubilities are also plotted in Figure 2-7 as lines LA and G, respectively, based on data from the EQ3/6 database data0.com.R16. Thermodynamic interpretations of groundwater data from near Yucca Mountain are plotted in Figure 2-7 as open circles and squares. The trend of these data and their magnitudes closely follow line A, strongly suggesting that the natural water chemistries are controlled by equilibrium with analcime. Some deviation of the groundwater data from the plotted analcime solubility line would be expected even if there were no uncertainty in the analyses of water from the field and all the waters were in perfect equilibrium with analcime. The aqueous silica activities in the groundwaters were not all equal to  $10^{-3}$  (though they were all close), and the temperatures of the waters were not all 25 °C (though they were all close). The solubility limits plotted as lines in Figure 2-7 are based on these conditions.

## 2.4 ASSESSMENT OF PROGRESS IN THE GEOCHEMISTRY RESEARCH PROJECT

The Geochemistry Research Project was planned and undertaken to address a broad scope of issues related to isolation of radioactive waste at Yucca Mountain. Specific topics of investigation were

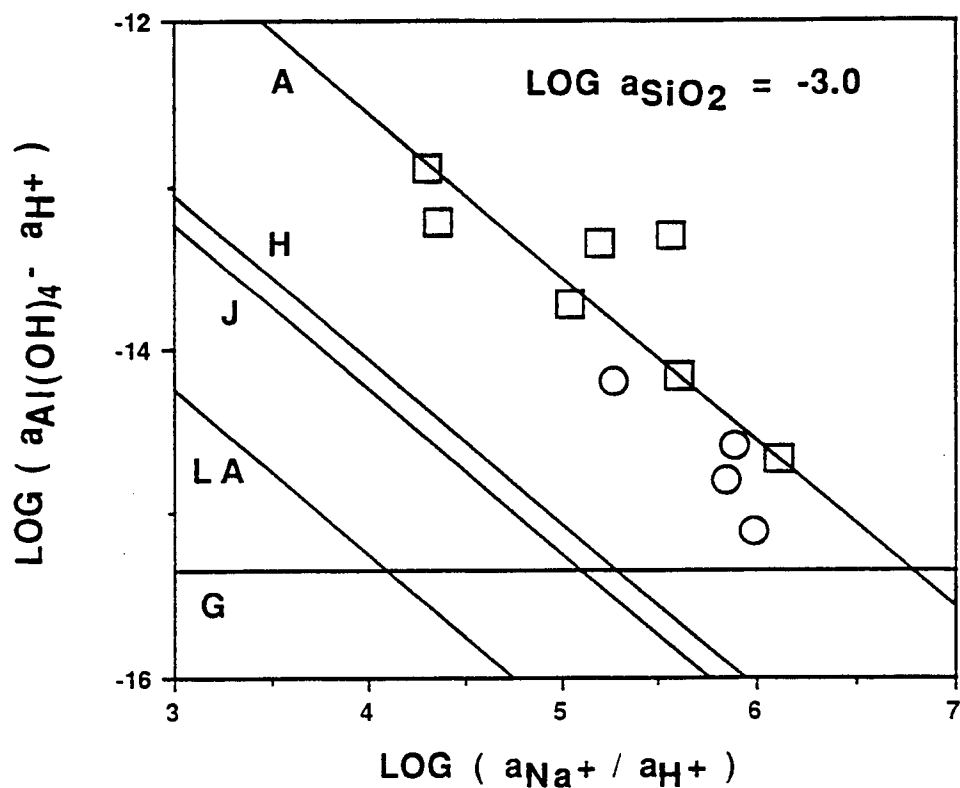


Figure 2-7. Aqueous solution properties represented as the logarithm of the product of the  $\text{Al(OH)}_4^-$  and  $\text{H}^+$  ion activities plotted as a function of the logarithm of the quotient of the  $\text{Na}^+$  and  $\text{H}^+$  activities. Line A represents the solubility of analcime in a solution of  $\log a_{\text{SiO}_2} = -3.0$  at  $25^\circ\text{C}$ , and was generated using thermodynamic data derived from line A in Figure 2-6. Lines H and J are analcime solubility limits at  $\log a_{\text{SiO}_2} = -3.0$  and  $25^\circ\text{C}$  derived from the thermodynamic data of Helgeson et al. (1978) and Johnson et al. (1982), respectively. Lines LA and G represent solubility limits of low albite and gibbsite, respectively, at  $\log a_{\text{SiO}_2} = -3.0$  (for albite) and  $25^\circ\text{C}$  derived from thermodynamic data from Johnson et al. (1992). Circles and squares are based on equilibrium speciations of groundwater chemistry data from the Yucca Mountain area and Oasis Valley, respectively.

designed to resolve technical uncertainties concerning fundamental aspects of the geochemical system at Yucca Mountain. Experimental studies and data interpretation have focused on interactions between water and the zeolite minerals analcime and clinoptilolite. The abundance of these secondary minerals at Yucca Mountain, their relations in the field, and the relationship between their chemistries suggest that they play a controlling role in active water-rock interactions. In addition, clinoptilolite is widely cited as a natural barrier to radionuclide migration because of its sorptive characteristics. Knowledge of the fundamental thermodynamic and kinetic properties of these minerals and their interactions with water is required to make defensible projections of the evolution of the water-rock system and retardation of radionuclide transport in the Yucca Mountain repository system. Nevertheless, at the inception of the project, major uncertainties existed concerning these properties. Furthermore, limited attempts had been made to use thermodynamic and kinetic reaction-path modeling to predict in detail the evolution of unsaturated zone gas, groundwater, and mineral chemistry in a nonisothermal repository at Yucca Mountain.

CDS for issues in geochemistry are under development, and development of Compliance Determination Methodologies (CDM) has not been initiated in this area. The Geochemistry Research Project was designed prior to definition of KTUs as they are being identified in CDS. Nevertheless, by focusing on clear issues relating to the gas-water-rock evolution of the natural and repository systems at Yucca Mountain, the project has produced results that will contribute significantly to the development of CDS and CDM and to the identification, if not resolution, of KTUs identified in them. Significant advances have been made in these fields in the Geochemistry Research Project. A summary of major accomplishments of the project is provided below, together with CDS (from the list in Section 2.1 with associated KTU) to which the results are most directly related.

- Experimental Data

- Clinoptilolite ion-exchange isotherms were determined at 25 °C for the Na-K, Na-Ca, Na-Sr, and K-Sr systems as a function of the total normality of the aqueous solution (3.2.3.2, 3.2.3.5)
- Analcime dissolution rate was measured, and dissolution mechanism was evaluated at 25 °C and pH 9 (3.2.3.1)
- Reversed solubility limit for analcime was determined (3.2.3.4, 3.2.3.5)
- Dissolution rate was measured, and dissolution mechanism was evaluated for clinoptilolite at 25 °C and pH 9 (3.2.3.1, 3.2.3.5)

- Kinetic and Thermodynamic Parameters

- Mixing parameters for clinoptilolite solid solutions were regressed from experimental data (3.2.3.2, 3.2.3.5)
- Rate constants and rate laws were determined for analcime and clinoptilolite dissolution (3.2.3.1, 3.2.3.5)
- Standard Gibbs free energy of formation for analcime was derived from experimental data (3.2.3.4, 3.2.3.5)

- Reaction-Path Modeling Capabilities

- The EQ3/6 geochemical modeling software and thermodynamic data package were acquired from the DOE and brought under configuration control (3.2.3.1, 3.2.3.2, 3.2.3.3, 3.2.3.4, 3.2.3.5, 3.2.3.7)
- Open-system, equilibrium (Rayleigh) gas fractionation modeling capabilities were implemented in EQ6 (3.2.3.3, 3.2.3.4, 3.2.3.5, 3.2.3.7)
- Nonisothermal, variable, imposed fugacity modeling was implemented with EQ6 (3.2.3.3, 3.2.3.4, 3.2.3.5, 3.2.3.7)

- System Models

- Models were developed for Yucca Mountain groundwater and mineral chemistry (3.2.3.1, 3.2.3.2, 3.2.3.4, 3.2.3.5, 3.2.3.7)
- Models were developed for nonisothermal, repository-induced chemical variations at Yucca Mountain (3.2.3.3, 3.2.3.4, 3.2.3.5, 3.2.3.7)
- Models were developed for water and mineral variations during boiling of Yucca Mountain groundwater (3.2.3.3, 3.2.3.4, 3.2.3.5)

Interactions of the principal investigators in the Geochemistry Project with researchers in other research and technical assistance activities have demonstrated the utility of the research results. Direct relations with other research projects include: acquisition and preparation of materials and design and interpretation of experiments for the Sorption Modeling for HLW PA Research Project, use of techniques and expertise for geochemical modeling of aqueous solutions in the IWPE Research Project, use of modeling techniques for modeling of aqueous uranium chemistry at the Peña Blanca site for the Geochemical Analogs Research Project, and application of general knowledge of Yucca Mountain area geochemistry in development of the Regional Hydrology Research Project. For IPA, techniques and expertise have been derived from the Geochemistry Research Project for the computation of solubilities of radionuclide-bearing solids and for the development of conceptual and simplified numerical models for the carbon system for use in modeling coupled heat flow, gas flow, and carbon-14 transport. In general, expertise and information developed in the Geochemistry Research Project have been useful for numerous technical reviews and in the development of CDS.

## **2.5 PLANS FOR NEXT REPORTING PERIOD**

In future activities in the Geochemistry Research Project, ongoing experimental studies will be completed, data will be analyzed and incorporated into final models for the Yucca Mountain system, and topical reports of research results for the project will be completed.

Review of preliminary KTU in CDS under development indicates a concentration of uncertainty in issues related to the interactions between the geochemical environment and the engineered materials of the repository under conditions of elevated repository temperatures. The need for a new research project in near-field geochemistry is indicated. This project would expand on the present Geochemistry Research Project, which focused on the ambient geochemical system and on predictions of its nonisothermal evolution in the absence of interactions with engineered materials. The modeling results, new data, and numerical modeling capabilities developed in the Geochemistry Research Project would provide initial and boundary conditions for research in near-field geochemistry. Specific topics that need to be addressed to resolve the KTU associated with near-field geochemistry are presently being developed in interactions between the CNWRA and NRC staff members. Technical issues in near-field geochemistry of particular significance to repository performance and licensing are:

- Water chemistry — Effects of temperature, evaporation, and condensation (e.g., properties of concentrated solutions), and interactions with the host rock, engineered materials (e.g., grout, rock bolts, and backfill), containers, and waste forms

- Source term controlling secondary mineralogy — Properties of uranyl oxy-hydroxides and silicates
- Host mineralogy — Effects of temperature, dehydration, and interactions with near-field aqueous solutions on sorptive capacity and other properties of zeolite and clay minerals

A research project focused on these issues would provide information to resolve KTUs associated particularly with the following Regulatory Requirement Topics (RRT):

- RRT 3.2.3.2: Assessment of Compliance with Siting Criteria; Geochemical System; Individual Favorable Conditions; Geochemical Conditions
- RRT 3.2.3.3: Assessment of Compliance with Siting Criteria; Geochemical System; Individual Favorable Conditions; Mineral Assemblages
- RRT 3.2.3.4: Assessment of Compliance with Siting Criteria; Geochemical System; Potentially Adverse Conditions; Groundwater Conditions and the Engineered Barrier System
- RRT 3.2.3.5: Assessment of Compliance with Siting Criteria; Geochemical System; Potentially Adverse Conditions; Geochemical Processes

## 2.6 REFERENCES

- Barrer, R.M. 1978. Cation-exchange equilibria in zeolites and feldspathoids. *Natural Zeolites: Occurrence, Properties, Use*. L.B. Sand and F.A. Mumpton, eds. New York: Pergamon Press: 385-395.
- Daniels et al. 1982. Summary report on the geochemistry of Yucca Mountain and environs. LANL Report LA-9328-MS. Los Alamos, NM: Los Alamos National Laboratory.
- Flanigen, E.M. 1986. *Crystal Structure and Chemistry of Natural Zeolites*. E.A. Mumpton, ed. Mineralogy and Geology of Natural Zeolites. *Reviews in Mineralogy* 4: 19-52.
- Helgeson, H.C., J.M. Delany, H.W. Nesbitt, and D.K. Bird. 1978. Summary and critique of the thermodynamic properties of rock-forming minerals. *American Journal of Science* 278A:229.
- Johnson, G.K., H.E. Flowtow, and P.A.G. O'Hare. 1982. Thermodynamic studies of zeolites: analcime and dehydrated analcime. *American Mineralogist* 67: 736-748.
- Johnson, G.K., I.R. Tasker, R. Jurgens, and P.A.G. O'Hare. 1991. Thermodynamic studies of zeolites: clinoptilolite. *Journal of Chemical Thermodynamics* 23: 475-484.
- Johnson, J.W., E.H. Oelkers, and H.C. Helgeson. 1992. SUPCRT92: (A Software Package for Calculating the Standard Molal Thermodynamic Properties of Minerals, Gases, Aqueous Species, and Reactions from 1 to 5000 bars and 0° to 1000 °C.) *Computer and Geosciences* 18: 899-947.
- Murphy, W.M., R.T. Pabalan, J.D. Prikryl, and C.J. Goulet. 1992. Dissolution rate and solubility of analcime at 25 °C. *Proceedings, Seventh International Symposium on Water-Rock Interactions*, Rotterdam, The Netherlands: 1:107-110.

- Pabalan, R.T. 1991a. Nonideality effects on the ion-exchange behavior of the zeolite mineral clinoptilolite. *Scientific Basis for Nuclear Waste Management XIV*. T. Abrajano, Jr. and L.H. Johnson, eds. Pittsburgh, PA: Materials Research Society: Symposium Proceedings 212: 559-567.
- Pabalan, R.T. 1991b. Unsaturated mass transport (Geochemistry): Experimental studies. *Report on Research Activities for Calendar Year 1990*. W.C. Patrick, ed. NUREG/CR-5817. Washington, DC: U.S. Nuclear Regulatory Commission: 2-1 to 2-24.
- Pabalan, R.T. 1992. Unsaturated mass transport (Geochemistry): Experimental studies. *Report on Research Activities for Calendar Year 1991*. W.C. Patrick, ed. CNWRA 91-01A. San Antonio, TX: Center for Nuclear Waste Regulatory Analyses: 2-1 to 2-24.
- Pabalan, R.T. 1993. Unsaturated mass transport (Geochemistry): Experimental studies. *NRC High-Level Radioactive Waste Research at CNWRA: January-June 1992*. W.C. Patrick, ed. NUREG/CR-5817, Vol 3, No. 1: Washington, DC: U.S. Nuclear Regulatory Commission: 2-1 to 2-8.
- Pabalan, R.T. and T.J. Griffin. 1993. Thermodynamics of ion-exchange between clinoptilolite and aqueous solutions of  $\text{Na}^+/\text{K}^+$  and  $\text{Na}^+/\text{Ca}^{2+}$ . *4th International Conference on the Occurrence, Properties, and Utilization of Natural Zeolites*. Boise, ID: publisher: Extended Abstracts.
- Pabalan, R.T. and W.M. Murphy. 1992a. Unsaturated Mass Transport (Geochemistry) *Report for Research Activities for Calendar Year 1991*. W.C. Patrick, ed. CNWRA 91-01A. San Antonio, TX: Center for Nuclear Waste Regulatory Analyses: 2-1 to 2-50.
- Pabalan, R.T. and W.M. Murphy. 1992b. Unsaturated Mass Transport (Geochemistry) *NRC High-Level Radioactive Waste Research at CNWRA January 1 through June 30, 1992*. W.C. Patrick, ed. CNWRA 92-01S. San Antonio, TX: Center for Nuclear Waste Regulatory Analyses: 2-1 to 2-25.
- Robie, R.A., B.S. Hemingway, and J.R. Fischer. 1978. *Thermodynamic Properties of Minerals and Related Substances at 298.15K and 1 bar ( $10^5$  Pascals) Pressure and at Higher Temperatures*. USGS, Bulletin 1452, Reston, VA: U.S. Geological Survey.
- Viani, B.E. and C.J. Bruton. 1992. *Modeling Fluid-Rock Interaction at Yucca Mountain, Nevada: A Progress Report*. UCRL-ID-109921. Livermore, CA: Lawrence Livermore National Laboratory.
- White, A.F. 1979. *Geochemistry of Ground Water Associated with Tuffaceous Rocks, Oasis Valley, Nevada*. USGS, Professional Paper 712-E. Reston, VA: U.S. Geological Survey.
- Wolery, T.J. 1992. EQ3/6, *A Software Package for Geochemical Modeling of Aqueous Systems: Package Overview and Installation Guide (Version 7.0)*. UCRL-MA-110662 PT I. Livermore, CA: Lawrence Livermore National Laboratory.

Young, R.A. 1972. *Water Supply for the Nuclear Rocket Development Station at the U.S. Atomic Energy Commission's Nevada Test Site*. USGS Water Supply Paper 1938. Reston, VA: U.S. Geological Survey.

# 3 THERMOHYDROLOGY

by *Randall D. Manteufel and Ronald T. Green*

*Investigators: Franklin T. Dodge (SwRI); Ronald T. Green (CNWRA); Randall D. Manteufel (CNWRA); Steve J. Svedeman (SwRI); and Terrie Perry (CNWRA)*

*NRC Project Officer: John Randall*

## 3.1 TECHNICAL OBJECTIVES

The technical objective of the Thermohydrology Research Project is to provide laboratory, computational, and theoretical analyses of the thermal and fluid regimes to be expected proximal to heat-generating waste at the proposed high-level radioactive waste (HLW) repository at Yucca Mountain. This information is necessary to predict the performance of the overall system (10 CFR 60.112) and the performance of the barriers that comprise the subsystems of the repository — the Engineered Barrier System (EBS), 10 CFR 60.113(a)(1) and the Geologic Setting (GS), 10 CFR 60.113(a)(2). However, predicting the status of the environment of the repository is difficult because of the time and size scales associated with the proposed Yucca Mountain repository. The laboratory-scale analyses are designed to develop a better understanding of the coupled processes expected to be important at the repository, but performed at a scale that will permit meaningful results to be gained in a reasonable time frame. To accomplish this, the principles of dimensional analysis are applied to laboratory-scale experiments in order to assess longer-time and larger-scale repository performance.

Information developed within the Thermohydrology Research Project will be used to support specific portions of the License Application Review Plan (LARP) (NRC, 1993). Fluid and temperature interactions observed at the laboratory scale and computational exercises conducted to apply these results to a more meaningful scale, such as the canister or repository scale, will provide practical experience and knowledge applicable to the review of Description of the Individual Systems and Characteristics of the Site (Sections 3.1.1, 3.1.2, 3.1.3, and 3.1.5). Similarly, these studies will provide an information basis for the development of portions of the LARP relating to both favorable and potentially adverse thermohydrological conditions (Sections 3.2.2.1, 3.2.2.2, 3.2.2.3, 3.2.2.4, 3.2.3.1, 3.2.3.2, 3.2.3.4, 3.2.3.5, and 3.2.3.7), because these require information on the coupled flow of heat and water through partially saturated, fractured media. The Thermohydrology Research Project provides for an opportunity to assess the interaction of the thermal impact of the HLW upon water present in the repository environment. This knowledge will be critical in the development of and support of Section 3.3, Assessment of Compliance with the Groundwater Travel Time Performance Objective, and Section 3.4, Effectiveness of Natural Barriers against the Release of Radioactive Material to the Environment. Additionally, knowledge of the thermal and fluid regimes that will exist in the presence of heat-generating HLW will provide information needed to develop Sections 5.1, Description of Engineered Systems and Components that provide a Barrier between the Waste and the Geologic Setting and 5.4, Assessment of Compliance with the EBS Performance Objectives.

Compliance Determination Strategies (CDS) for the LARP sections noted earlier have not been finalized. Nevertheless, information derived from results of the Thermohydrology Research Project will be germane in addressing key technical uncertainties (KTU) raised in several CDSs. For example, CDSs 3.3 and 5.4 have both been classified as requiring a Type 5 review, which requires independent research to resolve KTU that pose a high risk of arriving at a wrong conclusion regarding compliance with the

performance objectives and design criteria of 10 CFR Part 60. Specific KTU topics that will be addressed by work within the Thermohydrology Research Project include the transient regimes of temperature and moisture that are expected to occur proximal to the emplacement of heat-generating HLW. These transient regimes are expected to affect many processes, including the travel time of groundwater, the performance of the EBS, geochemical transport, and thermomechanical mechanisms.

Information resulting from the Thermohydrology Research Project is of critical importance to investigations involving geochemistry, hydrogeology, and material science. This intrinsic reliance is demonstrated in the interaction that exists with other projects sponsored by the U.S. Nuclear Regulatory Commission (NRC) Office of Nuclear Regulatory Research (RES) projects at the Center for Nuclear Wastes Regulatory Analyses (CNWRA). In particular, the EBS research project requires knowledge of the expected temperature and liquid saturation of the canister environment in order to determine the performance of the waste package. Of particular interest to the EBS project is the duration of dry out proximal to the canisters and the expected time and nature of re-wetting. Likewise, the Geochemistry Research Project will base thermodynamic predictions upon the anticipated thermal and fluid regimes. Additionally, the Performance Assessment (PA) Research Project requires this same information for several aspects of the analyses that are conducted as part of the overall PA. Design information provided by the Geochemistry, EBS, and PA projects will assist the Thermohydrology Research Project establish the properties of the waste package and the GS environments. This interaction is crucial to the success of all affected projects.

Several projects sponsored by the NRC Office of Nuclear Material Safety and Safeguards (NMSS) are also integrated with the Thermohydrology Research Project. These include the resolution of uncertainties in the groundwater travel time rule, which requires an understanding of the nature and extent of the disturbed zone resulting from the heat-generating HLW. Likewise, the design issues related to thermal loading need knowledge about the thermal and moisture environment to be expected (Nataraja and Brandshaug, 1992). Similar information is also utilized in the Iterative Performance Assessment (IPA) task.

Research within the Thermohydrology Research Project entails laboratory-scale experiments, numerical simulations, computational analyses, and dimensional analysis. A summary of the results of the Thermohydrology Research Project through 1991 can be found in CNWRA 92-006 (Green et al., 1992a). Subsequent reports documenting progress and results of this project include Manteufel and Green (1992); Manteufel et al. (1992a); and Green et al. (1992b). This report describes the results of the Thermohydrology Research Project during the first half of 1993.

## **3.2 LABORATORY EXPERIMENTS**

Two laboratory experiments have been performed to investigate thermally driven liquid redistribution in a partially saturated porous medium. The experiments consist of a sealed rectangular enclosure packed with unconsolidated medium (glass beads or alumina powders) and subjected to a horizontal steady-state temperature profile across the largest dimension of the enclosure. The two experiments were designed to be similar, yet with sufficient difference to resolve uncertainties that developed during the interpretation of the results of the first experiment (herein called test 6). In particular, the second experiment (herein called test 12) differed from test 6 by: (i) additional tensiometers; (ii) additional thermistors; and (iii) different medium. Alumina powder was used in test 12, and glass beads were used in test 6. The solid medium was changed in order to eliminate potential

chemical impairment of the medium observed in test 6. The primary purpose of performing test 12 was to investigate the development of a wet band in front of the dryout zone and assess the existence and importance of hysteresis in the medium characteristic curves as a potential driving mechanism for liquid redistribution.

### 3.3 EXPERIMENTAL APPARATUS

The laboratory experiments consisted of a sealed rectangular enclosure ( $20.3 \times 15.2 \times 5.3$  cm) with a clear plexiglass front wall (see Figure 3-1 for test 12). Each setup was instrumented with heat exchangers located on opposing sides across the longest dimension of the enclosure. The heat exchangers were connected to recirculating-fluid, constant-temperature baths that were used to maintain the side walls at specified temperatures. With this arrangement, an approximately linear temperature profile was established horizontally throughout the medium. Experimental measurements were obtained using a gamma-ray densitometer, porous cup tensiometers, thermistors, and visual observation of periodically injected dye. The locations of each of these measurements are shown in Figure 3-1.

Test 12 contained six tensiometers (whereas test 6 only had two), which entered from the back of the apparatus and resided in the middle of the porous medium. In test 12, a thermistor was installed inside each of the tensiometers. Test 12 contained more thermistors than test 6, in order to assess both the horizontal and vertical temperature gradients. Gamma-ray densitometer measurements were taken at 24 locations (e.g., A1, A2, A3, ..., D6) throughout the duration of both tests. In test 12, horizontal gamma scans were taken at three levels designated as B, C and D. In both tests, two liquid-dye injection tubes entered from the back of the enclosure and extended to the front wall, as shown in Figure 3-1.

The major differences between the setup of the two experiments were:

- Glass beads were used in test 6, while alumina powder was used in test 12 as the unconsolidated porous medium
- The size distribution of glass beads used in test 6 was bi-modal with 50 percent by volume of factory-sieved beads from 28 to 53  $\mu\text{m}$  and 50 percent from 74 to 105  $\mu\text{m}$ , and the alumina powder used in test 12 was factory sieved to particle sizes below 44  $\mu\text{m}$
- A simulated fracture was included in test 6, but not in test 12
- The right side heat exchanger temperature was controlled to be 60 °C in test 6 and 90 °C in test 12
- The initial saturation was 65 percent in test 6 and 50 percent in test 12

Test 12 parameters were chosen to be different from test 6 for the following reasons:

- The test medium was changed to alumina powder to eliminate the possibility for thermal-chemical effects due to the dissolution, mobilization, and precipitation of the glass that was observed in test 6

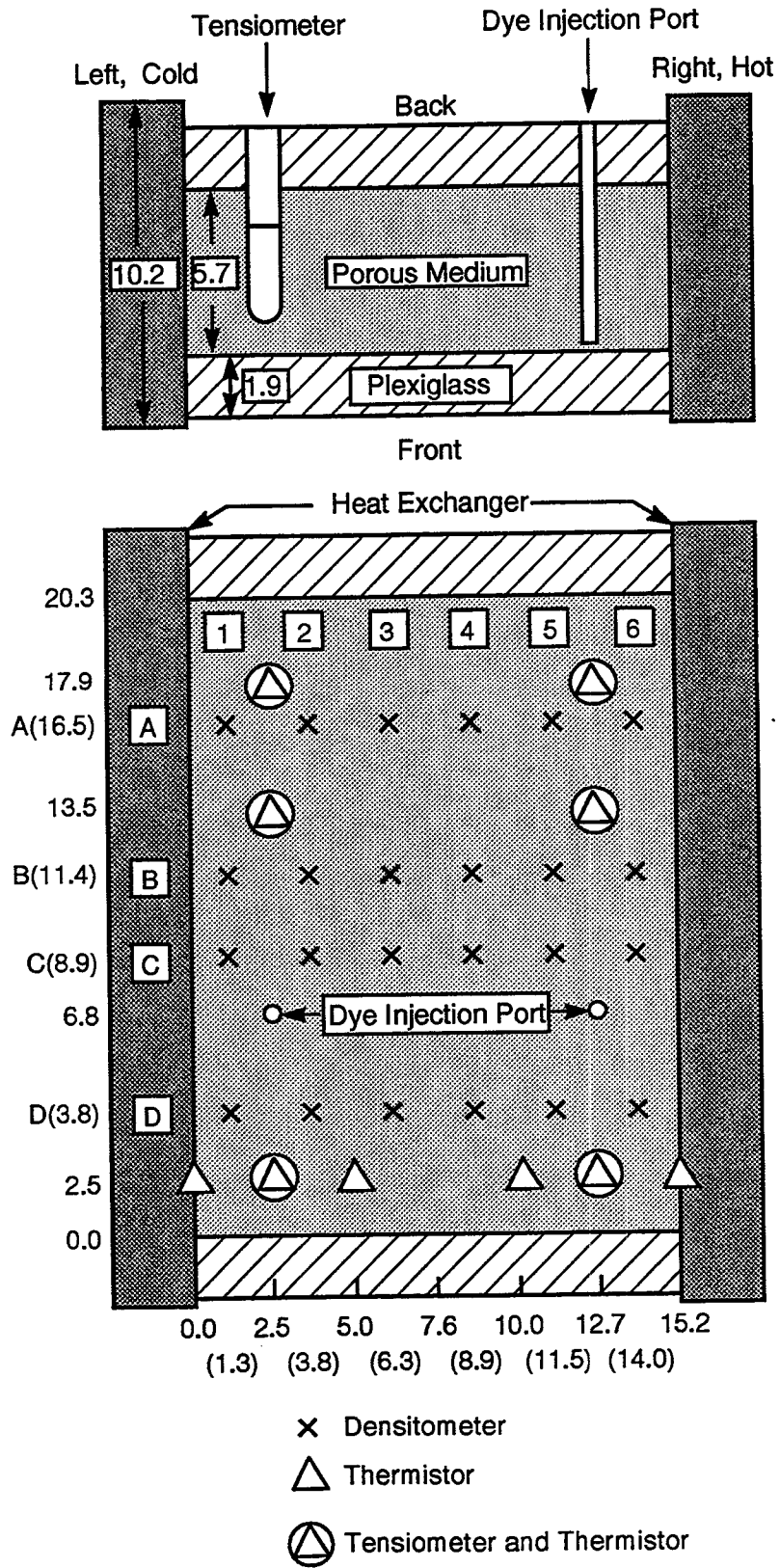


Figure 3-1. Test 12 experimental setup (all dimensions in cm)

- A less well-sorted medium was used to establish a less nonlinear characteristic or retention curve (capillary pressure versus liquid saturation) to be more representative of a homogeneous unconsolidated medium
- Smaller sized particles were used to decrease the saturated permeability of the medium in order to accentuate the dryout zone
- The temperature of the heated boundary was increased to 90 °C to increase the thermal driving force for vaporization and vapor flow in order to accentuate the dryout zone
- The simulated fracture was eliminated because its effects (e.g., inhibiting liquid flow across the fracture) were not of interest in this study, which focused on the development of a highly saturated zone and associated dryout zone

### 3.4 EXPERIMENTAL RESULTS

Both tests were conducted for approximately 200 days consisting of five distinct phases: (i) an ambient settling phase of 10–15 days; (ii) a heating phase of 85–100 days; (iii) a second ambient settling phase of 15–20 days; (iv) a drying phase of 15–20 days; and (v) a saturating phase of 15–20 days. The initial ambient settling phase allowed the liquid water to redistribute under the influence of gravity, and was also used to setup and test instrumentation. In order to achieve an approximately uniform initial saturation distribution, the water and medium were mixed prior to packing in the enclosure. During the heating period, the heat exchangers were maintained at the desired temperatures (20 and 60 °C for test 6, and 20 and 90 °C for test 12). A second ambient cooling period followed the heating period. The medium in test 12 was then dried by heating both heat exchangers to 90 °C and passing dry nitrogen gas through the medium. The flow rate of nitrogen was controlled at a low rate so that the solid medium would not be disturbed or redistributed. The final phase of the tests consisted of introducing liquid water into the bottom of the enclosure at a sufficiently low rate in order to saturate the medium without disturbing it. Gamma-ray densitometer measurements were taken during the drying and saturating phases in order to calibrate gamma-ray measurements taken during the heating phase.

An approximately linear temperature profile was established horizontally across the largest dimension of the enclosure in each test, thereby creating the thermal driving force for vaporization, vapor flow, condensation, and liquid flow. As a result, the observations were primarily one-dimensional (1D) in the horizontal direction. Experimental parameters were measured with a gamma-ray densitometer, porous cup tensiometers, thermistors, and by visual observation aided with periodically injected dye. In both experiments, liquid was observed to vaporize near the hot side, creating a dry zone, and condense in cooler regions, thereby increasing liquid saturation. In test 6, a thin near-vertical band of high saturation (called a wet band) was observed to develop on the cool side of the dryout zone, and liquid (containing dye) was observed to be advected from the cooler regions toward the heated boundary and into this region of increased saturation. The presence of a wet band was deduced from: (i) visual observations of the contrast of the medium through the front plexiglass wall (where wetter regions appeared darker and dryer regions appeared lighter) and (ii) gamma-ray densitometer measurements indicating an increased attenuation (hence increased liquid saturation) at the wet band and decreased attenuation (hence decreased liquid saturation) at measurement locations near the hot wall. In addition, the tensiometer data indicated that the hot side developed higher capillary/adsorptive pressures ( $P_{CAP/ADS}$ ). Following an interpretation of test 6 results (Manteufel et al., 1992a), it was hypothesized

that either thermal-chemical effects or hysteresis in the characteristic curves of the medium or both were responsible for the observed liquid flow from apparently lower to higher saturation values. As a result, test 12 was designed and executed in order to: (i) eliminate thermal-chemical effects; (ii) reproduce (if possible) the development of a wet band in front of the dryout zone; and (iii) assess the transport mechanisms.

### 3.4.1 Visual Observation

In test 6, visual observations (without the aid of dye) indicated that a dry zone developed near the hot side, and a nearly vertical wet band developed in front of the dry zone. The medium near the hot wall was visually observed to lighten, which was interpreted as the lower local liquid saturation. The dry zone was observed to be larger near the bottom and narrower at the top of the apparatus. Just to the left (or cool side) of the dry zone, a near-vertical band was visually observed to be darker than the surrounding medium, and this was interpreted that the local liquid saturation increased. The wet band appeared thinner ( $\sim 0.5$  cm) and lighter near the top, while wider ( $\sim 1$  cm) and darker near the bottom of the medium. Hence, based on visual observations, a dry zone and a near-vertical wet band were interpreted to have developed in test 6. In test 12, the anticipated dry zone was observed visually, but the anticipated wet band was not (however, the horizontal gamma-ray densitometer scans suggest a zone of increased liquid saturation at  $\sim 1$  cm).

Visual information was also obtained by periodically injecting dye through the dye injection tubes (see Figure 3-1) and then photographing the dye as it moved with the liquid in the medium. It is assumed that the dye did not affect the liquid flow, but only allowed the flow to be visualized. Dye was injected into test 6 during the 63rd day of heating and was observed for approximately 7 days. Dye injected on the left side (near the cold wall) spread due to diffusion and had a small downward bulk movement. The dye on the right side (near the hot wall) diffused also, but it displayed a distinguishable bulk movement to the right (into a region of high liquid saturation) and then downward (within the region of high saturation).

In test 12, dye was injected at the same locations as in test 6, but with faster liquid velocities than observed in test 6 (the difference in liquid velocities is related to the capillary diffusivity and is discussed in the analyses section). Within minutes after injection, the dye on the right side was observed to be advected towards the hot wall. In comparison, the dye on the left side exhibited primarily transport by diffusion, but also some bulk advection toward the hot side.

### 3.4.2 Thermistors

Temperatures were measured at ten locations in test 12 (see Figure 3-1 for locations) and the results are plotted in Figure 3-2. On day 6, the two vertical heat exchangers were set to  $20$  °C, and on day 12 the heater was activated, raising the temperature of the right heat exchanger to  $90$  °C. Within less than one day, a steady-state temperature profile was established throughout the apparatus, indicating the insensitivity of heat transfer to fluid flow. Temperature scans for test 12 are plotted for five horizontal locations in Figure 3-2. From thermistors installed inside the tensiometers, the vertical temperature gradient was assessed to be approximately  $0.09$  °C/cm near the hot side and approximately  $0.026$  °C/cm near the cold side. In comparison, the horizontal temperature gradient was approximately  $4.47$  °C/cm; hence the temperature profile is considered to be primarily horizontally oriented.

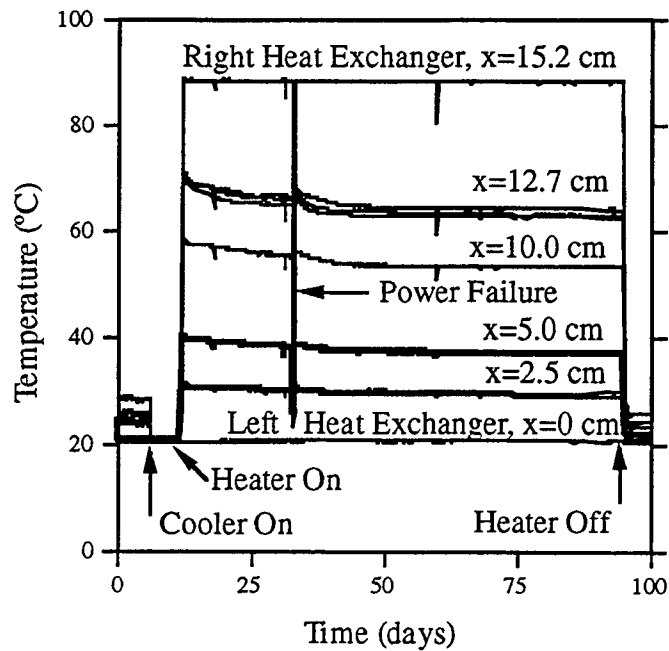


Figure 3-2. Temperature measurements in test 12

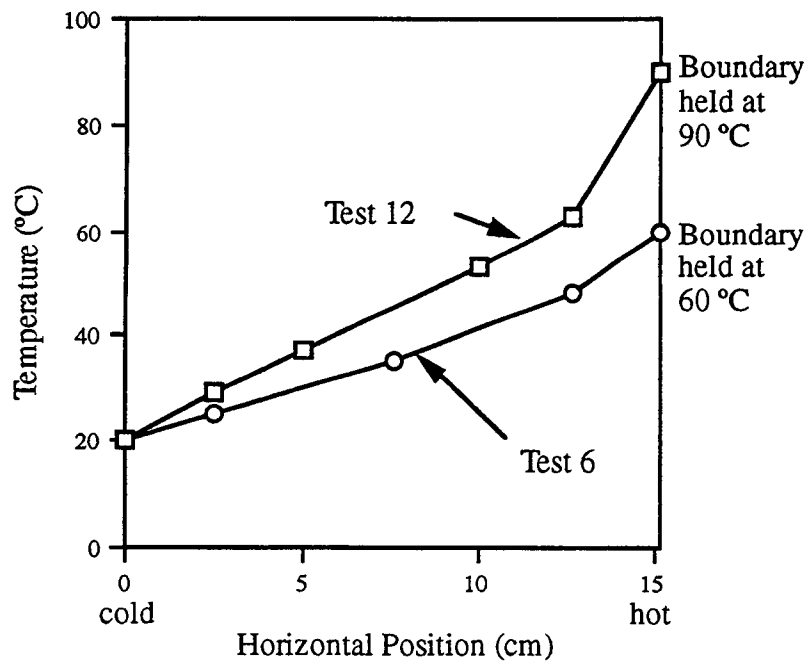


Figure 3-3. Steady-state, horizontal temperature profiles

The horizontal temperature profiles for tests 6 and 12 are compared in Figure 3-3. As previously noted, the hot-side temperature was increased from 60 to 90 °C from test 6 to 12. The horizontal temperature profile for both tests is approximately linear throughout the domain with the exception of a sharper temperature drop near the hot side wall.

### 3.4.3 Tensiometers

Tensiometer measurements are plotted in Figure 3-4 for test 12. The general trend of increasing capillary/adsorption pressure,  $P_{CAP/ADS}$ , near the hot side is evident. Throughout the tests, the tensiometers near the hot side experienced higher  $P_{CAP/ADS}$ , indicating dryout. As illustrated, the hot side tensiometers experienced higher  $P_{CAP/ADS}$  and dried out quickly. Despite attempts to refill the tensiometers, the three tensiometers on the hot side failed to yield meaningful results, except that they experienced high values of  $P_{CAP/ADS}$ . The cold-side tensiometers did not dry out and yielded much better results. A trend in test 12 was that the  $P_{CAP/ADS}$  rapidly decreased on the cold side and rapidly increased on the hot side after the heater was turned on. If one assumes that  $P_{CAP/ADS}$  is proportional to surface tension ( $\sigma$ ), then changes in  $\sigma$  should result in changes in  $P_{CAP/ADS}$ . By increasing the temperature on the hot side,  $\sigma$  would decrease, thereby creating a gradient in  $P_{CAP/ADS}$  that would move liquid from the hot to the cold side (this is discussed later). The time scale for liquid redistribution due to temperature-dependent surface tension appears to be small so that the redistribution process occurred quickly (within the first day). It appears that the liquid redistributed by accumulating on the cold side, hence increasing the liquid saturation and decreasing  $P_{CAP/ADS}$ .

### 3.4.4 Gamma-ray Densitometer

A  $^{137}\text{Cs}$  gamma-ray source was used to produce a collimated beam (2.5-mm diameter), which was aimed at the locations indicated in Figure 3-1. The attenuation of the gamma-ray beam through the test medium was measured using the detector. The number of counts was then used to infer the local liquid saturation using the attenuation principle:

$$I = I_d \exp(-\mu_w \phi S_L) \quad (3-1)$$

Equation (3-1) can be solved for the saturation,  $S_L$ . Typically, the initial saturation is known so that liquid saturation can be expressed as a function of the corresponding initial counts according to:

$$S_L = 0.65 + \frac{1}{\mu_w \phi} \ln \left[ \frac{I_{0.65}}{I} \right] \quad (3-2)$$

In Figure 3-5, the liquid saturation values are plotted at eight locations during the execution of test 12. The gamma-ray measurements at the fixed locations do not indicate the presence of a wet band. Test 12 measurements do not appear to have a vertical trend where measurements in each column (e.g., columns 1 and 6) are similar regardless of the row (e.g., A or D). However, the differences between column measurements are much more pronounced between the hot and cold side (i.e., between columns 1 and 6). Soon after increasing the temperature of the right boundary, the cold side measurements indicated a rapid increase in liquid saturation (from 0.5 to 0.58), which remained constant throughout the duration of the test. At the same time, the hot-side measurements indicated a rapid decrease in liquid saturation (from 0.5 to 0.38) which also remained constant throughout the remainder of the test. After the heating

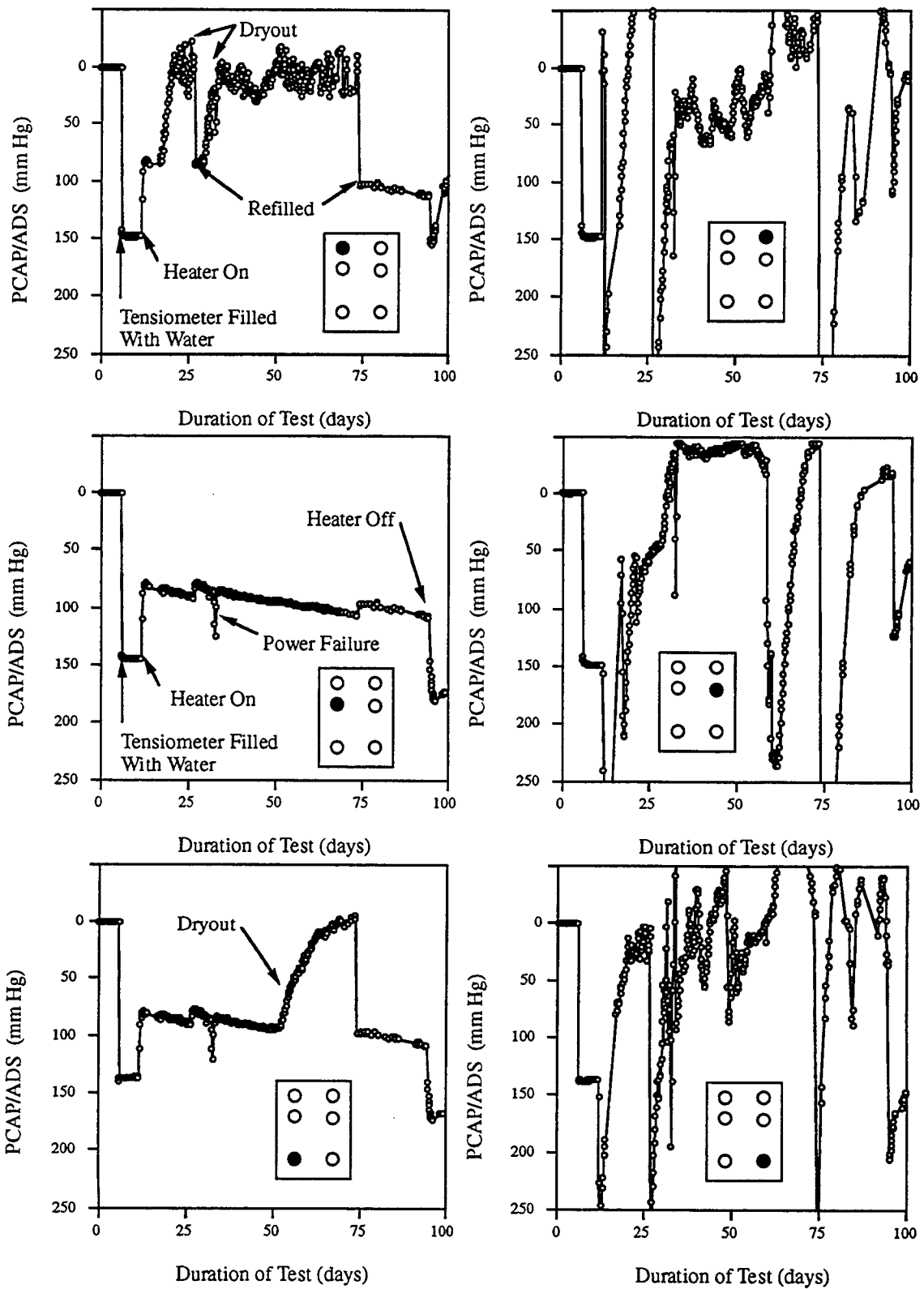


Figure 3-4. Tensiometer measurements in test 12 (insets show measurement locations)

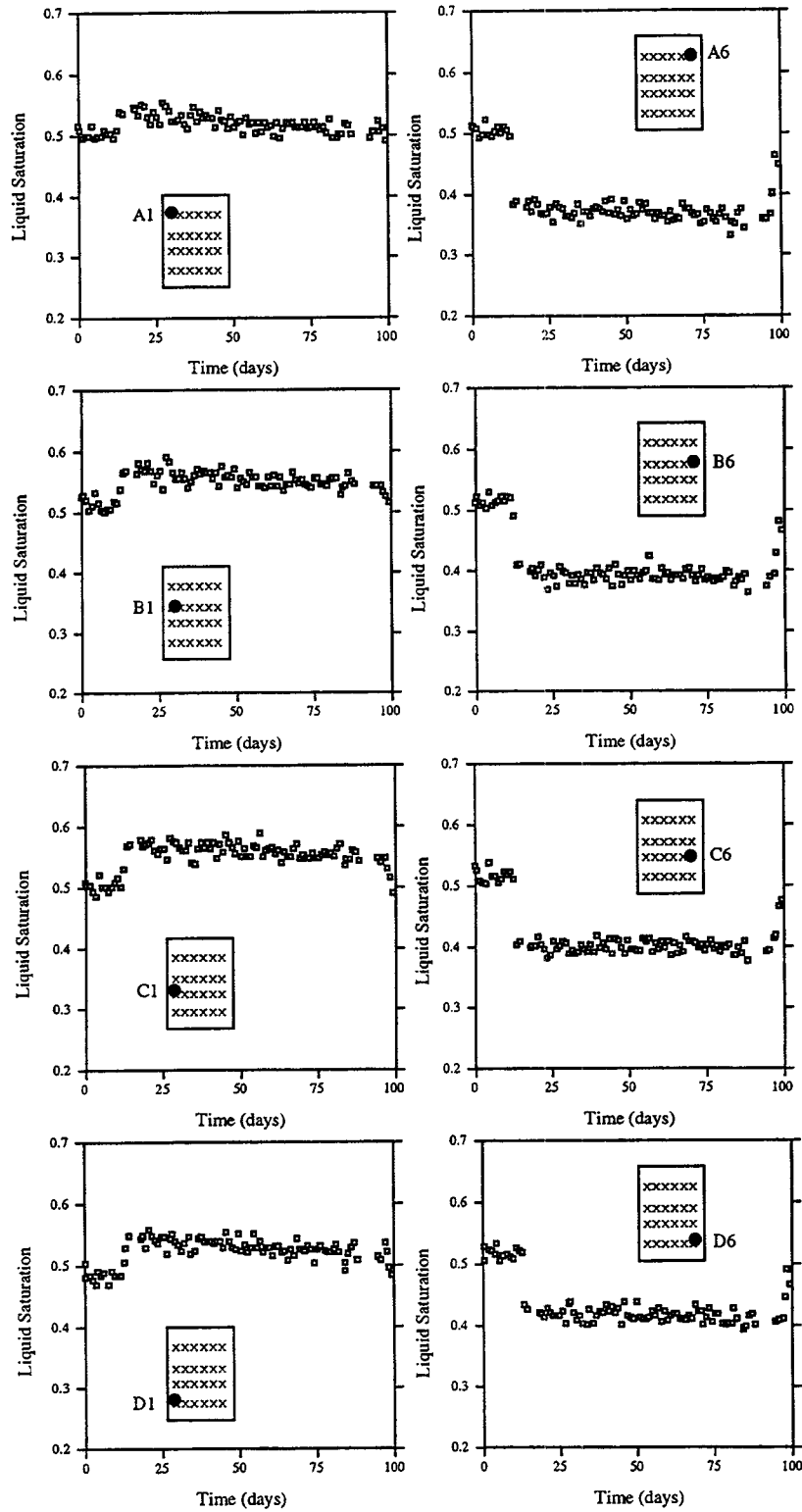


Figure 3-5. Liquid saturation based on gamma-ray densitometer measurements in test 12 (insets show measurement locations)

phase, the liquid saturation values returned to the ambient condition of 0.5 liquid saturation.

Additional gamma-ray data along horizontal scans were recorded in test 12 but not in test 6. Scans recorded during two periods of test 12 are illustrated in Figure 3-6. The scans were performed midway through the heating phase (~60th day) and near the end of the cooling phase (~105th day). The horizontal scans were recorded at three elevations (levels B, C, and D). The scans taken after heating indicate a gradual decrease (from left to right) in liquid saturation over most of the medium, with a sharper decrease near the hot side. From these measurements, the dryout zone is noticeable near the hot side. There appears to be a slight buildup of saturation ( $\Delta S_L \sim 0.05$ ) near the dryout zone, indicating the presence of a wet band. This region of increased saturation was not visibly distinguishable from observations through the front plexiglass wall (where in test 6 it was distinguishable), hence the horizontal gamma-ray scans are the only data indicating this phenomenon. As illustrated in the scans taken after heating was discontinued, liquid redistributed throughout the medium to an ambient level of 0.5 liquid saturation. The only noticeable exception is near the hot side where the liquid saturation only partially recovered to the initial 0.5 saturation level.

### 3.5 ANALYSES

A 1D mathematical model was developed for the conservation of water in a nonisothermal, partially saturated ( $S_L < 1.0$ ) porous medium that includes liquid advection and vapor diffusion. The governing equation is presented here:

$$\rho_L \phi \frac{\partial S_L}{\partial t} = \frac{\partial}{\partial x} \left\{ \frac{\rho_L k_{SAT} k_{REL,L}}{\mu_L} \left[ \left[ \frac{-dP_{CAP/ADS}}{dS_L} \right] \frac{\partial S_L}{\partial x} + \frac{P_{CAP/ADS}}{\sigma} \left[ \frac{-d\sigma}{dT} \right] \frac{\partial T}{\partial x} \right] \right\} \quad (3-3)$$

$$+ \frac{\partial}{\partial x} \left[ \eta D \left[ \frac{d\rho_{W,G}}{dT} \frac{\partial T}{\partial x} + \frac{d\rho_{W,G}}{dS_L} \frac{\partial S_L}{\partial x} \right] \right]$$

In Eq. (3-3), the transfer mechanisms have been related to either saturation or temperature gradients, which are useful because saturation typically is the independent variable of interest, and temperature is typically a known quantity (or an experimentally controlled dependent variable). Three aspects of the theoretical model are discussed below: (i) capillary diffusivity; (ii) liquid redistribution due to temperature-dependent surface tension; and (iii) the condensation/vaporization source term for liquid water.

#### 3.5.1 Capillary Diffusivity

The capillary diffusivity can be identified in Eq. (3-3) (which is consistent with the literature) to be:

$$D_C = \frac{k_{SAT} k_{REL,L}}{\phi \mu_L} \left[ \frac{-d P_{CAP/ADS}}{d S_L} \right] \quad (3-4)$$

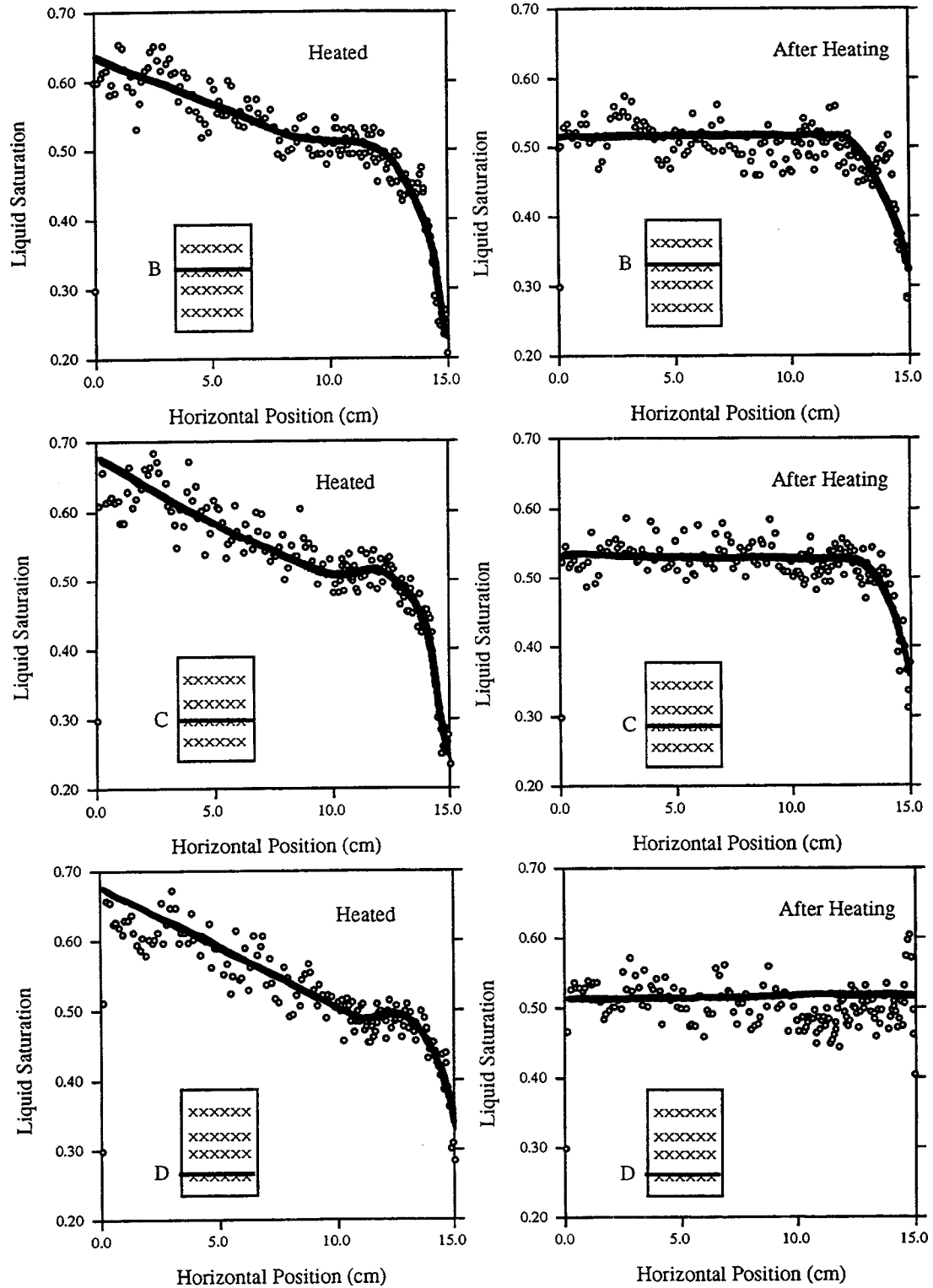


Figure 3-6. Horizontal liquid saturation profiles based on gamma-ray densitometer measurements in test 12 (insets show measurement locations)

The diffusivity can be used to indicate how quickly the liquid saturation can respond to changes in the system (such as changes in saturation at the boundary). For test 12, the capillary diffusivity was estimated to be  $D_C \sim 10^{-6} \text{ m}^2/\text{s}$  (near  $S_L = 0.5$  and decreases slightly with decreasing  $S_L$ ), while for test 6 it was estimated to be at least an order of magnitude smaller. The difference in  $D_C$  is due primarily to differences in  $dP_{CAP/ADS}/dS_L$ .

The capillary time scale for liquid advection is given by the familiar equation:

$$t_C \sim \frac{L^2}{D_C} \quad (3-5)$$

For test 12, the capillary time scale was estimated to be  $t_C \sim 6$  hours, while for test 6 it was  $t_C \sim 60$  hours (2.5 days). The permeability for test 6 was assessed to be comparable to that of test 12, which was  $k_{SAT} \sim 10^{-15} \text{ m}^2$ . The derivative of capillary/adsorptive pressure with respect to liquid saturation can be estimated from the retention curves illustrated in Figure 3-7 to be  $dP_{CAP/ADS}/dS_L \sim 5 \times 10^5 \text{ Pa}$  per 100 percent saturation for test 12 and  $dP_{CAP/ADS}/dS_L \sim 2 \times 10^4 \text{ Pa}$  per 100 percent saturation for test 6. This simple analysis helps explain the experimental observation that test 12 responded more rapidly to changes than did test 6. By comparison, the dye in test 6 was tracked from time of the injection for  $\sim 7$  days, while in test 12 it was tracked for  $\sim 1/3$  day (which is approximately one order of magnitude smaller). Hence, the capillary diffusivity and the capillary time scale have been identified in the mathematical model and assessed to be in qualitative agreement with the observation that test 12 responded faster than test 6.

### 3.5.2 Liquid Redistribution Due to Temperature-Dependent Surface Tension

One observation in test 12 was that liquid quickly redistributed (within  $\sim 1$  day) after the heater was turned on, thereby increasing the saturation on the cool side and decreasing the saturation on the hot side. One possible mechanism for this redistribution is that temperature-dependent surface tension pulled liquid from the hot side toward the cool side, because surface tension decreases with increasing temperature. At equilibrium (neglecting the influence of vaporization/condensation), the temperature gradient induces a gradient in  $P_{CAP/ADS}$ , which is balanced by a saturation gradient [from Eq. [(3-3)]:

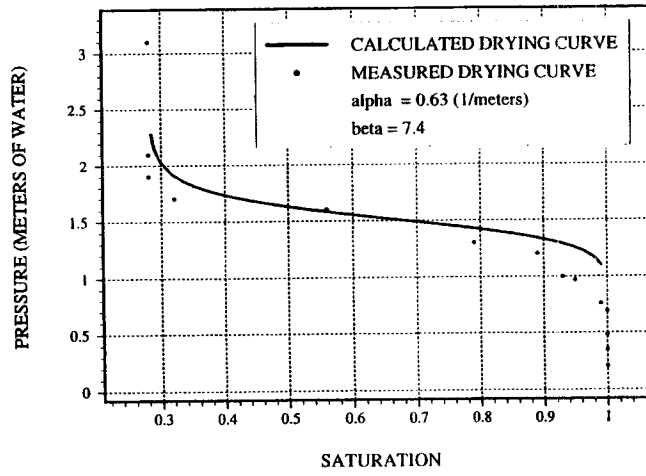
$$\left[ \frac{-dP_{CAP/ADS}}{dS_L} \right] \frac{\partial S_L}{\partial x} = - \frac{P_{CAP/ADS}}{\sigma} \left[ \frac{-d\sigma}{dT} \right] \frac{\partial T}{\partial x} \quad (3-6)$$

For small changes in  $x$ , Eq. (3-6) can be expressed as:

$$\Delta S_L \cong - \frac{\frac{1}{\sigma} \left[ \frac{-d\sigma}{dT} \right]}{\frac{1}{P_{CAP/ADS}} \left[ \frac{-d P_{CAP/ADS}}{d S_L} \right]} \Delta T \quad (3-7)$$

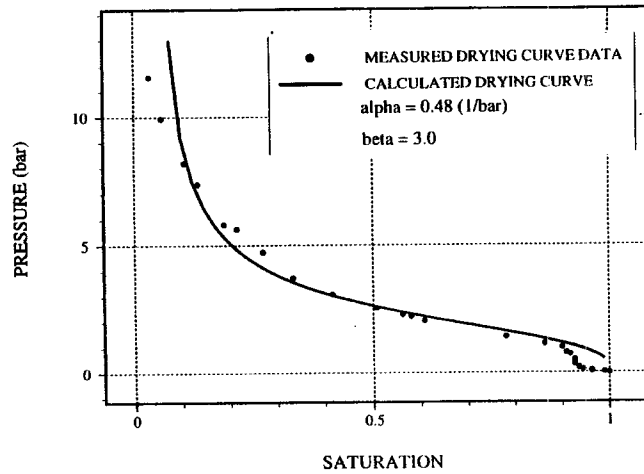
With  $\sigma \sim 0.073 \text{ N/m}$  and  $d\sigma/dT \sim 0.00017 \text{ N/(m-C)}$ , the imposed temperature gradient in test 12 ( $\Delta T \sim 70 \text{ }^\circ\text{C}$ ) leads to an assessment that the maximum change in saturation from the hot to cool side would be  $\Delta S_L \sim 0.07$ , which is less than the experimentally observed value of  $\Delta S_L \sim 0.2$ . Nevertheless, the direction and approximate magnitude of the liquid redistribution predicted by the theoretical model

### RETENTION CURVE - GLASS BEADS



(a)

### RETENTION CURVE - 44 MICRON



(b)

Figure 3-7. Characteristic curves for the porous medium used in: (a) test 6 and (b) test 12

(due only to temperature-dependent surface tension) is in qualitative agreement with the experimental observations.

### 3.5.3 Condensation/Vaporization Source Term for Liquid Water

The second term on the right-hand side of Eq. (3-3) represents a source/sink term of liquid water due to vapor flow with condensation/vaporization. When a medium is subjected to a temperature gradient, liquid should vaporize in the regions of higher temperature (which represents a sink for liquid water) and condense in regions of lower temperature (which represents a source for liquid water). The distribution of condensation/vaporization can be assessed where two groups of terms are present in the second term on the right-hand side of Eq. (3-3) due to the dependence on temperature (through the vapor pressure and Claperyon equation) and the dependence on saturation (through the capillary/adsorptive pressure and the Kelvin equation). The temperature gradient is considered the primary driving mechanism for vapor flow, and the gradient in saturation becomes important only as  $P_{CAP/ADS}$  becomes large (i.e., the medium becomes dry). In a dry medium, the relative humidity can be less than 100 percent due to vapor pressure lowering, as predicted by the Kelvin equation. Outside the dryout zone, the condensation/vaporization source term can be approximated as:

$$Q_{VIC} \cong \frac{\partial}{\partial x} \left[ \eta D \frac{h_{LG} (M_w)^2 P_V}{R^2 T^3} \frac{\partial T}{\partial x} \right] \quad (3-8)$$

In Eq. (3-8), three terms are noted to be temperature dependent (hence spatially dependent):  $\eta$ ,  $T^3$ , and  $P_V$ . In Figure 3-8, the temperature dependence of the terms is compared, where it can be noted that the  $P_V$  is the most temperature-dependent term. Hence, the other terms can be considered approximately constant and removed outside the spatial derivative, leading to a simplified model for  $Q_{VIC}$ :

$$Q_{VIC} \cong \frac{\eta D (h_{LG})^2 (M_w)^3 P_V}{R^3 T^5} \left[ \frac{\partial T}{\partial x} \right]^2 \quad (3-9)$$

From Eq. (3-9), the condensation source term is proportional to the temperature gradient squared and proportional to the vapor pressure. Hence, in an experiment, the importance of vaporization/condensation (i.e., vapor flow) can be increased by increasing the temperature gradient. The vapor pressure is strongly temperature dependent [i.e.,  $P_V \sim \exp(-1/T)$ ], as illustrated in Figure 3-8. Liquid condensation occurs over a fairly broad zone near the highest temperature. In comparison, the zone of vaporization is small and located at the point of maximum temperature. As time progresses, vaporization removes enough liquid to create a dryout zone (within which vapor pressure lowering may be important). With this model, the region of vaporization is predicted to be small and located near the region of maximum temperature, and the region of condensation is much larger and strongest near the region of vaporization, as illustrated in Figure 3-9. Because the region of maximum condensation is located to the cool side of the vaporization, it should tend to increase locally the liquid saturation (i.e., create a wet band) as observed in the tests. Hence, the model predicts a distribution of  $Q_{VIC}$ , which accentuates the development of a wet band and is in qualitative agreement with the experimental observations.

## 3.6 CONCLUSIONS

A laboratory study of thermally driven liquid redistribution in a partially saturated porous medium has been conducted and reported herein. The experimental setup consisted of a sealed rectangular

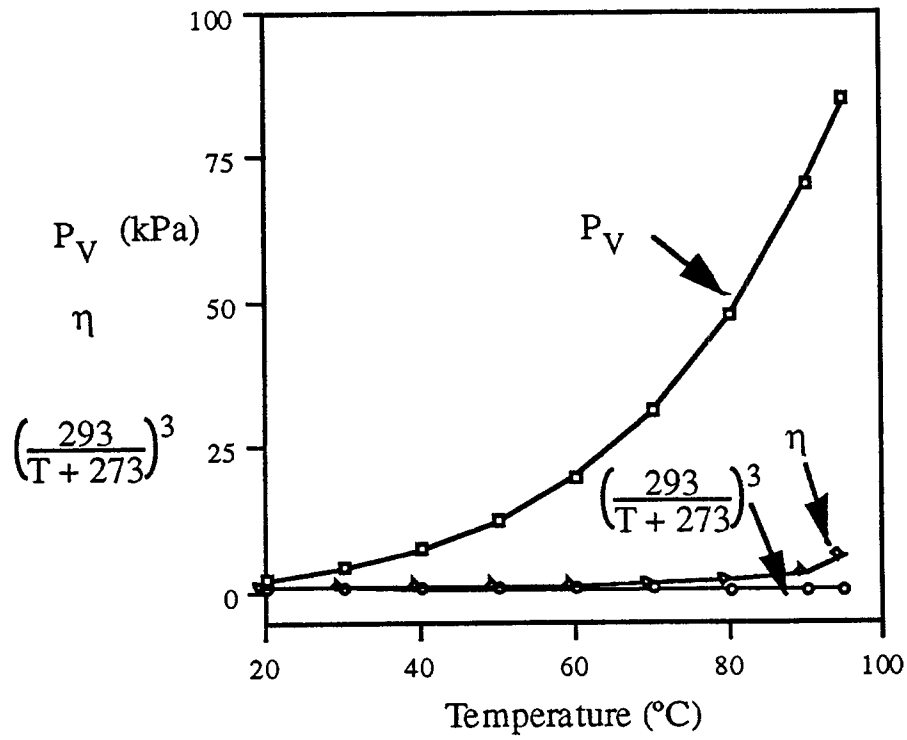


Figure 3-8. Comparison of the temperature dependence of  $P_v$ ,  $\eta$ , and  $[293/(T+273)]^3$

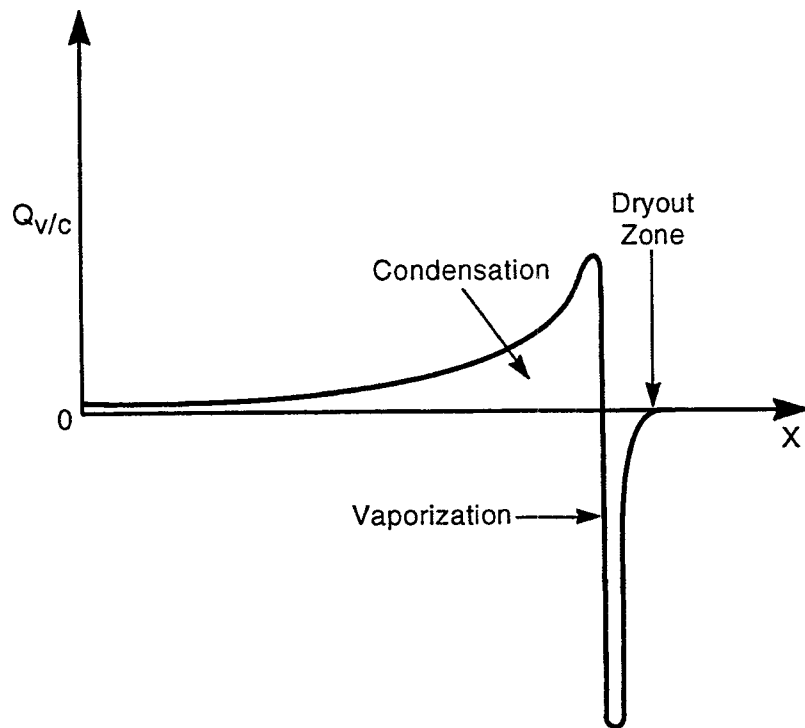


Figure 3-9. Illustration of  $Q_{v/c}$  showing the condensation, vaporization, and dryout zones

enclosure subjected to a steady-state temperature profile across the largest enclosure dimension. The experimental results indicate that:

- Vaporization, vapor flow, condensation, and liquid advection were shown to be important mass-transfer mechanisms for water in a nonisothermal porous medium
- A relatively small dryout zone developed near the hot side in both tests
- The local liquid saturation increased throughout the major portion of the porous volume of the experiment due to the displacement of liquid in the dryout zone
- The liquid saturation profile was predominately 1D (due to the imposed temperature profile being predominately 1D)
- The largest gradients in liquid saturation occurred near the dryout zone
- A wet band developed in front of the dryout zone and was more pronounced in test 6, which used glass beads (instead of alumina powder as in test 12) for the porous medium and was subjected to a smaller temperature gradient

A simplified mathematical model was developed and used to assess the effect of capillary diffusivity, temperature-dependent surface tension, and the condensation/vaporization source term. Conclusions from the theoretical analyses include:

- The capillary diffusivity and time scale were determined and found to be in qualitative agreement with the experimental observation that test 12 responded more quickly than test 6
- A model for liquid redistribution due to temperature-dependent surface tension was developed and found to be in qualitative agreement with experimental observations
- A model for the condensation/vaporization source term for liquid water has been developed and found to be in qualitative agreement with the experimental observation of the development of a wet band

### **3.7 ASSESSMENT OF PROGRESS**

Information regarding the transience of the thermal and liquid regimes at a HLW repository is critical if the performance of a HLW repository is to be understood and predicted. The repository temperatures and saturations will be a function of numerous physical properties, both of the GS and the EBS. The Thermohydrology Research Project has identified processes that appear to dominate distribution of heat and water at the repository. Determination of the extent and duration of dryout proximal to the emplaced canisters and the nature of the timing of reflux of water to the canisters, however, have not been accomplished.

Dimensional analysis has provided a methodology with which to assess the significance of processes observed in the laboratory-scale experiments and in other larger-scale experiments. This analysis has been important to the Thermohydrology Research Project and the U.S. Department of Energy

(DOE) in identifying which processes are important for a particular setting and scale, either experiment or repository.

The DOE has used the numerical codes TOUGH and VTOUGH to model two-phase flow through fractured porous media proximal to heat-generating HLW. VTOUGH has been used in the Thermohydrology Research Project to simulate processes observed in the laboratory-scale experiments. This exercise has provided an opportunity to independently assess the ability of VTOUGH to model accurately the thermal processes observed in the laboratory. Although reasonable simulations of some of the processes observed in the laboratory-scale experiments have been accomplished, a definitive assessment of the ability of the code to replicate all feasible processes to be expected at the repository (the subject of a KTU) has not been completed. Preliminary results were presented in Green et al. (1992b); subsequent results will be presented in future progress reports.

### 3.8 FUTURE PLANS

A second densitometer should be operational at the beginning of the next reporting period. This densitometer is oriented in the x-y plane, and experiments conducted using it will provide an opportunity to assess concepts developed in the dimensional analysis that currently cannot be assessed using the x-z oriented densitometer. The mechanism of water refluxing toward the heat source has been identified as an important transport mechanism. Additional experiments will investigate the nature of refluxing water resulting from condensation and gravity drainage. The effect of heat-pipe-type mechanisms on refluxing will also be assessed. These phenomena and mechanisms will also be assessed using VTOUGH, a two-phase heat and fluid transport code used by the DOE to model these types of processes.

### 3.9 NOMENCLATURE

$D$	effective porous medium diffusion coefficient = $\tau\phi S_G D_{WA,G}$ ( $m^2/s$ )
$D_C$	capillary diffusivity ( $m^2/s$ )
$D_{WA,G}$	diffusion coefficient of water vapor in air ( $m^2/s$ )
$g$	gravitational constant ( $9.81 m/s^2$ )
$h_{LG}$	enthalpy of vaporization ( $J/kg$ )
$I$	counts in 60 s time period
$I_d$	counts in 60 s time period for dry medium ( $S_L = 0$ )
$I_{0.65}$	counts in 60 s time period for medium with $S_L = 0.65$
$\bar{j}_{W,G}$	diffusive flux of water vapor in the gas [ $kg/(m^2 \cdot s)$ ]
$k_{SAT}$	saturated permeability ( $m^2$ )
$k_{REL,L}$	relative liquid permeability (dimensionless)
$M_W$	molecular weight of water (18.02 kg/kgmole)
$P$	total gas pressure ( $N/m^2$ )
$P_V$	vapor pressure of water ( $N/m^2$ )
$P_{W,G}$	partial pressure of water vapor in the gas ( $N/m^2$ )
$P_{CAP/ADS}$	capillary/adsorptive pressure ( $N/m^2$ )
$R$	ideal gas constant [8314 J/(kgmole-K)]
$R_{VP}$	relative humidity (dimensionless)
$S_G$	gas saturation ( $m^3$ gas/ $m^3$ void)
$S_L$	liquid saturation ( $m^3$ liquid/ $m^3$ void)
$t$	time (s)

$t_C$	capillary time scale (s)
$T$	temperature (C)
$T_0$	reference temperature (C)
$\bar{v}_L$	liquid (Darcy) velocity (m/s)
$\alpha$	van Genuchten parameters (1/m)
$\beta$	van Genuchten parameters (dimensionless)
$\eta$	advective enhancement factor (dimensionless)
$\sigma$	surface tension (N/m)
$\sigma_0$	reference surface tension (N/m)
$\rho_L$	liquid density (kg/m <sup>3</sup> )
$\rho_{W,G}$	density of water vapor in the gas (kg/m <sup>3</sup> )
$\phi$	porosity (m <sup>3</sup> void/ m <sup>3</sup> medium)
$\mu_L$	liquid viscosity [kg/(m-s)]
$\mu_w$	linear attenuation coefficient for liquid water (1/cm)
$\tau$	tortuosity (dimensionless)

### 3.10 REFERENCES

- Green, R.T., R.D. Manteufel, F.T. Dodge, and S.J. Svedeman. 1992a. *Theoretical and Experimental Investigation of Thermohydrologic Processes in a Partially Saturated, Fractured Porous Medium*. NUREG/CR-6026. Washington, DC: U.S. Nuclear Regulatory Commission.
- Green, R.T., R.D. Manteufel, and F.T. Dodge. 1992b. *NRC High-Level Radioactive Waste Research at CNWRA, July 1 through December 31, 1992*. CNWRA 92-02S. San Antonio, TX: Center for Nuclear Waste Regulatory Analyses: 3-1 to 3-22.
- Manteufel, R.D., and R.T. Green. 1992. *NRC High-Level Radioactive Waste Research at CNWRA, January 1 through June 30, 1992*. CNWRA 92-01S. San Antonio, TX: Center for Nuclear Waste Regulatory Analyses: 3-1 to 3-18.
- Manteufel, R.D., R.T. Green, F.T. Dodge, and S.J. Svedeman. 1992a. An experimental investigation of two-phase, two-component, nonisothermal flow in a porous medium with a simulated fracture. I. Catton, ed. *Heat and Mass Transfer in Porous Media*. HTD-216. New York: American Society of Mechanical Engineers: 9-18.
- Nataraja, M.S., and T. Brandshaug. 1992. *Staff Technical Position on Geologic Repository Operations Area Underground Facility Design - Thermal Loads*. NUREG-1466. Washington, DC: U.S. Nuclear Regulatory Commission.
- U.S. Nuclear Regulatory Commission. 1993. *Draft License Application Review Plan for the Review of a License Application for a Geologic Repository for Spent Nuclear Fuel on High-Level Radioactive Waste, Yucca Mountain Site, Nevada (LARP)*. NUREG-1323. Washington, DC: U.S. Nuclear Regulatory Commission.

## 4 SEISMIC ROCK MECHANICS

by *Simon M. Hsiung, Mikko P. Ahola, Amitava Ghosh, and Asadul H. Chowdhury*

*Investigators: Mikko P. Ahola, Asadul H. Chowdhury, Amitava Ghosh, Simon M. Hsiung, Randall D. Manteufel (CNWRA); Daniel D. Kana (SwRI)*

*NRC Project Officer: Jacob Philip*

### 4.1 TECHNICAL OBJECTIVES

The technical objective of the Seismic Rock Mechanics Research Project is to conduct laboratory, field, and theoretical analyses to develop techniques that could be used to predict the response of near-field jointed rock mass at the proposed high-level waste (HLW) repository at Yucca Mountain, Nevada, when it is subjected to repetitive seismic (including earthquakes and nuclear explosions at the Nevada Test Site) and thermal conditions. The near-field response includes the response both at the emplacement borehole and the emplacement drift scales. These analyses are designed to develop a better understanding of near-field rock mass behavior under repetitive seismic and thermally induced loads and to obtain fundamental data on the seismic and thermal effects that are important to validate predictive models and verify computer codes for review of repository design [10 CFR 60.131(b)(1), 60.133(e)(1), 60.133(e)(2), 60.133(i), and 60.134], waste retrievability [10 CFR 60.111, 60.133(c), 60.133(e)(1), 60.133(i), and 60.134], and post-closure performance assessment [10 CFR 60.112, 60.113, 60.122(c)(5), 60.122(c)(12), 60.122(c)(14), and 60.122(c)(23)]. Many factors controlling the effect of seismic and thermally induced loads on the near-field jointed rock mass behavior of the proposed repository are poorly understood. The problem is further complicated when the potential coupled effects of thermal loads are considered.

Information developed within the Seismic Rock Mechanics Research Project will be used to support specific portions of the License Application Review Plan (LARP). Detailed laboratory and field studies of stability of underground openings (including vertical emplacement boreholes, if adopted as a concept for waste emplacement) will provide a basis for development and implementation of portions of the LARP relating to Section 4.3, Assessment of Compliance with Design Criteria for Shafts and Ramps, Section 4.4, Assessment of Compliance with Design Criteria for Underground Facility, Section 4.5.2, Assessment of Integrated GROA Compliance with the Performance Objectives: Retrievability of Waste, and Section 5.3, Assessment of Compliance with the Design Criteria for the Post-Closure Features of the Underground Facility. Knowledge regarding prediction of long-term stability of vertical emplacement boreholes and emplacement drifts (for in-drift emplacement) and potential near-field fluid flow resulting from the coupled effects (including repetitive seismic effects) will support implementation of Section 5.4, Assessment of Compliance with the Engineered Barrier System (EBS) Performance Objectives. Further, knowledge of effects of repetitive seismic and thermal loads (including long-term deterioration of underground openings in the emplacement area) on near-field hydraulic conductivity changes and on the potential to create preferential pathways that may compromise the waste isolation capability of the proposed repository will provide input for Section 6.0, Overall System Performance Assessment.

The Compliance Determination Strategies (CDS) for the LARP sections noted above have been identified as types 4 and 5. It is clear that the Seismic Rock Mechanics Research Project is important in addressing uncertainties raised in CDS 4.3, 4.4, 4.5.2, 5.3, 5.4, and 6.1, requiring an independent review capability for assessing Key Technical Uncertainties (KTU) that pose a high risk of noncompliance

with performance objectives of 10 CFR Part 60. Specific KTU topics that will be addressed by the Seismic Rock Mechanics Research Project include the ability to predict the effects of thermal and repetitive seismic loads on stability of emplacement drifts and emplacement boreholes that may have implication on the performance of the EBS, retrievability of waste, and long-term isolation of waste. For instance, it has already been determined through field experimental studies of the Seismic Rock Mechanics Research Project that repetitive, lower magnitude seismic events can have a much greater influence on the degree of damage to underground openings than a single large magnitude event.

The Seismic Rock Mechanics Research Project addresses needs identified by the Office of Nuclear Material Safety and Safeguards (NMSS) of the U.S. Nuclear Regulatory Commission (NRC) concerning development of independent capabilities for assessing impacts of repetitive seismic loads on repository design and performance and predicting coupled thermal-mechanical-hydrological (TMH) effects to near-field repository performance. Specific NRC research needs that may be met through this project include: attainment of a better understanding of dynamic response of a jointed rock mass, evaluation of existing rock joint constitutive models, evaluation of scale effects such that laboratory results can be applied to the field, assessment of potential effects of repetitive seismic loads on change of hydrological properties, identification, through a better understanding, of coupled TMH processes that are relevant to the unsaturated environment, and verification of a selected computer code that will be used in the LARP for seismic analyses and prediction of coupled TMH effects on near-field rock mass response.

The Seismic Rock Mechanics Research Project is an integrated effort combining expertise in rock mechanics, mining engineering, engineering geology, and hydrology. The key areas of integration between seismic, thermohydrology, Integrated Waste Package Experiments (IWPE), and Performance Assessment (PA) research projects are in the prediction of opening stability and changes in near-field hydraulic conductivity. The seismic and thermohydrology projects will complement each other to develop techniques to predict near-field hydraulic conductivity, and flow and transport environment taking into account matrix flow and stress-dependent fracture flow under thermal conditions. The seismic research will assist in evaluating the mechanical loads that may cause stress corrosion or structural failure of waste packages, which is a component of EBS evaluations. The combined research and modeling efforts of seismic and thermohydrology projects will be useful to evaluate the presence of aqueous environments near the waste package for IWPE research and the near-field flow and transport environment for the PA research.

Research within the Seismic Rock Mechanics Research Project includes characterization of dynamic behavior of single-joint rock in the laboratory using tuff specimens from Apache Leap near Superior, Arizona, scale model experiment of a rock mass, field studies on the effects of mining-induced seismicity on the rock mass near underground openings and local hydrology, collection of ground shock data, participation in the DEvelopment of COupled models and their VALidation against EXperiments (DECOVALEX) program for evaluation of computer codes that are capable of simulating coupled TMH processes, and laboratory studies to understand and identify important thermally induced coupled processes in an unsaturated environment. Earlier reports in this series documenting progress to date include: Hsiung, et al. (1993a; 1993b); Hsiung and Chowdhury (1992); Hsiung et al. (1992); Hsiung and Chowdhury (1991); Kana, et al. (1991); Kana et al. (1990); Brady et al. (1990); Brandshaug et al. (1990). This report describes the results of activities in the Seismic Rock Mechanics Research Project during the first half of 1993.

## 4.2 SIGNIFICANT TECHNICAL ACCOMPLISHMENTS

### 4.2.1 Assessment of Analytical Models/Computer Codes

This research activity is based on two phases of qualification studies. In the first phase, a few currently available computer codes were selected and evaluated for the response of four benchmark problems that have closed-form solutions. Codes with an acceptable performance will be candidates for the second phase of the qualification studies, where the dynamic response of well-designed and executed laboratory experiments on single-joint rock specimens will be analyzed. The first phase of the qualification studies on the HONDO II, SPECTROM-331, UDEC, 3DEC, and DECICE codes has been completed, and the results have been reported previously (Hsiung and Chowdhury, 1991 and 1992; Hsiung et al., 1993a). This first phase study showed that only UDEC and 3DEC were able to reproduce the analytical solutions of all four benchmark problems. These two codes were selected for the second phase study. The objective of the second phase study is to determine whether the existing rock-joint models and associated computer codes can simulate the behavior of a single-joint rock specimen when subjected to dynamic loads.

There are two steps involved in the second phase study. The first is to model the single-joint rock experiments subjected to pseudostatic loads, and the second is to model the joint experiments under dynamic loads. Currently, the modeling of the pseudostatic single-joint experiments using the UDEC code is under way. Preliminary results of this work are presented in this section of the report.

#### 4.2.1.1 Model Setup

Figure 4-1 shows a model that was developed to simulate the results of pseudostatic direct shear tests carried out in the laboratory under Task 2. This model consists of two rock blocks separated by a rough joint or interface. These blocks have the same dimensions of those used in the laboratory tests. A loading block is attached to the side of the upper rock block for application of a shearing force at a constant velocity to the top block. This loading block represents the loading mechanisms of the shear apparatus in actual experiments. The lower block is fixed on the bottom and on the vertical sides. The top surface of the upper block is under a vertical confining pressure that can be changed in each simulation. Other boundaries of the two rock blocks are free to move. The rock blocks are modeled as fully deformable blocks and discretized into finite difference zones, as shown in Figure 4-1. The loading block is modeled as a rigid block, as the stiffness of the loading system is much larger than the rock block stiffness. The numbers shown in the figure denote contact points.

The vertical interface between the top block and the rigid loading block is modeled as a Mohr-Coulomb joint with extremely high uniaxial tensile strength ( $10^{10}$  MPa) to prevent separation between the loading block and the top rock block. Free sliding along the interface between the loading block and the top rock block is allowed so that the loading block can accommodate the rotation of the top block during sliding.

The material properties, which were obtained by conducting the uniaxial compressive tests on cylindrical core specimens from the Apache Leap tuff rocks, and the dimensions of the rock blocks are listed on page 4-4.

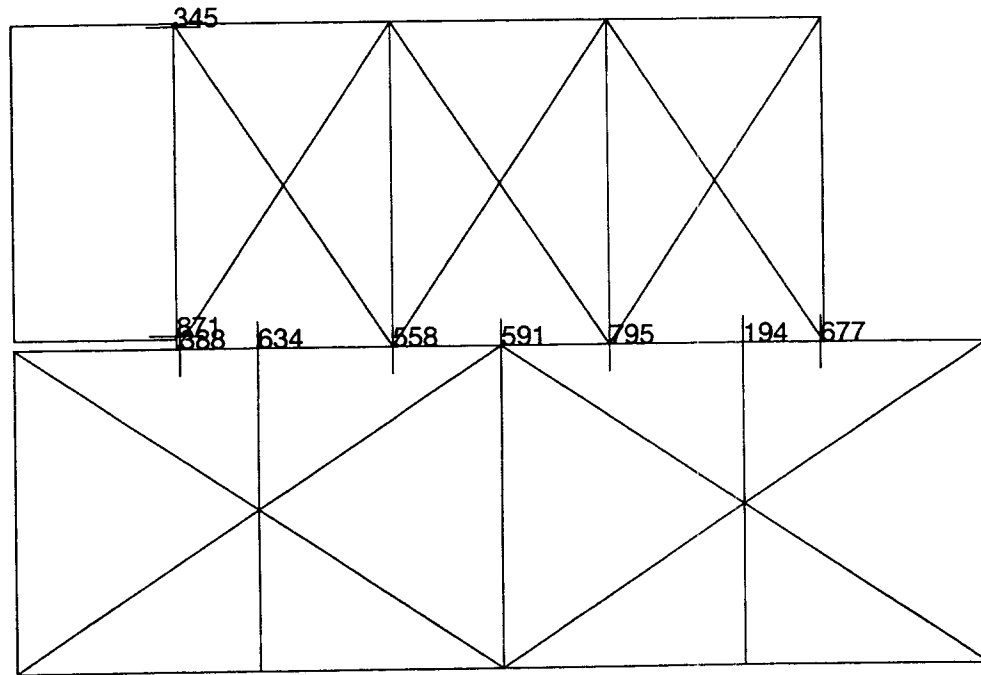


**Figure 4-1. UDEC model for simulating laboratory test on single-joint specimen**

Bulk Modulus	20.0 GPa
Shear Modulus	13.17 GPa
Density	2420 kg/m <sup>3</sup>
Top Block Dimensions	
height	0.1016 m
width	0.2032 m
Bottom Block Dimensions	
height	0.1016 m
width	0.3048 m

The UDEC code has the capability of simulating rock joint behavior (the interface between the rock blocks) using three different constitutive relationships—Mohr-Coulomb, Continuously Yielding, and Barton-Bandis. In the second phase qualification study, all three joint constitutive laws are being evaluated. During this reporting period, only the Continuously Yielding model was evaluated. Simulation on ten different pseudostatic single-joint specimens has been completed so far. The discussion of the modeling results for the Test No. 11 specimen is provided here.

The properties of the rock joint of Test Specimen No. 11 for the Continuously Yielding model are:

Joint Normal Stiffness	78.7 GPa
Maximum Joint Normal Stiffness	100.0 GPa
Minimum Joint Normal Stiffness	1.0 GPa
Joint Shear Stiffness	13.9 GPa
Maximum Joint Shear Stiffness	13.9 GPa
Minimum Joint Shear Stiffness	13.9 GPa
Joint Friction Angle	39.3°
Joint Initial Friction Angle	47.4°
Joint Roughness Parameter	0.0132
Exponent of Joint Normal Stiffness	0.7098

Joint shear stiffness is assumed to be independent of normal stress applied in this study. The above joint properties were back-calculated based on the laboratory measured data including joint shear stress and dilation information during forward shear. The normal stress applied for Test No. 11 was 1.08 MPa.

#### 4.2.1.2 Modeling Results

In order to simulate the actual loading rate as was used in the laboratory, a constant horizontal velocity of 0.42 mm/sec was applied to the centroid of the loading block. The direction of the velocity was pointed toward the right-hand side of the model. This velocity combined with the small rock density resulted in an extremely small critical time step ( $5.337 \times 10^{-6}$  sec). Based on this time step, the UDEC run needed 178 million steps of calculations for the top rock block to displace 40 mm as it did for the laboratory tests. The UDEC is a single-precision numerical code. A large number of calculation steps is expected to cause numerical instability. This was confirmed by the peculiar result shown in Figure 4-2. This figure shows a distorted mesh of the top rock block as compared to that in Figure 4-1.

To get around this numerical instability problem, the running time has to be shortened to reduce the number of calculations. It was decided to increase the input velocity. Although increase in input velocity deviates from the actual experimental condition, the modeling results were not significantly different from the experimental results since the Continuously Yielding rock joint model is not velocity-dependent. After some tests, a velocity of 100 mm/sec was used for further study. Caution needed to be exercised to provide adequate damping (i.e., Rayleigh) to the model. The natural frequency required for the Rayleigh damping was determined by running the UDEC model with no shear load.

Figure 4-3 shows the relation between the shear stress and shear displacement at three contact points along the joint interface. The shear stress versus shear displacement curve for contact point 388 appears to be incorrect. This incorrect result is related to the logic used in the UDEC for the calculation of joint shear stress. At each time step, UDEC calculates forces and displacements at each contact point in the model. The shear stress at each contact point along a joint interface, if required, is then calculated by dividing the shear force at the point by its associated joint length. The joint length of a contact point is equal to the sum of half distances from this point to the immediate contact points on both sides. For example, in Figure 4-1, the joint length for contact point 558 is one-half the length between contact points 634 and 591. If one looks carefully, joint length for contact point 388 is half the length between only this point and contact point 634 since contact point 388 is at the edge of the top rock block. As the top block moves to the right, contact point 388 follows. However, since contact point 634 is located at the bottom block, it remains stationary. As a result, the joint length at contact point 388 tends to decrease and, at some point, becomes zero when contact points 388 and 634 overlap each other. Since the joint shear force

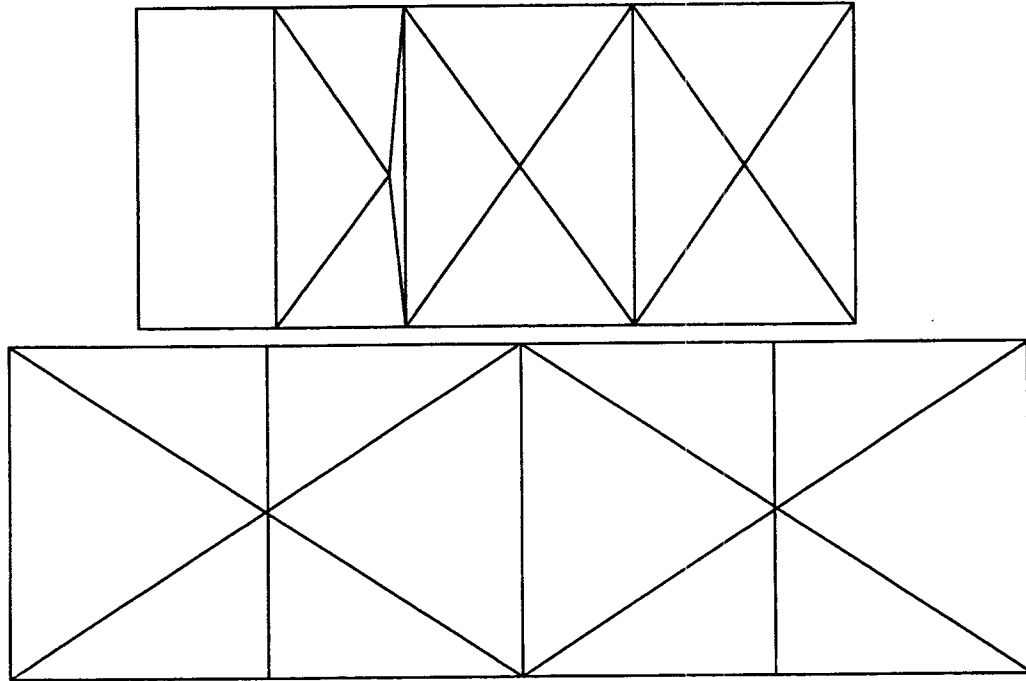


Figure 4-2. Plot showing distorted mesh for the top block due to numerical instability resulting from large number of calculations

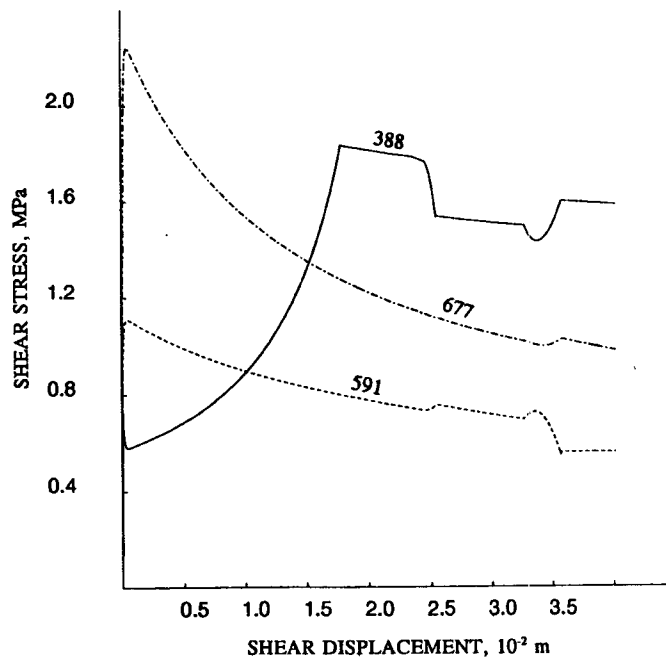


Figure 4-3. Joint shear stress versus shear displacement plot using model in Figure 4-1

at contact point 388 does not decrease at the same rate as its joint length, the resulting shear stress tends to increase, as indicated in Figure 4-3. This can be avoided by adopting a model, as shown in Figure 4-4, where no contact points are assigned on the bottom block. Consequently, the joint length at contact point 388 remains constant during shearing. Figure 4-5 shows the shear stress versus shear displacement curves along the joint interface using the model in Figure 4-4. All four curves correctly reflect the joint behavior.

Figure 4-6 shows joint shear stress versus shear displacement plots of UDEC modeling and laboratory test results for Test No. 11. The normal stress applied on the top of the upper block for both laboratory test and modeling was 1.08 MPa. The joint shear stress for the UDEC modeling was calculated using the horizontal force history at the centroid of the loading block. This shear stress is comparable to the shear stress measured on the horizontal actuator during testing. As shown in the figure, the upper rock block was displaced along one direction, forward shearing, for about 40 mm (top half of the figure) and then pushed back, reverse shearing, to its initial position (bottom half of the figure). A reasonably good agreement was observed between the modeling results and the laboratory measurements for forward shearing. This is expected since the parameters used for the UDEC model were back-calculated from the laboratory data. A small difference between the UDEC results and the laboratory data during reverse shearing was also observed. A detailed discussion regarding this difference will be presented later.

Figure 4-7 shows joint dilation plots of UDEC results and test measurements. Although good agreement is shown for dilation during forward shearing between the two sets of results, the UDEC prediction of dilation during reverse shearing is inaccurate. This gives a clear indication that the model implemented in UDEC for calculation of shear dilation is inadequate. This present deficiency with the Continuously Yielding rock joint model in UDEC code will be corrected or a new joint model developed such that the actual joint dilation behavior under cyclical shear loading can be simulated. The work for modifying an existing or developing a new joint model will be performed under RDCO Task 3.

#### **4.2.2 Thermal-Mechanical-Hydrological Coupled Modeling (DECOVALEX)**

The purpose of this research activity is to increase the understanding of TMH processes for rock mass stability and radionuclide release and transport from a geologic repository. This is being accomplished by participation of the NRC/Center for Nuclear Waste Regulatory Analysis (CNWRA) in an international project called DECOVALEX. DECOVALEX was organized by the Swedish Nuclear Power Inspectorate (SKI) to increase the understanding of coupled TMH processes applied to the underground disposal and isolation of HLW. Eleven funding organizations are currently involved, each supporting one or more research teams. In the DECOVALEX project, modeling is being used to develop and design validation tests of TMH-coupled processes. DECOVALEX is expected to lead to the development and validation of coupled TMH models, which are believed to be important to the licensing of a HLW repository.

Phase I of DECOVALEX was recently completed, and the comparison of results among the various research teams, including the CNWRA, for the two benchmark tests (BMT) and one test case (TC) problem is presented in a report by Jing et al., 1993. These study problems for Phase I were the Far-Field THM Model (BMT1), Multiple Fracture Model (BMT2), and Coupled Stress-Flow Model (TC1).

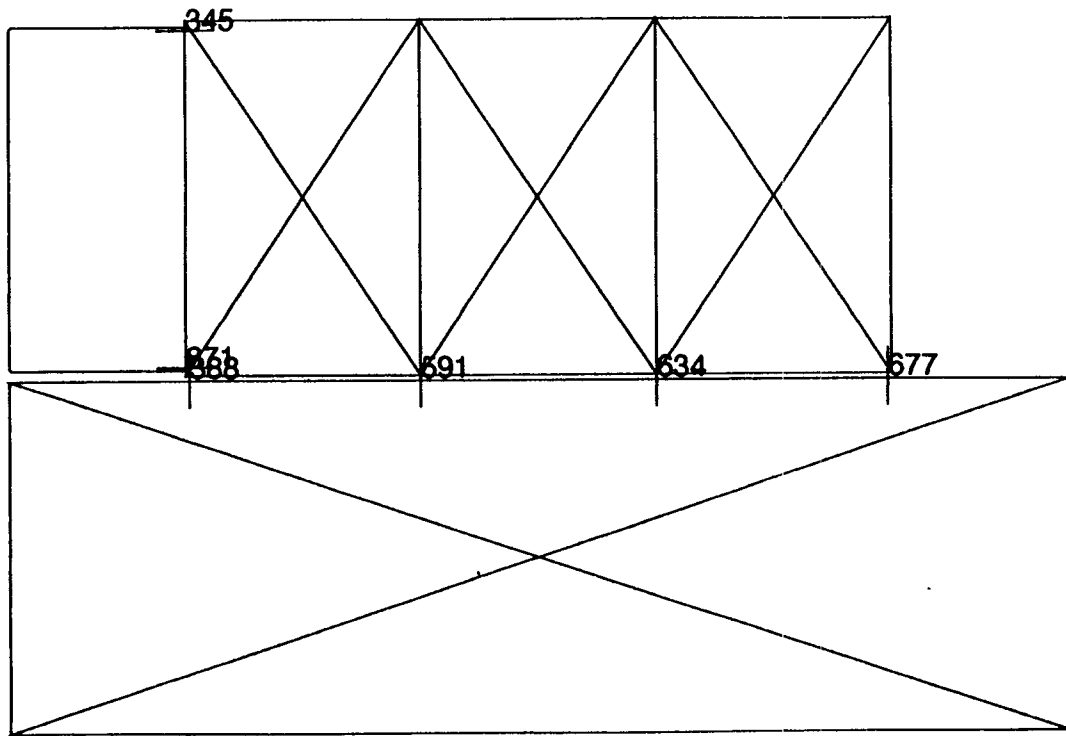


Figure 4-4. Modified UDEC model for simulating laboratory test on single-joint specimen

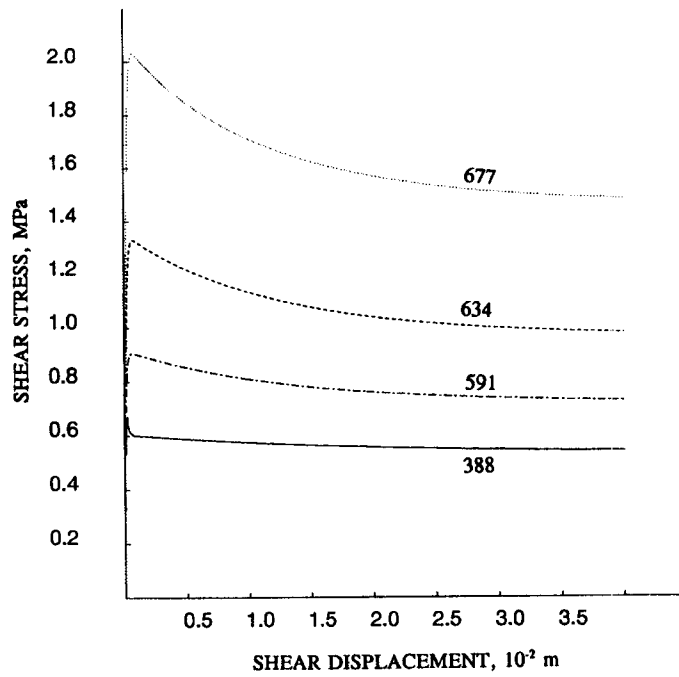


Figure 4-5. Joint shear stress versus shear displacement plot using model in Figure 4-4

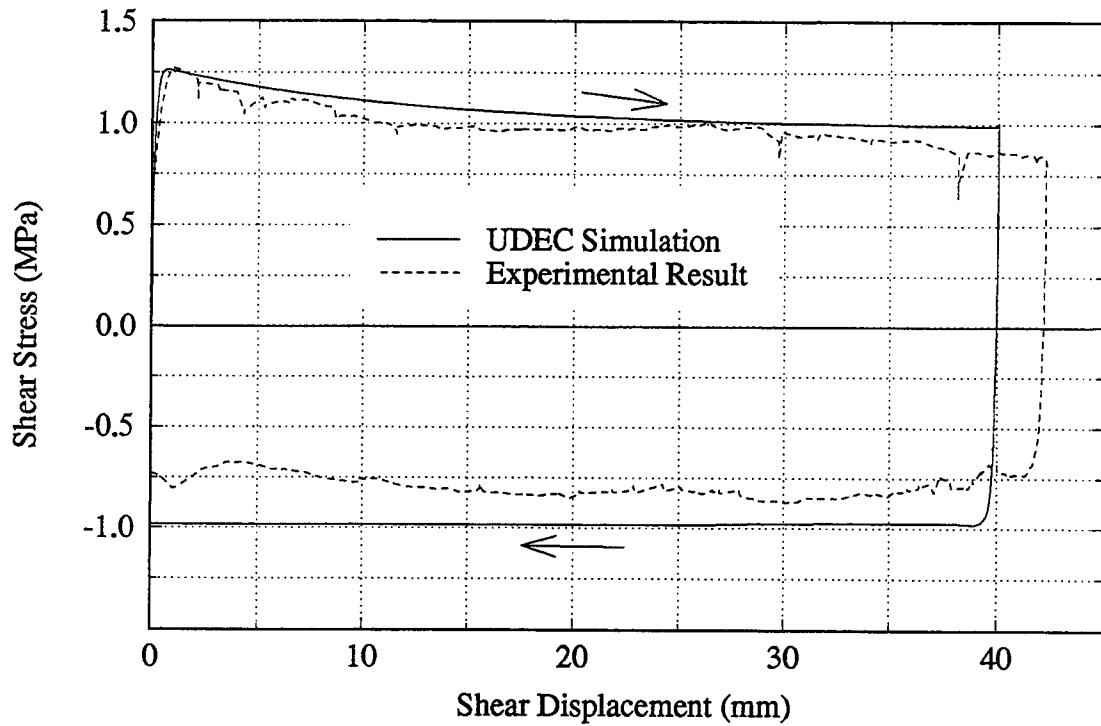


Figure 4-6. UDEC and laboratory test results of shear stress versus shear displacement plot for Test No. 11 under normal stress of 1.08 MPa

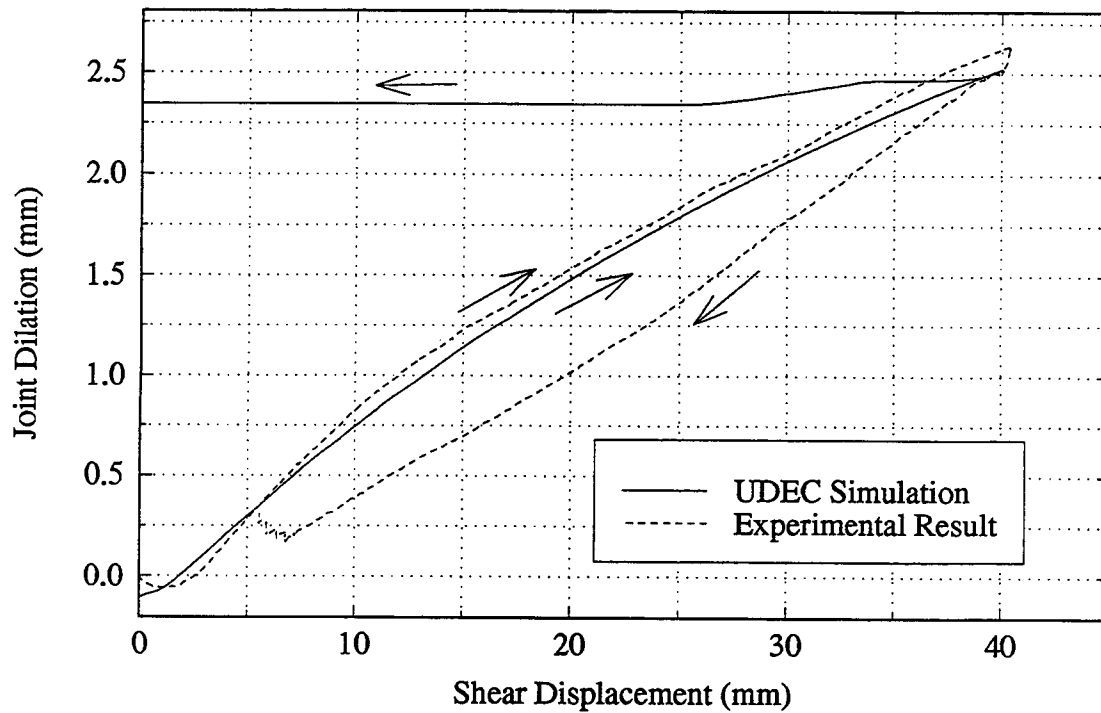


Figure 4-7. UDEC results and laboratory measurements of joint dilation for Test No. 11 under 1.08 MPa normal stress

#### 4.2.2.1 DECOVALEX Phase II Modeling Studies

For the Phase II modeling studies of DECOVALEX, one BMT problem and one TC problem were identified. The TC problem (TC1:2) was an extension of the Coupled Stress-Flow Model defined in the Phase I studies. This TC problem was revised to provide a more appropriate description of the biaxial testing apparatus designed at the Norwegian Geotechnical Institute (NGI) for conducting coupled stress-flow experiments on jointed core samples. Revised material parameters and loading procedures were also specified for this TC so that the modeling results could be directly compared to experimental test results. The BMT identified for Phase II was the Near-Field Repository Model (BMT3). Of these two problems, the BMT3 was modeled by the CNWRA team using the discrete-element code UDEC. This section presents a summary of the Phase II modeling studies. A detailed discussion of the CNWRA study results is presented by Ahola et al., 1993.

#### 4.2.2.2 Near-Field Repository Model (BMT3)

BMT3 was formulated as a BMT problem for both continuum and discontinuum codes to simulate TMH-coupled processes in a near-field, highly fractured, repository environment containing a waste emplacement tunnel and decaying heat source representing the waste canister. The two-dimensional model has dimensions of  $50 \times 50$  m and is centered about an origin located at a depth of 500 m below the ground surface. Figure 4-8 shows the locations and dimensions of the tunnel and heater for this near-field problem. The mechanical boundary conditions are such that all outward boundary surfaces of the

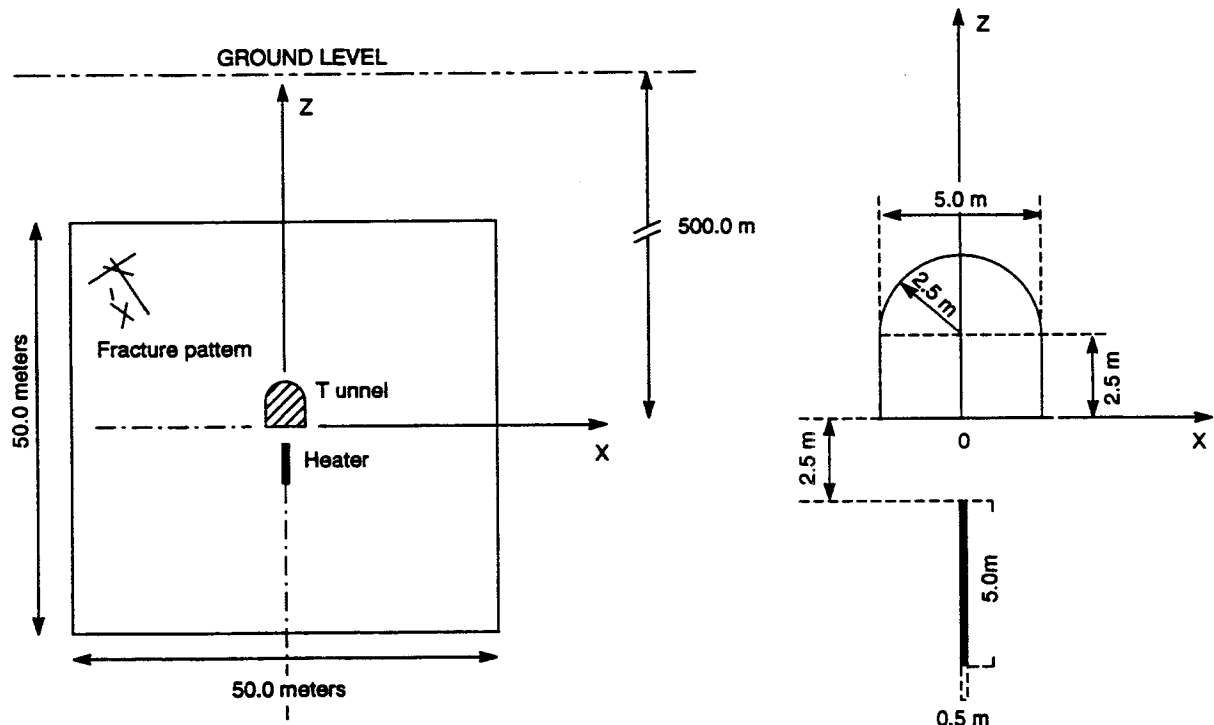


Figure 4-8. Near-field repository model, BMT3

model are fixed in the normal direction, except the top surface, at which the overburden stress is applied. The *in situ* stresses in the x and z directions are assumed equal, and a function of the overburden depth. No fluid flux is specified along the two vertical and bottom boundaries, while a constant water pressure is given along the top boundary, corresponding to a depth of 475 m. Along the tunnel perimeter, the fluid pressure is fixed at zero once the tunnel is excavated. Initial thermal conditions consist of a constant temperature of 27 °C throughout the model. This initial temperature is held fixed along the top boundary, while the remaining boundary surfaces are assumed adiabatic. The tunnel surface is assumed to behave as a convective boundary upon excavation. The heater is given an initial volumetric heat flux of 470 W/m<sup>3</sup>, and decays exponentially with time.

The rock mass is assumed to be highly fractured, containing a total of 6580 distinct fractures for the 50 × 50 m model (Figure 4-9a). The location of each fracture was given along with its associated aperture. All other fracture properties (e.g., normal and shear stiffnesses, cohesion, etc.) were assumed to be the same for each fracture. The fracture apertures ranged from 1 to 50 microns; however, 70 percent were less than 5 microns. In addition, no preferential fracture orientation existed in the model.

In order to analyze this BMT problem using the UDEC discrete element code, several simplifying assumptions had to be made to address the overwhelming number of fractures given. The first assumption was that of vertical symmetry about the z axis, which is justified by the geometry and boundary conditions as well as the fact that the equivalent permeabilities given in the x and z directions on the 50 × 50 m scale were approximately equal. This is somewhat expected due to the random nature of the fracture orientations. The second major assumption in the UDEC modeling approach was that beyond a certain distance from the tunnel boundary, the rock mass could be represented as an equivalent set of uniformly spaced joints to further reduce the overall number of fractures in the model. Figure 4-9b shows the UDEC model used for the analysis based on these assumptions. In this outer region, the hydraulic apertures as well as mechanical properties of the rectangular blocks are adjusted to account for the equivalent behavior of this region. Each of the discrete element blocks shown in Figure 4-9b is discretized into triangular finite difference zones to simulate the elastic block deformation.

Figure 4-10a shows the principal stress and displacement field around the tunnel after excavation of the tunnel and attainment of mechanical equilibrium. The figure shows relatively large inward displacements along the right wall of the tunnel, due to slip along the high angled fractures in this region, which transfers the stresses further into the tunnel wall. The maximum displacement is calculated to be 24.2 mm. Likewise, after tunnel excavation, the magnitude of the maximum principal stress is 58.9 MPa, and is located in the lower right portion of the tunnel. A minimum principal stress (tension) of 6.8 MPa also exists in this region. Figure 4-10b shows a similar plot after the maximum temperature of 172 °C is reached at the center of the heat source, corresponding to a heating period of 4 years. The maximum inward tunnel displacement increases to a value of 47.3 mm, causing some slight separation of the blocks in the tunnel wall. In addition, thermal expansion of the rock around the heater also induces upward vertical displacements around the tunnel. The maximum compressive principal stress increases 23 percent to 76.4 MPa, while the minimum tensile principal stress increases only slightly to 7.7 MPa. Within the UDEC code, heat transfer is assumed to take place through conduction only, with the fractures having no influence on the calculated temperature field.

Fluid flow in the UDEC model is assumed to take place only in the fractures, and is governed by the cubic law for parallel flat plates. Also, since UDEC contains no thermal-hydrologic coupling, heat convection within the fractures as well as other processes such as thermally induced buoyancy are completely neglected. Figures 4-11a and 4-11b show the fracture flow rates after mechanical-hydrological

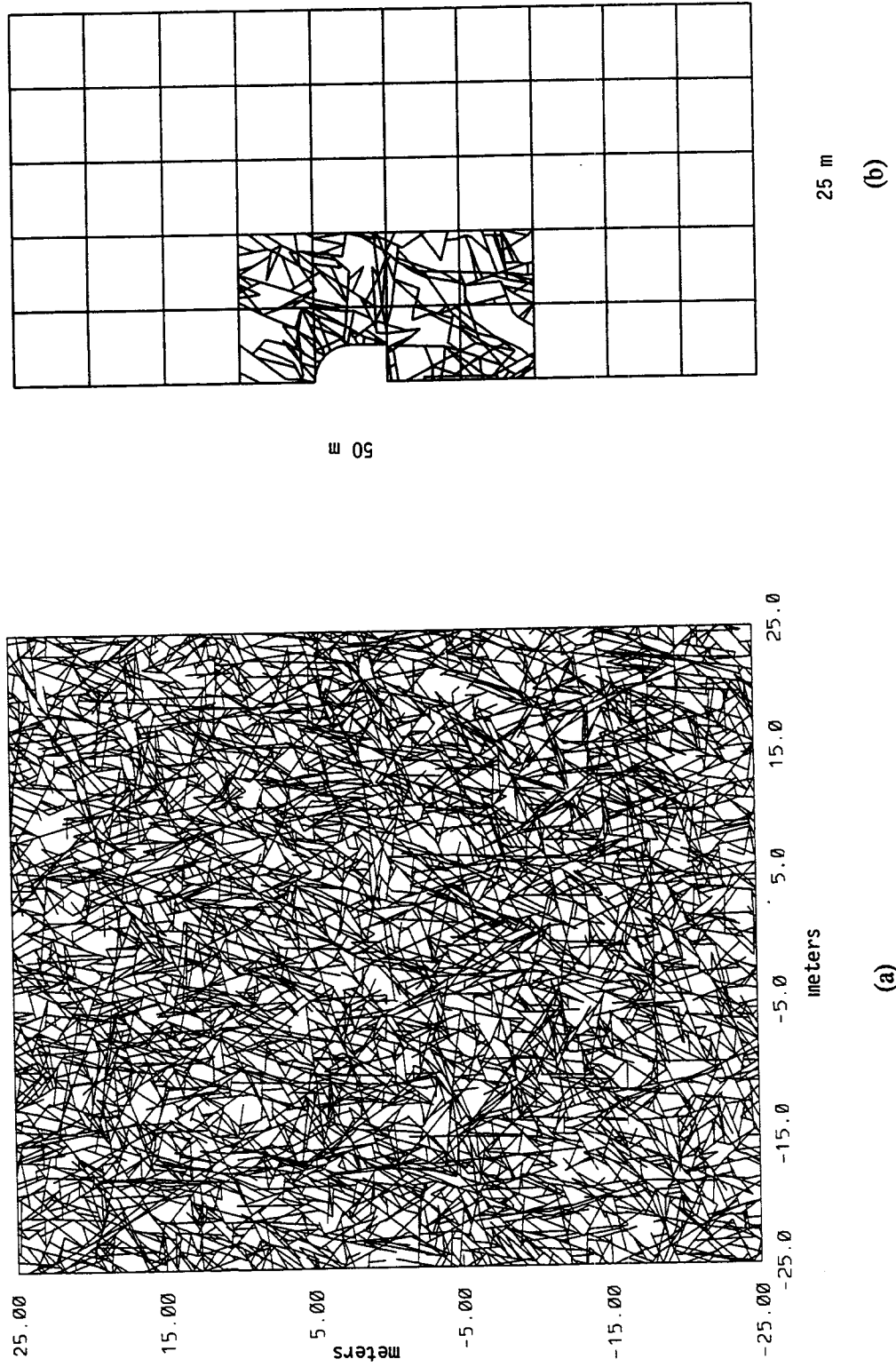
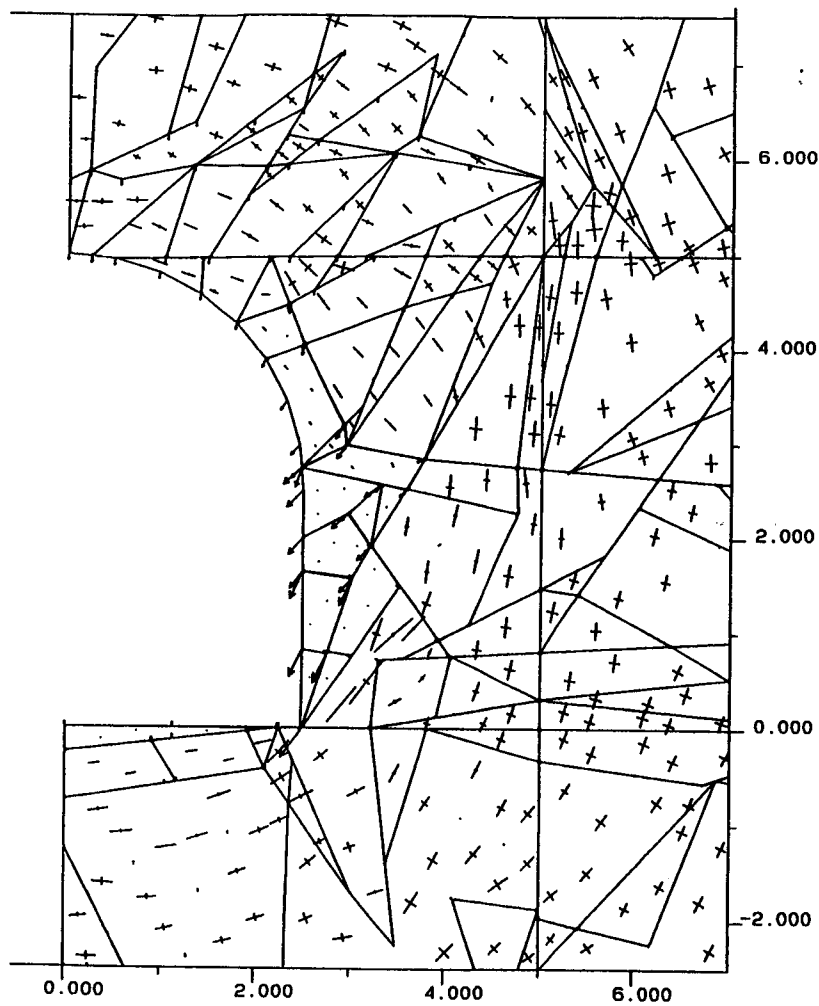
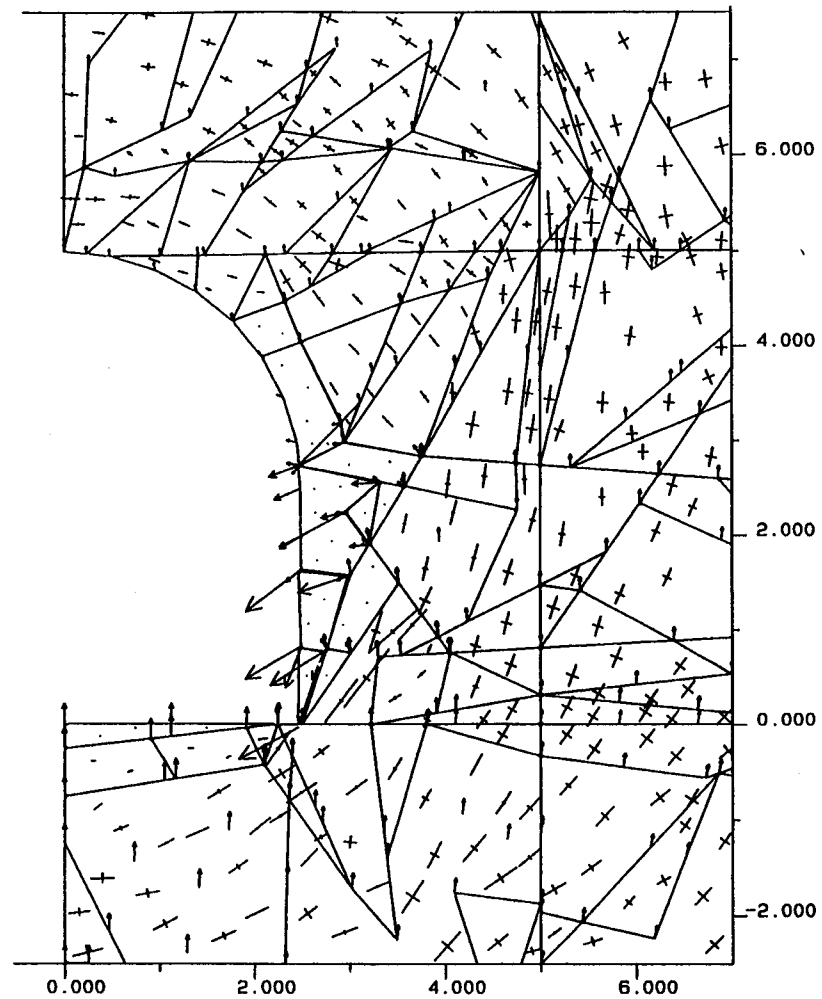


Figure 4-9. (a) Fracture geometry for near field repository model, BMT3, and (b) UDEC model

4-13



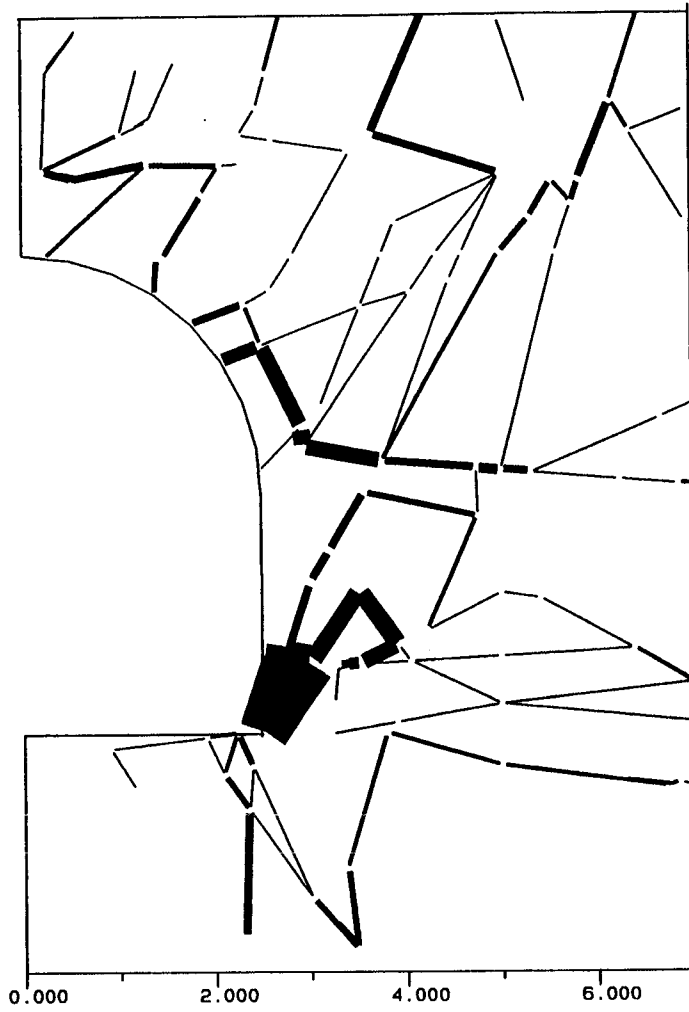
(a)



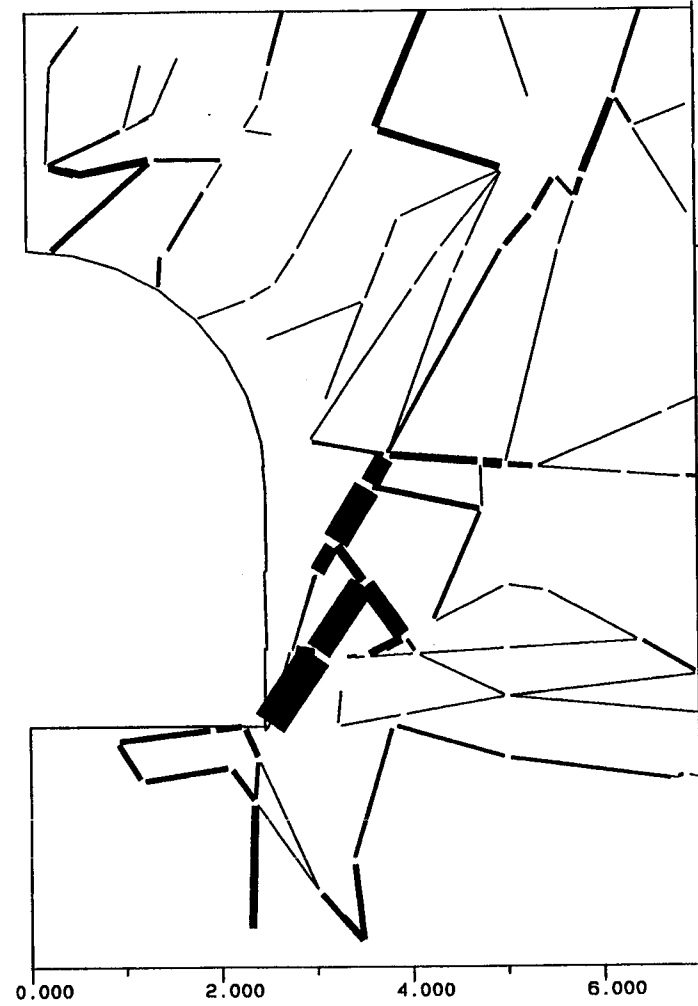
(b)

**Figure 4-10. UDEC results for the principal stresses (indicated by line segments) and displacements (indicated by arrows) after (a) tunnel excavation, (b) 4 years of heating**

4-14



(a)



(b)

$5 \times 10^{-10} \text{ m}^2/\text{s}$

Figure 4-11. UDEC results for the fracture flow rates after (a) tunnel excavation, and (b) 4 years of heating (one line thickness represents a flowrate of  $5 \times 10^{-10} \text{ m}^2/\text{s}$ )

equilibrium is reached upon tunnel excavation and 4 years of heating, respectively. Each individual line thickness in both figures represents a flow rate of  $5.0 \times 10^{-10}$  m<sup>2</sup>/s. Large fracture flow rates are seen to exist along the lower right corner of the tunnel due to movement of the blocks in this region. After excavation (Figure 4-11a), some flow also enters the tunnel through the crown, the upper portion of the tunnel wall, and the tunnel floor. The flow rate into the tunnel at this time is  $2.124 \times 10^{-8}$  m<sup>2</sup>/s. This is still a relatively small flow rate as a result of the small aperture size distribution. After the maximum temperature is reached at a time of 4 years (Figure 4-11b), it can be seen that the flow rate through the upper portion of the tunnel wall has decreased as a result of the thermal expansion of the rock mass, pinching off the fractures in this region. The total flow rate into the tunnel at this time period is  $8.425 \times 10^{-9}$  m<sup>2</sup>/s, a significant reduction of 60 percent. This result tends to support the concept that during the period of high thermal output from the waste canisters, the overall permeability through the disturbed zone around the emplacement boreholes and drifts could be substantially reduced. This would lead to better isolation of the canisters from inflowing groundwater, as well as prevention of release of radionuclides from a breached container.

### 4.3 ASSESSMENT OF PROGRESS TOWARDS MEETING PROJECT OBJECTIVES

The primary objective of the Seismic Rock Mechanics Research Project is to identify seismic-related, KTUs that will affect repository design and performance and to develop techniques that could be used to predict the response of near-field jointed rock mass at the proposed HLW repository at Yucca Mountain, Nevada, when it is subjected to repetitive seismic (including earthquakes and nuclear explosions at the Nevada Test Site) and thermal loads. This is being accomplished through laboratory and field experiments as well as computer modeling studies. Closure on several seismic-related issues has been accomplished. For instance, it has been determined through field experimental studies that repetitive, lower magnitude seismic events can have a much greater influence on the degree of damage to underground tunnels than a single large magnitude event. Most designs today consider only the maximum credible seismic event. Such results have been presented to the Nuclear Waste Technical Review Board (NWTRB), and the NWTRB has incorporated these findings in their annual report as guidance for the U.S. Department of Energy (DOE) to consider in its Exploratory Studies Facility (ESF) and repository design (NWTRB, 1992). The findings on the effect of repetitive seismic events have also directly supported the development of the Compliance Determination Methodologies (CDM) for shafts and ramps design, specifically with regard to establishing review method steps for assessing protection against natural phenomena and environmental conditions [10 CFR 60.131(b)(1)]. These findings will further be used in the development of CDM for RRT 4.4 Assessment of Compliance with Design Criteria for Underground Facility, 5.3 Assessment of Compliance with the Design Criteria for the Post-Closure Features of the Underground Facility, 5.4 Assessment of Compliance with the Engineered Barrier System Performance Objectives, and 6.1 Assessment of Compliance with the Requirement for Cumulative Releases of Radioactive Materials. Also, based on the field experiments performed at the Lucky Friday Mine, Mullan, Idaho (Task 5), both the magnitude and duration of water pressure changes due to seismic events were measured to be small (Hsiung and Chowdhury, 1992). These results would tend to indicate that significant changes in the water pressure below the proposed repository site due to seismic events of large magnitude may not be credible.

Through the research tasks involved in laboratory experiments and modeling studies, it has been found that the rock joint models presently incorporated in the computer codes under consideration for use in seismic design in jointed rock masses do not correctly simulate the pseudostatic and dynamic

experimental rock joint behavior. Through identification of these problems and subsequent enhancement of the rock joint models, the staff will be better able to review the DOE repository seismic design, and support assessment of repository performance. In addition, several of the design-related CDMs have KTUs related to the impact of repetitive seismic motion on long-term performance of seals. Having a verified code for seismic analysis, the staff will have better capabilities to perform independent detailed safety reviews regarding these issues.

The objective of DECOVALEX (Task 9) TMH modeling and coupled experiments is to address KTUs related to the impact of coupled TMH processes on repository design and performance. These activities are to evaluate methodologies including model validation and code verification for coupled TMH modeling of jointed rocks. The work being done in this task is supporting the development of a compliance determination code under technical assistance work for simulating coupled processes that can be used by the NRC and the CNWRA for determination of DOE compliance with NRC regulations on thermal and repetitive seismic loads. The results of seismic research have been used for Site Characterization Plan (SCP) reviews and are currently being used for ESF Title II Design reviews.

Since the currently used rock joint models cannot simulate jointed rock mass behavior, the model validation and code verification activities will not be conducted under this project. These activities will be conducted under RDCO Task 2.3 as parts of coupled code development work.

#### **4.4 PLANS FOR NEXT REPORTING PERIOD**

The laboratory tests on single-joint rock specimens under pseudostatic and dynamic loading conditions for the characterization of joint shear behavior and generation of a data set on joint dynamic behavior for rock-joint model validation have been completed. These test results are currently being analyzed. The preparation of a topical report to document the test activities and the results of data analysis is under way. This topical report is scheduled to be completed and submitted to NRC Office of Nuclear Regulatory Research, Division of Regulatory Applications. The second phase qualification studies on the UDEC code is well under way. During the next reporting period, qualification studies of the UDEC code using the Mohr-Coulomb and Barton-Bandis rock joint models will be completed, and a topical report to document the results of the qualification studies (including both the first and second phases) will be submitted by the end of 1993. A dynamic scale model experiment on a jointed rock mass to study the cumulative seismic effects and generate a complete data set for code verification will be performed during the next reporting period. Work on DECOVALEX Phase II modeling and the coupled mechanical and hydrological experiments will continue, and a topical report will be prepared.

#### **4.5 REFERENCES**

- Ahola, M.P., L. J. Lorig, A. Chowdhury, and S.M. Hsiung. 1993. *Thermo-Hydro-Mechanical Coupled Modeling: Near Field Repository Model, (BMT3)*. DECOVALEX-Phase II. CNWRA 93-002. San Antonio, TX: Center for Nuclear Waste Regulatory Analyses.
- Brady, B.H.G., S.M. Hsiung, and A.H. Chowdhury. 1990. *Qualification Studies on the Distinct Element Code UDEC Against Some Benchmark Analytical Problems*. CNWRA 90-004. San Antonio, TX: Center for Nuclear Waste Regulatory Analyses.

- Brandshaug, T., B. Dasgupta, B.H.G. Brady, S.M. Hsiung, and A.H. Chowdhury. 1990. *Qualification Studies on the Finite Element Code HONDO II Against Some Benchmark Analytical Problems*. CNWRA 90-006. San Antonio, TX: Center for Nuclear Waste Regulatory Analyses.
- Hsiung, S.M., and A.H. Chowdhury. 1991. *Report on Research Activities for Calendar Year 1990*. W. Sagar, ed. NUREG/CR-5817, CNWRA 90-01A. San Antonio, TX: Center for Nuclear Waste Regulatory Analyses.
- Hsiung, S.M., and A.H. Chowdhury. 1992. *Report on Research Activities for Calendar Year 1991*. W. Sagar, ed. CNWRA 91-01A. San Antonio, TX: Center for Nuclear Waste Regulatory Analyses.
- Hsiung, S.M., A.H. Chowdhury, W. Blake, M.P. Ahola, and A. Ghosh. 1992. *Field Site Investigation: Effect of Mine Seismicity on a Jointed Rock Mass*. CNWRA 92-012. San Antonio, TX: Center for Nuclear Waste Regulatory Analyses.
- Hsiung, S.M., M.P. Ahola, and A.H. Chowdhury. 1993a. *NRC High-Level Radioactive Waste Research at CNWRA January-June 1992*. W.C. Patrick, ed. NUREG/CR-5817, CNWRA 92-01S. San Antonio, TX: Center for Nuclear Waste Regulatory Analyses.
- Hsiung, S.M., M.P. Ahola, A. Ghosh, and A.H. Chowdhury. 1993b. *NRC High-Level Radioactive Waste Research at CNWRA July 1 through December 31, 1992*. W. Sagar, ed. CNWRA 92-02S. San Antonio, TX: Center for Nuclear Waste Regulatory Analyses.
- Jing, L., J. Rutqvist, O. Stephansson, C-F. Tsang, and F. Kautsky. 1993. *DECOVALEX—Mathematical Models of Coupled H-T-M Processes for Nuclear Waste Repositories. Report of Phase I*. Stockholm, Sweden: Swedish Nuclear Power Inspectorate.
- Kana, D.D., D.C. Scheidt, B.H.G. Brady, A.H. Chowdhury, S.M. Hsiung, and B.W. Vanzant. 1990. *Development of a Rock-Joint Dynamic Shear Test Apparatus*. CNWRA 90-005. San Antonio, TX: Center for Nuclear Waste Regulatory Analyses.
- Kana, D.D., B.H.G. Brady, B.W. Vanzant, and P.K. Nair. 1991. *Critical Assessment of Seismic and Geomechanics Literature Related to a High-Level Nuclear Waste Underground Repository*. NUREG/CR-5440, CNWRA 89-001. San Antonio, TX: Center for Nuclear Waste Regulatory Analyses.
- Nuclear Waste Technical Review Board (NWTRB). 1992. *Fifth Report of the U.S. Congress and the U.S. Secretary of Energy*. Washington, DC: Nuclear Waste Technical Review Board.

## 5 INTEGRATED WASTE PACKAGE EXPERIMENTS

*by Narasi Sridhar, Gustavo Cragnolino, and Darrell Dunn*

*Investigators: Narasi Sridhar, Gustavo Cragnolino, Darrell Dunn (CNWRA)*

*NRC Project Officer: Michael McNeil*

### 5.1 TECHNICAL OBJECTIVES

The overall technical objectives of the Integrated Waste Package Experiments (IWPE) project are to:

- Conduct waste package experiments to scope and study the key parameters affecting long-term material performance
- Assess waste package materials and designs selected by the U.S. Department of Energy (DOE) and provide independent evaluation for reasonable assurance of long-term performance
- Support the Office of Nuclear Regulatory Research (RES) in addressing the needs of the Division of High-Level Waste Management (DHLWM).

Two key technical uncertainties (KTU), developed as part of the compliance determination strategy (CDS) and listed in the License Application Review Plan (LARP), Section 5.4 (LARP, 1992), are addressed in the IWPE program. These are:

- The extrapolation of short-term laboratory and prototype test results to predict long-term performance of waste packages and engineered barrier systems (EBS)
- The prediction of environmental effects on the performance of waste packages and the EBS

To address the above objectives, the IWPE program is divided into five tasks: Task 1, corrosion; Task 2, stress corrosion cracking (SCC); Task 3, thermal stability of materials; Task 4, microbially influenced corrosion; and Task 5, other degradation modes and alternate container material performance issues. Since the effects of environmental factors on localized corrosion are complex and interactive, these effects have been studied using relatively short-term tests and various factorial designs. The use of parameters derived from these short-term tests for long-term prediction has also been examined specifically in terms of repassivation potential. The results of these studies were published in a topical report (Sridhar et al., 1993). The effect of fabrication thermal cycles on container material stability has been examined for alloy 825 and reported recently (Cragnolino and Sridhar, 1993). The possibility of microbial activity and resulting effects on corrosion under repository environmental conditions has been evaluated through a literature assessment and reported as a major milestone report (Geesey, 1993).

The results generated within the IWPE program are being used to guide the waste package performance assessment tasks. The overall strategy with respect to experimental studies and modeling of

slow degradation processes, such as corrosion and SCC, is outlined in the next section. As described in the following sections, a key area of integration between the IWPE, thermohydrology, and geochemistry projects is in the prediction of environmental evolution very near the waste packages. The fundamental assumption in waste package corrosion studies is the presence of an aqueous environment, at least episodically. The corrosion rate in a dry steam or dry air environment at the repository temperatures is negligible. The experimental research and modeling efforts within the thermohydrology project will assist in the evaluation of the presence of aqueous environments near the waste package. The results of the IWPE project will identify the environmental factors of importance to waste package performance and thus guide the investigations of rock-water interactions in the geochemistry projects.

## 5.2 LONG-TERM PREDICTION OF CONTAINER CORROSION

In the U.S. geologic disposal program, two types of waste package emplacement concepts are being considered: (i) vertical emplacement of a single-wall or double-wall container in a borehole with an air gap between the container and the borehole; and (ii) horizontal emplacement of a double-wall container surrounded by a suitable backfill in the drifts of the underground repository. The vertical emplacement of a thin (e.g., 12-mm thick), single-wall container made of an austenitic alloy is the present reference design, although the horizontal drift emplacement of a double-wall container is receiving increasing attention (Doering, 1993). It has also been proposed that high thermal loading via horizontal drift emplacement of large waste packages, containing up to 21 Pressurized Water Reactor (PWR) fuel assemblies, be used to create a dry-out zone around the EBS for thousands of years that will minimize corrosion and nongaseous radionuclide transport (Ruffner et al., 1993; Buscheck et al., 1993). The drying-out process may create deposition of solids rich in Ca and Si (Beavers et al., 1992; Pabalan and Murphy, 1993). In addition, backflow of the condensate through fractures may result in an aqueous environment around the container, as indicated by the results of some field heater tests (Patrick, 1986; Zimmerman et al., 1986; Ramirez, 1991). The rewetting of the dried solids may cause the formation of solutions rich in chloride and sulfate (Abraham et al., 1986; Beavers et al., 1992; Walton, 1993). Hence, a conservative approach to life prediction is to assume the presence of aqueous conditions surrounding the containers. The chemical composition of such an aqueous environment is not known, and a range of concentrations of various species must be explored.

The approach used in Source Term Code (SOTEC) for the Iterative Performance Assessment (IPA) activity for the prediction of performance of container materials (Sagar et al., 1992) is illustrated schematically in Figure 5-1. This approach assumes that corrosion failure modes of importance to life prediction occur under aqueous conditions. As shown in Figure 5-1a, the corrosion potential of the container material, which is a mixed potential dictated by the kinetics of the anodic and cathodic reactions at the surface exposed to the repository environment, changes with time in response to factors such as radiolysis, pH, temperature, and oxygen concentration (Macdonald and Urquidi-Macdonald, 1990). A simple increase in the corrosion potential to a constant upper limit is indicated in Figure 5-1a, although a more complex behavior may be observed in reality. Additionally, significant variation in the corrosion potential of containers may be expected, depending upon their location and thermal output. It is also indicated in Figure 5-1a that, if the corrosion potential exceeds the pit-initiation potential ( $E_p$ ), pits initiate and propagate into the container wall. If the corrosion potential drops below  $E_p$ , pits already initiated continue to grow, but no new pits initiate. Finally, if the corrosion potential drops below the repassivation potential ( $E_{rp}$ ), all pits repassivate and cease to grow. After repassivation, the corrosion of the container continues in a uniform manner at a low rate determined by the passive current density. This concept of critical potentials has been well established in the literature for pitting and crevice corrosion (Szklaarska-

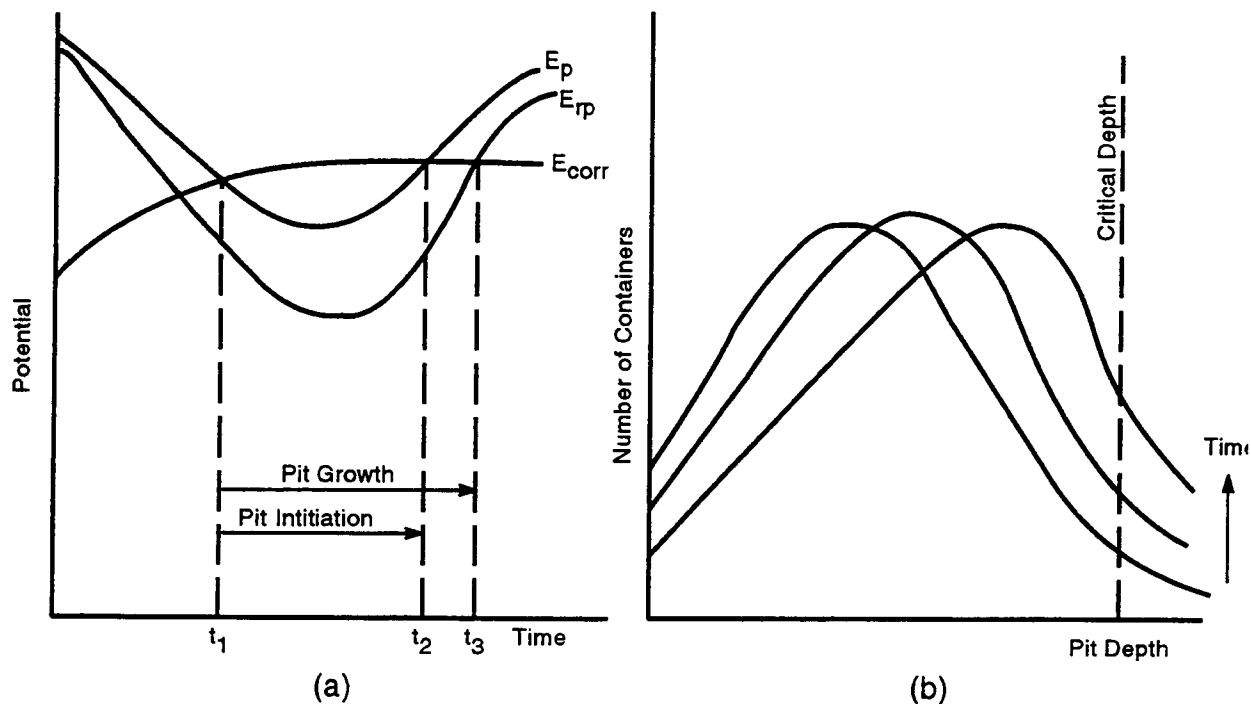


Figure 5-1. Schematic illustration of the approach used for long-term life prediction of container materials under localized corrosion conditions

Smialowska, 1986). Both  $E_p$  and  $E_{rp}$  are distributed values, and depend on both material and environmental factors. Hence, significant variability in the performance of various containers can be expected. The stochastic nature of localized corrosion (distributed values for  $E_p$  and  $E_{rp}$ ) and the variations in the corrosion potential of the containers in the repository can be taken into consideration by varying input parameters, for example by a Monte-Carlo driver, to obtain a distribution of containers with pit depths exceeding a certain value for any given time period (Figure 5-1b). This is termed a damage function (Macdonald and Urquidi-Macdonald, 1992). Containment can then be evaluated by comparing the fraction or number of containers with the deepest pits exceeding the critical pit depth at any given time period to a predetermined requirement. Although two potentials,  $E_p$  and  $E_{rp}$ , are defined, in long-term prediction, these two potentials may coincide to one critical potential (Tsuji-kawa and Hisamatsu, 1984; Thompson and Syrett, 1992). Additionally, while the method is illustrated for pitting, analogous parameters have been used to characterize the crevice-corrosion behavior of these alloys (Tsuji-kawa and Hisamatsu, 1984; Okayama et al., 1987). The concept of critical potential has been applied to SCC of many alloy-environment combinations (Cragno-lino and Sridhar, 1992a), but there are no data for the alloys and environments of interest to the Yucca Mountain repository. Other environmental degradation phenomena such as hydrogen embrittlement also depend on the corrosion potential, but do not exhibit a critical potential.

The crucial questions in the measurement and use of  $E_{rp}$  are its dependence on the extent of prior pit/crevice corrosion, measurement technique, environmental parameters, and microstructural characteristics. The research results reported previously (Cragno-lino and Sridhar, 1992b; Sridhar and Cragno-lino, 1992a; Sridhar and Cragno-lino, 1992b; Sridhar et al., 1992) have addressed some of these questions for pitting and crevice corrosion. It was shown that the  $E_{rp}$  was independent of the extent of

prior pitting and that it decreased logarithmically with an increase in chloride concentration. To a more limited extent, it was also shown that  $E_{rp}$  was not dependent on the pH and sulfate concentration. Another factor that is important in predicting the corrosion resistance of an alloy in the repository is the surface condition of the alloy container. Corrosion data obtained from laboratory tests on polished specimens can overestimate the performance of a material if significant differences in the near-surface chemistry exists between the mill-finished surface and the polished alloy. An important issue with respect to long-term prediction of container performance is the degree of conservatism entailed in the use of repassivation potentials irrespective of the variations in surface conditions. The effect of surface chromium depletion on localized corrosion of alloy 825 is addressed in the present report.

The environment near the waste packages is anticipated to be essentially dry with either periodic or episodic occurrences of water intrusion. Hence, it is important to understand the effects of wet and dry cycles on corrosion. One effect of wet and dry cycles is the increased concentration of species such as chloride. The effects of changing environmental composition have been studied by the use of factorial matrix of various anionic and cationic species (Thompson et al., 1992; Sridhar et al., 1993). However, the effects of dry thermal oxidation (hereafter referred to as thermal aging) on subsequent corrosion behavior in a wet environment have not been studied in detail. Some preliminary results of the effect of dry exposure on subsequent corrosion in wet environments are presented in this report.

Studies on the effects of environmental factors and potential on the SCC of candidate container materials are also included in this report. Slow strain rate tests are being used to define environmental conditions, in terms of solution composition, pH, and temperature, as well as potential ranges that promote SCC in chloride-containing solutions. The goal is to determine if a critical potential for SCC exists, and then to define the relationship between this potential and the  $E_{rp}$  for pitting/crevice corrosion. If such a critical potential for SCC exists, it can be used as a bounding parameter for the prediction of long-term behavior assuming, as a worst case, that the level of residual and imposed stresses on the container would be sufficiently high to induce cracking under the range of environmental conditions anticipated at the repository site.

## **5.3 EXPERIMENTAL PROCEDURES**

### **5.3.1 Localized Corrosion Studies**

The test program on the effects of surface Cr-depletion effects focused on alloy 825. The origin of Cr-depletion at the surface has been described previously (Sridhar et al., 1993). Rectangular specimens of dimensions  $12.5 \times 12.7 \times 38.1$  mm were cut from the mill-finished plate of alloy 825 such that the top and bottom surfaces of the plate were left intact. The four cut surfaces were then wet-ground to a 600-grit finish, cleaned ultrasonically in a detergent bath, rinsed in high-purity water, degreased with acetone, and dried before each test. The specimens undergoing thermal aging were placed in forced air convection ovens at 100 or 300 °C for periods of 1, 10, and 30 days. Upon thermal aging, the specimens were cooled and reweighed. In all cases, there was a small weight loss (approximately 0.1 mg), possibly due to loss of adsorbed moisture. The weight gain due to aging at these temperatures is below the resolution of the balance (0.1 mg). Visual observation of the specimens after thermal aging showed that all specimens treated at 300 °C exhibited a gold color film, with the mill-finished surfaces exhibiting a darker film. The specimens treated at 100 °C did not show any coloration. This suggests that the oxide film formed at 300 °C is thick enough to form interference colors. In the case of nickel, the film thicknesses corresponding to yellow to dark brown coloration have been indicated to range from 1260

to 1720 Å (Evans, 1961). This is an approximate estimation for the present case since the refractive index of the film and the phase changes at the metal-film and film-air interfaces can be different for alloy 825 than for nickel.

The solution contained 85 ppm  $\text{HCO}_3^-$ , 1000 ppm  $\text{Cl}^-$ , 20 ppm  $\text{SO}_4^{2-}$ , 10 ppm  $\text{NO}_3^-$ , and 2 ppm  $\text{F}^-$ , all added as Na salts. The choice of the chloride concentration was guided by prior results of repeated wetting and drying tests using J-13 water (Abraham et al., 1986). The initial pH of the solution at room temperature was approximately 8, while the final pH at room temperature was approximately 9. The rationale for the choice of this solution is provided in a previous report (Sridhar et al., 1993). The solution chemistry has been discussed in a previous report (Pabalan et al., 1990). All tests were performed at  $95 \pm 2$  °C. All solutions were prepared using high-purity water (17 MΩ/cm resistivity). Unless otherwise noted, the solutions were purged with high-purity nitrogen (potentiostatic tests) or argon (cyclic polarization tests). In the corrosion potential tests, the solution redox condition was changed by purging with nitrogen, a 79:21 mixture of high purity nitrogen and oxygen ( $< 1$  ppm  $\text{CO}_2$ ), and by the addition of 5 mmol/L  $\text{H}_2\text{O}_2$ . Hydrogen peroxide additions were made to simulate one of the effects of radiolysis of an aqueous environment.

The specimens were attached to a brass electrical contact surrounded by a glass holder with a polytetrafluoroethylene (PTFE, Teflon®) plug such that the brass did not come into contact with the test solution. The specimen assembly was partially immersed in the solution in order to avoid crevice corrosion in the specimen-PTFE interface. Post-test examination confirmed the absence of crevice corrosion. In some cases, preferential corrosion of the Cr-depleted surfaces at or slightly above the water-vapor interface occurred. These specimens were not considered for the present analysis, although they indicate the possible importance of alternate wet-dry conditions to corrosion. At the end of the tests, the specimens were ultrasonically cleaned in a mixture of 4 mL 2-butyne-1,4-diol (35 percent aqueous solution) + 3 mL concentrated HCl + 50 mL high purity water to remove corrosion products. Previous tests on control specimens indicated that this cleaning procedure did not result in measurable corrosion of the substrate. The specimens were then reweighed and examined using a 70× stereoscope. The weight loss after the corrosion tests was in good agreement with the weight loss calculated from the charge density measurements using Faraday's law (correlation coefficient,  $R^2 = 0.99$ ). Selected specimens were examined using scanning electron microscopy (SEM) for pit depth and density, and energy dispersive spectrometry (EDS) for near-surface composition.

The effect of Cr-depletion was studied initially using a potentiodynamic, cyclic polarization technique. This technique, which is a variation of the ASTM G-61 test technique, consists of varying the potential at a rate of 0.17 mV/s from the open-circuit potential to a high value and then cycling back to the open-circuit potential. The resultant current is monitored continuously. In order to study the effect of changing Cr content of the surface as a result of corrosion, the polarization scan was repeated several times on the same specimen, with fresh solution being used for each successive scan. Further longer-term studies of the Cr-depleted specimens were conducted using potentiostatic tests where a constant potential was applied and the current monitored over several days. The apparatus for these tests has been described in a previous report (Sridhar et al., 1993). The corrosion potentials under different redox conditions were measured separately using a high-impedance electrometer (Keithley model 614). All potentials were measured with respect to saturated calomel electrodes (SCE).

### 5.3.2 Slow Strain Rate Tests

Initial tests are being conducted on type 316L stainless steel to demonstrate the validity of the slow strain rate technique for evaluating SCC susceptibility. In the slow strain rate technique, a tensile specimen is pulled to complete failure, in a given environment, at a relatively slow strain rate (ranging from  $10^{-6}$  to  $10^{-7}$  s<sup>-1</sup>). Parameters representing the ductility of the material, such as time to failure, percent elongation, and reduction in cross-sectional area, are compared between the environment of interest and an inert environment (air, silicone oil, or glycerine) at the same temperature. Additionally, the specimen is examined after the test for evidence of SCC in terms of altered fracture morphology and presence of secondary cracks along the specimen gage length. The absence of an altered fracture morphology or secondary cracks indicates failure by purely ductile processes. It is known (Cragolino and Sridhar, 1992a) that type 316 stainless steel is susceptible to SCC in relatively dilute chloride-containing solutions at temperatures above 60 °C. However, some contradictory results have been obtained in the application of this technique to nonsensitized austenitic stainless steels, suggesting that the tests have been conducted at strain rates that are too high to detect SCC or at open-circuit potentials located outside the cracking susceptibility range (Beavers and Koch, 1992).

The chemical composition of the heat of type 316L used in this study is given in Table 5-1. The material was obtained in the form of hot-rolled plates, 12.7 mm (0.5 in.) thick. Round specimens were machined with the tensile axis perpendicular to the rolling direction from bars cut from the plates, after the bars were centerless ground to a diameter of 6.35 mm. Two types of specimens were used. One was a round tensile specimen with a waisted section having a gage length of 12.7 mm (0.5 in.) and a diameter of 3.175 mm (0.125 in.). The other type was a round-notched specimen, in which a circumferential notch with a depth of 1.588 mm (0.0625 in.), an aperture of 60°, and a radius of 51 μm was machined. The notched specimen was used to facilitate crack initiation with the additional advantage that the absence of secondary cracks simplifies the measurement of crack velocities. In some tests, an O-ring was placed in the notch position to create an artificial crevice. All the tests were conducted with the alloy in the as-received condition, without any heat treatment after machining. The specimens were wet-ground longitudinally along the gage length with 600 grit SiC paper and washed with acetone and deionized water just before the tests.

The slow strain tests were conducted using two machines in which the pull-rods holding the specimens were electrically isolated from the test frame. Solutions were contained in electrochemical cells made of glass and PTFE, in which the temperature was maintained at the desired value by using external heating tapes, a platinum resistance temperature detector (RTD), and a temperature controller. The cells were fitted with a gas bubbler and a water-cooled condenser connected to a water trap to prevent evaporation of water and back-diffusion of air. A platinum electrode and a SCE were used as counter and reference electrodes, respectively. A salt bridge consisting of a cotton wick passing through a PTFE tube connected the cell to the SCE located in a separate reservoir at room temperature. Accordingly, all the potentials are referred to the SCE scale at ambient temperature (22 °C), because no correction was made for the thermal diffusion potential along the nonisothermal salt bridge.

Most of the tests were conducted under potentiostatic conditions. Potentials were controlled using a Electrosynthesis Model 440 multichannel potentiostat, connected through a Strawberry Tree ACPC-16-16, 16-bit, 16-channel analog-digital converter (ADC) and an ACAO 12-8, 12-bit, 8-channel, digital-analog converter (DAC) to an Austin 386 computer. In addition to the potential and the current, measured as a potential drop through a 10 Ω resistor, voltage signals from load cells and linear voltage

Table 5-1. Chemical compositions of the heat of type 316L SS used in this study

Source of Analyses	Elemental Composition, wt. %										
	Al	C	Cr	Cu	Fe	Mn	Mo	Ni	P	S	Others
Manufacturer	—	0.014	16.35	0.27	Bal.	1.58	2.07	10.04	0.026	0.018	Si:0.49 N:0.06
Independent Laboratory	—	0.019	16.64	0.29	Bal.	1.56	2.16	10.43	0.025	0.014	Si:0.45 N:0.06

differential transducers (LVDT) were also fed into the ADC. The load cell and the LVDT were used to measure the load on the specimen and its extension, respectively, during the course of the test. The data acquisition was performed using Workbench software. This is an icon-based program through which external instruments are controlled, signals acquired, and algebraic and logical operations performed in order to obtain the required data in the appropriate units. In addition, the potential and the current were checked independently by using a Keithley Model 614 electrometer and a Keithley Model 485 picoammeter, respectively. The load cells and the LVDTs, in conjunction with their corresponding signal conditioners, were calibrated using as standards a proving ring and a micrometer, respectively.

In the initial set of tests, the solutions contained 85 ppm  $\text{HCO}_3^-$ , 10 ppm  $\text{NO}_3^-$  and 2 ppm  $\text{F}^-$ , with the addition of 1000 or 10,000 ppm  $\text{Cl}^-$ , and 20, 1000, or 10,000 ppm  $\text{SO}_4^{2-}$ . All these anions were added as  $\text{Na}^+$  salts. The solutions were prepared with reagent grade chemicals and high-purity (17 M $\Omega$ /cm resistivity) water. Solution compositions were selected on the basis of the localized corrosion studies previously reported, in which  $E_p$ ,  $E_{tp}$ , and  $E_{corr}$  values for type 316L stainless steel were determined (Sridhar et al., 1993). All these tests were conducted at 95 °C under potentiostatic conditions and the solutions were purged either with  $\text{N}_2$  gas to remove the dissolved oxygen, or with  $\text{CO}_2$  to attain a pH close to 5.0, simultaneously removing oxygen. A single test was conducted under open-circuit conditions, and, in this case, air was bubbled into the solution. In some tests, the pH of the solutions was initially adjusted to pH 4.0 by the addition of HCl. The environmental conditions for all these tests are summarized in Table 5-2, in which the type of specimen used in each test is described.

A second set of tests was conducted in more concentrated chloride solutions, prepared with salts of different cations ( $\text{Mg}^{2+}$ ,  $\text{Li}^+$ , and  $\text{Na}^+$ ) but without the presence of additional anions. The solution compositions for these tests are summarized in Table 5-3, in which additional information, such as the test temperature and the initial pH values, is also provided. The solutions in this set of tests were fully deaerated with nitrogen.

All of these slow strain rate tests, with the exception of the last four tests, were conducted at an extension rate of  $1.27 \times 10^{-5}$  mm/s ( $5.0 \times 10^{-7}$  in./s), which represents an initial strain rate of  $1.0 \times 10^{-6}$  s $^{-1}$  for the tensile specimens. For the notched specimens, the initial strain rate at the notch tip may represent a strain rate at least two orders of magnitude greater for the same nominal extension rate. The extension rate was reduced to  $4.6 \times 10^{-6}$  mm/s ( $1.8 \times 10^{-7}$  in./s) in the last four tests to increase the sensitivity of the slow strain rate technique.

Table 5-2. Experimental conditions for slow strain rate tests (extension rate =  $1.3 \times 10^{-5}$  mm/s) of type 316 L stainless steel in dilute chloride solutions

Test	Specimen	Machine	T (°C)	Gas	$E_{app}$ (mV <sub>SCE</sub> )	Cl <sup>-</sup> (ppm)	HCO <sub>3</sub> <sup>-</sup> (ppm)	SO <sub>4</sub> <sup>2-</sup> (ppm)	NO <sub>3</sub> <sup>-</sup> (ppm)	Initial pH
SS01	Tensile	1	95	N <sub>2</sub>	0	10000	85	10000	10	4.0
SS02	Tensile	2	95	air	O.C.	10000	85	10000	10	4.0
SS03	Tensile	1	95	N <sub>2</sub>	0	1000	85	1000	10	4.0
SS04	Tensile	2	95	N <sub>2</sub>	0	1000	85	1000	10	7.0
SS05	Tensile	2	95	N <sub>2</sub>	50	1000	85	1000	10	7.0
SS06	Notched <sup>a</sup>	1	95	N <sub>2</sub>	50	1000	85	1000	10	—
SS07	Notched <sup>a</sup>	1	95	CO <sub>2</sub>	0 to -280	1000	85	20	10	—
SS08	Notched <sup>a</sup>	2	95	CO <sub>2</sub>	50	1000	85	20	10	—
SS09	Tensile	1	95	CO <sub>2</sub>	50 to 0	1000	85	20	10	—
SS10	Tensile	2	95	CO <sub>2</sub>	100	1000	85	20	10	—
SS11	Tensile	2	95	CO <sub>2</sub>	-100	10000	85	20	10	—
SS12	Tensile	1	95	CO <sub>2</sub>	-50	10000	85	20	10	—
SS13	Tensile	2	95	CO <sub>2</sub>	-50	10000	85	20	10	—
SS14	Tensile <sup>b</sup>	1	95	CO <sub>2</sub>	-100	10000	85	20	10	—
SS15	Tensile <sup>b</sup>	2	95	CO <sub>2</sub>	-125	10000	85	20	10	—
SS16	Notched	2	95	CO <sub>2</sub>	-100	1000	85	20	10	—
SS17	Notched <sup>a</sup>	2	95	CO <sub>2</sub>	75	1000	85	20	10	8.1
SS18	Notched <sup>a</sup>	2	95	CO <sub>2</sub>	-100	10000	85	20	10	7.8

O.C. — Open circuit

<sup>a</sup> — with O-ring

<sup>b</sup> — with PTFE tape

Table 5-3. Experimental conditions for slow strain rate tests (extension rate =  $1.3 \times 10^{-5}$  mm/s) of type 316 L stainless steel in concentrated chloride solutions

Test	Specimen	Machine	T (°C)	Gas	$E_{app}$ (mV <sub>SCE</sub> )	Solution	Initial pH
SS19	Tensile	1	120	N <sub>2</sub>	O.C.	40% MgCl <sub>2</sub> (14.0 moles Cl <sup>-</sup> /kg water)	—
SS20	Tensile	2	120	N <sub>2</sub>	-260 to -275	40% MgCl <sub>2</sub> (14.0 moles Cl <sup>-</sup> /kg water)	—
SS21	Tensile	1	110	N <sub>2</sub>	-310 to -340	30% MgCl <sub>2</sub> (9.1 moles Cl <sup>-</sup> /kg water)	4.9
SS22	Tensile	2	110	N <sub>2</sub>	O.C.	30% MgCl <sub>2</sub> (9.1 moles Cl <sup>-</sup> /kg water)	4.9
SS23	Tensile	1	95-100	N <sub>2</sub>	O.C.	5.5 moles/L NaCl (6.2 moles Cl <sup>-</sup> /kg water)	2.6
SS24	Tensile	2	95-100	N <sub>2</sub>	-345 to -370	5.5 moles/L NaCl (6.2 moles Cl <sup>-</sup> /kg water)	2.6
SS25	Tensile	1	120	N <sub>2</sub>	-322	10.5 moles/L LiCl (13.9 moles Cl <sup>-</sup> /kg water)	1.6
SS26	Tensile	2	120	N <sub>2</sub>	O.C.	10.5 moles/L LiCl (13.9 moles Cl <sup>-</sup> /kg water)	1.6
SS27	Tensile	1	110	N <sub>2</sub>	-320 to -340	7.5 moles/L LiCl (9.1 moles Cl <sup>-</sup> /kg water)	2.1
SS28	Tensile	2	110	N <sub>2</sub>	O.C.	7.5 moles/L LiCl (9.1 moles Cl <sup>-</sup> /kg water)	2.1
SS29 <sup>a</sup>	Tensile	1	95	N <sub>2</sub>	-320 to -348	5.2 moles LiCl/830 mL water (6.2 moles Cl <sup>-</sup> /kg water)	2.4
SS30 <sup>a</sup>	Tensile	2	95	N <sub>2</sub>	-340 to -380	5.2 moles NaCl/830 mL water (6.2 moles Cl <sup>-</sup> /kg water)	2.7
SS31 <sup>a</sup>	Tensile	1	95	N <sub>2</sub>	-340 to -380	5.2 moles LiCl/830 mL water (6.2 moles Cl <sup>-</sup> /kg water)	2.5
SS32 <sup>a</sup>	Tensile	2	95	N <sub>2</sub>	-360 to -380	5.2 moles NaCl/830 mL water (6.2 moles Cl <sup>-</sup> /kg water)	2.7

O.C. — Open circuit

<sup>a</sup> — extension rate =  $4.6 \times 10^{-6}$  mm/s

After a specimen was mounted inside the cell, the solution was purged with the selected gas and then heated to the desired temperature. The specimen was allowed to attain a steady-state corrosion potential before the selected potential was applied. An initial load of approximately 133 N (30 lb) was applied to the specimen, and straining was started as soon as a steady current was obtained. After failure, the fracture and side surfaces of all specimens tested were examined with a stereoscope. Selected specimens were further examined by SEM. Such examination was conducted after corrosion products deposited in the fracture and side surfaces were ultrasonically removed using a mixture of 4 mL 2-butyne-1,4-diol (35 percent aqueous solution) + 3 mL HCl + 50 mL high-purity water.

## 5.4 RESULTS

### 5.4.1 Localized Corrosion of Cr-Depleted Surfaces

#### 5.4.1.1 Cyclic Polarization Behavior

A typical set of cyclic, potentiodynamic polarization curves for mill-finished specimens of alloy 825 is shown in Figure 5-2. In the first scan, the specimen exhibits only uniform corrosion even though the polarization curve exhibited a slight hysteresis. In the second scan (with fresh solution), the hysteresis is significantly less. In the third scan, there was significant hysteresis attended by pitting on the Cr-depleted surfaces. This behavior of initial narrowing of hysteresis followed by a widening and localized corrosion was reproducible even for specimens that had been thermally oxidized prior to the test, although the specific shapes of the polarization curves varied between specimens.

A better understanding of the cyclic polarization behavior may be obtained by relating the polarization behavior to the surface Cr concentration for each condition. Two potentials in the polarization curves are used in this relationship: the  $E_p$  and  $E_{rp}$ . The  $E_p$  corresponds to the potential at which the current increases rapidly. As mentioned before, in some cases no pitting was observed, and, hence, in these cases this potential is not a true  $E_p$ . Nevertheless it is used as a characteristic of the polarization curve. The  $E_{rp}$  is the potential on the reverse scan at which the current decreases to a low value. Typically, this is taken at the point of intersection of the forward and reverse scans. The effect of surface Cr concentration measured after various scans on the  $E_p$  and  $E_{rp}$  is shown in Figure 5-3. During the early scans, the Cr concentration at the surface was low (along with the Mo concentration) and the alloy corroded in a uniform manner. In this context, the initial large hysteresis in the polarization curve is probably due to the formation of surface film during the mill-annealing operations, which was not removed by mechanical polishing. The hysteresis may also be due to a change in solution composition during forward scan since the solution turned brown due to corrosion of the Cr-depleted surfaces. As the corrosion front progressed through the Cr-depleted layer, it encountered a more corrosion-resistant material. This resulted in a switch from a uniform corrosion mode to one of localized corrosion. The  $E_p$  and  $E_{rp}$  values increase with depth of penetration until the bulk alloy is reached. The data points for the bulk material were obtained using polished specimens whose Cr-depleted layer had been removed mechanically. Thus, there exists a region below the mill-finished surface whose resistance to localized corrosion is less than that of ground and polished surfaces typically tested in laboratories.

#### 5.4.1.2 Constant Potential Studies

The results of the potentiostatic tests on mill-finished specimens of alloy 825 are shown in Figures 5-4 and 5-5. Previous experiments on polished specimens of alloy 825 have shown that a potential of 600 mV<sub>SCE</sub> or higher is required to initiate pits. Below this potential, the alloy corrodes at a low rate

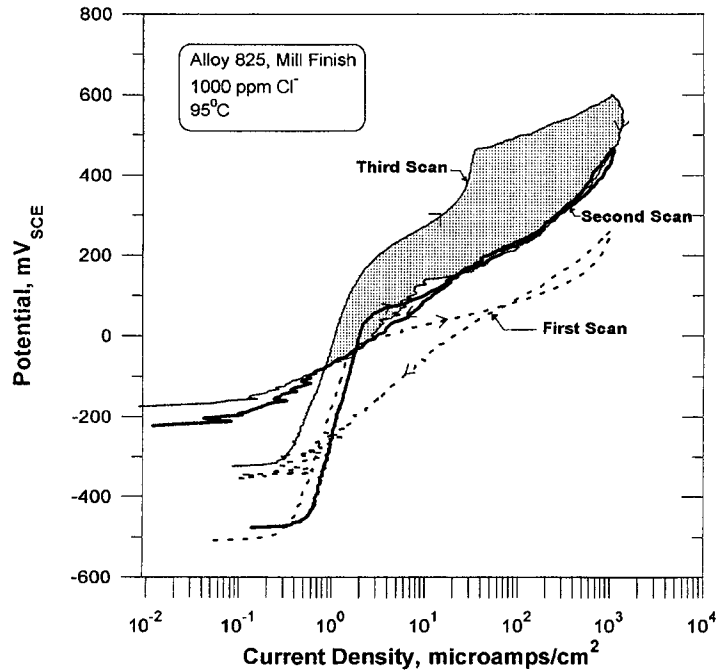


Figure 5-2. Successive cyclic potentiodynamic polarization scans for mill-finished alloy 825 in deaerated 1000 ppm  $\text{Cl}^-$  at 95 °C. Scan Rate = 0.17 mV/s. Fresh solution was used for each scan.

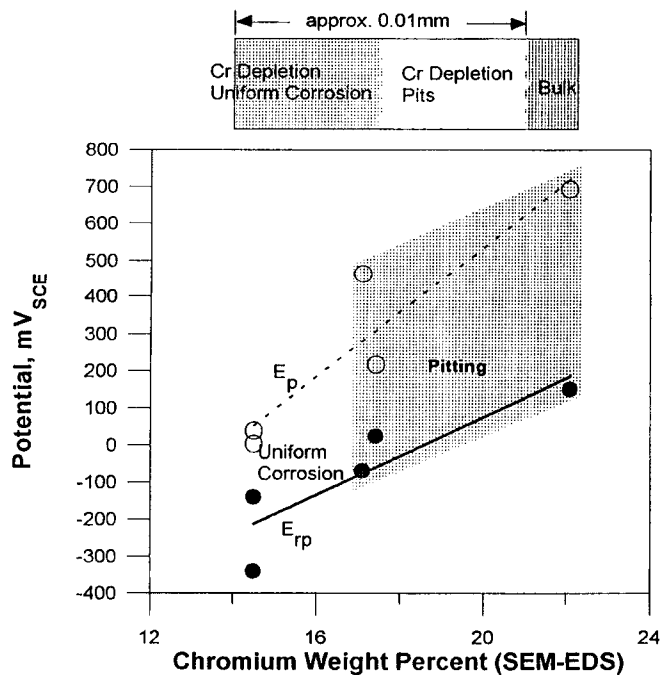


Figure 5-3. Breakdown and repassivation potentials in deaerated 1000 ppm  $\text{Cl}^-$  solution at 95 °C versus surface Cr concentration on corroded and cleaned specimens

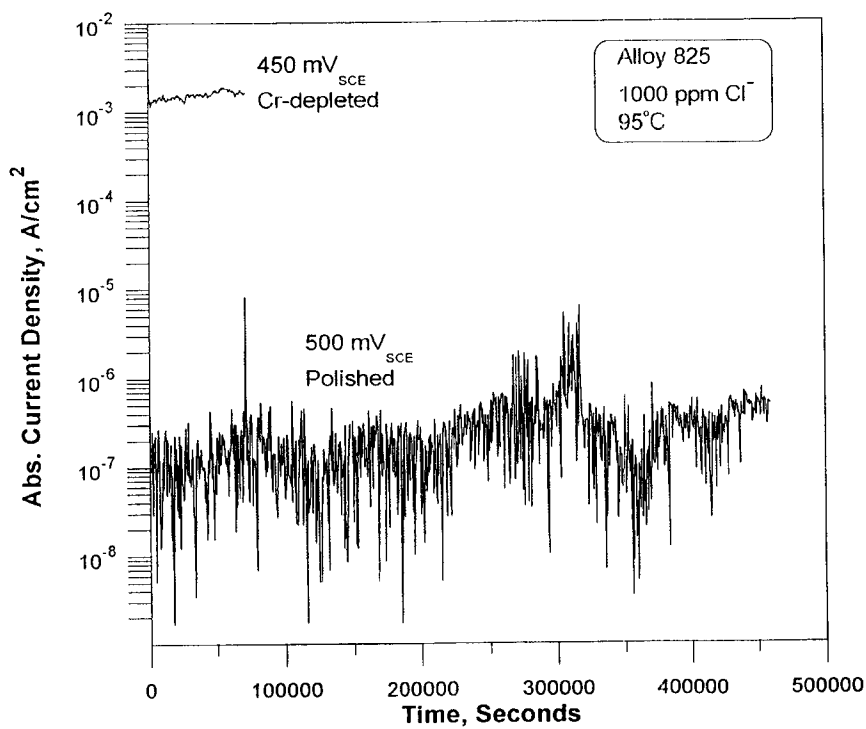


Figure 5-4. Current density as a function of time for polished and mill-finished (Cr-depleted) specimens of alloy 825 in 1000 ppm Cl<sup>-</sup> solution at 95 °C. The solution was purged with high-purity nitrogen.

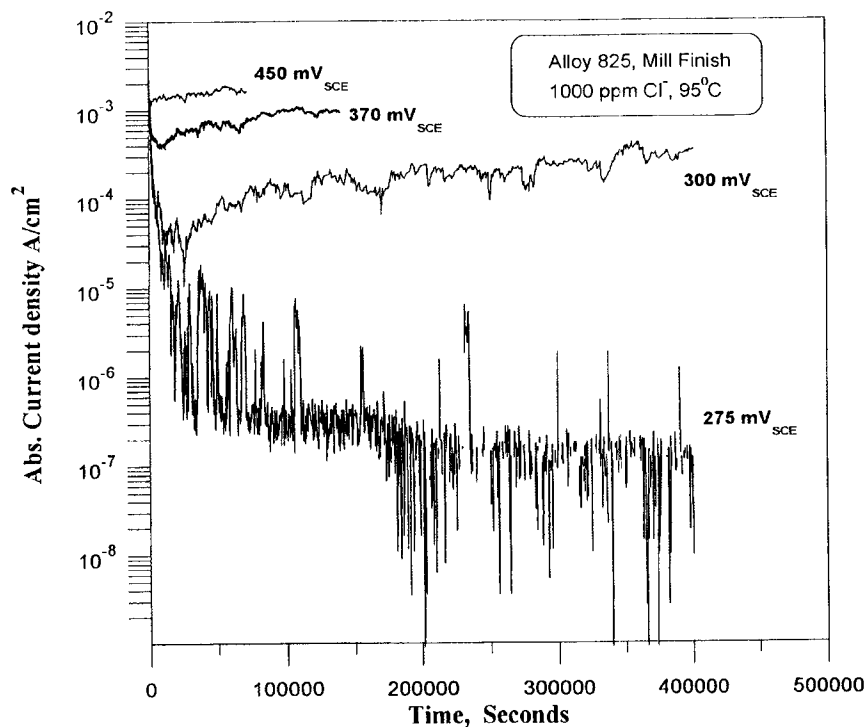


Figure 5-5. Current density as a function of time for mill-finished alloy 825 specimens at various applied potentials. The solution was purged with high-purity nitrogen.

corresponding to the passive current density of the alloy. This is shown in Figure 5-4 for a polished specimen held at 500 mV<sub>SCE</sub>. The absolute value of the current density is plotted because at the low current densities observed on this specimen there were brief bursts of cathodic (negative) current density. On the other hand, even at 450 mV<sub>SCE</sub>, the mill-finished surface exhibited a very high corrosion rate. Post-test examination of the specimen indicated that deep pits were formed. The Cr content away from the pits was 14.9 percent, indicating that the uniform corrosion front did not advance too far in the Cr-depleted zone. The dissolution rate of the Cr-depleted surface is high even at applied potentials as low as 300 mV<sub>SCE</sub> (Figure 5-5). At the applied potential of 275 mV<sub>SCE</sub>, the specimen exhibited a high current initially which then decreased to a value corresponding to the passive current density. Again current noise was observed, but no pits were observed under a stereoscope at 70× magnification.

#### 5.4.1.3 Corrosion Potential Measurements

As mentioned in Section 5.2, long-term prediction of the occurrence of localized corrosion is made by comparing the critical potentials to the corrosion potential. Critical potential is obtained by measuring the response of a material to applied potentials, as discussed in Section 5.4.1.2. Corrosion potential is measured on freely corroding specimens exposed to an environment containing the various anticipated redox species. In the present investigation, the effects of oxygen and hydrogen peroxide were investigated, the former because the repository environment is expected to be saturated with air and the latter because it is expected to form upon radiolysis of an aqueous environment. The corrosion potentials of alloy 825 in a 1000 ppm Cl<sup>-</sup> + 85 ppm HCO<sub>3</sub><sup>-</sup> + 20 ppm SO<sub>4</sub><sup>2-</sup> + 10 ppm NO<sub>3</sub><sup>-</sup> + 2 ppm F<sup>-</sup> solution after various thermal treatments are shown in Figure 5-6. When the solutions were completely deaerated by argon, the corrosion potential was low and unaffected by surface Cr-depletion. Thermal aging of the polished specimen resulted in an increase of over 400 mV in the corrosion potential. The increase in corrosion potential was quite rapid for the specimen aged at 300 °C, attaining a relatively constant or slowly rising value within a day, but the rate of increase was lower for that at 100 °C. In contrast, the Cr-depleted surface did not exhibit any significant change due to thermal aging. Introduction of oxygen into the solution raised the corrosion potential of the polished specimen by about 200 mV in the unaged condition. Thermal aging reduced the effect of oxygen on corrosion potential. It must be noted that the corrosion potential of alloy 825 in an oxygenated environment even in the thermally aged condition was quite low compared to that of platinum (Sridhar et al., 1993). The Cr-depleted specimen exhibited a higher corrosion potential in the oxygenated solution than the polished specimen in the unaged condition, but a lower value in the aged condition. The corrosion potential of the Cr-depleted specimen was also higher by about 300 mV in the oxygenated environment than in the deoxygenated environment under all aging conditions. The addition of 5 mmol/L H<sub>2</sub>O<sub>2</sub> caused an increase in the corrosion potential of both polished and Cr-depleted specimens, the former exhibiting a much stronger positive shift. Thermal aging did not have a significant effect on the corrosion potential in the H<sub>2</sub>O<sub>2</sub> solution.

#### 5.4.2 Slow Strain Rate Tests of Type 316L Stainless Steel

As noted previously, one of the main objectives of these tests was to demonstrate a possible relationship between the E<sub>rp</sub> for pitting/crevice corrosion and a critical potential for SCC that defines the lower limit of the susceptibility range. To select the appropriate potentials for slow strain rate testing of type 316L stainless steel, E<sub>p</sub>, E<sub>rp</sub>, and E<sub>corr</sub> from previous localized corrosion tests (Sridhar et al., 1993) were plotted as a function of chloride concentration, as shown in Figure 5-7. Following an abrupt decrease at low chloride concentrations, both E<sub>p</sub> and E<sub>rp</sub> decrease linearly with the logarithm of chloride concentration at concentrations above 100 ppm. These two potentials define a potential range that

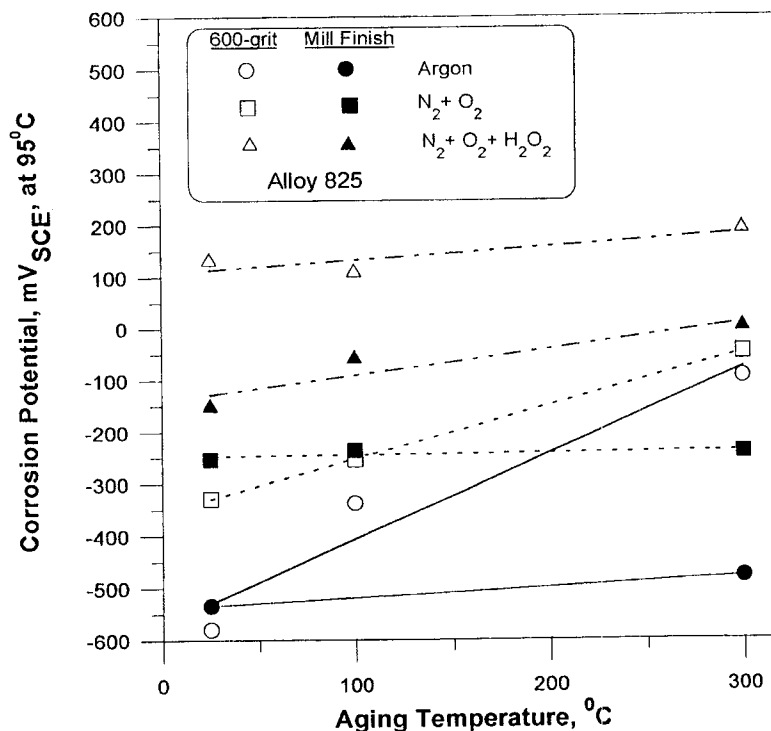


Figure 5-6. Effect of surface condition, thermal treatment, and redox species on the corrosion potential of alloy 825 at 95 °C. Solution used contained 1000 ppm  $\text{Cl}^-$  + 85 ppm  $\text{HCO}_3^-$  + 20 ppm  $\text{SO}_4^{2-}$  + 10 ppm  $\text{NO}_3^-$  + 2 ppm  $\text{F}^-$ .

contracts from approximately 400 mV at 100 ppm  $\text{Cl}^-$  to 200 mV at  $10^5$  ppm  $\text{Cl}^-$ . This is the potential range within which SCC could be expected, because pitting corrosion should predominate at higher potentials, whereas at lower potentials, repassivation of the locally damaged passive film would overcome any tendency for crack initiation (Cragolino and Sridhar, 1992a). It is also seen in Figure 5-7 that  $E_{\text{corr}}$  is practically independent of the chloride concentration with values slightly lower than  $-600 \text{ mV}_{\text{SCE}}$ , indicating that the predominant cathodic reaction is the reduction of hydrogen ions because oxygen has been removed from the solution. As shown in Table 5-2, potentials located between  $E_{\text{TP}}$  and  $E_{\text{p}}$  were selected for slow strain rate testing in a variety of solutions in which not only the chloride concentration was changed from 1000 to 10,000 ppm, but the sulfate concentration was decreased (from 10,000 to 20 ppm). The initial pH of these solutions was modified from 8.1 to 4.0 or 5.4, either by the addition of HCl or by bubbling  $\text{CO}_2$ .

The results of these tests are detailed in Table 5-4 and summarized in Figure 5-8. It is seen that no SCC was observed in all these tests, even at relatively high potentials within the range defined above. The elongation to failure was found to be 55.6 percent in average for all the tensile specimens, with a standard deviation of approximately 10 percent, indicating a high degree of ductility but a relatively large dispersion in the elongation values. In a single case, a specimen failed as a result of severe pitting corrosion, exhibiting an elongation of only 20.2 percent. This occurred at the highest potential tested in the solution of pH 4.0 containing 10,000 ppm  $\text{Cl}^-$  and 10,000 ppm  $\text{SO}_4^{2-}$ , even though this potential ( $0 \text{ mV}_{\text{SCE}}$ ) was lower than the corresponding  $E_{\text{p}}$ . From this result, it is apparent that pitting can be initiated at potentials lower than  $E_{\text{p}}$  in prolonged tests, but pits do not seem to act as initiation sites for cracks under these experimental conditions. All these tests were conducted potentiostatically, with the exception of one test that was carried under open-circuit conditions in a solution in which synthetic air

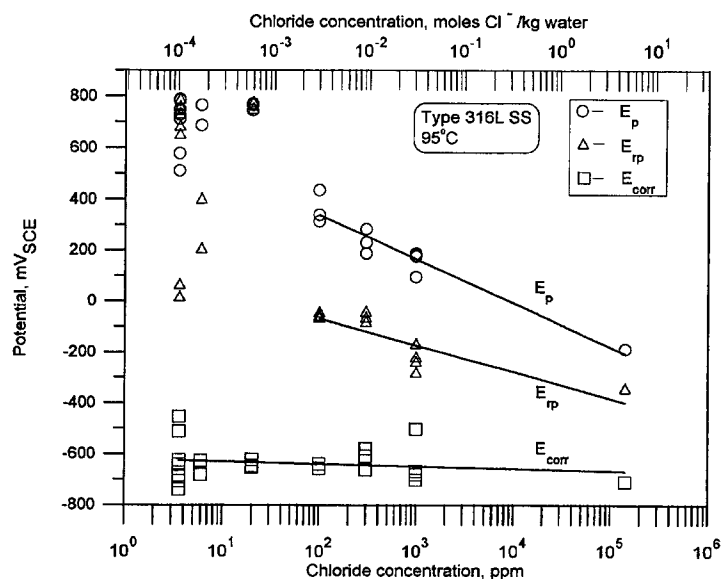


Figure 5-7. Effect of chloride concentration on pitting ( $E_p$ ), repassivation ( $E_{rp}$ ), and corrosion ( $E_{corr}$ ) potentials of type 316L stainless steel in chloride-containing solutions (pH 8.1 to 8.4) at 95 °C

( $N_2$ -20 vol%  $O_2$ ) was bubbled into the solution. The corrosion potential decreased during the test from 0 to  $-200$  mV<sub>SCE</sub>, but only ductile failure was observed. Even in some specific tests, in which a piece of PTFE tape was wrapped around the gauge section of tensile specimens in order to promote crevice conditions that may lead to crack initiation, no SCC was observed. The use of notched specimens did not lead to the initiation of cracks, although an O-ring was used to create crevice conditions. It was expected that a notch would facilitate crack initiation by localized intensification of the stress, avoiding the simultaneous initiation of several cracks, but it appears that the extension rate at the root of the notch is too high and ductile failure occurred before any crack could be initiated. It should be noted that the failure times for tests conducted with notched specimens were shorter, by about a factor of four, than those for tensile specimens, which significantly decreases the exposure time. It appears that the extension rate should be reduced, at least by an order of magnitude, to promote crack initiation in a notched specimen. In addition, tests should be conducted at other potentials.

An additional set of tests was conducted using tensile specimens under the environmental conditions described in Table 5-3, which essentially represent various concentrated chloride solutions of different cations. Magnesium chloride is a well-known cracking environment for austenitic stainless steels such as type 316L. Hence, the initial tests of this set were conducted at 120 °C in 40%  $MgCl_2$  solution (14.0 moles  $Cl^-$ /kg water) at the corrosion potential (approximately  $-300$  mV<sub>SCE</sub>) and at a slightly anodic potential ( $-280$  mV<sub>SCE</sub>). The boiling point of this solution is 138 °C at 1 atm pressure. SCC was observed under both conditions in which elongation values of 7.4 percent and 4.6 percent were obtained, respectively, as shown in Table 5-5. Similar results were obtained at a lower temperature (110 °C) in a less concentrated solution (30%  $MgCl_2$ ) in which the chloride concentration is 9.1 moles/kg water. In

**Table 5-4. Results of slow strain rate tests of type 316L stainless steel in dilute chloride solutions at 95 °C (test conditions are given in Table 5-2)**

Test	Spec.	T (°C)	Gas	$E_{corr}$ (mV <sub>SCE</sub> )	$E_{app}$ (mV <sub>SCE</sub> )	Current (Amps)	Cl <sup>-</sup> (ppm)	SO <sub>4</sub> <sup>2-</sup> (ppm)	Elong (in)	Failure Time (h)	TEST RESULTS
SS01	T	95	N <sub>2</sub>	—	0	10 <sup>-2</sup>	10000	10000	0.101	59.5	Severe pitting
SS02	T	95	air	0 to -200	O.C.	—	10000	10000	0.289	167.9	Ductile failure
SS03	T	95	N <sub>2</sub>	—	0	Cathodic	1000	1000	—	24.0	Test interrupted
SS04	T	95	N <sub>2</sub>	—	0	10 <sup>-5</sup> to 10 <sup>-6</sup>	1000	1000	0.305	221.0	Ductile failure
SS05	T	95	N <sub>2</sub>	—	50	9 × 10 <sup>-6</sup> to 1.3 × 10 <sup>-3</sup>	1000	1000	—	171.0	Test interrupted
SS06	N <sup>a</sup>	95	N <sub>2</sub>	-142	50	—	1000	1000	—	—	Test interrupted
SS07	N <sup>a</sup>	95	CO <sub>2</sub>	-256	0 to -280	5.2 × 10 <sup>-6</sup>	1000	20	0.060	57.5	No SCC
SS08	N <sup>a</sup>	95	CO <sub>2</sub>	—	50	5.3 × 10 <sup>-5</sup> oscillated	1000	20	0.070	48.9	No SCC
SS09	T	95	CO <sub>2</sub>	-514	50 to 0	3 × 10 <sup>-4</sup> to -3 × 10 <sup>-6</sup>	1000	20	0.340	196.0	Ductile failure
SS10	T	95	CO <sub>2</sub>	-523	100	1 × 10 <sup>-4</sup> to 8 × 10 <sup>-4</sup>	1000	20	0.231	131.5	Ductile failure
SS11	T	95	CO <sub>2</sub>	-260	-100	—	10000	20	0.275	—	Data lost
SS12	T	95	CO <sub>2</sub>	-260	-50	10 <sup>-4</sup> to 10 <sup>-3</sup>	10000	20	0.219	89.4	No SCC
SS13	T	95	CO <sub>2</sub>	-311	-50	2.0 × 10 <sup>-4</sup>	10000	20	0.207	135.6	No SCC
SS14	T <sup>b</sup>	95	CO <sub>2</sub>	-322	-100	5 × 10 <sup>-4</sup> to 3 × 10 <sup>-3</sup>	10000	20	0.289	162.9	No SCC
SS15	T <sup>b</sup>	95	CO <sub>2</sub>	-332	-125	5 × 10 <sup>-6</sup> to 1 × 10 <sup>-5</sup>	10000	20	0.343	188.9	Ductile failure
SS16	N	95	CO <sub>2</sub>	-253	-100	5 × 10 <sup>-3</sup>	1000	20	0.095	58.9	No SCC
SS17	N <sup>a</sup>	95	CO <sub>2</sub>	-250	75	10 <sup>-4</sup> to 10 <sup>-3</sup>	1000	20	0.083	45.5	No SCC
SS18	N <sup>a</sup>	95	CO <sub>2</sub>	-247	-100	3 × 10 <sup>-4</sup>	10000	20	0.086	47.3	No SCC

T — Tensile specimen

N - Notched specimen

O.C. — Open circuit

<sup>a</sup> — with O-ring

<sup>b</sup> — with PTFE tape

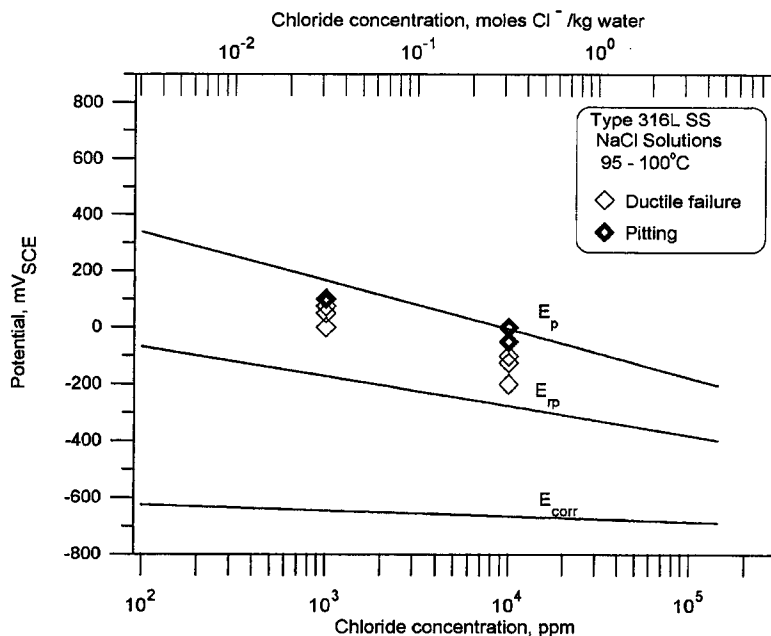


**Figure 5-8. Potentials and chloride concentrations selected for slow strain rate tests of type 316L stainless steel in dilute chloride solutions at 95 °C in relation to pitting ( $E_p$ ) and repassivation ( $E_{rp}$ ) potentials, indicating the failure mode**

this case again, a decrease in the elongation to failure from 49.4 to 15.2 percent was observed by increasing the potential to slightly anodic values with respect to the open-circuit potential. Extensive secondary cracking was observed on the side surfaces of these specimens, with the exception of the specimen tested at the open-circuit potential in the less concentrated solution in which very few incipient cracks were detected. Figure 5-9 shows the typical appearance of these secondary cracks, as well as a view of the area close to the fracture surface exhibiting no signs of ductility. Figure 5-10 shows the morphology of the fracture surface at low magnification. Higher magnification fractographs revealed that, besides the cleavage-like features typical of the transgranular cracking of austenitic stainless steels in boiling  $MgCl_2$  solutions (Figure 5-11), intergranular cracking (Figure 5-12) occurred over a large proportion of the fracture surface. Detailed examination seems to indicate that cracking initiated transgranularly but propagated mostly in an intergranular fashion through the specimen. The proportion of intergranular cracking diminished with the decrease in the severity of the environment, in terms of chloride concentration and temperature and also with the decrease in potential.

As shown in Table 5-5, two tests were conducted at 95-100 °C in a concentrated NaCl solution in which the pH was adjusted to 2.6 by the addition of HCl. An elongation to failure of 64 percent was obtained under open-circuit conditions that decreased to 28.8 percent at a slight anodic potential. The potential was diminished by about 25 mV during the course of the test in order to avoid pitting, and this was controlled by maintaining the current below 1 mA. Whereas the specimen tested at the corrosion potential exhibited ductile failure, the one tested at an anodic potential exhibited a relatively unusual, flat topography on a significant fraction of the fracture surface. However, no quasi-cleavage features, typical of transgranular SCC (TGSCC), or the grain faces characteristic of intergranular SCC (IGSCC), were noted in the fractographs. Some irregular pits, around 100  $\mu m$ , were observed on the side surfaces. The complete absence of secondary cracks, however, was the dominant feature.

Table 5-5. Results of slow strain rate tests of type 316L stainless steel in concentrated chloride solutions (test conditions are given in Table 5-3)

Test	T (°C)	E <sub>corr</sub> (mV <sub>SCE</sub> )	E <sub>app</sub> (mV <sub>SCE</sub> )	Current (Amps)	Solution	Initial pH	Final pH	Elong. (in.)	Failure Time (h)	Test Results
SS19	120	-311	O.C.	—	40% MgCl <sub>2</sub> (14.0 moles Cl <sup>-</sup> /kg water)	—	—	0.037	22.9	IGSCC and TGSCC
SS20	120	-280	-260 to -275	10 <sup>-5</sup> to 10 <sup>-3</sup>	40% MgCl <sub>2</sub> (14.0 moles Cl <sup>-</sup> /kg water)	—	—	0.023	12.4	IGSCC and TGSCC
SS21	110	-326	-310 to -340	10 <sup>-5</sup> to 10 <sup>-3</sup>	30% MgCl <sub>2</sub> (9.1 moles Cl <sup>-</sup> /kg water)	4.9	5.9	0.076	44.7	IGSCC and TGSCC
SS22	110	-331	O.C.	—	30% MgCl <sub>2</sub> (9.1 moles Cl <sup>-</sup> /kg water)	4.9	5.9	0.247	138.6	Ductile and some IGSCC
SS23	95-100	-361	O.C.	—	5.5 moles/L NaCl (6.2 moles Cl <sup>-</sup> /kg water)	2.6	—	0.320	177.7	Ductile failure
SS24	95-100	-363	-345 to -370	10 <sup>-6</sup> to 10 <sup>-3</sup>	5.5 moles/L NaCl (6.2 moles Cl <sup>-</sup> /kg water)	2.6	7.0	0.144	80.2	Ductile and brittle fracture regions
SS25	120	-353	-322	10 <sup>-6</sup> to 4.7 × 10 <sup>-4</sup>	10.5 moles/L LiCl (13.9 moles Cl <sup>-</sup> /kg water)	1.6	2.0	0.013	7.2	TGSCC some IGSCC
SS26	120	-356	O.C.	—	10.5 moles/L LiCl (13.9 moles Cl <sup>-</sup> /kg water)	1.6	1.4	0.078	44.2	TGSCC and IGSCC
SS27	110	-343	-320 to -340	10 <sup>-4</sup>	7.5 moles/L LiCl (9.1 moles Cl <sup>-</sup> /kg water)	2.1	5.9	0.066	38.25	TGSCC, IGSCC some ductile regions

O.C. — Open circuit      <sup>a</sup> — extension rate = 4.6 × 10<sup>-6</sup> mm/s  
 IGSCC — Intergranular SCC    TGSCC — Transgranular SCC

Table 5-5. Results of slow strain rate tests of type 316L stainless steel in concentrated chloride solutions (test conditions are given in Table 5-2) (cont'd)

Test	T (°C)	E <sub>corr</sub> (mV <sub>SCE</sub> )	E <sub>app</sub> (mV <sub>SCE</sub> )	Current (Amps)	Solution	Initial pH	Final pH	Elong. (in.)	Failure Time (h)	Test Results
SS28	110	-353	O.C.	—	7.5 moles/L LiCl (9.1 moles Cl <sup>-</sup> /kg water)	2.1	6.1	0.147	79.2	TGSCC, IGSCC some ductile regions
SS29 <sup>a</sup>	95	-340	-320 to -348	10 <sup>-3</sup>	5.2 moles LiCl/830 mL water (6.2 moles Cl <sup>-</sup> /kg water)	2.4	7.9	0.054	90.3	Severe pitting
SS30 <sup>a</sup>	95	-356	-340 to -380	10 <sup>-3</sup>	5.2 moles NaCl/830 mL water (6.2 moles Cl <sup>-</sup> /kg water)	2.7	8.2	0.066	104.3	Severe pitting
SS31 <sup>a</sup>	95	-347	-340 to -680	10 <sup>-7</sup> to 10 <sup>-3</sup>	5.2 moles LiCl/830 mL water (6.2 moles Cl <sup>-</sup> /kg water)	2.5	5.6	0.280	435.1	Ductile failure/ Pitting
SS32 <sup>a</sup>	95	-359	-360 to -380	10 <sup>-7</sup> to 10 <sup>-4</sup>	5.2 moles NaCl/830 mL water (6.2 moles Cl <sup>-</sup> /kg water)	2.7	6.7	0.178	267.2	Ductile failure/ Pitting

O.C. — Open circuit      <sup>a</sup> — extension rate =  $4.6 \times 10^{-6}$  mm/s  
 IGSCC — Intergranular SCC    TGSCC — Transgranular SCC

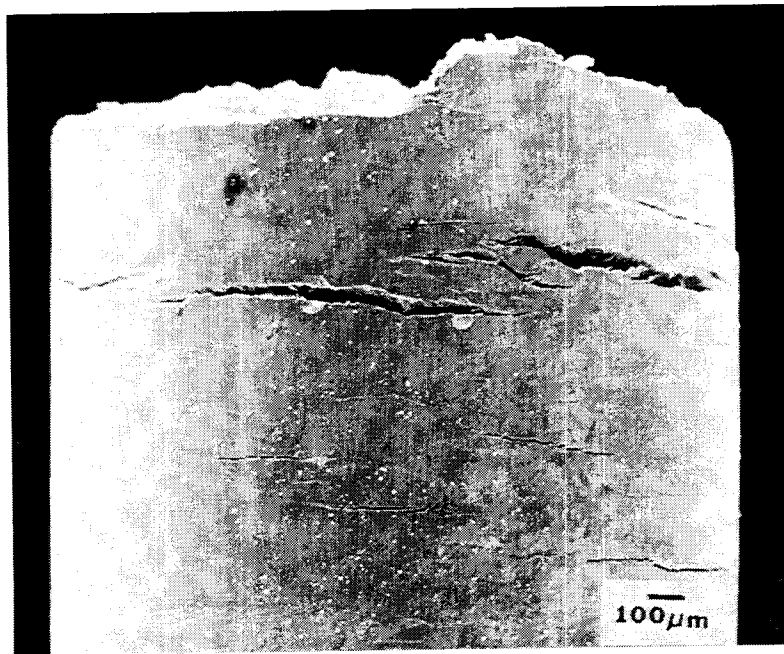


Figure 5-9. Side surface of specimen tested under open-circuit conditions in 40%  $\text{MgCl}_2$  solution at 120 °C showing the presence of many secondary cracks

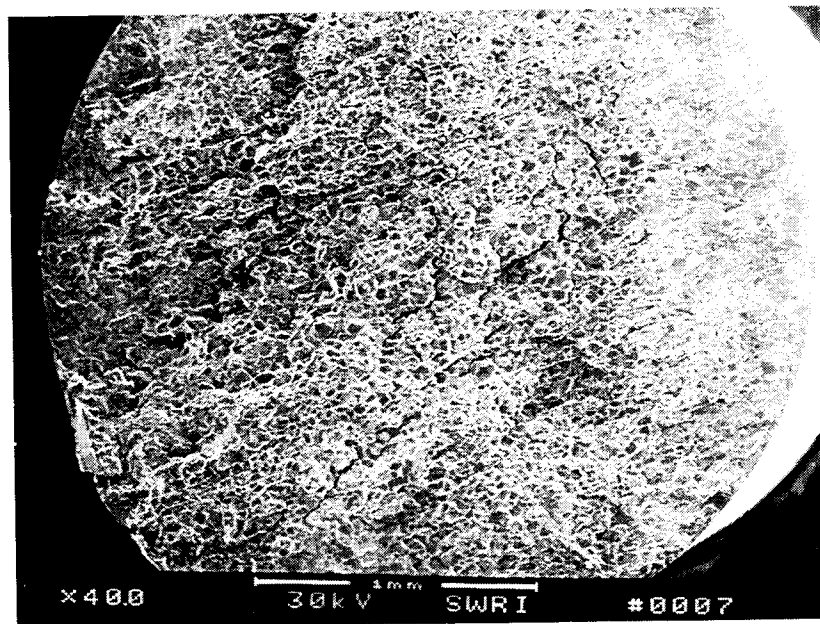
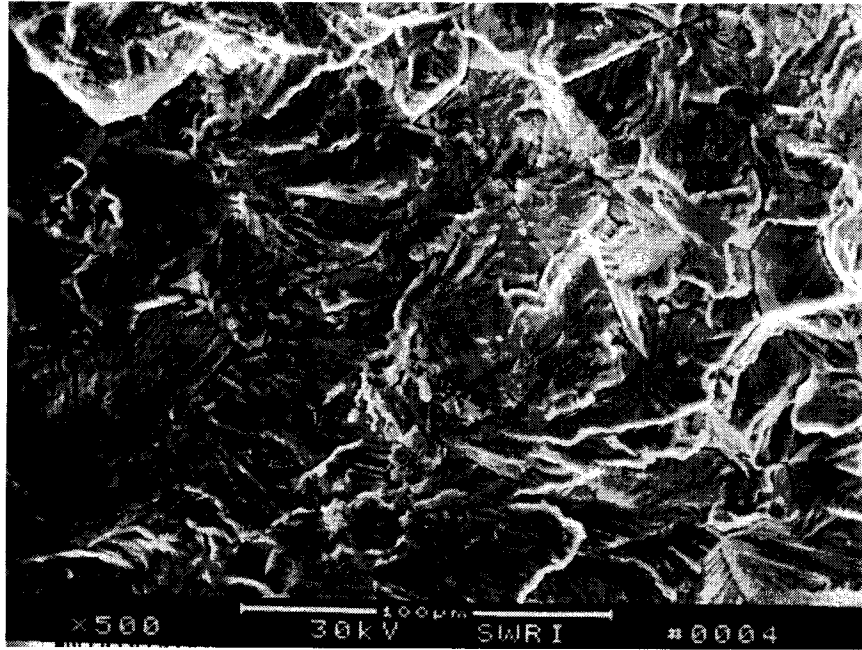
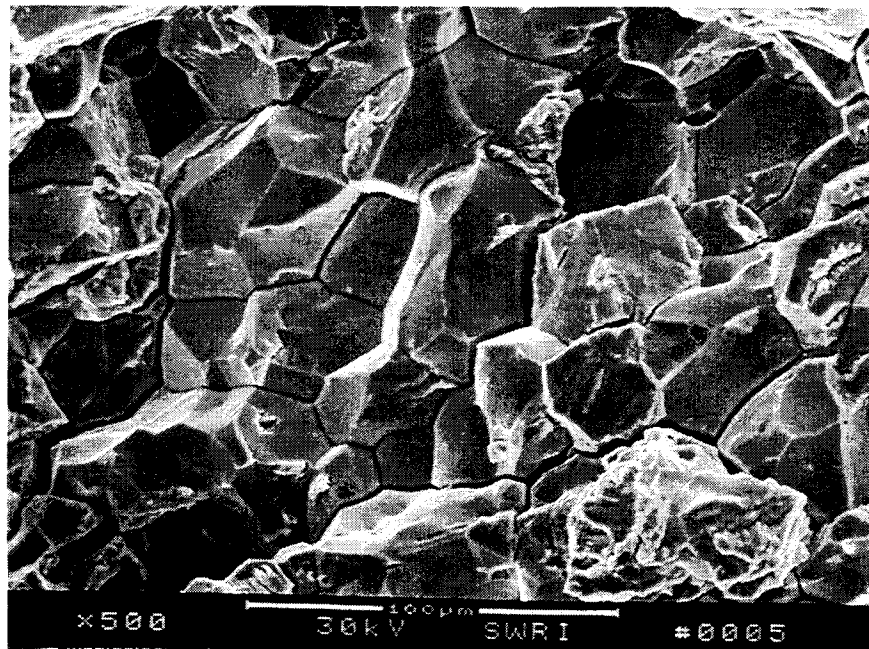


Figure 5-10. Fracture surface of specimen tested under open-circuit conditions in 40%  $\text{MgCl}_2$  solution at 120 °C



**Figure 5-11. Fractograph showing the transgranular SCC area of the specimen tested under open-circuit conditions in 40% MgCl<sub>2</sub> solution at 120 °C**



**Figure 5-12. Fractograph showing the intergranular SCC area of the specimen tested under open-circuit conditions in 40% MgCl<sub>2</sub> solution at 120 °C**

On the other hand, SCC was observed in four tests conducted at 120 and 110 °C in concentrated LiCl solutions acidified to pH 2.0 by the addition of HCl, as summarized in Table 5-5. The pattern was similar to that found in MgCl<sub>2</sub> solutions at equivalent chloride concentrations. SCC occurred under open-circuit conditions, but cracking susceptibility increased significantly with anodic polarization, as can be concluded from the decrease in the elongation to failure. These observations were confirmed by fractographic examination. Extensive areas of IGSCC and TGSCC were observed in these fractographs. It appears, however, that the proportion of intergranularly cracked areas was smaller than that observed under equivalent conditions in MgCl<sub>2</sub> solutions. The susceptibility to SCC, as evaluated from the elongation to failure values and the appearance of the fracture surfaces, decreased with decreasing chloride concentration and temperature.

Four additional tests were conducted at 95 °C to compare the behavior in NaCl solutions with that in LiCl solutions at an equivalent chloride concentration of 6.2 moles/kg water. This concentration was chosen because it is close to the solubility of NaCl at 90 °C. The pH was adjusted to  $2.5 \pm 0.2$  with the addition of HCl. Also, the extension rate was decreased to  $4.6 \times 10^{-6}$  mm/s to increase the sensitivity of the technique. However, as shown in Table 5-5, no SCC was observed in these tests. Severe pitting occurred in the first two of this set of tests causing the premature failure of the specimens. In the remaining tests, ductile failure predominated, but was accompanied by pitting corrosion.

Several stress versus elongation curves obtained in some of the tests conducted in concentrated LiCl solutions are plotted for comparison in Figure 5-13. The different curves represent the range of behaviors from severe SCC to ductile failure with minor pitting corrosion. The significant decrease in ductility promoted by the application of an anodic overpotential of only 30 mV with respect to the corrosion potential is clearly seen in the curves for the solution containing 9.1 moles Cl<sup>-</sup>/kg water. The slow relaxation of the load, caused by the propagation of cracks, is particularly noticeable in this test. On the other hand, a very high elongation to failure, close to 55 percent, accompanied by a sudden drop in the load characterizes the predominantly ductile behavior in the solution containing 6.1 moles Cl<sup>-</sup>/kg water.

## 5.5 DISCUSSION

### 5.5.1 Localized Corrosion of Mill-Finished Alloy 825

It is sometimes assumed that surface Cr-depletion is of no great long-term consequence because the depleted layer is dissolved rapidly and uniformly and the sound material underneath exposed. The results shown in Figures 5-3 and 5-5 clearly demonstrate that localized corrosion in the form of pits can be more easily initiated (i.e., in less oxidizing environments) on mill-finished surfaces than on polished surfaces due to lower surface Cr concentration. A possibility exists that once pits are initiated, they will continue to grow through the bulk material. Since the container surfaces in the repository are most likely to be in the mill-finished condition, laboratory tests used to select materials and predict their performance must include an evaluation of this surface condition. The tests to date have shown that, depending upon the potential, corrosion initially proceeds by uniform dissolution. Then pits are initiated and propagate inward. If the potential is higher than the  $E_{tp}$  of the base alloy (polished specimen), then the pits will continue to grow. If the potential is lower than the  $E_{tp}$  of the polished alloy, then the pits will cease to grow once they encounter the bulk alloy. For a given alloy composition, the  $E_{tp}$  decreases with an increase in pit depth up to a certain value and then becomes independent of pit depth (Sridhar et al.,

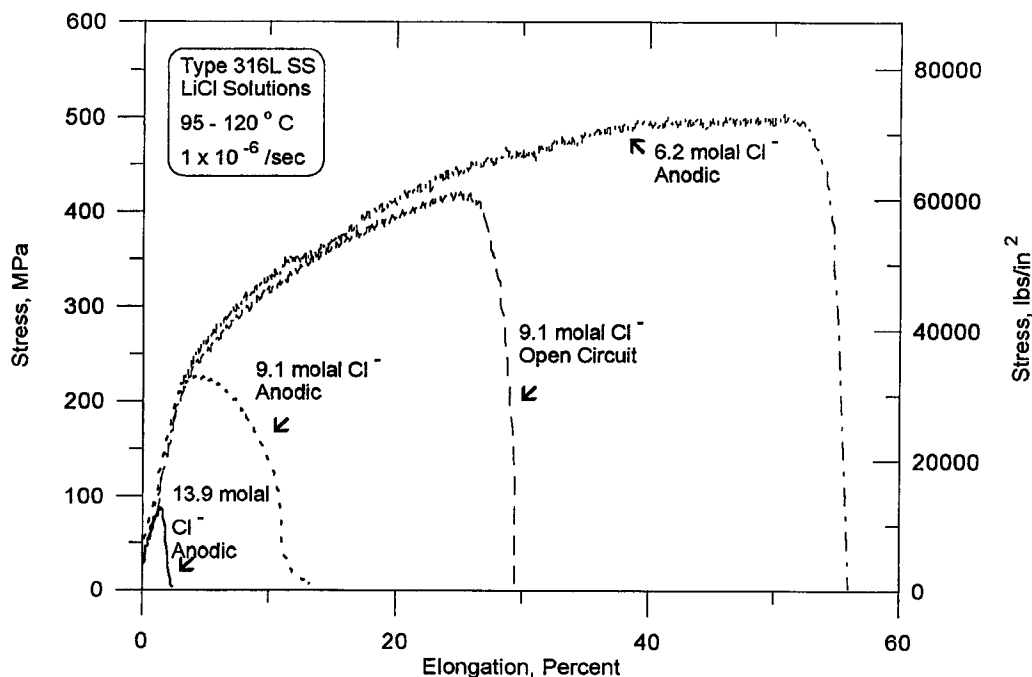


Figure 5-13. Stress versus elongation curves obtained in slow strain rate tests of type 316L stainless steel in concentrated LiCl solutions at temperatures ranging from 95 to 120 °C

1993). For shallow pits (pit depth less than about 400  $\mu\text{m}$ ), the  $E_{\text{rp}}$  can be as high as 350  $\text{mV}_{\text{SCE}}$ . The pits that grow through the Cr-depletion zone have a small depth. Hence, as shown in Figure 5-5, at potentials below about 275  $\text{mV}_{\text{SCE}}$ , which is below the  $E_{\text{rp}}$  for shallow pits, there is an initially high current density followed by a rapid decay to a low value. At potentials above this value, pits continue to grow through the bulk alloy because they are above repassivation potentials for even shallow pits. In this context, the  $E_{\text{rp}}$  for deep pits (pit depth greater than about 500  $\mu\text{m}$ ) can be considered to be a conservative parameter irrespective of the surface condition. If the corrosion potential is maintained at or below the  $E_{\text{rp}}$  for deep pits, then no pits can initiate or any propagative pit will repassivate.

The corrosion potential is a mixed potential determined by the kinetics of redox reactions and dissolution reactions on a given substrate. This is illustrated schematically in Figure 5-14a and b. Here, the anodic (oxidation) and cathodic (reduction) currents are plotted on the same side of the axis although they are of opposite signs. The  $E_{\text{eq}}^{\text{c}}$  is the equilibrium potential of the cathodic reaction (e.g., oxygen reduction), and  $E^{\text{a}}$  is the open-circuit potential of the anodic reaction (e.g., metal dissolution), under reducing conditions. The  $i_0^{\text{c}}$  is the exchange current density for the cathodic reaction that corresponds to the rates of forward and backward reactions at equilibrium. The anodic kinetics of a passive alloy, such as alloy 825, consists of an essentially potential-independent current region (passive regime) and a transpassive region of sharply increasing current with potential that can be a mixture of anodic dissolution and oxygen evolution from the oxidation of water. A prepassive region of high current is ignored in this analysis because of the rapid passivation kinetics of alloy 825. The passive current density, which arises from the formation of a thin film of hydrated oxide, is dependant upon several factors including passive film thickness, electronic properties of the passive film, alloy composition, and environmental factors such as pH and temperature. The cathodic reduction kinetics is indicated by the downward sloping line

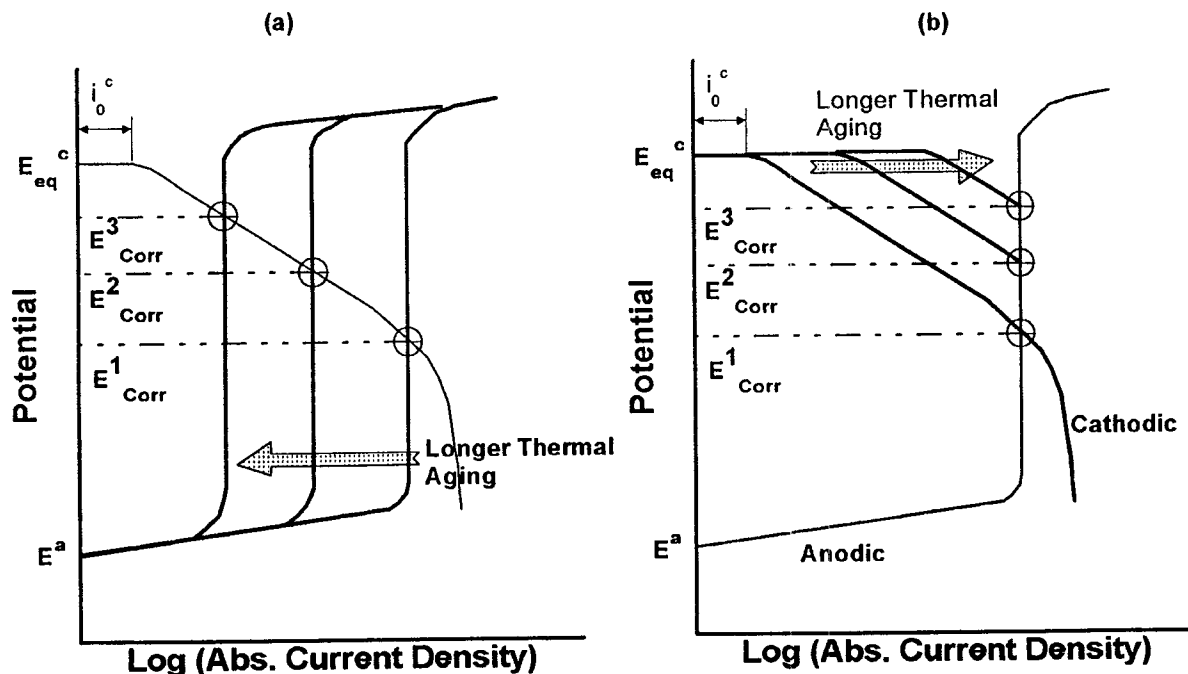


Figure 5-14. Schematic illustration of the formation of a corrosion potential as a result of anodic dissolution kinetics and cathodic redox reaction kinetics. A single redox reaction is assumed for simplicity and a passive behavior for the anodic dissolution of the alloy. (a) variation of  $E_{Corr}$  due to changes in anodic kinetics and (b) variation of  $E_{Corr}$  due to changes in cathodic kinetics.

that is characterized by a flat region corresponding to an exchange current density ( $i_0^c$ ), a log-linear Tafel region, and a diffusion limited region where the current is independent of applied potential. As indicated in Figure 5-14a, increasing the film thickness, for example by thermal aging, can result in a lowering of passive current density. The corrosion potential is the potential at which the sum of all currents equals zero, as indicated by the intersection of anodic and cathodic curves in Figures 5-14a and b. If it is assumed that the thermal aging did not affect the reduction kinetics but reduced the passive current density either through film thickening or through an alteration of the electronic property of the film, then the corrosion potential will increase with thermal aging (Figure 5-14a). If, on the other hand, passive current density is increased by surface Cr-depletion, then a decrease in corrosion potential of the Cr-depleted alloy can be explained. Alternatively, the reduction reaction kinetics can be affected by surface changes (Figure 5-14b).

The oxygen reduction reaction kinetics on Fe-Ni-Cr alloys have not been studied extensively. However, limited data that are available suggest that the exchange-current density for oxygen reduction reaction on Cr-containing alloys is quite low (about  $10^{-10}$  amps/cm<sup>2</sup>) compared to that on platinum (about  $10^{-5}$  to  $10^{-6}$  amps/cm<sup>2</sup>). This explains the much lower corrosion potential of alloy 825 in an oxygenated environment than that of platinum. Typically, the oxygen reduction reaction on stationary electrodes is controlled by diffusion of oxygen to the metal surface and hence is not expected to be affected by changes in the surface film or Cr concentration. Thus, the changes in the observed corrosion

potential in an oxygenated environment due to thermal aging and Cr-depletion (Figure 5-6) is most probably due to changes in the passive current density (anodic reaction kinetics). This also may explain the relative independence of corrosion potential of the Cr-depleted specimens to thermal aging (closed squares in Figure 5-6) since the effects of Cr-depletion (increasing passive current density) and thermal aging (decreasing passive current density) compensate each other. The results of cyclic polarization curves on polished and thermally aged specimens confirm the effect of aging on the decrease in passive current density (Table 5-6). However, the effect of aging on passive current density does not explain why the corrosion potential of the 300 °C aged specimen in oxygenated environment is close to that in the deoxygenated environment. In this case, it is possible that aging had an effect on the oxygen reduction kinetics. Further experiments under controlled hydrodynamic conditions are necessary to understand these effects. The corrosion potentials in the solutions containing  $H_2O_2$  were independent of thermal aging for both the polished and Cr-depleted specimens. This may be due to the opposing effects of decreasing passive current density (Figure 5-14a) and increasing cathodic kinetics (Figure 5-14b) as a result of thermal aging. Further experiments on the cathodic reaction kinetics of  $H_2O_2$  are necessary to understand the factors affecting the corrosion potential in this solution.

A comparison of Figures 5-5 and 5-6 suggests that under natural exposure conditions, assuming that  $O_2$  and  $H_2O_2$  are the only oxidizing species, pits will not initiate or propagate even on a Cr-depleted surface of alloy 825. Although the critical potential for pit initiation of the Cr-depleted surface is lower than that of the polished surface, the corrosion potential is also lower. However, several important considerations must temper this conclusion:

- The critical potentials for pit initiation and repassivation depend on the test time and pit size. It has been argued that, for long-term tests, the  $E_p$  will be lower (Rosenfeld et al., 1978; Thompson and Syrett, 1992). The  $E_{rp}$  decreases with pit depth and attains a lower-bound value of about 100 mV<sub>SCE</sub> (Sridhar et al., 1993). This potential is slightly below the corrosion potential of the bulk alloy in the  $H_2O_2$  solution (Figure 5-6), and, hence, pit growth is possible under natural conditions if radiolysis products of aqueous solutions are present.
- The  $E_{rp}$  for deep pits is also important for crevice corrosion since a crevice may be regarded as a deep pit. It has been shown that the  $E_{rp}$  for crevice corrosion is the same as initiation potential for crevice corrosion in long-term exposure studies (Tsuji-kawa and Hisamatsu, 1984). Under such conditions, crevice corrosion may be a possibility for alloy 825 if aqueous solution radiolysis products are present in the repository environment. Long-term testing of alloy 825 with well-defined crevices under controlled potentials is necessary to verify this possibility.
- The critical potentials discussed thus far pertain to one environmental composition. If the chloride concentration increases beyond 1000 ppm due to evaporative effects, the critical potentials can decrease below the corrosion potentials to initiate localized corrosion. The effect of chloride concentration and test technique on critical potentials has been discussed in a previous report (Sridhar et al., 1993), as shown in Figure 5-15 for alloy 825 using a cyclic potentiodynamic polarization test technique. In this figure, the corrosion potentials of alloy 825 in aerated and  $H_2O_2$  added solutions (horizontal lines) are compared to the  $E_p$  and  $E_{rp}$  at various chloride concentrations. The corrosion potential of the unaged, polished specimen in oxygenated solution is below the critical potentials for alloy 825 at all chloride concentrations up to 4 M. However, in  $H_2O_2$  containing solutions,  $E_{corr}$  is higher than  $E_{rp}$ .

**Table 5-6. Effect of thermal aging on the electrochemical parameters of alloy 825 in a solution of 1000 ppm Cl<sup>-</sup> + 85 ppm HCO<sub>3</sub><sup>-</sup> + 20 ppm SO<sub>4</sub><sup>2-</sup> + 10 ppm NO<sub>3</sub><sup>-</sup> + 2 ppm F<sup>-</sup> at 95 °C**

Specimen Treatment	E <sub>corr</sub> (mV <sub>SCE</sub> )	Passive Current Density (μA/cm <sup>2</sup> )	Pitting Potential, E <sub>p</sub> (mV <sub>SCE</sub> )	Repassivation Potential, E <sub>rp</sub> (mV <sub>SCE</sub> )
As polished	-595	1.42	692	158
100 °C, 1 day	-534	1.25	684	115
100 °C, 10 days	-400	1.00	683	166
100 °C, 30 days	-339	0.92	706	137
300 °C, 1 day	-158	0.04	693	156
300 °C, 10 days	-151	0.10	705	156
300 °C, 30 days	-96	0.06	678	141

at even 0.007 M chloride. It must be emphasized that the effect of environmental factors is complex since aggressive species such as chloride can be counteracted by inhibitive species such as nitrate and there may be synergistic effects (Sridhar et al., 1993).

### 5.5.2 Stress Corrosion Cracking of Type 316L Stainless Steel

The results summarized in Figure 5-16 clearly indicate that mill-annealed type 316L stainless steel failed by SCC in slow strain rate tests (extension rate =  $1.0 \times 10^{-6} \text{ s}^{-1}$ ) when exposed to MgCl<sub>2</sub> and LiCl solutions at chloride concentrations equal to or higher than 9.1 moles/kg water and temperatures above 100 °C. Although SCC was observed under open-circuit conditions, it was significantly enhanced at slightly anodic potentials. As shown in Figure 5-10, the fracture surfaces exhibited a relatively large proportion of intergranularly cracked area besides the transgranular features typical of the SCC of annealed, nonsensitized austenitic stainless steel in concentrated chloride-containing solutions.

Several authors (Takano, 1974; Stalder and Duquette, 1977; Manfredi et al., 1987; Duffo et al., 1988) have reported the simultaneous occurrence of transgranular and intergranular SCC of type 304 stainless steels in slow strain rate tests conducted in concentrated MgCl<sub>2</sub> or LiCl solutions at temperatures above 90 °C. The proportion of intergranular to transgranular SCC changes with chloride concentration, temperature, potential, and strain rate, but it is difficult to establish a well-defined pattern as a function of these variables. It appears, however, that the tendency towards intergranular SCC increases with decreasing chloride concentration, temperature, and potential, and also with increasing strain rate. Although no similar studies have been conducted with type 316L stainless steel, Okada et al. (1971) have suggested, by studying the SCC behavior of types 304 and 316 stainless steels and Fe-16Cr-15Ni-xMo (x = 1,2,4) alloys in hot CaCl<sub>2</sub> solutions, that the fracture mode became more and more intergranular with increasing Mo content. This was attributed by Okada et al. (1971) to the increasing corrosion

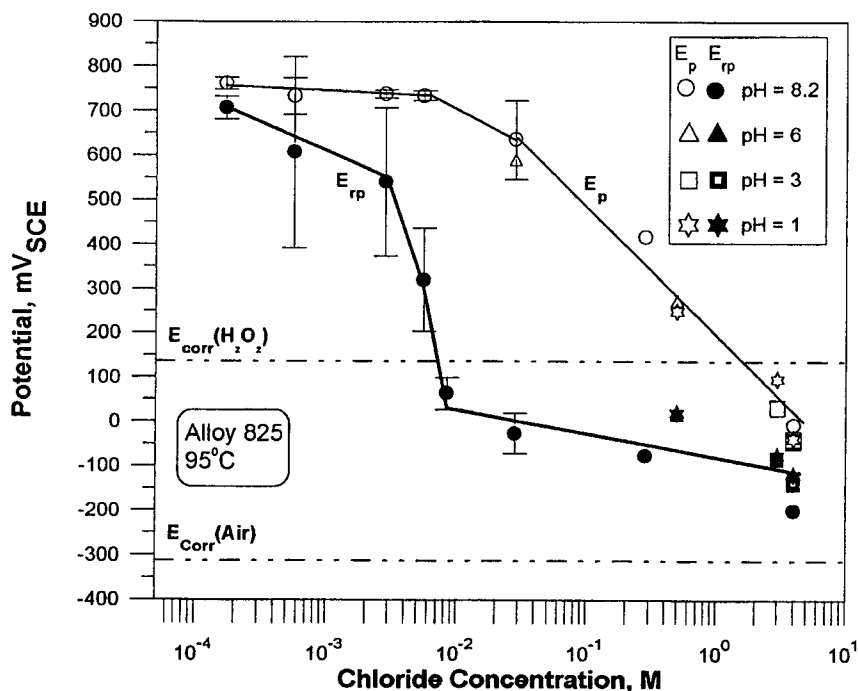
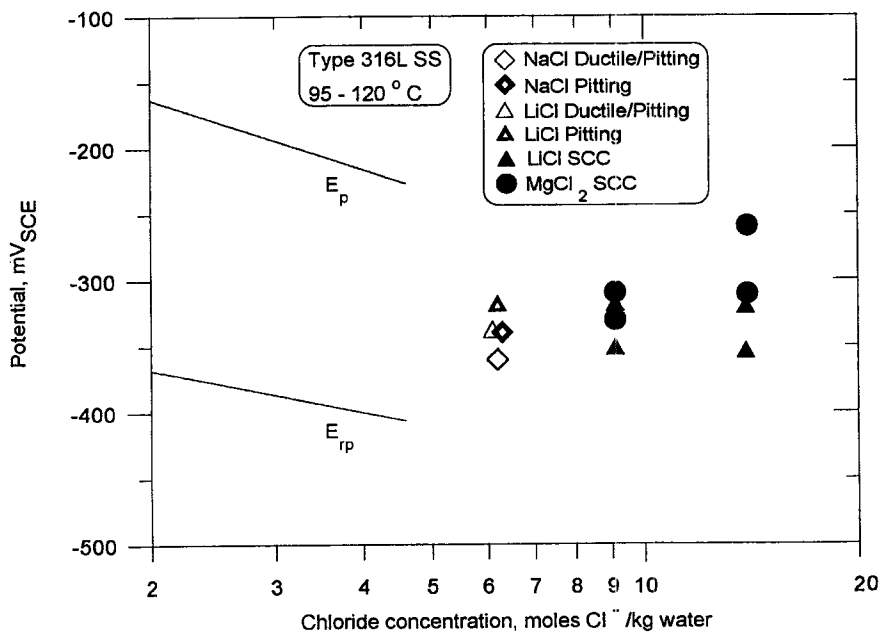


Figure 5-15. Effect of chloride concentration on the pit initiation ( $E_p$ ) and repassivation ( $E_{rp}$ ) potentials of alloy 825 and corrosion potential ( $E_{corr}$ ) in the presence of air and  $H_2O_2$

resistance of the alloys brought about by the increasing Mo content, which parallels the effect of decreasing corrosivity of the solutions as a result of lower chloride concentrations and temperatures.

The results shown in Table 5-5 and Figure 5-16 indicate that SCC did not occur in NaCl solutions in which the chloride concentration was 6.2 moles/kg water. This is the maximum concentration attainable in NaCl due to solubility limitations. However, the same results were obtained in LiCl solutions of equivalent chloride concentration. These results indicate that, under the experimental conditions used in these tests, particularly in terms of temperature and strain rate, no SCC can be promoted regardless of the cation at chloride concentrations equal to or lower than 6.2 moles/kg water, even at acidic pHs. It should be noted, however, as shown in Table 5-5, that in these tests the pH changes from values close to 2.5 before the test to values higher than 6.0 at the end of the test, probably due to the evaporation of HCl. At temperatures well above 100 °C, transgranular cracking of solution-annealed type 316 stainless steel has been observed in slow strain rate tests in the presence of very low chloride concentrations (Yang et al., 1992). Beavers and Koch (1992) claimed that the inability to reproduce the SCC of austenitic stainless steels in dilute chloride solutions may be due to the use of relatively high extension rates. In these particular tests, the strain rate was decreased by almost three times from  $1 \times 10^{-6}$  to  $3.6 \times 10^{-7} \text{ s}^{-1}$ , but, nevertheless, no cracks were initiated. In this concentration range, however, it is very difficult to avoid the occurrence of pitting as a predominant phenomenon. Although the potential selected seems to be well below the extrapolation of the line representing the dependence of  $E_p$  with chloride concentration, pitting corrosion was observed in all these specimens, as noted in Table 5-5 and Figure 5-16.



**Figure 5-16. Potential and chloride concentrations selected for slow strain rate tests of type 316L stainless steel in concentrated chloride solutions (MgCl<sub>2</sub>, LiCl, and NaCl) at temperatures ranging from 95 to 120 °C**

At even lower chloride concentrations (1000 to 10,000 ppm), no SCC was observed under a wide range of experimental conditions (Table 5-2), even in the presence of crevice geometries introduced to promote crack initiation through the localized modification of the environment expected in the occluded region. It can be hypothesized that the exposure time available in slow strain rate tests, limited by the occurrence of ductile failure, is not long enough to facilitate such environmental modification and, therefore, crack initiation. A substantial decrease of at least one order of magnitude in the extension rate may be required to induce crack initiation under similar environmental conditions. Another possibility is the alteration of surface or near-surface conditions by introducing very localized plastic deformation via cold work or microchemical modifications through surface depletion of some alloying element or thickening of the passive film by oxidation in air.

Additional experiments are needed to clarify these uncertainties. In particular, more prolonged tests using U-bend specimens under well-controlled potential conditions are required to attain a better understanding of the events leading to crack initiation.

## 5.6 CONCLUSIONS AND RECOMMENDATIONS

### 5.6.1 Localized Corrosion

Presence of surface Cr-depletion of mill-finished surface of alloy 825 can be detrimental to localized corrosion resistance of the alloy. Pits can be nucleated at lower initiation potentials than those measured on polished specimens, and can then propagate into the bulk alloy. The E<sub>rp</sub> for pitting measured

on a polished specimen can serve as a conservative lower bound parameter for predicting localized corrosion. The corrosion potential of alloy 825 in the presence of oxygen in the air as the redox controlling species is quite low and is not expected to initiate or propagate localized corrosion even in a highly concentrated chloride environment. However, in the presence of  $H_2O_2$ , the corrosion potential values fall between the pit-initiation and repassivation potentials for the 1000 ppm  $Cl^-$  solution. If  $E_{rp}$  is indeed a better critical parameter for predicting the long-term localized corrosion, then alloy 825 may be expected to be susceptible to this failure mode under the redox conditions established by the presence of  $H_2O_2$ . Long-term tests under controlled potential conditions are necessary to verify the validity of using the  $E_{rp}$  as a critical parameter.

There is a lack of fundamental data on various redox reaction kinetics of relevance to repository environment. For example, parameters such as exchange current density and Tafel slopes for oxygen and hydrogen peroxide reduction reactions on substrates of interest are necessary to model the evolution of the corrosion potential of candidate container materials (Macdonald and Urquidi-Macdonald, 1990). Furthermore, while some recent experimental results (Okuyama and Haruyama, 1990) have shown that these two reduction reaction kinetics are additive; further studies are necessary to verify this assertion. Eventually, the effect of radiation on the kinetics of cathodic reactions (photoelectrochemical effects) on alloys such as alloy 825 needs to be understood (Gorse et al., 1990).

### 5.6.2 Stress Corrosion Cracking

Slow strain rate tests were used to investigate the SCC susceptibility of type 316L stainless steel in chloride containing solutions as a basis for further studies on alloy 825. The occurrence of transgranular and intergranular SCC was demonstrated in hot, concentrated  $MgCl_2$  and  $LiCl$  solutions in which the chloride concentration was equal to or higher than 9.1 moles/kg water and the temperature was above 110 °C. On the other hand, no SCC was observed in solutions containing  $NaCl$  or  $LiCl$  at lower chloride concentrations and temperatures. Under these conditions, pitting corrosion became the predominant degradation mode at anodic potentials close to the pitting potential. However, there are many reported cases of SCC of austenitic stainless steels in solutions of low chloride concentrations at temperatures above 60 °C. The cause of these discrepancies between field experience and laboratory studies is not understood yet, but prolonged tests adopting other stressing methods, such as constant deflection using U-bend specimens, may promote crack initiation and be used to study the variables affecting this process.

## 5.7 PROGRESS TOWARDS MEETING PROJECT OBJECTIVES

The approach that is currently being used in the IPA and the Substantially Complete Containment Example Analysis programs for assessing the container performance involves consideration of critical potentials for localized corrosion and the corrosion potential. These programs will eventually support the development of Compliance Determination Methodologies (CDM). The results of the IWPE program described in the previous sections support the methodologies of performance assessment adopted thus far. It has been shown, for example, that  $E_{rp}$  can be a conservative parameter for a wide range of surface conditions. While the current IPA and SCC Example Problem codes consider only type 304L stainless steel containers, which are not the focus of the IWPE project, the same methodology can be used in the future for alloy 825. The experimental data on the effects of environmental factors on  $E_{rp}$  for alloy 825 can then be used as input parameters in these codes. The experimental results described in this and previous reports can also provide guidance to the DOE in conducting their experimental and field studies.

For example, the results to date clearly demonstrate the need to monitor the corrosion potentials of materials that are tested in the field. Unfortunately, many of the corrosion coupon tests [e.g., at the Waste Isolation Pilot Plant (WIPP) site] have not included any provision for measuring this important parameter (Sorensen and Molecke, 1992). Long-term laboratory tests also need to consider means of either controlling potentials (electronically) or monitoring corrosion potentials so that these results can be compared to model predictions. The studies also point out the limitations or inadequacies of certain test techniques, such as slow strain rate tests to reproduce field observations. This technique has been used by DOE laboratories (Park et al., 1992) to evaluate SCC of container materials.

## 5.8 PLANS FOR THE NEXT REPORTING PERIOD

Long-term tests under controlled potentials, anticipated to continue for time periods ranging from a few months to 5 years, are necessary to verify several of the concepts discussed before. These tests, which are under way, will verify whether the  $E_{rp}$  for deep pits is a conservative parameter for predicting pit initiation and repassivation for all surface conditions. Tests with intentional crevices under potentiostatic control will also verify whether the  $E_{rp}$  for deep pits can be used to predict initiation and repassivation of crevice corrosion. In conjunction with these controlled potential tests, tests under naturally aerated conditions will also be conducted where the corrosion potential will be monitored. The status of these tests will be reported in following semi-annual reports.

Modeling of crevice corrosion has been performed within the EBS element (Walton and Kalandros, 1992). This model and others similar to this (Sharland, 1992) predict the environmental conditions inside a crevice or a deep pit, which are important to understand repassivation as well as other localized events such as SCC. Experiments are under way that attempt to verify some of these model predictions. These experiments use microelectrodes in a simulated crevice of well-defined geometry to monitor changes in the pH,  $Cl^-$ , and potential inside the crevice. The results of these studies will be reported in the next semi-annual report.

Slow strain rate testing of type 316 stainless steel at lower extension rates will be completed and studies on alloy 825 will be initiated. However, the main effort will be devoted to the studies on crack initiation using constant deflection tests. These studies will address several important issues related to crack initiation, encompassing the role of pits and crevices, near surface changes in alloy composition, and surface films formed in dry and moist air.

In order to understand the long-term behavior of container materials, their microstructural changes as a result of thermal exposure need to be understood. These studies are being performed in Task 3. As part of this task, methods to quantify the grain boundary sensitization of alloy 825 are being developed. While such test techniques exist for stainless steels such as type 304L, no method for rapidly and sensitively estimating grain boundary sensitization of alloy 825 exists. The results from these studies will be presented in the next semi-annual report as a basis for further studies in this area.

## 5.9 REFERENCES

- Abraham, T., H. Jain, and P. Soo. 1986. *Stress Corrosion Cracking Tests on High-Level Waste Container Materials in Simulated Tuff Repository*. NUREG/CR-4619. Upton, NY: Brookhaven National Laboratories.

- Beavers, J.A., and G.H. Koch. 1992. Limitations of the slow strain rate test for stress corrosion cracking testing. *Corrosion* 48: 256-264.
- Beavers, J.A., N.G. Thompson, and C.L. Durr. 1992. *Pitting, Galvanic, and Long-Term Corrosion Studies on Candidate Container Alloys for the Tuff Repository*. NUREG/CR-5709. Columbus, OH: Cortest Columbus Technologies, Inc.
- Buschek, T.A., D.G. Wilder, and J.J. Nitao. 1993. Large-scale *in situ* heater tests for hydrothermal characterization at Yucca Mountain. *High Level Radioactive Waste Management. Proceedings of the Fourth Annual International Conference*. La Grange Park, IL: American Nuclear Society: 1854-1872.
- Cragolino, G.A., and N. Sridhar. 1992a. *A Review of Stress Corrosion Cracking of High-Level Nuclear Waste Container Materials — I*. CNWRA 92-021. San Antonio, TX: Center for Nuclear Waste Regulatory Analyses.
- Cragolino, G.A., and N. Sridhar. 1992b. *Integrated Waste Package Experiments. NRC High-Level Radioactive Waste Research at CNWRA, January 1 Through June 30, 1992*. W.C. Patrick, ed. CNWRA 92-01S. San Antonio, TX: Center for Nuclear Waste Regulatory Analyses.
- Cragolino, G.A., and N. Sridhar. 1993. *Long-Term Stability of High-Level Nuclear Waste Container Materials: I — Thermal Stability of Alloy 825*. CNWRA 93-003. San Antonio, TX: Center for Nuclear Waste Regulatory Analyses.
- Doering, T.W. 1993. Robust waste package concept (multibarrier). *High Level Radioactive Waste Management. Proceedings of the Fourth Annual International Conference*. La Grange Park, IL: American Nuclear Society: 551-557.
- Duffo, G.S., I.A. Maier, and J.R. Galvele. 1988. The influence of temperature on the susceptibility of type 304 stainless steel to intergranular and transgranular stress corrosion cracking in LiCl solutions. *Corrosion Science* 28: 1003-1018.
- Evans, U.R. 1961. *The Corrosion and Oxidation of Metals: Scientific Principles and Practical Applications*. London, U.K.: Edward Arnold Publishers, Ltd.
- Geesey, G. 1993. *A Review of The Potential for Microbially Influenced Corrosion of High-Level Nuclear Waste Containers*. G.A. Cragolino, ed. CNWRA 93-014. San Antonio, TX: Center for Nuclear Waste Regulatory Analyses.
- Gorse, D., B. Rondot, and M. DA Cunha Belo. 1990. Irradiation effects on passive films formed on a type 304 stainless steel. *Corrosion Science* 30(1): 23-36.
- LARP. 1992. *Draft License Application Review Plan for the Review of a License Application for a Geologic Repository for Spent Nuclear Fuel and High-Level Radioactive Waste Yucca Mountain, Nevada*. NUREG-1323. Nuclear Regulatory Commission. Office of Nuclear Material Safety and Safeguards. Washington, DC: U.S. Nuclear Regulatory Commission.

- Macdonald, D.D., and M. Urquidi-Macdonald. 1990. Thin-layer mixed-potential model for corrosion of high-level nuclear waste canisters. *Corrosion* 46(5): 380-390.
- Macdonald, D.D., and M. Urquidi-Macdonald. 1992. Corrosion damage function—interface between corrosion science and engineering. *Corrosion* 48(5): 354-367.
- Manfredi, C., I.A. Maier, and J.R. Galvele. 1987. The susceptibility of AISI type 304 stainless steel to transgranular and intergranular SCC in 40% MgCl<sub>2</sub> solution at 100 °C. *Corrosion Science* 27: 887-903.
- Okada, H., Y. Hosio, and S. Abe. 1971. Scanning electron microscopic observations of fracture surfaces of austenitic stainless steels in stress corrosion cracking. *Corrosion* 27: 424-428.
- Okayama, S., Y. Uesugi, and S. Tsujikawa. 1987. The effect of alloying elements on the repassivation potential for crevice corrosion of stainless steels in 3% NaCl solution. *Corrosion Engineering* 36: 157-168.
- Okuyama, M., and S. Haruyama. 1990. The cathodic reduction of oxygen on stainless steels in a neutral solution. *Corrosion Science* 31: 521-526.
- Pabalan, R.T., W.M. Murphy, and P. Bertetti. 1990. Unsaturated mass transport (Geochemistry). *Report on Research Activities for the Quarter July 1 Through September 30, 1990*. CNWRA 90-03Q. San Antonio, TX: Center for Nuclear Waste Regulatory Analyses.
- Pabalan, R.T., and W.M. Murphy. 1993. Unsaturated mass transport (Geochemistry). *Report on Research Activities for July 1 Through December 31, 1992*. CNWRA 92-02S. San Antonio, TX: Center for Nuclear Waste Regulatory Analyses.
- Park, J.Y., P.S. Maiya, W.K. Soppet, D.R. Diercks, W.J. Shack, and T.F. Kassner. 1992. *Stress Corrosion Cracking of Candidate Waste Container Materials — Final Report*. ANL-92/28. Argonne, IL: Argonne National Laboratory.
- Patrick, W.C. 1986. *Spent Fuel Test — Climax: An Evaluation of the Technical Feasibility of Geologic Storage of Spent Nuclear Fuel in Granite — Final Report*, UCRL-53702. Livermore, CA: Lawrence Livermore National Laboratory.
- Ramirez, A.L., ed. 1991. *Prototype Engineered Barrier System Field Test (PEBSFT) Final Report* UCRL-ID-106159. Livermore, CA: Lawrence Livermore National Laboratory.
- Rosenfeld, I.L., I.S. Danilov, and R.N. Oranskaya. 1978. Breakdown of the passive state and repassivation of stainless steels. *Journal of the Electrochemical Society* 125(11): 1729-1735.
- Ruffner, D.J., G.L. Johnson, E.A. Platt, J.A. Blink, and T.W. Doering. 1993. Drift emplaced waste package thermal response. *High Level Radioactive Waste Management. Proceedings of the Fourth Annual International Conference*. La Grange Park, IL: American Nuclear Society: 538-543.

- Sagar, B., R.B. Codell, J.C. Walton, and R.W. Janetzke. 1992. *SOTEC: A Source Term Code for High-Level Nuclear Waste Geologic Repositories. User's Manual Version 1.0*. CNWRA 92-009. San Antonio, TX: Center for Nuclear Waste Regulatory Analyses.
- Sharland, S.M. 1992. A mathematical model of the initiation of crevice corrosion in metals. *Corrosion Science* 33(2): 183-201.
- Sorensen, N.R., and M.A. Molecke. 1992. Summary of the WIPP materials interface interactions test — Metal corrosion. *Workshop on In Situ Tests on Radioactive Waste Forms and Engineered Barriers. Corsendok. Belgium*. SAND92-1921C. Albuquerque, NM: Sandia National Laboratory.
- Sridhar, N., and G.A. Cragnolino. 1992a. Long-term life prediction of localized corrosion of Fe-Ni-Cr-Mo high-level nuclear waste container materials. *Corrosion/93, Paper No. 93197*. Houston, TX: National Association of Corrosion Engineers.
- Sridhar, N., and G.A. Cragnolino. 1992b. Integrated waste package experiments. *NRC High-Level Radioactive Waste Research at CNWRA, July 1 Through December 31, 1992*. W.C. Patrick, ed. CNWRA 92-02S. San Antonio, TX: Center for Nuclear Waste Regulatory Analyses.
- Sridhar, N., G.A. Cragnolino, J.C. Walton, and D. Dunn. 1992. Prediction of crevice corrosion using modeling and experimental techniques. *Application of Accelerated Corrosion Tests to Service Life Prediction of Materials*. G.A. Cragnolino, and N. Sridhar, eds. ASTM STP 1194. Philadelphia, PA: American Society for Testing and Materials.
- Sridhar, N., G.A. Cragnolino, and D. Dunn. 1993. *Experimental Investigations of Localized Corrosion of High-Level Waste Container Materials*. CNWRA 93-004. San Antonio, TX: Center for Nuclear Waste Regulatory Analyses.
- Stalder, F., and D.J. Duquette. 1977. Slow strain rate stress corrosion cracking of type 304 stainless steels. *Corrosion* 33: 67-72.
- Szklarska-Smialowska, Z. 1986. *Pitting Corrosion of Metals*. Houston, TX: National Association of Corrosion Engineers: 201-236.
- Takano, M. 1974. Effect of strain rate on stress corrosion cracking of austenitic stainless steel in MgCl<sub>2</sub> solutions. *Corrosion* 30: 441-446.
- Thompson, N.G., and B.C. Syrett. 1992. Relationship between conventional pitting and protection potentials and a new, unique pitting potential. *Corrosion* 48(8): 649-659.
- Thompson, N.G., J.A. Beavers, and C.L. Durr. 1992. *Potentiodynamic Polarization Studies on Candidate Container Alloys for Tuff Repositories*. NUREG/CR-5708. Columbus, OH: Cortest Columbus Technologies, Inc.

- Tsujikawa, S., and Y. Hisamatsu. 1984. Repassivation potential as a crevice corrosion characteristic for austenitic and ferritic stainless steels. *Improvement of Corrosion Resistance of Structural Materials in Aggressive Media*. Ya. M. Kolotykin, ed. Moscow, Russia: Nauka Publishers.
- Walton, J.C., and S.K. Kalandros. 1992. *TWITCH — A Model for Transient Diffusion, Electromigration, and Chemical Reaction in One Dimension*. CNWRA 92-019. San Antonio, TX: Center for Nuclear Waste Regulatory Analyses.
- Walton, J.C. 1993. Effects of evaporation and solute concentration on presence and composition of water in and around the waste package at Yucca Mountain. *Waste Management* Vol. 13. In press.
- Yang, W., J. Conglenton, O. Kohneh-Chari, and P. Sajdl. 1992. The strain for stress corrosion cracking initiation in type 316 stainless steel in high temperature water. *Corrosion Science* 33: 735-750.
- Zimmerman, R.M., R.L. Schuch, D.S. Mason, M.L. Wilson, M.E. Hall, M.P. Board, R.P. Bellman, and M.P. Blanford. 1986. *Final Report: G-Tunnel Heated Block Experiment*. SAND84-2620. Albuquerque, NM: Sandia National Laboratories.

## 6 STOCHASTIC ANALYSIS OF UNSATURATED FLOW AND TRANSPORT

by *Amyrossios C. Bagtzoglou and Sitakanta Mohanty*

Investigators: *Amyrossios C. Bagtzoglou, M. Rashidul Islam, and Sitakanta Mohanty (CNWRA); Rachid Ababou (CEA); Jim Yeh (University of Arizona); Ashok Nedungadi and Michael Muller (SwRI); and David E. Dougherty (University of Vermont)*

*NRC Project Officer: T.J. Nicholson*

### 6.1 TECHNICAL OBJECTIVES

The technical objective of the Stochastic Analysis of Unsaturated Flow and Transport Research Project, hereafter called Stochastic Project, is to provide and document the methods and tools necessary for realistic modeling and analyses of the complex, heterogeneous flow and transport processes expected or anticipated to occur in the far-field of the proposed high-level waste (HLW) repository at Yucca Mountain, Nevada. These analyses will be necessary to predict the performance of the overall system (10 CFR 60.112), the Geologic Setting (GS) (10 CFR 60.113), and also to evaluate compliance with siting criteria (10 CFR 60.122). The variability of many processes and parameters affecting the long-term behavior of the flow system at the scale of the Yucca Mountain site are poorly known. More specifically, there is a lack of acceptable hydrogeologic parameters, theories, and conceptual and mathematical models that are considered applicable for the conditions prevailing at Yucca Mountain. Even if such models are developed, many fundamental questions regarding their applicability over the period of regulatory concern and the spatial scales of the subregional and regional hydrologic systems remain to be addressed. Moreover, there will remain a high level of uncertainty in the hydrogeologic parameter space due to the fact that realistically, only a limited amount of data can be collected. The Stochastic Project aims to provide a natural platform to address issues related to the quantitative characterization of large-scale flow and transport in unsaturated, highly fractured, heterogeneous rock. Furthermore, this work will lead to an understanding of the effects of small-scale variability on large-scale flow and transport processes anticipated at Yucca Mountain.

The Stochastic Project interfaces with other projects of the NRC Office of Nuclear Regulatory Research (RES) at the Center for Nuclear Waste Regulatory Analyses (CNWRA) and the University of Arizona (UAZ). More specifically, technical exchanges, interactions, and synergism exist with the following projects: (i) FIN B5753 (UAZ) on the application of alternative Eulerian-Lagrangian methods for modeling contaminant transport; (ii) FIN L1282 (UAZ), Task 4, on geometric fracture modeling and associated preferential flow development at the Apache Leap Tuff Site (ALTS); (iii) FIN L1283 (UAZ), Tasks 3 and 6, on developing ways to model large systems of fractures and matrices and associated scaling issues; (iv) FIN L1152 (CNWRA), Task 2, on developing efficient algorithms for generating conditional random hydraulic property fields (potential interfaces also exist with Task 3 on evaluating the effects of highly heterogeneous, preferential flow processes on the coupling of flow and reactive transport); and (v) FIN L2198 (CNWRA) on implementing geometric fracture modeling to validation exercises of flow and transport at the Peña Blanca natural analogue site. Finally, the Stochastic Project interfaces actively with projects of the U.S. Nuclear Regulatory Commission (NRC) Office of Nuclear Material Safety and Safeguards (NMSS), FIN D1035 (CNWRA). More specifically, stochastic methods have been previously applied for Groundwater Travel Time (GWTT) uncertainty evaluation; and the BIGFLOW numerical code and its associated pre- and post-processors have been applied to study the

effects of common geologic features on unsaturated flow and transport as part of the Iterative Performance Assessment (IPA) Phase 2 exercise.

Information, methodologies, and numerical tools developed within the Stochastic Project will be used to support specific portions of the License Application Review Plan (LARP). Parameter heterogeneity effects on flow and transport at a scale similar to that of Yucca Mountain will provide knowledge relevant to the Description of the Individual Systems and Characteristics of the Site (Sections 3.1.1, 3.1.2, and 3.1.3). Similarly, detailed numerical analyses of the flow processes occurring in highly fractured, heterogeneous rock will provide the necessary framework for the development of portions of the LARP specifically related to favorable hydrogeological conditions (Sections 3.2.2.3 and 3.2.2.4) and potentially adverse hydrogeological conditions (Sections 3.2.2.9, 3.2.2.11, 3.2.2.12, and 3.2.4.2). Moreover, the Stochastic Project serves as the natural platform to study and assess the variability in model parameters and its effect on various performance measures. This information will be of importance for the development of Section 3.3, Assessment of Compliance with the GWTT Performance Objective.

Compliance Determination Strategies (CDS) for the LARP sections noted earlier are not yet finalized and, therefore, the Key Technical Uncertainties (KTU) are not fully defined. Nevertheless, results obtained and methodologies/tools developed under the Stochastic Project will be important in addressing several KTU identified in the CDS. Specifically, Regulatory Requirement Topics (RRT) 3.3 and 3.2.2.12 have been judged to require a Type 5 review, thus requiring independent research to resolve the following KTU: (i) there exists uncertainty in determining effective hydrologic characteristics (e.g., effective porosity, hydraulic conductivity) as a function of scale for the saturated zone; (ii) there is great uncertainty in determining the relative proportion of fracture/matrix flow in the vadose zone, including identification of the conditions under which fracture flow will dominate; and (iii) in order for the potential for future perched water bodies to be evaluated, knowledge of the flow behavior of unsaturated fractured rock for different flux rates through Yucca Mountain is required.

Current research within the Stochastic Project focuses on: (i) enhancements to the BIGFLOW code; (ii) development and documentation of a working methodology to calculate effective hydraulic properties for highly fractured, heterogeneous rock; and (iii) development of the executive code Stochastic analysis of Unsaturated FLOW And Transport (SUFLAT) to be used in the conduct of large-scale, stochastic flow and transport simulations. Earlier reports documenting progress to date include: Ababou (1991a; b); Ababou et al. (1991); Bagtzoglou et al. (1992); Ababou (1993a; b); Ababou and Bagtzoglou (1993); and Bagtzoglou (1993). This report describes the results of activities in the Stochastic Project during the first half of 1993.

## **6.2 LIMITATIONS IN THE REGULATORY USE OF NUMERICAL SOLUTE TRANSPORT MODELS by A.C. Bagtzoglou and D.E. Dougherty**

Numerical models of solute transport in water-saturated porous media are routinely used to make decisions regarding contamination risks, remediation designs, and the effects of pollution. For many contaminants, decisions are based on concentrations of 5 parts per billion (ppb) or less, a so-called action level. The action level is usually a small fraction of the concentrations near a source of contamination, usually less than 0.01. Decisions based on numerical modeling that utilize information in the low concentration ( $c/c_{\max}$ ) range, such as the action level, should be carefully examined. Numerical errors at these low dimensionless concentrations tend to be of overwhelming magnitude relative to the correct solution, even in the case of uniform and steady flows in one space dimension. In addition, the

mathematical transport model itself may contain errors (e.g., in the description of the dispersion process) not considered here that affect both solutions and error propagation. It is vital to keep in mind that the purpose of modeling is to form a basis for making decisions, not to make decisions themselves. Research is needed to identify methods that extend the region for which the error-to-signal ratio in these models is acceptably small. Modern numerical methods for the solution of transport equations provide better behavior, in this sense, than classical methods. Particle tracking methods (PTM) and, in particular, the Random Walk Particle Method (RWPM), exhibit favorable noise-to-signal ratios and their performance improves as the flow becomes more advection-dominated. Even though there is no direct concentration criteria to be applied under this project, the formulation introduced by Bagtzoglou et al. (1991) following the work of Dagan (1982) establishes a proportionality between the expected value of concentration and a probability density function (PDF) field of particle locations. This PDF field is used to make inferences regarding GWTT estimates and associated uncertainties. The accuracy, therefore, of a PTM-based solute transport simulator is very much related to the accuracy of GWTT estimates under the formulation described in Bagtzoglou et al. (1991). This is especially important since PTM are the current method of choice within the Stochastic Project, and flow in the unsaturated zone of Yucca Mountain is expected to be strongly hyperbolic.

Consider the transport of a nonreactive solute in a constant-porosity, water-saturated porous medium, which for one-dimensional (1D) space is governed by the equation

$$\frac{\partial c}{\partial t} + v \frac{\partial c}{\partial x} - D \frac{\partial^2 c}{\partial x^2} = 0 \quad (6-1)$$

Here the usual notations of  $c$  for solute concentration in the water phase,  $v$  for the average water phase velocity within the pores, and  $D$  for the hydrodynamic dispersion tensor are used. Sources of solute are assumed negligible.

The general problem of solute transport was simplified to a problem involving one spatial dimension with constant velocity and dispersion, as indicated in Eq. (6-1). On the one hand this problem is less difficult to solve numerically than two- or three-dimensional (2D or 3D) cases that are usually encountered in practice. On the other hand, one can compare numerical solutions with closed-form (analytical) solutions quite easily. If problems are experienced by any of the numerical methods for the 1D problem used here, it is anticipated that greater difficulties will be encountered in multiple space dimensions. The analysis presented here is specified as: Solve Eq. (6-1) for  $0 \leq x \leq \infty$ , and subject to

$$c(x,0) = 0 \quad (6-2)$$

$$c(0,t) = 1 \quad (6-3)$$

and

$$c(\infty,t) = 0 \quad (6-4)$$

The analytical solution ( $c^a$ ) for this problem is

$$c^a(x,t) = \frac{1}{2} \left[ \operatorname{erfc} \left( \frac{x-vt}{\sqrt{4Dt}} \right) + \exp \left( \frac{vx}{D} \right) \operatorname{erfc} \left( \frac{x+vt}{\sqrt{4Dt}} \right) \right] \quad (6-5)$$

The numerical parameters were specified as: Compute for  $0 \leq x \leq 12800$ , grid spacing of  $\Delta x = 200$ ,  $v = 0.5$ , time step size of  $\Delta t = 96$  or  $960$ , total simulation time of  $T = 9600$ , and  $D = 0, 2$ , or  $50$ . Results are presented for moderate Peclet number ( $Pe = v\Delta x/D = 2$ ,  $\Delta t = 96$ ,  $D = 50$ ) and Courant number ( $Co = v\Delta t/\Delta x = 0.24$  for  $\Delta t = 96$ ).

Several numerical methods were implemented for this problem. Classical explicit methods (e.g., Roache, 1976) used were central finite differences (CFD), upwind finite differences (UFD), Lax-Wendroff (LW) finite differences, and the Fromm (FR) modification of LW finite differences. The first two are widely used in groundwater studies. The RWPM is widely used in groundwater hydrology and was also included. With the exception of the particle method, all these techniques use fixed grids to discretize space. The analytical and numerical solutions to this standard test problem are shown in Figure 6-1. The classical methods lead to excessive smearing of the front, incorrect traveling wave speed, and, especially for higher velocities, oscillations. The particle method, because of the finite number of particles used (here 400), yields noisy solutions unless the diffusion is negligible.

Consider now the difference between the numerical concentration ( $c^n$ ) and the analytical (true) concentration ( $c^a$ ), relative to the analytical concentration, at different spatial locations for time  $T$ . Figure 6-2 shows this error-to-signal (or noise-to-signal) ratio for the test problem under study. The error-to-signal ratio in the concentration field is given by

$$\eta = \frac{\sqrt{(c^n - c^a)^2}}{c^a} \quad (6-6)$$

The error-to-signal ratio is virtually constant and negligible for a wide range of  $x$ . However, at large  $x$ , where the concentration  $c$  is small, the error grows in all classical methods to large values (RWPM is a special case due to its Lagrangian formulation). The error-to-signal ratio ( $\eta$ ) measure, employed in this study, is compatible with the reliability index used by Yen (1988) to "offer a comparative reliability evaluation rather than a risk evaluation."

It is clear from Figure 6-1 that numerical modeling errors using classical methods are largest where concentrations are lowest. This implies that in regions of low dimensionless concentration, that is near the action level, large relative errors can be expected. Figure 6-2 shows that the RWPM provides significantly better solutions near this region. As the flow problem becomes more advection dominated, the particle method exhibits better performance.

### 6.3 RECENT ENHANCEMENTS OF THE BIGFLOW NUMERICAL CODE by A.C. Bagtzoglou, A. Nedungadi, and M.R. Islam

Documentation, benchmarking, and verification of the BIGFLOW (Version 1.1) numerical code were recently completed and published as NUREG/CR-6028 (Ababou and Bagtzoglou, 1993). During the

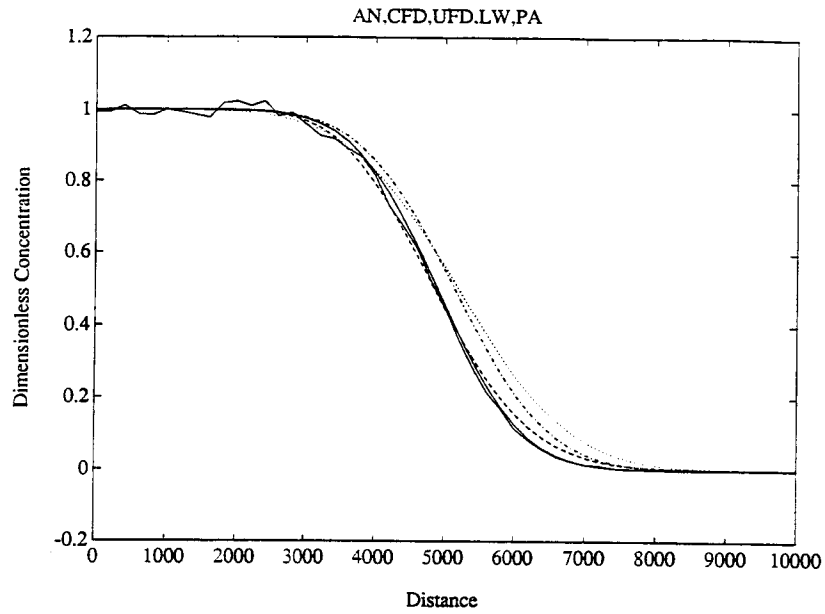


**Figure 6-1. Concentrations versus  $x$  for the advancing front problem obtained using several numerical methods. LEGEND: smooth solid line: analytical; noisy solid line: RWPM; dashed line: CFD; dotted line: UFD; dashed-dotted line: LW.**

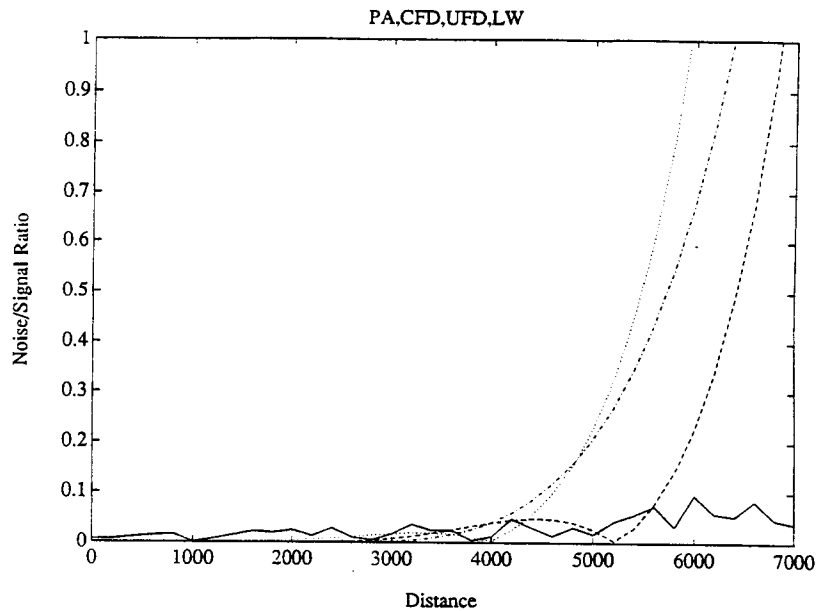


**Figure 6-2. Error-to-signal ratios versus  $x$  for the advancing front problem obtained using several numerical methods. LEGEND: noisy solid line: RWPM; dashed line: CFD; dotted line: UFD; dashed-dotted line: LW.**

course of the review process and subsequent analyses, several limitations of the code were identified. These are: (i) only the exponential Gardner model can be used to characterize the hydraulic conductivity-pressure head relationship of the soil; and (ii) the van Genuchten model used to represent the water retention curve is restricted to homogeneous residual water moisture content ( $\theta_r$ ) and exponent ( $n$ ).

These limitations are now eliminated due to recent enhancements of the BIGFLOW code (Version 2.0). The new version of the code bases (at the user's request) all soil properties on the van Genuchten (1978) formulation of the Mualem model given by

$$\theta(h) = \theta_r + (\theta_s - \theta_r) [1 + (-\beta h)^n]^{-m} \quad (6-7)$$

where

- $\theta$  = the water content at pressure head ( $h$ )
- $\theta_s$  = saturated water content
- $\theta_r$  = residual water content
- $n$  = a fitting exponent
- $\beta$  = a characteristic inverse length scale
- $m$  =  $(n-1)/n$ , and

$$K(h) = K_s \sqrt{S} [1 - (1 - S^{1/m})^m]^2 \quad (6-8)$$

where

- $K(h)$  = hydraulic conductivity at pressure head ( $h$ )
- $K_s$  = saturated hydraulic conductivity, and
- $S$  = saturation at pressure head ( $h$ ) given by

$$S(h) = \frac{\theta(h) - \theta_r}{\theta_s - \theta_r} \quad (6-9)$$

In this formulation, BIGFLOW (Version 2.0) accommodates a fully 3D description of the  $\theta_r$  and  $n$  parameters. Preliminary numerical tests indicate an approximate 15-percent increase in the number of nonlinear iterations relative to the corresponding Gardner formulation despite extensive modifications of the code to maintain its level of vectorization. BIGFLOW (Version 2.0) has been verified for the following test problems: (i) 1D vertical infiltration in a homogeneous soil; (ii) 2D vertical infiltration from a strip source in a fully heterogeneous soil; and (iii) 1D vertical infiltration in a layered soil with hydraulic properties characteristic of the Yucca Mountain site. Results from this third verification exercise are presented in this section.

The hydraulic properties used in this analysis were slightly modified from the COVE-2A exercise (Dykhuizen and Barnard, 1992) and are characteristic of unsaturated flow in the matrix of a 530.4 m long vertical column of rock similar to Yucca Mountain. These properties can be found in Table 6-1 on a layer-by-layer basis. The simulation was conducted under a constant net infiltration rate

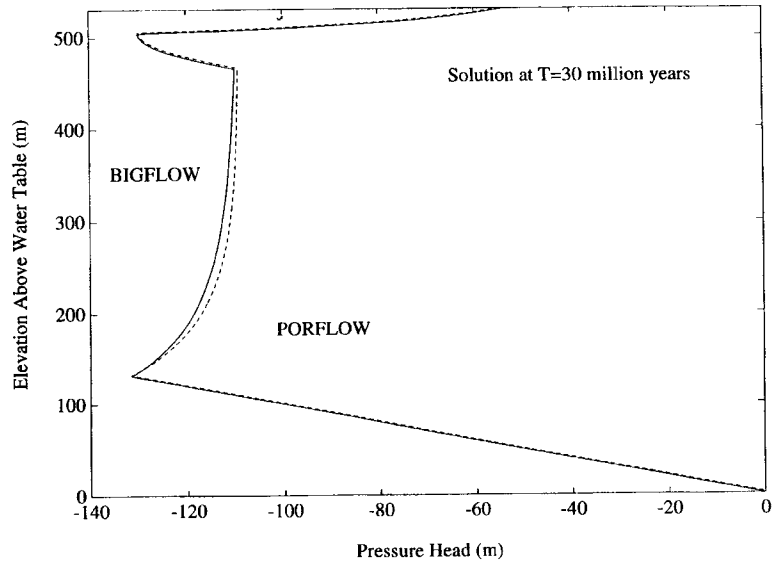
**Table 6-1. Material hydraulic properties used in the modified COVE-2A exercise**

Property	$TC_w$	$PT_n$	$TS_{w(1-2-3)}$	$CH_{nv}$
$\theta_s$	0.08	0.40	0.11	0.46
$\theta_r$	$1.6 \times 10^{-4}$	$1.6 \times 10^{-2}$	$9.68 \times 10^{-4}$	$8.694 \times 10^{-3}$
$\beta(1/m)$	$8.21 \times 10^{-3}$	$1.5 \times 10^{-2}$	$5.07 \times 10^{-3}$	$3.08 \times 10^{-3}$
n	1.558	6.872	1.798	1.602
$K_s(m/s)$	$9.02 \times 10^{-12}$	$3.369 \times 10^{-7}$	$1.645 \times 10^{-11}$	$2.33 \times 10^{-7}$

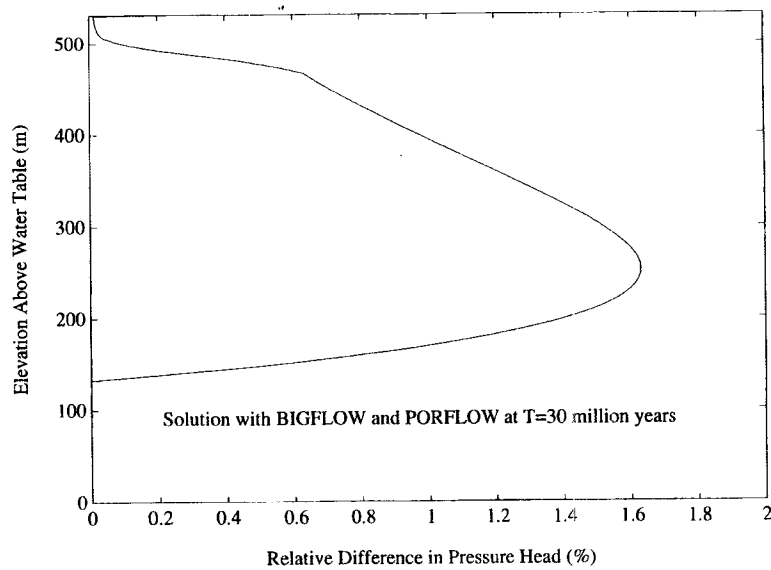
of 0.1 mm/yr, and steady-state conditions were attained by time-marching the solution. Two comparisons were made with: (i) the numerical code PORFLOW (Runchal and Sagar, 1993); and (ii) a semi-analytical solution developed by Baca et al. (1993) in Chapter 9 of this report. Figure 6-3a shows the comparison of pressure head as a function of elevation above water table for BIGFLOW and PORFLOW at a time  $T = 30$  million years. A good agreement is observed for the largest portion of the domain. The differences in solutions between the two codes are more pronounced near the Topopah Spring welded - Calico Hills nonwelded, vitric ( $TS_w - CH_{nv}$ ) unit interface, which is characterized by a ratio in saturated hydraulic conductivities of 1/14,164. However, as seen in Figure 6-3b, the relative difference in the pressure head solution is less than 1.6 percent anywhere in the computational domain. Finally, Figure 6-4 depicts a similar comparison between BIGFLOW and the semi-analytical solution. Again, a very good agreement is observed. Minor differences may be attributed to the fact that the BIGFLOW solution is possibly not at an absolute steady-state condition.

#### **6.4 SEMI-ANALYTICAL PREDICTION OF THE EFFECTIVE HYDRAULIC CONDUCTIVITY OF SATURATED AND UNSATURATED MEDIA** by A.C. Bagtzoglou, S. Mohanty, and A. Nedungadi

Assessing the performance of the potential HLW repository at Yucca Mountain, Nevada, requires the determination of the rate of radionuclide transport via groundwater through the unsaturated and/or saturated zone to the accessible environment. The unsaturated zone extends approximately over 500 m of interbedded welded and nonwelded ash flow tuffs. This tuffaceous rock exhibits a large variation in petrophysical properties due to the post-depositional fracturing, faulting, and erosion (Flint et al., 1993). It has been postulated (Nitao and Buscheck, 1991) that as the water infiltrates down from the surface, it may, at first, flow mainly through the fractures in the rock. As this filtration occurs, water may also imbibe into the matrix blocks. The rate at which imbibition takes place determines whether or not the water from a precipitation event can reach the repository level. The accessibility is also strongly governed by the fracture characteristics such as density, connectivity, and orientation. As it is virtually impossible to describe the exact fracture topology in a deterministic fashion to conduct a full-scale simulation, it is worthwhile to investigate an alternative approach. This approach consists of stochastically generating several fracture realizations to estimate the most likely flow behavior of the fractured composite. These realizations may be conditioned to the constraints dictated by experimental data. To stochastically generate and analyze many realizations in a reasonable amount of time, it is required that



(a)



(b)

**Figure 6-3. Comparison of pressure head versus elevation solution for BIGFLOW and PORFLOW at a time  $T = 30$  million years: (a) absolute values of pressure head; and (b) relative difference in pressure head**

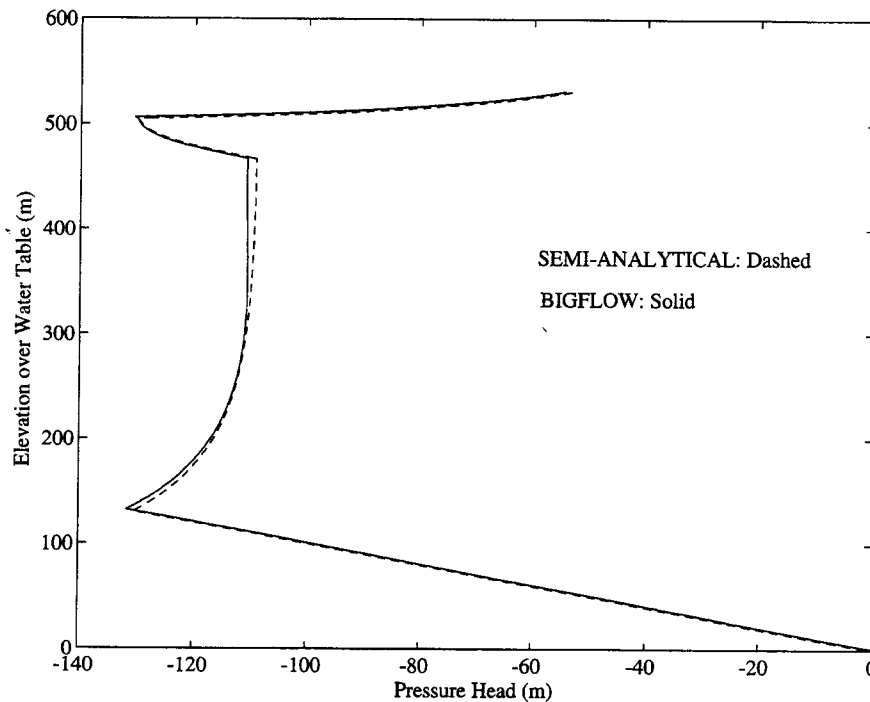


**Figure 6-4.** Comparison of pressure head versus elevation solution for **BIGFLOW** and semi-analytical solution. Note that the semi-analytical solution results are at steady-state, whereas the **BIGFLOW** results were obtained through time-marching up to a time of  $T = 30$  million years.

the simulation of flow using each realization of the stochastic field be able to be conducted relatively quickly. A minimum requirement is to be able to determine the essential or dominant flow behavior by using fewer discretized flow units without sacrificing the important contributions from features smaller than the grid block scale.

The object of this work is to study the effective flow behavior of an ensemble of fractures in the presence of fracture-matrix interaction. Presented here are salient features of a simple, but efficient, 2D fracture network generator code developed at the CNWRA. Then, the implementation of the Real Space Renormalization Group (RSRG) method to upscale petrophysical and flow properties from the scale of measurements to the large-scale simulation grid block scale is presented.

#### 6.4.1 Fracture Network Generator and Verification

A numerical code has been developed to generate 2D fracture networks consisting of horizontal and vertical fractures. This network topology is not as restricting as it may seem since it is very much consistent with fracture data observed at the Apache Leap Tuff Site (ALTS) and several pavements at Yucca Mountain, Nevada (Yeh et al., 1988; Barton and Hsieh, 1990; Thornburg, 1990; Bagtzoglou, 1993). Therefore, if the fracture sets are to be observed and studied along vertical planes, as is the case in hand, the adopted fracture network topology is applicable.

The approach used to place the fractures in space is similar to the methodology used by Sheridan (1992) for estimating the probability of occurrence of future volcanic dikes in the vicinity of Yucca Mountain. Sheridan's model is based on a geometric approach that assumes the centers of the volcanic dikes to be spatially distributed according to a bivariate Gaussian distribution. In a similar fashion, the generator presented here distributes the fracture center locations following either a spatially random or exponential distribution around a pre- or arbitrarily specified point within the domain. This point is called, in our formulation, the centroid of the cluster of fractures. The distribution of fracture centers becomes a Poisson process in the case of the exponential distribution. The clustering or development of spatial structure of fracture centers is controlled by defining the centroid of the cluster of fractures to be either fixed or randomly distributed in space. The number of fracture centers is determined based on a user defined fracture density along the horizontal direction. The horizontal fracture density is specified as a fraction of the total number of pixels (or computational cells). Anisotropy in fracture density can be introduced by assigning the density of the vertical fractures as a fraction of the density of the horizontal fractures. Obviously, when the fracture density is isotropic, this ratio is equal to one and for every fracture center two orthogonal fractures exist creating a fracture feature with the shape of a cross. After the center of a fracture has been set, the fractures get placed by determining their half-length in each possible direction through sampling from an exponential distribution. This choice is corroborated by trace length data presented by Barton and Hsieh (1990), who fitted power-law functions of the form  $f = aL^b$ , where  $f$  is the frequency,  $L$  is the trace length, and  $a$  and  $b$  are some fitting parameters. A power-law distribution of this form is a strong indication of self-similarity and, therefore, analyses of such features by recursive scale transformations are expected to prove extremely compatible. The generator also provides for the fractures to have uniform lengths. If the length of a fracture is greater than the system length, it is assumed that the fracture is fully connecting the two opposite ends of the system.

The width of the fracture is considered as the width of a pixel, and the length of the fracture is represented as a row or column of pixels, where the pixels are assumed to have the shape of a square. Obviously, the aperture assigned to the fracture is dependent on the resolution with which the domain has been discretized. What is important to keep in mind is that all subsequent analyses can be considered dimensionless since by changing the characteristic length of the domain (in this case the side of a square), all lengths and related properties are scaled appropriately. It is also important to define at this point the physical significance of a fracture in the analyses. As shown in Figure 6-5, a fracture is represented by a continuum that possesses distinctly different hydraulic properties from the surrounding matrix. It can be conceptualized as a relatively rubblized zone, with the fracture walls being rugged or smooth and with the fracture space being filled with material or not. In any case, this disturbed zone of material in and around a lineal discontinuity of the rock mass, together with some small portion of the surrounding undisturbed matrix, is considered in this conceptual model as possessing different hydraulic properties than the undisturbed matrix.

In order to mimic large system behavior (i.e., reduce the effects of finite domain size), the generator has been enhanced by a periodic boundary. This means that fractures loop around and appear at the opposite face of the computational domain when they are intercepted by a boundary. Provision has been made also for two parallel fractures to be separated from each other by at least one pixel. However, two parallel fractures can connect each other at their tips, thus giving rise to connectivity even when two fractures are not collinear. Thus, while sampling the center of fractures from a specified distribution, provision is made to reject candidate fractures that are not at least one pixel away from existing ones in every direction. This process of rejection of fractures was suspected of violating the distributional assumptions of centers and, therefore, a variogram analysis was conducted in a manner similar to the

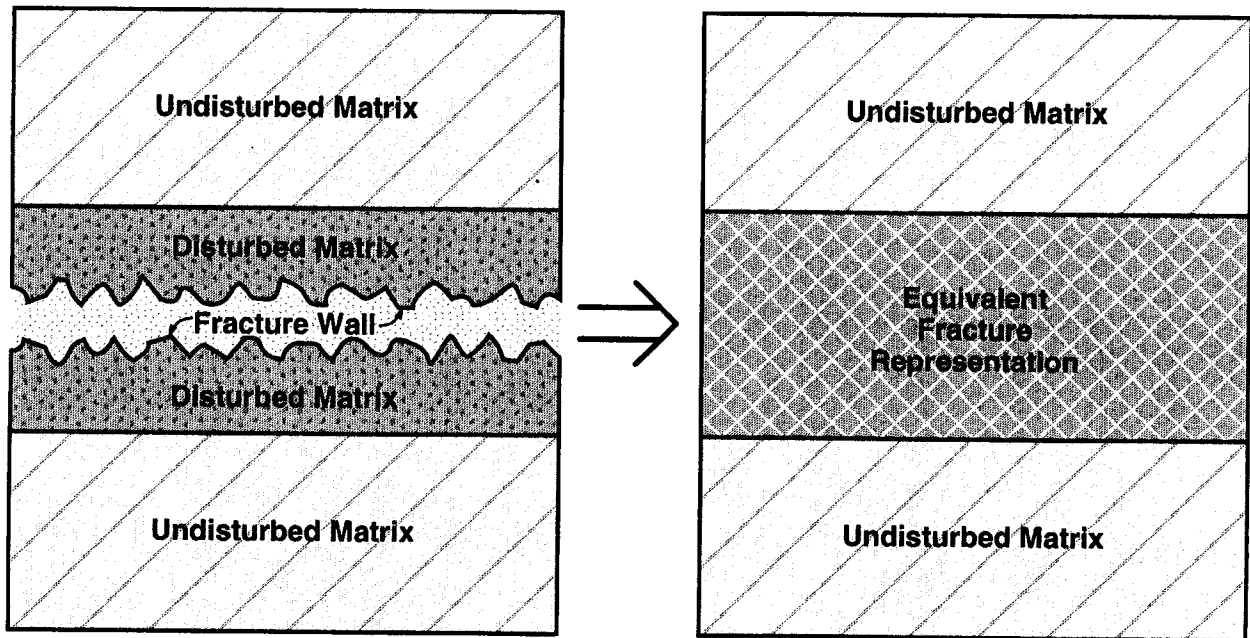


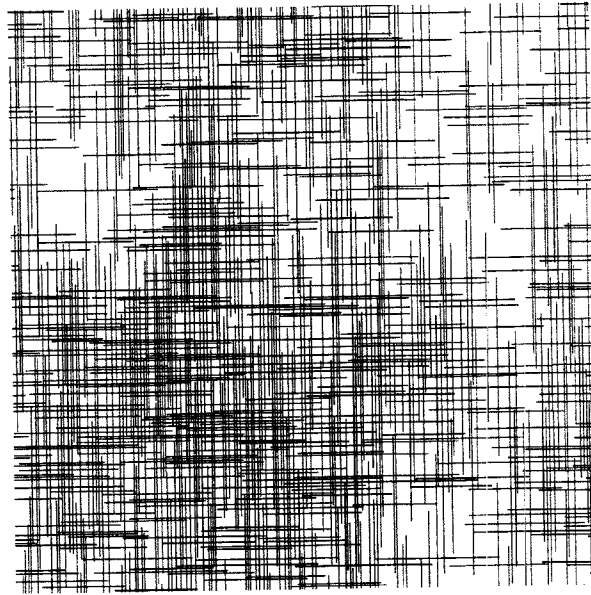
**Figure 6-5. Schematic depicting the conceptual model for a fracture and its corresponding continuum approximation**

study by Hestir et al. (1987). No biasing of the generator was obvious from the semivariogram plots, indicating that the distributional assumptions were honored.

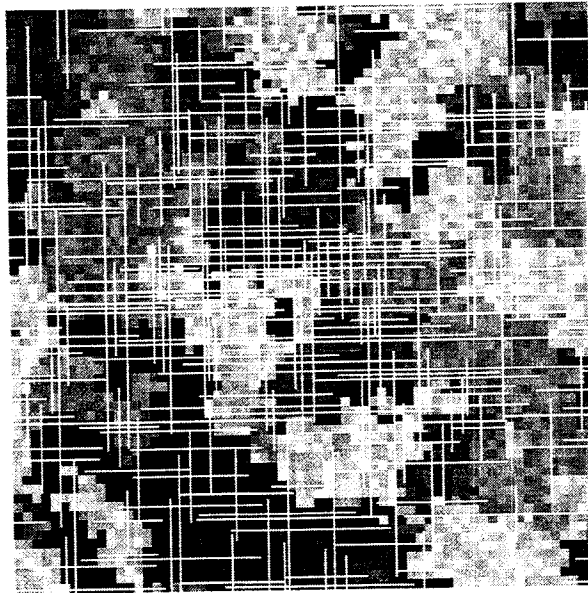
Finally, the fracture network generator is capable of superimposing the fracture sets on either a homogeneous or a heterogeneous matrix background. In this way, the user may choose to analyze a binary system or a fracture network superimposed on a stochastically generated matrix hydraulic property field. Typical examples of complex, highly fractured, heterogeneous structures generated by the numerical code discussed in this section are shown in Figure 6-6.

#### **6.4.2 Determination of Effective Hydraulic Properties**

Scaling effects come into the picture when the scale of measurements differs from the scale of application. Scale effects arise as the relative importance of different flow and transport processes shift as the scale of analysis changes. As Tidwell et al. (1993) pointed out, the scaling models are designed to provide a means of transforming heterogeneous small-scale data to larger scale in terms of effective properties, while preserving the signature of the small-scale flow and transport processes and media heterogeneity. Effective hydraulic conductivity means the conductivity that preserves the fluid flux-potential drop quotient between a heterogeneous block and an equivalent (same size, geometry, and fluid viscosity) homogeneous block (Kasap and Lake, 1990). The scaling (averaging) process for moving from a smaller scale to a larger scale is complicated particularly for properties like saturated and unsaturated conductivities that are nonadditive. In addition to the many empirical models proposed in the



(a)



(b)

**Figure 6-6. Examples of highly fractured, heterogeneous structures: (a) binary matrix-fracture system; and (b) stochastic matrix-fracture system**

past, the following are the methods that are traditionally used and are based on theoretical foundations to determine effective properties: (i) Direct simulation; (ii) Monte Carlo approach; (iii) Effective Medium Approximation (EMA); and (iv) RSRG. The direct simulation and Monte Carlo approaches are extremely time consuming for large numbers of computational cells. The effective medium approximation gives accurate results only when the fraction of the dispersed phase is small. In a binary matrix-fracture system the fracture is assumed to be the dispersed phase. Moreover, EMA provides less accurate estimates of effective properties in 3D than in 2D domains. David et al. (1990) and Wang (1991) pointed out that systems with nearly uniform distribution can be treated with EMA, whereas the systems with broad distributions can be treated with critical path analysis. The RSRG method works equally well for any fraction of the dispersed phase, especially near the percolation threshold (fixed point), defined as the minimum volume fraction of the conducting component at which a conductor/nonconductor binary mixture allows conduction. Owing to the sharp contrast in the fracture and matrix hydraulic conductivity, percolation-type behavior is expected in a fracture/matrix system. The following is a brief description on the background of the method and its implementation in its simplest form.

### 6.4.3 Real Space Renormalization Group Method

The renormalization group (RG) method (Wilson and Kogut, 1974) is a statistical mechanics approach originally developed to study the phase transition behavior of fluids near a critical point. This method involves a recursive scale transformation process in which while going from the smallest to the largest length scale, the small-scale fluctuations are integrated and only the important features that contribute toward the macroscopic behavior are preserved. This method is suitable for dealing with any problem in which complex microscopic effects underlie macroscopic properties (i.e., a problem that involves many length scales). The method has largely been applied in the past to study the Ising problems in magnetic systems (Wilson and Kogut, 1974).

RG theory has been formulated in Fourier space and in real space. In the Fourier space method, the Fourier transform of the partition function or the probability distribution function is manipulated. Its implementation in real space is referred to as the RSRG method. RSRG methods are of greater practical importance, and the method is intuitively appealing because of its geometric description on a lattice, which provides a direct analogy to a network model of conduction. The first application of the RSRG formalism to percolation problems was by Young and Stinchcombe (1975). In a binary site percolation problem, the sites/nodes are considered to be occupied by either Phase A or Phase B. The correlation length of the dispersed phase (i.e., fractures) is the first moment of the cluster size distribution. As the system approaches the percolation threshold, the correlation length tends to infinity. This implies that infinite or sample-spanning clusters are formed. The renormalization transformation is directly applied to the probability distribution of sites (nodes) or bonds (conductive links between the nodes). Application of the method to a system in which both phases are conducting is a logical extension of the conductor-insulator problem. The percolative behavior can still be observed, primarily because of the sharp contrast in the hydraulic conductivity of fracture and matrix cells. There is nothing in the method itself that prevents it from being applied to a system in which two or more phases are conducting.

Bernasconi (1978) implemented the RSRG approach using a bond disordered conductance distribution on a square lattice, and a simple cubic lattice with a binary distribution of conductances. He applied the theory only to conductor-insulator systems. As evident from the previous discussion, the RG has primarily been applied to fully random systems or to site percolation problems posed as a correlated

bond percolation problem. Several applications have also been reported on anisotropic bond percolation problems.

Mohanty and Sharma (1991) developed a cluster-counting method for correlated isotropic and anisotropic systems that honors the true spirit of the RG formalism in keeping the nature of the conductance distribution invariant through the recursion steps. They used the explicit cluster-counting method to calculate degeneracy, which is necessary for implementing the recursion relation. Although their implementation minimized the finite lattice size effects, the method was more suitable for an ensemble of realizations rather than determining the conductivity of a given field. A much simpler and quicker alternative to the above method is to simply ignore the effect of finite lattice size and to recursively calculate the average property (Lobb et al., 1981; King, 1989; Ahmed et al., 1991; and Aharony et al., 1991). The implementation of this procedure is demonstrated in Figure 6-7. In this approach, a lattice, preferably a square lattice in 2D or a cubic in 3D, is overlaid on the given heterogeneous field. Each node on the lattice on a binary system represents either a matrix pixel or a fracture pixel. In reality, as the pixel size may be larger than the fracture width, an equivalent property is assigned to the fracture pixel, which is calculated by assuming that the fracture is surrounded by some matrix material that coexists in the same pixel as that of the portion of a fracture. Then the whole lattice is subdivided into cells that contain a few matrix and/or fracture pixels. A cell of size  $b = 2$  is shown in Figure 6-7. The average property of each cell is calculated by imposing a no-flow boundary condition in the transverse direction and a unit pressure gradient in the flow direction. This process of subdividing the lattice into cells and averaging the heterogeneities inside the cell is continued until only a single site/bond is obtained. The number of cells is reduced by a factor of  $2^d$  ( $d$  is the dimensionality of the problem) at each step in the recursion until only one conductance remains.

The limitation of this method lies in the fact that, in some cases, an artificially created connectivity between disconnected conductors will lead to an overestimation of the conductivity. Independent of exactly how the RSRG method is implemented, the following assumptions hold: (i) the field is of infinite extent; (ii) steady-state conditions have been established; and (iii) the transformation keeps the random conductance field invariant. The comparison between the above two methods using isotropically and anisotropically correlated fields can be found in Mohanty (1993). The two methods give similar results away from the percolation threshold.

The above methods are expected to give poor results when the fractures are oriented at an angle to the global flow and also when many of the conductivities in one direction are set equal to zero, which is reflected through large relative errors when the effective conductivity in that direction is small.

#### **6.4.4 Determining Effective Hydraulic Conductivity by the RSRG Method**

To obtain effective unsaturated conductivities, a fluid is conducted in a heterogeneous medium and the flow rate and the pressure gradients at any cross section are averaged to obtain the effective relative conductivity for each phase. The primary issue in the steady-state analysis of heterogeneous media is the determination of the saturation distribution. For small capillary number flows (viscous forces  $\ll$  capillary forces), capillary pressure will dictate the distribution of fluids. Indeed, if no flow occurs, the pressure in the wetting component and the nonwetting component will be constant everywhere, and the difference will be controlled entirely by the capillarity. For such low-capillary number flows, the effective unsaturated conductivity will be a strong function of the structure of the permeability distribution.

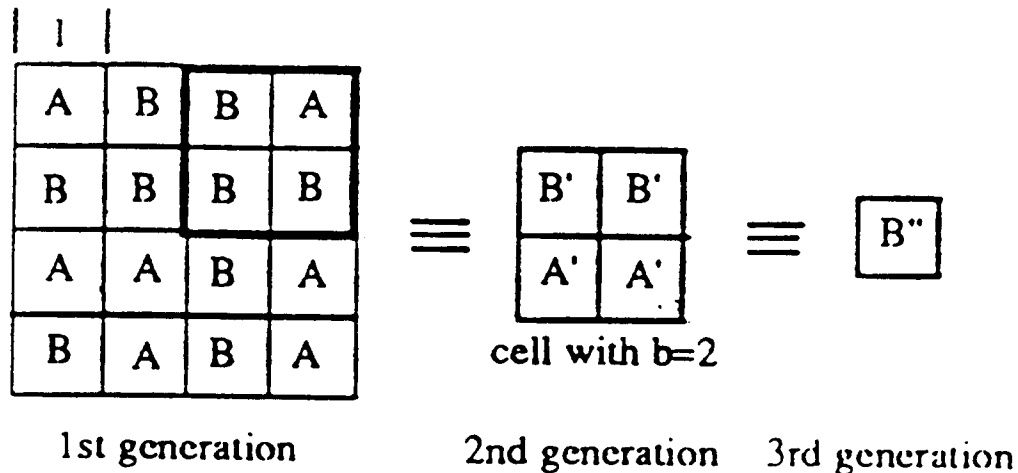


Figure 6-7. Schematic of the RSRG transformation: cluster of cells transforms to a cell, cell transforms to a site, etc.

The fractured porous medium, whether in the composite porosity or effective continuum models (Peters and Klavetter, 1988; Pruess et al., 1990b), is represented by saturation and permeability functions. The properties of the composites are represented by an arithmetic average of the fracture property and matrix property. This sort of averaging mimics a physical condition as if the flow in the fracture is parallel to the flow in the matrix. The study of Rasmussen et al. (1987) indicated that harmonic and geometric means would also be appropriate averaging methods, depending on the fracture orientation. Clearly, there is a need for a method that is robust enough for representing the composite properties for a broad range of fracture properties (such as distribution and orientation).

The applicability of the RSRG method to determine composite unsaturated properties is described in this section. The following are the assumptions under which this method is applicable:

- Capillary-dominated flow regime exists
- Capillary equilibrium has been reached (i.e., the difference in pressure between air and water is the same everywhere)
- For every change in pressure, the equilibrium is reached instantaneously

Wang and Narasimhan (1985) and Pruess et al. (1990a) have pointed out that when the matrix blocks are small, that is, the formation is highly fractured, the pressure and temperature within the matrix block will

quickly equilibrate with the surrounding fractures. The quick attainment of thermodynamic equilibrium eliminates the need to determine pressure separately in the matrix and in the fracture.

To implement the RSRG method, the following relationships can be used: (i) saturation and pressure head represented by van Genuchten's moisture retention relation given in Eq. (6-7); and (ii) Gardner's unsaturated conductivity-pressure relation which is defined as

$$K(h) = K_s \exp[\alpha (h - h_b)] \quad (6-10)$$

where

- $K(h)$  = hydraulic conductivity at pressure head ( $h$ )
- $K_s$  = saturated conductivity
- $h_b$  = air entry pressure head (bubbling pressure), and
- $\alpha$  = scaling parameter

The algorithm developed for determining effective unsaturated conductivity for a binary system can be summarized as follows:

- Assign equivalent saturated fracture conductivity to the fracture pixels
- Choose a water saturation value for the matrix region
- Calculate the corresponding suction head in the matrix region, assume that suction heads in the matrix and fracture are at equilibrium, and calculate the fracture saturation corresponding to this suction
- Determine the corresponding hydraulic conductivities using Gardner's (or any other appropriate) model
- Apply RSRG method to average the values for the binary system
- Assign weighted average saturation to the homogenized region

When a fracture-matrix binary system is used, for every matrix saturation, a unique value of saturation can be determined for the fracture, as for every matrix saturation value there exists one and only one fracture saturation. But for a distribution of matrix conductivities, this cannot be done as there is no unique value of pressure or saturation that characterizes the matrix. Therefore, two methods have been implemented: Method A and Method B. In Method A, the saturation in each matrix block is evaluated at the specified pressure head in the fracture. The average of all the saturations in the matrix blocks is used to determine the matrix unsaturated conductivity. Then, the RSRG method is applied to obtain the effective hydraulic unsaturated conductivity of the matrix-fracture composite. In Method B, the pressure head distribution is calculated for a specified saturation. Then, the average value of the pressure heads in the matrix is used to determine the unsaturated conductivity in the fracture before the RSRG is applied to determine the effective unsaturated conductivity of the matrix-fracture composite.

## 6.4.5 Results and Discussion

In the first part of this study, the effective saturated and unsaturated conductivities were obtained by using fully connected fracture networks. Figure 6-8 depicts a schematic representation of such a network. The computational burden is not expected to be significantly different for stochastically generated fracture networks. The following is a comparison of approximate CPU time between direct numerical simulations and the RSRG method. The execution times for saturated and unsaturated conductivities are presented in Table 6-2 and Table 6-3, respectively. Clearly, as the system size grows, the RSRG method becomes much faster than the numerical method. The accuracy of the RSRG method was compared against the numerical solution by using a fully connected fracture network on a  $64 \times 64$  grid, with a fracture conductivity 1000 times that of the matrix conductivity. A maximum error of 1.5 percent was observed.

Results of effective unsaturated conductivity were also compared against numerical simulations using the BIGFLOW code (Ababou and Bagtzoglou, 1993). Two types of fractured heterogeneous fields were used: (i) a binary field with the distribution of fracture and matrix; and (ii) a field in which the homogeneous matrix was replaced by a distribution of matrix conductivities. The effective unsaturated conductivity for the binary system with a fracture density anisotropy of two and a saturated hydraulic conductivity ratio of 1000 is presented in Figure 6-9a. A good match was obtained between the numerical simulation and the RSRG method both at low and high suctions. When the saturated hydraulic conductivity contrast was reduced to 25, a good match was obtained between the two methods only at low suctions (Figure 6-9b).

## 6.4.6 Summary and Conclusions

A 2D fracture generator code has been developed such that horizontal and vertical fractures can be created on a matrix background with distributed or binary conductivities. The program has the capability to generate exponentially distributed fracture centers and fracture lengths. Periodic boundary conditions have been implemented to mimic a large-flow system. Anisotropic fracture densities can be specified in the vertical and horizontal directions. The program is capable of calculating effective saturated conductivity and unsaturated conductivities of the composite using the RSRG approach as a function of relative saturation or pressure head.

The results obtained from the numerical experiments using a fully connected fracture network are summarized below:

- The RSRG method has been used to determine effective saturated and unsaturated conductivities. The method is nearly 100 times faster than the steady-state flow solver for the saturated case. It is nearly 350 times faster than the available unsaturated flow simulator (BIGFLOW) in determining effective unsaturated conductivity.
- For a fully connected fracture network, effective saturated conductivity increases almost linearly with the density of fractures in the direction of flow.
- Effective saturated conductivity is insensitive to vertical fracture density, suggesting that cross flow is not important.

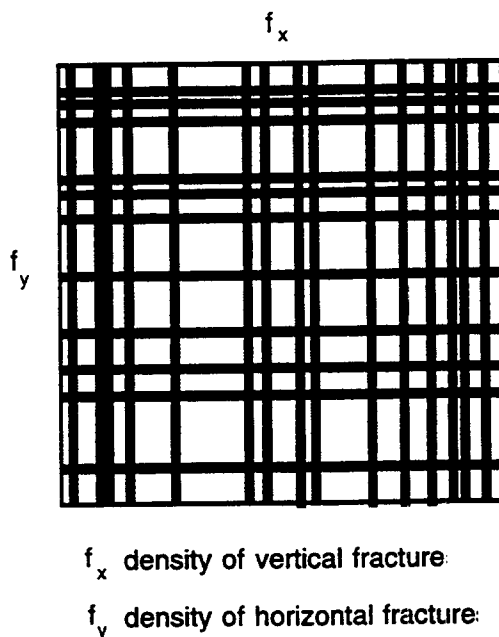


**Figure 6-8. Schematic of a fully connected fracture network with anisotropic fracture density**

- Capillary force-dominated flow regime has been considered for unsaturated conductivity calculations.
- When the saturated conductivity contrast is high, the RSRG solution matches well with the results from numerical simulation (BIGFLOW) at low suction heads. At low saturated conductivity contrasts, a quantitative match is observed for low suction heads. Overall a good qualitative match was obtained for all suction values.
- There is a certain saturation range for which the effective unsaturated conductivity of a fractured system is identical to that of a fully random system, suggesting that a stochastic continuum approach may be appropriate.

## **6.5 ASSESSMENT OF PROGRESS TO DATE**

The Stochastic Project so far has contributed to the conceptualization of issues related to the quantitative characterization of large-scale flow and transport in unsaturated, highly fractured, heterogeneous rock. It has also contributed to the conceptualization of methods for incorporating small-scale variability effects in the conduct of large-scale simulations of flow and transport processes expected or anticipated to occur at the far-field of the proposed HLW repository at Yucca Mountain, Nevada.

**Table 6-2. Execution time comparison between numerical simulation and RSRG method for the determination of effective saturated conductivity. The calculation of the time ratio assumes that the Cray X-MP is about seven times faster than a SUN Sparc workstation.**

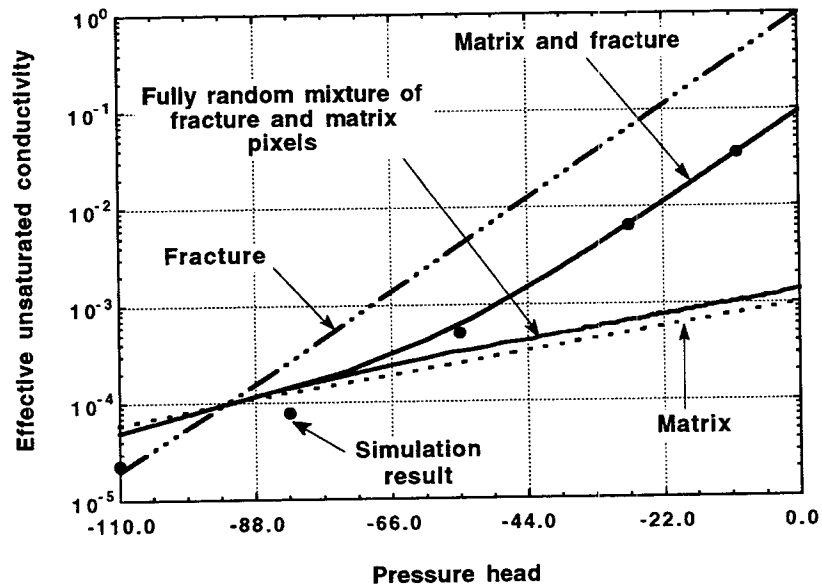
Grid Size	Numerical (Cray X-MP)	RSRG (SUN Sparc)	Approximate Ratio
128×128	100 sec	24 sec	30
512×512	500 sec	30 sec	115

**Table 6-3. Execution time comparison between numerical simulation and RSRG method for the determination of effective unsaturated conductivity. The calculation of the time ratio assumes that the Cray X-MP is about seven times faster than a SUN Sparc workstation.**

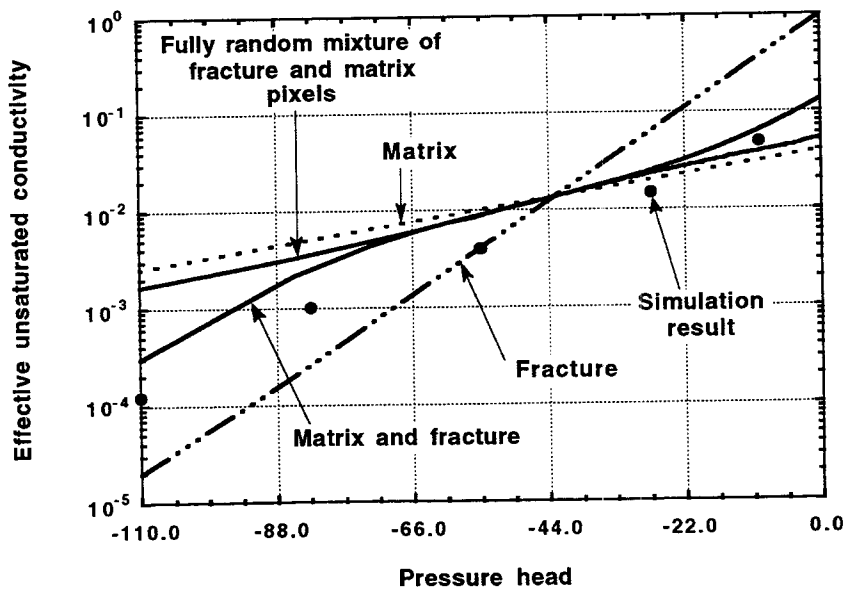
Grid Size	Numerical (Cray X-MP)	RSRG (SUN Sparc)	Approximate Ratio
64×64	1200 sec	24 sec	350
1024×1024	N/A	100 sec	N/A

More specifically, a thorough review of the state-of-the-art literature resulted in NUREG/CR-5743, Approaches to Large Scale Unsaturated Flow in Heterogeneous, Stratified, and Fractured Geologic Media (Ababou, 1991b). This work has, to a large extent, covered the lack of acceptable hydrogeologic theories and conceptual/mathematical modes that are considered applicable for the conditions prevailing at Yucca Mountain. Furthermore, the development, continuing enhancements, and documentation of an efficient unsaturated flow simulator [NUREG/CR-6028, BIGFLOW: A Numerical Code for Simulating Flow in Variably Saturated, Heterogeneous Geologic Media (Theory and User's Manual — Version 1.1), Ababou and Bagtzoglou (1993)] provided a much needed software platform to study the flow behavior of unsaturated fractured rock for different flux rates, an issue that directly affects resolution of a KTU. It has also contributed to the IPA Phase 2 exercises. Moreover, the development and documentation of a working methodology to calculate effective hydraulic properties for highly fractured, heterogeneous rock are activities that address directly a KTU on the determination of effective hydrologic characteristics as a function of scale.

The most important contribution of the Stochastic Project is that it provides the necessary platform to study and assess the variability in model parameters and the effect of the variability on various performance measures. This contribution, in the form of numerical models, executive codes, or the documentation of working methodologies, is of critical importance for the development of the GWTT performance objective. A preliminary successful application of such a methodology has been conducted for GWTT uncertainty evaluation.



(a)



(b)

Figure 6-9. Comparison of effective unsaturated hydraulic conductivity between a fracture system with fully connecting fractures and a system with a random binary distribution of fracture and matrix pixels. The fracture density anisotropy is 2 and the ratio of saturated hydraulic conductivities is: (a) 1000; and (b) 25.

Finally, the experience and knowledge obtained in the course of analyses conducted under the Stochastic Project have already contributed and will continue to do so in the future to the efficient and in-depth review of the following U.S. Department of Energy (DOE) Study Plans (SP): (i) SP 8.3.1.2.3.3, Site Saturated-Zone Hydrologic System Synthesis and Modeling; (ii) SP 8.3.1.2.2.9, Site Unsaturated-Zone Modeling and Synthesis; (iii) SP 8.3.1.2.1.4, Regional Hydrologic System Synthesis and Modeling; (iv) SP 8.3.1.2.2.1, Characterization of Unsaturated-Zone Infiltration; (v) SP 8.3.1.2.2.8, Fluid Flow in Unsaturated, Fractured Rock; and (vi) SP 8.3.1.5.2.2, Characterization of the Future Regional Hydrology due to Climate Changes.

The Stochastic Project is scheduled to conclude at the end of March 1994 with the publication of a project final report on large-scale flow and transport simulations conducted for a Yucca Mountain-like environment. During the recent compilation of the large-scale flow characteristics database, it had become apparent that there exists no computational platform that can accommodate such detailed large-scale flow and transport simulations for a  $4,600 \times 4,600 \times 530$  m domain. The option currently under consideration is to conduct these simulations for a subset of the larger domain at approximately the central part of the repository.

## 6.6 PLANS FOR NEXT REPORTING PERIOD

The executive code SUFLAT is expected to be operational at the onset of the next reporting period. This code will: (i) stochastically generate all appropriate 3D hydrogeologic property fields using the Turning Bands Method as incorporated in the code MKPROP; (ii) solve the flow problem with BIGFLOW (Version 2.0); (iii) post-process all flow results in order to calculate 2D or 3D flux and velocity fields using the numerical code FLUX; and (iv) conduct transport simulations with SLIM (2.41).

The analyses pertaining to the efficient calculation of effective hydraulic properties are expected to be completed early next reporting period. Documentation of this methodology will be put in a report to be published as a NUREG/CR by December 1993. Finally, large-scale flow and transport simulations of a  $1200 \times 530 \times 530$  m portion of the Yucca Mountain HLW proposed repository will be conducted using the executive code SUFLAT to assess uncertainty in GWTT estimates as manifested by variability in hydrogeologic properties.

## 6.7 REFERENCES

- Ababou, R. 1991a. Stochastic analysis of unsaturated flow and transport. *Report on Research Activities for Calendar Year 1991*. CNWRA 91-02Q. San Antonio, TX: Center for Nuclear Waste Regulatory Analyses: 6-1 to 6-45.
- Ababou, R. 1991b. *Approaches to Large Scale Unsaturated Flow in Heterogeneous, Stratified, and Fractured Geologic Media*. NUREG/CR-5743. Washington, DC: U.S. Nuclear Regulatory Commission.
- Ababou, R., G. Wittmeyer, and B. Sagar. 1991. Stochastic analysis of unsaturated flow and transport. *Report on Research Activities for the Quarter July 1, 1991 through September 30, 1991*. CNWRA 91-03Q. San Antonio, TX: Center for Nuclear Waste Regulatory Analyses: 6-1 to 6-29.

- Ababou, R. 1993a. Stochastic analysis of unsaturated flow and transport. *Report on Research Activities for Calendar Year 1991*. NUREG/CR-5817. Washington, DC: U.S. Nuclear Regulatory Commission.
- Ababou, R. 1993b. Stochastic analysis of unsaturated flow and transport. *NRC High-Level Radioactive Waste Research at CNWRA, January — June, 1992*. NUREG/CR-5817. Washington, DC: U.S. Nuclear Regulatory Commission 3(1): 6-1 to 6-16.
- Ababou, R., and A.C. Bagtzoglou. 1993. *BIGFLOW: A Numerical Code for Simulating Flow in Variably Saturated, Heterogeneous Geologic Media (Theory and User's Manual — Version 1.1)*. NUREG/CR-6028. Washington, DC: U.S. Nuclear Regulatory Commission.
- Aharony, A., E.L. Hinrichsen, A. Hansen, J. Feder, T. Jossang, and H.H. Hardy. 1991. Effective renormalization group algorithm for transport in oil reservoirs. *Physica A*. 177: 260-266.
- Ahmed, E., A. Tawansi, and M.A. Soliman. 1991. Grey scaling, a new approximation for random resistor networks. *Physics Letters A*:151 (5,6): 301.
- Bagtzoglou, A.C., A.F.B. Tompson, and D.E. Dougherty. 1991. Probabilistic simulation for reliable solute source identification in heterogeneous porous media. *Water Resources Engineering Risk Assessment*. J. Ganoulis, ed. Berlin Heidelberg: Springer-Verlag: NATO ASI Series. G29: 189-201.
- Bagtzoglou, A.C., R. Ababou, and A. Nedungadi. 1992. *BIGFLOW: A Multi-Dimensional Code for Flow in Heterogeneous and Variably Saturated Geologic Media (Theory and User's Manual — Version 1.0)*. CNWRA 92-026. San Antonio, TX: Center for Nuclear Waste Regulatory Analyses.
- Bagtzoglou, A.C. 1993. Stochastic analysis of unsaturated flow and transport. *NRC High-Level Radioactive Waste Research at CNWRA July 1 Through December 31, 1992*. CNWRA 92-02S. San Antonio, TX: Center for Nuclear Waste Regulatory Analyses: 6-1 to 6-23.
- Barton, C.C., and P.A. Hsieh. 1990. *Physical and Hydrologic-Flow Properties of Fractures*. Washington, DC: 28th International Geological Congress.
- Bernasconi, J. 1978. Real space renormalization of bond-disordered conductance lattices. *Physics Review B* 18(5): 2185-2191.
- Dagan, G. 1982. Stochastic modeling of groundwater flow by unconditional and conditional probabilities, 2. The solute transport. *Water Resources Research* 18(4): 835-848.
- David, C., Y. Guegnen, and A. Pamponkis. 1990. Effective medium theory and network theory applied to the transport properties of rock. *Journal of Geophysical Research* 95(B5): 6993-7005.
- Dykhuisen, R.C., and R.W. Barnard. 1992. *Groundwater Flow Code Verification "Benchmarking" Activity (COVE-2A): Analysis of Participants' Work*. SAND89-2558, UC-814. Albuquerque, NM: Sandia National Laboratories.

- Flint, A., L.E. Flint, and J.A. Havesi. 1993. The influence of long term climate change on net infiltration at Yucca Mountain, Nevada. *Proceedings of the Fourth High-Level Radioactive Waste Management Conference*. Las Vegas, NV: American Nuclear Society and American Society of Civil Engineers: 152-159.
- Hestir, K., J.-P. Chiles, J. Long, and D. Billaux. 1987. Three dimensional modeling of fractures in rock: From data to a regionalized parent-daughter model. *Flow and Transport Through Unsaturated Fractured Rock; Geophysical Monograph 42*. D.D. Evans and T.J. Nicholson, eds. Washington, DC: American Geophysical Union: 133-140.
- Kasap, E., and W.L. Lake. 1990. Calculating the effective permeability tensor of a gridblock. *Society Petroleum Engineering Formation Evaluation*: 192-200.
- King, P. 1989. The use of renormalization for calculating effective permeability. *Transport in Porous Media* 4: 37-58.
- Lobb, C.J., D.J. Frank, and M. Tinkham. 1981. Percolative conduction in anisotropic media: A renormalization-group approach. *Physics Review B* 23(5): 2262-2268.
- Mohanty, S., and M.M. Sharma. 1991. A Monte Carlo RSRG method for the percolation/conduction properties of correlated lattices. *Physics Letters A* 154(9): 475-481.
- Mohanty, S. 1993. *Experimental Determination and Theoretical Prediction of Effective Thermal Conductivity of Porous Media*. Ph.D. Thesis. Austin, TX: University of Texas at Austin.
- Nitao, J.J., and T.A. Buscheck. 1991. Infiltration of a liquid front in an unsaturated, fractured porous medium. *Water Resources Research* 27: 2099-2112.
- Peters, R.R., and E.A. Klavetter. 1988. A continuum model for water movement in an unsaturated fractured rock mass. *Water Resources Research* 24(3): 416-430.
- Pruess, R., J.S.Y. Wang, and Y.W. Tsang. 1990a. On thermohydrological conditions near high level nuclear wastes emplaced in partially saturated fractured tuff 1. Simulation studies with explicit consideration of fracture effects. *Water Resources Research* 26(6): 1235-1248.
- Pruess, K., J.S.Y. Wang, and Y.W. Tsang. 1990b. On thermohydrologic conditions near high level nuclear wastes emplaced in partially saturated fractured tuff 2. Effective continuum approximation. *Water Resources Research* 26(6): 1249-1261.
- Rasmussen, T.C., T.C.J. Yeh, and D.D. Evans. 1987. Effect of variable fracture permeability/matrix permeability ratios on three-dimensional fractured rock hydraulic conductivity. *Proceedings from Geostatistical, Sensitivity, and Uncertainty Methods for Ground-Water Flow and Radionuclide Transport Modeling*. B.E. Buxton, ed. New York: Battele Press: 337-358.
- Roache, P.J. 1976. *Computational Fluid Dynamics*. Albuquerque, NM: Hermosa Publishers.

- Runchal, A., and B. Sagar. 1993. *PORFLOW: A Multifluid Multiphase Model for Simulating Flow, Heat Transfer, and Mass Transport in Fractured Porous Media, User's Manual, Version 2.41*. NUREG/CR-5991. CNWRA 92-003. Washington, DC: U.S. Nuclear Regulatory Commission.
- Thornburg, T.M. 1990. *Electrical Resistivity of Unsaturated, Fractured Tuff: Influence of Moisture Content and Geologic Structure*. M.S. Thesis. University of Arizona: Department of Hydrology and Water Resources.
- Tidwell, V.C., J.D. Von Doemming, and K. Martinez. 1993. Scale dependence of effective media properties. *Proceedings of the Fourth High-Level Radioactive Waste Management Conference*. Las Vegas, NV: American Nuclear Society and American Society of Civil Engineers: 1059-1065.
- Sheridan, M.F. 1992. A Monte Carlo technique to estimate the probability of volcanic dikes. *Proceedings of the Third International Conference on High-Level Radioactive Waste Management*. Las Vegas, NV: American Nuclear Society and American Society of Civil Engineers: 2033-2038.
- van Genuchten, M.Th. 1978. *Calculating the Unsaturated Hydraulic Conductivity with a New Closed-Form Analytic Model*. Report 78-WR-08. Princeton, NJ: Princeton University: Department of Civil Engineering: Water Resources Program.
- Wang, J.S.Y., and T.N. Narasimhan. 1985. Hydrologic mechanisms governing partially saturated fluid flow in fractured porous medium. *Water Resources Research* 21(12): 1861-1874.
- Wang, J.S.Y. 1991. Flow and transport in fractured rocks. *Review of Geophysics Supplement*: 254-262.
- Wilson, K.G., and J. Kogut. 1974. The renormalization group and the  $\epsilon$  expansion. *Physics Reports* 12C: 75-200.
- Yeh, T.C., T.C. Rasmussen, and D.D. Evans. 1988. *Simulation of Liquid and Vapor Movement in Unsaturated Fractured Rock at the Apache Leap Tuff Site, Models and Strategies*. NUREG/CR-5097. Washington, DC: U.S. Nuclear Regulatory Commission.
- Yen, B.C. 1988. Stochastic methods and reliability analysis in water resources. *Advances in Water Resources* 11: 115-122.
- Young, A.P., and R.B. Stinchcombe. 1975. A renormalization group theory for percolation problems. *Journal of Physics C: Solid State Physics* 8: L585-540.

## 7 GEOCHEMICAL NATURAL ANALOG RESEARCH

*by English Percy and Bret Leslie*

*Investigators: English Percy, Bret Leslie, William Murphy, James Prikryl, Peggy Hunka*

*NRC Project Officer: L.A. Kovach*

### 7.1 TECHNICAL OBJECTIVES

The technical objective of the Geochemical Natural Analog Research Project is to provide field, laboratory, and theoretical analyses of natural systems that are analogous to some aspects of the proposed high-level waste (HLW) repository at Yucca Mountain, Nevada. These analyses are designed to develop a better understanding of the utility and limitations of natural analog studies when employed to support a license application for a HLW repository and to provide fundamental data on the long-term behavior of HLW within a repository environment. Natural systems that have operated for periods comparable to that required for HLW disposal {i.e.,  $10^3$  to  $10^4$  years and greater, [U.S. Environmental Protection Agency (EPA), 1989]} provide the only opportunity to obtain observational knowledge of the long-term behavior of HLW components. Such information is important for support of long-term predictive models of repository performance assessment (PA) [U.S. Nuclear Regulatory Commission (NRC), 1987]. Many factors affecting the long-term behavior and interaction of the waste form and engineered barrier system (EBS) with the geochemical environment of the proposed repository are poorly known. The absence of this basic information severely limits the confidence with which performance assessment models may be evaluated.

Information developed within the Geochemical Natural Analog Project will be used to support specific portions of the License Application Review Plan (LARP). Site characterization and evaluation activities carried out on sites comparable to Yucca Mountain as part of the Analog Project will provide practical experience and knowledge applicable to the Description of the Individual Systems and Characteristics of the Site (Sections 3.1.1, 3.1.2, 3.1.3, and 3.1.5). Detailed field, laboratory, and theoretical studies of mineral stabilities and elemental transport mechanisms and rates, which are integral to the Analog Project, will provide an independent basis for development of portions of the LARP relating to both favorable and potentially adverse geochemical conditions and processes (Sections 3.2.3.1, 3.2.3.2, 3.2.3.3, and 3.2.3.5). One result of the Analog Project will be knowledge of the long-term and large-scale behavior of radioelements in natural systems comprising the integrated effects of lithology, structural geology, hydrology, and geochemistry. Knowledge of the net transport behavior resulting from the interaction of these systems will support preparation and implementation of Section 3.4, Effectiveness of Natural Barriers Against the Release of Radioactive Material to the Environment. Further, material and corrosion analogs studied within the Analog Research Project may provide information required to develop Section 5.4, Assessment of Compliance with the Engineered Barrier System (EBS) Performance Objectives.

At this time, Compliance Determination Strategies (CDS) for the LARP sections noted earlier are not yet finalized. Nevertheless, it is clear that the Analog Research Project will be important in addressing uncertainties raised in the CDS. For example, CDS 3.2.3.5 on geochemical processes has been identified as a Type 5, requiring independent research to resolve Key Technical Uncertainties (KTU) that pose a high risk of noncompliance with performance objectives of 10 CFR Part 60. Specific KTU topics that will be addressed by work within the Analog Project include the long-term, large-scale effects of

geochemical processes on the transport and retardation of radionuclides and on the performance of the EBS.

The Analog Research Project is required by its nature to be an integrated effort combining expertise in geochemistry, hydrology, and structural geology. This need for interdisciplinary input is reflected in a number of technical interfaces with other NRC Office of Nuclear Regulatory Research (RES) projects. An active and ongoing relationship has been established with the PA Research Project. This work consists of characterizing the hydrologic properties of welded silicic tuff from the Nopal I analog site to allow more complete interpretation of long-term transport of U through tuff at the site. The Sorption Research Project is developing plans to initiate short-term U diffusion experiments using Nopal tuff to experimentally evaluate diffusion coefficients and sorption behavior. Those results will be used within the Analog Project to interpret the existing record of U diffusion and sorption at the Nopal I site. Results from the Analog Research Project are being used to guide and develop the Near-Field Geochemistry Research Project. Specifically, at the Nopal I site, it has been observed that alteration phases formed after uraninite (a spent fuel analog material) are dominated by the minerals uranophane, soddyite, and weeksite. The Nopal I analog suggests that these phases are likely to be important to radionuclide transport in a Yucca Mountain repository; the Near-Field Geochemistry Research Project may include experiments to determine thermodynamic properties of those minerals so that their behavior can be modeled. Similarly, results and expertise from the uraninite characterization at Nopal I are being used to guide the design of potential spent fuel waste from experiments within the EBS Waste Form Characterization work for the NRC Office of Nuclear Material Safety and Safeguards (NMSS).

The Geochemical Natural Analog Research Project addresses needs identified by NMSS concerning assessment of the degree to which data from analogous sites may be extrapolated to support modeling for a repository site and evaluation of means to derive reasonable assurance that performance assessment models can be validated using data from natural analogs. Specific NRC research needs that may be met through this project include: comparison of laboratory sorption, mineral stability, leaching, and chemical reaction kinetics data with observations from natural systems; evaluation of radionuclide transport in unsaturated tuff; assessment of the effects of the oxidizing power of the environment on leaching and radionuclide release; and investigation of coupled interactions affecting radionuclide release and transport.

Research within the Geochemical Natural Analog Research Project includes work at two sites: the Nopal I U deposit in the Peña Blanca district, Chihuahua, Mexico (field work initiated February 1991), and at the Akrotiri archaeological site on Thera (Santorini), Greece (field work initiated June 1992). Earlier reports in this series documenting progress to date include: Percy et al., 1993; Percy et al., 1992; Leslie et al., 1993a; Percy and Murphy, 1991a; 1991b; 1991c; Percy et al., 1991; Percy and Murphy, 1990).

## **7.2 SIGNIFICANT TECHNICAL ACCOMPLISHMENTS**

Analogous aspects of the Nopal I deposit to the proposed repository at Yucca Mountain have been discussed earlier (Percy and Murphy, 1991d; Percy and Murphy, 1992) and include the silicic, tuffaceous host rocks, the semi-arid climate, the unsaturated hydrologic regime, the chemically oxidizing environment, and the presence of reduced U mineralization. Previous research within this project has provided an understanding of the geologic, mineralogic, and hydrologic framework of the Peña Blanca natural analog (Percy et al., 1992). This work has included measurement and interpretation of the

chemical composition of waters collected near and at the Nopal I deposit (Pearcy et al., 1992) and development of preliminary source-term constraints (Murphy and Pearcy, 1992; Pearcy et al., 1992). The details of the mineralogy and paragenesis of the deposit have been established (Pearcy et al., 1993; Leslie et al., 1993a, 1993b), and the spatial distribution of U within and adjacent to the U ore deposit has been measured and mapped (Leslie et al., 1993b). Most recently, the alteration of uraninite (nominally  $UO_{2+x}$ ) at Nopal I has been studied and compared to spent fuel degradation processes expected in a Yucca Mountain repository environment (Pearcy et al., 1993).

The Nopal I U deposit is hosted by rhyolitic tuffs of the Nopal and Coloradas Formations (Pearcy et al., 1992), and the U mineralization is located within a breccia pipe structure (about 20 × 40 m wide and about 100 m high) located at the intersection of several faults.<sup>1</sup> Exposure of the deposit at Nopal I is unusually good; the mineralization is presently exposed on broad mined benches at the 0 and +10 m levels, which together provide surface access across the deposit (Figure 7-1). The removal of the loose rock and gravel cover from a 1,250 m<sup>2</sup> section of Level +10 m has provided an extraordinary exposure of the geologic and mineralogic relationships that comprise the analog.

Recent work has examined the transport of U in the host tuff over a wide range of spatial scales. Preliminary measurements are presented here of the distances of U transport along a discrete fracture (tens of meters), through generally fractured tuff (meters), through relatively unfractured tuff (centimeters), and through homogeneous portions of the tuff matrix ( $\mu\text{m}$ ). Uranium concentration profiles along these transport paths are examined and compared with data on the mineralogy of the bulk rock and the mineralogy of fracture fillings. These measurements and interpretations are an initial attempt to define working hypotheses for mechanisms of U transport at Nopal I.

### 7.2.1 Sampling Uranium Distributions at Varying Scales

The gross distribution of U within and around the Nopal I deposit has been previously delineated at a coarse scale (measurements every 0.5 to 1.0 m) using a contact gamma survey and discrete gamma spectrometry measurements of the U content in the bulk rock (Leslie et al., 1993a; 1993b). Those studies indicated that the western margin of the deposit on Level +10 m is abrupt, with the transition to unmineralized tuff occurring in a systematic fashion over a distance of about 0.5 m, whereas the distribution of U along a N-S transect on Level +10 m is more variable and appears to be fracture related. It was suggested by Leslie et al. (1993a) that the redistribution of U from its original locations within primary uraninite was strongly influenced by fracture geometry and fracture intensity, but that flow of U-bearing fluids was not restricted to fractures.

To better constrain these working hypotheses, the distribution of U has been evaluated at a variety of scales ( $10^{-6}$  to  $10^1$  m). This range allows initial assessment of both fracture and matrix transport of U at the Nopal I deposit. Guided by information from earlier gamma surveys and geologic mapping of the +10 m level, samples were collected: (i) along a prominent East-West trending fracture located at about 13.5 m North (13.5 m N); (ii) across a 2-m traverse spanning the western boundary of the deposit at 9.1 m North (9.1 m N); (iii) perpendicular to the 13.5 m N fracture at several locations; and (iv) perpendicular to microfractures from two locations within the deposit (Figure 7-1).

---

<sup>1</sup>This interpretation was received orally from Professor Ignacio Reyes, *Universidad Autonoma de Chihuahua*, during a field trip in 1991.

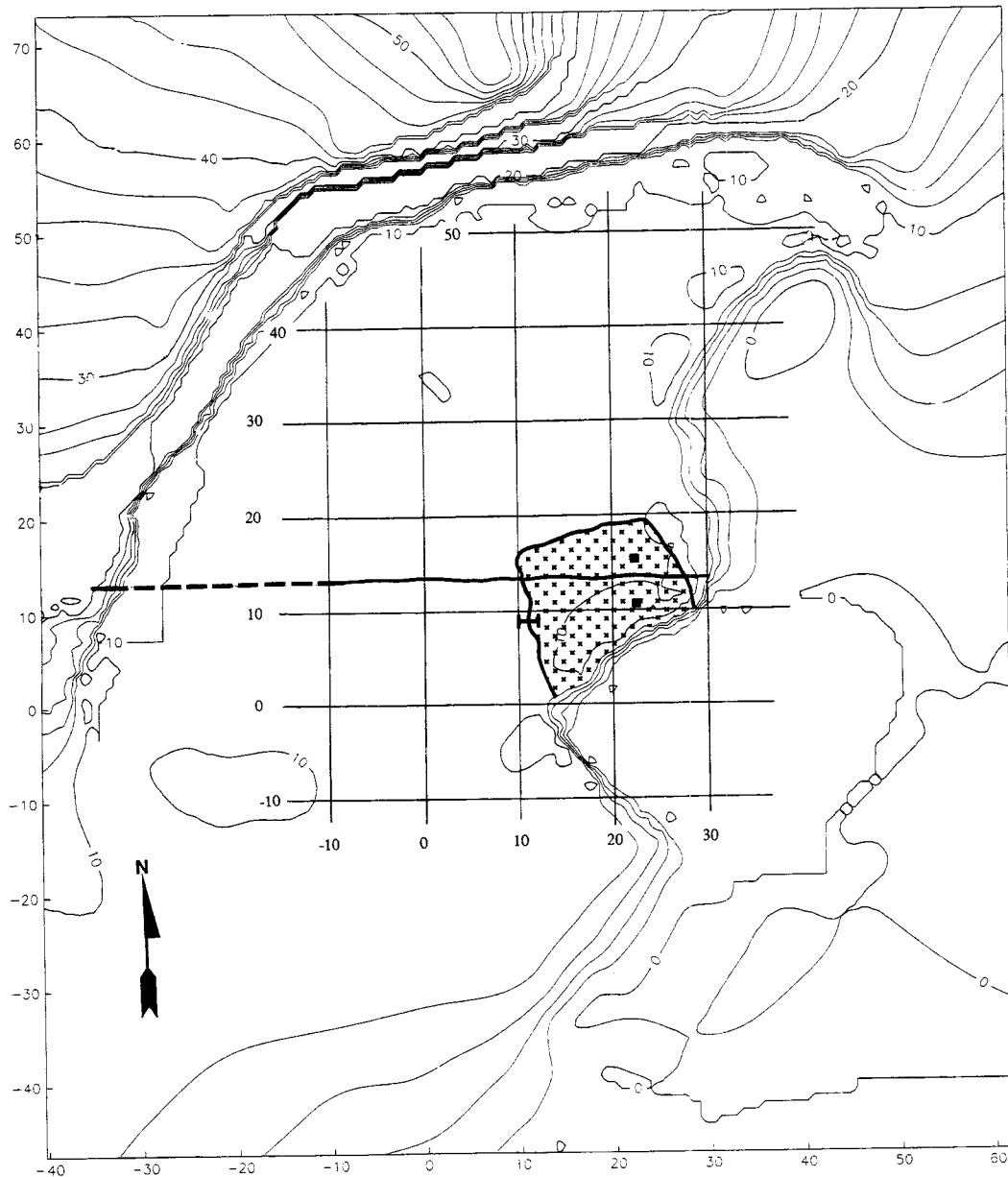


**Figure 7-1. Location map of the Nopal I analog site. Topographic contour interval is 2 m. Topography is based on plane-table mapping conducted as part of this project. Original topographic data were gridded and contoured with ARCINFO software. Coordinates are in meters East-West and North-South within the permanent sampling grid established on Level +10 m. The stippled area is the area in which visible U mineralization occurs on Level +10. The East-West line at about 13.5 m N is the location of the large, through-going fracture discussed in the text. The dashed portion of the fracture trace indicates the portion yet to be cleared of soil and debris. At the far west end of the trace, the fracture is exposed on the near-vertical face between Level +10 and Level +20. The line at 9.1 m north is the location of the 2 m East-West transect across the edge of the deposit. The solid squares indicate the locations of samples NOPI-ECP-22.35/15.3-TS1 and NOPI-ECP-22.5/10.4-TS1 used in autoradiographic studies.**

The major fracture at 13.5 m N, with an aperture of 1 mm to 1 cm, runs approximately East-West and was chosen for sampling because it cross-cuts the deposit (dip of  $85^\circ \pm 5^\circ$  N), is visibly filled with iron oxides, appears to be laterally continuous, and extends well beyond the western edge of the deposit (Figure 7-1). The trend of the fracture can be projected toward the western edge of Level +10 m where it appears to be present on the vertical wall between the +10 and +20 m levels as an iron oxide-filled fracture. Clearing the portion of the fracture that remains covered, planned during the next 6-month period, should clarify the extent, location, and continuity of the fracture. The fracture location and orientation can also be projected down into the Level 0 m adit where it is observed. Sampling of the material filling the fracture was accomplished by scraping the loose material from the rock surfaces using a steel pocketknife. Although these samples may contain small and variable portions of the wall rock, the samples are generally reflective of the mineralogy and U content of the fracture-filling material. Samples were collected at 1-m intervals along the fracture on the +10 m level over a distance of 20 m, from the fracture on the vertical wall between the +10 and +20 m levels (Sample 393-10-7/0), and at three sites along the fracture within the Level 0 m adit (Samples 393-11.2/14.7/1.5, 393-5.0/14.2/2.0, and 393-3.2/14.0/1.7).

A 2-m profile was sampled across the western margin of the deposit at 9.1 m N (a location just south of the 13.5 m N fracture, Figure 7-1). The 2-m profile was sampled every 20 cm along the traverse in an effort to clarify the nature of the edge of the deposit. Bulk tuff samples of 1 to 2 kg were collected with hammer and chisel. The location of the 2-m traverse was chosen to avoid major fractures. The area is generally fractured and is presently thought to be representative of the degree of fracturing of the host rock surrounding the deposit (except for the lack of major through-going fractures).

Several 20-cm long bulk rock sample traverses were collected perpendicular to the 13.5 m N fracture at locations about 0.5, 6.0, 10.2, 15.9, and 20.1 m from the western edge of the deposit. Samples along these traverses were collected as 2- to 6-cm thick pieces of tuff on either side of the fracture at each location. The locations of the traverses were chosen to avoid heavily broken rock and other fractures. Samples were taken at 6.0 m (NOPI-ECP-4.5/13.73), 10.2 m (393-0.30/13.41), 15.9 m (393-(-5.4)/14.22), and 20.1 m (393-(-9.6)/14.70) from the edge of the deposit, with each sample including both the wallrock and the fracture surface material. These samples were cut into approximately 2-mm thick sections parallel to the surface of the fracture. The sections were washed with deionized water, dried at 100 °C in a drying oven, and cooled in a desiccator. Portions of these thick sections, all other bulk rock samples, and fracture fillings were powdered using a tungsten carbide vial set with a SPEX mixer/mill. These powders were analyzed by x-ray diffractometry (XRD) to determine bulk mineralogy and by gamma spectrometry (Leslie et al., 1993a) to determine their U contents.

The distribution of U perpendicular to microfractures (apertures of 100 to 230  $\mu$ m) was examined at a  $\mu$ m scale using alpha autoradiographic techniques. Samples were selected for autoradiography based on the occurrence of a uranium-bearing microfracture with a simple geometry located in mineralogically and texturally homogeneous tuff. Samples that contained complex fracture patterns or other heterogeneities were rejected. Samples were prepared as standard polished petrographic thin sections 46 by 27 mm, 30  $\mu$ m thick. Autoradiographic techniques used in this study were based on Basham (1981). Alpha radiation intensities and distributions were measured using CR39 film as a solid-state alpha particle detector. CR39 is a thermoset polymer plastic used commercially for a variety of eyeglass and eye shield applications. For alpha autoradiography, CR39 has many practical attributes that are superior to other materials used in the past (e.g., CA80-15, CN85) (Basham, 1981): (i) uniform response to alpha particles up to 6 MeV energy, (ii) optical clarity and lack of color, (iii) high-resolution recording of alpha impacts, and (iv) ease of development (simple etching).

### 7.2.1.1 Distribution of U at Meter and Centimeter Scales

In Figure 7-2, U concentrations in the fracture-filling material from the major fracture at 13.5 m N are compared to bulk tuff U contents at comparable distances from the deposit. The concentration of U in the portion of the fracture located within the deposit is quite high (> 7 weight percent U), and there is a general decrease in the concentration of U in the fracture-filling material with distance from the western edge of the deposit. The concentration of U in the fracture-filling material is 1 to 2 orders of magnitude greater than U concentrations in the bulk tuff at comparable distances from the western boundary of the deposit. This distribution suggests that U was transported through this major fracture for a distance of at least 20 m, and possibly as much as 50 m from its source (i.e., the edge of the deposit). The decrease in U content with distance from the edge of the deposit could be due to physicochemical interaction (e.g., sorption), or chemical reaction (e.g., dissolution of silicates and a concomitant pH increase) of the U-transporting fluid with the wall rock, or differences in the nature of the interaction of the fluid with the wall rock due to varying composition/mineralogy of the bulk rock with distance from the deposit (George-Aniel et al., 1991; Ildefonse et al., 1990).

The mineralogical composition of the fracture-filling material offers possible constraints on the distribution of U in the 13.5 m N fracture. Samples of the fracture-filling material were powdered and analyzed by XRD ( $2 - 70^\circ$  2-theta, at  $0.02^\circ$  2-theta/sec). Diffraction patterns were collected electronically with a DATABOX controller, and the graphics interface program JADE was used to provide output of the absolute intensity of the diffraction signal at each  $0.02^\circ$  2-theta angle. The patterns were normalized to the 100 percent absolute intensity peak of each sample pattern. Representative portions of these patterns are shown in Figure 7-3, including the distance from the edge of the deposit at which each sample was collected and the measured concentration of U.

Minerals identified in the 13.5 m N fracture filling include jarosite [ $\text{KFe}_3(\text{SO}_4)_2(\text{OH})_6$ ], quartz ( $\text{SiO}_2$ ), goethite ( $\alpha\text{-FeO}\cdot\text{OH}$ ), hematite ( $\text{Fe}_2\text{O}_3$ ), and kaolinite [ $\text{Al}_2\text{Si}_2\text{O}_5(\text{OH})_4$ ] (Figure 7-3). Absolute abundances of these minerals cannot be determined from the XRD patterns because variable amounts of wall rock were incorporated during sample collection, because variable amounts of sample powders were used, and because appropriate standards for calibration were not available at the time of the analyses. However, the relative proportions of the different minerals can be compared in a semiquantitative fashion. It is clear that jarosite is the most abundant and that the ratio of jarosite to goethite is highest within the deposit and close to the western edge of the visible U mineralization. The relative proportion of goethite to jarosite increases with distance from the source region. By about 15 m from the edge of the visible U mineralization, jarosite is no longer detected by XRD (XRD may not detect abundances of < 5 volume percent). The presence of XRD-detectable hematite is limited to locations along the fracture that do not show any jarosite.

Jarosite occurs most commonly in acidic, sulfate-rich environments developed as a result of pyrite ( $\text{FeS}_2$ ) oxidation during weathering (Nordstrom, 1982), but has also been reported from inferred paleo-hot springs (Cunningham et al., 1984), and hydrothermal ore deposits (Hayba et al., 1985). The primary mineral assemblage of the Nopal I deposit has been established as uraninite+kaolinite+pyrite (Pearcy and Murphy, 1991c); this original mineralization was limited to the "breccia pipe" area (Leslie et al., 1993a). This occurrence, and the absence of significant concentrations of S or U in the host rocks outside the deposit, suggest that the deposit itself was the source of both the S in the jarosite and the U in the fracture filling. The original pyrite was also likely the source of the locally abundant iron oxides within and near the deposit. Although both the U content of the fracture filling and the quantity of jarosite decrease with distance from the deposit, it is unlikely that jarosite is directly responsible for this U

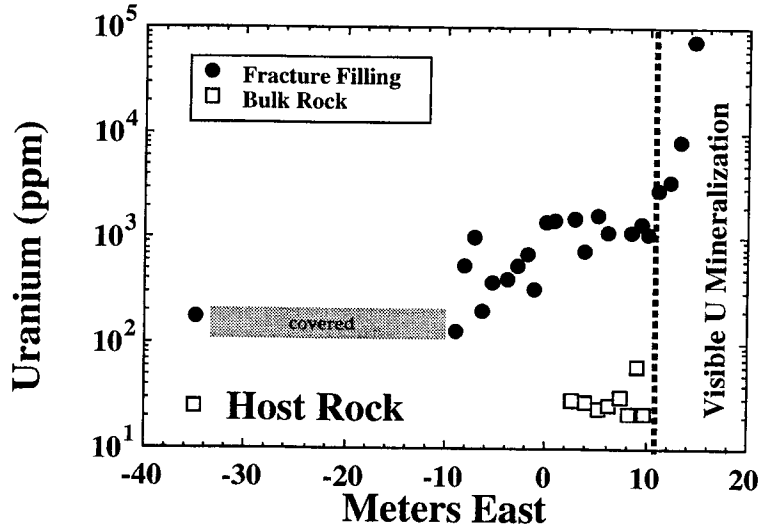


Figure 7-2. Concentration of U in the fracture-filling material of a major fracture at 13.5 m North. The concentration of U in the bulk rock (open squares) is derived from measurements of U along an E-W traverse at about 7.5 m North (Leslie et al., 1993a). The limit of the area of visible U mineralization on the +10 m level at this location is noted with a dashed line. The stippled area represents the portion of the fracture presently covered by soil and debris.

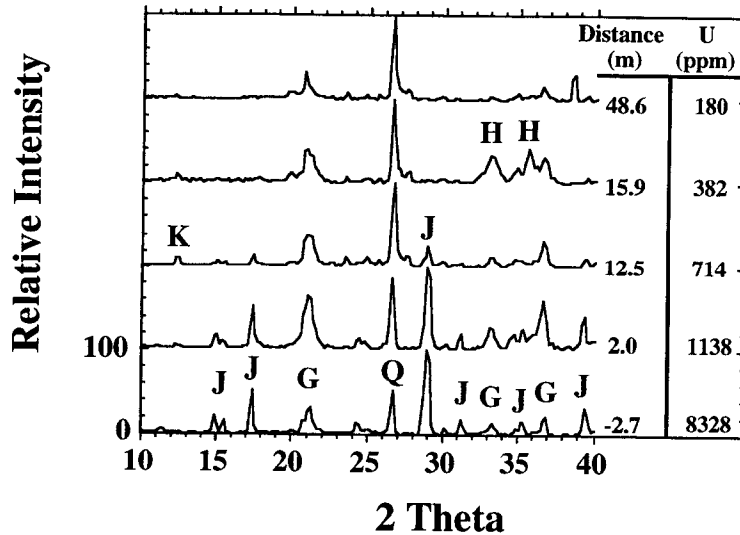


Figure 7-3. Selected XRD patterns of the fracture-filling material collected at varying distance from the edge of the visible U mineralization. The pattern of each sample has been normalized to the 100 percent intensity peak. Kaolinite (K), jarosite (J), goethite (G), quartz (Q), and hematite (H) were identified based upon their 2 theta values. The U concentration of the fracture material and distance from the edge of the deposit are listed next to each sample spectra.

distribution because jarosite tends not to sequester U or Th during its formation (Dickson and Herzceg, 1992). Though it is presently unclear under what conditions and during what time interval the transport occurred, it appears that fluids carrying both U and S were able to travel tens of meters away from the deposit along the 13.5 m N fracture.

The results of U measurements of powdered bulk rock samples collected along the 2-m traverse (Figure 7-4) support the earlier interpretation of a sharp transition from the high U-content rock within the deposit to unmineralized rock across generally fractured tuff (i.e., randomly broken on a scale of centimeters) along the western margin of the deposit. There appears to be a systematic decrease in the concentration of U away from the edge of the visible U mineralization. The concentration of U within the deposit ranges from about 1,000 to 33,000 ppm (Leslie et al., 1993b). Uranyl silicate minerals occur along fracture surfaces of samples collected along this traverse east of 12.18 m east. XRD analyses of the powdered samples indicate the presence of weeksite [nominally  $K_2(UO_2)_2Si_6O_{15} \cdot 4H_2O$ ] in several of those samples in the region of visible U mineralization. Other minerals detected by XRD are quartz, kaolinite, sanidine ( $KAl_3Si_3O_8$ ), and hematite in two samples outside of the visibly U mineralized zone.

In a preliminary attempt to model the distribution of U along this profile, it was decided to try to fit the U concentration in the bulk rock to a classical diffusion equation (Neretnieks, 1980):

$$C = C^0 \left[ 1 - \operatorname{erf} \left( \frac{x}{2\sqrt{Dt}} \right) \right] \quad (7-1)$$

where:

- $C$  = U concentration at location,  $x$ , and time,  $t$
- $C^0$  = constant U boundary concentration
- $x$  = distance from the boundary
- $D$  = diffusion coefficient (diffusivity)
- $t$  = time for diffusion

This equation governs one-dimensional diffusion in a semi-infinite medium with a constant concentration boundary condition (Neretnieks, 1980). It should be noted that chemical data most often fit to the diffusion equation are the concentrations of a solute in a liquid rather than concentrations in a solid as measured here. The present calculation assumes that the measured concentrations in the tuff represent the concentrations of U formerly present as mobile, diffusing species. This use of the diffusion equation to model solid-phase U bulk concentrations assumes a simple linear relationship between the concentration of U in the solid and the concentration of U in the fluid that diffused through the 2-m domain (i.e.,  $C = K\bar{C}$ , where  $\bar{C}$  is the concentration of U in the bulk solid and  $K$  is a dimensionless distribution coefficient). Modelling the solid phase U concentration using the diffusion equation also assumes that the media through which the U diffused had uniform hydrologic properties. The diffusivity ( $D$ ) used here is an apparent diffusivity (i.e., a function of porosity, tortuosity, constrictivity, and a volumetric sorption constant). This simple linear relationship between concentrations of U in the bulk rock and the postulated fluid concentration could be explained by a linear  $K_d$  sorption model (Turner, 1991). For these calculations, the constant concentration boundary condition was taken to be the U

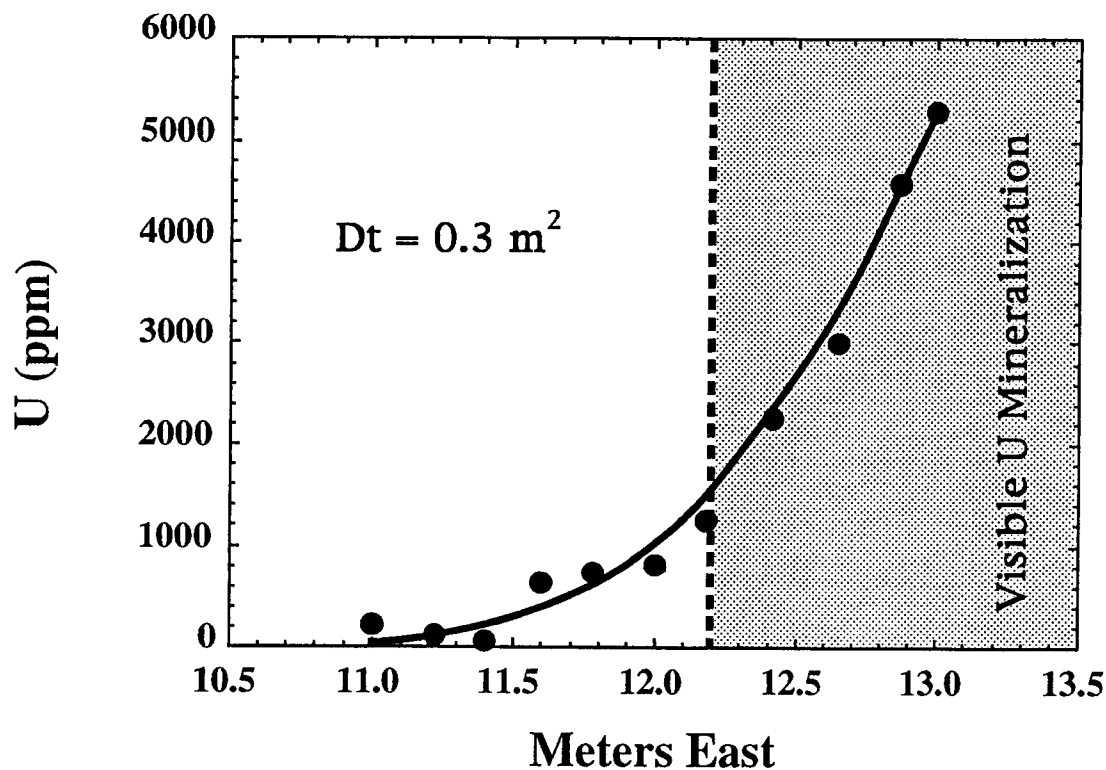


**Figure 7-4.** East/West profile of U content in bulk rock at 9.1 m North. Stippled region is the area of visible U mineralization (uranyl silicates). The solid line is the fit of the diffusion equation to the solid U concentration with the boundary condition of  $U^{\circ} = 5,282$  ppm at 13.0 m East.

concentration at 13.0 m East. Normally, fitting the profile of the dissolved species concentration as a function of distance to the diffusion equation allows estimation of either the diffusivity ( $D$ ) (if the time for the diffusion process is known), or the time ( $t$ ) necessary to generate the diffusion profile (if the diffusivity of the dissolved species is known). In this case, however, neither one is known. Therefore, the fit of the diffusion equation to the profile results in an estimate of the product  $Dt$  (with units of distance<sup>2</sup>).

Uranium concentrations along the 2-m profile can be fit to the diffusion equation of a solute through a porous medium if the product  $Dt$  is about  $0.3 \text{ m}^2$ . Uncertainties in the amount of time for diffusion (e.g., Percy et al, 1993), and the wide range of tenable values for  $D$  (e.g., van Brakel and Heertjes, 1974) preclude complete evaluation of these results at this time. It should be strongly emphasized that modeling of the data from this profile is tentative and that further analysis (petrographic, mineralogic, chemical, and theoretical) is required to evaluate any implications of the model for performance assessment sorption/transport modeling.

Figures 7-5 and 7-6 illustrate the distribution of U perpendicular to the 13.5 m N fracture at various distances from the western edge of the deposit. These profiles were collected to examine the movement of U away from the 13.5 m N fracture and into the bulk tuff host rock at scales of centimeters. Figure 7-5 shows four profiles: two at 0.5 m west of the deposit boundary (one North of the 13.5 m N fracture and one south of the 13.5 m N fracture); and two at 6.0 m west of the deposit boundary (one North and one South of the 13.5 m N fracture). The vein filling of the 13.5 m N fracture has a U content of about 1500 ppm at these locations. The 0.5 m and 6.0 m profiles show that within the first 2 cm from

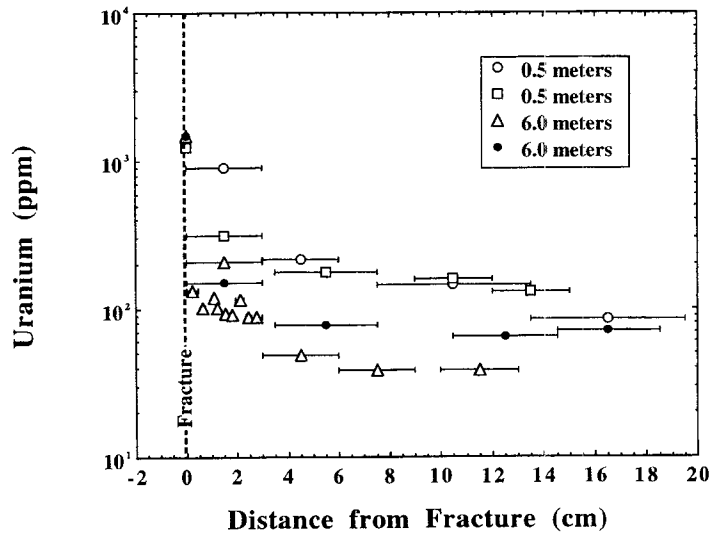


Figure 7-5. Centimeter-scale profiles of U content of bulk rock as a function of distance from the edge of the fracture. Different symbols represent the distances from the edge of the deposit along the East-West fracture at 13.5 m N. Different symbols for the same distance represent data points North and South of the East-West fracture. Error bars indicate the length of each sample; gaps between adjacent samples of a traverse indicate material not recovered during sampling.

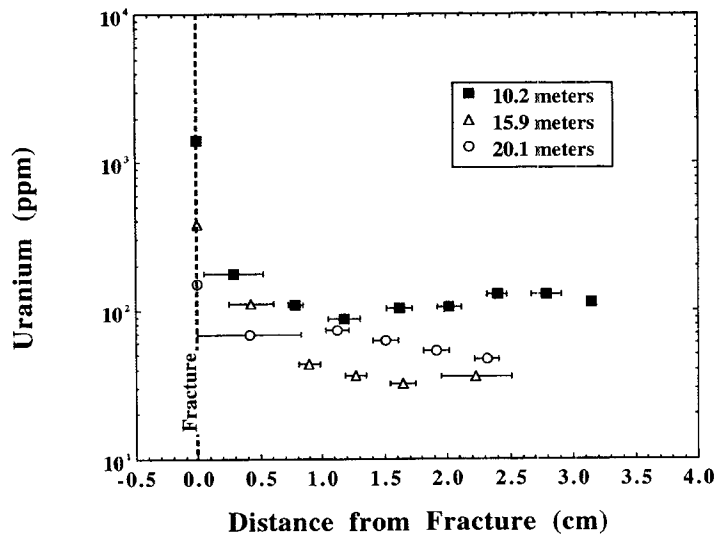


Figure 7-6. Centimeter-scale profiles of U content of bulk rock as a function of distance from the edge of the fracture. Different symbols represent the distances from the edge of the deposit along the East-West fracture at 13.5 m N. Different symbols for the same distance represent data points North and South of the East-West fracture. Error bars indicate the length of each sample; gaps between adjacent samples of a traverse indicate material not recovered during sampling.

the fracture the U content of the bulk rock drops steeply from the vein-filling concentration; concentrations within 2 cm of the fracture range from 900 to less than 100 ppm U. Beyond 2 cm perpendicular to the fracture, the U concentration profiles collected at 0.5 m from the deposit still trend downward though with a reduced gradient, whereas those collected at 6.0 m from the deposit tend to flatten toward values approximating a local background U content.

Figure 7-6 shows three profiles perpendicular to the 13.5 m N fracture at distances of 10.2, 15.9, and 20.1 m from the edge of the deposit. The U content of the fracture filling at these locations is lower (1400, 380, and 150 ppm U, respectively) than for the profiles nearer the deposit. Within the first 2 cm of the fracture, the U content ranges from 177 to 32 ppm U. These more detailed profiles show some irregularities in the U concentrations, which may be caused by inclusion in the sample of small microfractures or other heterogeneities in the tuff. Beyond 0.5 m from the edge of the deposit, the concentration gradients from the fracture filling to the first 2-cm interval decrease with distance from the deposit. This decrease in concentration gradient perpendicular to the fracture corresponds to the decrease in concentration of the fracture filling at each profile location. The profiles shown in Figures 7-5 and 7-6 are not well fit by the simple diffusion model used earlier to fit the data from the 2-m transect across the deposit boundary (Figure 7-2). This discrepancy may have been caused by many factors, including: chemical reactions along the transport paths, heterogeneities in porosity or other hydrologic differences within each transport domain, or formation of the extant U concentration profiles by advective processes or complex combinations of processes of which the measured profiles are the integrated result.

#### 7.2.1.2 Distribution of U at $\mu\text{m}$ Scales

Autoradiographic analyses were performed on samples from the Nopal I site to measure the spatial variation in U concentration perpendicular to microfractures (aperture widths of 100 to 230  $\mu\text{m}$ ) within the deposit. This small scale allows observation of U concentrations in portions of the tuff matrix free of heterogeneities such as other fractures or xenoliths. Selected polished thin sections were placed facedown on CR39 film. Corner locations were marked, and the samples were taped to the CR39 to preclude shifting. Exposure times for the samples varied according to their U contents; the time necessary to produce a measurable pattern was determined by trial and error. For example, sample NOPI-ECP-22.35/15.3-TS1 was exposed for 21 days, whereas NOPI-ECP-22.5/10.4-TS1 was exposed for 59 days. These exposure times are consistent with the field locations of the samples: NOPI-ECP-22.35/15.3-TS1 was collected from within the high U ring on Level +10, and NOPI-ECP-22.5/10.4-TS1 was collected from the outer edge of the low U area within the Level +10 deposit outcrop (Figure 7-1).

After exposure, the CR39 was etched in 6 N NaOH at 80 °C for 2 to 3 hr. The resulting CR39 film contains etched pits, each corresponding to an individual alpha particle impact. The distribution of these alpha impacts was mapped using standard point counting techniques and an ocular micrometer reticule. For each sample, 40 traverses perpendicular to the microfractures were counted, 20 on each side of the microfracture. Counting locations were chosen to avoid other microfractures, xenoliths, or other heterogeneities in the tuff matrix. Counting was extended away from each microfracture until a constant alpha impact density was reached. This constant value is interpreted to correspond to the local background U concentration in the tuff matrix.

For these analyses, it is assumed that there is a direct correspondence between alpha impacts per unit area, per unit time and U content of the sample. There are other alpha emitters in the system in addition to U, including  $^{232}\text{Th}$  and its daughters. However, the Th concentration in the bulk rock is less than 30 ppm (Leslie et al., 1993a), and U concentrations greatly exceed those of Th. Further support for

the correspondence of alpha impacts to U concentrations is provided by energy dispersive x-ray (EDX) analyses, including x-ray element mapping of polished thin sections for which autoradiographic analyses were also conducted. Uranium was the only alpha emitter observed in significant concentrations in these samples.

The resulting alpha distributions are illustrated in Figure 7-7. Each data point is the result of 40 individual measurements. Raw data for each sample were converted to alpha impacts per unit area per unit time to provide a common basis for comparison. Other samples, which will provide information on U transport perpendicular to microfractures in areas of the deposit with lower U concentrations have been partially counted. Additional exposures of those samples continue; data from those samples will be reported when measurements are complete. The portion of each curve farthest from its respective microfractures (e.g., from about 0.35 to 0.50 mm) was observed to flatten to an approximately constant value. This value is interpreted to represent the local background U concentration in the tuff adjacent to each microfracture. These background values were subtracted from the respective curves so that the remaining measurements are representative of U transported into the matrix from the microfractures of interest.

The microfractures contain relatively high concentrations of U, including U minerals [mainly uranophane,  $\text{Ca}(\text{UO}_2)_2\text{Si}_2\text{O}_7 \cdot 6\text{H}_2\text{O}$ ]. The U within the microfractures was transported by water moving through the deposit. From the measured concentration profiles, it is clear that a portion of the U (or its radioactive daughters) within the microfractures was transported perpendicular to the microfracture into the matrix of the host tuff.

Mineralogic and geometric comparisons of the sample profiles find them to be generally comparable but to have differences that may be significant for U transport. Optical microscopy indicates that the mineralogic composition of the matrix of both samples is similar (fine grained to cryptocrystalline quartz, sanidine, and kaolinite). The matrix of sample NOPI-ECP-22.35/15.3-TS1, however, contains significant iron oxide, which is absent from sample NOPI-ECP-22.5/10.4-TS1. Nominal apertures of the microfractures in the two samples are also different. The microfracture in sample NOPI-ECP-22.35/15.3-TS1 has an aperture of about 100  $\mu\text{m}$ , whereas sample NOPI-ECP-22.5/10.4-TS1 has a microfracture width of about 230  $\mu\text{m}$ . Both samples were collected on the Level +10 m surface of the Nopal I deposit from locations about 5 m apart. The higher alpha intensity close to the microfracture of sample NOPI-ECP-22.35/15.3-TS1 is consistent with its location in an area of the deposit that contains higher U concentrations than sample NOPI-ECP-22.5/10.4-TS1. General U abundances and alteration mineral distributions suggest that these locations may have had different alteration histories (Leslie et al., 1993b).

Given these differences (iron oxide content of the matrix, aperture widths, U concentration close to the microfractures, and apparent alteration histories), it is interesting that the maximum U transport distances are comparable; the maximum distance of U transport through the matrix appears to be 0.30 to 0.35 mm (distance measured perpendicular to the microfractures). This similarity of maximum transport distances may indicate insensitivity to the differences listed above or may result from a balance of competing effects produced by the differences. For example, sample NOPI-ECP-22.35/15.3-TS1 has the higher U source concentration, hence a stronger concentration gradient (which would tend to increase the U transport distance), but it also has a greater iron oxide content in the surrounding matrix [which would tend to restrict transport because U tends to be sorbed onto hydrated iron oxides, (Guthrie, 1991)]. The similarity in U profiles may also indicate that the measured U transport away from the microfractures is a product of earlier or later events than those that produced the difference in gross alteration histories for the two locations.

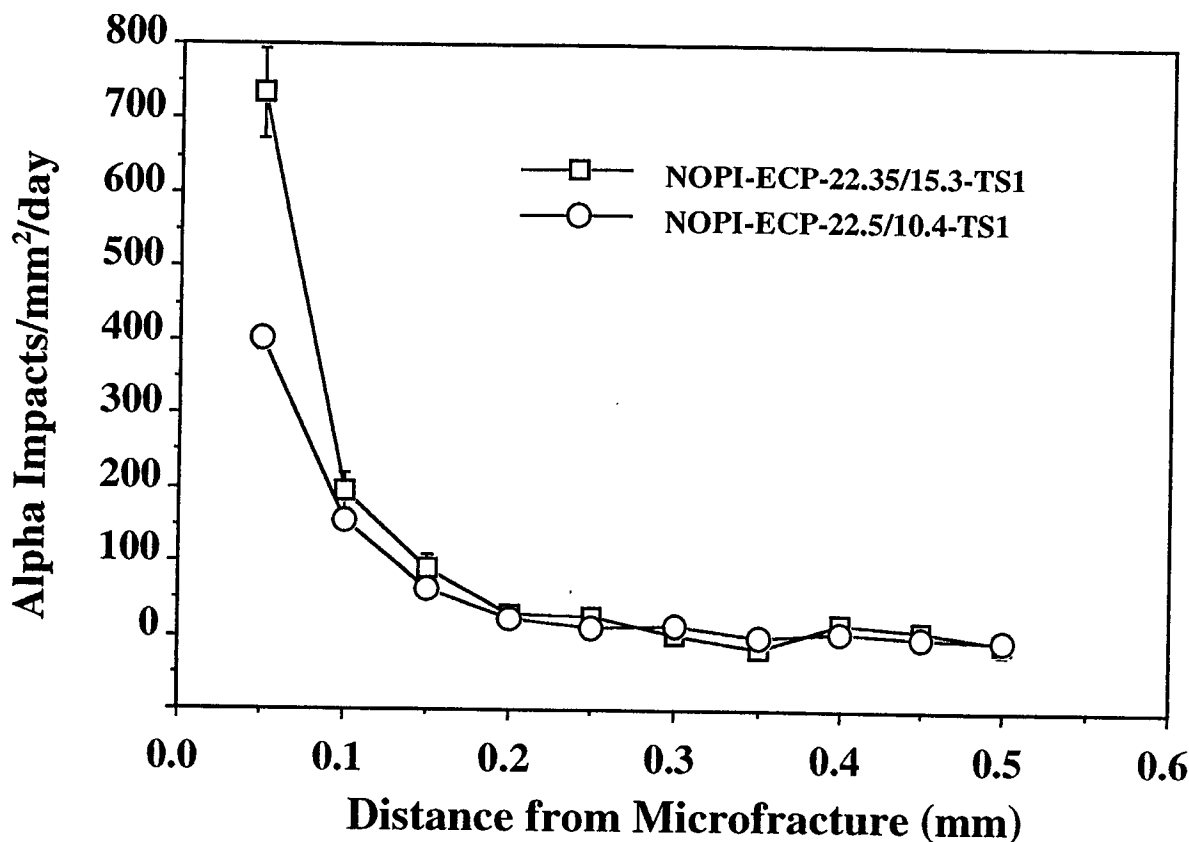


Figure 7-7. Plots of total alpha impacts per unit area, per unit time for samples NOPI-ECP-22.35/15.3-TS1 and NOPI-ECP-22.5/10.4-TS1 corrected for local background U concentration. Each data point on this plot represents 40 individual measurements. Error bars are one standard deviation uncertainties among those measurements.

The conditions under which U was transported out of the microfractures and into the surrounding tuff are not well known. The occurrence of  $U^{+6}$  within the microfracture (i.e., uranophane) suggests that U was transported out into the matrix by an oxidizing, aqueous solution that moved along the microfracture. It is not known if this solution was the same solution that precipitated the uranophane or some later solution. The solution that carried U out into the matrix may have been hot or cold, may have occurred in one event or many, may have moved the U relatively rapidly or over considerable time, and may have carried the U by advection or by diffusion. Future research will attempt to resolve these uncertainties.

It is likely that the measured profiles represent the net U transport into the matrix from more than one event. Recently (i.e., since tilting and relative uplift of the structural host block of the Nopal I deposit), the most likely mechanism for introduction of oxidizing fluids to transport U is episodic penetration of the host tuffs by meteoric water. If the observed U distributions are the result of diffusive transport of U through the matrix during such events, and if there is little effect on diffusion by chemical reactions or by differences in hydrologic properties within the domain, the U distributions should correspond closely to a diffusive distribution as described earlier.

Allowing the closest measurement point to the microfractures to approximate a constant concentration boundary condition, and making adjustments for the local U background concentrations as

described earlier, the U profiles measured for NOPI-ECP-22.35/15.3-TS1 and NOPI-ECP-22.5/10.4-TS1 can be modelled using the diffusion equation (Figures 7-8 and 7-9). Because the diffusion coefficient ( $D$ ), and the time over which the diffusion may have occurred ( $t$ ) are not known, the model can only be solved for the product,  $Dt$ . Sample NOPI-ECP-22.35/15.3-TS1 produces a  $Dt$  of  $1.5 \times 10^{-3} \text{ mm}^2$ , whereas sample NOPI-ECP-22.5/10.4-TS1 has a  $Dt$  of  $2.5 \times 10^{-3} \text{ mm}^2$ . This difference may result from disparities in the effective local diffusion coefficient, the time over which diffusion occurred, or other discrepancies between the samples.

## 7.2.2 Conclusions

Uranium transport at the Nopal I site has been strongly influenced by fractures, but clearly U-bearing solutions have not been restricted to fractures. Transport of U at the Nopal I site has been documented in a major, continuous fracture for a distance of about 45 m from the nearest edge of the original U deposit. Distribution of U within the fracture corresponds to distributions of fracture-filling minerals, suggesting that U was transported by advection away from the deposit. Uranium appears to have been deposited as the fluid interacted physically and/or chemically with the wall rocks of the fracture. Smaller scale transport of U through highly fractured tuff across the western boundary of the deposit has been measured along a 2 m transect. Uranium distribution across this domain drops abruptly from more than 5,000 ppm U to local background levels (about 50 ppm U). Uranium concentration profiles perpendicular to a large, continuous fracture have been measured. The U concentration gradient close to the fracture generally drops with distance from the deposit and appears to be related to the drop in the concentration of U in the vein filling with distance from the deposit. The concentrations of U perpendicular to uranophane-bearing microfractures have been measured by autoradiography. These profiles are the first at Nopal I in which U transport is examined through mineralogically and texturally homogeneous, otherwise unfractured tuff (i.e., other than the microfracture of interest).

These measurements establish that at Nopal I transport of U along a large, continuous fracture has achieved greater distances than U transport through tuff heavily fractured at a centimeter scale or U transport through homogeneous, unfractured tuff. Uranium transport distances along a major fracture are at least 25 times larger than U transport distances through generally fractured tuff. This disparity may reflect different durations and conditions of transport.

Some of the profiles reported here have relatively simple forms whereas others do not. Uranium concentration profiles across a 2-m transect through generally fractured tuff and those away from microfractures through otherwise unfractured tuff can be fit closely by a simple model assuming pure diffusion in a semi-infinite medium with a constant concentration boundary condition. This model could strictly be correct only if the U mobility occurred without effects on U transport by chemical reactions or variations in hydrologic properties within the domain. This relationship could be explained by a linear  $K_d$  sorption model. Alternatively, profiles measured away from a large fracture, through tuff with only a few hairline fractures do not have a simple form and cannot be fit by the diffusion model used to fit the other transects. This difference may be caused by mineralogic or textural heterogeneities in the sample domain, by chemical reactions between the U-bearing fluids and the tuff, by formation of the extant U profiles by advection rather than diffusion, or by combinations of these or other processes.

These measurements and interpretations are initial attempts to define conceptual models for mechanisms of U transport at Nopal I. The significance of these measurements for performance assessment modeling remains uncertain and requires definition of the conditions under which the U transport occurred.

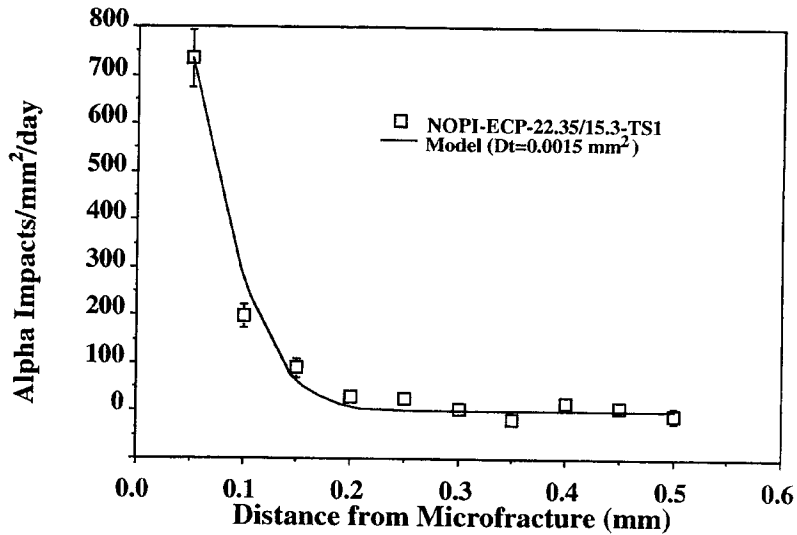


Figure 7-8. Plot of total alpha impacts per unit area, per unit time for sample NOPI-ECP-22.35/15.3-TS1 versus a model alpha impact intensity profile calculated assuming one-dimensional diffusion of U in a semi-infinite medium with a constant concentration boundary condition and a linear relationship between liquid and solid U concentrations. Error bars are one standard deviation uncertainties among those measurements.

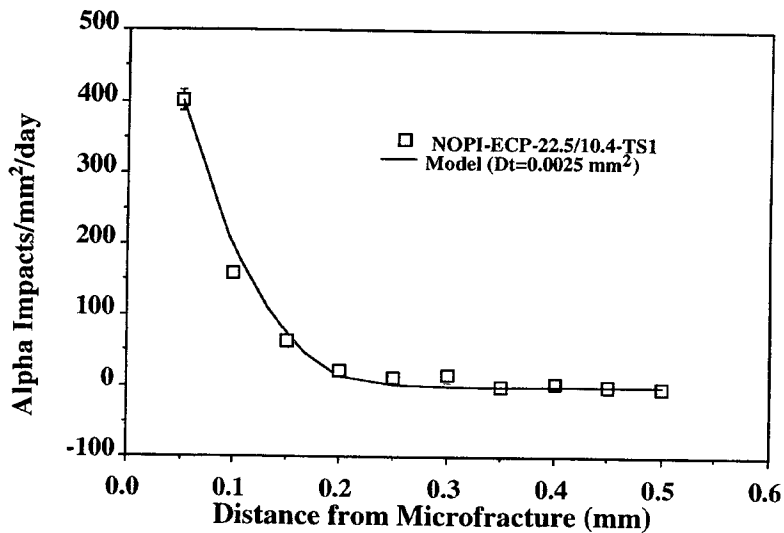


Figure 7-9. Plot of total alpha impacts per unit area, per unit time for sample NOPI-ECP-22.5/10.4-TS1 versus a model alpha impact intensity profile calculated assuming one-dimensional diffusion of U in a semi-infinite medium with a constant concentration boundary condition and a linear relationship between liquid and solid U concentrations. Error bars are one standard deviation uncertainties among those measurements.

### 7.3 ASSESSMENT OF PROGRESS TOWARDS MEETING PROJECT OBJECTIVES

Work at both the Nopal I site and at Akrotiri is proceeding well. Research results presented in this report and elsewhere (e.g., Percy et al., 1993) have begun to provide a realistic understanding of the utility and limitations of natural analog studies when employed to support a license application for a HLW repository. Specifically, fundamental data have been gathered and interpreted on U mineral characteristics, stabilities, and alteration sequences in a geologic environment comparable to that anticipated for the proposed Yucca Mountain repository. This information is required for development and evaluation of reasonable performance assessment models for radionuclide transport. For example, limiting rates for uraninite (a spent fuel analog mineral) alteration derived from constraints at the Nopal I site (Murphy and Percy, 1992) were used to support Iterative Performance Assessment (IPA) Phase 2 work<sup>2</sup>. Additionally, progress has been made in evaluation of the roles of fracture and matrix transport of U in a Yucca Mountain-like environment. This information has been used in the development of CDS 3.2.3.3 (mineral assemblages), 3.2.3.5 (geochemical processes), and 5.4 (engineered barrier system).

The Akrotiri project (first field examination June 1992) is necessarily less well developed at this point than the Nopal I work (first field examination February 1991). Because of limited access to the field site, work is likely to continue more slowly at Akrotiri than at Nopal I. Progress to date at Akrotiri includes definition of specific areas for analog study and completion of initial analyses that indicate the usefulness of further study.

The U.S. Department of Energy (DOE) has initiated analog research related to a Yucca Mountain repository. The DOE is studying water/rock interactions in hot springs in New Zealand in an attempt to validate the EQ3/6 computer code. In addition to these efforts, other DOE analog research is under consideration (e.g., Chapman et al., 1992). CNWRA work at Peña Blanca and at Akrotiri provides a strong base of experience from which to evaluate DOE analog studies. Results from the Center for Nuclear Waste Regulatory Analyses (CNWRA) analog research allows informed comment on selection of sites, site characterization techniques, applications of the analog data, and use of the analog data for assessment of aspects of a Yucca Mountain repository.

### 7.4 PLANS FOR NEXT REPORTING PERIOD

Field research anticipated during the next reporting period (July 1, 1993 to December 31, 1993) includes work at both the Peña Blanca site and at the Akrotiri site. Geologic mapping of the cleared area on Level +10 m of the Nopal I site at Peña Blanca is expected to be completed. Clearing, geologic mapping, gamma mapping, and sampling of a portion of Level 0 m spanning the outcrop of the deposit are all planned to be completed. Equipment has been acquired and will be constructed to attempt contact gamma mapping across the deposit outcrop on the 10-m vertical face between Levels 0 and +10 during the next report period. This map will provide a partial view of the third dimension of U transport at Nopal I. Field research at Akrotiri is planned to include detailed mapping and sampling of the Delta 3 site identified during the first field study, possible excavation of the locations identified to have anomalous

---

<sup>2</sup> Information provided orally by Richard Codell, NRC-NMSS, during a meeting in Washington in February 1993.

magnetic properties, geophysical mapping of the pre-eruptive land surface topography, and sampling of the Minoan tuff and the pre-Minoan Cape Riva tuff for petrologic and hydrologic studies.

Laboratory research during the next period is planned to include continued U-series, U content, and rare earth content measurements on samples from Nopal I. Optical microscopy, scanning electron microscopy, EDX analyses, and powder diffraction x-ray analyses are planned for both Nopal I samples and Akrotiri samples. Microthermometric studies of Nopal I veinlet minerals are planned to continue as are transmission electron microscopy studies of the composition and structure of Nopal I uraninite and autoradiographic analyses of U distributions.

## 7.5 REFERENCES

- Basham, I.R. 1981. Some applications of autoradiographs in textural analysis of uranium bearing samples - Discussion. *Economic Geology* 76: 974-977.
- Chapman, N., P.L. Cloke, J.-C. Petit, J.A.T. Smellie, and A.E.J. van Luik. 1992. *Applications of natural analogue studies to Yucca Mountain as a potential high level radioactive waste repository*. Las Vegas: Office of Civilian Radioactive Waste Management, USDOE.
- Cunningham, C.G., R.O. Rye, T.A. Steven, and H.H. Mehnert. 1984. Origins and exploration significance of replacement vein-type alunite deposits in the Marysvale volcanic field, West Central Utah. *Economic Geology* 79: 50-71.
- Dickson, B.L., and A.L. Herzceg. 1992. Deposition of trace elements and radionuclides in the spring zone, Lake Tyrrell, Victoria, Australia. *Chemical Geology* 96: 151-166.
- George-Aniel, B., J.L. Leroy, and B. Poty. 1991. Volcanogenic uranium mineralization in the Sierra Peña Blanca District, Chihuahua, Mexico: Three genetic models. *Economic Geology* 86: 233-248.
- Guthrie, V. 1991. Determination of recent  $^{238}\text{U}$ ,  $^{234}\text{U}$  and  $^{230}\text{Th}$  mobility in granitic rocks: Application of a natural analogue to the high-level waste repository environment. *Applied Geochemistry* 6:63-74.
- Hayba, D.O., P.M. Bethke, P. Heald, and N.K. Foley. 1985. Geologic, mineralogic, and geochemical characteristics of volcanic-hosted epithermal precious-metal deposits. *Geology and Geochemistry of Epithermal Systems*. B.R. Berger and P.M. Bethke, eds. El Paso, TX: The Economic Geology Publishing Company: 129-167.
- Ildefonse, P., J.-P. Muller, B. Clozel, and G. Calas. 1990. Study of two alteration systems as natural analogues for radionuclide release and migration. *Engineering Geology* 29: 413-439.
- Leslie, B.W., E.C. Percy, and J.D. Prikryl. 1993a. Geochemical Natural Analogs. *NRC High-Level Radioactive Waste Research at CNWRA January 1 through June 30, 1992*. W.C.Patrick, ed. NUREG/CR-5817, CNWRA 92-01S. San Antonio, TX: Center for Nuclear Waste Regulatory Analyses.

- Leslie, B.W., E.C. Percy, and J.D. Prikryl. 1993b. Oxidative alteration of uraninite under hydrologically unsaturated conditions at Peña Blanca, Chihuahua, Mexico: Contaminant transport and source term constraints for the proposed repository at Yucca Mountain, Nevada. *Symposium Procs. 294 Scientific Basis for Nuclear Waste Management XVI*. C.G. Interrante and R.T. Pabalan, eds. Pittsburgh, PA: Materials Research Society: 505-512.
- Murphy, W.M., and E.C. Percy. 1992. Source-term constraints for the proposed repository at Yucca Mountain, Nevada, derived from the natural analog at Peña Blanca, Mexico. *Scientific Basis for Nuclear Waste Management*. C.G. Sombret, ed. Pittsburgh, PA: Materials Research Society: 521-527.
- Neretnieks, I. 1980. Diffusion in the rock matrix: An important factor in radionuclide retardation? *Journal of Geophysical Research* 85: 4379-4397.
- Nordstrom, D.K. 1982. Aqueous pyrite oxidation and the consequent formation of secondary iron minerals. *Acid Sulfate Weathering*. J.A. Kittrick et al., eds. Soil Science Society of America Special Publication 10: 37-56.
- Percy, E.C., and W.M. Murphy. 1990. Geochemical Natural Analogs: *Report on Research Activities for Calendar Year 1990*. CNWRA 90-01A, NUREG/CR-5817. W.C. Patrick, ed. San Antonio, TX: Center for Nuclear Waste Regulatory Analyses: 7-1 to 7-7.
- Percy, E.C., and W.M. Murphy. 1991a. Geochemical Natural Analogs: *Report on Research Activities for the Quarter January 1 through March 31, 1991*. W.C. Patrick, ed. CNWRA 91-01Q. San Antonio, TX: Center Nuclear Waste Regulatory Analyses: 7-1 to 7.7.
- Percy, E.C., and W.M. Murphy. 1991b. Geochemical Natural Analogs: *Report on Research Activities for the Quarter April 1 through June 30, 1991*. W.C. Patrick, ed. CNWRA 91-02Q. San Antonio, TX: Center Nuclear Waste Regulatory Analyses: 7-1 to 7-7.
- Percy, E.C., and W.M. Murphy. 1991c. Geochemical Natural Analogs: *Report on Research Activities for the Quarter July 1 through September 30, 1991*. W.C. Patrick, ed. CNWRA 91-03Q. San Antonio, TX: Center Nuclear Waste Regulatory Analyses: 7-1 to 7-9.
- Percy, E.C., and W.M. Murphy. 1991d. *Geochemical Natural Analogs Literature Review*. CNWRA 90-008. San Antonio, TX: Center Nuclear Waste Regulatory Analyses.
- Percy, E.C., W.M. Murphy, R.T. Green, B.W. Leslie, and J.D. Prikryl. 1991. Geochemical Natural Analogs: *Report on Research Activities for Calendar Year 1991*. W.C. Patrick, ed. CNWRA 91-01A. San Antonio, TX: Center Nuclear Waste Regulatory Analyses: 7-1 to 7-32.
- Percy, E.C., and W.M. Murphy. 1992. *Site Selection and Workplan Report for the Geochemical Natural Analog Research Project*. CNWRA 92-014. San Antonio, TX: Center Nuclear Waste Regulatory Analyses.

- Pearcy, E.C., B.W. Leslie, W.M. Murphy, and R.T. Green. 1992. *Geochemical Natural Analogs. NRC High-Level Radioactive Waste Research at CNWRA July 1 through December 31, 1992*. W.C. Patrick, ed. CNWRA 92-02S. San Antonio, TX: Center Nuclear Waste Regulatory Analyses: 7-1 to 7-27.
- Pearcy, E.C., J.D. Prikryl, W.M. Murphy, and B.W. Leslie. 1993. *Uranium Mineralogy of the Nopal I Natural Analog Site, Chihuahua, Mexico*. CNWRA 93-012. San Antonio, TX: Center Nuclear Waste Regulatory Analyses.
- Turner, D.R. 1991. *Sorption Modeling for High-Level Waste Performance Assessment: A Literature Review*. CNWRA 91-011. San Antonio, TX: Center for Nuclear Waste Regulatory Analyses.
- U.S. Nuclear Regulatory Commission. 1987. *Disposal of High-Level Radioactive Wastes in Geologic Repositories*. Title 10, Energy, Part 60 [10 CFR 60.21(c)(1)(ii)(F)]. Washington, DC: U.S. Government Printing Office.
- U.S. Environmental Protection Agency. 1989. *Environmental Radiation Protection Standards for Management and Disposal of Spent Nuclear fuel, High-Level and Transuranic Radioactive Wastes*. Title 40, Protection of Environment, Part 191 (40 CFR 191.13). Washington DC: U.S. Government Printing Office.
- van Brakel, J., and P.M. Heertjes. 1974. Analysis of diffusion in macroporous media in terms of a porosity, a tortuosity, and a constrictivity factor. *International Journal of Heat and Mass Transfer* 17: 1093-1103.

# 8 SORPTION MODELING FOR HIGH-LEVEL WASTE PERFORMANCE ASSESSMENT

*by Roberto T. Pabalan and David R. Turner*

*Investigators: Roberto T. Pabalan, David R. Turner, Bret W. Leslie, James D. Prikryl, Paula Muller, Todd Dietrich, and Stephen Sassman (CNWRA)*

*NRC Project Officer: George F. Birchard*

## 8.1 TECHNICAL OBJECTIVES

A fundamental concern in evaluating the suitability of Yucca Mountain, Nevada, as a repository for high-level nuclear wastes (HLW) is the possibility of radionuclide migration from the repository to the accessible environment as dissolved constituents in groundwaters. An important mechanism for attenuating radionuclide migration is sorption of radionuclides on minerals encountered along the flow paths. Sorption is specifically referred to in 10 CFR 60.122(b) as a favorable geochemical condition that will tend to inhibit radionuclide migration and "favorably affect the ability of the geologic repository to isolate the waste." Conversely, geochemical processes that "would reduce sorption of radionuclides" are listed [10 CFR 60.122(c)(8)] as potentially adverse conditions that could reduce the effectiveness of the natural barrier system.

To support the U.S. Nuclear Regulatory Commission (NRC) HLW program, the Center for Nuclear Waste Regulatory Analyses (CNWRA) is conducting research activities under the Sorption Modeling for HLW Performance Assessment Research Project. The broad objectives are to develop sufficient understanding of radionuclide transport issues so that timely precicensing guidance can be provided to the U.S. Department of Energy (DOE) and a sound basis can be available for evaluating the DOE license application. The results will be used to support the NRC License Application Review Plan (LARP), particularly Sections 3.2.3.2 and 3.2.3.5 pertaining to favorable and potentially adverse geochemical conditions and processes at a potential repository site, and Section 3.4, which addresses the effectiveness of natural barriers against the release of radioactive material to the environment. Laboratory and modeling studies of radionuclide transport, sorption, and retardation, which are central to the Sorption Research Project, will provide an independent basis for addressing Key Technical Uncertainties (KTU) identified during development of Compliance Determination Strategies (CDS), which are an integral part of the LARP. Specifically, a KTU regarding parametric representation of retardation processes will be addressed by this research project. This KTU is relevant to the regulatory requirement topic (RRT) regarding geochemical conditions that favor inhibition of radionuclide migration, i.e., those that is: (i) promote precipitation or sorption of radionuclides; (ii) inhibit the formation of particulates, colloids, and inorganic and organic complexes that increase the mobility of radionuclides; or (iii) inhibit the transport of radionuclides by particulates, colloids, and complexes. This KTU is also related to the RRT on potentially adverse conditions concerning geochemical processes that would reduce sorption of radionuclides. Compliance Determination Methods (CDM) for evaluating compliance with the regulatory requirements associated with the RRT will be developed using data and models, including those arising from this research project.

Results arising from this project will be integrated with those from other CNWRA activities. For example, data on uranium sorption will be used in interpreting data on uranium distribution and migration at the Peña Blanca field site of the Geochemical Natural Analog Research Project (Chapter 7),

as well as in developing conceptual models for radionuclide transport/retardation in near-field and far-field environments related to the Performance Assessment Research Project (Chapter 9) and the Iterative Performance Assessment (IPA) Phase 3. Results of activities undertaken during the first half of 1993 are discussed in the following.

## 8.2 TASK 2 — SORPTION MODELING

### 8.2.1 Introduction

Many studies have been conducted during the past several decades to examine the complex sorption behavior of toxic elements such as  $Zn^{2+}$ ,  $Cd^{2+}$ ,  $Pb^{2+}$ , and  $Hg^{2+}$  on a number of different mineral surfaces. Given the increasing concern with radioactive waste, similar experiments have begun to be performed for key radionuclides, with the results only recently reaching the peer-reviewed literature. Because of the acknowledged limitations of empirical methods (Kent et al., 1988; Davis and Kent, 1990), mechanistic modeling approaches to data interpretation are necessary to take full advantage of this research (Bradbury and Baeyens, 1992).

Surface complexation models (SCM) represent one type of mechanistic approach that has been used to interpret contaminant sorption on oxide surfaces over a wide range of chemical conditions (e.g., pH, ionic strength, total concentration of adsorbate). Three commonly used types of SCM include the Constant Capacitance (CCM), Diffuse-Layer (DLM), and Triple-Layer (TLM) models. These models rely on a set of model-dependent parameters to represent the acid-base and electrostatic behavior of the mineral surface. Unfortunately, SCM have tended to be applied in an *ad hoc* fashion, adjusting a number of different model parameters to fit a specific data set. This has made uniform application and comparison of model results difficult, if not impossible (Westall and Hohl, 1980; Pabalan and Turner, 1993).

One recently advocated approach is the development of a standard set of parameters that is uniformly applied in all systems (Davis and Kent, 1990; Hayes et al., 1991; Bradbury and Baeyens, 1992; Mesuere, 1992). While this approach may not truly represent the exact physical, electrostatic, and chemical processes operating at the mineral-water interface, it does limit the number of adjustable parameters and serves to establish a baseline that will allow future direct comparison of modeling results and evaluation of model performance. In addition, such an approach is desirable from the point of view of developing simple, flexible sorption models with internally consistent databases for performance assessment.

To date, this type of uniform approach has largely been limited to one model and one surface. Dzombak and Morel (1990) present an extensive tabulation, evaluation, and application of the DLM to heavy and transition metal sorption on ferrihydrite [ $Fe(OH)_3$ ]. Based on the literature available on ferrihydrite, Dzombak and Morel (1990) established a constant value for site density ( $N_S$  in sites/nm<sup>2</sup>). This value was then applied to available potentiometric titration data to derive a single standard set of DLM equilibrium constants for the reactions that represent the acid-base chemistry of the ferrihydrite surface. These parameters were used in turn to interpret available sorption data for a number of contaminant elements. Hayes et al. (1990; 1991) performed a series of sensitivity analyses for goethite,  $\alpha$ - $Al_2O_3$ , and rutile to determine the relative importance of different parameters in determining constants for the DLM, CCM, and TLM surface complexation models.

Radionuclide sorption data are available for a number of minerals (e.g.,  $\text{SiO}_2$ ) that have not received the same amount of attention. Therefore, to take advantage of the data available for different surfaces and to compare different SCM, the approaches of Dzombak and Morel (1990) and Hayes et al. (1990; 1991) need to be extended to provide the necessary model constants for different minerals. This is also important for common rock-forming minerals such as feldspar and kaolinite where it may be possible to model the sorption characteristics assuming a combination of different sites such as aluminol ( $\text{AlOH}^\circ$ ) and silanol ( $\text{SiOH}^\circ$ ) (Benjamin and Leckie, 1981; Kent et al., 1988; Siegel et al., 1992).

Although the ultimate goal of this research is to use a uniform approach to obtain the necessary equilibrium (or binding) constants for sorption reactions that involve the radionuclides themselves, a more basic first step is necessary. This involves deriving acidity constants that describe the acid-base chemistry of the mineral surface that is responsible for generating the sorption sites. Therefore, to demonstrate the feasibility of a uniform approach, the objectives of research presented in this report were to obtain potentiometric titration data from readily available peer-reviewed literature for different relevant minerals and to interpret these data following, where possible, the techniques developed by Dzombak and Morel (1990) and Hayes et al. (1990; 1991). In this fashion, a consistent set of constants that characterize the acid-base behavior of each mineral was developed for each of the three surface complexation models listed above. These parameters are necessary to construct the mass balance/mass action equations used by geochemical sorption/speciation programs such as MINTQA2 (Allison et al., 1991) and HYDRAQL (Papelis et al., 1988). Once these parameters are in place, it will be possible to move to the next step of obtaining binding constants for the sorption of radionuclides.

### 8.2.2 Potentiometric Titration Data

Potentiometric titration is commonly used to determine the acid-base behavior of a surface. Procedures are described in detail elsewhere (e.g., Dzombak and Morel, 1990), but titration generally involves the incremental addition of known amounts of acid or base to a solid suspension of the mineral of interest, while monitoring changes in solution pH. The ionic strength ( $I$ ) of the suspension is adjusted to a desired value using a supporting background electrolyte such as  $\text{NaNO}_3$ ,  $\text{NaClO}_4$ , or  $\text{KCl}$ ; the experiment is performed under closed atmosphere conditions, purging the solution with an inert gas such as nitrogen or argon to eliminate  $\text{CO}_2$  and the formation of carbonate and bicarbonate species that would otherwise contaminate the surface. Changes in pH between acid/base additions are monitored potentiometrically; pH equilibration is generally assumed when the pH drift falls below some threshold value (pH units/min). Ideally, the time between additions is kept short (on the order of minutes) to focus on surface protonation/deprotonation. Longer times allow proton exchange with the interior of the solid or dissolution, and result in continuous pH drift and hysteresis in the titration curves (Dzombak and Morel, 1990).

Potentiometric titration data and point-of-zero charge data were identified through several compilations (e.g., James and Parks, 1982; Smith and Jenne, 1988; Kent et al., 1988) and a search of the peer-reviewed literature. Several data sets identified were not used (e.g., Breeuwsma and Lyklema, 1973) due to uncertainty regarding experimental conditions that were necessary for data interpretation. This was particularly true for solid concentrations ( $c_s$ ) and specific surface area ( $A_{sp}$ ), which were necessary to convert charge data to total  $\text{H}^+$  but not always reported. The sources for potentiometric titration data used in this study are listed in Table 8-1. In most cases, the original data were obtained, although in some cases, data compiled in survey reports were used [e.g., ferrihydrite titration data reported in Dzombak and Morel (1990)]. Generally, data were presented in graphical form only; an

Table 8-1. Mineral properties used in interpreting potentiometric titration (25 °C) with data sources

Mineral	A <sub>SP</sub> (m <sup>2</sup> /g)	pH <sub>ZPC</sub> (±1 σ)	Reference(s)
Goethite	50	8.0±0.8 (n=11)	Hsi and Langmuir (1985); Hayes et al. (1990); Yates and Healy (1975); Balistrieri and Murray (1981); Mesuere (1992)
Ferrihydrite	600 <sup>(a)</sup>	8.0±0.1 (n=9)	Hsi and Langmuir (1985); Davis (1977); Swallow (1978); Yates (1975)
Magnetite	5	6.7±0.1 (n=2)	Regazzoni et al. (1983)
amorphous-SiO <sub>2</sub>	175	2.8±0.3 (n=3)	Abendroth (1970); Bolt (1957)
α-Al <sub>2</sub> O <sub>3</sub>	12	8.9±0.4 (n=4)	Hayes et al. (1990)
γ-Al <sub>2</sub> O <sub>3</sub>	120	8.4±0.3 (n=3)	Huang and Stumm (1972); Sprycha (1989)
δ-MnO <sub>2</sub>	270 <sup>(b)</sup>	1.9±0.5 (n=7)	Murray (1974); Balistrieri and Murray (1982); Catts and Langmuir (1986)
TiO <sub>2</sub> (anatase)	125	6.1±0.2 (n=2)	Sprycha (1984); Berube and de Bruyn (1968)
TiO <sub>2</sub> (rutile)	30	5.9±0.3 (n=4)	Berube and de Bruyn (1968); Yates (1975)

(a) Value recommended in Dzombak and Morel (1990).

(b) Although the same methods were used, Balistrieri and Murray (1983) report 74 m<sup>2</sup>/g, Murray (1974) reports 263 m<sup>2</sup>/g, and Catts and Langmuir (1986) report 290 m<sup>2</sup>/g.

electronic digitizing tablet linked to a personal computer was used to convert graphical data to numerical values in the appropriate coordinates [typically pH versus surface charge (μC/cm<sup>2</sup>)]. Surface charge data were then converted to total H<sup>+</sup> with a spreadsheet application based on procedures described in Dzombak (1985).

### 8.2.3 Data Interpretation

The strengths and limitations of surface complexation theory and models are described in detail elsewhere (Westall and Hohl, 1980; Hayes et al., 1990; Pabalan and Turner, 1992 a,b) and will only be covered briefly here. All SCM assume a mineral surface comprised of a finite number of amphoteric sites (XOH<sup>0</sup>) that can become positively charged (XOH<sub>2</sub><sup>+</sup>) by sorption of H<sup>+</sup>, or negatively charged (XO<sup>-</sup>) through desorption of a proton (Table 8-2). If the equilibrium (or acidity) constants K<sub>+</sub> and K<sub>-</sub>, and site concentrations for these reactions can be determined, sorption of protons can be modeled as an equilibrium process using the mass balance/mass action approach common to many geochemical programs.

Table 8-2. Summary of surface complexation model parameters (modified from Hayes et al., 1991)

MODEL EQUATION/REACTION (MASS ACTION)	CHARGE/POTENTIAL RELATIONSHIPS (25 °C)	MODEL-SPECIFIC ADJUSTABLE PARAMETERS (a)
<p><u>1. Diffuse-Layer (DLM):</u></p> $\text{XOH}^\circ + \text{H}^+ = \text{XOH}_2^+ \quad (K_+)$ $\text{XOH}^\circ = \text{XO}^- + \text{H}^+ \quad (K_-)$ $\text{XOH}^\circ + \text{M}^+ = \text{XO} \cdot \text{M}^\circ + \text{H}^+ \quad (K_{M^+})$	$-\sigma_o = \sigma_d = -0.1174\sqrt{I} \sinh\left(\frac{zF\Psi_d}{2RT}\right)$ $\Psi_o = \Psi_d$	$K_+, K_-, K_{M^+}$
<p><u>2. Constant Capacitance (CCM):</u></p> <p>Same as DLM</p>	$\sigma_o = C_1\Psi_d$	$K_+, K_-, C_1, K_{M^+}$
<p><u>3. Triple-Layer (TLM):</u></p> $\text{XOH}^\circ + \text{H}^+ = \text{XOH}_2^+ \quad (K_+)$ $\text{XOH}^\circ = \text{XO}^- + \text{H}^+ \quad (K_-)$ $\text{XOH}^\circ + \text{C}^+ = \text{XO} \cdot \text{C}^\circ + \text{H}^+ \quad (K_{\text{Cation}})$ $\text{XOH}^\circ + \text{A}^- + \text{H}^+ = \text{XOH}_2 \cdot \text{A}^\circ \quad (K_{\text{Anion}})$ $\text{XOH}^\circ + \text{M}^+ = \text{XO} \cdot \text{M}^\circ + \text{H}^+ \quad (K_{M^+})$	$-\sigma_o = \sigma_d = -0.1174 \sqrt{I} \sinh\left(\frac{zF\Psi_d}{2RT}\right)$ $\sigma_o = (\Psi_o - \Psi_\beta) C_1$ $\sigma_o + \sigma_\beta = -\sigma_d = (\Psi_\beta - \Psi_d) C_2$	$K_+, K_-, K_{\text{Cation}}, K_{\text{Anion}}, C_1, C_2, K_{M^+}$

(a) Adjustable parameters are:  $K_+$ ,  $K_-$  = Protonation and Deprotonation equilibrium constants, respectively;  $K_{M^+}$  = Intrinsic equilibrium constant for sorption of contaminant  $M^+$ ;  $K_{\text{Cation}}$ ,  $K_{\text{Anion}}$  = Intrinsic equilibrium constant for cations and anions in background electrolyte, respectively;  $C_1$ ,  $C_2$  = Capacitance for inner and outer electrostatic layers (Farads/m<sup>2</sup>). Parameters not specific to each model include:  $N_s$  = surface site density (sites/nm<sup>2</sup>).

The data selected for this study covered a range in ionic strength from 0.0004 to 1 M. In constructing the geochemical equilibrium problem, the mass action was corrected for ionic strength effects on activity using the Davies Equation (e.g., Dzombak and Morel, 1990). For reactions involving a surface species such as  $XOH_2^+$ , an additional correction is added for the electrostatic effects of the charged surface using the exponential Boltzmann relationship

$$a_{i,s} = a_i \left[ e^{\frac{-\Psi_j F}{RT}} \right]^z \quad (8-1)$$

where  $a_{i,s}$  is the activity of a given ion  $i$  in the aqueous phase near the charged surface,  $a_i$  is the activity in the bulk solution,  $e^{-\Psi_j F/RT}$  is the Boltzmann factor,  $\Psi_j$  is electrostatic potential of the  $J$ th layer (volt),  $z$  is the valence of the ion,  $F$  and  $R$  are the Faraday (J/volt equiv) and ideal gas (J/K mole) constants, respectively, and  $T$  is absolute temperature (K). The relationship between surface charge as derived from the titration data and potential at the surface differs among SCM models (Westall and Hohl, 1980).

Surface complexation models differ in how the mineral/water interface is represented. For this reason, different adjustable parameters are necessary for each model (Table 8-2). Drawing on the recommendations of several recent studies (Hayes et al., 1990; Dzombak and Morel, 1990; Davis and Kent, 1990), it was attempted in this study to fix several of these parameters *a priori* to minimize the number of fitted parameters and to establish a baseline to facilitate comparison between models.

To consider mass balance constraints on site availability, all SCM require a single value for  $A_{SP}$ . However, surface area, generally determined in titration experiments by BET/ $N_2$  techniques, is subject to uncertainty and can vary from study to study, depending on grain size, how the mineral was prepared, and how long the mineral was allowed to age. Since one objective of this research is the development of a simplified uniform approach to modeling titration data, a single generalized  $A_{SP}$  has been assumed for each mineral and applied consistently for each SCM considered (Table 8-1). This maintains the distinction in  $A_{SP}$  between minerals, and in most cases the use of similar mineral preparation techniques between studies provides some support for this assumption.

In the case of magnetite and  $\alpha$ - $Al_2O_3$ , only one data set was modeled, and the reported  $A_{SP}$ , rounded to the nearest whole number, was used. In most cases where several studies were interpreted, each study reported following the same mineral preparation procedures. For example, each of the five goethite studies listed in Table 8-1 reported using the methods of Atkinson et al. (1967; 1968; 1972), leading to relatively close agreement in  $A_{SP}$  (48 to 66  $m^2/g$ ). In other cases, however, such as  $\delta$ - $MnO_2$ , surface area measurements differ markedly, even though identical methods of synthesis were reported. Other surface area measurements for  $\delta$ - $MnO_2$  support assuming a higher surface area (270  $m^2/g$ ). Finally, in some cases (e.g.,  $\gamma$ - $Al_2O_3$ , am- $SiO_2$ ), commercial grade materials were used and reported surface area measurements agreed closely.

### 8.2.3.1 Fixed Model Parameters

Site Density ( $N_S$ ). Based on a sensitivity analysis of titration data using the CCM, DLM, and TLM models, Hayes et al. (1990) suggested that model results were relatively insensitive to differences in site density and proposed a constant site density of 10 sites/ $nm^2$ . The study of Mesuere (1992), however, suggested that for a broader pH range, goethite titration data was sensitive to  $N_S$  and better modeled assuming a small site density of 1.5 sites/ $nm^2$  for the DLM and 5 sites/ $nm^2$  for the TLM. Based

on a literature survey, Dzombak and Morel (1990) recommended a total site density of 2.31 sites/nm<sup>2</sup> for ferrihydrite. Since the goal of this study was a uniform application rather than taking a best fit approach, the recommendation of Davis and Kent (1990) was followed and the site density of Dzombak and Morel (1990) has been assumed for all minerals. Because there does not appear to be a physical reason for assuming different site densities for different models, the same site density has also been maintained for the different SCM.

Also implicit in the approach taken here is the equivalence of all sites. Other studies (Benjamin and Leckie, 1981; Dzombak and Morel, 1990) have employed heterogeneous sites to explain observed sorption behavior. Since simplification is one desired goal of this study, and because of a lack of data on site heterogeneities for many of the minerals considered here, a single site type is assumed.

Capacitances. All three models require values for  $N_S$  and  $A_{SP}$  to construct the mass balance relationships. In addition, the CCM and TLM require capacitances to describe the charge-potential relationships across one or more model-defined planes at the mineral/water interface. The CCM requires a single value. Based on the sensitivity analysis of Hayes et al. (1990), this has been set at 1.0 F/m<sup>2</sup>. The TLM requires capacitances for its two inner layers. By convention (Hayes et al., 1990), the outer  $\beta$ -layer capacitance ( $C_2$ ) is set at 0.2 F/m<sup>2</sup>. As with the CCM, the sensitivity analysis of Hayes et al. (1990) has been used to set the inner  $\alpha$ -layer capacitance at 0.8 F/m<sup>2</sup>. The DLM does not require capacitance values.

### 8.2.3.2 Parameter Estimation Using FITEQL

Several studies advocating a uniform approach to SCM applications (Dzombak and Morel, 1990; Hayes et al., 1990; Mesuere, 1992) have used Version 2.0 of the FITEQL parameter estimation code (Westall, 1982) to determine acidity constants ( $K_+$  and  $K_-$ ) and cation/anion binding constants ( $K_{\text{Cation}}$  and  $K_{\text{Anion}}$ ). This study also used FITEQL to interpret the titration data. For the DLM and CCM models, values were determined for  $\text{Log } K_+$  and  $\text{Log } K_-$  simultaneously. However, unlike the single layer DLM and CCM, the TLM allows for sorption of the background electrolyte ( $\text{Na}^+$  and  $\text{NO}_3^-$  for example). This leads to four equilibrium constants,  $K_+$ ,  $K_-$ ,  $K_{\text{Cation}}$ , and  $K_{\text{Anion}}$  to describe the interface. While FITEQL can, in theory, fit these four constants simultaneously, in practice the code does not converge unless two of these can be specified. The relationship between  $K_+$ ,  $K_-$ , and  $\text{pH}_{\text{ZPC}}$  can be expressed

$$(\text{Log } K_+ - \text{Log } K_-)/2 = \text{pH}_{\text{ZPC}} \quad (8-2)$$

and the sensitivity analysis of Hayes et al. (1990) recommended a value for  $\Delta\text{pK}$  such that

$$\Delta\text{pK} = |\text{Log } K_+ + \text{Log } K_-| = 4.0 \quad (8-3)$$

In this fashion, if  $\text{pH}_{\text{ZPC}}$  is known for a given mineral, values can be set for the TLM acidity constants and FITEQL can be used to solve for  $K_{\text{Cation}}$  and  $K_{\text{Anion}}$ . Turning again to the peer-reviewed literature, values for  $\text{pH}_{\text{ZPC}}$  were obtained for the different minerals considered. In general, the differences between values reported for a given mineral were small, and a mean value was chosen for  $\text{pH}_{\text{ZPC}}$ . The values used are reported in Table 8-1. It should also be noted that  $\delta\text{-MnO}_2$  and amorphous- $\text{SiO}_2$  have such low  $\text{pH}_{\text{ZPC}}$  that most of the available titration data is at  $\text{pH} > \text{pH}_{\text{ZPC}}$ . In this range, only deprotonation and adsorption of cations are assumed to be significant (Kent et al., 1988), and the FITEQL runs were set up to determine equilibrium constants ( $K_-$  and  $K_{\text{Cation}}$ ) for only these reactions.

Output from FITEQL includes a "goodness-of-fit" parameter and standard deviations for the estimated parameters (Westall, 1982). These values are determined based on the experimental error specified in the optimization run and the size of the data set. For example, because the chemical system is not as well constrained, goodness-of-fit and parameter uncertainty generally deteriorate for smaller data sets (Dzombak and Morel, 1990). In most cases, error is not reported for potentiometric titration data, and the approach of Hayes et al. (1990) has been adopted with only slight modification. Relative error has been assumed to be  $\pm 1$  percent (0.01), while absolute error has been assumed to be  $1 \times 10^{-8}$  M instead of the  $2 \times 10^{-8}$  M used by Hayes et al. (1990). Their sensitivity analyses indicated that the dissimilarities in acidity constants due to differences in experimental error are negligible, but the calculated uncertainty in the estimated values increases with increasing error. The goodness-of-fit parameter generated by FITEQL can be used as a measure of how well the data are described by the assumed chemical and adsorption models. In a strict sense, however, goodness-of-fit cannot be compared directly unless the experimental error limits imposed on the problem are known.

## 8.2.4 Discussion of Results

After interpretation of the data, the chief objective of this parameter estimation exercise was to combine the results for separate potentiometric titration data sets into a single set of weighted values for the desired SCM parameters ( $K_+$ ,  $K_-$ ,  $K_{\text{Cation}}$ , and  $K_{\text{Anion}}$ ). This involved combining experiments performed at different ionic strengths using different background electrolytes. In a strict sense, this approach is not valid for the CCM. This is because there is no ionic strength correction in the charge-potential relationship (Table 8-2) and, in theory, the capacitance used should be adjusted for each ionic strength (Hayes et al., 1990; 1991). By arbitrarily fixing the capacitance used in the model at a single value, the calculated equilibrium constants are adjusted by FITEQL to fit the data. The resultant values are therefore valid only for the ionic strength at which the data were measured. Also implicit in this approach is the assumption that different background electrolytes behave in an identical manner and have no effect on the modeling results. While this is probably reasonable for the simple CCM and DLM models that assume an inert background electrolyte, it is likely to be an oversimplification in the TLM.

The values resulting from the FITEQL analysis were tabulated for each study at each ionic strength considered. In some cases, the numerical scheme did not converge. For the DLM and TLM, the method of Dzombak and Morel (1990) was used to obtain convergence for one of the values. This involves fixing one of the constants using values obtained from runs at other ionic strengths in the data set, and rerunning the input file to fit the remaining parameter. In almost all cases, convergence was achieved quickly. Because of its lack of ionic strength dependence, however, this was not done for the CCM. For some data sets, however, plotting the Log of the acidity constants ( $\text{Log } K_+$  and  $\text{Log } K_-$ ) versus the base-10 logarithm of the ionic strength resulted in a linear relationship. The correlation was generally strong ( $r^2 > 0.9$ ) and could be used to extrapolate acidity constants for ionic strengths outside of the range of the experiments.

Dzombak and Morel (1990) proposed a scheme for deriving a single set of acidity constants for the DLM. This approach relies on using the standard deviation calculated by FITEQL to develop a weighting factor ( $w_i$ ) according to the following relationship

$$w_i = \frac{(1/\sigma_{\text{Log } K})_i}{\sum (1/\sigma_{\text{Log } K})_i} \quad (8-4)$$

The weighting factor is then used to derive a "best-estimate" of the equilibrium constant of interest

$$\overline{\text{Log K}} = \sum w_i (\text{Log K})_i \quad (8-5)$$

In this fashion, a value with a lower standard deviation (i.e., a better fit) is more heavily weighted and will have more influence on the final value. Dzombak and Morel (1990) used this approach to combine acidity constants for different ferrihydrite data sets at different ionic strengths. This technique is valid for the DLM, which contains an ionic strength term in the charge-potential relationship. Because it also adjusts potential to reflect ionic strength, a similar approach should be valid for the TLM. Again, however, for the reasons given earlier, this approach is not valid for the CCM, and was not used. The weighted results (DLM and TLM only) are presented in Table 8-3. The values reported for the CCM are for  $I = 0.1$  M. Generally, constants calculated at different ionic strengths within a given data set agreed very closely. This holds true even for different background electrolytes at the same concentration. For example, for the  $\gamma\text{-Al}_2\text{O}_3$  data of Sprycha (1989), DLM- $\text{Log K}_+$  ranged from 6.17 to 7.02 and DLM- $\text{Log K}_-$  varied from  $-8.82$  to  $-9.75$ . This was despite ionic strengths ranging from 0.001 to 0.1 M and background electrolytes ( $I = 0.1$  M) that included NaBr, NaCl, KCl, CsCl, and NaI. Agreement between data sets was not as good, which is not surprising given the differences in data set size, laboratory procedure, equipment, and sample preparation (perhaps exemplified in differences in measured  $A_{\text{SP}}$ ) that were noted for the different studies.

One factor complicating data comparison was the different pH ranges covered in the experiments. If the coverage is not as extensive on one side of the  $\text{pH}_{\text{ZPC}}$ , the chemical equilibrium model will not be well constrained and FITEQL will have more difficulty converging on equilibrium constants. One extreme example of this is  $\delta\text{-MnO}_2$ , where there are no data available below its low  $\text{pH}_{\text{ZPC}} \sim 2.0$ . In this case, as noted earlier, the protonation reaction and the anion adsorption reaction for the TLM (Table 8-2) are not constrained at all, and attempting to include them in the optimization leads to convergence problems.

One of the trade-offs inherent in the simplified uniform approach adopted here is the implicit assumption of similar mineral morphology between studies embodied in using a single  $A_{\text{SP}}$  for a given mineral. Although a systematic analysis has not been performed here, it is important to recognize the uncertainty inherent in estimated acidity constants due to differences in surface area measurements. It would be possible to construct a more complete model by maintaining the exact  $A_{\text{SP}}$  reported for each of the titration studies through the data interpretation. However, because of the uncertainty in  $A_{\text{SP}}$  measurements, a single generalized value was used. This assumption is supported by the similarity in reported mineral preparation techniques and the generally close agreement between measured  $A_{\text{SP}}$  values.

Similarity in mineral synthesis methods provides some justification for assuming a single  $A_{\text{SP}}$ . In addition, although some information is lost in this simplification, the general distinctions in  $A_{\text{SP}}$  between minerals are preserved. Also, relative to empirical models, the addition of geochemical considerations such as aqueous speciation, pH, and partial gas pressures to sorption models is the benefit received.

## 8.2.5 Conclusions

Despite disparities in experimental conditions, the agreement in acidity constants (and binding constants for background electrolytes in the TLM) between different data sets for several minerals (e.g.,

Table 8-3. Best estimate values for SCM constants (T = 25 °C)

Mineral	Model	$N_S$ (sites/nm <sup>2</sup> )	Log K <sub>+</sub>	Log K <sub>-</sub>	Log K <sub>Anion</sub>	Log K <sub>Cation</sub>
Goethite	CCM(0.1M)	2.31	6.47	-9.03	n.a.	n.a.
	DLM	"	7.35	-9.17	n.a.	n.a.
	TLM <sup>(a)</sup>	"	6.00	-10.00	8.78	-7.64
Ferrihydrite	CCM(0.1M)	2.31	7.35	-8.45	n.a.	n.a.
	DLM	"	7.29 <sup>(b)</sup>	-8.93 <sup>(b)</sup>	n.a.	n.a.
	TLM <sup>(a)</sup>	"	6.00	-10.00	8.43	-7.66
Magnetite	CCM(0.1M)	2.31	6.26	-7.32	n.a.	n.a.
	DLM	"	6.72	-6.37	n.a.	n.a.
	TLM <sup>(a)</sup>	"	4.70	-8.70	7.95	-5.47
am-SiO <sub>2</sub>	CCM(0.1M)	2.31	(c)	-7.05	n.a.	n.a.
	DLM	"	(c)	-7.20	n.a.	n.a.
	TLM <sup>(a)</sup>	"	0.90	-4.90	(c)	-6.29
α-Al <sub>2</sub> O <sub>3</sub>	CCM(0.1M)	2.31	9.08	-8.32	n.a.	n.a.
	DLM	"	8.33	-9.73	n.a.	n.a.
	TLM <sup>(a)</sup>	"	6.80	-10.80	10.12	-7.73
γ-Al <sub>2</sub> O <sub>3</sub>	CCM(0.1M)	2.31	6.92	-9.00	n.a.	n.a.
	DLM	"	6.85	-9.05	n.a.	n.a.
	TLM <sup>(a)</sup>	"	6.40	-10.40	8.28	-7.95
δ-MnO <sub>2</sub>	CCM(0.1M)	2.31	(c)	-2.14	n.a.	n.a.
	DLM	"	(c)	-3.27	n.a.	n.a.
	TLM <sup>(a)</sup>	"	-0.10	-3.9	(c)	-1.60
TiO <sub>2</sub> (anatase)	CCM(0.1M)	2.31	3.26	-8.98	n.a.	n.a.
	DLM	"	3.40	-8.67	n.a.	n.a.
	TLM <sup>(a)</sup>	"	4.10	-8.10	5.45	-7.55
TiO <sub>2</sub> (rutile)	CCM(0.1M)	2.31	3.91	-7.79	n.a.	n.a.
	DLM	"	4.23	-7.49	n.a.	n.a.
	TLM <sup>(a)</sup>	"	3.90	-7.90	5.24	-6.42

- n.a. Parameters not applicable to CCM and DLM models.  
(a) Log K<sub>+</sub> and Log K<sub>-</sub> fixed by convention. See text for discussion.  
(b) Dzombak and Morel (1990) constants for ferrihydrite.  
(c) Not considered for δ-MnO<sub>2</sub> and am-SiO<sub>2</sub>. See text for discussion.

goethite, ferrihydrite,  $\gamma$ - $\text{Al}_2\text{O}_3$ , and am- $\text{SiO}_2$ ) for a given SCM was often within two orders of magnitude. This supports combining these results into a single set of parameters. The similarity between the DLM and TLM constants calculated for goethite and ferrihydrite suggests that ferrinol ( $\text{FeOH}^0$ ) sites behave similarly for these two minerals despite differences in crystallinity, and indicates that they may be modeled using the same SCM parameters.

This modeling exercise pointed up some of the limitations in the different SCM. The CCM is perhaps the most restrictive of the three models in that it requires knowledge of the dependence of capacitance on ionic strength. For this reason, the type of generalized approach outlined here is not strictly applicable for the CCM. The TLM can model different ionic strengths, but it has a larger number of parameters and requires some means of fixing  $\text{Log } K_+$  and  $\text{Log } K_-$  to model titration data using FITEQL. This extra level of complexity tends to work against the ready incorporation of the TLM in performance assessment codes (Hayes et al., 1990; 1991). The simplest model, the DLM, is also able to model ionic strength changes, and also has the fewest number of parameters to fit. Examination of the values listed in Table 8-3 for the acidity constants and mineral  $\text{pH}_{\text{ZPC}}$  indicates that the values for both the CCM and DLM are reasonable, meeting the constraint set in Eq. (8-2).

Values determined in this study are necessary before data on radionuclide sorption on these minerals can be interpreted using surface complexation models. It is important to remember, however, that in an effort to establish a baseline, the constants in Table 8-3 were determined using fixed site density, capacitances, and, in the case of the TLM, acidity constants. Although these parameters were selected where possible, based on surveys of mineral properties, they may not be the same as properties reported for a given set of experimental data. For this reason, results cannot be compared directly to constants determined using a different set of parameters (Dzombak and Hayes, 1992). However, while there is some loss of conceptual (and numerical) accuracy in using a single set of parameters to model sorption data, this type of uniform approach is to be favored in trying to strike a balance between model completeness and performance assessment needs for efficient modeling.

### 8.3 SORPTION EXPERIMENTS

To develop an understanding of radionuclide sorption processes and the important physical and chemical parameters that affect actinide sorption behavior in the Yucca Mountain environment, experiments are being conducted to investigate the sorption behavior of uranium on geologic media. Results reported previously (Pabalan et al., 1993) regarding uranium (6+) sorption on clinoptilolite, which is the predominant zeolite mineral in the proposed HLW repository at Yucca Mountain, indicate that sorption of uranium is strongly dependent on pH and, to some extent, on uranium concentration in solution. Uranium sorption on clinoptilolite is important at near-neutral pH where  $\text{UO}_2(\text{OH})_{2(\text{aq})}$  is the predominant aqueous species calculated using the EQ3 geochemical code, whereas sorption is inhibited at alkaline pH where carbonate- and hydroxy-carbonate-complexes are the calculated primary uranium aqueous species. Those results indicate that, under certain geochemical conditions, the zeolite mineral clinoptilolite can be an important sorber of an actinide element, but quantitative prediction of uranium transport through zeolite-rich rocks will need to account for changes in solution chemistry.

Because the objective of this research project is to understand fundamental controls on radionuclide sorption on rocks, which are essentially mixtures of minerals, new uranium sorption experiments were initiated during this reporting period using the clay mineral montmorillonite, which is another important mineral phase present underneath Yucca Mountain, as the sorbing phase. In contrast

to zeolites, which are tectosilicates with relatively open three-dimensional pore structures, montmorillonite is a phyllosilicate with a layer-type crystal structure. These experiments were designed to evaluate the effects of pH, aqueous uranium speciation, and aqueous uranium concentration on uranium sorption on clays, and also to determine differences in uranium sorption behavior on different types of minerals. The results may help identify simplified approaches to modeling radionuclide sorption, which can be used in performance assessment calculations.

Additional uranium sorption experiments were also initiated using alpha-alumina as the sorbent phase. The primary objective of these experiments is to evaluate the effect of sorbent-surface-area/solution-volume ratio, recognizing that surface adsorption is the predominant uranium sorption mechanism, even for zeolites like clinoptilolite (Pabalan et al., 1993), and that the ratio of fluid-volume to mineral surface-area can vary significantly along a fluid flowpath. A secondary objective is to compare uranium sorption on clinoptilolite and montmorillonite with that on alpha-alumina, which is an oxide with very different structure and surface properties.

### 8.3.1 Experimental Procedures

#### Uranium sorption on Na-montmorillonite

The sorption experiments were conducted by reacting 0.1 g of Na-montmorillonite with 50 ml of uranium solutions in polypropylene bottles at 25 °C. In contrast to the experiments on clinoptilolite, which had initial uranium concentrations (as  $^{238}\text{U}$ ) of 476 or 4,760 ppb, the solutions used in these experiments had initial uranium concentrations of 5, 50, or 500 ppb (mostly as  $^{233}\text{U}$ ) in an 0.1 M  $\text{NaNO}_3$  matrix. The Na-montmorillonite was prepared from montmorillonite powder (source locality: Cheto, Arizona) obtained from the Source Clay Minerals Repository (University of Missouri-Columbia) by ion-exchange with 3 M  $\text{NaCl}$  solutions. Prior to addition of the solid phase, the initial pH of each solution was adjusted to a value in the range 2.5 to 9.0 at approximately 0.25 pH intervals by addition of  $\text{HNO}_3$  or  $\text{NaHCO}_3$ . The amount of reagent needed to achieve the desired initial pH of the uranium solution was estimated using the EQ3NR geochemical code (version 3245.R124) with database Data0.com.R12 (Wolery et al., 1990). The solutions, which were kept open to atmospheric  $\text{CO}_2(\text{g})$  throughout the experiment, were agitated using gyratory shakers.

The Na-montmorillonite powder was added after all solutions had attained a constant pH. For uranium solutions with added  $\text{NaHCO}_3$ , it took at least 10 days to equilibrate with atmospheric  $\text{CO}_2(\text{g})$  and reach a constant pH. Control experiments consisting of uranium solutions (in an 0.1 M  $\text{NaNO}_3$  matrix and initial pH adjusted to 2, 4, 6, 8, or 9.5) without added clay were used to determine potential losses of uranium to the container walls. After about 2 weeks, samples were taken from each mixture using polypropylene syringes tipped with 0.2  $\mu\text{m}$  DynaGard filters. Initial and final uranium concentrations of the experimental mixtures and control solutions were analyzed with a liquid scintillation analyzer. The equilibrium pH of each solution was also measured.

#### Uranium sorption on alpha-alumina

The sorption experiments on alpha-alumina were conducted by reacting 0.2 g of the solid with 100 ml of uranium solutions in polypropylene bottles at 25 °C. The solutions all had initial concentrations of 5 ppb (mostly as  $^{233}\text{U}$ ) in an 0.1 M  $\text{NaNO}_3$  matrix. The sorbent phase used consisted of alpha-alumina issued by the National Institute of Standards and Technology (NIST) as certified reference materials for

measurements of specific surface-area of powders, specifically Reference Materials (RM) 8005, 8006, and 8007, with reported surface-areas of 2.09, 0.23, and 0.0686 m<sup>2</sup>/g, respectively. The experiments were conducted at a constant solid-mass/solution-volume, but variable sorbent-surface-area/solution-volume ratio. In a manner similar to the montmorillonite experiments described earlier, the initial pH of the uranium solutions was adjusted by addition of HNO<sub>3</sub> or NaHCO<sub>3</sub>. The alpha-alumina was added after all solutions attained a constant pH. The solutions were agitated using gyratory shakers and were kept open to atmospheric CO<sub>2</sub>(g) throughout the experiment. After about 2 weeks, samples were taken using filter-tipped syringes for liquid scintillation analysis and the equilibrium pH of each solution was measured.

### 8.3.2 Results and Discussion

Initial results of the sorption experiments on Na-montmorillonite and alpha-alumina are presented in Figures 8-1 and 8-2. Figure 8-1 shows the percent of uranium lost from solution (initial uranium concentration = 50 ppb) versus the equilibrium pH in the Na-montmorillonite experiments. Figure 8-2 shows the percent of uranium lost from solution (initial uranium concentration = 5 ppb) versus the equilibrium pH in the alpha-alumina experiments. The solid circles in these figures, which represent data from the experimental mixtures, illustrate the strong dependence of uranium sorption on pH. This dependence is similar to that observed for uranium sorption on clinoptilolite (Pabalan et al., 1993), on iron oxides/oxyhydroxides (Tripathi, 1984; Payne et al., 1992), and on the clay mineral corrensite (Siegel et al., 1990). The data represented by the solid circles, however, are not corrected for uranium losses to the container walls or filters. The open circles in Figures 8-1 and 8-2, which are data from the control experiments, show that significant amounts of uranium are lost to the container and the filter. The control data also show that the losses to the container and filter mimic the pH-dependence of the results from the experimental mixtures. The significant losses of uranium from solution in the control experiments preclude meaningful interpretation of the results from the experimental mixtures. Although possible uranium losses to the containers and to syringe filters were anticipated based on data published in the literature and the low initial uranium concentrations used in this study, the uranium losses observed in the control experiments were higher than expected. For example, Tripathi (1984) assessed the possible loss of uranium from his experiments due to sorption on a syringe-Nucleopore filter assembly from solutions having initial concentrations of 20 ppb to 5 ppm uranium and reported that no significant losses were observed.

The experiments on uranium sorption on Na-montmorillonite and alpha-alumina are currently being redone. These new experiments use teflon (FEP), instead of polypropylene, bottles to minimize losses to the container walls, and filtration of aqueous samples was eliminated. Separation of sorbent from aqueous phase is being done only by centrifugation. A greater number of control solutions (ten, instead of the usual four) is also being used to determine the pH-dependence of uranium loss to the containers. Results of these experiments will be presented in the next semi-annual research report.

## 8.4 ASSESSMENT OF PROGRESS TOWARDS MEETING PROJECT OBJECTIVES

Electrostatic SCM have been used recently to describe complex sorption behavior for a number of contaminants. Each model employs a set of model-specific adjustable parameters to describe the mineral/water interface. Traditionally, several of these parameters have been adjusted simultaneously to achieve a best fit to a specific data set. This lack of uniformity has made comparison between different

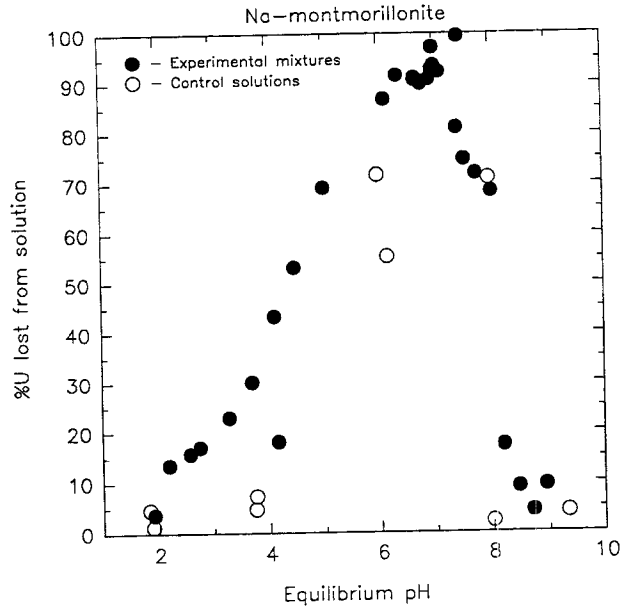


**Figure 8-1.** Data from the experiments on uranium sorption on Na-montmorillonite in terms of percent of uranium lost from solution versus equilibrium pH. Initial uranium concentration in solution is 50 ppb. The solid and open circles are data from the experimental and control mixtures, respectively.

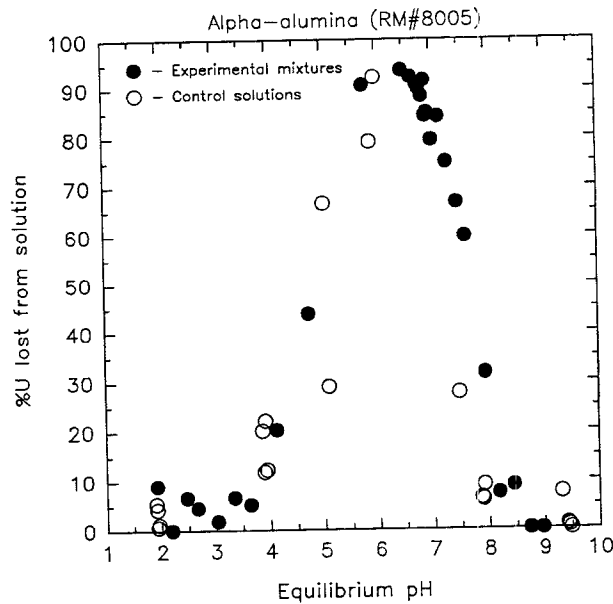


**Figure 8-2.** Data from experiments on uranium sorption on alpha-alumina in terms of percent of uranium lost from solution versus equilibrium pH. Initial uranium concentration in solution is 5 ppb. The solid and open circles are data from the experimental and control mixtures, respectively.

models and studies difficult, if not impossible. For three commonly used SCM, the current study has developed a uniform set of model parameters to provide a consistent baseline from which to determine the equilibrium constants needed to describe the acid-base chemistry of a number of different minerals. With these parameters in place, it is now possible to use surface complexation models to describe available radionuclide sorption data for these minerals. It may also be possible to combine values for different oxides to describe sorption site characteristics for common rock-forming minerals such as feldspar and clay. Because a uniform approach has been used, modeling results can be compared and the performance of the different models evaluated. These initial efforts have identified some of the strengths and weaknesses of the different SCM.

Results of laboratory experiments on uranium sorption have begun to provide an understanding of the important parameters that control the sorption behavior of an actinide element. For example, the results reported previously on uranium sorption on clinoptilolite (Pabalan et al., 1993) indicated that uranium(6+) species are strongly sorbed at near-neutral pH. However, the amount of uranium sorbed is strongly dependent on pH and decreases steeply away from near-neutral pH. Some dependence on total uranium concentration in solution was also observed. Because of the strong dependence on pH, modeling of sorption processes will likely require that changes in groundwater chemistry be properly accounted for in performance assessment calculations if retardation by sorption processes is included. Information derived from the laboratory experiments has been useful in developing CDS 3.2.3.3 and 3.2.3.5.

The similarity in the dependence of uranium sorption on parameters such as pH and uranium concentration observed for the zeolite mineral clinoptilolite and iron oxides/oxyhydroxides and clays is important. This may help identify simplified approaches to modeling sorption and thus help in developing CDM relevant to the KTU identified in Section 8.1, and in developing conceptual models related to the Performance Assessment Research Project and the IPA Phase 3. The information derived from the laboratory experiments may also help interpret data on uranium distribution and migration at the Peña Blanca field site of the Geochemical Natural Analog Research Project.

Experience gained and lessons learned from both sorption modeling and sorption experiments, including problems encountered such as uranium losses to containers and filters, will be useful in reviewing DOE study plans and prelicensing submittals on sorption studies. The experience will also be necessary to identify potential problems in sorption experiments and modeling exercises conducted by the DOE. Although losses of radionuclides to container walls and filters are mentioned in some publications, the strong pH-dependence of these losses is not discussed. Thus, sorption experiments that do not properly account for these losses are flawed.

## **8.5 PLANS FOR NEXT REPORTING PERIOD**

Available information on the acid-base chemistry and surface area of minerals important at Yucca Mountain will be examined for incorporation into surface complexation approaches. Sorption modeling will continue, using the parameters determined in this study. Radionuclide sorption data will be obtained from the peer-reviewed literature and experimental studies at the CNWRA, and modeled using different surface complexation approaches. Comparison of model results will allow evaluation of SCM performance, and should further indicate how these models can be simplified for practical incorporation into hydrogeochemical transport codes. In addition, calibration of sorption models will provide an understanding of what chemical conditions control radionuclide sorption.

Experiments studying uranium sorption on Na-montmorillonite, alpha-alumina, and clinoptilolite will continue. In order to obtain data on the surface properties of these minerals such as  $\text{pH}_{\text{zpc}}$ , a Mettler potentiometric titrator is being set up for acid-base titration of mineral samples, as well as a Micromeritics Zeta Potential Analyzer for electrophoretic measurements. Because the batch sorption experiments on single minerals only provide phenomenological information, that is, how much radionuclide is lost from solution, an attempt will be made to utilize molecular dynamics simulation to provide more mechanistic information by computer simulation of sorption of different aqueous species.

## 8.6 REFERENCES

- Abendroth, R.P. 1970. Behavior of pyrogenic silica in aqueous electrolytes. *Journal of Colloid and Interface Science* 34: 591-596.
- Allison, J.D., D.S. Brown, and K.J. Novo-Gradac. 1991. *MINTEQA2/PRODEFA2, A Geochemical Assessment Model for Environmental Systems: Version 3.0 User's Manual*. EPA/600/3-91/021. Athens, GA: U.S. Environmental Protection Agency.
- Atkinson, R.J., A.M. Posner, and J.P. Quirk. 1967. Adsorption of potential determining ions at the ferric oxide-aqueous electrolyte interface. *Journal of Physical Chemistry* 71: 550-558.
- Atkinson, R.J., A.M. Posner, and J.P. Quirk. 1968. Crystal nucleation in Fe(III) solutions and hydroxide gels. *Journal of Inorganic Nuclear Chemistry* 30: 2371-2381.
- Atkinson, R.J., A.M. Posner, and J.P. Quirk. 1972. Kinetics of isotopic exchange of phosphate at the  $\alpha$ -FeOOH-aqueous solution interface. *Journal of Inorganic Nuclear Chemistry* 34: 2201-2211.
- Balistrieri, L., and J.W. Murray. 1981. The surface chemistry of goethite ( $\alpha$ -FeOOH) in major ion sea water. *American Journal of Science* 281: 788-806.
- Balistrieri, L., and J.W. Murray. 1982. The surface chemistry of  $\delta$ -MnO<sub>2</sub> in major ion sea water. *Geochimica et Cosmochimica Acta* 46: 1253-1265.
- Benjamin, M.M., and J.O. Leckie. 1981. Multiple site adsorption of Cd, Cu, Zn, and Pb on amorphous iron oxyhydroxide. *Journal of Colloid and Interface Science* 79: 209-221.
- Berube, Y.G., and P.L. de Bruyn. 1968. Adsorption at the rutile-solution interface. 1. Thermodynamic and experimental study. *Journal of Colloid and Interface Science* 27: 305-318.
- Bolt, G.H. 1957. Determination of the charge density of silica soils. *Journal of Physical Chemistry* 61: 1166-1169.
- Bradbury, M.H., and B. Baeyens. 1992. A mechanistic approach to the generation of sorption databases. *Radionuclide Sorption From the Safety Evaluation Perspective. Proceedings of an NEA Workshop*. Nuclear Energy Agency (NEA). Paris: Organization for Economic Cooperation and Development: 121-162.

- Breeuwsma, A., and J. Lyklema. 1973. Physical and chemical adsorption of ions in the electrical double layer on hematite ( $\alpha$ -Fe<sub>2</sub>O<sub>3</sub>). *Journal of Colloid and Interface Science* 43: 437-448.
- Catts, J.G., and D. Langmuir. 1986. Adsorption of Cu, Pb and Zn by  $\delta$ -MnO<sub>2</sub>: Applicability of the site binding surface complexation model. *Applied Geochemistry* 1: 255-264.
- Davis, J.A. 1977. *Adsorption of Trace Metals and Complexing Ligands at the Oxide/Water Interface*. Ph.D. Dissertation Stanford, CA: Stanford University.
- Davis, J.A., and D.B. Kent. 1990. Surface complexation modeling in aqueous geochemistry. *Reviews in Mineralogy: Volume 23. Mineral-Water Interface Geochemistry*. M.F. Hochella, Jr. and A.F. White, eds. Washington, DC: Mineralogical Society of America: 177-260.
- Dzombak, D.A. 1985. *Toward a Uniform Model for the Sorption of Inorganic Ions on Hydrous Oxides*. Ph.D. Dissertation Cambridge, MA: Massachusetts Institute of Technology.
- Dzombak, D.A., and K.F. Hayes. 1992. Comment on recalculation, evaluation, and prediction of surface adsorption constants for metal adsorption on iron and manganese oxides. *Environmental Science and Technology* 26:1251-1253.
- Dzombak, D.A., and F.M.M. Morel. 1990. *Surface Complexation Modeling: Hydrous Ferric Oxide*. New York: John Wiley and Sons.
- Hayes, K.F., G. Redden, W. Ela, and J.O. Leckie. 1990. *Application of Surface Complexation Models for Radionuclide Adsorption: Sensitivity Analysis of Model Input Parameters*. NUREG/CR-5547. Washington, DC: U.S. Nuclear Regulatory Commission.
- Hayes, K.F., G. Redden, W. Ela, and J.O. Leckie. 1991. Surface complexation models: An evaluation of model parameter estimation using FITEQL and oxide mineral titration data. *Journal of Colloid and Interface Science* 142: 448-469.
- Hsi, C.-K.D., and D. Langmuir. 1985. Adsorption of uranyl onto ferric oxyhydroxides: Application of the surface complexation site-binding model. *Geochimica et Cosmochimica Acta* 49: 1931-1941.
- Huang, C.P., and W. Stumm. 1972. The specific surface area of  $\gamma$ -Al<sub>2</sub>O<sub>3</sub>. *Surface Science* 32: 287-296.
- James, R.O., and G. Parks. 1982. Characterization of aqueous colloids by their electrical double-layer and intrinsic surface chemical properties. *Surface and Colloid Science* 12: 119-216.
- Kent, D.B., V.S. Tripathi, N.B. Ball, J.O. Leckie, and M.D. Siegel. 1988. *Surface-Complexation Modeling of Radionuclide Adsorption in Subsurface Environments*. NUREG/CR-4807. Washington, D.C: U.S. Nuclear Regulatory Commission.
- Mesuerre, K.L.G. 1992. *Adsorption and Dissolution Reactions Between Oxalate, Chromate, and an Iron Oxide Surface: Assessment of Current Modeling Concepts*. Ph.D. Dissertation. Beaverton, OR: Oregon Graduate Institute of Science and Technology.

- Murray, J.W. 1974. The surface chemistry of hydrous manganese dioxide. *Journal of Colloid and Interface Science* 46: 357-371.
- Pabalan, R.T., and D.R. Turner. 1992(a). *Sorption Modeling for HLW Performance Assessment. Report on Research Activities for Calendar Year 1991*. W.C. Patrick, ed. CNWRA 91-01A. San Antonio, TX: Center for Nuclear Waste Regulatory Analyses: 8-1 to 8-66.
- Pabalan, R.T., and D.R. Turner. 1992(b). *Sorption Modeling for HLW Performance Assessment. NRC High-Level Radioactive Waste Research at CNWRA January 1 Through June 30, 1992*. W.C. Patrick, ed. CNWRA 92-01S. San Antonio, TX: Center for Nuclear Waste Regulatory Analyses: 8-1 to 8-24.
- Pabalan, R.T., and D.R. Turner. 1993. *Sorption Modeling for HLW Performance Assessment. NRC High-Level Radioactive Waste Research at CNWRA July 1 Through December 31, 1992*. W.C. Patrick, ed. CNWRA 92-02S. San Antonio, TX: Center for Nuclear Waste Regulatory Analyses: 8-1 to 8-18.
- Pabalan, R.T., J.D. Prikryl, P.M. Muller, and T.B. Dietrich. 1993. Experimental study of uranium (6+) sorption on the zeolite mineral clinoptilolite. C.G. Interrante and R.T. Pabalan, eds. *Scientific Basis for Nuclear Waste Management XVI. MRS Symp. Proc. 212*, Pittsburgh, PA: Materials Research Society: 777-782.
- Papelis, C., K. F. Hayes, and J. O. Leckie. 1988. *HYDRAQL: A Program for the Computation of Chemical Equilibrium Composition of Aqueous Batch Systems Including Surface-Complexation Modeling of Ion Adsorption at the Oxide/Solution Interface*. Technical Report No. 306., Stanford, CA: Stanford University.
- Payne, T.E., K. Sekine, J.A. Davis, and T.D. Waite. 1992. Modeling of radionuclide sorption processes in the weathered zone of the Koongarra ore body. *Alligator Rivers Analogue Project Annual Report, 1990-1991*. P. Duerden, ed. Menai, New South Wales, Australia: Australian Nuclear Science and Technology Organization: 57-85.
- Regazzoni, A.E., M.A. Blesa, and A.J.G. Maroto. 1983. Interfacial properties of zirconium dioxide and magnetite. *Journal of Colloid and Interface Science* 91: 560-570.
- Siegel, M.D., J.O. Leckie, S.W. Park, S.L. Phillips, and T. Sowards. 1990. *Studies of Radionuclides Sorption by Clays in the Culebra Dolomite at the Waste Isolation Pilot Plant Site, Southeastern New Mexico*. SAND89-2387. Albuquerque, NM: Sandia National Laboratories.
- Siegel, M.D., V.S. Tripathi, M.G. Rao, and D.B. Ward. 1992. Development of a multi-site model for adsorption of metals by mixtures of minerals: 1. Overview and preliminary results. *Water-Rock Interaction: Proceedings 7th International Symposium on Water-Rock Interaction*. Y.F. Kharaka and A.S. Maest eds. Rotterdam, Netherlands: A.A. Balkema.

- Smith, R.W., and E.A. Jenne. 1988. *Compilation, Evaluation, and Prediction of Triple-Layer Model Constants for Ions on Fe(III) and Mn(IV) Hydrous Oxides*. PNL-6754. Richland, WA: Pacific Northwest Laboratory.
- Sprycha, R. 1984. Surface charge and adsorption of background electrolyte ions at anatase/electrolyte interface. *Journal of Colloid and Interface Science* 102: 173-185.
- Sprycha, R. 1989. Electrical double layer at alumina/electrolyte interface. *Journal of Colloid and Interface Science* 127: 1-11.
- Swallow, K.C. 1978. *Adsorption of Trace Metals by Hydrous Ferric Oxide*. Ph.D. Dissertation. Cambridge, MA: Massachusetts Institute of Technology.
- Tripathi, V.S. 1984. *Uranium(VI) Transport Modeling: Geochemical Data and Submodels*. Ph.D. Dissertation. Stanford, CA: Stanford University.
- Westall, J.C. 1982. *FITEQL: A Computer Program for Determination of Chemical Equilibrium Constants From Experimental Data, Version 2.0*. Rpt. 82-02. Corvallis, OR: Oregon State University.
- Westall, J.C., and H. Hohl. 1980. A comparison of electrostatic models for the oxide/solution interface. *Advances in Colloid and Interface Science* 12: 265-294.
- Wolery, T.J., K.J. Jackson, W.L. Bourcier, C.J. Bruton, B.E. Viani, K.G. Knauss, and J.M. Delany. 1990. Current status of the EQ3/6 software package for geochemical modeling. D.C. Melchior and R.L. Bassett, eds. *Chemical Modeling of Aqueous Systems II. ACS Symp. Series 416*. Washington, DC: American Chemical Society: 104-116.
- Yates, D.A. 1975. *The Structure of the Oxide/Aqueous Electrolyte Interface*. Ph.D. Dissertation. Melbourne, Australia: University of Melbourne.
- Yates, D.A., and T.W. Healy. 1975. Mechanism of anion adsorption at the ferric and chromic oxide/water interfaces. *Journal of Colloid and Interface Science* 52: 222-228.

## 9 PERFORMANCE ASSESSMENT RESEARCH

*by Robert G. Baca, Gordon W. Wittmeyer, Ronald T. Green,  
and Sitakanta Mohanty*

*Investigators: Robert G. Baca, Gordon W. Wittmeyer, Ronald T. Green, and Sitakanta Mohanty  
(CNWRA); Chris Freitas (SwRI); Hoa D. Nguyen and Mohan S. Seth (Consultants)*

*NRC Project Officer: T. J. McCartin*

### 9.1 TECHNICAL OBJECTIVES

Postclosure Performance Assessment (PA), as a scientific evaluation process, will provide the quantitative basis for judging the acceptability of the proposed repository system at Yucca Mountain. In conducting a PA, the U.S. Nuclear Regulatory Commission (NRC) will utilize a hierarchy of models and codes. The top level or total-system PA code, which is being developed under the NRC Nuclear Material Safety and Safeguards (NMSS) Iterative Performance Assessment (IPA) activity, models a wide variety of processes, phenomenological interactions, and future states, but in a necessarily simplified manner. In contrast, the lower-level codes in this hierarchy are very sophisticated, but model only a few processes in a very detailed manner. Quite interestingly, both types of codes typically exceed the computational limits of conventional computers and push the capability of the most advanced, high-performance supercomputers. The technical objectives of the PA Research Project are to develop advanced PA modeling technology in three specific areas: (i) alternate conceptual models of key phenomena and disruptive scenarios (i.e., future system states); (ii) efficient and robust computational and computer techniques for solving the model equations; and (iii) formalized approaches for testing and evaluating (i.e., validating) computer models.

One of the primary programmatic objectives of the PA Research Project is to provide modeling technology that will benefit the NRC IPA exercises. Another, and equally important, programmatic objective is to provide the knowledge base necessary for supporting: (i) revision of the postclosure PA Compliance Determination Strategies (CDS) (i.e., CDS 6.1, 6.2, and 6.3); and (ii) development of postclosure performance Compliance Determination Methods (CDM) that will be incorporated into appropriate sections of the License Application Review Plan (LARP). Specifically, this research project is providing the knowledge base for addressing key technical uncertainties (KTU) associated with:

- (1) Conceptual models
- (2) Mathematical models
- (3) Model parameters
- (4) Future system states
- (5) Model validation

At present, the KTU related to the first three items resulted in the associated CDS being typed as Review Level 4, while the CDS associated with the fourth item is typed Review Level 5; these KTUs are broadly addressed in Tasks 1 and 2 of this research project. The last KTU requires a type Review Level 5 of

CDS 6.1, Assessment of Compliance with the Requirement for Cumulative Releases of Radioactive Materials, and is being addressed in a focused effort under Task 3 of this research project. In addition, the practical experience and expertise gained from this research project will place the NRC and the Center for Nuclear Waste Regulatory Analyses (CNWRA) in a position to thoroughly and independently evaluate the U.S. Department of Energy (DOE) PA models and codes.

Because of its multidisciplinary nature, the PA Research Project is an integrated programmatic effort drawing on expertise from such technical areas as hydrology, geochemistry, structural geology, volcanology, seismology, climatology, computational fluid dynamics, and computer science. At present, the PA Research Project is programmatically integrated with the NMSS IPA activity and three other Office of Nuclear Regulatory Research (RES) projects: (i) the Geochemical Natural Analog Research Project; (ii) the Sorption Research Project; and (iii) the Stochastic Unsaturated Flow and Transport Project. In relation to the Geochemical Natural Analog Research Project, data from rock cores obtained from the Peña Blanca field site are being analyzed to improve conceptual and mathematical models of: (i) variably saturated flow in the fractured-porous tuff; and (ii) radionuclide transport in discrete fractures and diffusion into and out of the rock matrix. In addition, data on diffusion and sorption coefficients, compiled under the Sorption Research Project, will contribute to conceptual/mathematical model development of radionuclide transport phenomena. Simulation studies conducted under the Stochastic Unsaturated Flow and Transport Research Project have identified a number of computational aspects that currently limit the practical application of detailed hydrologic codes (e.g., BIGFLOW) to the Yucca Mountain site. Work conducted under Task 2 of the PA Research Project is being focused to reduce or remove these limitations.

The PA Research Project is designed to address a number of user needs identified by the NMSS for postclosure PA. Specific research needs include: (i) means to identify and screen scenarios; (ii) efficient integration of mathematical models into high-level waste (HLW) PA methodology; (iii) validation of mathematical models; (iv) evaluation of mathematical models; (v) evaluation of mathematical flow and transport models applicable to unsaturated fractured rock and application to a range of scales and heterogeneities; and (vi) appraisal of the applicability of existing mathematical models of hydrologically and chemically coupled flow and transport.

Research conducted under the PA Research Project is divided among three major tasks. The first task, Conceptual Model Development, focuses on developing conceptual/mathematical models in two areas: (i) flow and transport phenomena; and (ii) disruptive event scenarios. In the second task, Computational Model Development, research is directed toward the development of advanced numerical methods necessary to implement PA conceptual and mathematical models. Under the third task, Model Evaluation, a general model validation strategy is being developed using data from the INTRAVAL project test cases. Work completed on these tasks has been reported in two earlier semi-annual research reports. This section describes the results of the PA Research Project for the first half of 1993.

## **9.2 SIGNIFICANT TECHNICAL ACCOMPLISHMENTS**

Progress towards the primary technical objectives has been made in all three tasks of the PA Research Project. Work under Task 1 actively pursued an integration activity with the Geochemical Natural Analog Research Project. As part of Task 2, research was continued on evaluation of adaptive grid methods and advanced computational fluid dynamics (CFD) methods for solving the flow and transport equations. For Task 3, a steady flow model was developed and applied to field data from the Yucca

Mountain site as part of the INTRAVAL Project. Research results and findings for each task are presented separately in the following subsections.

### **9.2.1 Task 1 — Conceptual Model Development: Flow and Transport in Fractured Tuff**

Understanding solute transport through fractured-porous media is of fundamental importance to predicting the isolation performance of the proposed repository at Yucca Mountain. Natural analog field sites where transport has occurred over many thousands of years can provide a setting at which such processes can be investigated. An investigation of this type requires the availability of data and information concerning the hydrologic, geochemical, and structural properties of the site. A reconnaissance-level effort was initiated in this reporting period to analyze the hydraulic properties of the unsaturated matrix of volcanic tuff at a natural analog field site and to relate those properties to geochemical and transport characteristics.

As part of the Geochemical Natural Analog Research Project (Pearcy et al., 1993a), the Peña Blanca natural analog site, located near Chihuahua, Mexico, hydraulic data for cores from Nopal I are being analyzed to provide a basis for assessing solute transport through the fractured-porous tuff. This high-grade uranium deposit, located in the Nopal Formation, is a welded silicic tuff that is very similar to the Topopah Spring Formation. Uranium from the ore deposit has migrated through both the rock matrix and the fractures that permeate the breccia pipe through which the high-grade uranium deposit is located. Veinlets that emanate from the Nopal I deposit have mineral alteration halos and uranium concentration gradient halos. It is likely that these halos represent past fluid flow out from the veinlets into the matrix of the host rock during episodic flooding by meteoric water. The nature and rate of transport from the veinlet into the rock matrix is an important question that is very relevant to similar issues related to the Topopah Spring Formation at Yucca Mountain.

Several tuff rock samples from the Peña Blanca site have been collected as part of the Geochemical Natural Analog Project. Hydraulic properties are being analyzed as part of this task. The rock samples show varying degrees of mineralogic alteration ranging from the unaltered country rock to the highly altered rock found at the Nopal I deposit (Pearcy et al., 1993b). The hydraulic properties are being analyzed and interpreted to help formulate conceptual models of solute transport of uranium through the tuff. Comparison of the hydraulic properties of the Nopal Formation samples to the properties of the Topopah Spring Formation will also help define the similarities (or differences) between the transport characteristics of these two formations.

The hydraulic properties currently being analyzed in this task include porosity, saturated hydraulic conductivity, air permeability, and the moisture content-pressure relationship (i.e., retention curve). Since these properties are being determined for rock samples representing variable degrees of mineralogic alteration, the relationship of the hydraulic character to the degree of alteration will also be assessed. This assessment will be conducted as a collaborative effort with the principal investigations of the Geochemical Natural Analog Project. Air permeability and saturated hydraulic conductivity are being measured using a flex-wall permeameter. Moisture retention curves are being determined using several different apparatus, including two variations of a pressure plate and a centrifuge. One of the pressure plates is capable of characterizing hysteretic curves (e.g., both the drying and wetting curves) at pressures up to 5 bars, while the other is capable of exposing samples to pressures up to 15 bars. The centrifuge is capable of applying forces equivalent to a pressure of about 12 bars. The centrifuge has the ability to determine

the retention curve of a sample with relatively low permeability (i.e.,  $10^{-15} \text{ m}^2$ ) in significantly shorter times (i.e., 72 hr) than the standard pressure plate method (i.e., weeks to months, especially in media of low permeability).

In preparation for analyzing retention curve data for samples from the Nopal Formation, the centrifuge was used to determine the moisture retention characteristics of samples of alumina powder that were prepared to exhibit permeabilities similar to those of volcanic tuff. Particles greater than  $44 \mu\text{m}$  were removed by sieving to produce a porous medium with a measured permeability of about  $10\text{--}15 \text{ m}^2$ , similar to permeabilities measured on samples from the Topopah Springs Formation (Klavetter and Peters, 1986). Moisture content and pressure data from these samples will be analyzed using the RETC computer code (van Genuchten et al., 1991). Data obtained for a low permeability sample are shown in Figure 9-1. Of particular interest is the similarity and repeatability among the various moisture retention curves.

## **9.2.2 Task 2 — Computational Model Development: Adaptive Mesh and Spectral Element Methods**

### **9.2.2.1 Adaptive Mesh Methods**

Computational grids are commonly used in the numerical solution, by finite difference and finite element methods, of boundary value problems that arise in engineering design and scientific analysis. For complicated spatial domains, hundreds of thousands of grid points may be required to represent the problem geometry accurately and to limit the truncation errors associated with the discretized equations. Very fine grids may also be required to obtain accurate solutions of highly nonlinear problems, or of those problems that possess pronounced features, such as chemical reaction or shock fronts across which the gradient of the solution is large. Unfortunately, fine grids require that large amounts of computer memory, as well as large amounts of computational time, be used to solve the linear or linearized system of equations arising from the discretized form of the governing equations. Often these fine grids arise due solely to the presence of pronounced local solution features whose accurate solution requires an extremely high spatial resolution that must be extended uniformly throughout the solution domain. It is readily apparent that if the computational mesh could be locally refined at the temporal and spatial location where these pronounced solution features are generated and then moved through the solution domain, the excessive use of computer resources arising from the use of uniformly fine spatial discretization could be avoided. Any procedure in which the local spatial and temporal discretization of a computational grid is correspondingly refined or coarsened, depending on the behavior of the solution, is generally referred to as adaptive mesh refinement.

The general precept that underlies the method of adaptive refinement of either finite difference or finite element meshes is that to make the most economical use of a limited number of grid points these nodes should be located in space and/or time so as to minimize some measure of the truncation error. This same precept is commonly used by numerical analysts to guide the design of a computational mesh; refining the mesh in areas where large gradients in the solution are expected and coarsening the mesh where little spatial change in the solution is expected. For designing fixed grids, the analyst is guided by experience and physical intuition as to where shocks or other important features of the solution will develop and where the mesh must be correspondingly refined. Such grids may be adequate for steady-state solutions; however, if the problem is time dependent and includes features such as shocks or reaction fronts, some automatic truncation error estimation and grid refinement procedure must be used.

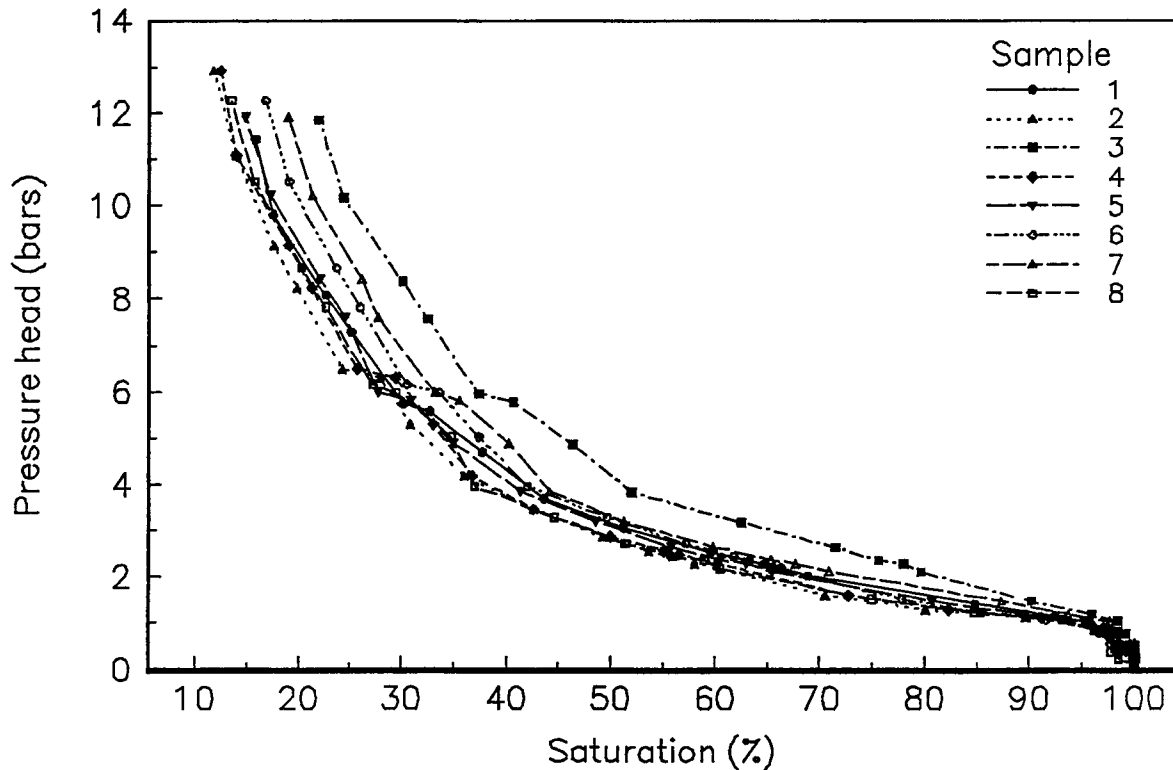


Figure 9-1. Moisture retention curves for low permeability sample obtained by centrifuge method

### Mesh Redistribution

A brief review of the technical literature on adaptive mesh refinement as well as a brief tutorial on the mathematical methods used in adaptive mesh refinement were presented in Chapter 9 of the previous semi-annual research report. As noted previously (Baca et al., 1993), adaptive mesh refinement algorithms may be divided into two basic methods: grid refinement procedures and grid redistribution procedures. Grid refinement methods add or subtract grid points or elements in response to some measure of the grid error, while grid redistribution methods adjust the location of a fixed number of grid points so that the mesh spacing is, in some sense, optimally graded. While the emphasis in the present work is on the application of these methods to one-dimensional (1D) grids, the ultimate goal of this work is to investigate the feasibility of implementing these methods for the two-dimensional (2D) and three-dimensional (3D) flow problems whose solution is required for IPA. The literature suggests that for 2D and 3D problems, grid refinement methods are more commonly implemented than are grid redistribution methods. Apparently, redistributing grid points in more than 1D increases the likelihood that the topology of the mesh will become tangled, requiring the use of computationally expensive routines such as Delaunay triangulation to construct a new grid topology. For problems in 1D, redistribution methods are ideal since grading functions for the grid are readily computable and mesh topology remains fixed. While the focus of this work is on grid redistribution, insight gained here should aid in assessing the utility of implementing appropriate refinement methods for 2D and 3D domains.

Consider the nonlinear Richards' equation for unsaturated flow in a porous medium

$$\frac{\partial}{\partial z} \left[ K(\psi) \left( \frac{\partial \psi}{\partial z} + 1 \right) \right] = \frac{\partial \theta}{\partial t} + q \quad (9-1)$$

subject to the general boundary conditions

$$-K(\psi) \left( \frac{\partial \psi}{\partial z} + 1 \right) = -\alpha(\psi - \Psi) + Q, \quad z=0, \quad z=l \quad (9-2)$$

and initial conditions

$$\psi(z,0) = \psi_0 \quad (9-3)$$

where  $\psi(z,t)$  is the pressure head or matric potential,  $\theta$  is the volumetric water content,  $K$  is the hydraulic conductivity that is a known function of  $\psi$  and possibly  $z$ ,  $q$  is an internal source/sink term, for  $\alpha = 0$  Eq. (9-2) is a Neumann boundary condition with prescribed flux  $Q$ , for  $\alpha = \infty$  Eq. (9-2) is a Dirichlet boundary condition with prescribed data  $\Psi$ , and for intermediate values of  $\alpha$  Eq. (9-2) is a mixed or Robin boundary condition. The vertical coordinate  $z$  in Eqs. (9-1) and (9-2) is positive upward.

When Eqs. (9-1) to (9-3) are spatially discretized on a 1D grid using the Galerkin weighted residual finite element method with linear basis functions, and the time derivative is approximated by a forward Euler finite difference scheme, the resulting system of nonlinear algebraic equations is tridiagonal and has the form

$$\sum_{i=1}^{N_n} A_{ij}(\psi) \left[ (1-\omega)\psi_i^{k+1} + \omega\psi_i^k \right] + \sum_{i=1}^{N_n} D_{ij}(\psi) \frac{\psi_i^{k+1} - \psi_i^k}{\Delta t^{k+1}} = r_j \quad \forall j \quad (9-4)$$

where  $A_{ij}$  is an  $n \times n$  tridiagonal conductance matrix,  $\psi_i$  is a  $n \times m$  vector of unknown nodal values,  $\omega$  is a weighting factor such that  $0 \leq \omega \leq 1$ ,  $D_{ij}$  is an  $n \times m$  capacitance matrix that is diagonal in the case where a lumped mass finite element procedure is employed and tridiagonal when the consistent finite element procedure is employed, and  $r_j$  is an  $n \times 1$  load vector that includes the effects of the gravity drainage term, internal sources and sinks, and boundary conditions.

Because the computational mesh used to obtain Eq. (9-4) is fixed, the grid spacing may be too coarse to permit accurate estimation of the pressure head in regions where sharp fronts develop. The accuracy of the pressure head estimates may be improved by allowing the spatial resolution of the mesh to increase in those areas where sharp fronts are developing and computational performance enhanced by decreasing the spatial resolution of the mesh in regions where gradients of the solution approach zero. One method that may be employed to increase or decrease the spatial resolution of the mesh where required is the so-called moving finite element method proposed by Miller and Miller (1981), wherein the spatial location of the nodal points and the nodal values are determined simultaneously by solving an expanded coupled system of equations. Unlike the moving finite element method, the mesh redistribution procedure used here is based on the principle of projecting a uniform mesh to a nonuniform or graded mesh using grading functions. This type of mesh redistribution procedure is more general and allows problems with

large diffusive components to be solved without concurrently solving for the nodal location and the partial differential equation (PDE) solution. Relatively straightforward mesh redistribution schemes can be constructed in 1D based on grading functions. A detailed outline of the theory and application of grading function to mesh redistribution has been presented in CNWRA (1993).

### Application to Unsaturated Flow

Numerical modeling of the infiltration of water into desiccated soils is difficult when using fixed computational grids because of the typically insufficient number of grid points required to accurately resolve the shape of the wetting front as it propagates through the soil profile. To test whether or not a mesh redistribution scheme based on the grading function (Baca et al., 1993) could improve the overall performance of infiltration modeling, a computer code was developed in which the discretized version of Richards' equation given by Eq. (9-4) was solved on a 1D vertical domain. Following Celia et al. (1990), the mixed formulation of the capacitance term in the finite element equations was incorporated into the Picard iteration procedure to reduce mass balance errors. The following mesh redistribution algorithm was implemented in the computer program:

- (1) Define an initial computational grid with a uniform grid spacing
- (2) Assemble and solve the finite element equations at a specified time
- (3) Estimate the second derivative of the solution at each internal node in the domain once the solution at the current time has converged
- (4) Solve an integral equation for the new location of each node
- (5) Project the converged pressure head solution from the old mesh to the new mesh
- (6) Return to step 2 and repeat steps 3-5 until the final solution time is achieved

To ensure that the finite element equations were correctly formulated and coded, the program was benchmarked against the 1D unsaturated flow finite element code, UNSAT1D, written by Celia (1991). This code was selected for benchmarking because it has been compared against other more sophisticated unsaturated flow codes (Baca and Magnuson, 1992), for example, PORFLOW and FLASH. Figure 9-2 shows that the results of the code compare very favorably with those from UNSAT1D for a specific vertical infiltration problem consisting of a 100 cm deep vertical homogeneous soil profile with Dirichlet boundary conditions at the top and bottom of  $\psi = -75$  cm and  $\psi = -1000$  cm, respectively, and uniform initial conditions of  $\psi = -1000$  cm. Soil properties were described by the van Genuchten-Mualem model:

$$\theta(\psi) = \theta_r + \frac{\theta_s - \theta_r}{\left[1 + (\alpha|\psi|)^n\right]^m} \quad (9-5)$$

and

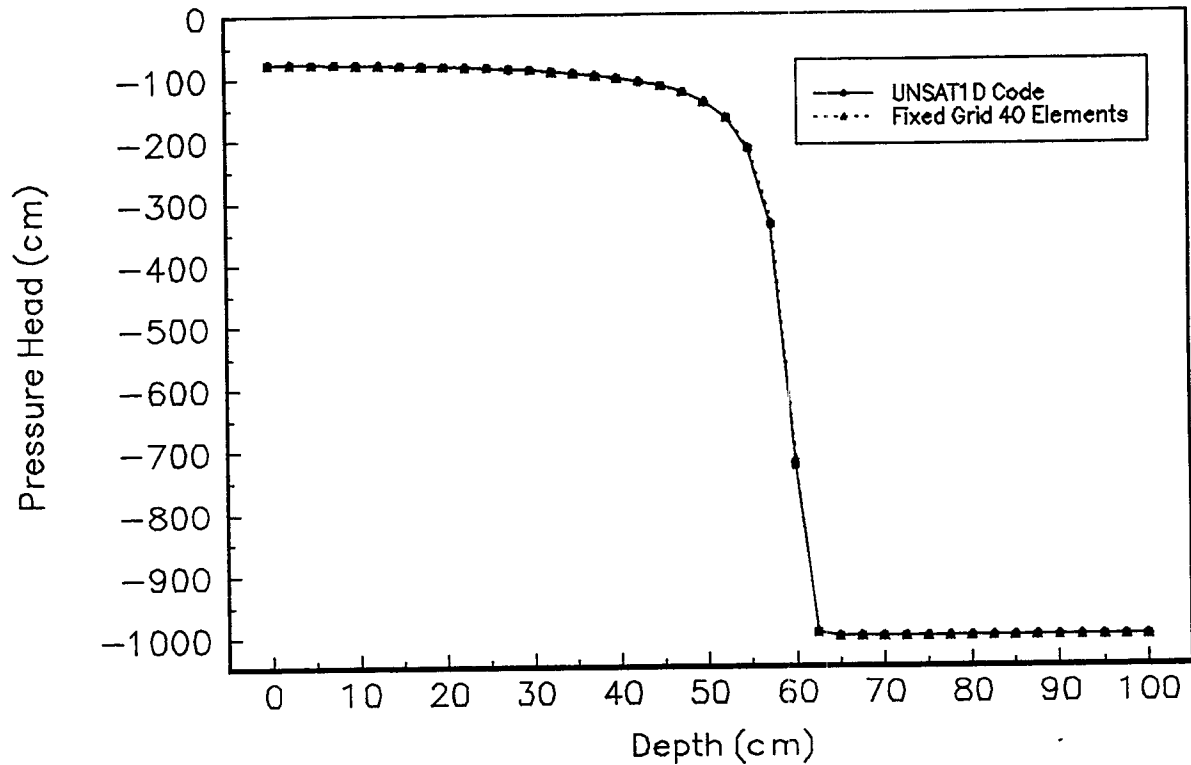


Figure 9-2. Comparison of calculated pressure heads at  $T = 1$  day from UNSAT1D Code (Celia, 1991) and from the adaptive meshing code developed by the authors

$$K(\psi) = K_s \frac{\left\{ 1 - (\alpha|\psi|)^{n-1} \left[ 1 + (\alpha|\psi|)^n \right]^{-m} \right\}^2}{\left[ 1 + (\alpha|\psi|)^n \right]^{m/2}} \quad (9-6)$$

where  $\alpha = 0.0335 \text{ cm}^{-1}$ ,  $\theta_s = 0.368$ ,  $\theta_r = 0.102$ ,  $n = 2$ ,  $m = 0.5$ , and  $K_s = 0.00922 \text{ cm/s}$ . For purposes of comparison, both spatial domains were divided into 40 equal-sized elements of a length of 2.5 cm and constant time steps of 144 s were used to reach a final time of 1 day (86400 s).

Initial attempts at using the integral equation approach (Baca et al., 1993) to redistribute the nodes led to serious problems with oscillation of the nodal positions over time. To prevent this oscillation, which was believed to have a deleterious effect on mass balance, a Laplacian smoothing routine was implemented to prevent nodes from clustering up too tightly in regions where the second derivative was large and spreading out too much in regions where it was near zero. While the Laplacian smoothing procedure did reduce node oscillation, there was no significant improvement in mass balance errors.

Figure 9-3 compares the predicted position of the wetting front for the infiltration problem described previously when computed using a fixed grid with 40 elements, a fixed grid of 200 elements,

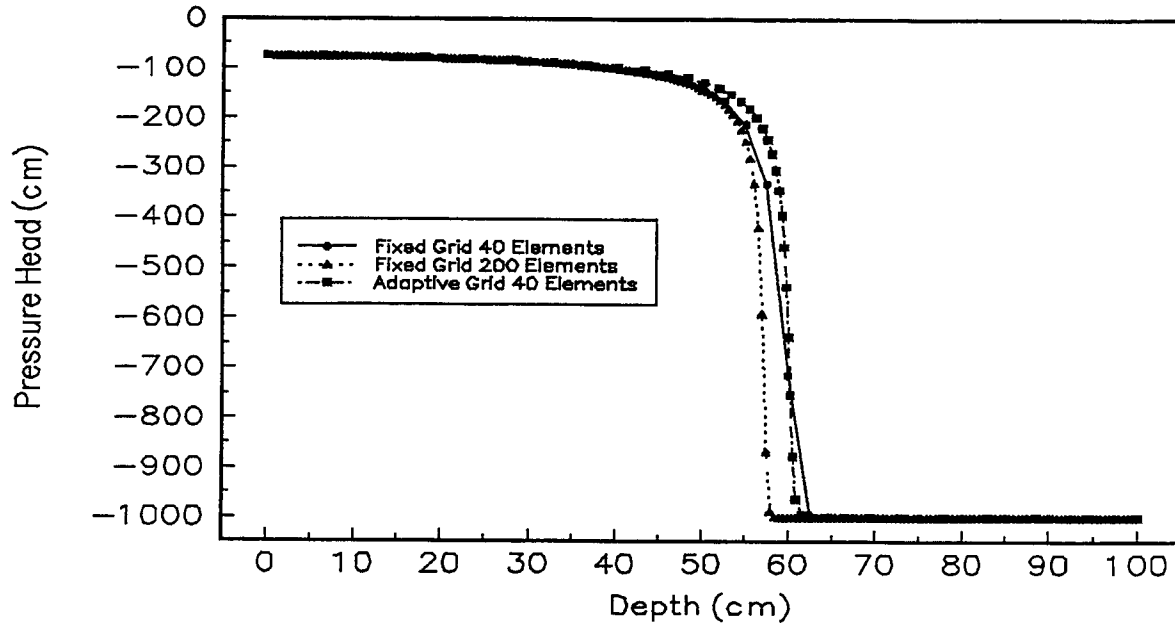


Figure 9-3. Comparison of adaptive grid and fixed grid pressure head solutions

and an adaptive grid consisting of 40 elements. While it is not unexpected that the position of the wetting front predicted by the fixed grid of 200 equal-sized elements should lag behind that predicted for 40 fixed elements, it is somewhat surprising that the adaptive grid solution for 40 elements lags even farther behind. Inspection of the cumulative mass balance errors indicate that while the 40-element and 200-element fixed grid solutions achieve relatively small mass balance errors at  $T = 1$  day of  $-0.001809$  percent and  $-0.001311$  percent, respectively, the mass balance error for the adaptive grid solution is  $-9.075$  percent. Here the mass balance error is given by

$$MBE = \frac{\text{Net Inflow} - \text{Mass Accumulated}}{\text{Net Inflow}} \times 100 \quad (9-7)$$

The relatively large mass balance error for the adaptive grid is believed to be caused by the procedure used to project the converged solution at a given time step to the new grid. The projection procedure used to obtain the results shown in Figure 9-3 simply uses the linear basis functions defined on the old grid to interpolate the converged solution estimates to the new nodal points. As shown in Figure 9-4, using linear interpolation to project from the old grid to the new grid causes a net loss of mass when the nodes are moved in the same direction as the wetting front. Attempts at explicitly adjusting the global mass balance so that no mass was gained or lost during the projection procedure resulted in the generation of a spurious second wetting front that preceded the true wetting front.

A second projection procedure was developed in which the elliptic portion of Eq. (9-1) was solved locally on an element to obtain estimates of pressure head at nodes placed in the element by the redistribution procedure. Dirichlet conditions were imposed on the boundary by setting the pressure head at the endpoints of the element to the converged values obtained at the previous time step. When using the elliptic projection procedure, the mass balance error for the 40-element grid was  $+4.41$  percent. While

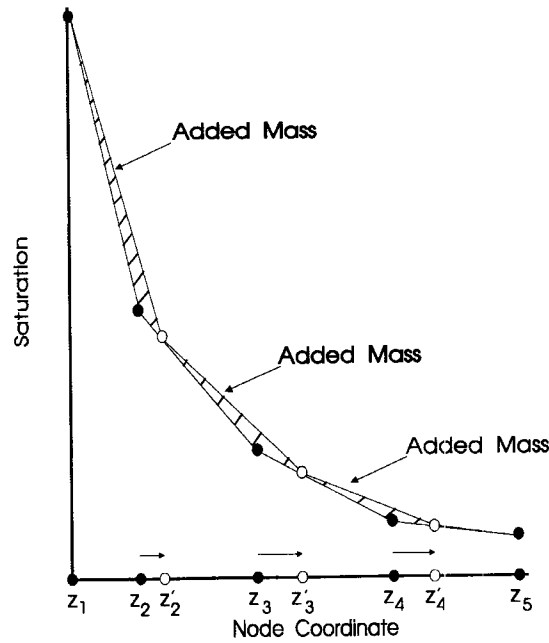


Figure 9-4. Mass balance error caused by grid projection using linear basis functions

this projection procedure produces smaller errors than the linear interpolation procedure, the mass balance error is still too large to be satisfactory. From the results of many simulations, it has been determined that both projection procedures cause the mass balance error to continue to increase in magnitude as the wetting front propagates through the domain. Projection methods based on linear interpolation of water contents and first-order Taylor series extrapolation of pressure heads were also implemented, but neither was found to improve mass balance.

Gottardi and Venutelli (1992) applied the moving finite element method to modeling 1D infiltration into unsaturated soil using the basic procedure outlined by Miller and Miller (1981). As noted previously, the moving finite element method differs from the procedure used here to redistribute the nodal points, however, Gottardi and Venutelli (1992) also observed that their procedure was less mass conserving than either standard finite element or finite difference methods using fixed grids. It must be noted that the results presented by Gottardi and Venutelli (1992) indicate that the moving finite element method appears to be less affected by errors in mass balance than the mesh redistribution procedure presented here. Unlike the mesh redistribution procedure, the moving finite element procedure cannot accommodate infiltration into layered soils because the method appears to have difficulty when nodes cross into new material property zones. In contrast, the mesh redistribution procedure used here has no such problems with layered soils and has been successfully tested by simulating steady-state infiltration into a vertical profile that consists of layers of bedded and welded tuffs similar to the those used for the COVE-2A (Dykhuizen and Barnard, 1992) exercise by solving the transient equation up to a large time.

#### Summary of Preliminary Findings

The recent literature indicates that adaptive mesh techniques significantly improve computational performance when applied to problems with steep fronts. However, applications of adaptive meshing (based on a mesh redistribution procedure) to 1D unsaturated flow are, at best, discouraging. In order for

these methods to prove useful for unsaturated flow modeling, a grid projection procedure that does not introduce local mass balance errors must be developed. Future efforts will be devoted to incorporating existing mesh refinement algorithms, such as that incorporated into the program PLTMG by Bank (1990), into existing IPA auxiliary analysis codes that use fixed grids. These hybrid codes will be carefully analyzed to ensure that the mass balance errors that plague the 1D test program do not affect the accuracy of the solution.

### 9.2.2.2 Spectral Element Method

Two of the most popular numerical techniques for solving nonlinear, hyperbolic, partial differential equations are low-order finite difference and finite element techniques. In recent years, higher-order numerical techniques have received significant attention in the CFD community. These methods are referred to as spectral methods (Canuto et al., 1988) and are based on use of orthogonal functions such as Chebyshev polynomials. Spectral methods have the unique property that their accuracy increases exponentially with grid refinement, unlike the low-order methods that typically converge linearly. The result is that, for comparable accuracy, the spectral methods require fewer grid points (i.e., coarser computational mesh) than the low-order finite difference or finite element methods. In order to apply the spectral methods to problems with complex domains, Patera (1984) has combined the spectral method approach with Galerkin finite elements to produce the so-called Spectral Element Method (SEM). Motivated by the possibility of taking advantage of the capabilities of this new approach, the SEM was applied to solve the two equations typically solved in performance assessment, namely: (i) the convection-dispersion equation for solute transport; and (ii) Richards' equation for unsaturated flow. The results of these applications are presented in the following subsections.

#### Application to Convection Dispersion Equation

The movement of a solute in media is described by the linear convection-dispersion equation, which is written in simplified (e.g., neglects sorption and decay) form (1D) as

$$\frac{\partial C}{\partial t} + u \frac{\partial C}{\partial x} = D \frac{\partial^2 C}{\partial x^2} \quad (9-8)$$

where  $C$  is the solute concentration,  $u$  is the fluid velocity, and  $D$  is the dispersion coefficient. The main difficulty of solving this governing equation is its mixed parabolic and hyperbolic character. An SEM solution algorithm was developed using the approach outlined by Patera (1984) and Basdevant et al. (1986). In their approach, the convection-dispersion equation is integrated over a single time step from  $t_n$  to  $t_{n+1}$  using operator splitting (i.e., the convection term solved explicitly and dispersion terms treated implicitly), where  $n$  and  $n+1$  represent the time levels. As a result, the integration is broken up into two steps

$$\hat{C}^{n+1} = C^n - \delta t \sum_{j=0}^{J-1} \alpha_j \left( u \frac{\partial C}{\partial x} \right)^{n-j} \quad (9-9)$$

and

$$C^{n+1} - \beta \delta t \left( D \frac{\partial^2 C}{\partial x^2} \right)^{n+1} = \hat{C}^{n+1} + \delta t \sum_{j=0}^{J-2} \beta_j \left( D \frac{\partial^2 C}{\partial x^2} \right)^{n-j} \quad (9-10)$$

where  $\delta t$  is the time increment and the coefficients,  $\alpha$  and  $\beta$ , are simply the weights of quadrature formulas. Quadrature formulas commonly used in SEM codes are the Adams-Bashforth and Crank-Nicolson formulas, which correspond to  $\alpha_0=3/2$ ,  $\alpha_1=1/2$ ,  $\beta=1/2$ , and  $\beta_0=1/2$ . By adopting these values, Eqs. (9-9) and (9-10) are second-order accurate in time.

Over an arbitrary element, the dependent variable,  $C$ , is approximated using the expansion

$$C(\zeta) = \sum_{j=0}^{N^e} \tilde{c}_j T_j(\zeta) \quad (9-11)$$

where  $T_j(\zeta)$  is the Chebyshev polynomial of order  $j$ , and  $\tilde{c}$  is the set of spectral coefficients. Note that the superscript has been omitted for convenience. Upon evaluation of Eq. (9-11) at the collocation points, a relation between the spectral coefficients and the physical variables is obtained. That is

$$\{C\} = [T]\{\tilde{c}\} \quad (9-12)$$

The computational domain is partitioned into nonoverlapping elements whose individual interval is denoted by  $[a^e, b^e]$ . For each element, there are  $N^e$  grid points, which are distributed according to the Gauss-Lobatto quadrature points  $\zeta_i = \cos(i\pi/N^e)$ , herein referred to as collocation points, where  $\zeta$  is the local coordinate that maps  $(a^e, b^e)$  onto  $(-1, 1)$  by means of the transformation

$$\zeta = \frac{2}{b^e - a^e} (x - a^e) - 1 \quad (9-13)$$

The explicit solution of the convective part of Eq. (9-9) is easily advanced through time. To solve the dispersive part, however, requires the application of the Galerkin finite element approach and solution of a linear system of equations (Patera, 1984).

To test the SEM algorithm, the method was coded in a simple finite element program and then applied to solve Eq. (9-8), the initial and boundary condition of

$$C(x, 0) = 0, \quad C(t, 0) = 1, \quad \text{and} \quad C(t, \infty) = 0 \quad (9-14)$$

Numerical solutions were generated for the case of  $u = 1$  and  $D = 0.01$ . The comparisons of the numerical results against the exact solution is shown in Figure 9-5. The plot shows the agreement is quite good. The propagation of the sharp front is predicted correctly. The solution is almost free of oscillations with 11 collocation points in each of the 5 elements used to discretize the domain from  $x = 0$  to 10.

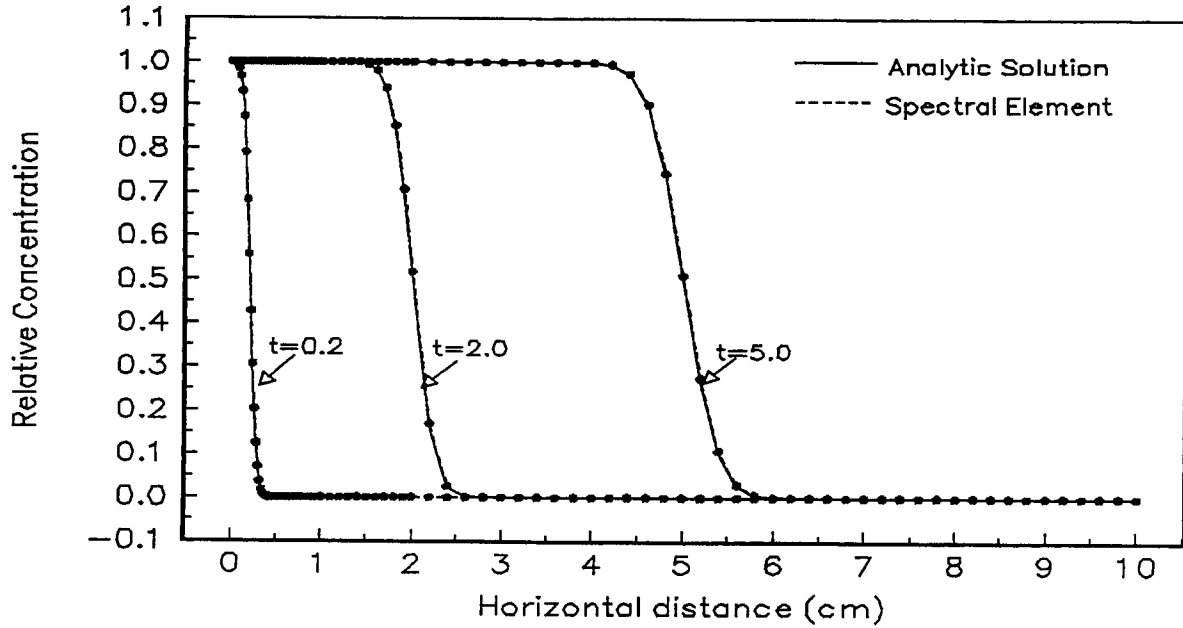


Figure 9-5. Comparisons of SEM and analytic solutions for  $u = 1$  and  $D = 0.01$

#### Application to Unsaturated Flow Equation

Vertical movement of water through unsaturated soil is described by the 1D form of Richards' equation [see Eq. (9-1)]. Efficient and mass conservative solutions of this equation are obtained if expressed in the following mixed form (Baca and Magnuson, 1992)

$$C(\psi) \frac{\partial \delta}{\partial t} = \frac{\partial}{\partial z} \left[ K(\psi) \left( \frac{\partial \delta}{\partial z} + 1 \right) \right] + \frac{\partial}{\partial z} \left[ K(\psi^m) \frac{\partial \psi^m}{\partial z} \right] - \frac{\partial \theta^m}{\partial t} \quad (9-15)$$

in which the second-order and higher terms have been omitted and  $\delta\psi = \psi^{m+1} - \psi^m$ , with  $m$  and  $m+1$  representing successive iterations. To solve this equation, the Galerkin finite element method was applied, which yields the Picard-based weak statement

$$\int \left\{ \omega_j \left[ C(\psi) \frac{\partial \delta}{\partial t} + \frac{\partial \theta^m}{\partial t} \right] + \frac{\partial \omega_j}{\partial z} \left[ k(\psi) \left( \frac{\partial \delta}{\partial z} + 1 \right) + K(\psi^m) \frac{\partial \psi^m}{\partial z} \right] \right\} dl \quad (9-16)$$

$$- \left[ K(\psi) \left( \frac{\partial \delta}{\partial z} + 1 \right) + K(\psi^m) \frac{\partial \psi^m}{\partial z} \right]_{GAMM}$$

where  $\Gamma$  designates the boundaries of the soil column.

Within each element domain, say  $e$ , the following quantities are expanded as a linear combination of a set of basis functions as

$$\{\psi, \theta, C, K\}^e \approx \sum_{j=0}^{N^e} \{\psi, \theta, C, K\}_j^e \omega_j^e(\zeta) \quad (9-17)$$

where  $\zeta$  is the local coordinate defined by  $\zeta = \frac{2}{\Delta^e} (z - a^e) - 1$  and  $\omega_j$  is the Lagrangian interpolant of the form:

$$\omega_j^e(\zeta) = \frac{2}{n^e} \sum_{n=0}^{N^e} \frac{1}{d_j d_n} T_n(\zeta_j) T_n(\zeta) \quad (9-18)$$

which has the property  $\omega_j^e(\zeta_k) = \delta_{jk}$  where  $\delta_{jk}$  is the Kronecker delta. The constant  $\bar{d}_j$  in Eq. (9-18) has a value of two if  $i = 0$  or  $N^e$  and one otherwise. Continuing the above equations and integrating produced a system of linear equations for an individual iteration. These equations are solved until convergence to an appropriate level is achieved.

In order to test the SEM algorithm, the test problem with the following characteristics (Celia et al., 1990) was solved. The column depth is 40 cm and is filled with an unsaturated porous material whose retention functions obey the Haverkamp model

$$\theta(\psi) = \theta_r + \frac{\alpha(\theta_s - \theta_r)}{\alpha + |\psi|^\beta} \quad (9-19)$$

and

$$K(\psi) = K_s \frac{A}{A + |\psi|^\gamma} \quad (9-20)$$

with values of empirical parameters listed in Table 9-1. Initially, the soil has a uniform moisture content of 0.0999, which corresponds to a pressure head of -61.5 cm. The pressures at the top and bottom of the column are maintained at -20.7 cm and -61.5 cm, respectively.

Table 9-1. Summary of soil properties (adapted from Celia et al., 1990)

$\alpha$	$\beta$	$\gamma$	$\theta_r$	$\theta_s$	A	$K_s$ , cm/s
$1.611 \times 10^6$	3.96	4.74	0.075	0.287	$1.175 \times 10^6$	0.00944

To perform the simulation, the column is divided into 13 elements with variable sizes. Figure 9-6 shows the results for the pressure head at three different times: 36.72; 158.2; and 368.2 s based on linear

fitting of the hydraulic properties. The numerical results compared very well to those published by Celia et al. (1990).

### **Summary of Preliminary Findings**

The SEM was successfully applied to solve the 1D equations for flow and transport in unsaturated porous media. The numerical results obtained to date on simple computational test cases indicate a very promising capability. Additional computational tests of the SEM with direct comparisons to finite difference and finite element techniques appear to be warranted. In particular, computational tests are needed to determine how well the method accommodates convection-dominated transport and very low saturation conditions.

### **9.2.3 Task 3 — Model Evaluation: Yucca Mountain INTRAVAL Test Case**

The objective of this task is to develop practical quantitative and qualitative methods for determining the validity of flow and transport models applicable to unsaturated media. Prior research conducted at the CNWRA, in conjunction with participation in the international INTRAVAL project on model validation, focused on the unsaturated flow and transport field experiment conducted at the Las Cruces Trench site in unconsolidated alluvial soil. While the Las Cruces Trench experiment was less directly relevant to CNWRA concerns regarding the use of models for simulating flow at the proposed Yucca Mountain repository than were other INTRAVAL test cases, it was felt that the sheer abundance of site characterization data available from the trench experiment made it better suited for developing and testing model validation strategies. The Yucca Mountain INTRAVAL test case was proposed by Alan Flint, U.S. Geological Survey (USGS), at the February, 1992, workshop in Sydney, Australia. Because of the obvious direct relevance of such a test case to NRC and CNWRA research efforts, and because INTRAVAL is scheduled to end in September, 1993, it was decided that both the NRC and CNWRA teams would actively participate in this validation exercise.

The problem, as posed to the modelers, was to use rock-hydraulic property data, detailed micro-stratigraphic data, and measured saturation profiles in near-surface boreholes provided by the DOE to construct a model and predict the saturation profile at the to-be-drilled USW UZ-16 borehole (henceforth referred to as UZ-16). Upon completion of the modeling efforts and drilling of borehole UZ-16, measured saturations in UZ-16 would be released so that direct comparisons of observations and predictions could be made.

#### **9.2.3.1 Conceptual Model Development**

The strategy used to construct a model for predicting the saturation profile in UZ-16 was to first concentrate on determining the appropriate steady-state infiltration rate and then refine the hydrostratigraphic description of the portion of UZ-16, which lies below the bottoms of adjacent boreholes USW UZN-54 and UZN-55. Although the assumption that the unsaturated flow regime at Yucca Mountain is in steady-state is certainly questionable, the low mean annual infiltration rates estimated by other researchers (Gauthier, 1993; Long and Childs, 1993) suggest that, at depths below the root zone, this assumption may be useful as a first approximation.

Boreholes USW UZN-54 and 55, which are 60 m apart, are located just to the northeast of the proposed repository and were drilled to determine the current hydrologic conditions in the unsaturated

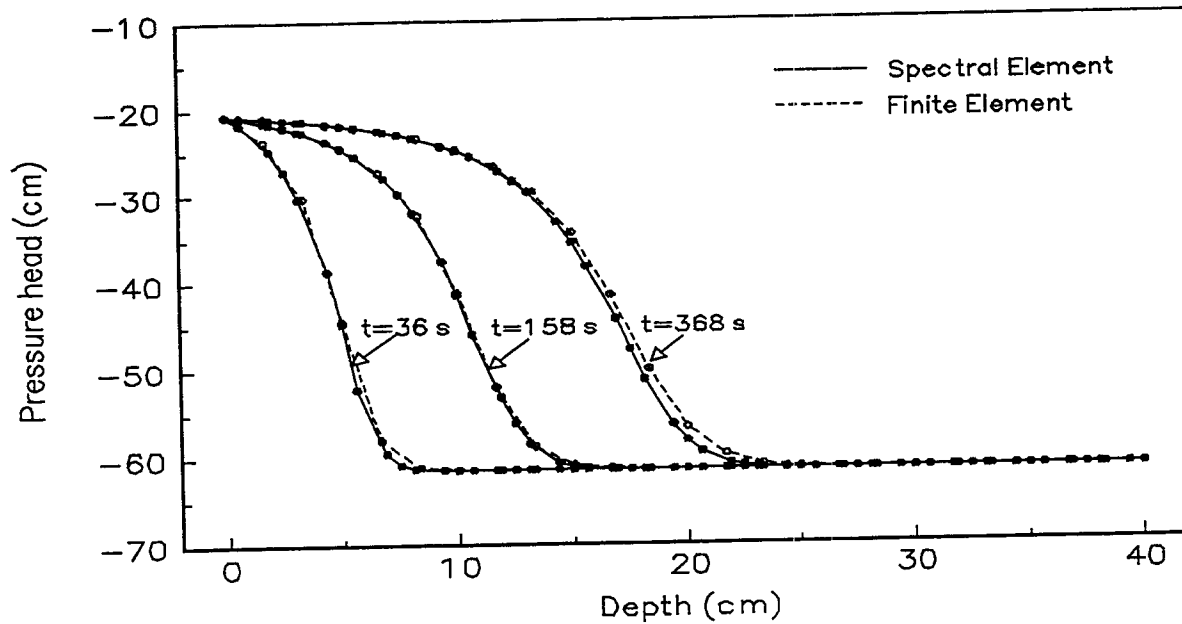


Figure 9-6. Pressure head profiles at three different times computed using SEM code

zone. UZN-54 lies in a wash, whereas UZN-55 lies to the north of the side slope of the erosionally controlled wash. UZ-16 is planned to be drilled 100 m downslope from and east of UZN-55. UZ-16 is expected to penetrate through the entire unsaturated zone and terminate at the water table. In comparison, UZN-54 is only 73 m deep penetrating the entire Tiva Canyon and the upper portion of the Topopah Spring member. Attempts to predict the infiltration rate at UZ-16 were based on UZN-54 since the saturation profile was less complicated than that in UZN-55.

No information was available on the depth of the water table for UZN-54. Therefore, the projected water table for UZ-16 was assumed to hold for UZN-54. The surface elevation for UZ-16 was not available; however, the surface elevation data for UZN-54 were provided by Sandia National Laboratories (SNL). Therefore, to associate the depth of water table with UZN-54, the top of the nonbedded welded tuff was chosen as the reference point. This location was chosen because it was a distinct level in the projected stratigraphy for UZ-16 and also because samples have been taken on either side of this interface close enough that the midpoint between these neighboring samples depths can be approximated as the depth of this interface. The thicknesses used for various members up to the depth of UZN-54 were inferred from the provided lithology. The thickness of various members for the region below the bottom of UZN-54 to the water table was obtained from the projected stratigraphy of UZ-16.

The structure inferred from the lithologic information provided for well UZN-54 was too uniform to explain the large variations in the saturation profile observed within each member. Therefore, the more detailed lithostratigraphic structure obtained from the Yucca Mountain composite vertical transect data provided to the INTRAVAL participants was projected onto various members at UZN-54. The porosity, saturated conductivity, residual water saturation, and moisture retention curves from the transect data were also projected onto UZN-54. The transect data consisted of 51 samples characterizing 19 microstratigraphic units. These microstratigraphic units were lumped into 14 layers based on their porosity, rock density, and saturated conductivity values. Porosity values assigned to each layer were the arithmetic average of the

porosities of various units in that layer. Harmonic averaging was used to assign saturated conductivity to each layer. The van Genuchten model parameters were obtained for each layer by using nonlinear regression to simultaneously fit the model to all saturation-pressure head curves for samples from that layer. The residual saturation values were estimated from plots of the water retention data. There was generally good correspondence between the thickness of various units interpreted from the transect data and the borehole data below the Tiva Canyon member. However, for the Tiva Canyon member, since the transect data showed much greater thickness than the thickness observed from the well data, the properties were assigned only to the projected thickness of various layers in the well.

Saturation information for UZN-54 was not available all the way down to the water table, therefore, the boundary was fixed at the bottom of the borehole. The pressure head at this depth was inferred from the measured saturation by using van Genuchten's relationship and assuming a very thin matrix layer at the bottom of the borehole with the same properties as that of the bottom layer. The pressure head thus obtained was used as the fixed bottom boundary condition. For each layer, the fracture density was interpreted from the information gathered from UZ-6 (Whitfield et al., 1993).

### 9.2.3.2 Numerical Methods

Because of difficulties encountered in attempting to use standard finite difference and finite element models for estimating the steady-state saturation profile for a 1D vertical transect through Yucca Mountain, a simple numerical model based on a fourth-order Runge-Kutta integration scheme for solving the Darcy equation was developed. For 1D vertical infiltration in unsaturated rock with lower boundary condition  $\psi(z=-L) = \psi_0$  and upper boundary condition (at  $z=0$ ) of

$$-K(\psi) \left( \frac{d\psi}{dz} + 1 \right) = q_0 \quad (9-21)$$

the mass-conservation equation can be integrated once to obtain

$$\frac{d\psi}{dz} = -1 - \frac{q_0}{K(\psi)} \quad (9-22)$$

which, while not being separable, may be readily integrated using standard numerical methods for solving initial value problems. The hydraulic conductivity,  $K(\psi)$ , for the fractured-porous rock is computed using the composite fracture-matrix continuum model of Klavetter and Peters (1986). The IMSL routine IVPAG was used to solve the initial value problem given by Eq. (9-22) and the lower boundary condition.

### 9.2.3.3 Summary of Preliminary Results

Except at the top of the formation, the match between results from the simplified 1D steady-state analytical solution and the field saturation profile is good. It may be emphasized that the properties are derived from the transect data to make the saturation prediction at UZN-54. As the description of the stratigraphic units do not have one-to-one correspondence with the stratigraphic description at UZN-54, the property selections heavily demanded the application of judgment.

To predict the water saturation profiles, two approaches are proposed. In the first approach, the bottom boundary could be fixed at the bottom of the well. In this case, the existing stratigraphic information could be honored. In the second approach, the bottom boundary could be fixed at the work table. In this case, the stratigraphy below the bottom of UZN-54 could be assumed to be the same projected stratigraphy for UZ-16. Both these boundary conditions are currently being investigated, and only the results from the first approach will be presented here.

The effects of infiltration rate on the saturation profile are presented in Figure 9-7. The saturation in the Tiva Canyon member was found to be more sensitive to the infiltration rate than in the Topopah Spring member. Figure 9-8 shows a comparison between the measured saturation profile and the profile predicted by using the 1D model. The best fit was obtained with an infiltration rate of  $10^{-14}$  m/sec ( $\approx 0.003$  mm/year).

### 9.3 ASSESSMENT OF PROGRESS

In the current reporting period, priority attention was given to the following research topics: (i) the INTRAVAL model validation exercise; (ii) development of conceptual models of flow and transport in fractured-porous tuff; and (iii) development of efficient and robust computational techniques for flow and transport. The model validation work was given high priority because the KTU requires a Type 5 review for CDS 6.1, Assessment of Compliance with the Requirement for Cumulative Releases of Radioactive Materials, and is an NMSS identified user need. The research on conceptual models for flow and transport in fractured-porous tuff is a high priority activity because: (i) understanding this phenomena is of fundamental importance to assessing isolation performance of the proposed repository site; (ii) research on this topic addresses the KTU on Mathematical Models in CDS 6.1 (Type 4); and (iii) both the NRC and DOE IPA activities have identified infiltration rate (and therefore unsaturated flow) as the most important factor controlling total-system performance. Research on advanced computational methods was conducted to address PA model implementation issues important to license review methods such as IPA. Specific issues being addressed are: (i) the need to reduce the long computer execution times of the total-system code (e.g., typically 30 hours on the Cray X/MP supercomputer) and stochastic auxiliary analysis codes such as BIGFLOW (e.g., greater than 48 hours on the Cray X/MP supercomputer when applied at a Yucca Mountain scale); and (ii) the need for more realistic models with fewer simplifying assumptions, which is also related to the Mathematical Model KTU.

Model validation, as a scientific process for assessing the accuracy/reliability of hydrologic models and building confidence in models, is slowly evolving. The investigators of this research project have been active participants in the international model validation project called INTRAVAL. Through the involvement in INTRAVAL, hydrologic models have been applied to experimental data sets from the Las Cruces Trench and, more recently, to field data from the Yucca Mountain site. This latest validation exercise, which is in progress, has provided an appreciation for the difficulty in collecting adequate field data for a model validation exercise and the limitations of numerical models in simulating unsaturated flow in the fractured-porous media. While participation in the latest INTRAVAL test case has definite merit from the perspective of collaborating with the international community, the current exercise is not likely to: (i) help make significant progress towards development of a systematic validation methodology; and (ii) provide insight to the complex, 3D, transient unsaturated flow regime in Yucca Mountain. Because the available field data are so limited and the boundary conditions and forcing term were not controlled, interpreting the significance of the comparison between measured and computed moisture profiles is expected to be highly speculative.

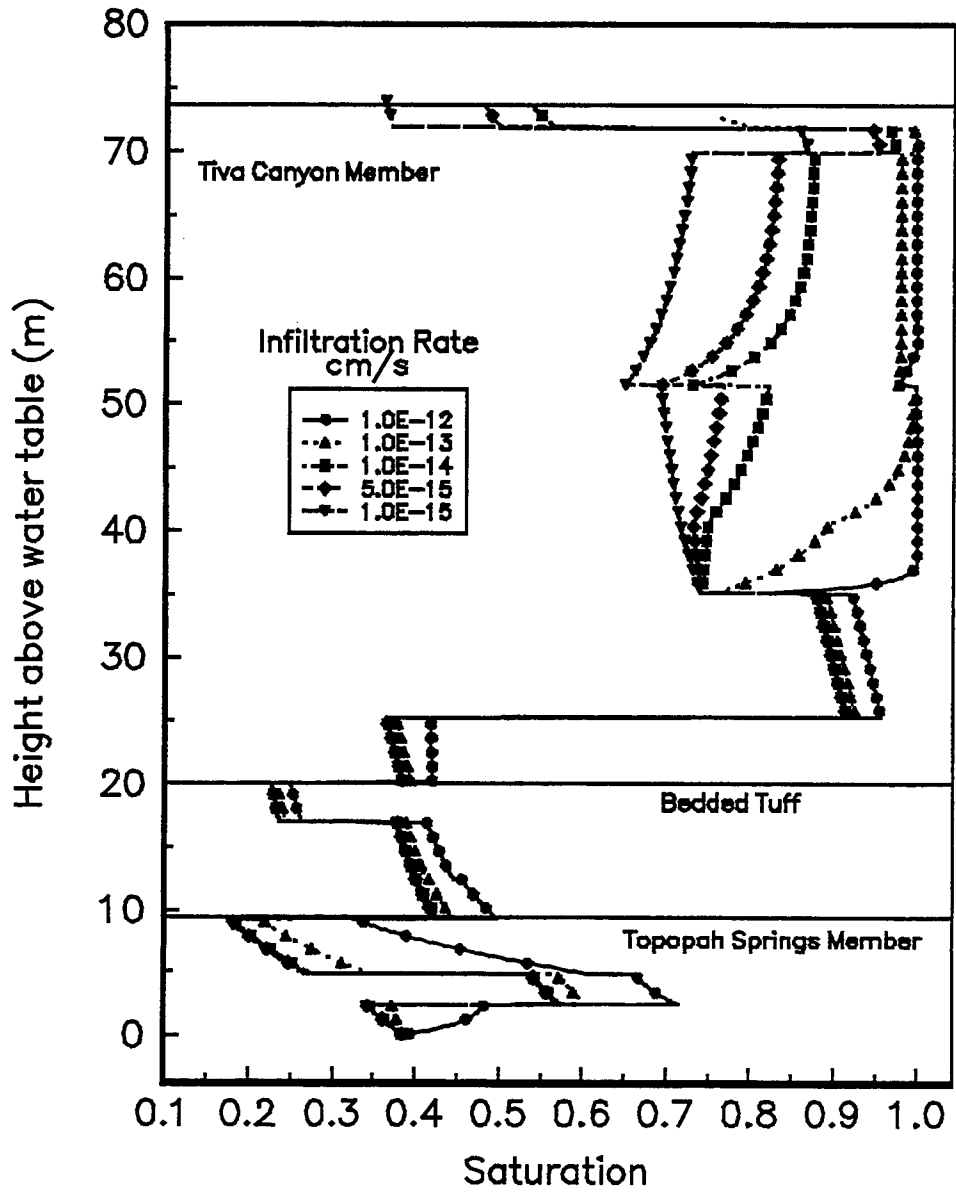


Figure 9-7. Effect of steady-state infiltration rates (m/s) on the predicted water saturation profile at well bore UZN-54

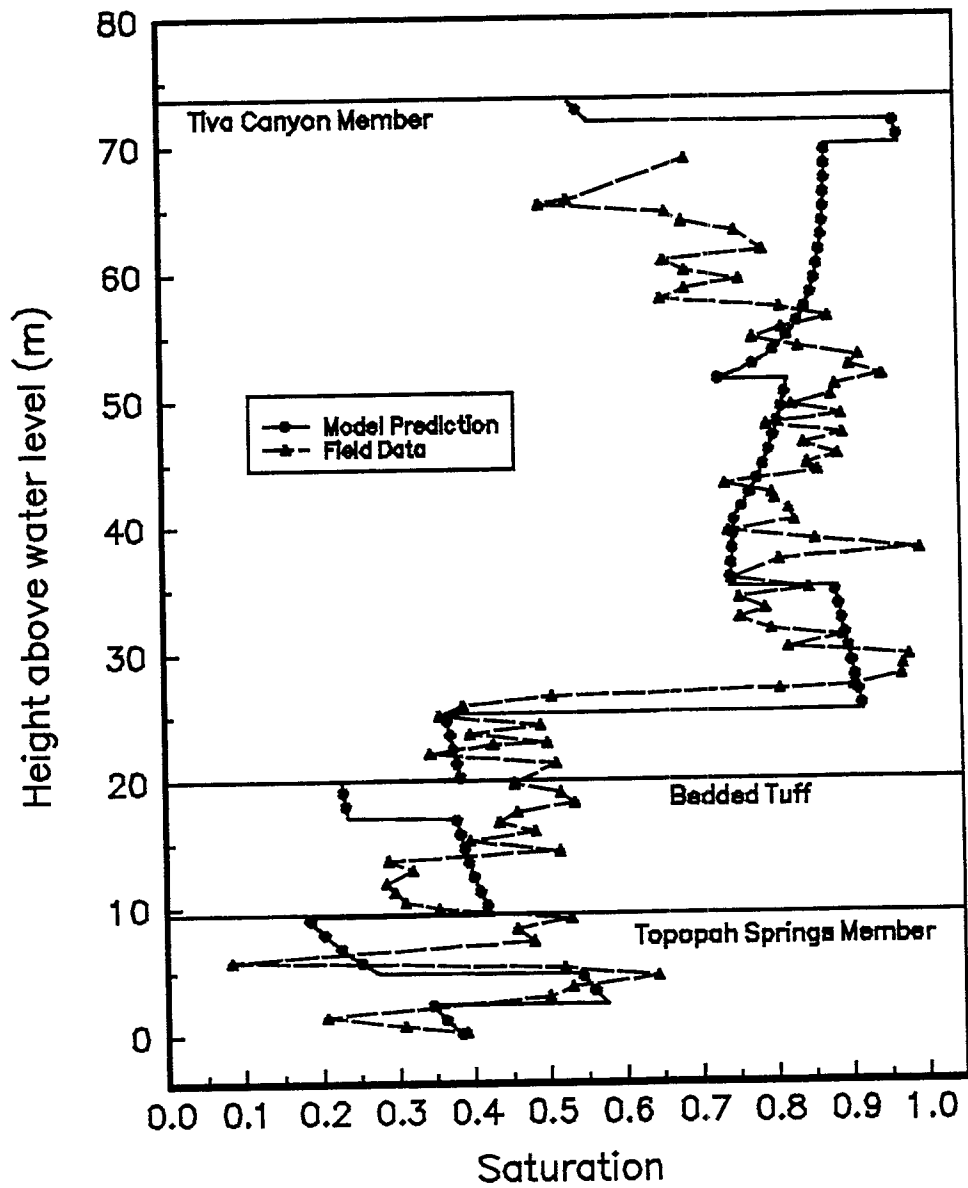


Figure 9-8. Comparison between the predicted and measured water saturation profiles at well bore UZN-54 for a steady-state infiltration rate of  $\sim 0.003$  mm/yr

Research on conceptual models of flow and transport in fractured-porous tuff was only recently initiated. This research activity is integrated with two other research projects. During this reporting period, techniques were assembled for use in determining the unsaturated hydraulic conductivity properties of welded tuff. As these properties are compiled and analyzed, they will be used in conjunction with data from the Geochemical Natural Analog Research Project and Sorption Research Project to formulate conceptual and mathematical models. This activity is at too early a stage to assess its progress toward addressing specific KTU, user needs, or supporting the NMSS IPA activity.

A number of CFD techniques have been evaluated in terms of their applicability to solution of the governing equations of flow and transport in unsaturated fractured-porous media. Many of these CFD methods have been found to be very promising in terms of their accuracy, computational speed, and robustness. However, the degree to which they demonstrate superior performance over numerical techniques currently being used in existing hydrologic models is yet to be determined. It is expected that this research will yield significant benefits to the enhancement of the total-system and subsystem PA codes. Specific benefits expected include: (i) reduction of computer memory and execution time requirements; (ii) higher spatial resolution; and (iii) robust numerical solutions.

#### **9.4 PLANS FOR NEXT REPORTING PERIOD**

In the next reporting period, research activity will be focused on: (i) the INTRAVAL model validation exercise; (ii) compilation of hydraulic properties for tuff core samples and formulation of conceptual models; and (iii) comparisons of CFD techniques and conventional numerical methods used in hydrologic models. In addition, work will be conducted on the adequacy of current conceptual models of the four disruptive event scenario classes (i.e., volcanism, drilling, seismic, and climatic change) being used in IPA.

Regarding activity on model validation, the model comparisons with the Yucca Mountain field data will be completed and documented. The report on this work will be submitted to the INTRAVAL group for use in the subsequent meeting. During the last quarter of 1993, plans will be developed for continuation of model validation studies through a possible collaboration with the University of Arizona (UAZ). In previous meetings with R. Bassett (UAZ), discussions were held regarding possible use of data from infiltration experiments at Queen Creek (in the vicinity of the Never Sweat Tunnel) as part of a model validation exercise. This possible collaboration with UAZ will be explored in the next reporting period.

Using the hydraulic and geochemical properties for the Peña Blanca cores, conceptual, and mathematical models will be proposed. These models will focus on describing possible matrix-fracture interactions important to long-term migration of radionuclides.

The CFD techniques investigated to date will be compared against the conventional finite difference and finite element techniques used in hydrology. A set of computational test cases will be developed that will challenge the capabilities of both classes of numerical methods. In addition, current work on evaluation of various iterative matrix solution techniques (not reported here) will be completed and documented. Those CFD techniques and matrix methods that prove superior to current techniques will be transferred to existing codes such as PORFLO (Runchal and Sagar, 1992) and BIGFLOW (Bagtzoglou et al., 1992).

## 9.5 REFERENCES

- Baca, R.G., and S.O. Magnuson. 1992. *FLASH – A Finite Element Computer Code for Variably Saturated Flow*. EGG-GEO-10274. Idaho Falls, ID: EG&G Idaho, Inc.
- Baca, R.G., G.W. Wittmeyer, and S. Yokuda. 1993. Chapter 9 Performance Assessment Research. *NRC High-Level Radioactive Waste Research at CNWRA, July 1 through December 31, 1992*. CNWRA 92-02S. San Antonio, TX: Center for Nuclear Waste Regulatory Analyses: 9-1 through 9-26.
- Bagtzoglou, A.C., R. Ababou, and A. Nedungadi. 1992. *BIGFLOW: A Multi-Dimensional Code for Flow in Heterogeneous and Variably Saturated Geologic Media (Theory and User's Manual, Version 1.0)*. CNWRA 92-026. San Antonio, TX: Center for Nuclear Waste Regulatory Analyses.
- Bank, R.E. 1990. *PLTMG: A software package for solving elliptic partial differential equations; User's Guide 6.0*. Philadelphia, PA: *Society for Industrial and Applied Mathematics*.
- Basdevant, C., M. Deville, P. Haldenwang, J.M. Lacroix, J. Quazzani, R. Peyret, and A.T. Patera. 1986. Spectral and finite difference solutions of the Burgers equation. *Computers and Fluids* 14: 23-41.
- Canuto, C., M.Y. Hussaini, A. Quarteroni, and T.A. Zang. 1988. *Spectral Methods in Fluid Dynamics*. New York: Springer-Verlag.
- Celia, M.A., E.T. Bouloutas, and R.L. Zarba. 1990. A general mass-conservative numerical solution for the unsaturated flow equation. *Water Resources Research* 26: 1483-1496.
- Celia, M.A. 1991. *The One-Dimensional Princeton Unsaturated Code*. Fundamentals of Unsaturated Zone Modeling Short Course. Princeton, NJ: Princeton University.
- Dykhuisen, R.C., and R.W. Barnard. 1992. *Groundwater Flow Code Verification "Benchmarking" Activity (COVE-2A): Analysis of Participant's Work*. SAND89-2558. Albuquerque, NM: Sandia National Laboratories.
- Gauthier, J.H. 1993. The most likely groundwater flux through the unsaturated tuff matrix at USW H-1. *Proceedings of the Fourth High-Level Radioactive Waste Management Conference, Las Vegas, Nevada, April 26-30, 1993*. American Nuclear Society and American Society of Civil Engineers.
- Gottardi, G., and M. Venutelli. 1992. Moving finite element model for one-dimensional infiltration in unsaturated soil. *Water Resources Research* 28(12): 3259-3267.
- Klavetter, E.A., and R.R. Peters. 1986. *Estimation of Hydrologic Properties of an Unsaturated, Fractured Rock Mass*. SAND 84-2642. Albuquerque, NM: Sandia National Laboratories.
- Long, A., and S.W. Childs. 1993. Rainfall and net infiltration probabilities for future climate conditions at Yucca Mountain. *Proceedings of the Fourth High-Level Radioactive Waste Management Conference, Las Vegas, Nevada, April 26-30, 1993*. American Nuclear Society and American Society of Civil Engineers.

- Miller, K., and R.N. Miller. 1981. Moving Finite Elements, I. *Society for Industrial and Applied Mathematics Journal of Numerical Analysis* 18(6): 1019-1032.
- Nguyen, H.D., S. Paik, and J.N. Chung. 1993. Application of vorticity integral conditioning to Chebyshev pseudospectral formulation for the Navier-Stokes equations. *Journal of Computational Physics* 106: 115-124.
- Pearcy, E.C., B.W. Leslie, W.M. Murphy, and R.T. Green. 1993a. *Geochemical Natural Analogs: Report on Research Activities for the Quarter July 1 through December 31, 1992*. B. Sagar, ed. CNWRA 92-02S. San Antonio, TX: Center for Nuclear Waste Regulatory Analyses: 7-1 through 7-24.
- Pearcy, E.C., J.D. Prikryl, W.M. Murphy, and B.W. Leslie. 1993b. *Uranium Mineralogy of the Nopal I Natural Analog Site, Chihuahua, Mexico*. CNWRA 93-012. San Antonio, TX: Center for Nuclear Waste Regulatory Analyses.
- Runchal, A.K. and B. Sagar. 1992. *PORFLOW: A Multifluid Multiphase Model for Simulating Flow, Heat Transfer, and Mass Transport in Fractured Porous Media, User's Manual, Version 2.40*. CNWRA 92-003. San Antonio, TX: Center for Nuclear Waste Regulatory Analyses.
- Whitfield, S., C.M. Cope, and C.L. Loskot. 1993. *Borehole and Geohydrologic Data for Test Hole USW UZ-6, Yucca Mountain Area, Nye County, Nevada*. Open-File Report 92-28. U.S. Geological Survey: 34.
- Patera, A.T. 1984. A spectral element method for fluid dynamics: Laminar flow in a channel expansion. *Journal of Computational Physics* 54: 468-488.
- van Genuchten, M.Th., F.J. Leij, and S.R. Yates. 1991. *The RETC Code for Quantifying the Hydraulic Functions of Unsaturated Soils*. EPA/600/2-91/065. Ada, OK: U.S. Environmental Protection Agency: Office of Research and Development: Robert S. Kerr Environmental Research Laboratory.

# 10 VOLCANISM RESEARCH

*by Charles B. Connor and Brittain E. Hill*

*Investigators: Charles B. Connor, Brittain E. Hill, Kathy H. Spivey (CNWRA)*

*NRC Project Officer: L.A. Kovach*

## 10.1 TECHNICAL OBJECTIVES

Characterization of the frequency and nature of past volcanic events in the Yucca Mountain region (YMR) and assessment of the probability and consequences of future volcanism are critical aspects of prelicensing scientific investigation. The technical objectives of the Volcanic Systems of the Basin and Range Research Project are to: (i) assess the probability of continued magmatic activity in the YMR; (ii) develop models that better predict the interaction between structure and volcanism in this tectonic setting; and (iii) develop scenarios for the potential impact of volcanism on the candidate Yucca Mountain repository. Effective review of the U.S. Department of Energy (DOE) license application will require insight into volcanic processes operating in the YMR on several scales. These processes include assessment of: western Great Basin tectonic and structural controls on volcanism on local scales ( $10^2$  to  $10^3$  km<sup>2</sup>), the longevity of vent complexes and individual volcanoes in the western Great Basin, and the relationship between specific mappable faults, joints and fractures, and volcanic conduits such as dikes and dike swarms. The western Great Basin has been the site of recurring small-volume basaltic volcanism throughout the Quaternary. Modern analogs and theoretical studies have demonstrated convincingly that this activity encompasses a variety of eruption styles, from the gentle effusion of lavas to sub-Plinian and Plinian-style activity that has produced large and highly dispersive ash columns (e.g., Williams, 1950; McGetchin et al., 1974; Wilson et al., 1978; Wilson, 1980; Amos et al., 1983; Head and Wilson, 1989). The Volcanic Systems of the Basin and Range research project has been designed to assess the probability of future volcanism in the YMR, taking into account the range of activity and the structural controls on activity that are an inherent part of western Great Basin volcanism.

Insight gained through the Volcanic Systems of the Basin and Range research project will support the following sections of the License Application Review Plan (LARP): (i) evidence of igneous activity as a potentially adverse condition, Section 3.2.1.9, (ii) impact of volcanism on groundwater movement, Section 3.2.2.7, and (iii) assessment of compliance with the requirement for cumulative releases of radioactive materials, Section 6.1. Research is necessary to develop these three sections of the LARP for the purpose of providing the U.S. Nuclear Regulatory Commission (NRC) with the methodology and acceptance criteria to determine DOE compliance with 10 CFR Part 60 requirements. Compliance Determination Strategies (CDS) and Compliance Determination Methods (CDM) for these LARP sections are currently under development. However, the CDS associated with evidence of Quaternary volcanism includes Key Technical Uncertainties (KTU) of Type 5, indicating that independent research by NRC may be required to evaluate volcanism, and that volcanism poses a high risk of NRC reaching unwarranted conclusions regarding compliance with 40 CFR Part 191 and 10 CFR Part 60.122(c)(15).

To date, three KTUs related to igneous activity have been identified as part of the CDS concerned with evidence of Quaternary igneous activity. These KTUs are:

- Low resolution of exploration techniques to detect and evaluate igneous features (Type 4)

- Inability to sample igneous features (Type 5)
- Development and use of conceptual tectonic models as related to igneous activity (Type 5)

Evaluation of these KTUs will require detailed safety review supported by analyses (Type 4), and detailed safety review supported by independent tests, analyses, and other investigations (Type 5). Additional KTUs related to igneous activity will likely be identified in a forthcoming CDS on rates of tectonic activity. The Volcanic Systems of the Basin and Range project will address each of these KTUs. For example, development of a computerized database of volcanism in the western Great Basin will provide a basis for assessment of spatial and temporal patterns in volcanism in this region. This database, in conjunction with other ongoing research programs, will aid in the development of models describing the mechanisms that control the formation of igneous features. This investigation addresses KTUs related to development and use of conceptual tectonic models as related to igneous activity (Type 5). Successful completion of the Volcanic Systems of the Basin and Range project and efficient integration with the LARP will require interaction with the Field Volcanism research project, an NRC research project that concentrates on eruption energetics, degassing, and controls on magma movement at shallow levels; the Tectonic Setting of the central Basin and Range research project; and Geologic Setting Element Task 3 (Division of High-Level Waste Management) on faulting and dike interaction. The Volcanic Systems of the Basin and Range project, together with these associated investigations, will form the basis of volcanism models in Iterative Performance Assessment (IPA). The link between volcanism studies and IPA has been established, with preliminary probability models serving as the basis for IPA phase 2 scenarios for volcanism. Volcanism research also provides support of NRC reactive work during the precicensing stage. Results of the Volcanic Systems of the Basin and Range research project are utilized in reactive work, including at NRC-DOE Technical Exchanges and in the review of Topical Reports, Study Plans, and related reports.

Research efforts in the Volcanic Systems of the Basin and Range project are primarily directed toward the development of probability models of potential volcanic events in the YMR, based on geologic insight into tectonic processes operating in the western Great Basin and geologic controls on areal basaltic volcanism in general. Key elements of the research design include the development of robust probability models for basaltic volcanism and creation of a comprehensive database on basaltic volcanism in the southwestern United States. Review of the regional tectonic setting of basaltic volcanism in the Great Basin, Task 1 of this project, is provided by Stirewalt et al. (1992). Connor and Hill (1993) discuss initial work on probability model development and the nature of basaltic volcanism in the YMR. This current report describes research activities since January 1993.

## **10.2 SIGNIFICANT TECHNICAL ACCOMPLISHMENTS**

Work during this reporting period has concentrated on data-gathering activities and probability model development. Data have been compiled for several volcanic fields in the southwest United States. These fields include the Cima Volcanic Field, California; the San Francisco Volcanic Field (SFVF), Arizona; and the Lunar Crater - Pancake Range Volcanic Field, Nevada. Probability model development under Tasks 3 and 4 of this project has focused on near-neighbor nonhomogeneous Poisson models. Furthermore, a review of geochronological information on the volcanoes of the YMR and estimates of recurrence rate has been undertaken as part of Task 2 activities. Most model development and probability analysis accomplished in this research project have been applied directly to the YMR. Additional statistical analyses have been made for the San Francisco volcanic field. These analyses include:

performance of statistical tests to characterize volcano distributions, preparation of a density kernel cluster analysis of volcano distribution in the San Francisco Volcanic Field, and completion of an alignment analysis of vents using Hough transform and two-point azimuth techniques. The primary goal of these analyses has been to characterize important aspects of volcano distribution, such as the development of cinder cone clusters, alignment development, and the relationship between alignments and mapped faults. Volcanism in the SFVF is in several respects analogous to that of the YMR. The SFVF, however, has been the site of a great deal more volcanic activity in the Quaternary. The large number of volcanoes in the SFVF enables more rigorous statistical analysis and investigation of the mechanisms governing cinder cone formation and distribution than is possible in the YMR.

Specific improvements made during the last 6 months to probability models of volcanism in the YMR include:

- Review and analysis of models of recurrence rate for new volcanoes in the YMR
- Analysis of the uncertainty in the age of volcano formation in the YMR
- Development of an approach to differentiate between various near-neighbor nonhomogeneous Poisson models based on comparison with expected regional recurrence rate
- Incorporation of uncertainty in volcano age, YMR recurrence rate, and area affected by sub-volcanic igneous intrusion during volcanic activity into nonhomogeneous probability models

These improvements are discussed in the next subsection, followed by a discussion of initial work on the computerized database and an analysis of vent distribution in the SFVF.

### 10.2.1 Recurrence Rates for Volcano Formation in the YMR

Most estimates of recurrence rate for basaltic volcanism in the YMR during the late Quaternary vary from about 1 volcano/million years (v/my) to 8 v/my (e.g., Ho, 1991; Ho et al., 1991; Crowe et al., 1982, 1992; Margulies et al., 1992). This range in estimated recurrence rate is a result of the application of various averaging techniques and statistical estimators. For example, one approach is to consider the number of volcanoes formed in the YMR over the last 1.8 million years (Crowe et al., 1982). A total of eight volcanoes formed in the YMR during this period of time, which gives a recurrence rate of approximately 4 v/my. Crowe et al. (1992) consider the two Little Cones to represent a single magmatic event, and, therefore, conclude that there are seven Quaternary centers in the region (Figure 10-1). This conclusion lowers the estimated recurrence rate slightly. However, five of these volcanoes are thought to be  $1.2 \pm 0.4$  Ma (e.g., Vaniman and Crowe, 1981; Crowe et al., 1992), and the remaining three are less than 0.5 Ma (Table 10-1). By averaging over this period of activity, the late Quaternary recurrence rate is  $7 \pm 2$  v/my and is slightly lower if the Little Cones are considered to be a single event. Quaternary recurrence rate estimates based on maximum likelihood estimation and repose times are between 5 v/my and 5.9 v/my (Ho et al., 1991).

Basalts emplaced since the formation of the Timber Mountain caldera complex are collectively termed post-caldera basalts (Crowe et al., 1986) and can be used to estimate the regional recurrence rate since the late Miocene. These basalts include late Miocene and Pliocene rocks of the Nye Canyon, Pahute Mesa, Paiute Ridge, and Rocket Wash areas, as well as Plio-Quaternary basalts of the Crater Flat area (Figure 10-1). Average post-caldera basalt recurrence rate during the last 9 million years is about 3 v/my.

Table 10-1. Locations of volcanic centers and ages used for statistical models. Vent locations from Crowe (1990), and ages from Crowe et al. (1982; 1983), Vaniman and Crowe (1981), Crowe and Perry (1991), and Crowe, B.M., 1992, written communication. Vent coordinates in Universal Transverse Mercator, zone 11, Clarke 1866 spheroid.

Name	Age (Ma)	UTM easting	UTM northing	Name	Age (Ma)	UTM easting	UTM northing
Amargosa Valley SW	≈ 4.0	543376	4048820	Hidden Cone	0.3±0.2	523301	4113698
Amargosa Valley	≈ 4.0	544817	4050859	Thirsty Mesa	≈ 4.5	528129	4112249
Amargosa Valley NE	4.4	550306	4053139	Rocket Wash	8.0±0.2	535539	4109028
Lathrop Wells	0.13±0.05	543737	4060073	Buckboard Mesa	2.8±0.1	554946	4109111
Crater Flat S	3.7±0.2	541493	4066057	Pahute Mesa W	9.8±0.4	548758	4133489
Crater Flat E	3.7±0.2	543704	4067644	Pahute Mesa	8.8±0.1	554170	4134467
Crater Flat W	3.7±0.2	540584	4067787	Pahute Mesa E	≈ 9.8	561927	4132182
Crater Flat NW	3.7±0.2	539915	4070959	Paiute Ridge S	8.5±0.3	593698	4101888
Crater Flat W	3.7±0.2	536879	4068573	Paiute Ridge N	8.5±0.3	593611	4103166
Little Cone SW	1.2±0.4	534626	4069423	Scarp Canyon	8.7±0.3	595625	4103906
Little Cone NE	1.2±0.4	534825	4069884	Nye Canyon N	6.8±0.2	603210	4091744
Red Cone	1.2±0.4	537259	4071648	Nye Canyon	6.8±0.2	602370	4085671
Black Cone	1.2±0.4	538257	4074275	Nye Canyon SE	6.8±0.2	600999	4082470
Northern Cone	1.2±0.4	540088	4079455	Nye Canyon SW	6.8±0.2	599557	4083139
Little Black Peak	0.3±0.2	521298	4111346				

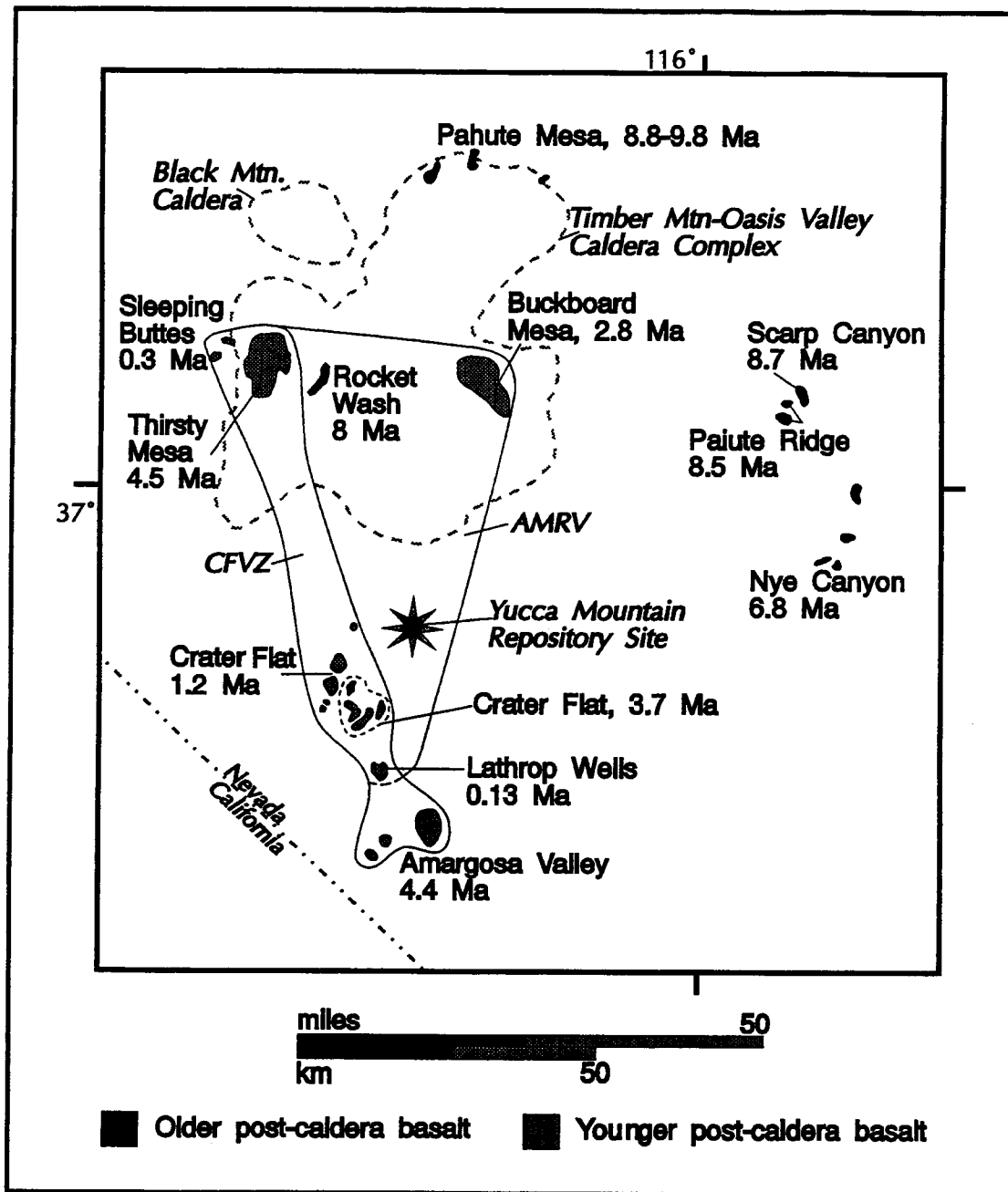


Figure 10-1. Post-caldera basaltic vent locations in the YMR, modified from Crowe (1990). Basaltic units are shaded by relative age, and mean numeric age is posted (also see Table 10-1). Miocene calderas of the Timber Mountain caldera complex are outlined by the dashed lines. The area of most recent volcanism (AMRV) defined by Smith et al. (1990) and the Crater Flat volcanic zone (CFVZ) defined by Crowe and Perry (1989) are outlined and shaded. The AMRV includes all volcanoes in the region younger than about 4.5 Ma; the CFVZ is a narrow zone, approximately 12 km in width and 70 km long, that includes all Quaternary volcanoes in the YMR, Thirsty Mesa, and the Amargosa Valley vents. The location of the proposed HLW repository is also indicated (star).

The lower regional recurrence rate since the late Miocene compared to the late Quaternary rate may be due to either a true increase in the recurrence rate of basaltic volcanism through time in the region, or may simply reflect the increased difficulty in identifying poorly preserved, older vents in the region. The latter seems likely, given the relatively large amounts of erosion and deposition in the area. For example, three Amargosa Valley vents (Figure 10-1) were identified through the interpretation of distinctive aeromagnetic anomalies (Kane and Bracken, 1983; Langenheim et al., 1993). It seems likely that other Miocene and Pliocene volcanoes may have been eroded or buried deeply enough to make vents undetectable. A recurrence rate of less than about 3 v/my is anomalously small for the area, even averaged over the last 9 million years. However, Perry and Crowe (1992) have argued that volcanism is waning in the YMR, and, therefore, lower recurrence rates should be considered. Although volumes of Quaternary eruptions apparently are smaller than Neogene eruptions (Crowe et al., 1982), the Quaternary rate of cinder cone formation is higher than Neogene rates. The available geochronological and volcanological data can be used to support models of waxing (e.g., Ho, 1991), waning (e.g., Perry and Crowe, 1992), or steady-state magmatism (Crowe and Perry, 1989). Probability models for volcanic disruption of the candidate high-level waste (HLW) geological repository must encompass a range of regional recurrence rates.

Several models assessing the probability of future volcanic events and the likelihood of a repository-disrupting event rely on the assumption that Plio-Quaternary vents have been emplaced in a temporally or spatially uniform random distribution over some bounded area (e.g., Crowe et al., 1982; Crowe et al., 1992; Margulies et al., 1992). The model proposed by Margulies et al. (1992) is typical. This model assumes a temporally and spatially homogeneous Poisson distribution for volcanic centers. The recurrence rate in the Margulies et al. (1992) model is estimated by summing the number of volcanoes within the area of most recent volcanism (AMRV) of Smith et al. (1990) (Figure 10-1), dividing this number by the area of the AMRV and the time interval over which the vents have been active. Crowe et al. (1982) calculated recurrence rates based on areas drawn out by circles and ellipses about the repository site.

However, homogeneous Poisson models do not accurately describe volcano distributions and are unlikely to reflect accurately the probability of future volcanic activity and may underestimate the probability of volcanic events. Spatial vent clustering has been observed in every large volcanic field in the world, where such patterns have been searched for in a systematic way (Heming, 1980; Hasenaka and Carmichael, 1985; Wadge and Cross, 1988; Connor, 1990; Connor et al., 1992). Crowe et al. (1992) and Sheridan (1992) also have noted that basaltic vents appear to cluster in the YMR. Several investigators have argued that temporally homogeneous Poisson models are inappropriate for volcanic fields in general and the probability of future volcanic events in the YMR in particular (Ho, 1991, 1992; McBirney, 1992; Sheridan, 1992). Sheridan (1992) suggests that one method of accounting for spatial heterogeneity in vent distribution is to assume that post 4 Ma vents in the Crater Flat system are formed as a result of steady-state activity, and that the dispersion of these vents represents two standard deviations on an elliptical Gaussian surface. Sheridan (1992) then modeled the probability of repository disruption by Monte Carlo simulation for both volcanic events and dike intrusions, noting that variations in the shape of the probability surface significantly alter the probability of igneous disruption of the HLW repository. An alternative approach has been to define specific areas in which the recurrence rate of igneous events is increased. For example, Smith et al. (1990) and Ho (1992) define narrow NNE-trending zones within which the average recurrence rate exceeds that of the region. These zones correspond to cinder cone alignment orientations that Smith et al. (1990) and Ho (1992) hypothesize may develop as a result of structural control.

Statistical tests, such as the Hopkins F-test and the Clark-Evans test, indicate that, spatially, volcanoes in the YMR do not have a homogeneous Poisson distribution (Connor and Hill, 1993). The underlying cause of volcano clustering is unknown (Connor, 1990); however, it is likely that cinder cone clustering is related to mantle processes. A possible explanation is that volcano clusters form because successive mantle melting events may occur beneath the same area within a region. In the Springerville Volcanic Field, which consists of approximately seven large clusters (Connor et al., 1992), the mean age of clusters is older in the western part of the field than in the eastern part of the field, possibly because of westward movement of North American lithosphere through time. A similar pattern is seen in the SFVF. In both of these fields, however, activity may occur in more than one cluster simultaneously.

Given that homogeneous Poisson models do not accurately model cinder cone distribution in the YMR, alternative probability models need to be explored. One approach is to estimate expected recurrence rate per unit area at an arbitrary point,  $\lambda_r$ , using varying numbers of near neighbors (Connor and Hill, 1993):

$$\lambda_r = \frac{m}{\sum_{i=1}^m u_i t_i} \quad (10-1)$$

where near-neighbor volcanoes are determined as the minimum,  $u_i t_i$ ,  $t_i$  is the time elapsed since the formation of the  $i^{\text{th}}$  nearest neighbor volcano, and  $u_i$  is an area term dependent on the distance from the point to the  $m^{\text{th}}$  near neighbor, with  $u_i \geq 1 \text{ km}^2$ .

It is possible to differentiate between various near-neighbor nonhomogeneous Poisson models by comparing the observed recurrence rate for the region with the expected regional recurrence rate calculated using near-neighbor methods, determined by integrating the estimated recurrence rates [Eq. (10-1)] over the YMR:

$$\lambda_t = \iint_{XY} \lambda_r(x,y) dy dx \quad (10-2)$$

where  $\lambda_t$  is the estimated YMR recurrence rate, based on the nonhomogeneous model. In practice, recurrence rates,  $\lambda_r$ , are calculated on a grid, and these values are summed over the region of interest:

$$\lambda_t = \sum_{i=0}^m \sum_{j=0}^n \lambda_r(i,j) \Delta x \Delta y \quad (10-3)$$

where, in this case,  $\Delta x$  and  $\Delta y$  are each 2000 m, the grid spacing used in the calculations, and  $m$  and  $n$  are the number of grid points used in the  $x$  and  $y$  directions, respectively. The dependence of expected regional recurrence rate,  $\lambda_r$ , on the number of near-neighbor volcanoes,  $m$ , used in the calculation is illustrated in Figure 10-2. The relationship between the number of nearest neighbor volcanoes and

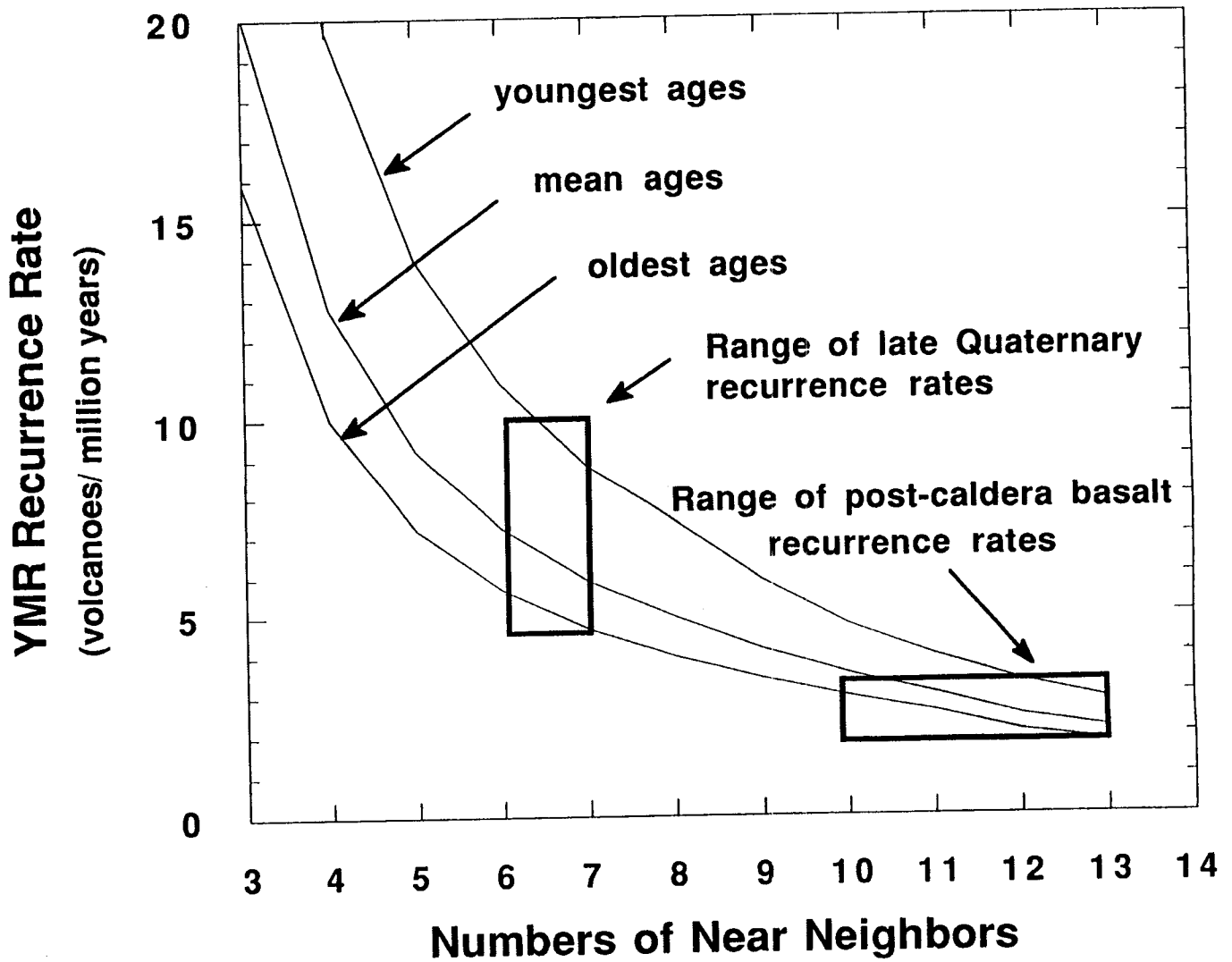


Figure 10-2. Recurrence rate for the formation of new volcanoes in the YMR is estimated using a number of near-neighbor nonhomogeneous Poisson models. Curves are calculated using mean volcano ages, oldest estimated ages, and youngest estimated ages (Table 10-1) to illustrate the effect of uncertainty in volcano age on the models. Calculated recurrence rates decrease with increasing numbers of near neighbors because nearest neighbor volcanoes are young [see Eq. (10-1)]. Comparison with recurrence rates calculated directly from geochronological data indicates that six and seven near-neighbor models most closely approximate late Quaternary recurrence rates; ten to thirteen near-neighbor models most closely approximate post-caldera basalt recurrence rates.

regional recurrence rate depends on the ages of the volcanoes [Eq. (10-1)], which are known with varying precision and accuracy. Consequently, Eq. (10-3) is used to calculate regional recurrence rates using mean volcano ages, and the youngest and oldest ages for each volcano (Table 10-1), based on reported uncertainties (Vaniman and Crowe, 1981; Crowe et al., 1982, 1983; Crowe and Perry, 1991; Crowe, B.M., written comm., 1992). Nonhomogeneous Poisson models using six to seven near-neighbor volcanoes give regional recurrence rates close to those directly calculated for late Quaternary activity in the YMR for mean, oldest, and youngest volcano ages (Figure 10-2). Ten to thirteen near-neighbor volcanoes are required to model recurrence rates similar to the estimated post-caldera recurrence rate of  $\approx 3$  v/my. Therefore, if steady-state volcanism is assumed, in the sense that the frequency of new volcanic center formation is not expected to change during the next 10,000 years, near-neighbor models using between six and seven vents are the most appropriate, because these models most closely reflect rates of late Quaternary activity.

### 10.2.2 Probability Models

The probability of volcanic disruption of the candidate repository site can be estimated assuming a nonhomogeneous Poisson distribution,

$$P [N \geq 1] = 1 - \exp \left[ -t \iint_{XY} \lambda_r(x,y) dy dx \right] \quad (10-4)$$

where the limits of integration define the area of the repository. This relation is closely approximated by:

$$P [N \geq 1] = 1 - \exp \left[ -t \sum_a \lambda_r \Delta x \Delta y \right] \quad (10-5)$$

where  $\Delta x$  and  $\Delta y$  are 1 km and  $a$  is the approximate total area of the repository. These probabilities are very close to the probability of one volcanic event because the probability of two or more events is vanishingly small ( $\approx 1 \times 10^{-9}$ ). The probabilities of volcanic disruption of the repository calculated from a range of near-neighbor models are presented in Figure 10-3. The probability of disruption also is determined for various repository areas calculated using mean volcano ages (Figure 10-4). The area of the candidate repository is currently estimated to be approximately 6 km<sup>2</sup>. Larger area terms are presented to indicate the effects of an increase in repository size, and, more importantly, to account for the area affected by the emplacement of a new volcanic center. Scoria mounds and related satellite vents at Red Cone, Black Cone, and Lathrop Wells (Smith et al., 1990; Crowe et al., 1988) extend for at least 0.5 km around the main vent, which indicates that establishing a new volcanic center within roughly 0.5 km of the repository boundary may result in direct disruption of the candidate HLW repository and potentially transport HLW to the surface. Thus, an area of 8 to 10 km<sup>2</sup> may more accurately reflect the area of concern for establishing a new volcanic center that disrupts the candidate HLW repository. Using the 8 km<sup>2</sup> area, the probability of disruption during a 10,000-year confining period is between  $1.4 \times 10^{-4}$  and  $1.7 \times 10^{-4}$  for a mean late-Quaternary recurrence rate (six to seven near neighbors), and  $6.9 \times 10^{-5}$  to  $9.2 \times 10^{-5}$  for a post-caldera basalt recurrence rate (ten to thirteen near neighbors). Using a range of late Quaternary rates and an 8 km<sup>2</sup> area, the probability of disruption is between  $1.1 \times 10^{-4}$  and

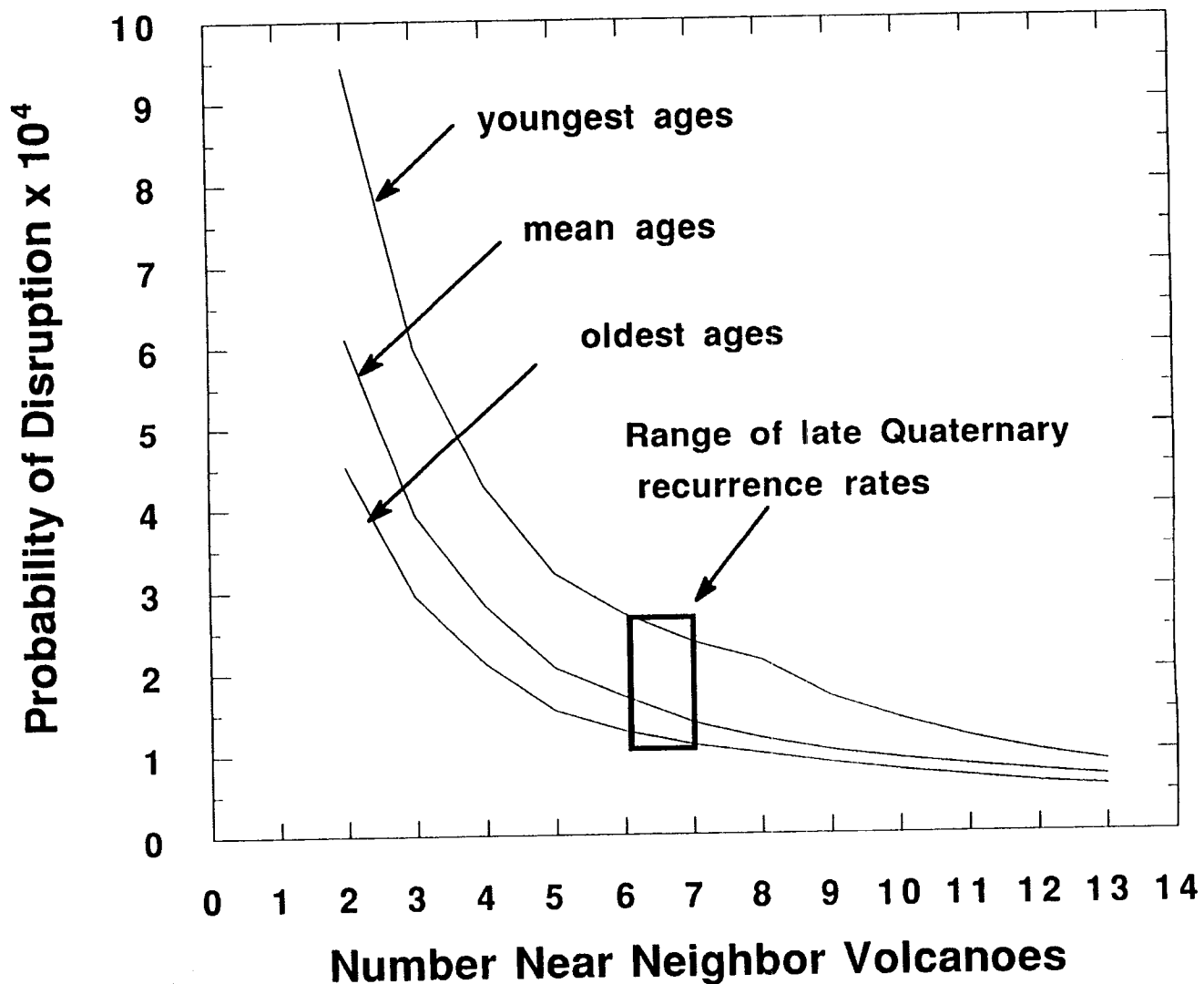


Figure 10-3. Estimated probability of disruption of the HLW repository varies with the number of near neighbors used in nonhomogeneous Poisson models and because of uncertainty in the ages of Quaternary YMR cinder cones (Table 10-1). Calculations are made for the probability of a volcano forming within an 8 km<sup>2</sup> block at the Yucca Mountain repository site (Figure 10-1) during the next 10,000 years. Six to seven near-neighbor models most closely approximate the late Quaternary recurrence rate. Ten to thirteen near-neighbor models most closely approximate the post-caldera basalt recurrence rate.

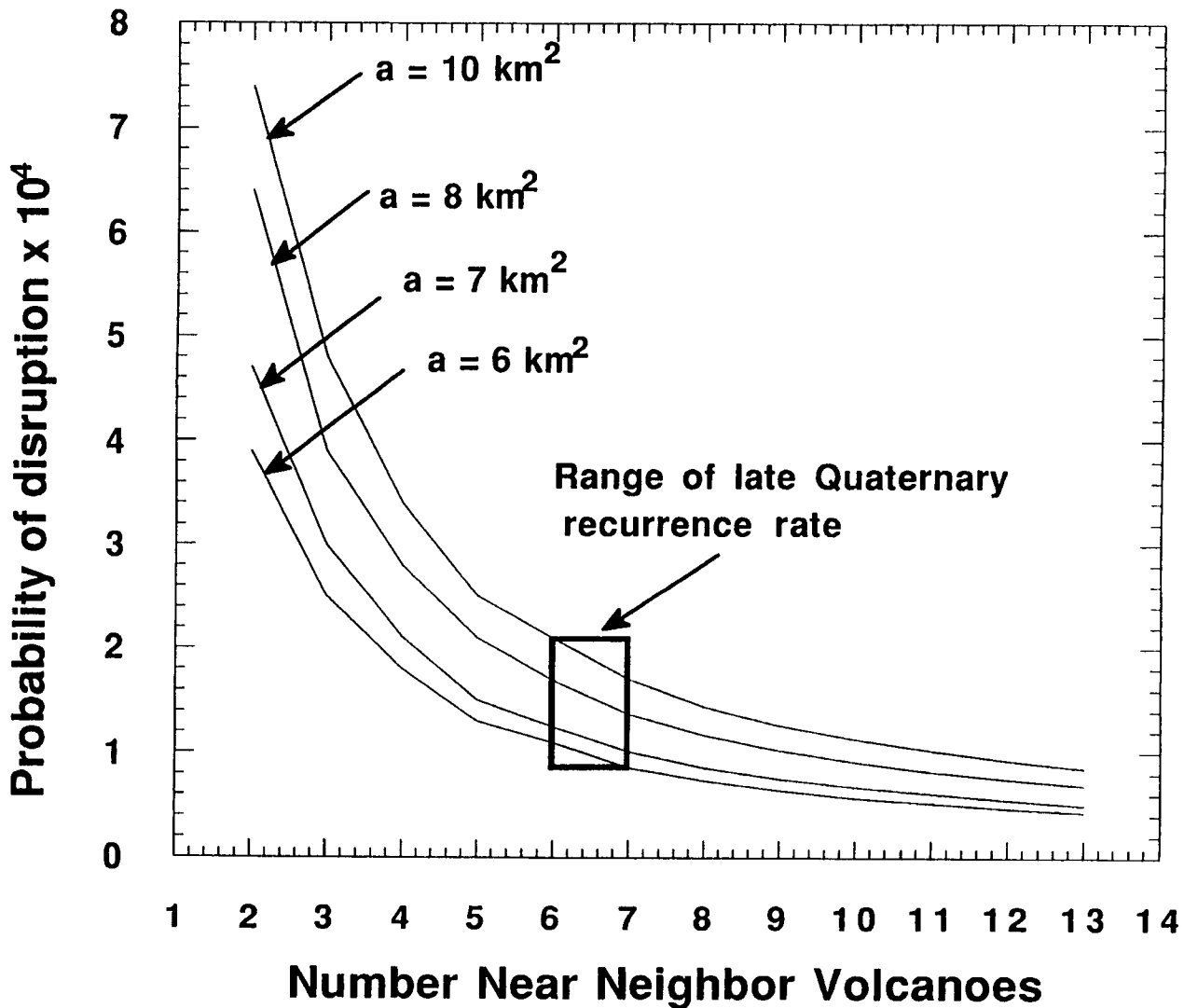


Figure 10-4. Estimated probability of a volcano forming at the repository site (Figure 10-1) increases with increasing area of the site. Magma erupting at main vents located outside the repository perimeter may disrupt the repository, as cinder cones in the region often have satellite vents within 0.5 km of the main vent. Larger area calculations (e.g.,  $a = 10 \text{ km}^2$ ) indicate the probability of disruption taking this factor into account. Calculations are made using mean volcano ages (Table 10-1) and indicate the probability of disruption during the next 10,000 years. Six to seven near-neighbor models most closely approximate the late Quaternary recurrence rate. Ten to thirteen near-neighbor models most closely approximate the post-caldera basalt recurrence rate.

$2.7 \times 10^{-4}$ . For a larger area,  $a = 10 \text{ km}^2$ , and using young volcano ages, the probability of volcanic disruption in 10,000 years increases to  $3.4 \times 10^{-4}$ . Conversely, using the oldest ages for volcanoes and a smaller area,  $a = 6 \text{ km}^2$ , the probability of disruption is  $8.0 \times 10^{-5}$ . Based on the nonhomogeneous Poisson models for various Quaternary recurrence rates and areas, most estimates of the probability of repository disruption are between  $1 \times 10^{-4}$  and  $3 \times 10^{-4}$  for the next 10,000 years (Figures 10-3 and 10-4).

One way to illustrate spatial variation in estimated recurrence rate in the YMR, and hence, the probability of disruptive volcanic events, is to map probabilities calculated from nonhomogeneous Poisson models. Applying Eq. (10-1), the expected recurrence rate is estimated at points on a grid (grid node spacing 2 km) using varying numbers of near neighbors. Probabilities of at least one event occurring within one repository control area ( $8 \text{ km}^2$ ) about each grid point during the next 10,000 years are then calculated [Eq. (10-5)]. Two such maps are illustrated in Figures 10-5a and 10-5b, generated using six and eleven near neighbors, respectively. The tendency for vents to cluster is well illustrated by the  $m = 6$  near neighbors probability map. On this map (Figure 10-5a), the probability of renewed volcanic activity is highest in Crater Flat. South of Red Cone, for example, the probability of a new volcanic center forming in the next 10,000 years within an  $8 \text{ km}^2$  area is between  $1.6 \times 10^{-3}$  and  $2.0 \times 10^{-3}$  for a mean late Quaternary recurrence rate (six to seven near neighbors) and between  $2.0 \times 10^{-4}$  and  $8.0 \times 10^{-4}$  for a post-caldera basalt recurrence rate (ten to thirteen near neighbors). Furthermore, the NNW-trending Crater Flat volcanic zone (Crowe and Perry, 1989) is reflected as an elongation of probability contours due to the presence of young volcanoes at Sleeping Butte. Although the probability of disruption is less using an  $m = 10$  near-neighbor model (Figure 10-5b), the Crater Flat cluster persists as an area of high probability on this plot, and probability contours remain elongated in a NNW direction. In all cases, the probability of volcanic disruption of the candidate HLW repository is high compared with most homogeneous Poisson models (c.f. Crowe et al., 1982; Crowe et al., 1992) because the repository site is relatively close to one of the youngest and largest volcano clusters in the YMR.

### 10.2.3 Summary of Probability Analysis

The distribution of existing volcanic centers in the YMR is not adequately described by a homogeneous Poisson model. Vent clustering in the YMR is statistically significant, and any probability model should reflect this clustering. Nonhomogeneous Poisson probability models calculated by near-neighbor methods can be used to estimate the probability of volcanic disruption of the candidate HLW. Assuming a late Quaternary recurrence rate of  $7 \pm 2 \text{ v/my}$ , these models estimate probability of disruption of between  $8.0 \times 10^{-5}$  and  $3.4 \times 10^{-4}$  in 10,000 years, with most estimates between  $1 \times 10^{-4}$  and  $3 \times 10^{-4}$ . Estimates based on a lower, post-caldera basalt recurrence rate of approximately 3 v/my are between  $6.9 \times 10^{-5}$  and  $9.2 \times 10^{-5}$  in 10,000 years. The repository site is positioned on a probability gradient. West of the candidate site, the probability of volcanism within the next 10,000 years increases substantially due to the presence of late Quaternary volcanoes in Crater Flat Valley. The probability of volcanism within the next 10,000 years decreases east of the candidate repository site. Further refinement of probability models will likely alter these estimates, and they are not intended to represent a complete analysis of the probability of repository disruption by igneous activity. The nonhomogeneous model takes into account one important geological feature of volcanic fields: vents tend to cluster within these fields through time. Additional geological information, such as the importance of pre-existing structure (Smith et al., 1990) or strain rate on volcanism, will need to be taken fully into account before a more refined assessment of the probability of future volcanic activity in the YMR can be made with confidence.

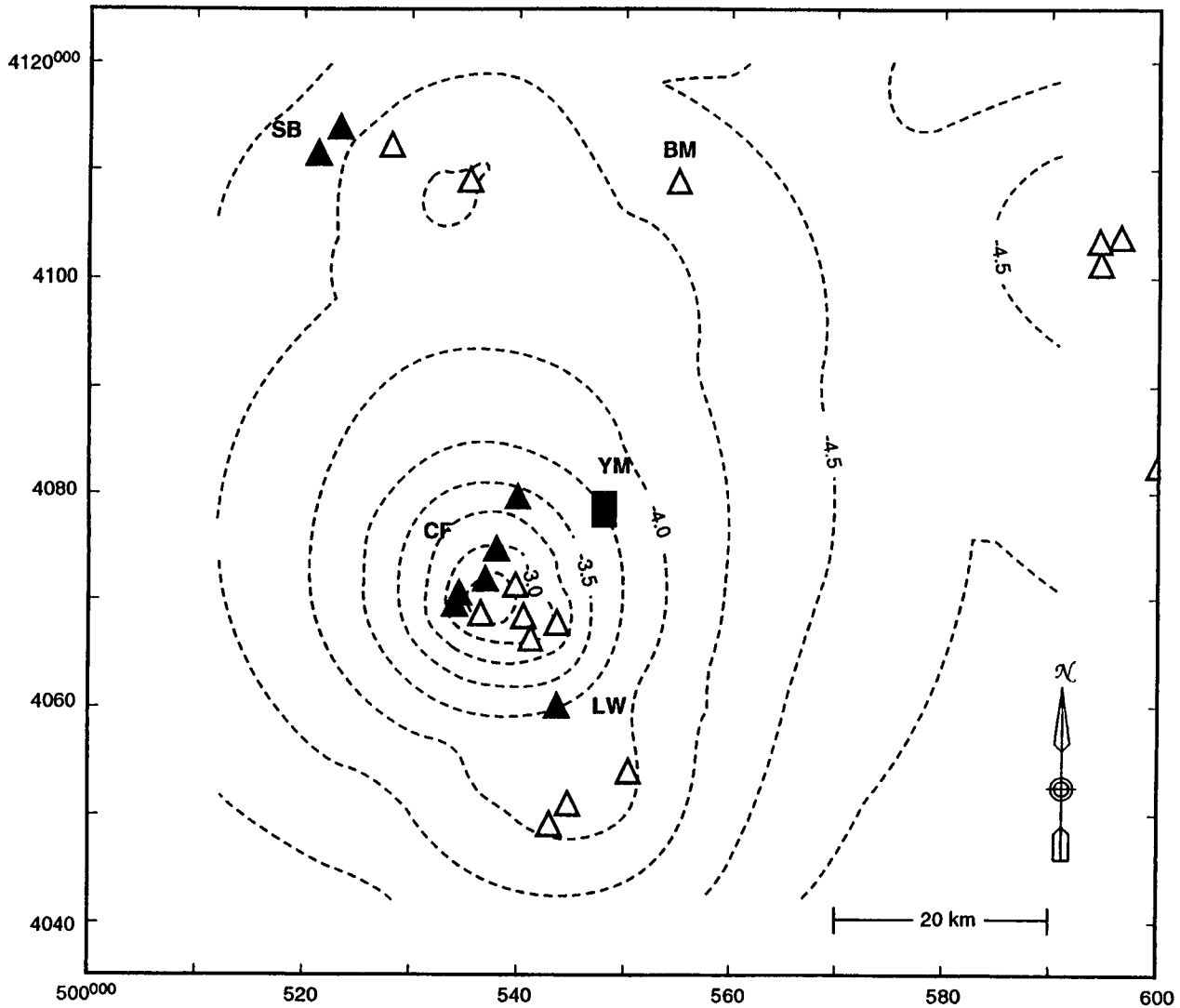


Figure 10-5. Probability of a new volcano forming during the next 10,000 years varies in the YMR because of the tendency for volcanoes to cluster. Here the logarithm of probability of a volcano forming within an  $8 \text{ km}^2$  area during the next 10,000 years is contoured using six near-neighbor (a) and ten near-neighbor (b) nonhomogeneous Poisson models. These models reflect late Quaternary and post-caldera basalt recurrence rates, respectively. Both models indicate that the probability of disruption of the proposed repository (solid rectangle) is higher than in the YMR as a whole due to the relative proximity of the site to Quaternary Crater Flat volcanoes. Solid triangles are Quaternary volcanoes, open triangles are Neogene vents, YM - Yucca Mountain repository, CF - Crater Flat, SB - the Sleeping Butte volcanoes (Little Black Peak and Hidden Cone), BM - Buckboard Mesa, and LW - Lathrop Wells (Table 10-1). The contour interval is  $0.25 \log(P[N \geq 1 \text{ in } 10,000 \text{ yr}])$  (e.g., -4 is a probability of  $1 \times 10^{-4}$  of a new volcano forming within an  $8 \text{ km}^2$  area in 10,000 years). Across the YMR, probabilities vary from more than  $1 \times 10^{-3}$  in Crater Flat Valley (Figure 10-5a) to less than  $1 \times 10^{-5}$ . Map coordinates are in Universal Transverse Mercator, Clarke 1866 Spheroid.

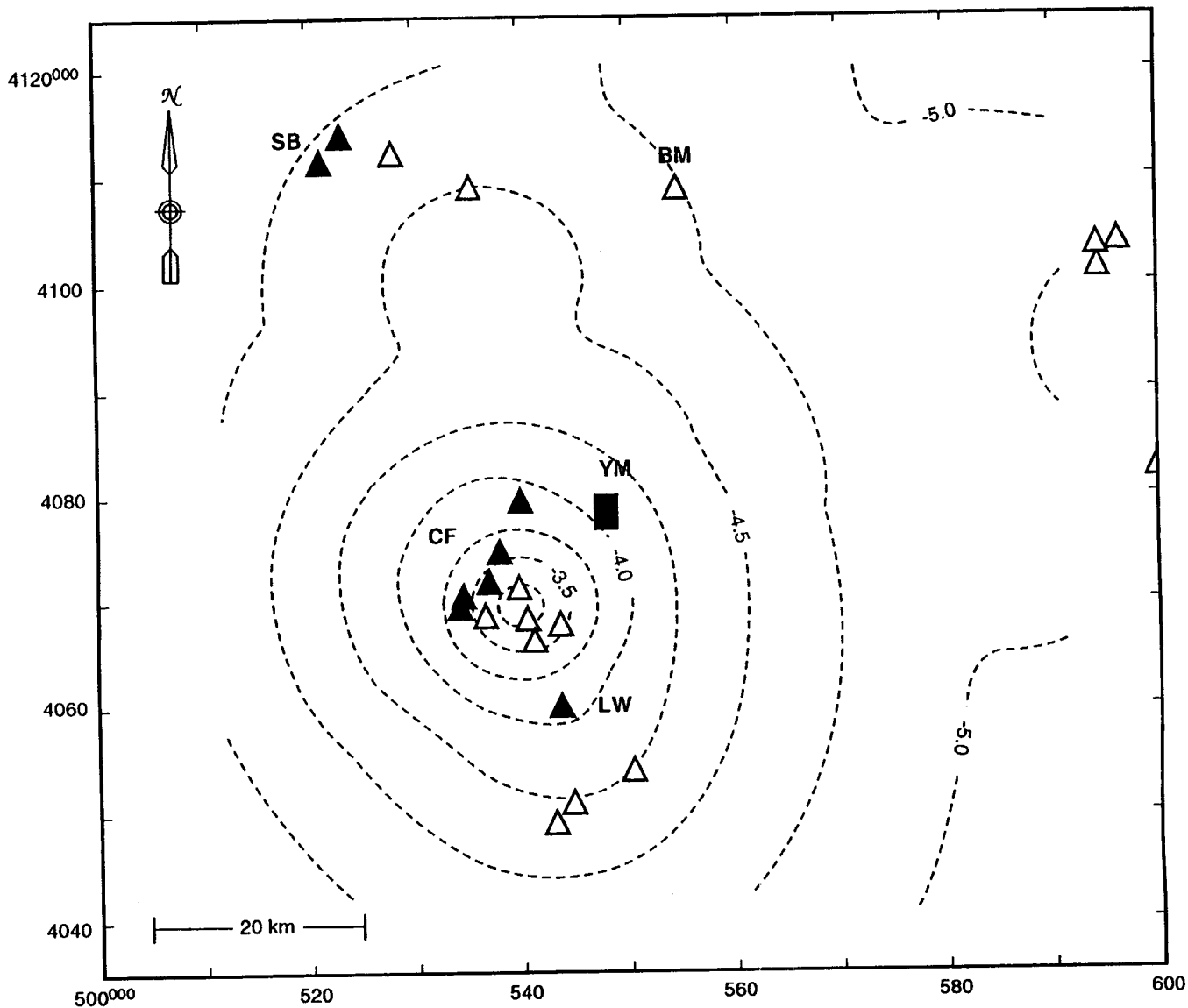


Figure 10-5 (Cont'd). Probability of a new volcano forming during the next 10,000 years varies in the YMR because of the tendency for volcanoes to cluster. Here the logarithm of probability of a volcano forming within an  $8 \text{ km}^2$  area during the next 10,000 years is contoured using six near-neighbor (a) and ten near-neighbor (b) nonhomogeneous Poisson models. These models reflect late Quaternary and post-caldera basalt recurrence rates, respectively. Both models indicate that the probability of disruption of the proposed repository (solid rectangle) is higher than in the YMR as a whole due to the relative proximity of the site to Quaternary Crater Flat volcanoes. Solid triangles are Quaternary volcanoes, open triangles are Neogene vents, YM - Yucca Mountain repository, CF - Crater Flat, SB - the Sleeping Butte volcanoes (Little Black Peak and Hidden Cone), BM - Buckboard Mesa, and LW - Lathrop Wells (Table 10-1). The contour interval is  $0.25 \log(P[N \geq 1 \text{ in } 10,000 \text{ yr}])$  (e.g.,  $-4$  is a probability of  $1 \times 10^{-4}$  of a new volcano forming within an  $8 \text{ km}^2$  area in 10,000 years). Across the YMR, probabilities vary from more than  $1 \times 10^{-3}$  in Crater Flat Valley (Figure 10-5a) to less than  $1 \times 10^{-5}$ . Map coordinates are in Universal Transverse Mercator, Clarke 1866 Spheroid.

#### **10.2.4 Cluster Analysis of San Francisco Volcanic Field Vents Using Computerized Databases**

A computerized geographic information system (GIS) provides the means necessary to construct models relating quantitative physical data to spatial data. In the volcanism research project, a computerized GIS is being constructed to support empirical and theoretical models of volcanism and tectonism for the Basin and Range Province. The volcanism data compiled and manipulated in the GIS originate in the published literature, and include maps, data tables, digitized images, and complex binary geophysical data. Thus, the GIS also will be useful in evaluating the completeness and adequacy of the DOE volcanism database used to demonstrate compliance with 10 CFR Part 60 requirements relating to igneous activity. The GIS and volcanism database will provide confirmatory data for addressing issues related to waste isolation, and provide data that may be required to explore safety issues not adequately addressed by the DOE.

Arc/Info® is a series of computer programs designed to relate tabular and spatial data using real-world geographic coordinates. Arc/Info® also is used by both the NRC and DOE as primary GIS software for the Yucca Mountain Project, and is used by the Center for Nuclear Waste Regulatory Analyses (CNWRA) for the computerized database of volcanic and tectonic data for the Basin and Range. Some of the questions being considered in the volcanism research project include:

- What are the boundaries to volcano clusters, and how can these clusters be described quantitatively?
- Are any specific geologic characteristics unique to a certain vent cluster, or are specific characteristics common to only several clusters?
- Do volcano clusters reflect temporal clusters of activity within the SFVVF, or do clusters develop without any time dependence?
- What are the relationships between exposed faults and volcano locations?
- With a large number of cinder cones, it is possible to create numerous alignments that may or may not be significant. Which of the myriad of possible vent alignments are statistically significant?
- Do cinder cone alignments have the same trends as fault alignments?

It is possible to address these points using a volcanism database and input from spatial analysis programs. Early GIS work with the volcanism database has focused on four areas in the Basin and Range that have relatively abundant geological data: San Francisco Volcanic Field (SFVVF), Arizona; Yucca Mountain and Lunar Crater Volcanic Fields, Nevada; and the Cima Volcanic Field, California (Figure 10-6).

The SFVVF is an ideal area to examine relationships between volcanism and structure, because large amounts of data are available for this regionally extensive field. The SFVVF contains over 600 different basaltic volcanoes, most of which were erupted within the last several million years (Tanaka et al., 1986). Quaternary normal faults are also exposed in the SFVVF, and the area has been mapped in

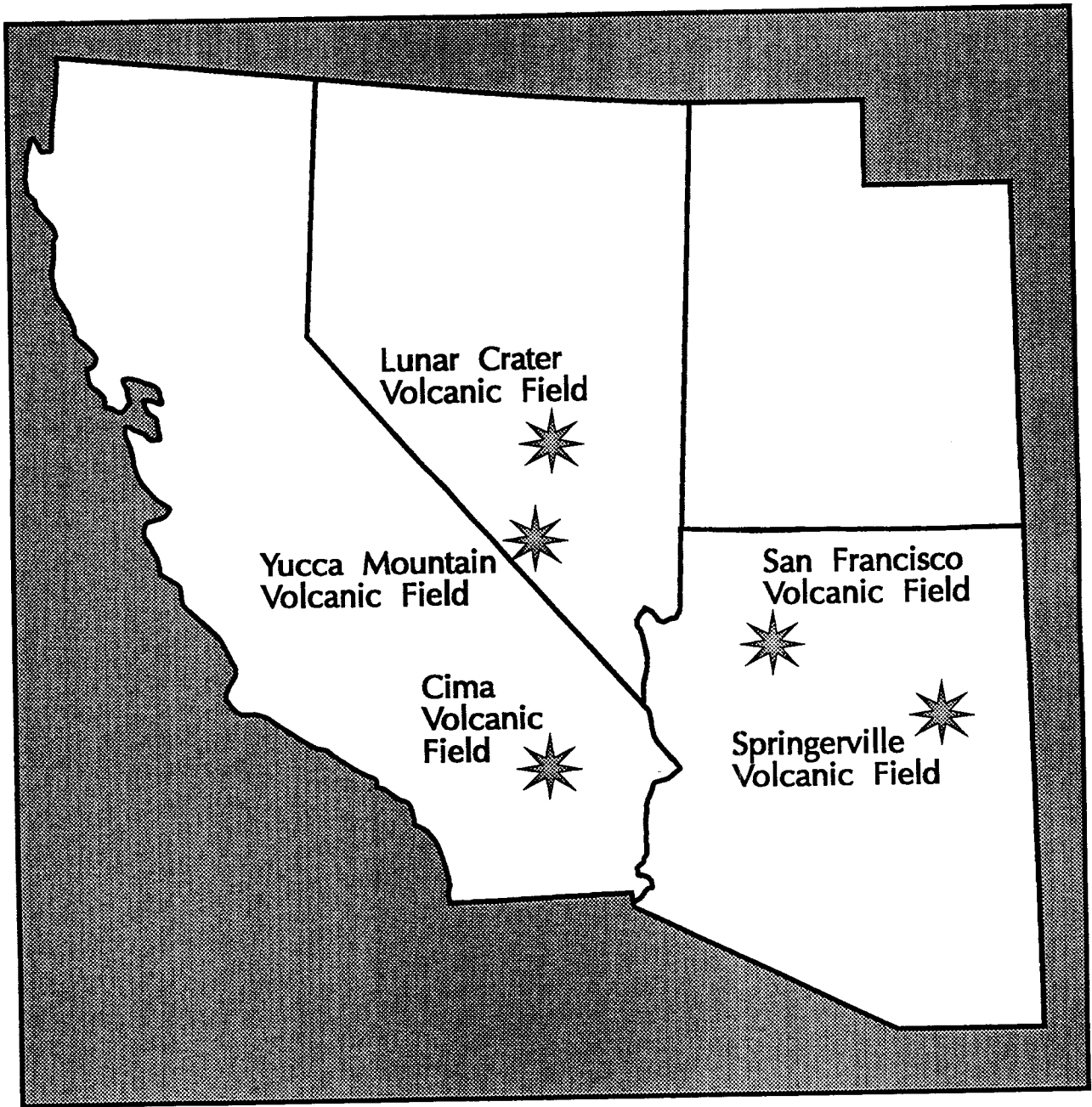


Figure 10-6. Volcanic fields currently under investigation using the GIS and volcanism database

detail by the U.S. Geological Survey (Moore and Wolfe, 1987; Newhall et al., 1987; Ulrich and Bailey, 1987; Wolfe et al., 1987a, 1987b). Detailed geochemical, geochronological, and geophysical data also are available for the SFVF. The distribution of volcanoes and faults in the SFVF appears irregular (Figure 10-7). Visual inspection reveals that volcanoes appear to cluster in certain areas of the field, and at times form alignments. Some apparent volcano alignments are parallel to the strike of nearby faults. A subjective evaluation of volcano clustering and alignment, however, is insufficient to rigorously test hypothesized relationships between volcanism and structure. These features must be characterized quantitatively in order to truly examine possible relationships between volcanism and structure.

Common characteristics of many large volcanic fields are that cinder cones tend to form clusters and that significant geochemical, temporal, and structural variations exist between clusters (e.g., Hasenaka and Carmichael, 1985; Condit et al., 1989; Connor, 1990; Connor et al., 1992). Identification of volcano clusters is also important in quantitative alignment analysis because volcano clustering can affect the distribution and significance of volcano alignments (Connor, 1990). Application of the Hopkins F-test and Clarke-Evans test (Connor and Hill, 1993) indicates that volcano clustering is a significant aspect of distribution in the SFVF. The locations of volcano clusters in the SFVF can be calculated using a variation of the uniform kernel density fusion cluster analysis technique (Wong, 1982; Wong and Lane, 1983; Wong and Schaak, 1982), which is described in detail by Connor (1990). This method searches for spatial groupings of volcanoes based on measured variations in the spatial density of volcanoes. Density fusion analysis does not require any assumptions about cluster shape and is able to distinguish different clusters that overlap slightly. Other cluster analysis techniques require assumptions about cluster shape (e.g., Wong, 1982) or identify clusters solely on the basis of individual points and thus cannot distinguish overlapping clusters (Connor, 1990).

The uniform kernel density fusion cluster analysis is performed by constructing a circle of radius  $r$  around each volcano in the field. The number of volcanoes within this circle is  $f(X_i)$ , for volcano  $X_i$ . An  $n \times n$  matrix is created where  $n$  is the number of volcanic vents in the field and each element in the lower triangle of the matrix is:

$$d^*(X_i, X_j) = \frac{1}{2} \left[ \frac{1}{f(X_i)} + \frac{1}{f(X_j)} \right] \text{ if } d(X_i, X_j) < r \quad (10-6)$$

$$d^*(X_i, X_j) = \infty, \text{ otherwise}$$

and  $d(X_i, X_j)$  is the map distance between  $X_i$  and  $X_j$  volcanoes. An element in the matrix thus will have a small value if volcanoes  $i$  and  $j$  are separated by any distance less than  $r$  and there is a high density of volcanoes around them. Separations less than  $r$  result in large matrix values if there is a low density of volcanoes. If volcano  $i$  and  $j$  are not within  $r$  distance of each other, the element value is set equal to infinity.

After the lower triangle of the matrix is calculated, individual elements in the matrix are joined using a single linkage algorithm that starts with the highest density elements (smallest values of  $d^*$ ) and progresses toward less dense elements (larger values of  $d^*$ ) in the immediate neighborhood. If some elements of the matrix  $d^*(X_i, X_j) = \infty$ , then some volcanoes are separated from near-neighbor volcanoes by a distance greater than the search radius,  $r$ , and a finite number of clusters will be identified. In volcanic fields that consist of comparatively few cinder cones, such as in the YMR, this algorithm is adequate.

## San Francisco Volcanic Field

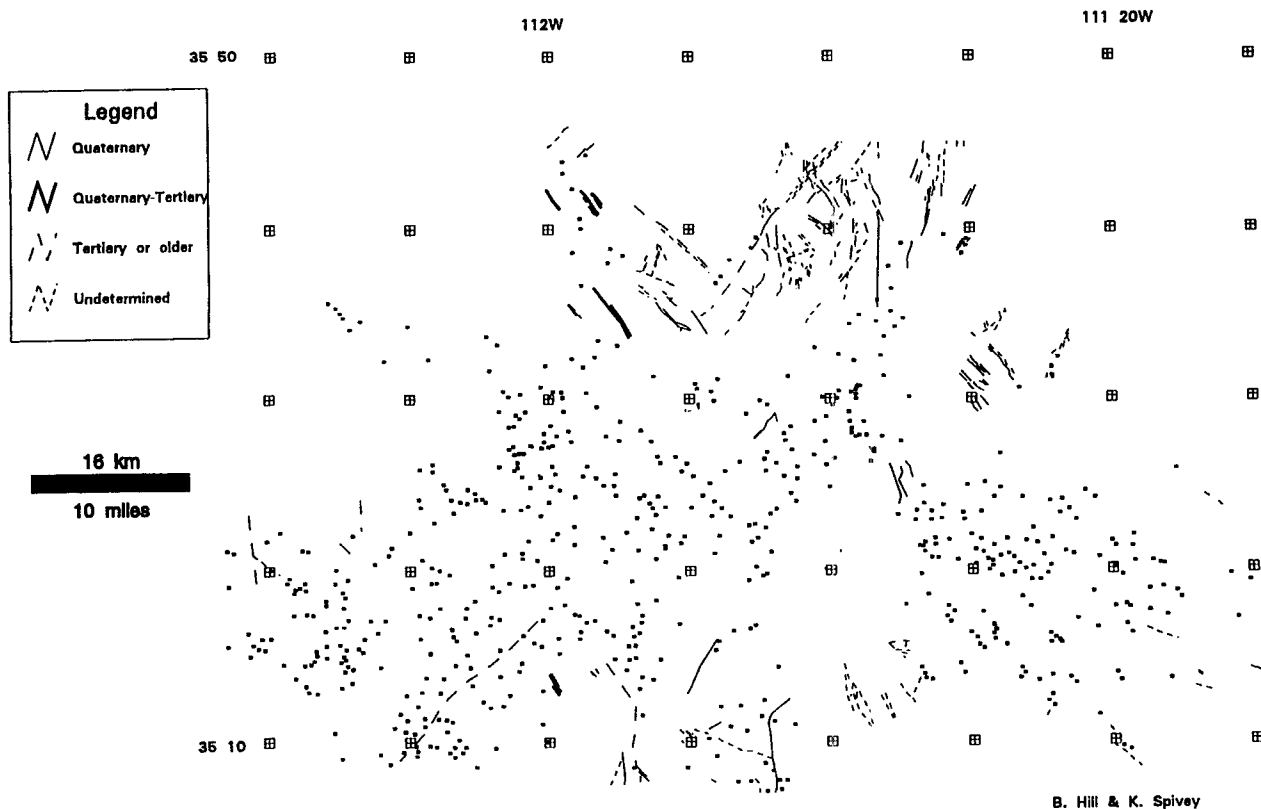


**Figure 10-7. Volcanoes and mapped faults of the SFVF, Arizona. Note that many of the volcanoes form alignments that are subparallel to fault strike and that some volcanoes appear to cluster. Map coordinates are in Universal Transverse Mercator, Clark 1866 spheroid. Map has been reduced 22% during reproduction; actual map scale is 1:700,280. Data from Moore and Wolfe (1987); Newhall et al. (1987); Ulrich and Bailey (1987); and Wolfe et al. (1987a, 1987b).**

In many volcanic fields the large number of cinder cones creates overlap between clusters. In this case clusters are not completely discrete, but are separated by areas of low cinder cone density. This is the case in the SFVF. The Hopkin's F-test and Clark-Evans test indicate that cinder cone clustering is a statistically significant aspect of volcano distribution, but clusters are not isolated; rather, there are significant modes in cinder cone distribution. In order to identify overlapping clusters, the algorithm is modified slightly. If the maximum volcano density in both clusters exceeds the fusion density between the clusters, then the clusters are not joined because each represents a mode in volcano density. In this case, the single linkage algorithm is used iteratively until a stable number of clusters is identified. The number of clusters will depend on the search radius, the density of vents, and the occurrence of gaps in vent distribution.

Cluster analysis of volcanoes in the SFVF was performed by varying the search radius  $r$  from 2 km to 18 km. An individual cluster is significant if its location and membership remains relatively constant with large (i.e., 1 to 10 km) changes in the search radius. For a radius of  $<5$  km, the number and location of clusters vary significantly with decreasing  $r$ . However, the number and location of clusters are relatively stable for a search radius between 6 and 8 km, indicating that clustering is significant at that scale. The results of a cluster analysis using a search radius of 8 km are shown in Figure 10-8. For a search radius greater than about 8 km, there are only a few clusters in the field, indicating that the search radius is too large and is probably combining discrete clusters into anomalously large clusters.

Several of the cinder cones clusters in Figure 10-8 are relatively obvious. For example, cluster 1 forms a fairly distinct group of volcanoes, which is also apparent in Figure 10-7. This cluster is distinct, and its membership remains relatively constant for all search radii between 5 and 12 km, indicating that this clustering is significant. Other volcano clusters, however, are qualitatively indistinct. For example, it is extremely difficult to make a subjective judgment as to the division between clusters 2 and 3 (Figure 10-8). These two clusters are distinct for search radii between 7 and 12 km, indicating that the clustering is significant. Studies are continuing to determine if these clusters are temporally or petrogenetically distinct, or are associated with other unique geological characteristics. Application of the uniform kernel density fusion cluster analysis removes subjective distinctions between apparent volcano clusters and provides a relatively robust and reproducible method to determine volcano clustering.

One of the main goals of the volcanism research program is to examine how faults may influence the location and petrogenesis of volcanoes. Quaternary volcanoes in the YMR align with or are located along normal faults that at times strike into the candidate repository block. Determining how faults can control the location of volcanoes is thus critical to examining the risks that igneous activity may present to the candidate repository.

Many researchers have noted an apparent correlation between the local strike of faults and the trends of volcano alignments in the SFVF and elsewhere (Colton, 1936; Nakamura, 1977; Thompson and Zoback, 1979; Bacon, 1985; Hasenaka and Carmichael, 1985; Tanaka et al., 1986). There are, however, several examples of Basin and Range volcanic fields that lack obvious alignments with mapped faults (e.g., the Cima, Darwin Plateau, and Coso Volcanic Fields, California). Vent locations in other Basin and Range volcanic fields, such as the Yucca Mountain, Piute, Amboy-Pisgah, Tahoe, Battle Mountain and Monarch Divide (e.g., Smith and Luedke, 1984), may be fault controlled, but there are too few volcanoes in these fields to adequately test this hypothesis.

Faults in the SFVF range in age from pre-Tertiary to Quaternary (Tanaka et al., 1986). Examination of Figure 10-8 reveals that some volcanoes form alignments that trend subparallel to the

## San Francisco Volcanic Field

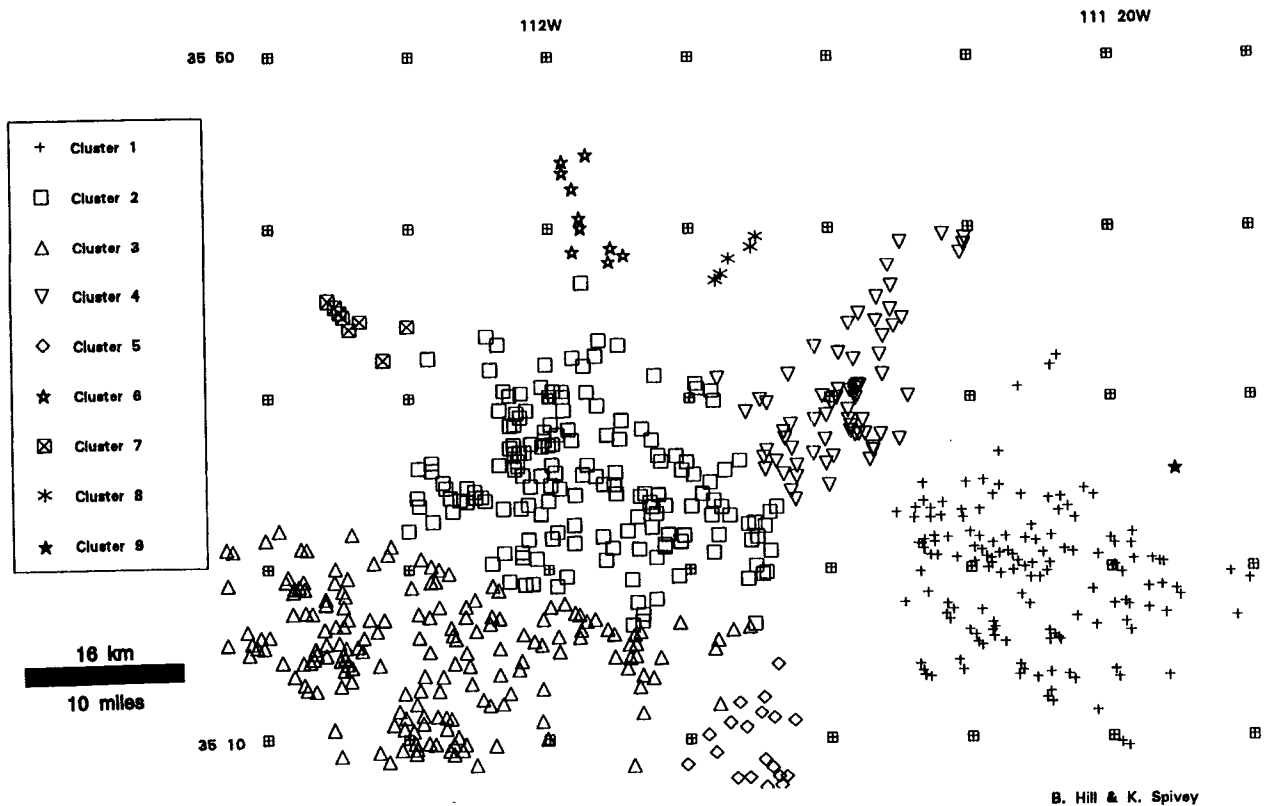


Figure 10-8. Vent clusters of the SFVF, Arizona. Clusters calculated using the uniform kernel density fusion cluster analysis technique described in text. The calculated clusters are at times similar to some of the apparent clusters in Figure 10-7, but additional significant clusters can be calculated. Search radius is 8 km, actual map scale is 1:700,280, Universal Transverse Mercator, Clark 1866 spheroid. Vent locations from Moore and Wolfe (1987); Newhall et al. (1987); Ulrich and Bailey (1987); and Wolfe et al. (1987a, 1987b).

strike of nearby faults. One hypothesis that the SFVF volcanism database can test is that if volcano location is controlled by faults, then some vents should be located close to mapped faults. To test this hypothesis, a buffer zone of 1 km was established around all of the mapped faults in Figure 10-7. Volcanoes located within the 1 km fault buffer are then extracted from the main database (Figure 10-7) and plotted in Figure 10-9. Although only 47 volcanoes out of 604 are located within 1-km of a mapped fault, most of the vent clusters in the SFVF have some volcanoes located within 1 km of mapped faults. This relationship fails to disprove the working hypothesis that some volcanoes are located close to mapped faults.

### 10.2.5 Alignment Analysis of the SP<sup>1</sup> Mountain Cluster

Quantitative cinder cone alignment analysis is an important aspect of volcano distribution studies. The previous section concluded that most of the volcanoes in the SFVF are not located near mapped faults. This finding may indicate that the faults that localized these volcanoes were buried in the ensuing eruptions, or that there is no significant control of vent location by faults. In order to relate volcanic alignments with regional fault alignments, these features must be described quantitatively.

Two-point azimuth (Monte Carlo) simulation (Lutz, 1986) shows that NE-trending alignments are statistically significant within the SP Mountain cluster (#4, Figure 10-8). The two-point azimuth method assumes that the overall shape of the cluster is unimportant and weights the analysis accordingly. This weighting makes it more difficult to identify significant trends in the direction of cluster elongation. Nonetheless, in the SP Mountain cluster, trends of N10-40E are significant with greater than 95 percent confidence, with trends of N30-40E being the most prominent (Figure 10-8). Not only is the cluster elongated NE, but vents align in NE directions within the cluster. This trend is parallel to the Mesa Butte Fault Zone, which is manifested by a prominent set of grabens that trend approximately N35-40E through the area. However, the cinder cones are offset from the Mesa Butte Fault Zone at least 10 to 15 km SE from the main scarp of the Mesa Butte fault. A relationship appears to exist between the trend of SFVF cinder cone alignments and some regional structural trends, which seems analogous to the alignment of late Quaternary cinder cones in Crater Flat Valley. However, as is also the case in the YMR, the exact relationship between the alignment and structure is unclear. For example, it is not clear if the alignments in the SP Mountain cluster are directly related to buried Precambrian faults, such as a splay along the Mesa Butte fault, or whether the alignments reflect the orientation of compressional stress in the crust only and are not related to pre-existing structure.

The Hough transform is used to map actual alignments in the SP Mountain cluster. This transform is a computer enhancement technique, first applied to the study of cinder cone distributions by Wadge and Cross (1988). Alignments are identified using a specified alignment width and angle. In this case, an alignment width of 500 m is used, which may reflect the width of fracture or fault zones associated with cinder cone alignments (Wadge and Cross, 1988 and Connor, 1990). Alignments were searched for in all orientations, at two degree intervals. One problem with the application of the Hough transform to the SP Mountain cluster is the occurrence of a dense concentration of vents near the center of the cluster (Figure 10-10). Because these vents are closely grouped, they control the alignment analysis. Consequently, this group of vents is considered to be one cluster in the analysis.

---

<sup>1</sup>SP Mountain is an official U.S. Geological Survey name and is not an abbreviation.

## San Francisco Volcanic Field

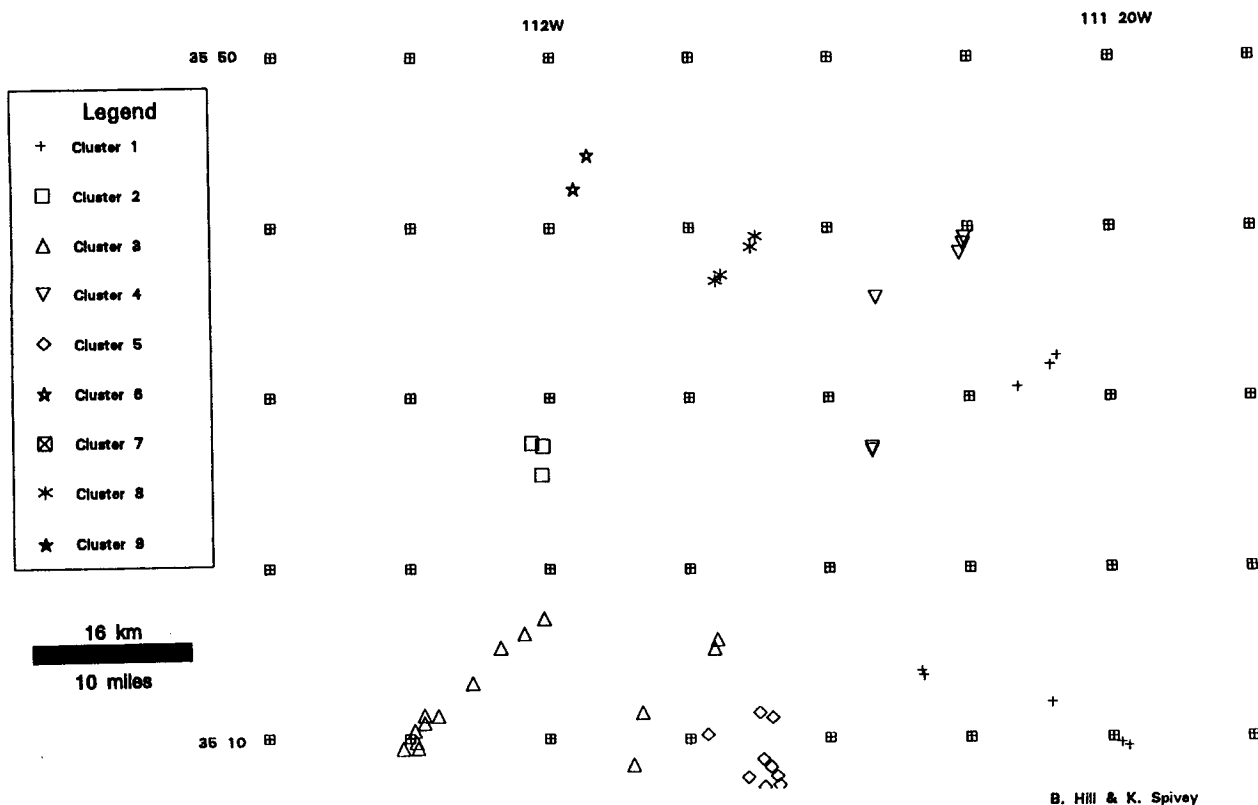


Figure 10-9. Volcanoes of the SFVF, Arizona, that are located within 1 km of a mapped fault. Only 47 of 605 vents are located within 1 km of a mapped fault, which may indicate a lack of direct fault control on vent location or that faults have been buried by subsequent eruptions. Cluster symbols are the same as in Figure 10-8. Actual map scale is 1:700,280, Universal Transverse Mercator, Clark 1866 spheroid. Fault and vent locations from Moore and Wolfe (1987); Newhall et al. (1987); Ulrich and Bailey (1987); and Wolfe et al. (1987a, 1987b).

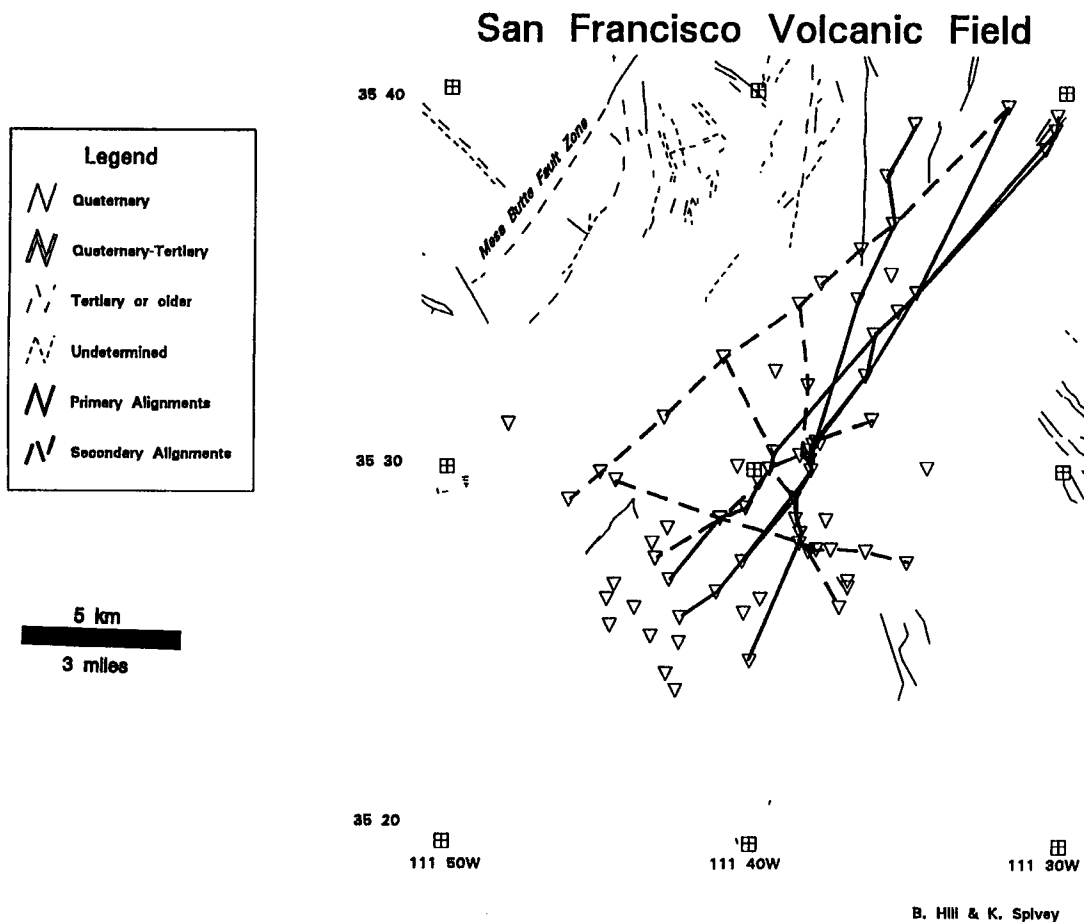


Figure 10-10. Vent alignments of the SP Mountain cluster (#4, Figure 10-8) calculated with the Hough transform every two degrees and an alignment width of 0.5 km. Primary alignments (solid lines) contain 11 or more vents and are oriented N10-40E. Secondary alignments (dashed lines) contain 9 or more vents and are not oriented N10-40E. Fault and vent locations from Ulrich and Bailey (1987). Map coordinates are in Universal Transverse Mercator, Clark 1866 spheroid. Map has been reduced 22 percent during reproduction; actual map scale is 1:204,200.

Alignments mapped using the Hough transform are divided into two groups. Primary alignments are alignments that contain numerous vents and are aligned in an orientation found to be statistically significant by the two-point azimuth analysis, which, in this case, trend N10-40E and consist of 11 or more vents. Secondary alignments consist of fewer vents and are not oriented NE, but may reflect structural control that is simply less pervasive. Three primary alignments have trends of N38-39E, N36-40E, and N25-35E through the center of the cluster (Figure 10-10). Together these alignments form a prominent NE-trending alignment zone that is approximately 30 km long and 5 km wide. Older Quaternary basalt vents (Ulrich and Bailey, 1987) comprise the NE part of the alignment zone, and younger Quaternary basalt vents comprise the SW part. Cinder cones are not evenly spaced along the alignments, rather they tend to form in groups of three or more. Some vents within these smaller groups are of different ages and petrology. A fourth primary alignment trends N15-20E through the center part of the field. This alignment also consists of groups of younger Quaternary cones. This direction is consistent with normal fault orientations in the north-central and NE parts of the SP Mountain cluster.

Relaxing the criteria for the Hough transform by mapping alignments of nine or more vents has two effects: (i) more combinations of the NE trends are plotted to further define the alignment zone, and (ii) five secondary alignments are found (Figure 10-10). These secondary alignments consist of fewer vents than the primary alignments and are not oriented N10-40E, the direction found to be significant by the two-point azimuth method.

One of these secondary alignments is coincident with the western bounding normal fault of the N-trending SP Graben, which extends north of the alignment. There are actually two alignments in this direction, which consist of nearly the same vents but are not resolvable in Figure 10-10. Each of these alignments has a total of 10 vents. This similarity in number of vents likely indicates a zone in this area wider than the 500-m fracture zone width specified as input for the Hough transform. Other alignment orientations are NW, parallel to antithetic faults in the region, and east, which cannot be related to any mapped structure in the area.

Vent alignments are important features of the SP Mountain cluster. Because of the coincidence of alignment orientations and mapped faults in the region, two models for the formation of these alignments appear to be reasonable. First, the SP Mountain cluster may overlie a fault system that is subparallel to the Mesa Butte. This fault zone would have to be more diffuse than the Mesa Butte Fault Zone and completely buried by the voluminous late Quaternary lava flows from the cones. An alternative possibility is that there is no underlying fault zone serving as a conduit. Rather, when magma is available, strain is largely accommodated by the intrusion of dikes rather than by brittle deformation along the Mesa Butte fault (e.g., Spence and Turcotte, 1990; Baer and Reches, 1991; Lister and Kerr, 1991). In the first model, magma passively responds to pre-existing fabric in the crust through which it ascends. In the latter model, magma actively relieves stress in the rocks through which it ascends, and dike emplacement is a critical aspect of cumulative finite strain of the region.

In either case, volcano formation is not a spatially random process in the SP Mountain cluster, which has important implications for the YMR. Smith et al. (1990) have developed models based on the presence of NE-trending vent alignments in the YMR. The probability of disruption of the repository is comparatively high in their models because the repository block is located NE of late Quaternary Crater Flat volcanoes. Because of the small number of cinder cones in the YMR, it is difficult to assess the validity of their arguments. By analogy with other areas, such as the SP Mountain cluster, it is clear that alignments can be an important aspect of vent distribution and do, in some cases, reflect structural control on magmatism. In the future, it will be necessary to differentiate between models of alignment formation,

because the first model indicates that mappable faults, such as the Solitario Canyon fault, may be preferential conduits for magma ascent whereas the latter model would indicate that this is not the case. Additional work planned in the Volcanic Systems of the Basin and Range research project and related investigations will attempt to quantify this relationship more thoroughly.

### **10.3 ASSESSMENT OF PROGRESS**

The Volcanic Systems of the Basin and Range research project is in its early stages. Nonetheless, significant progress has been made toward understanding basic issues in basaltic volcanism in the YMR and the developing of comprehensive probability models for volcanic disruption. Although these models are clearly preliminary, they have begun to be incorporated into the IPA and have resulted in additional guidance to the DOE on development and utilization of probability models. Specifically, these preliminary models were presented to the DOE at a technical exchange in Las Vegas, Nevada, on June 9, 1993. Based on these models, it was concluded that DOE volcanism studies do not yet adequately constrain the probability of future volcanic events in the YMR, the likelihood that this activity would affect the candidate repository, or the consequences of volcanic activity. The development of nonhomogeneous Possion models for calculating the probability of volcanic disruption of the candidate repository represents an attempt to incorporate additional geologic information into probability models. Further refinement of these models, in light of data gathered in other western Great Basin fields and elsewhere, should result in a more comprehensive and justifiable probability model. The current approach of the project is appropriate and will likely lead to the resolution of these issues.

Progress is being made toward resolution of volcanism issues related to the LARP. It should be noted, however, that the CNWRA staff only recently initiated investigation of the relationship between finite strain, faulting, and igneous intrusion. Previous work indicates that incorporation of faults into probability models can strongly influence calculations of the probability of volcanic disruption (Ho et al., 1991; Ho, 1992), but it is difficult to evaluate their validity until the geologic basis of these models is better understood. Investigation of the relationship between volcanism and other tectonic parameters involves the interaction of several CNWRA projects and the development of new geophysical models of this process. Additional work may be required, beyond the scope of the Volcanic Systems of the Basin and Range project, to resolve this issue adequately to support NRC pre-licensing interactions with DOE and determine compliance with 10 CFR Part 60 requirements.

### **10.4 PLANNED PROGRESS IN THE NEXT SIX MONTHS**

A major milestone will be delivered to the NRC during September 1993. This milestone will discuss the geochronological methods used to date young volcanic rocks and the assumptions and uncertainties inherent in these methods. The milestone will also discuss the impact of these uncertainties on estimates of the recurrence rate of new volcano formation in the YMR and on probability models of volcanic disruption of the repository, several aspects of which have been discussed in this report. This information will be directly applicable to CDS/CDM development and the LARP.

During the previous 6 months, considerable effort has been devoted to developing further expertise in the use of the Arc/Info® system and determining the best strategy for using this software to develop and utilize a comprehensive geographic information system database on Basin and Range basaltic volcanism. This process is coming to fruition, and it is anticipated that most relevant data on several volcanic fields will be collected and entered into the database by the end of the next reporting period.

Volcanic fields represented in the database at that time will include: the SFVF, Coso Volcanic Field, the Pisgah-Amboy volcanoes, the Lunar Crater-Pancake Field, and the Cima Volcanic Field. By using these data, it will be possible to further test nonhomogeneous Poisson and similar models. Particular attention will be focused during the next 6 months on tectonic controls on volcanism. This effort will include study of the spatial and temporal relationships between volcanism and deformation, as represented by the results of the study of the SP Mountain cluster of the SFVF described previously.

## 10.5 REFERENCES

- Amos, R.C., S. Self, and B.M. Crowe. 1983. Pyroclastic activity at Sunset Crater: Evidence of a large magnitude, high dispersal strombolian eruption. *EOS, Transactions of the American Geophysical Union* 62: 1085.
- Bacon, C.R. 1985. Implications of silicic vent patterns for the presence of large crustal magma chambers. *Journal of Geophysical Research* 90(B13): 11,243-11,252.
- Baer, G., and Z. Reches. 1991. Mechanics of emplacement and tectonic implications of the Ramon dike systems, Israel. *Journal of Geophysical Research* 96(B7): 11,895-11,910.
- Colton, H.S. 1936. *The Basaltic Cinder Cones and Lava Flows of the San Francisco Volcanic Field*. Flagstaff, AZ: Museum of Northern Arizona.
- Condit, C.D., L.S. Crumpler, J.C. Aubele, and W.E. Elston. 1989. Patterns of volcanism along the southern margin of the Colorado Plateau: The Springerville Field. *Journal of Geophysical Research* 94(B6): 7975-7986.
- Connor, C.B. 1990. Cinder cone clustering in the TransMexican volcanic belt: Structural and petrologic implications. *Journal of Geophysical Research* 95: 19,395-19,405.
- Connor, C.B., C.D. Condit, L.S. Crumpler, and J.C. Aubele. 1992. Evidence of regional structural controls on vent distribution: Springerville volcanic field, Arizona. *Journal of Geophysical Research* 97: 12,349-12,359.
- Connor, C.B., and B.E. Hill. 1993. Volcanism Research. *NRC High-Level Radioactive Waste Research at CNWRA, July 1 Through December 31, 1992*. San Antonio, TX: Center for Nuclear Waste Regulatory Analyses: 10-1-10-31.
- Crowe, B.M. 1990. Basaltic volcanic episodes of the Yucca Mountain region. *High-Level Radioactive Waste Management, International Conference*. Las Vegas, Nevada. La Grange Park, IL. American Nuclear Society: 1:65-73.
- Crowe, B.M., and F.V. Perry. 1989. Volcanic probability calculations for the Yucca Mountain site: Estimation of volcanic rates. *Proceedings Nuclear Waste Isolation in the Unsaturated Zone, Focus '89*. La Grange Park, IL. American Nuclear Society: 326-334.

- Crowe, B., and F.V. Perry. 1991. *Preliminary Geologic Map of the Sleeping Butte Volcanic Centers*. Los Alamos National Laboratory Report LA-12101-MS. Los Alamos, NM: Los Alamos National Laboratory.
- Crowe, B.M., M.E. Johnson, and R.J. Beckman. 1982. Calculation of the probability of volcanic disruption of a high-level nuclear waste repository within southern Nevada, USA. *Radioactive Waste Management and the Nuclear Fuel Cycle* 3: 167-190.
- Crowe, B.M., S. Self, D.T. Vaniman, R. Amos, and F. Perry. 1983. Aspects of potential magmatic disruption of a high-level nuclear waste repository in southern Nevada. *Journal of Geology* 91: 259-276.
- Crowe, B.M., K.H. Wohletz, D.T. Vaniman, E. Gladney, and N. Bower. 1986. *Status of Volcanic Hazard Studies for the Nevada Nuclear Waste Storage Investigations*. LA-9325-MS, Vol. II. Los Alamos, NM: Los Alamos National Laboratory.
- Crowe, B.M., C. Harrington, L. McFadden, F. Perry, S. Wells, B. Turrin, and D. Champion. 1988. *Preliminary Geologic Map of the Lathrop Wells Volcanic Center*. Los Alamos National Laboratory Report LA-UR-88-4155. Los Alamos, NM: Los Alamos National Laboratory.
- Crowe, B.M., R. Picard, G. Valentine, and F.V. Perry. 1992. Recurrence Models for Volcanic Events: Applications to Volcanic Risk Assessment. *Third Conference on Radioactive Waste Management*. Las Vegas, NV: La Grange Park, IL. American Nuclear Society: 2:2344-2355.
- Hasenaka, T., and I.S.E. Carmichael. 1985. The cinder cones of Michoacán-Guanajuato, central Mexico, their age, volume, distribution, and recharge rate. *Journal of Volcanology and Geothermal Research* 25:195 -204.
- Head, J.W., III, and L. Wilson. 1989. Basaltic pyroclastic eruptions: Influence of gas-release patterns and volume fluxes on fountain structure, and the formation of cinder cones, spatter cones, rootless flows, lava ponds and lava flows. *Journal of Volcanology and Geothermal Research* 37: 261-271.
- Heming, R.F. 1980. Patterns of Quaternary basaltic volcanism in the northern North Island, New Zealand. *New Zealand Journal of Geology and Geophysics* 23: 335-344.
- Ho, C.-H. 1992. Risk assessment for the Yucca Mountain high-level nuclear waste repository site: Estimation of volcanic disruption. *Mathematical Geology* 24: 347-364.
- Ho, C.-H. 1991. Time trend analysis of basaltic volcanism at the Yucca Mountain site. *Journal of Volcanology and Geothermal Research* 46: 61-72.
- Ho, C.-H., E.I. Smith, D.L. Feurbach, and T.R. Naumann. 1991. Eruptive probability calculation for the Yucca Mountain site, USA: Statistical estimation of recurrence rates. *Bulletin of Volcanology* 54: 50-56.

- Kane, M.F., and R.E. Bracken. 1983. *Aeromagnetic Map of Yucca Mountain and Surrounding Regions, Southwest Nevada*. U.S. Geological Survey Open-File Report 83-616.
- Langenheim, V.E., K.S. Kirchoff-Stein, and H.W. Oliver. 1993. Geophysical investigations of buried volcanic centers near Yucca Mountain, Southwest Nevada. *High-Level Radioactive Waste Management: Proceedings of the Fourth International Conference* Las Vegas, NV: LaGrange Park, IL. American Nuclear Society 2: 1840-1846.
- Lister, J.R., and R.C. Kerr. 1991. Fluid-mechanical models of crack propagation and their application to magma transport in dykes. *Journal of Geophysical Research* 96(B6): 10,049-10,077.
- Lutz, T.M. 1986. An analysis of the orientations of large scale crustal structures: A statistical approach based on areal distribution of pointlike features. *Journal of Geophysical Research* 91: 421-434.
- Margulies, T., L. Lancaster, N. Eisenberg, and L. Abramson. 1992. Probabilistic analysis of magma scenarios for assessing geologic waste repository performance. *American Society of Mechanical Engineers, Winter Annual Meeting* Anaheim, CA: New York, NY. American Society of Mechanical Engineers.
- McBirney, A.R. 1992. Volcanology. *Techniques for Determining Probabilities of Geologic Events and Processes. Studies in Mathematical Geology No. 4*. R.L. Hunter and C.J. Mann, eds. New York: Oxford University Press: 167-184.
- McGetchin, T.R., M. Settle, and B.A. Chouet. 1974. Cinder cone growth modeled after Northeast Crater, Mount Etna, Sicily. *Journal of Geophysical Research* 79: 3257-3272.
- Moore, R.B., and E.W. Wolfe. 1987. *Geological Map of the East Part of the San Francisco Volcanic Field, North-Central Arizona*. U.S. Geological Survey Map MF-1960.
- Nakamura, K. 1977. Volcanoes as possible indicators of tectonic stress orientation - principles and proposal. *Journal of Volcanology and Geothermal Research* 2: 1-16.
- Newhall, C.G., G.E. Ulrich, and E.W. Wolfe. 1987. *Geological Map of the Southwest Part of the San Francisco Volcanic Field, North-Central Arizona*. U.S. Geological Survey Map MF-1958.
- Perry, F.V. and B.M. Crowe. 1992. Geochemical evidence of waning magmatism and polycyclic volcanism at Crater Flat, Nevada. *High Level Radioactive Waste Management: Proceedings of the Third International Conference* Las Vegas, NV: La Grange Park, IL: American Nuclear Society: 2: 2344-2355.
- Sheridan, M.F. 1992. A Monte Carlo technique to estimate the probability of volcanic dikes. *High Level Radioactive Waste Management: Proceedings of the Third International Conference* Las Vegas, NV: La Grange Park, IL: American Nuclear Society: 2: 2033-2038.

- Smith, E.I., T.R. Feuerbach, and J.E. Faulds. 1990. The area of most recent volcanism near Yucca Mountain, Nevada: Implications for volcanic risk assessment. *High-level Radioactive Waste Meeting. Proceedings of the International Topical Meeting*. La Grange Park, IL.: American Nuclear Society 1:81-90.
- Smith, R.L., and R.G. Luedke. 1984. Potentially active volcanic lineaments and loci in western conterminous United States. *Explosive Volcanism: Inception, Evolution, and Hazards. Studies in Geophysics*: National Research Council/Geophysics Study Committee, eds. Washington, DC: National Academy Press: 47-66.
- Spence, D.A., and D.L. Turcotte. 1990. Buoyancy-driven magma fracture: A mechanism for ascent through the lithosphere and the emplacement of diamonds. *Journal of Geophysical Research* 95(B4): 5133-5139.
- Stirewalt, G.L., S.R. Young, and K.D. Mahrer. 1992. A review of pertinent literature on volcanic-magmatic and tectonic history of the Basin and Range. Center for Nuclear Waste Regulatory Analyses, San Antonio, TX.
- Tanaka, K.L., E.M. Shoemaker, G.E. Ulrich, and E.W. Wolfe. 1986. Migration of volcanism in the San Francisco volcanic field, Arizona. *Geological Society of America Bulletin* 97: 129-141.
- Thompson, G.A., and M.L. Zoback. 1979. Regional geophysics of the Colorado Plateau. *Tectonophysics* 61: 149-181.
- Ulrich G.E., and N.G. Bailey. 1987. *Geologic Map of the Northwestern Part of the San Francisco Volcanic Field, North-Central Arizona*. U.S. Geological Survey Map MF-1957.
- Vaniman, D.T., and B.M. Crowe. 1981. *Geology and Petrology of the Basalts of Crater Flat: Applications to Volcanic Risk Assessment for the Nuclear Waste Storage Investigations*. Los Alamos National Laboratory Report LA-8845-MS. Los Alamos, NM: Los Alamos National Laboratory.
- Wadge, G., and A. Cross. 1988. Quantitative methods for detecting aligned points: An application to the vents of the Michoacán-Guanajuato volcanic field, Mexico. *Geology* 16: 815-818.
- Williams, H. 1950. Volcanoes of the Parícutin region. *U.S. Geological Survey Bulletin* 965B: 165-275.
- Wilson, L., R.S.J. Sparks, T.C. Huang, and N.D. Watkins. 1978. The control of volcanic column heights by eruption energetics and dynamics. *Journal of Geophysical Research* 83(b4): 1829.
- Wilson, L. 1980. Relationships between pressure, volatile content, and ejecta velocity in three types of volcanic explosion. *Journal of Volcanology and Geothermal Research* 8: 297-313.
- Wolfe, E.W., G.E. Ulrich, R.F. Holm, R.B. Moore, and C.G. Newhall. 1987a. *Geologic Map of the Central Part of the San Francisco Volcanic Field, North-Central Arizona*. U.S. Geological Survey Map MF-1959.

- Wolfe, E.W., G.E. Ulrich, and C.G. Newhall. 1987b. *Geologic Map of the Northwest Part of the San Francisco Volcanic Field, North-Central Arizona*. U.S. Geological Survey Map MF-1957.
- Wong, M.A. 1982. A hybrid clustering method for identifying high density clusters. *Journal of the American Statistical Association* 77: 841-847.
- Wong, M.A., C. Schaak. 1982. Using the  $k^{\text{th}}$  nearest neighbor clustering procedure to determine the number of subpopulations. *American Statistical Association Proceedings of the Statistical Computational Section*. 1982: 40-48.
- Wong, M.A., T. Lane. 1983. A  $k^{\text{th}}$  near neighbor clustering procedure. *Journal of the Royal Statistical Society, Series B* 45: 362-368.

# 11 TECTONIC PROCESSES IN THE CENTRAL BASIN AND RANGE REGION

*by Stephen R. Young, Ronald H. Martin, and Brent Henderson*

*Investigators: Stephen R. Young, Ronald H. Martin, Brent Henderson, Richard Klar, Joyce Foegele*

*NRC Project Officer: G. Birchard*

## 11.1 TECHNICAL OBJECTIVES

The primary technical objectives of the Tectonics Research Project are: (i) to compile and integrate geological and geophysical data on late Neogene and Quaternary tectonic processes in the central Basin and Range region; and (ii) to develop and assess alternative models of tectonic processes at Yucca Mountain, Nevada. The primary purpose of these activities is to determine the adequacy of existing data, methods, and models for demonstrating and determining compliance with descriptive regulatory requirements, and especially quantitative performance objectives. At this time, it is not clear that existing data, analytical and simulation methods, and conceptual models are adequate to either demonstrate or determine compliance with a quantitative performance objective. Uncertainties and sources of error in estimates of important parameters are large and difficult to quantify. Thus, the initial focus of the project is on compilation of data, then on modeling, and finally on performance assessment. The common thread is uncertainty. The key questions are: (i) What are the important tectonic parameters for performance assessment and what are their associated ranges of uncertainties?; (ii) Can uncertainties in conceptual models and computational simulations be adequately quantified for inclusion in performance assessments?; (iii) How do these uncertainties affect performance assessments based on quantitative release standards?; (iv) Is the existing knowledge base adequate; if not, can an adequate knowledge base be achieved? Information and models resulting from this project will be used directly to develop and refine Compliance Determination Strategies (CDS) and Methods (CDM), and thus to establish review methods and acceptance criteria for sections 3.1.1, 3.2.1.5, 3.2.1.6, 3.2.1.7, 3.2.1.8, 3.2.2.8, and 6.1 of the License Application Review Plan (LARP). Input to performance assessment is expected to consist largely of quantitative estimates of uncertainty for key tectonic parameters.

Compliance determination strategies on Structural Deformation (LARP Section 3.2.1.5) and Structural Deformation and Groundwater (LARP No. 3.2.2.8) have drawn on information and specific references identified during the early phases of the literature review and data compilation tasks of the Tectonics Research Project. Development of CDM will likely draw more heavily from alternative tectonic models of the region, and from computational simulations of fault block deformation and fault propagation through alluvial materials that have been identified as Key Technical Uncertainties (KTU) in Section 3.2.1.5 of the LARP.

U.S. Environmental Protection Agency (EPA) environmental standards for release of radioactivity (40 CFR Part 191) require prediction of waste isolation performance of the proposed high-level waste (HLW) repository for up to 10,000 years. Based on the EPA standards, the overall system performance objective for a geologic repository (10 CFR 60.112) imposes limits on post-closure cumulative releases of radionuclides. Tectonic processes, such as faulting, earthquake seismicity, and ground-rupture, may substantially influence long-term (post-closure) performance. Thus, detailed information on geological features of the site, such as faults, that might affect repository design or performance, is required to be included in the Safety Analysis Report (SAR) of the U.S. Department of

Energy's (DOE) license application [10 CFR 60.21(c)(1)]. The SAR [10 CFR 60.21(a)] generally will include a description and assessment of the proposed repository site. Where subsurface conditions outside the controlled area may affect isolation within the controlled area, the description must include such information to the extent it is relevant [60.21(c)(1)(i)]. Detailed information required in the SAR includes orientation, distribution, aperture in-filling and origin of fractures, discontinuities, and heterogeneities; the presence and characteristics of other potential pathways such as solution features, breccia pipes, or other potentially permeable features; and the geomechanical properties and conditions, including pore pressure and ambient stress conditions [60.21(c)(1)(i)(A)(B)and(C)]. Required assessments, as described in 60.21(c)(1)(ii)(A)-(F), should include analysis of the geology, geophysics and hydrogeology; and analyses and evaluations of favorable and potentially adverse conditions, post-closure performance, and the effectiveness of natural barriers. The Tectonics Research Project will incorporate data acquired from potentially important fault systems outside the controlled area, such as the Furnace Creek fault. Data compiled by the Tectonics Research Project will be used in the review and assessment of those regulatory requirements.

The Tectonics Research Project will produce an improved knowledge base necessary for U.S. Nuclear Regulatory Commission/Center for Nuclear Waste Regulatory Analyses (NRC/CNWRA) assessment of the SAR, and for credible assessment of compliance with specific siting and performance criteria related to tectonics. In particular, information on patterns and rates of historic and prehistoric faulting and seismicity will be necessary to assess compliance with specific regulatory requirements in LARP Sections 3.2.1.5-3.2.1.8. Several specific concerns related to tectonics are stated in the regulations. Structural deformation such as uplift, subsidence, folding, and faulting during the Quaternary Period, if characteristic of the controlled area or if it could affect isolation within the controlled area, is specifically included as a potentially adverse condition [10 CFR 60.122(c)(11)]. Likewise, in 10 CFR 60.122(c)(4), structural deformation, such as uplift, subsidence, folding, or faulting that may adversely affect the regional groundwater flow system is considered to be a potentially adverse condition. Historic earthquakes which, if repeated, could affect the site significantly [10 CFR 60.122(c)(12)]; and indications, based on correlations of earthquakes with tectonic processes, that either the frequency or magnitude of earthquakes may increase [10 CFR 60.122(c)(13)] require assessment as potentially adverse conditions. Earthquake activity that may occur more frequently, or with higher magnitude than is typical of the area in which the geologic setting is located [10 CFR 60.122(c)(14)], would require assessment as a potentially adverse condition. This project will integrate the necessary regional data on Quaternary fault segmentation, distributive faulting [Nuclear Material Safety & Safeguards (NMSS) User Need No. 607], historic seismicity and paleoseismicity for evaluation of these adverse conditions. Assessments of estimates of fault slip, ground rupture, and earthquake seismicity at Yucca Mountain may thus be substantially improved. Thus, for instance, estimates of earthquake magnitudes based on fault characteristics (e.g. trace length, slip rate) may readily be compared to fault systems elsewhere within the geologic setting.

Models and analytical methods produced by Tectonics Research may also assist in review of detailed investigations and analyses of tectonic processes. As indicated by 10 CFR 60.122(a)(2)(i)-(iii), the following criteria must be demonstrated to show that a potentially adverse condition does not compromise performance of the repository: (i) the condition has been adequately investigated; (ii) the condition has been adequately evaluated using analyses sensitive to the condition and assumptions that are unlikely to underestimate its effects; and (iii) the combined set of potentially favorable and adverse conditions are shown by analyses not to significantly degrade waste isolation. Tectonics Research will provide a practical foundation of existing data and critically reviewed tectonic models on which to base assessments of the required investigations.

## 11.2 SIGNIFICANT TECHNICAL ACCOMPLISHMENTS

Three tasks have been initiated in the Tectonics Research Project. Two of these tasks are literature reviews and the third is digital compilation of tectonic data into the ARC/INFO Geographic Information System (GIS). Both literature reviews are ongoing. However, one of the reviews is being conducted to directly support the data compilation task. This review is focused on existing digital data and on published material that contains tectonic data that can be digitized. In particular, data on contemporary crustal-scale strain measured by geodetic methods and the distribution, slip history, seismology, and paleoseismology of Quaternary faults are being reviewed and processed for inclusion in the GIS. The other review is focused on methods used to measure and analyze the slip history of Quaternary faults.

These reviews of published literature and other relevant sources of data are being conducted to determine the type and extent of existing data related to Late Neogene and Quaternary tectonism in the central Basin and Range region. This task makes selective use of literature and data compiled for Task 1 of the Volcanic Systems of the Basin and Range research project (Stirewalt and Young, 1992). Current emphasis is on data required for assessment of seismic and fault rupture hazards, and to support development and evaluation of alternative conceptual models of seismic and tectonic processes. Thus, data on slip rates and paleoseismology of historically active faults are of particular interest.

Significant technical accomplishments to date include processing of digital terrain models and LandSat Thematic Mapper data, and compilation of a data base containing Quaternary fault traces, earthquake hypocenters, and Quaternary basaltic volcanic fields. These data are compiled in the ARC/INFO GIS. The different data types have subsequently been integrated onto a common mapping base for correlation. Maps of the central Basin and Range and Yucca Mountain areas are now available that show spatial and temporal associations between Quaternary faults, location and magnitude of earthquakes, location of Quaternary volcanic fields, and extant terrain features.

## 11.3 REVIEW OF LITERATURE AND OTHER SOURCES OF DATA ON LATE NEOGENE AND QUATERNARY TECTONISM IN THE CENTRAL BASIN AND RANGE REGION

The central Basin and Range region (Wernicke 1991) has undergone extensive crustal-scale tectonic extension during about the last 15 million years (Wernicke et al., 1988; Kruse et al., 1991). Spatial and temporal patterns of late Neogene [15 million years ago (Ma) to 1.6 Ma] and Quaternary (1.6 Ma to present) extensional deformation of the central Basin and Range region are not well constrained regionally (at spatial scales in excess of 500 - 1000 km), and are little known at more local scales (less than 100 - 200 km). In particular, substantial uncertainty exists as to how the contemporaneous regional displacement field may be partitioned locally onto specific faults and fault systems. Magnitude and recurrence intervals of earthquakes may be closely related to regional strain patterns.

Wernicke et al. (1988) have determined that 247 km ( $\pm 56$  km) of extensional displacement has been accommodated in a region between the Colorado Plateau and the Sierra Nevada Range during the last 15 million years. The total relative separation between the Colorado Plateau and the Sierra Nevada block is distributed along a net vector path oriented north  $73^\circ$  ( $\pm 12^\circ$ ) west. The regional displacement

field is heterogeneous. Displacement is distributed between two distinct highly extended terrains separated by a relatively weakly extended region. Yucca Mountain is situated within the western-most of the highly extended regions, referred to as the Death Valley normal fault system by Wernicke et al. (1988). Regional displacement rates varied from an estimated maximum of 20–30 mm/yr (millimeters per year) from 10 – 15 Ma, to a diminished rate of less than 10 mm/yr over the last 5 million years. This project will attempt to account for the distribution of this net 10 mm/yr of regional deformation by mapping slip measured across active fault zones.

Onset of Neogene tectonic extension across the greater Basin and Range region is time transgressive. The initial phases of extension are progressively younger from north to south in the northern Basin and Range (Gans et al., 1989; Lipman et al., 1972). In contrast, onset of deformation is younger from south toward the north and northwest in the southern Basin and Range (Gans et al., 1989; Glazner and Bartley, 1984). Yucca Mountain is located in the transitional area between the northern and southern Basin and Range regions. Within this central Basin and Range region, Wernicke et al. (1988) and Gans et al. (1989) have determined that onset of tectonic extension progressed from east to west. Thus, regional patterns of deformation are apparent. It is not clear that these patterns can be resolved well enough to have much predictive value.

As many as 32 discrete faults or fault segments through Yucca Mountain have recognized Quaternary displacement (Swadley et al., 1984; Scott, 1990). The proposed repository site is within a relatively intact fault block directly bounded to the east (Paintbrush Canyon, Bow Ridge, and Stagecoach Road faults) and west (Solitario Canyon fault) by major faults with discernable Quaternary displacement. The proposed location of the surface facilities and the subsurface excavation are in the hanging wall of the Paintbrush Canyon-Bow Ridge-Stagecoach Road fault system. These faults have a maximum combined net dip slip of over 1.4 km, with up to 400 m of dip slip accumulated on the segment of the Paintbrush Canyon fault due east of the proposed repository block. Most of the fault slip was accumulated during the time period from 13 Ma to present. Quaternary dip slip on the Paintbrush Canyon and Stagecoach Road faults is in the range of 4.1 to 4.6 m. The Solitario Canyon fault has as much as 400 m of dip slip. Menges et al. (1993) document five or six discrete ground-rupture events, and cumulative middle to late Pleistocene (approximately 700,000 – 10,000 years ago) slip of 76–132 cm on the Bow Ridge fault. They estimate that each event accrued 11–28 cm of net slip. Recurrence intervals are estimated to be between  $10^4$ – $10^5$  years. Slip rate is estimated to be less than about 0.001 mm/yr. Swan et al. (1993) suggest a middle to late Quaternary dip-slip rate of less than 0.01 mm/yr for part of the Paintbrush Canyon fault running through Midway Valley. Three to five discrete ground-rupture events were identified. Displacements for each of the older events are estimated to be between 40–85 cm of dip-slip. The youngest is estimated to have been displaced 15 cm. Swan et al. (1993) suggest  $10^3$  to  $10^4$  years between slip events. Estimates of the cumulative displacement of the oldest middle Pleistocene unit are between 170 and 270 cm.

At this time, the effects of fault slip on a potential repository block can only be grossly estimated. A fault slip threshold, below which no waste isolation would not be adversely effected, is not established. Faults that transect the repository, such as the Ghost Dance, may directly shear waste canisters. This is a highly localized effect. In contrast, slip on bounding faults, such as the Paintbrush Canyon, may cause distributed deformation throughout the proposed repository fault block. Finite element models of fault-block deformation are currently being developed by the CNWRA staff to estimate mechanical effects of fault slip on the proposed repository.

Major uncertainties persist with respect to geometry and rates of extension, spatial and temporal distribution of extensional deformation, and, of particular importance, styles of faulting that have accommodated late Neogene and Quaternary extensional deformation of the region around Yucca Mountain. Slip directions on Quaternary faults at Yucca Mountain are not well constrained. Contemporary earthquake foci do not correlate well with traces of Quaternary faults. Variation of fault slip directions through the Neogene and Quaternary has not been determined. It is unlikely that characterization at the scale of Yucca Mountain site alone will produce data sufficient to adequately address these issues. No single site within the central Basin and Range represents the full range of tectonic processes active within the region. For instance, correlations of earthquake magnitude with fault length, or with coseismic slip, cannot be established with data from Yucca Mountain alone. These relationships must be established using data from areas of modern earthquake seismicity, coseismic ground rupture, and good paleoseismic records. Studies of active fault zones elsewhere within the central Basin and Range region thus seem essential to estimate probabilities and effects of future tectonic events. However, major changes in the tectonic framework of the region during the last 5 to 10 million years place emphasis on determination of contemporary *in situ* conditions in the Yucca Mountain area.

Explanations of relationships between modern earthquake seismicity and geometric and kinematic descriptions of known fault systems are needed to substantially improve prediction and characterization of future potential seismic slip. In particular, modern seismicity is not consistent with the interpreted extensional style of much of the region. Earthquake focal mechanisms indicate slip on relatively deep ( $> 15$  km), high-angle ( $> 30^\circ$  dip) planar fault surfaces, while most of the region probably experienced significant extension by slip on low-angle (detachment) fault systems. An important implication for a potential repository is that planar faults that extend through the seismogenic crust (to depths greater than 15 - 20 km) are generally thought to be capable of producing large earthquakes. Low-angle fault systems are not generally known to be seismically active.

### 11.3.1 Patterns and Rates of Geodetic Strain

Approximately 9 mm/yr of net extensional displacement are currently accumulating across the Great Basin region (DeMets, et al. 1990; Minster and Jordan, 1987). The exact distribution of net Basin and Range displacement onto specific major fault systems is not known. However, space geodetic measurements of crustal-scale strain suggest that much of the Basin and Range displacement is localized within a relatively narrow corridor (e.g., Dokka and Travis 1990b and Savage et al., 1990) that includes the Death Valley fault system (Argus and Gordon, 1991). The contemporary Death Valley fault system is actively accommodating an unknown proportion of the total Great Basin displacement field. The Yucca Mountain site is about 70 km east of the northern Death Valley-Furnace Creek fault zone, which is the eastern limit of major Quaternary normal fault activity of the Death Valley fault system.

Contemporary deformation rates of the Great Basin region determined from space geodetic data are in good accord with models of relative tectonic plate velocity computed from sea floor geomagnetic anomaly data. Azimuths of contemporary extension, however, have significantly larger components of northward motion than those computed from the plate velocity models, or from the field work by Wernicke et al. (1988). This discrepancy may indicate that the geometry of the crustal-scale displacement field has changed substantially since the period of major crustal stretching, and has continued to rotate to a more northward orientation over about the last 3 to 5 million years. The plate velocity models of DeMets et al. (1990) are based on approximately the last 3 million years of sea floor spreading. Ward (1990) has determined that instantaneous, path-integrated extensional deformation measured from Very

Long Baseline Interferometry (VLBI) is in the range of  $8.2 (\pm 1.3)$  mm/yr directed north  $34^\circ \pm 7$  west to  $8.8 (\pm 1.1)$  mm/yr directed north  $25^\circ \pm 8$  west for the Basin and Range region. Anders et al. (1993) have determined a geological strain rate of about  $1 \times 10^{-16}$ /sec over the last 6.6 Ma for the portion of the Great Basin north of the eastern Snake River Plain.

### 11.3.2 Patterns and Rates of Quaternary Faulting and Seismic Strain Release

The relative motion between the Pacific and North American plates must be accommodated by a mix of distributed shear and relatively localized slip along discrete faults or fault zones. The shallow crust (less than about 15–20 km) deforms primarily by faulting. The key question is: How is the strain within the deforming margin partitioned between the major active fault systems? Contemporary partitioning may not be representative of longer term behavior. Seismic and aseismic slip may cluster significantly both spatially and temporally (Wallace 1984). Thus, the paleoseismic record and studies of Quaternary fault slip will yield a more realistic view of the potential distribution of fault slip over the next 10,000 to 100,000 years.

Dating of middle Holocene surface-rupturing slip events on faults in the western Lake Mead region suggests that these events may recur on an individual fault at periods in excess of 10,000 years, but that, for the region as a whole, recurrence of earthquakes larger than Ms 6.5 may be in the range of a few thousand years (Anderson and O'Connell 1993).

Beanland and Clark (1993) report that measurements made at one of their study sites indicate an average net slip rate of the Owens Valley Fault Zone (OVFZ) of  $1.5 \pm 1$  mm/yr over the last 300,000 years. Data from other of their sites along the OVFZ indicate an average net slip rate of  $2 \pm 1$  mm/yr over the last 10,000 years (Holocene). Coseismic displacement associated with the 1872 (Mm 7.5–7.7, Ms 8.0) earthquake averaged  $6 \pm 2$  m of right-lateral offset and  $1 \pm 0.5$  m of vertical offset. The maximum right-lateral displacement is about 10 m. Average net oblique slip is  $6.1 \pm 2.1$ . Maximum net oblique slip is 11 m. Three major Holocene earthquakes have occurred on the OVFZ. Beanland and Clark (1993) estimate that major earthquakes, with about the same types and magnitudes of displacement, occur at least every 3,300 to 5,000 years on the Owens Valley system. They also point out that slip is partitioned between the primarily right-slip OVFZ and the adjacent normal (dip-slip) faults that bound the eastern flank of the Sierra Nevada mountain range. They report average Holocene dip-slip rates of 0.1–0.8 mm/yr on these bounding normal faults.

Clark and Gillespie (1993) document late Quaternary slip rates from 0.1–3.0 mm/yr on the Hilton Creek fault at McGee Creek in the vicinity of Long Valley, and slip rates in excess of 2.0 mm/yr on the Mono Lake fault. Owens Valley range bounding faults (normal) have slip rates less than 1 mm/yr. At McGee Creek, slip rates over the last 140,000 – 10,000 years are estimated to be between 4.2 mm/yr and 1.1 mm/yr (10–15 ka = 1.3–2.5 mm/yr; 13.–20 ka = 1.4–2.6 mm/yr; 25–40 ka = 1.4–4.2 mm/yr; 65–140 ka = 1.1–3.5 mm/yr). They also report that slip rates increase from 0.1–0.4 mm/yr at the south end of the normal fault system to 0.1–0.8 mm/yr 3 km north, near Hilton Lake, to 1.4–3.0 mm/yr 9 km farther north, at McGee Creek, and then to 1.1–2.0 mm/yr 5 km farther north, at Tobacco Flat in the Long Valley area. A salient point made by Clark and Gillespie is that, even for a fairly well-studied, high slip-rate normal fault system like the Sierras, sufficient data have not been acquired to reliably, or adequately, characterize the slip history and paleoseismology. Uncertainty in dating of fault slip is a major contributor to uncertainty in estimates of earthquake recurrence.

Bell (1993) reports a slip rate of 0.2 mm/yr over the last 200,000 years, and a slip rate of 0.5–0.8 mm/yr over the last 7,000–12,000 years within the Dixie Valley (1954 M6.8) earthquake zone. He reports a slip rate of 0.2–0.7 mm/yr over the last 25,000–35,000 years, and a slip rate of 0.3–0.7 mm/yr over the last 6,000–13,000 years on the main fault segment of the Cedar Mountain (1932 M7.2) earthquake fault zone. Bell (1993) estimates that slip rates within the 1954 Rainbow Mountain (M6.6–M6.8) earthquake zone and the 1954 Fairview Peak (M7.1) earthquake zone were less than 0.1 mm/yr over the last 200,000 years. Bell points out that the Dixie Valley and Cedar Mountain zones have ruptured the ground surface previously during the Holocene, but that there is no evidence for older Holocene surface-rupturing earthquakes within the Rainbow and Fairview fault zones. Bell presents evidence that the Fairview Peak fault zone has not ruptured over at least the period of 120,000–60,000 years prior to the historical event, and that the Rainbow Mountain zone has not ruptured over at least the last 13,000 years. Bell states that slip rates over the last 10,000 years are higher on the Sierra Nevada bounding fault and on the Pyramid Lake fault zone ( $> 1$  mm/yr).

Caskey and Wesnousky (1993) document a maximum right-lateral coseismic displacement of about 2.8 m and a maximum vertical displacement of 3.5 m for the Fairview Peak earthquake. A net slip direction of S32E is indicated by offset tree roots, which is consistent with a focal mechanism solution of S26E.

Bryant (1993) reports slip rates over the last 10,000 years of at least 2mm/yr for several faults (Death Valley—right-lateral strike slip (rlss), Hilton Creek—dip-slip (ds), Honey Lake—rlss, Owens Valley—rlss, and Panamint Valley—rlss) in the eastern California part of the central Basin and Range. Hilton Creek is the only primarily dip-slip fault in this group. Two other Holocene faults (Deep Springs—ds and Genoa—ds) are reported to have slip rates less than 2 mm/yr (most likely less than 1 mm/yr for Genoa) and are both primarily dip-slip zones. Bryant concludes that most of the primarily normal faults in the eastern California region have slip rates substantially lower than the synchronous right-lateral strike slip systems. Range-bounding Holocene faults with maximum slip rates in excess of 1 mm/yr include the Genoa, Hilton Creek, Mono Lake, Round Valley, Surprise Valley, and White Mountains fault zones. Ground-rupture occurred on the Fort Sage (1950), Hilton Creek (1980), Little Lake (1982), and White Mountains-Volcanic Tablelands zone (1986).

Davis and Burchfiel (1993) report right-lateral strike slip (rlss) on the southern Death Valley fault zone to be less than the 35 km estimated by Butler et al. (1988), probably less than 18 km (Troxel personal communication to Davis 1993), and perhaps less than 10 km.

Hecker (1993) estimates that the latest Pleistocene-Holocene (ca. 130 ka) surface-faulting recurrence rate along the eastern flank of the Basin and Range province, essentially the northern Wasatch fault zone region (northern Utah), is 6.7 surface-faulting events per  $10^4$  yr per  $10^4$  km<sup>2</sup> over about the last 15 million years. More than half of the faulting events occurred on primary segments of the northern Wasatch fault zone. Hecker also reports an estimate of 1.3 events per  $10^4$  yr per  $10^4$  km<sup>2</sup> for the southeastern flank of the Basin and Range province in southern Utah. Hecker indicates that the longer-term (Quaternary) slip rates are lower than the latest Pleistocene-Holocene rates measured in northern Utah, but that the increase in activity may be caused locally by changes in the level of ancient Lake Bonneville.

Knuepfer (1993) reports a maximum late Quaternary slip rate across the main segments of each of the Lost River (1983 Borah Peak rupture), Lemhi and Beaverhead faults of 0.5 m/ka. The main segments of the Lost River ruptured previous to the 1983 events about 6,000–8,000 years ago. The Lemhi

fault segment ruptured previously from about 6,000–12,000 years ago. Kneupfer makes the important observation that the detailed historical patterns of faulting on this system are not predictable from the longer-term (Quaternary) record, and that the patterns of rupture of distinct fault segments is spatially and temporally heterogeneous. For example, distinct segments of the Lemhi system that ruptured two or three times during the period from 25–15 ka, have been inactive over that last 18–15 ka.

Kohler et al. (1993) suggest at least 35 km of riss on the Furnace Creek fault zone over the last 10 Ma. The Walker Lane fault is estimated to accommodate 50–70 km of riss. The north end of the Furnace Creek is linked to the south end of the Walker Lane by a right-stepping (releasing bend) pull-apart system of high-angle and low-angle extension fault systems.

Lund (1993) reports that the Wasatch fault zone has not ruptured in the last few hundred years. Considerable evidence has been acquired from trenching of at least 15 ground-rupturing earthquakes along the central Wasatch over the last 6,000 years. The composite recurrence interval is  $395 \pm 60$  years. Average recurrence of large events on distinct segment is  $1,980 \pm 310$  years. Actual intervals vary from 500–3,500 years. Most of the distinct central segments have each ruptured between 1,500 and 400 years ago, giving a late Holocene composite recurrence interval of about 220 years. Late Pleistocene-Holocene slip rates of 0.5–1.5 mm/yr are significantly larger than the 0.1–0.3 mm/yr measured for the older Quaternary interval. Again, cycles of Lake Bonneville are implicated.

Machette et al. (1993) suggest a recurrence interval of large earthquakes along the Pleasant Valley system (1915, M6.9–7.7) of 10–20 ky. McGill (1993) documents at least 1–3 mm/yr of left-lateral/normal slip on the Owl Lake fault over about the last 30,000 years, at the eastern end of the Garlock system. Ramelli and DePolo (1993) suggest a Quaternary slip rate of 0.1–0.2 mm/yr for the Railroad Valley fault zone.

Cinti et al., (1993) report that ground-surface ruptures caused by the Landers (1992 M7.5) earthquake occurred along parts of the Johnson Valley, Homestead Valley, and Emerson faults. These faults have been previously mapped. Ground rupture length on the 25 km long Homestead Valley segment was 21 km. Cinti et al. (1993) suggest, based on their field studies of the Homestead Valley fault, that large earthquakes are one to two orders of magnitude less frequent on faults comprising the Eastern California Shear Zone than on major faults that comprise the San Andreas system.

Several recent studies present convincing evidence and supporting statistical analyses that the Landers earthquake triggered a widespread set of earthquakes throughout the central and northern Basin and Range region (Anderson et al., 1993; Hill et al., 1993; Sieh et al., 1993).

#### **11.4 REVIEW OF LITERATURE ON PALEOSEISMOLOGY AND GEOCHRONOLOGY OF FAULTING**

The primary objective of this task is to assess the utility and reliability of methods used to determine the slip history of faulting and to estimate the ages of seismic (earthquake) slip events on Quaternary faults. Salient assumptions, sources of uncertainty and limitations related specifically to field methods used to determine fault slip are discussed. In particular, this review is focused on field geological methods used to determine direction and amount of slip, and the use of analytical dates and interpreted ages of geologic features to establish a chronology of slip.

Estimating probabilities of future seismic slip and fault rupture on any specific fault system depends, in part, on knowledge of the amount, direction, and rate of slip along particular fault surface or zone of distributed faulting. Interpretation of the slip history of a fault system is an important source of uncertainty in estimates of risk due to potential fault rupture and earthquake seismicity. Because fault patterns mapped in weakly consolidated or poorly indurated alluvium are often complex, it is difficult to simply relate the mapped patterns to the geometry and slip history of the underlying bedrock fault. However, the primary means of investigating Quaternary faulting at Yucca Mountain is by mapping fault and fracture patterns exposed in trenches excavated in Quaternary alluvium.

Conceptually, fault systems may be envisioned to accumulate slip in either continuous (creep) or episodic (stick-slip) modes. Earthquakes result from large scale stick-slip movement along faults. Historic earthquake rupture of a fault system is strong evidence that the fault moves characteristically by stick-slip, and a record of historic events may be used to establish a characteristic time period over which earthquake events recur along a specific fault system. However, interpretation of prehistoric earthquake rupture requires detailed study of disrupted soil and stratigraphic horizons within and adjacent to the fault. Field methods are not available to reliably interpret slip mode, or even to distinguish between end-member modes of fault slip. Interpretation of the occurrence and period of prehistoric earthquake slip often depends heavily on studies of fault-scarp degradation, discernment of rupture-related sediments adjacent to the fault, age-dating of secondary mineralization within the fault zone, and measurement of average slip rates. Average slip rate is generally calculated by dividing a measured increment of slip by the time period over which the slip accumulated. Average slip rate alone may be a significant indicator of seismic risk; instantaneous rates, which may have been seismic, are generally not directly discernable. There are two main sources of substantial uncertainty in estimates of slip rate. The first is in measurement of the total and incremental slip vectors (direction and magnitude) determined from relative displacement of geological markers offset by the fault. The second is in estimation of the age of these markers. In essence then, uncertainties in age-dates of fault movement may be classified as related either to: (i) the geology of the site; or (ii) the analytical methods used to obtain discrete absolute age estimates of rock samples.

At Yucca Mountain, Quaternary fault slip is currently being investigated by detailed cross-section mapping of trenches emplaced across fault zones. Consequently, stratigraphic horizons within the depositionally complex Quaternary alluvium must be correlated across an equally complex array of subsidiary faults and fractures that constitute the fault zone. Slip rate calculations are uncertain because it is difficult to determine the direction and amount of displacement of subtle stratigraphic markers in the alluvium. Once a displacement pattern is established, age-dates of displaced strata can be used to estimate average slip rates. Uncertainties related to determination of absolute age-dates will be addressed in the Volcanism Research task mentioned earlier. Accordingly, the focus of this task is on critical evaluation of the data and field methods available to characterize and distinguish seismic and aseismic slip of Quaternary fault systems.

In principle, field geologic studies of fault kinematics, and analytical methods used to determine absolute age-dates of specific rock units, can be considered as mostly distinct procedures. In practice, however, the interaction of complex fault and fracture patterns with the subtle layering common to Quaternary alluvial, volcanic, and paleosol horizons often requires close cooperation between sampling and analysis activities. Geological interpretation of the depositional, diagenetic, and structural environment of the rock unit being sampled for age-dating may be important for proper interpretation of the age-date results. Even though alternative sites may exist at which an improved framework for assessment of uncertainties in fault-slip chronology can be developed, the feasibility of finding an

'analog' site applicable to geochronologic studies of Quaternary fault systems at Yucca Mountain is doubtful. Limitations and uncertainties related to interaction between depositional, diagenetic, and deformation processes may be quite site-specific, and therefore may be of little real value in constraining uncertainties at seemingly similar sites. However, it is possible that a particular site, or area, may emerge from a focused literature review that can offer insight into uncertainties and limitations related to regional relationships between faulting and Quaternary volcanic and alluvial depositional systems. For example, air-fall volcanic ash beds within an alluvial sequence (e.g., the Bishop Tuff) may be stratigraphically correlative with the eruptive source of the ash. Whereas the ash may be difficult to date, lavas or intrusive equivalents at the source eruption may be comparatively easier to date with standard techniques. A similar situation exists at Yucca Mountain, in which basaltic ash, presumably erupted from one of the nearby cones, occurs in fissures within some of the fault zones. Likewise, age-dates of secondary calcite and silica deposited in veins and fractures associated with faults at Yucca Mountain may depend somewhat on regional groundwater chemistry. These secondary mineral and ash deposits were discovered by trenching across the faults, and may not be well exposed in natural outcrops. Although it seems likely that these types of concerns are best addressed by studies conducted specifically at Yucca Mountain, insight gained from a literature review may indicate potentially fruitful research opportunities at particular sites elsewhere in the region.

Hemphill-Haley et al., (1993) use a combination of stratigraphic relationships, thermoluminescence (TL) and radiocarbon dates, and soil development to date ground-rupturing slip events on the southern part of the Lemhi fault. At one site, they use TL dates of loess derived from the Eastern Snake River Plain to bracket the age of a discrete slip event on a single fault segment to between 19 and 15 ka. At another site, TL dates are used to estimate the age of a single faulting event to be about 75 ka. Subsequent faulting events at the same site are bracketed between 24-19 ka. Lifton and Jull (1993) report work on a new approach to estimating ages of geomorphic surfaces using statistical correlations between measured *in situ* and theoretical depth profiles of cosmogenic  $^{14}\text{C}$ . Lundstrom et al. (1993) report progress on dating and correlation of surficial (eolian, alluvial, and colluvial) deposits at Yucca Mountain. They use uranium-trend, uranium series disequilibrium, TL, and regional stratigraphic correlation to estimate ages of surficial map units. McGill (1993) reports conventional radiocarbon dates of  $1,583 \pm 90$  and  $1,656 \pm 88$  years ago of organic matter encased below varnish on cobbles sampled from the Owl Lake fault zone.

## 11.5 GEOLOGIC SETTING TECTONIC DATABASE

The objective of this task is to compile data on faulting, seismicity, and geodynamic strain in the central Basin and Range region. The purpose of this section is mainly to show a snapshot of the current data sets and to describe the status of the database. However, based on available information, some preliminary interpretations have been made to illustrate the utility of the current database. The database is not yet sufficiently advanced to support complex queries. The data are being compiled into the Environmental Systems Research Institute, Inc. (ESRI) ARC/INFO GIS software system. Use of a GIS approach to archive and manage tectonic data allows flexibility in structuring conditional queries, retrieving selected data, and creating integrated displays of spatially related tectonic features and processes.

The ARC/INFO software system currently functions primarily as a database management system for the Tectonics Research Project. However, GIS data management with the ARC/INFO system will allow the NRC and CNWRA staff to more easily utilize information stored in the ARC/INFO system

maintained by the DOE Yucca Mountain Project (YMP). Thus, using a common software environment, data acquired by site characterization activities may be archived and correlated with data developed by the NRC and CNWRA, and with data acquired from the literature or other existing databases.

The CNWRA is using the ARC/INFO software system to digitize geologic and tectonic data from source maps that have been previously published at a variety of scales and projections. This process essentially creates a map-like coverage of the data. The data are stored along with spatial coordinates and a set of attributes specific to the data type. These data can then be transformed to a selected scale and map projection. This is an extremely powerful facility, in that various combinations of the digital data can then be selected and displayed on a single map at a common scale and with a common projection. This is an essential capability for efficient assessment and use of the large body of regional tectonic data.

The ARC/INFO system is currently installed on a SUN SparcStation 2 and on a Silicon Graphics Iris 4D-210 VGX. Data are being entered by digitizing maps, reading digital data from existing archive media (e.g., 9-track tape, CD-ROM), and by direct entry at the console.

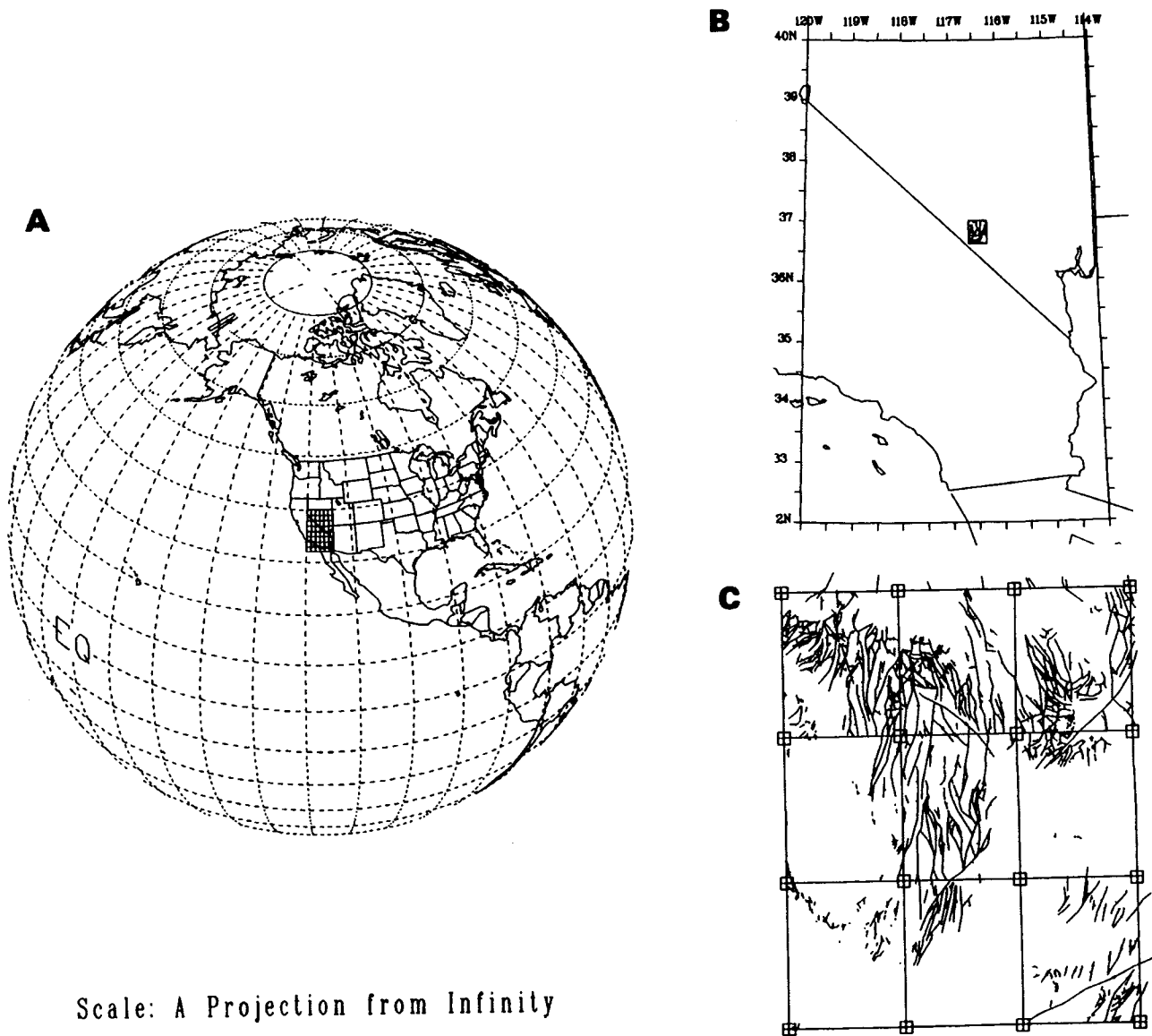
At this time, the Geologic Setting Tectonic Database (GSTDB) consists mostly of digital elevation data, Quaternary fault traces, earthquake hypocenters, and locations and age ranges of late Neogene and Quaternary basaltic volcanic systems. Data sets are being compiled at two geographic scales (Figure 11-1). The central Basin and Range Regional Tectonic Database (RTDB) (Figure 11-1B) covers a large area that encompasses the entire regional tectonic setting of Yucca Mountain. This particular area was chosen to specifically include all of the strike-slip dominated Mojave Desert/Death Valley region, and most of the Great Basin in which critical studies of normal and oblique slip faulting are being conducted. Data sets in this coverage are regional in scope and resolution. That is, they are positioned accurately within the regional-scale view. However, there is a practical limit to how much the regional view can be magnified. This limit depends on the precision and resolution of the source material. For example, faults digitized at a scale of 1:2,500,000 are difficult to precisely correlate with related terrain features at scales greater than about 1:100,000. The sub-regional scale Yucca Mountain Tectonic Database (YMTDB) (Figure 11-1C) comprises an area about 10–15 km around Yucca Mountain. The smaller region encompassed by the YMTDB allows compilation of the more detailed data acquired by site characterization and geologic studies of the Nevada Test Site.

### **11.5.1 Central Basin and Range Regional Tectonic Database**

The central Basin and Range RTDB covers an area that is 6° of longitude (114° W–120° W) by 8° of latitude (32–40° N). This area was chosen to encompass the central Basin and Range region (Wernicke, 1991), which includes the Mojave Shear Zone (Savage et al., 1990)/eastern California Shear Zone (Dokka and Travis, 1990a), the Walker Lane Belt (Carr, 1984), and part of the southern Great Basin.

#### **11.5.1.1 Digital Terrain Model**

The Digital Terrain Model (DTM) was developed from 3-arc, as shown in Figure 11-2, second digital elevation data acquired from the U.S. Geological Survey (USGS). The digital elevation data set consists of 47 1°×1° (latitude-longitude) cells of elevation points. Each cell is composed of  $1.44 \times 10^6$  (1200×1200) discrete elevation points. The spacing between elevation points is 3 seconds of latitude by 3 seconds of longitude or about 100 m within the latitude range of the RTDB. Elevations at each point



Scale: A Projection from Infinity

**Figure 11-1.** Location maps showing geographic areas covered by the GSTDB. The GSTDB consists of two parts: First is the central Basin and Range RTDB, which covers the area indicated by the grid of small squares in the center of the global projection (A). Each grid square is 1° of latitude. The RTDB coverage includes southern Nevada, Southern California, and a small part of western Arizona (B). Second, the YMTDB is a more detailed coverage of the region immediately around Yucca Mountain. The small square in the middle of the RTDB coverage (B) indicates the area covered by the YMTDB. The YMTDB covers an area comprised by nine 7.5 minute USGS topographic quadrangles (C).

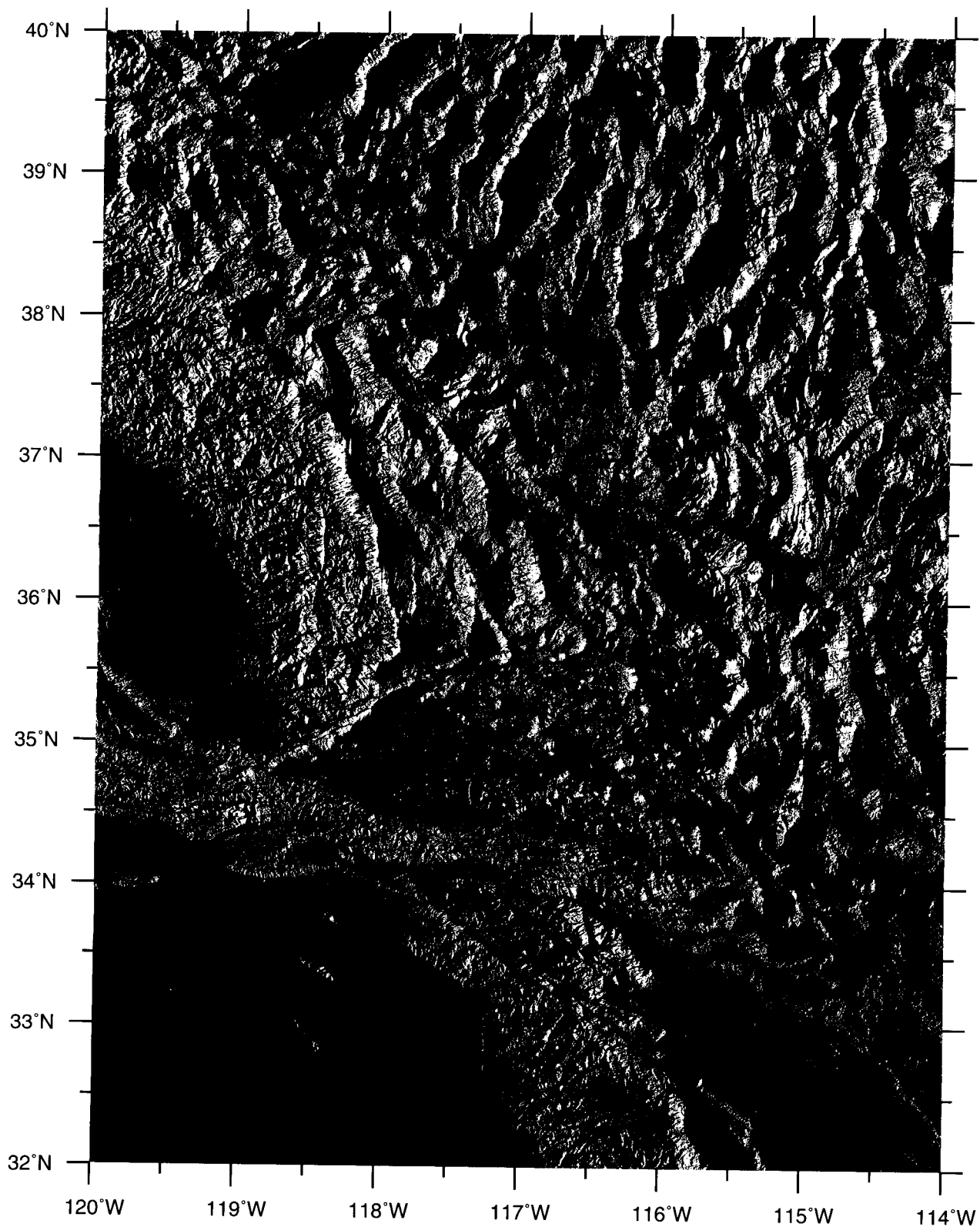


Figure 11-2. Digital Shaded-Relief Terrain Model (DTM) of the area covered by the central Basin and Range Regional Tectonic Database (RTDB). The DTM image of the RTDB area is produced from digital elevation data with a spacing of 3 arc-seconds between elevation points. Yucca Mountain is located in the center of the black square near the middle of the map. North is toward the top of the image. Distance and location in this projection is measured in latitude and longitude.

are known to  $\pm 20$  m. The DTM is used essentially as a backplane of terrain features on which to plot the geological and geophysical data. The value of the DTM is two-fold. First, the locations of faults, earthquake epicenters, volcanic fields, and geophysical anomalies, with respect to the mountain ranges and valleys, is immediately apparent. Second, the DTM can be used as a synthetic aerial photograph. The view-angle and the illumination-angle can be specified to enhance linear features, such as faults and fracture zones, in a specified range of orientations. Low illumination-angle views of the DTM simulate low sun-angle aerial photographs, and, thus, may be used to search for subtle fault scarps or structural trends that may not be apparent from other types of imagery. The resolution of this technique is limited by the resolution (spacing) of the digital elevation data. Closer spacing gives a higher resolution view.

#### **11.5.1.2 Earthquake Hypocenters**

Earthquake hypocenters are extracted from the Global Hypocenter Database of the USGS Earthquake Database System (USGS/NEIC 1992). As of this report, the RTDB contains most earthquakes recorded in the continental United States through 1988. This data set includes the Decade of North American Geology (DNAG) data set described by Engdahl and Rinehart (1988; 1991). The hypocenter data are currently being updated through 1993. Earthquake attribute data include date, magnitude, and focal depth. Figure 11-3 shows epicenter locations for earthquake magnitudes in excess of 4.0, plotted with Quaternary fault traces from Nakata et al. (1982).

#### **11.5.1.3 Quaternary Faults**

The current Quaternary fault coverage (Figure 11-3) has been digitized from Nakata et al. (1982) and Jennings (1992). Fault traces from Nakata et al. (1982) are shown plotted with earthquake epicenters on Figure 11-3. This is a generalized and incomplete coverage of Quaternary faults, but it reliably illustrates the overall pattern. A more detailed Quaternary fault coverage of California has been digitized from Jennings (1992). Comparable detailed Quaternary faults in Nevada are currently being digitized from a set of surficial geologic maps produced by Dohrenwend et al., (1982-1993). These data sets will be used to study the correlation between Quaternary faults and historic seismicity. The Jennings coverage includes the estimated age of most recent slip for each of the faults. An interesting preliminary observation from the Jennings coverage is that historic slip in southeastern California is generally restricted to Quaternary faults that show evidence of Holocene slip. Faults with Quaternary slip older than Holocene have not generally been active historically. This preliminary observation suggests that a time frame of 10,000-100,000 years may be a reasonably practical age range for definition of an active fault in the Mojave Desert/Death Valley area.

#### **11.5.1.4 Quaternary Volcanic Fields**

The locations of Quaternary volcanic fields (Figure 11-4) were digitized from Leudke and Smith (1981). The coverage at this time is quite general. A more detailed coverage is being produced from Leudke and Smith (1978; 1981; 1984). Detailed maps of selected Quaternary basaltic volcanic fields are currently being developed in the Volcanism Research project. These maps will be integrated with the detailed fault and seismicity maps produced by Tectonics Research. The integrated coverage will then be used to study correlations between Quaternary faulting, volcanism, and seismicity.

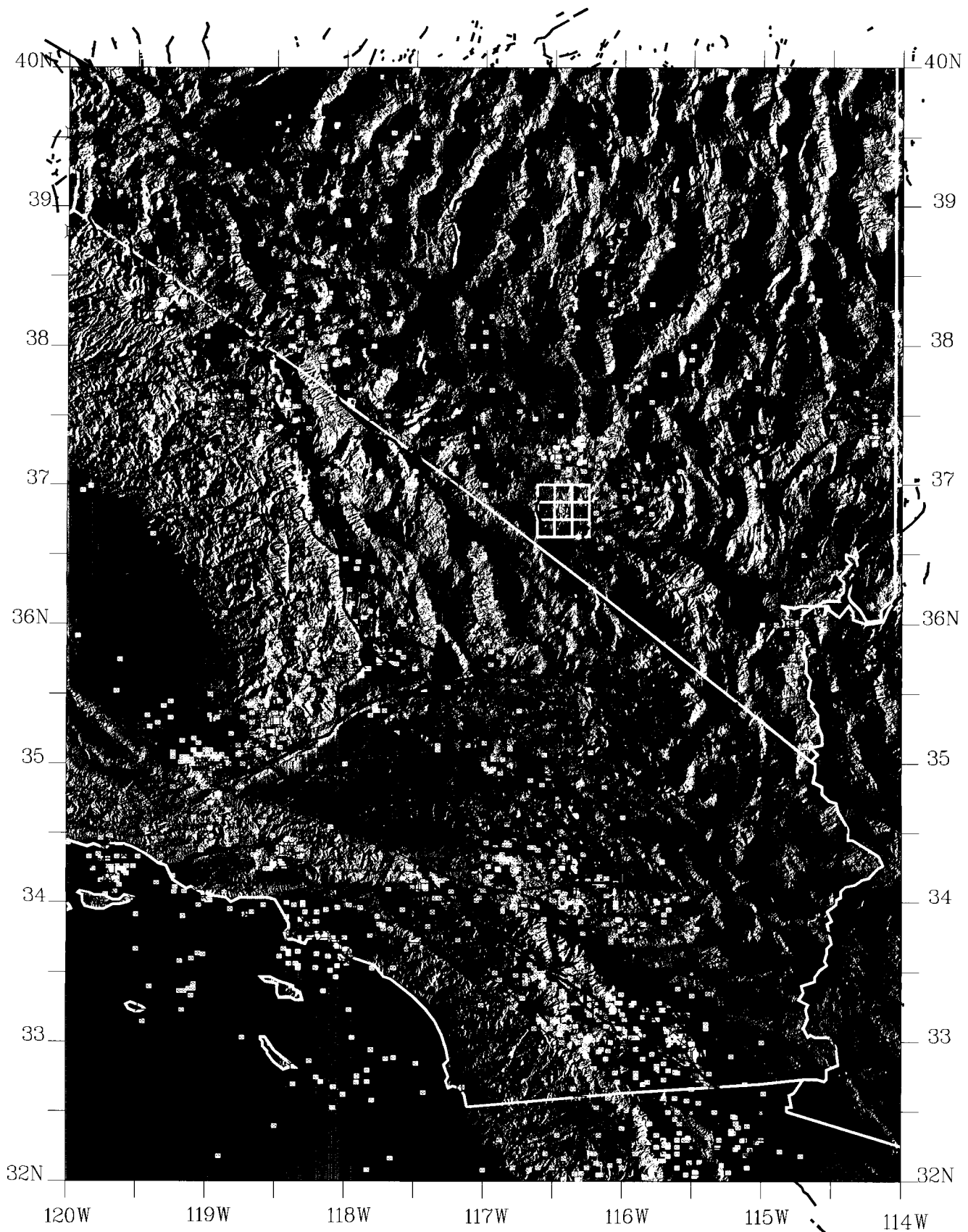


Figure 11-3. Map of Quaternary fault traces (Nakata et al., 1982) and earthquake epicenters (USGS/NEIC 1992b) from the Regional Tectonic Database plotted onto the regional digital terrain model from Figure 11-2. Quaternary fault traces are depicted as solid black lines. Earthquakes are indicated by small white squares (M4.0-M5.0); large black squares (M5.0-M6.0); and stars (M6.0+). Nevada and California state lines are in white. Yucca Mountain is at the center of the white square grid near the middle of the map. The white square grid indicates the nine 7.5 minute USGS topographic quadrangles that comprise the area covered by the more detailed Yucca Mountain Tectonic Database (Figure 11-5).

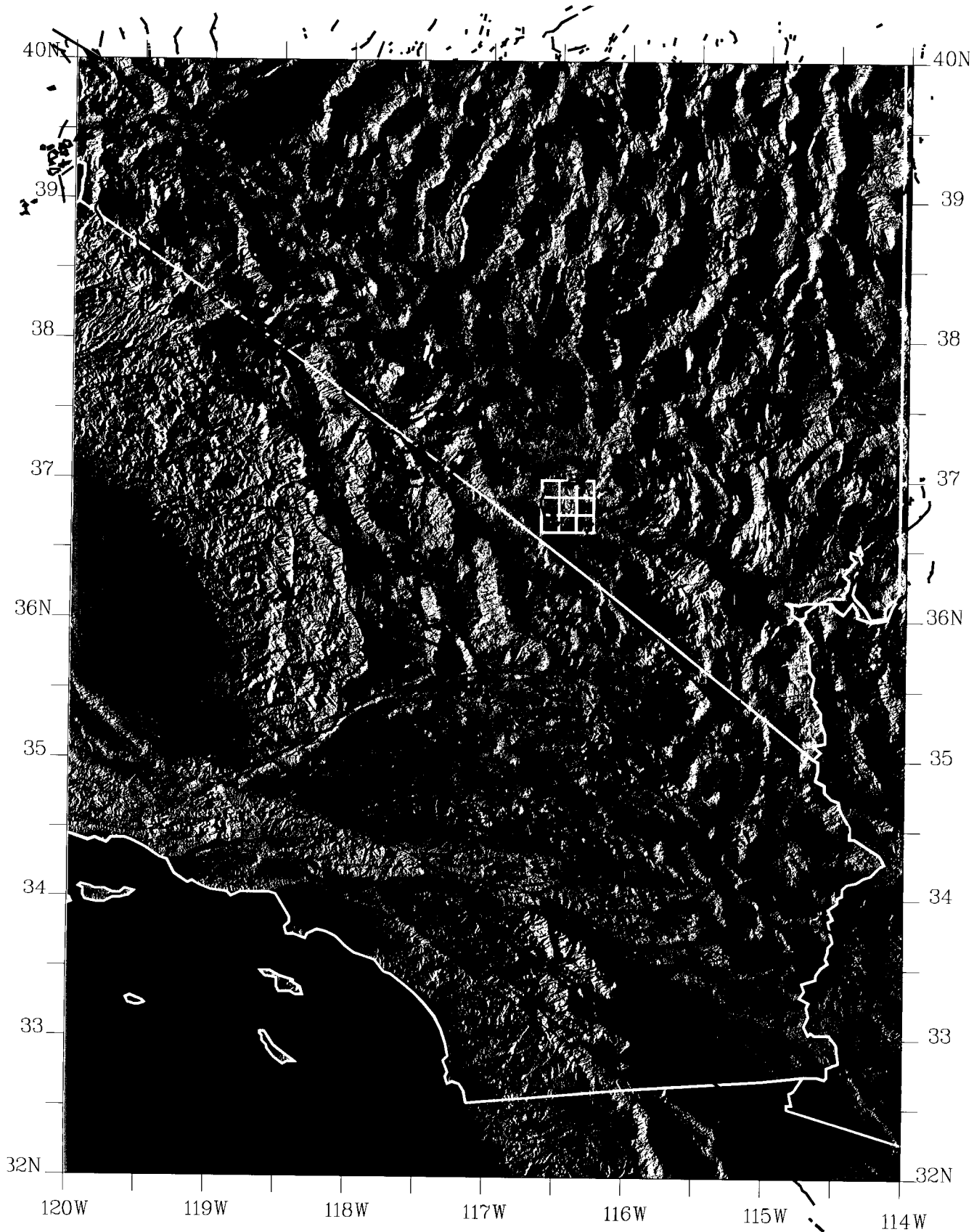


Figure 11-4. Map of Quaternary fault traces (Nakata et al., 1982) and late Neogene and Quaternary basaltic volcanic fields (Luedke and Smith, 1981) from the Regional Tectonic Database plotted onto the regional digital terrain model from Figure 11-2. Quaternary fault traces (same as Figure 11-3) are depicted in light gray lines. Basaltic volcanic fields are indicated by solid black outlines (0-5my); dark gray outlines (5my-10my); and light gray outlines (0-5my feldspathoidal basalts). Yucca Mountain is at the center of the white square grid near the middle of the map. The white square grid indicates the nine 7.5 minute USGS topographic quadrangles that comprise the area covered by the more detailed Yucca Mountain Tectonic Database (Figure 11-5).

## **11.5.2 Yucca Mountain Tectonic Database**

The YMTDB covers a much smaller area than the RTDB. The YMTDB is centered on Yucca Mountain, and covers the immediate surrounding area, including Crater Flat Valley, Fortymile Wash, Jackass Flats, and the Calico Hills. The YMTDB data sets cover an area comprised by nine 7.5 minute USGS map quadrangles.

### **11.5.2.1 Digital Terrain Model**

The DTM (Figure 11-5) for this database was developed from a higher resolution USGS digital elevation data set. The spacing between adjacent rows and columns of elevation points is 30 m. The DTM consists of nine 7.5 minute cells corresponding to the nine 7.5 minute topographic quadrangles that comprise the area.

### **11.5.2.2 Quaternary Faults**

Neogene and Quaternary faults in the YMTDB (Figure 11-6) were digitized from Frizzell and Shulters (1990). Photogeologic lineaments (Figure 11-7) were digitized from O'Neill et al. (1992). The lineaments generally correspond to fault scarps in Quaternary and Holocene alluvium, and connect to bedrock faults. The various fault maps produced for Yucca Mountain can now be selectively sampled to look for correspondence between features of interest. For example, the photogeologic lineament map may be overlain onto the more general fault map from Frizzell and Shulters (1990) to indicate which of the many interconnected faults may have Quaternary or Holocene slip. A separate map may then be produced that shows only those bedrock faults that correspond to a particular type of photo-lineament.

### **11.5.2.3 Topographic Contours and Borehole Locations**

Elevation contours currently available in the data base are derived from USGS Digital Line Graph (DLG) files (Figure 11-8). Additional contour maps will be generated directly from the digital elevation grid. The DLG contours can currently be displayed at a 20 foot or 100 foot contour interval. Elevation labels are being prepared for annotation of individual contours. Integration of elevation contours and the digital terrain model (Figure 11-8) allows elevation values to be estimated quickly for easily recognized terrain features. In the Yucca Mountain area, geologic structures are closely associated with particular geomorphic features such as distinct topographic ridges and valleys. Thus, construction of structural geologic cross sections is facilitated, and recognition of geologic structures based on terrain features is improved. Preliminary borehole locations (Figure 11-8) currently available in the data base are from Nelson et al. (1991).

### **11.5.2.4 Analysis of Terrain Data**

Digital elevation models (DEM) can be treated as synthetic aerial photographs. Because of the marked topographic expression of geological structures in the Yucca Mountain area, examination of the DEM from various view and illumination angles reveals substantial new insight on faulting. Visually distinct map-view geometries, interconnectivity, and dominant structural trends are dependant on how the model is viewed. Note the difference between views in Figure 11-9. Illumination of the model from west (Figure 11-9a) or east (Figure 11-9d) emphasizes the somewhat arcuate geometry of the Yucca Mountain ridge system as a whole, whereas illumination from north (Figure 11-9b) or south (Figure 11-9c)

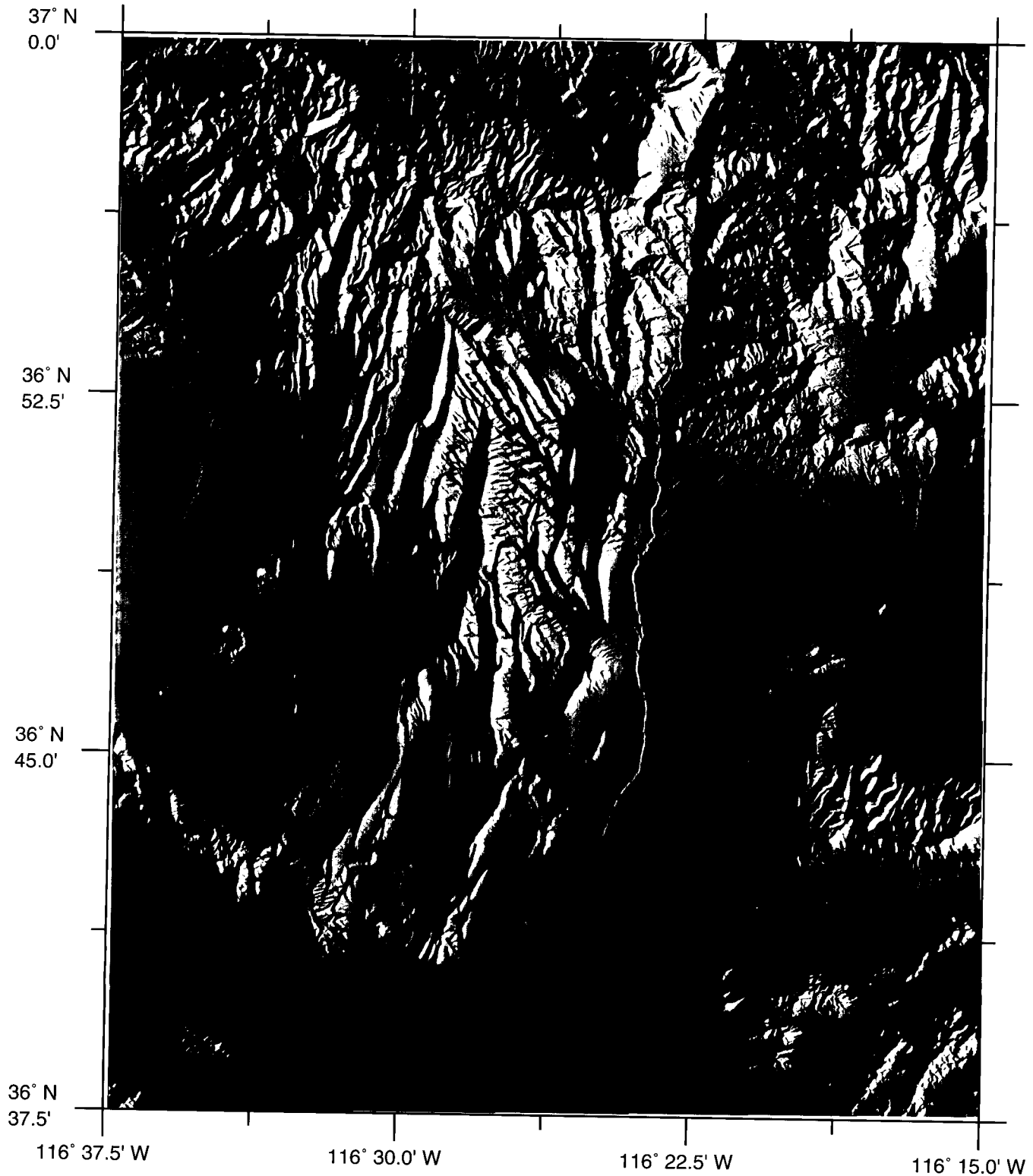


Figure 11-5. Digital Shaded-Relief Terrain Model (DTM) of the area covered by the Yucca Mountain Tectonic Database (YMTDB). The location of this area is indicated by the solid black square near the middle of Figures 11-1B and 11-2, and by the white square grids near the middle of Figures 11-3 and 11-4. The DTM image for the YMTDB area is produced from digital elevation data with a spacing of 30 meters between elevation points. The model is illuminated from an azimuth of 105° (east-southeast) and 35° above the horizon. Yucca Ridge is the prominent north-south ridge in the center-left of the image. Projection is Universal Transverse Mercator. North is toward the top of the map. 1 inch = 3.3 miles. 1 cm = 2.06 km.

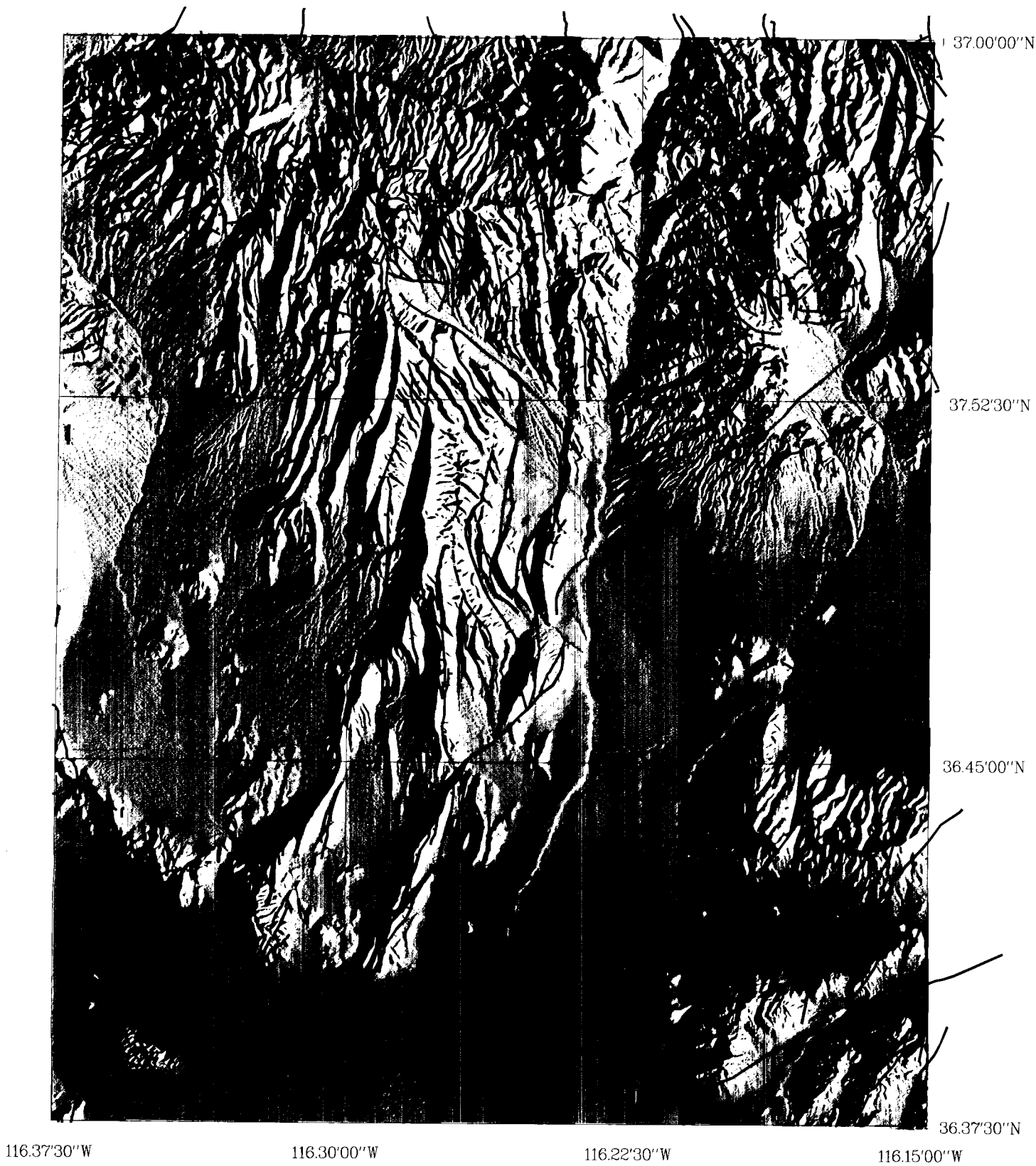


Figure 11-6. Map of Neogene and Quaternary faults (Frizzell and Shulters, 1990) from the Yucca Mountain Tectonic Database plotted onto the digital terrain model shown in Figure 11-5.

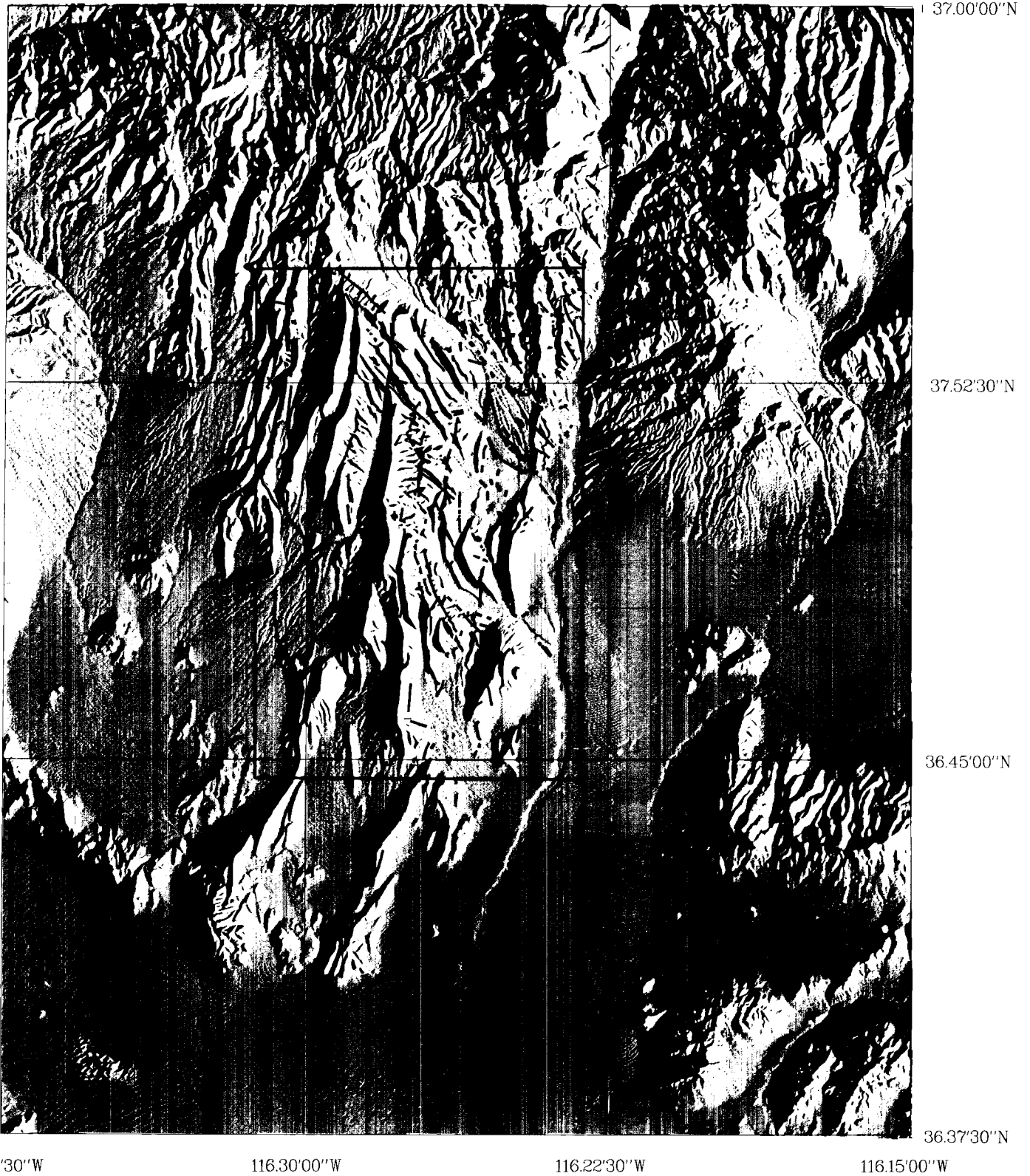


Figure 11-7. Map of photogeologic lineaments (O'Neill, 1992) from the Yucca Mountain Tectonic Database plotted onto the digital terrain model show in Figure 11-5.

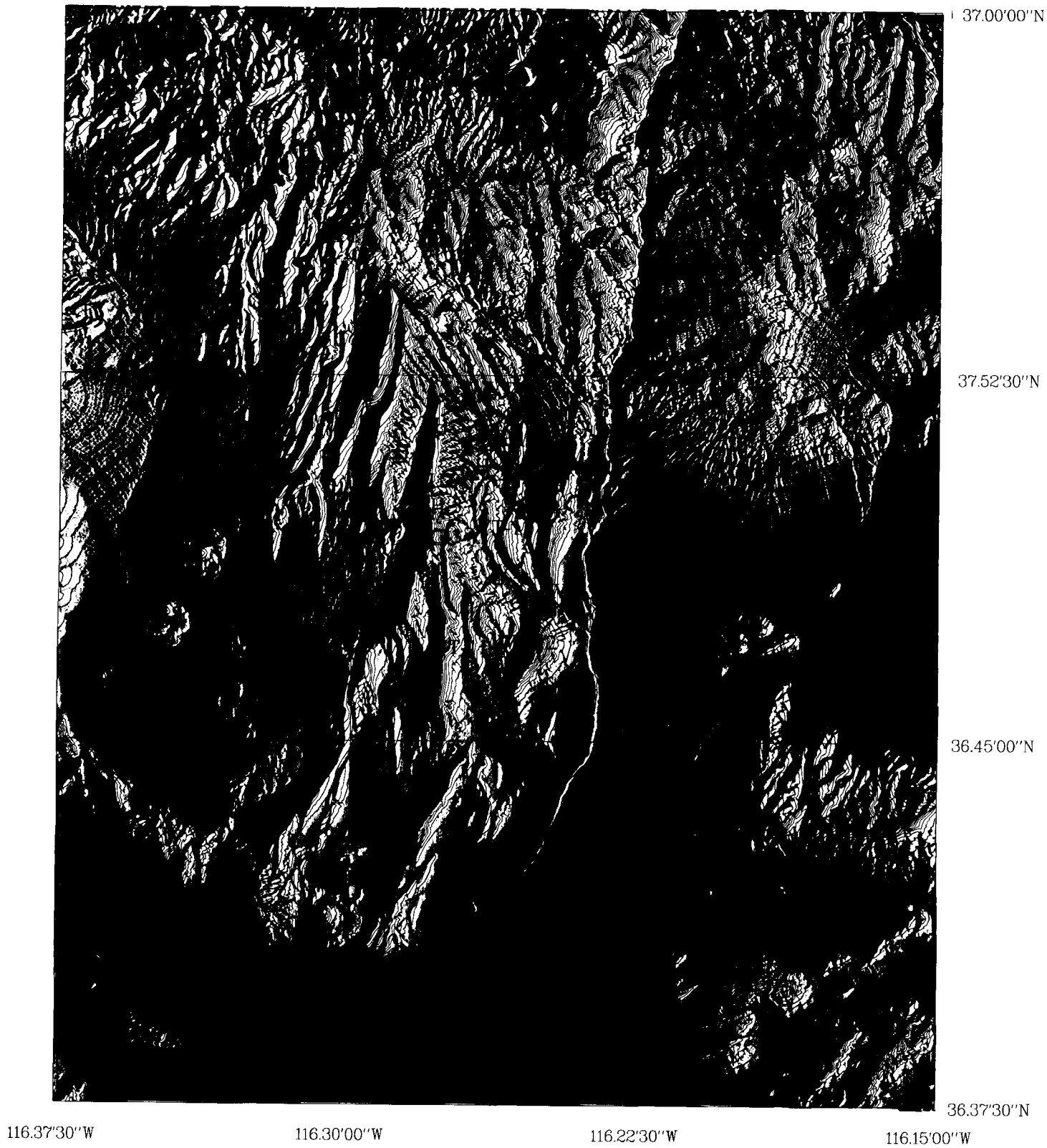
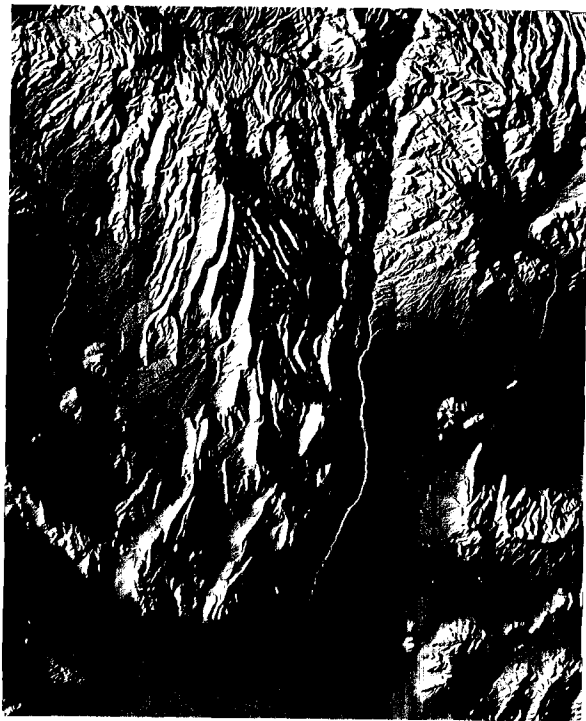
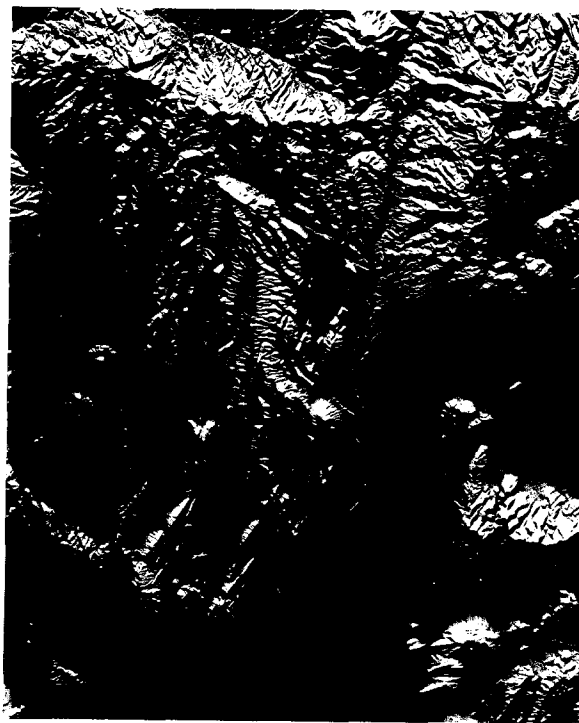


Figure 11-8. Map showing location of selected boreholes at Yucca Mountain plotted on Digital Terrain Model (DTM) shown in Figure 11-5. Topographic contour lines are plotted at an interval of 100 ft. Contour labels have been omitted for clarity.



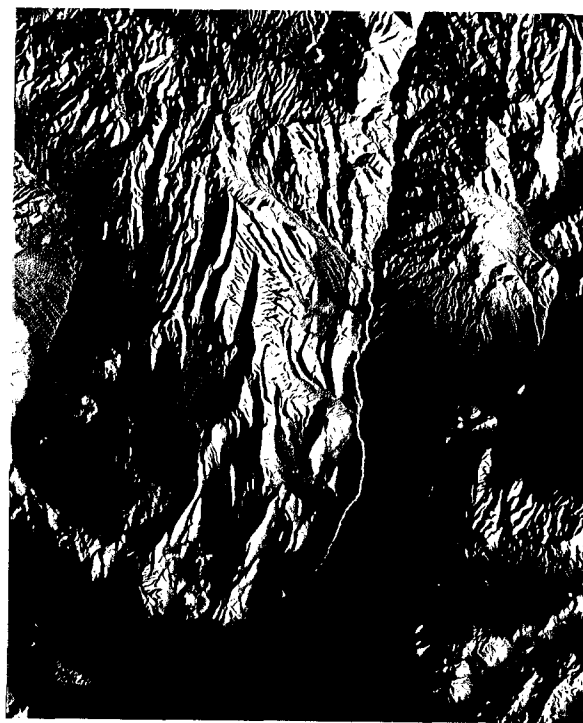
(a)



(b)



(c)



(d)

Figure 11-9. Shaded-relief digital terrain model shown in Figure 11-5 illuminated from west (a), north (b), south (c), and east (d). The computer generated terrain images may thus be treated as a synthetic alternative to low sun-angle aerial photographs. For instance, illumination from north (b) and south (c) enhances northeast trending structural/geomorphic fabric that is not as distinct in the images illuminated from west (a) and east (d).

enhances a strong northeast-southwest trending linear fabric. In particular, illumination from the north strikingly reveals the northeast trend and strongly enhances the small-scale fault-controlled ridges that transect the entire area. This method may prove to be valuable in distinguishing between distinct fault systems and in determining the interconnectivity of the entire fault system. A comprehensive set of experiments is planned to test these methods.

## **11.6 ASSESSMENT OF PROGRESS TOWARDS MEETING PROJECT OBJECTIVES**

Development of CDM for the primary regulatory requirements related to tectonics has not yet started. However, the Tectonics Research Project is expected to contribute particularly to CDM development for the following LARP sections: 3.2.1.5 Structural Deformation; 3.2.1.6 Historic Earthquakes; 3.2.1.7 Correlation of Earthquakes with Tectonic Processes; 3.2.1.8 Increasing Earthquake Frequency/Magnitude; and 3.2.1.9 Evidence of Igneous Activity. Substantial input was provided during development of the CDS on Structural Deformation and Groundwater (LARP Section 3.2.2.8), and it is likely that additional input will be provided for development of the CDM on the topic. At this time, input to Iterative Performance Assessment (IPA) is expected to consist mainly of uncertainty estimates for seismic and fault rupture risk analysis. For IPA input, the current emphasis is on slip-rate estimates for Quaternary and Holocene faults, and correlation of slip rate to earthquake recurrence an magnitude.

The project is generally on schedule. No significant technical problems have been encountered. Review of the literature on dating methods and age estimation of fault lip is a few months behind schedule. However, compilation of data and development of the GIS database are significantly further along than anticipated. Compilation of Quaternary faults and historic seismicity has gone particularly well. Good progress is being made in production of a detailed Quaternary fault coverage, and a significant number of slip-rate estimates are emerging in the current literature. Thus, correlations of historic seismicity and paleoseismicity (earthquake recurrence period) with Quaternary slip rate may be significantly improved. It is too early to determine progress toward resolution of specific issues or KTUs mentioned in the LARP. At this time, results of this project may be useful in developing guidance for the DOE on the extend of studies conducted outside of the controlled area. For instance, data required for correlations of fault slip with earthquake magnitudes must be acquired from many fault systems throughout the region. This project may point to analogous fault systems with particularly good paleoseismic and earthquake records.

## **11.7 PLANS FOR NEXT REPORTING PERIOD**

Data compilation will continue during the next report period. The effort level on review of literature on methods for dating fault slip will be increased somewhat, and this task is expected to be mostly finished. Planning for field work and some field reconnaissance will be conducted. Critical review of the database will be started. Preliminary correlations between earthquakes and fault characteristics will be made using conditional (Boolean) queries of the ARC/INFO database.

## 11.8 REFERENCES

- Anders, M.H., J.R. Hopper, R. Abad, and M. Spiegelman. 1993. Lower crustal flow: the origin of late Cenozoic extension north of the eastern Snake River Plain. Cordilleran and Rocky Mountain Section Meeting, Geological Society of America, May 19-21, Reno Nevada. Abstracts with Programs 25(5): 2.
- Anderson, J.G., J. Louie, Y. Zeng, G. Yu, M. Savage, D. DePolo, and J.N. Brune. 1993. Earthquakes in Nevada triggered by the Landers, California earthquake, June 28, 1992. Cordilleran and Rocky Mountain Section Meeting, Geological Society of America, May 19-21, Reno Nevada. Abstracts with Programs 25(5): 3.
- Anderson, L.W., and D.R. O'Connell. 1993. Late Quaternary faulting and historic seismicity in the western Lake Mead area, Nevada, Arizona, and California. Cordilleran and Rocky Mountain Section Meeting, Geological Society of America, May 19-21, Reno Nevada. Abstracts with Programs 25(5): 3.
- Argus, D.F., and R.G. Gordon. 1991. Current Sierra Nevada-North America motion from very long baseline interferometry: Implications for the kinematics of the western United States. *Geology* 19:1085-1088.
- Beanland, S. and M.M. Clark. 1993. Late Quaternary history of the Owens Valley Fault Zone, eastern California, and surface rupture associated with the 1872 earthquake. Cordilleran and Rocky Mountain Section Meeting, Geological Society of America, May 19-21, Reno Nevada. Abstracts with Programs 25(5): 7.
- Bell, J.W. 1993. Behavior of late Quaternary and historical faults in the western Basin and Range province. Cordilleran and Rocky Mountain Section Meeting, Geological Society of America, May 19-21, Reno Nevada. Abstracts with Programs 25(5): 8.
- Bryant, W.A. 1993. Holocene faulting in the western Basin and Range, California. Cordilleran and Rocky Mountain Section Meeting, Geological Society of America, May 19-21, Reno Nevada. Abstracts with Programs 25(5): 15.
- Butler, P.R., B.W. Tronel, and K.L. Verosub. 1988. Late cenozoic history and styles of deformation along the southern Death Valley Fault zone, California: *Geological Society of America Bulletin*. 11: 402-410.
- Carr, M. 1984. Regional structural setting of Yucca Mountain, southwestern Nevada, and late cenozoic rates of tectonic activity in part of the southwestern Great Basin. Nevada and California. *U.S. Geological Survey Open File report*. OF-84-854: 109.
- Caskey, S.J., and S.G. Wesnousky. 1993. Reinvestigation of fault trace complexity and slip distribution for the 16 December 1954 Fairview Peak ( $M_s=7.2$ ) and Dixie Valley ( $M_s=6.8$ ) earthquakes, central Nevada. Cordilleran and Rocky Mountain Section Meeting, Geological Society of America, May 19-21, Reno Nevada. Abstracts with Programs 25(5): 19.

- Cinti, F.R., T.E. Fumal, C.D. Garvin, J.C. Hamilton, T.J. Powers, and D.P. Schwartz. 1993. Earthquake recurrence and fault behavior on the Homestead Valley fault--central segment of the 1992 Landers surface rupture sequence. Cordilleran and Rocky Mountain Section Meeting, Geological Society of America, May 19-21, Reno Nevada. Abstracts with Programs 25(5): 21.
- Clark, M.M., and A.R. Gillespie. 1993. Variations in late Quaternary behavior along and among range-front faults of the Sierra Nevada, California. Cordilleran and Rocky Mountain Section Meeting, Geological Society of America, May 19-21, Reno Nevada. Abstracts with Programs 25(5): 21.
- Davis, G.A., and B.C. Burchfiel. 1993. Tectonic problems revisited: the eastern terminus of the Miocene Garlock fault and the amount of slip on the southern Death Valley fault zone. Cordilleran and Rocky Mountain Section Meeting, Geological Society of America, May 19-21, Reno Nevada. Abstracts with Programs 25(5): 28.
- DeMets, C., R.G. Gordon, D.F. Argus, and S. Stein. 1990. Current plate motions. *Geophysical Journal International* 101: 425-478.
- Dohrenwend, J.C., and B. Moring. 1993. Reconnaissance photogeologic map of late Tertiary and Quaternary faults in Nevada. Cordilleran and Rocky Mountain Section Meeting, Geological Society of America, May 19-21. Reno Nevada. Abstracts with Programs 25(5): 31.
- Dohrenwend, J.C. 1982. Surficial Geologic Map of the Walker Lake 1° by 2° quadrangle, Nevada - California. Scale 1:250,000. U.S. Geological Survey Miscellaneous Field Studies Map MF-1382-C.
- Dohrenwend, J.C., and B. C. Moring. 1991. Reconnaissance photogeologic map of young faults in the Vya 1° by 2° quadrangle, Nevada, Oregon, and California. Scale 1:250,000. U.S. Geological Survey Miscellaneous Field Studies Map MF-2174.
- Dohrenwend, J.C., and B. C. Moring 1991. Reconnaissance photogeologic map of young faults in the Winnemucca 1° by 2° quadrangle, Nevada. Scale 1:250,000. U.S. Geological Survey Miscellaneous Field Studies Map MF-2175.
- Dohrenwend, J.C., B. A. Schell, and B. C. Moring 1992. Reconnaissance photogeologic map of young faults in the Millett 1° by 2° quadrangle, Nevada. Scale 1:250,000. U.S. Geological Survey Miscellaneous Field Studies Map MF-2176.
- Dohrenwend, J.C., and B.C. Moring. 1991. Reconnaissance photogeologic map of young faults in the McDermitt 1° by 2° quadrangle, Nevada, Oregon, and Idaho. Scale 1:250,000. U.S. Geological Survey Miscellaneous Field Studies Map MF-2177.
- Dohrenwend, J.C., M.A McKittrick, and B.C. Moring. 1991. Reconnaissance photogeologic map of young faults in the Lovelock 1° by 2° quadrangle, Nevada and California. Scale 1:250,000. U.S. Geological Survey Miscellaneous Field Studies Map MF-2178.
- Dohrenwend, J.C., B.A. Schell, and B.C. Moring. 1991. Reconnaissance photogeologic map of young faults in the Elko 1° by 2° quadrangle, Nevada and Utah. Scale 1:250,000. U.S. Geological Survey Miscellaneous Field Studies Map MF-2179.

- Dohrenwend, J.C., B.A. Schell, and B.C. Moring. 1991. Reconnaissance photogeologic map of young faults in the Lund 1° by 2° quadrangle, Nevada and Utah. Scale 1:250,000. U.S. Geological Survey Miscellaneous Field Studies Map MF-2180.
- Dohrenwend, J.C., B.A. Schell, and B.C. Moring. 1991. Reconnaissance photogeologic map of young faults in the Ely 1° by 2° quadrangle, Nevada and Utah. Scale 1:250,000. U.S. Geological Survey Miscellaneous Field Studies Map MF-2181.
- Dohrenwend, J.C., C.M. Menges, B.A. Schell, and B.C. Moring. 1991. Reconnaissance photogeologic map of young faults in the Las Vegas 1° by 2° quadrangle, Nevada, California, and Arizona. Scale 1:250,000. U.S. Geological Survey Miscellaneous Field Studies Map MF-2182.
- Dohrenwend, J.C., B.A. Schell, M.A. McKittrick, and B.C. Moring. 1992. Reconnaissance photogeologic map of young faults in the Goldfield 1° by 2° quadrangle, Nevada and California. Scale 1:250,000. U.S. Geological Survey Miscellaneous Field Studies Map MF-2183.
- Dohrenwend, J.C., M.A. McKittrick, and B.C. Moring. 1991. Reconnaissance photogeologic map of young faults in the Wells 1° by 2° quadrangle, Nevada, Utah, and Idaho. Scale 1:250,000. U.S. Geological Survey Miscellaneous Field Studies Map MF-2184.
- Dokka, R.K., and C.J. Travis. 1990a. Role of the eastern California shear zone in accommodating Pacific-North American plate motion. *Geophysical Research Letters* 17(9): 1323-1326.
- Dokka, R.K., and C.J. Travis. 1990b. Late cenozoic strike-slip faulting in the Mojave Desert, California. *Tectonics* 9(2): 311-340.
- Engdahl, E.R., and W.A. Rinehart. 1991. Seismicity Map of North America Project, D.B Slemmons, E.R. Engdahl, M.D. Zoback, and D.D. Blackwell eds., Neotectonics of North America: Geological Society of America, Decade Map Volume I. Boulder CO: 21-27.
- Engdahl, E.R., and W.A. Rinehart. 1988. Seismicity map of North America, Continent-scale map-004, scale 1:5,000,000, The Geological Society of America, Boulder CO.
- Frizzel, V.A., Jr., and J. Shulters. 1990. Geologic map of the Nevada Test Site, southern Nevada. 1:100,000 U.S. Geological Survey Miscellaneous Investigations Series Map I-2046.
- Gans, P.B., G.A. Mahood, and E. Schermer. 1989. *Synextensional Magmatism in the Basin and Range Province: A Case Study from the Eastern Great Basin*. Geological Society of America Special Paper 233. Boulder, CO: Geological Society of America.
- Glazner, A.F., and J.M. Bartley. 1984. Timing and tectonic setting of Tertiary low-angle normal faulting and associated magmatism in the southwestern United States: *Tectonics*, 3: 385-396.
- Hecker, S. 1993. Rates and patterns of Holocene-latest Pleistocene faulting, eastern Basin and Range, Utah. Cordilleran and Rocky Mountain Section Meeting, Geological Society of America, May 19-21, Reno Nevada. Abstracts with Programs 25(5): 50.

- Hemphill-Haley, M.A. T.L. Sawyer, I.G. Wong, P.L.K. Knuepfer, S.L. Forman, and R.P. Smith. 1993. Late Quaternary faulting along the southern Lemhi fault, southeastern Idaho: a complex segmentation history. Cordilleran and Rocky Mountain Section Meeting, Geological Society of America, May 19-21, Reno Nevada. Abstracts with Programs 25(5): 51.
- Hill, D.P., et al. 1993. Seismicity remotely triggered by the magnitude 7.3 Landers, California, earthquake. *Science*, 260: 1617-1626.
- Jennings, C.W. 1992. Preliminary Fault Activity Map of California. DMG Open-File Report 92-03. The Resources Agency, California Department of Conservation, Division of Mines and Geology:76. Replaces the 1:750,000 scale Fault Map of California, Bulletin 201, California Dept. of Conservation, Division of Mines and Geology, and the Fault Map of California with location of volcanoes, thermal springs, and thermal wells (Jennings 1975).
- Kohler, G., J.S. Oldow, V.B. Sisson, and R.A. Donelick. 1993. Displacement transfer system linking the Furnace Creek and Walker Lane fault systems, west-central Nevada. Cordilleran and Rocky Mountain Section Meeting, Geological Society of America, May 19-21, Reno Nevada. Abstracts with Programs 25(5): 63.
- Knuepfer, P.L.K., 1993. Late Quaternary Basin-Range faulting north of the Eastern Snake River Plain, Idaho. Cordilleran and Rocky Mountain Section Meeting, Geological Society of America, May 19-21, Reno Nevada. Abstracts with Programs 25(5): 63.
- Kruse, S.M., McNutt, J. Phipps-Morgan, L. Royden, and B. Wernicke. 1991. Lithospheric extension near Lake Mead, Nevada: A model for ductile flow in the lower crust. *Journal of Geophysical research* 96(B3):4,435-4,456.
- Lifton, N.A., and A.J. Jull. 1993 A new method for estimating bedrock surface exposure ages and long-term erosion rates using a single in-situ-produced cosmogenic radionuclide. Cordilleran and Rocky Mountain Section Meeting, Geological Society of America, May 19-21, Reno Nevada. Abstracts with Programs 25(5): 70.
- Lipman, P.W., H.J. Protska, and R.L. Christiansen. 1972. Cenozoic volcanism and plate tectonic evolution of the western United States; 1. Early and middle Cenozoic. *Royal Society of London Philosophical Transactions*, 271(A): 217-248.
- Luedke, R.G., and R.L. Smith. 1978. Map showing distribution, composition and age of late Cenozoic volcanic centers in Arizona and New Mexico. U.S. Geological Survey Miscellaneous Investigations Series Map I-1091-A.
- Luedke, R.G., and R.L. Smith. 1981. Map showing distribution, composition and age of late Cenozoic volcanic centers in California and Nevada. U.S. Geological Survey Miscellaneous Investigations Series Map I-1091-C.
- Luedke, R.G., and R.L. Smith. 1984. Map showing distribution, composition and age of late Cenozoic volcanic centers in the western coterminous United States. U.S. Geological Survey Miscellaneous Investigations Series Map I-1523.

- Lund, W.R. 1993. summary of Holocene surface faulting and fault segmentation, Wasatch fault zone, Utah. Abstracts with programs, Vol 25, No. 5, Cordilleran and Rocky Mountain Section Meeting, The Geological Society of America, Reno, Nevada: 112.
- Lundstrom, S.C., J.R. Wesling, F.H. Swan, E.M. Taylor, and J.W. Whitney. 1993. Quaternary allostratigraphy of surficial deposit map units at Yucca Mountain, Nevada: a progress report. Cordilleran and Rocky Mountain Section Meeting, Geological Society of America, May 19-21, Reno Nevada. Abstracts with Programs 25(5): 112.
- Machette, M.N., K.M. Haller, and K.R. Berryman. 1993. Prehistoric movement along the 1915 Pleasant Valley fault zone and implications for the Central Nevada Seismic Belt. Cordilleran and Rocky Mountain Section Meeting, Geological Society of America, May 19-21, Reno Nevada. Abstracts with Programs 25(5): 112.
- McGill, S.F. 1993. Late Quaternary slip rate of the Owl Lake fault and maximum age of the latest event on the easternmost Garlock fault, S. California. Cordilleran and Rocky Mountain Section Meeting, Geological Society of America, May 19-21, Reno Nevada. Abstracts with Programs 25(5): 118.
- Menges, C.M., G. Vadurro, R. Cress, J. Coe and F.W. Simonds. 1993. Stratigraphic evidence for multiple small Quaternary displacements on the Bow Ridge fault at northeast Yucca Mountain, Nye County, Nevada. Cordilleran and Rocky Mountain Section Meeting, Geological Society of America, May 19-21, Reno Nevada. Abstracts with Programs 25(5): 120.
- Minster, J.B., and T.H. Jordan. 1987. Vector constraints on western U.S. deformation from space geodesy, neotectonics, and plate motions. *Journal of Geophysical Research* 92(B6): 4,798-4-808.
- Nakata, J.K., C.M. Wentworth, and M. Machette. 1982. Quaternary Fault Map of the Basin and Range and Rio Grande Rift Provinces, Western United States. U.S. Geological Survey Open-File Report 82-579.
- Nelson, P.H., D.C. Muller, U. Schimschal, and J.E. Kibler. 1991. Geophysical logs and core measurements from forty boreholes at Yucca Mountain, Nevada. U.S. Geological Survey Geophysical Investigations Map GP-1001.
- O'Neill, J. M., J.W. Whitney, and M.R. Hudson. 1992. Photogeologic and kinematic analysis of lineaments at Yucca Mountain, Nevada: Implications for strike-slip faulting and oroclinal bending. U.S. Geological Survey Open-File Report 91-623: 23.
- Ramelli, Alan R. and Craig M. Depolo. 1993. Examples of Holocene and latest Pleistocene faulting in northern and eastern Nevada. Cordilleran and Rocky Mountain Section Meeting, Geological Society of America, May 19-21, Reno Nevada. Abstracts with Programs 25(5):136.
- Savage, J.C., M. Lisowski and W.H. Prescott. 1990. An apparent shear zone trending north-northwest across the Mojave Desert into Owens Valley, eastern California, *Geophysical Research Letters*, 17(12): 2113-2116.

- Scott, R.B. 1990. Tectonic setting of Yucca Mountain, southwestern Nevada. B.P. Wernicke, ed. *Basin and Range Extensional Tectonics Near the Latitude of Las Vegas, Nevada*. Geological Society of America Memoir 176: 251-282
- Sieh, K.E., et al. 1993. Near-field investigations of the Landers earthquake sequence, April to July 1992. *Science* 260: 171-176.
- Stirewalt, G.L. and S.R. Young. 1992. A review of pertinent literature on volcanic-magmatic and tectonic history of the Basin and Range. Center for Nuclear Waste Regulatory Analyses Technical Report CNWRA 92-025. San Antonio, TX.
- Swadley, W.C., D.L. Hoover, and J.N. Rosholt. 1984. Preliminary report on late Cenozoic stratigraphy and faulting in the vicinity of Yucca Mountain, Nye County, Nevada: U.S. Geological Survey Open-File Report 84-788: 42.
- Swan, F.H., J.R. Wesling, and A.P. Thomas. 1993. Paleoseismic investigations of the Paintbrush Canyon fault in southern Midway Valley, Yucca Mountain, Nevada: Preliminary results. Cordilleran and Rocky Mountain Section Meeting, Geological Society of America, May 19-21, Reno Nevada. Abstracts with Programs 25(5):153.
- USGS/NEIC. 1992. U.S. Geological Survey, Global Hypocenter Database CD-ROM, National Earthquake Information Center, Denver.
- USGS/NEIC. 1992b. U.S. Geological Survey, Earthquake Database System (EDBS), National Earthquake Information Center, Denver.
- Wallace, R.E. 1984. Patterns and timing of late Quaternary faulting in the Great Basin province and relation to some regional tectonic features. *Journal of Geophysical Research* 89(B7): 5763-5769.
- Ward, S.N. 1990. Pacific-North American plate motions: New results from very long baseline interferometry. *Journal of Geophysical Research* 95(B13): 21,965-21,981.
- Wernicke, B.P. 1991. Cenozoic extensional tectonics of the U.S. Cordillera. The Cordilleran Orogen: Coterminous U.S., B.C. Burchfiel, P.W. Lipman, and M.L. Zoback, eds. *The Geology of North America G-3*. Boulder, CO: Geological Society of America.
- Wernicke, B.P., G.J. Axen, and J.K. Snow. 1988. Basin and Range extensional tectonics at the latitude of Las Vegas, Nevada. *Geological Society of America Bulletin* 100: 1,738-1,757.

## 12 FIELD VOLCANISM RESEARCH

*by Charles B. Connor*

*Investigators: Charles B. Connor, Brittain E. Hill, Gerry L. Stirewalt (CNWRA);  
Kenneth D. Mahrer, Jorge Parra (SwRI)*

*NRC Project Officer: L.A. Kovach*

### 12.1 TECHNICAL OBJECTIVES

The Yucca Mountain region (YMR) has been the site of recurring small volume basaltic eruptions during the last 10 million years (Crowe et al., 1983; Smith et al., 1990). This volcanic activity has led to the formation of numerous cinder cones, eight of which are less than 1.6 million years old. These volcanoes likely represent a range of eruptive activity, from extremely explosive eruptions to comparatively gentle effusive volcanic eruptions (Valentine et al., 1992; Amos et al., 1983; Walker, 1993). The technical objectives of the Field Volcanism project are to better characterize the effect of this type of volcanic activity on repository performance and, as a result, better constrain probability models of disruption of the repository. This characterization will be possible through investigation of the: (i) mechanics of mafic cinder cone eruptions; (ii) extent and characteristics of shallow hydrothermal systems and diffuse degassing associated with small volume mafic eruptions; and (iii) nature of mafic intrusive geometries at repository depths. Successful completion of the Field Volcanism project, which began in April 1993, will require study of Plio-Quaternary cinder cones in the western Great Basin and comparison with modern, recently active cinder cones located elsewhere.

Results of the Field Volcanism project will be used to support specific sections of the License Application Review Plan (LARP). Insight into the possible magnitude of volcanic processes likely to occur in the YMR in the event of further volcanic activity, the areas probably affected, and the likely duration of volcanic activity form an integral part of site characterization activities (evidence of igneous activity as a potentially adverse condition, Section 3.2.1.9; and impact of volcanism on groundwater movement, Section 3.2.2.7), and the description of overall system performance (assessment of compliance with the requirement for cumulative releases of radioactive materials, Section 6.1). Compliance Determination Strategies (CDS) for these LARP sections are currently under development. The CDS associated with evidence of Quaternary volcanism are of Type 5, indicating that independent research must be conducted to evaluate Key Technical Uncertainties (KTU) associated with volcanism and that volcanism poses a high risk to U.S. Nuclear Regulatory Commission (NRC) of reaching unwarranted conclusions regarding compliance with 40 CFR Part 191 and 10 CFR Part 60.122(c)(15). For example, until acceptable methods for the characterization of the likely magnitude and duration of eruptive activity and the determination of the impact of this activity on groundwater and geochemical transport are found, it will be difficult to ascertain compliance with 40 CFR Part 191.

To date, three KTUs related to igneous activity have been identified as part of the CDS concerned with evidence of Quaternary igneous activity. These KTUs are:

- Low resolution of exploration techniques to detect and evaluate igneous features (Type 4)
- Inability to sample igneous features (Type 5)

- Development and use of conceptual tectonic models as related to igneous activity (Type 5).

Evaluation of these KTUs will require detailed safety review supported by analyses (Type 4), and detailed safety review supported by independent tests, analyses, and other investigations (Type 5). Additional KTUs related to igneous activity will likely be identified in a forthcoming CDS on rates of tectonic activity. The Field Volcanism project will address each of these KTUs. For example, Task 4 investigations into geophysical techniques for identifying anomalies related to subsurface igneous dikes will address uncertainties resulting from the low resolution of exploration techniques, a Type 4 KTU. Many problems in eruption dynamics and the extent of volatile degassing following eruptive activity can only be addressed by comparison of past eruptions at recently active cinder cones with those of the YMR. Tasks 2 and 3 in the Field Volcanism project are designed to investigate eruptive activity and degassing, providing independent testing, analysis, and investigation addressing the inability to sample igneous features, a Type 5 KTU.

Successful completion of the Field Volcanism research project and efficient integration with the LARP will require interaction with the Volcanic Systems of the Basin and Range research project. This project concentrates on probability model development and the structural setting of volcanism in the Basin and Range, the Tectonic Setting of the central Basin and Range project, Geologic Setting Task 3 Nuclear Material Safety and Safeguards (NMSS) on faulting and dike interaction, and performance assessment projects. For example, the Field Volcanism project will provide data that are critical for review of alternate probability models. In addition, results of the Task 3 (NMSS) work on dike-fault interaction will be important to modeling mechanisms of dike emplacement in Task 4 of the Field Volcanism project. The Field Volcanism project, together with these associated investigations, will form an integral part of volcanism models in Iterative Performance Assessment (IPA). For example, the effects of development of a shallow diffuse degassing system about a cooling cinder cone, and estimates of the area likely to be influenced by such a system are not currently part of IPA models. This type of geological detail will be critical to the development of more comprehensive IPA models. In addition, understanding the range of possible consequences of direct disruption of the repository will have an important effect on probability calculations.

## 12.2 SIGNIFICANT TECHNICAL ACCOMPLISHMENTS

The Field Volcanism project has been under way for less than 2 months, and technical accomplishments during this period have been limited. Work, however, has been initiated on several aspects of the project. This work includes Task 1 research on selection of western Great Basin volcanoes and recently active cinder cones for detailed study and Task 4 research on the geology of intrusive igneous features. Work on these tasks to date has included initial site visits to the Cima Volcanic Field, the Fortification Hills dike set, and the Pisgah — Amboy volcanic area. Geophysical modeling of potential field anomalies associated with igneous features has also been initiated. This aspect of the project includes development of models of anomalies likely to result from shallow dikes in a variety of geologic settings and modeling of data collected at specific dikes and vents.

Rather than focus on site selection and initial geophysical investigations, which are quite preliminary, this report will review several aspects of eruption energetics and mechanics, in light of two recent cinder cone eruptions. This issue is critical to probability and consequence studies in volcanism in the YMR and constitutes a key aspect of Field Volcanism research.

Substantial uncertainty exists about the mechanics and energetics of cinder cone volcanism in the western Great Basin. Although cinder cone eruptions are commonly thought to result from exclusively low-energy Hawaiian, strombolian, or vulcanian eruptions (Barnard et al., 1991; Margulies et al., 1992), observations at numerous active or recently active cones indicate that this is frequently not the case. High-energy hydromagmatic eruptions of basaltic magmas have been observed at historically active cinder cones and have likely occurred in the YMR (Self et al., 1980; Valentine et al., 1992). Sub-Plinian and Plinian-style activity that does not result from interaction of magma with a significant amount of meteoric water or vapor, is also common at historically active cinder cones (e.g., Rose et al., 1973; Fedotov, 1983; Amos et al. 1983; Walker, 1991; Rowland et al., 1991; Walker, 1993; Connor et al., 1993). The Field Volcanism research project will work toward achieving better constraints on the range of potential eruptive activity in the YMR in view of observations made during cinder cone eruptions. This can be accomplished in a straightforward way by comparison of the products of monitored eruptions with those of the YMR and other western Great Basin cinder cones. Models of the mechanics of cinder cone eruptions will be integrated into probability models and will be critical to the review of site characterization and performance issues in the LARP.

Detailed characterization of cinder cones of the YMR and western Great Basin is an important area of research in consequence studies. Examination of cinder cone products at these volcanoes, for example, will provide the necessary quantitative detail about their eruptive histories. Specific aspects of the deposits that will be examined include: degree of fragmentation in the deposit (Walker, 1991), the nature of vesiculation in juvenile clasts (Walker, 1993), ballistic studies of volcanic bombs (Rose et al., 1973; Self et al., 1980), crustal xenolith concentration in the deposit, and variation in these features within a single cone and a volcanic field. The Center for Nuclear Waste Regulatory Analyses (CNWRA) study of these cinder cones will largely be limited to investigation of near vent deposits, because in most areas of the western Great Basin distal ashfall deposits are absent or poorly preserved due to rapid erosion rates and the age of the volcanoes. Lack of preservation is important because volcanologists have traditionally relied on distal deposits to characterize the magnitude, duration, and energy of volcanic eruptions. These distal deposits are largely absent in the western Great Basin. Furthermore, recent work has indicated that conceptual models of cinder cone volcanism will need to be modified to include significant variations in magma properties, explosive character of the eruption, and duration of the eruption (Walker, 1991; 1993). Therefore, direct comparison of the near vent facies of deposits resulting from historically active and monitored cinder cone eruptions with those of the western Great Basin will provide the most direct means for quantitative interpretation of cinder cone deposits in terms of the mechanics and energetics of cinder cone eruptions. The accuracy and utility of numerical models, such as those currently under development at Los Alamos (Valentine et al., 1992), will also be best assessed through careful study of monitored cinder cone eruptions.

Brief summaries of two cinder cone eruptions, Cerro Negro, 1992 and Tolbachik, 1975, are provided along with calculations of the thermal energy release of the eruptions. Initial conclusions based on these and related data that are relevant to site characterization and related LARP activities are:

- Highly explosive activity, lacking a significant hydromagmatic or phreatic component, is a common characteristic of monitored cinder cone eruptions.
- Energy release, mechanical fragmentation of country rock, and muzzle velocities may commonly be greater in some cinder cone eruptions than expected from hydromagmatic activity.

- Cinder cone eruptions are often sustained rather than instantaneous, and the terms vulcanian and strombolian do not describe these eruptions well.
- The range of eruptive activity in the western Great Basin is best determined through a combination of field observations, laboratory analyses, and direct comparison with the deposits of monitored cinder cone eruptions.

### 12.2.1 Data from the April 1992 Eruption of Cerro Negro, Nicaragua

Volcán Cerro Negro is a small cinder cone located 63 km NW of Managua, Nicaragua (Figure 12-1), in the Cordillera de los Marribios. Cerro Negro is a young cinder cone, first formed in 1850, and is part of the El Hoyo volcanic complex, a cluster of cinder cones and small shields (Figure 12-1) that has likely been active throughout the Quaternary. This complex is located midway between two large composite cones, Momotombo and Telica volcanoes, along the main trend of the Central America volcanic arc. Six cinder cones, including Cerro Negro, and one maar form a 12 km long, NNW-trending alignment across the west flank of the El Hoyo complex. Cerro Negro has erupted at least 19 times since its formation, with 13 eruptions occurring between 1947 and 1971. It is the site of the most recent small-volume basaltic eruption at a cinder cone in the western hemisphere, having last erupted in April 1992 (Global Volcanism Network, 1992; Connor et al., 1993). Typical 1971 activity is illustrated in Figure 12-2. During the 1992 activity, the summit crater widened from approximately 100 m (Figure 12-2) to approximately 400 m.

Cerro Negro is unique in the western hemisphere because three recent explosive eruptions (1968, 1971, and 1992) have been studied in detail (Dillard, 1968; Goldsmith, 1968; Taylor and Stoiber, 1973; Viramonte and Di Scala, 1970; Viramonte et al., 1971; Rose et al., 1973; Carr and Walker, 1987; Global Volcanism Network, 1992; Connor et al., 1993). Of these three, the 1992 eruption was the most energetic and dispersive. During the explosive phase of the 1968 eruption, the convective ash column reached heights between 150 to 1500 m above the cinder cone, and total erupted volume was approximately  $1.7 \times 10^7 \text{ m}^3$  of ash (Viramonte and Di Scala, 1970; Rose et al., 1973). This explosive activity took place over 46 days (Dillard, 1968; Goldsmith, 1968) and consisted of numerous strombolian and vulcanian bursts (Taylor and Stoiber, 1973). Explosive activity was followed by the effusion of lavas from the south flank of the volcano. In contrast, 1992 activity took place in two eruptive phases of 17.75 hours and 19 hours duration. During these episodes, eruptive columns were maintained at a much greater height (3.5 to 7.5 km) than ever occurred during 1968 activity and the resulting ash deposit was more voluminous and widely dispersed than the 1968 deposit (Figure 12-3). Total volume of erupted ash during 1992 activity was approximately  $6 \times 10^7 \text{ m}^3$  (GVN, 1992). Nearly all the ash released during the 1992 eruption fell during the first phase of activity (Global Volcanism Network, 1992). The city of Leon, for example, had reached a total ash accumulation of 4 cm after 18 hours of eruptive activity and only an additional 0.25 to 0.5 cm accumulated during subsequent activity. Eruption column heights were reported to be sustained at approximately 7.5 km during this initial period.

Relative seismic energy release was monitored during the second, less voluminous eruptive phase in April 1992 (Connor et al., 1993), using the real-time seismic amplitude method (Murray and Endo, 1989). These data are believed to be the first of their kind ever recorded for a cinder cone eruption. Seismic energy release was remarkably steady during the eruption, increasing rapidly from background immediately before the onset of eruptive activity and dropping to background levels following the eruption (Figure 12-4). This seismic energy release is largely a result of volcanic earthquakes

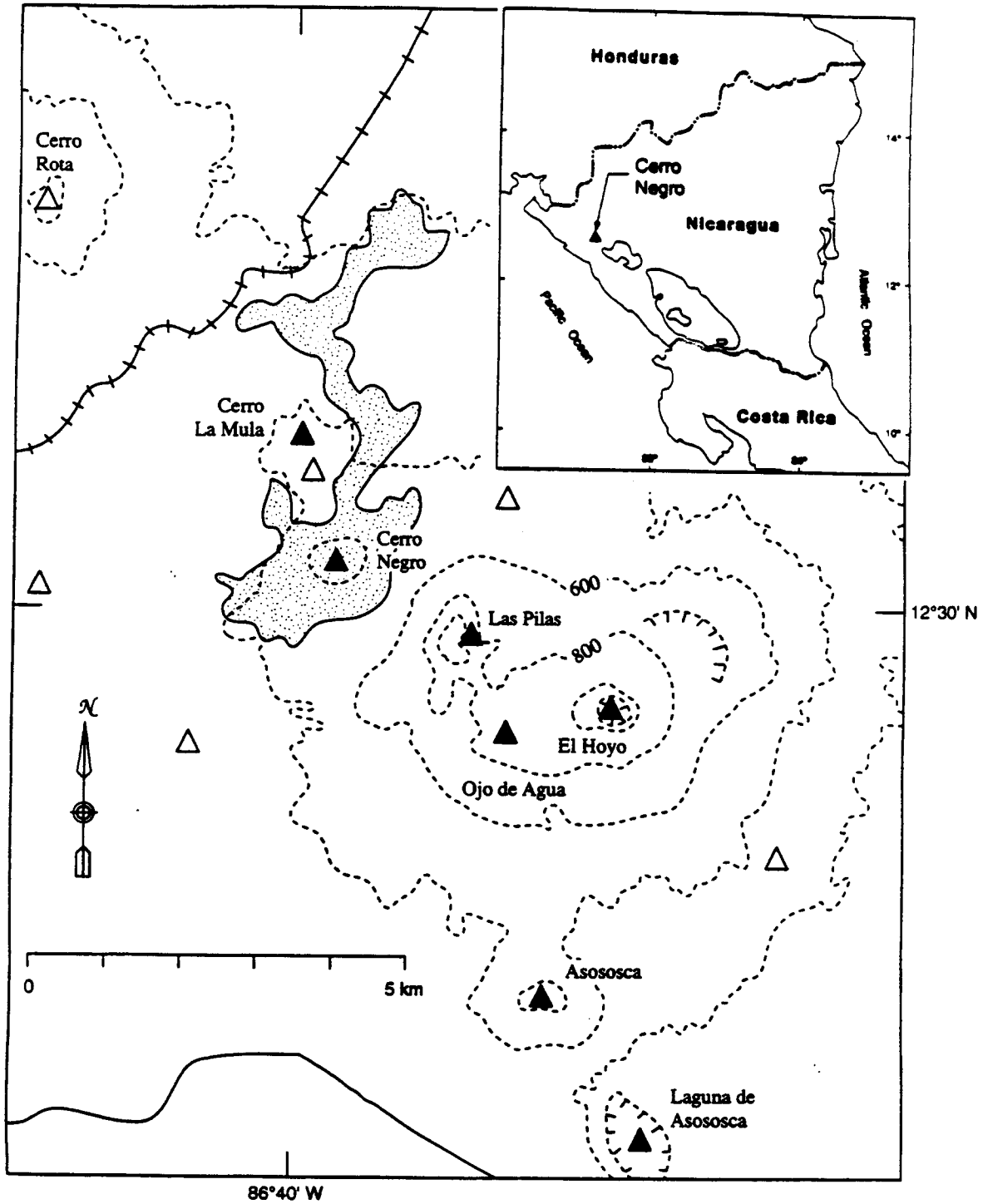
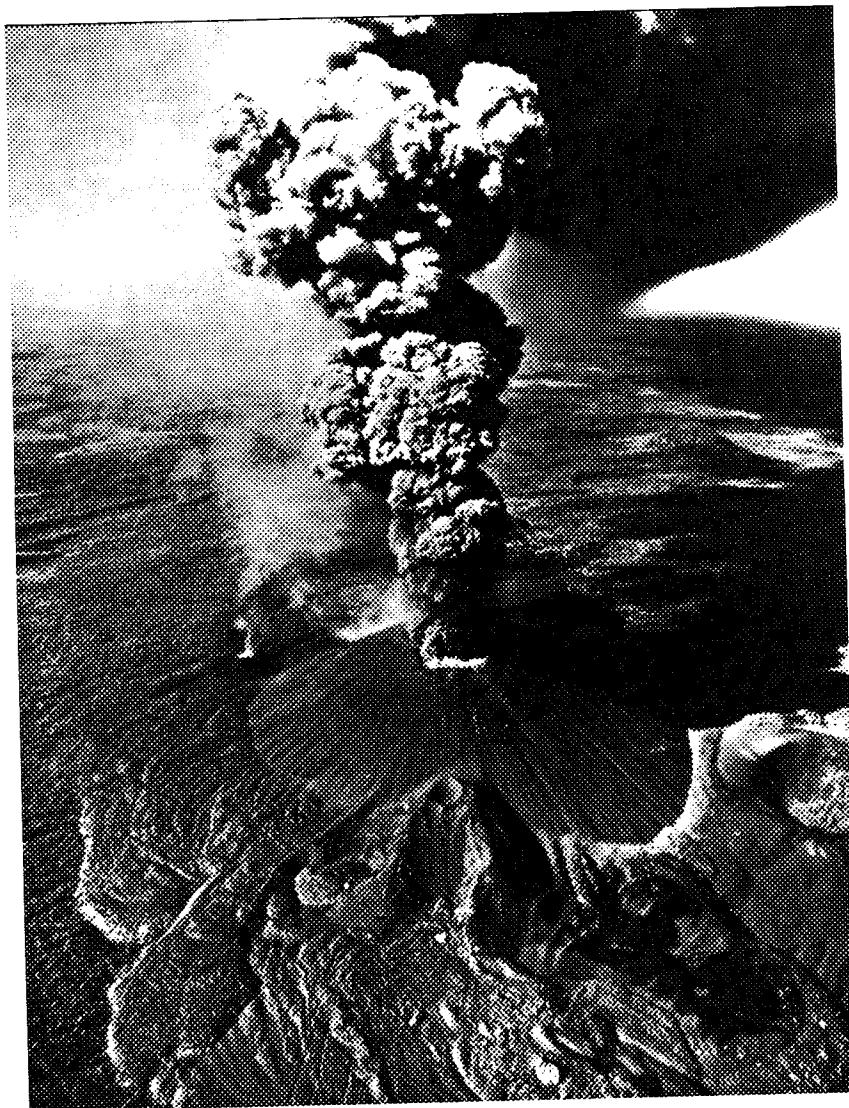


Figure 12-1. Location of Cerro Negro, Nicaragua. Late Quaternary cinder cones and maars of the El Hoyo complex are shown as solid triangles; older Quaternary(?) cones are shown as open triangles. The 1968 lavas of Cerro Negro are indicated by the stippled pattern.



**Figure 12-2. Photo of typical activity during the 1971 eruption of Cerro Negro. The vulcanian-style activity results in a tight, cauliflower-shaped eruption column rising approximately 500 m above the vent. Photo by Mark Hurd.**

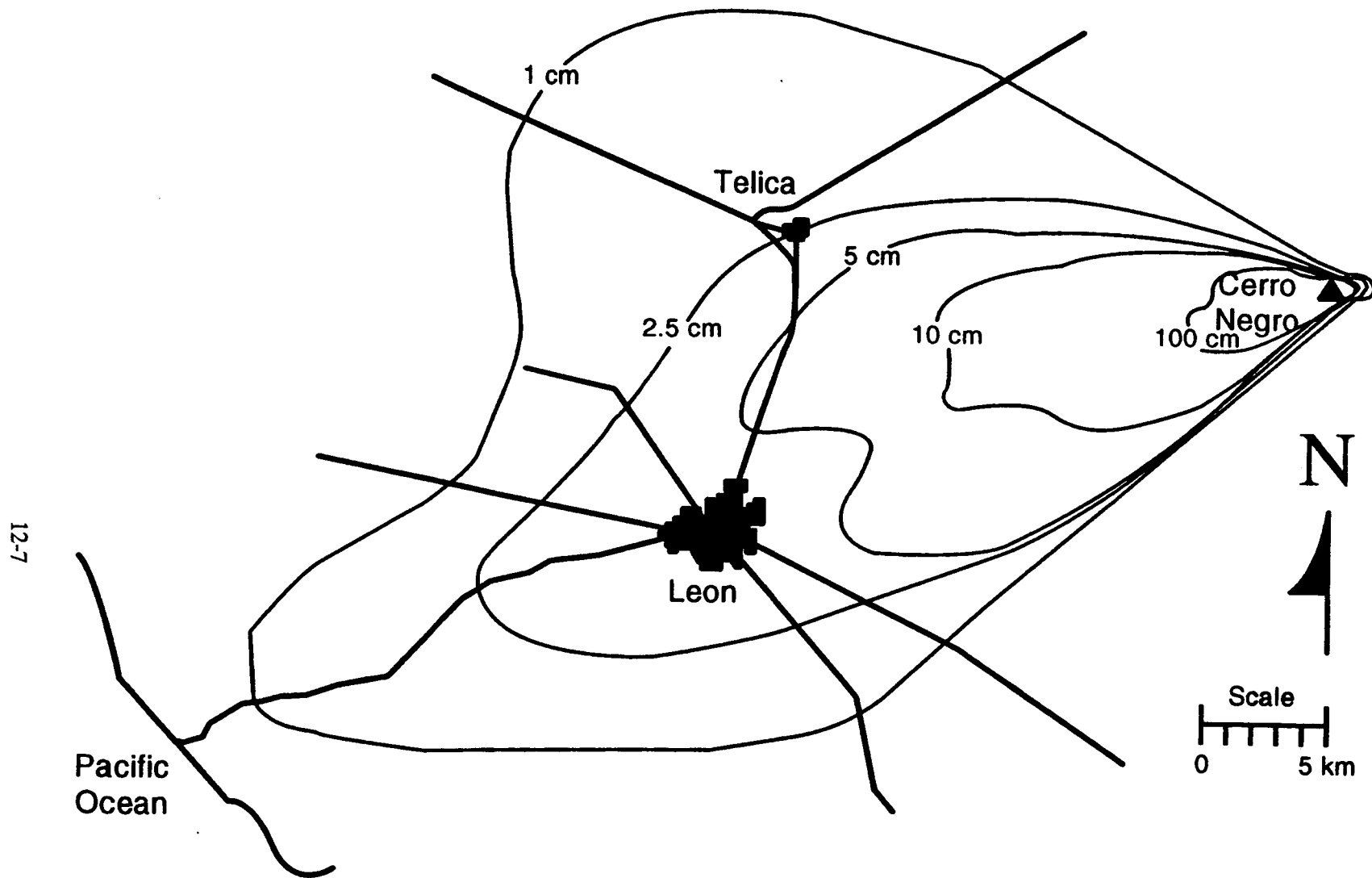


Figure 12-3. Isopach map of airfall from the April 1922 eruption of Cerro Negro. This eruption was voluminous and dispersive compared to 1968 or 1971 activity.

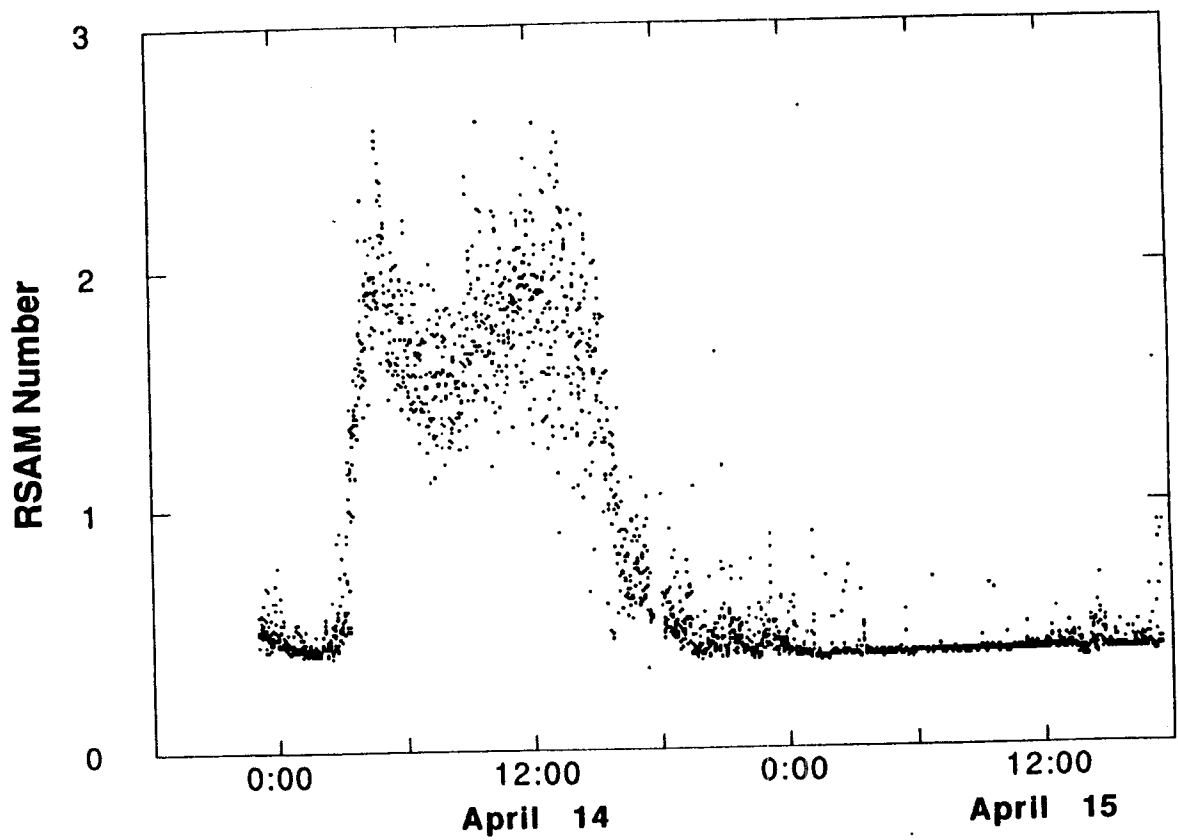


Figure 12-4. Real-time seismic amplitude measurements collected during the second phase of eruptive activity at Cerro Negro during the 1992 eruption. RSAM units are relative, calculated using the procedures of Murray and Endo (1989), and are indicative of total seismic energy release. Each sample point represents the root-mean-squared amplitude of the seismic signal collected at a site 5 km from the volcano.

associated with the movement of magma and hydrofracturing of rock at depths of less than 8 km (Connor et al., 1993). The seismic energy release pattern is very different than that expected if activity were characterized by a series of essentially instantaneous explosions, which would be characteristic of vulcanian or strombolian eruptive activity. During this phase of activity, magma apparently ascended from depth, and flow was maintained in the conduit until activity rapidly waned, which are characteristics of Sub-Plinian and Plinian eruptions.

Volatile concentration in erupting magma is believed to be a primary control on eruption style, energy release, and ash dispersion (Sparks, 1978; Wilson et al., 1978; Wilson, 1980; Wilson and Head, 1981). One of the simplest ways to learn about volatiles in erupting magmas is to monitor the chemistry of aerosols and salts adsorbed on ash particles in erupting ash columns. This can be done by collecting ash as it falls, or immediately after it falls, sieving the ash, and leaching the samples using a known amount of deionized water. The resulting ash leachate is then analyzed by ion chromatography for selected ions. Ion ratios, such as S/Cl, in leachates are indicative of volatile ratios within the erupting column (Taylor and Stoiber, 1973; Rose et al., 1973; Rose, 1977). Increases in S/Cl are indicative of increases in eruption magnitude and energy release (e.g., Menyaliyov, 1977; Nehring and Johnston, 1981; Rose, 1977). Ash leachate data collected from the April 1992 eruption are shown in Table 12-1. In comparison with the 1968 and 1971 Cerro Negro eruptions, the S/Cl ratio in the 1992 ash samples is higher. This is consistent with the more dispersive character of the 1992 eruption and suggests that variation in magmatic volatile chemistry is a fundamental control on eruption character of this cinder cone. Furthermore, there is a consistent change in S/Cl with stratigraphic position along the major axis of dispersion within the 1992 ash blanket (Figure 12-5). Early in the first eruptive phase, ash was less dispersive and S/Cl ratios were lower. Later, ash was more dispersive as eruption energy increased and S/Cl ratios were higher. This may be a result of overall change in magma chemistry during the eruption (cf. Carr and Walker, 1987), rather than simply a change in volatile chemistry.

### **12.2.2 Data From the 1975 Eruption of Tolbachik Cinder Cones, Kamchatka, Russia**

A series of basaltic eruptions created an alignment of cinder cones and fissure-fed lava flows on the Kamchatka Peninsula, Russia, during 1975. These cones are located approximately 10 km south of the summit caldera of the Ploskiy Tolbachik shield volcano in an area of numerous monogenetic cinder cones and spatter cones. Four other cinder cones in the area are thought to be less than 500 years old (Braytseva et al., 1983). Three cinder cones, Cones I, II, and III, and a series of small vents formed an alignment during several weeks of activity, known as the Northern Breakout, at Tolbachik in July and August of 1975. This activity was followed by a fissure eruption known as the Southern Breakout, 10 km south of the Northern Breakout and about 20 km from the summit caldera (Fedotov, 1983). A single cone formed as a result of Southern Breakout activity.

Budnikov et al. (1983), Tokarev (1983), and Maleyev and Vande-Kirkov (1983) summarized the initial activity at Tolbachik during the Northern Breakout. Activity at the first cone (Cone I) was initially mildly explosive and strombolian. This mild activity evolved into sustained explosive activity, during which a convective ash column was maintained at approximately 5 km altitude and effusion rates were on the order of  $1.25 \times 10^5$  kg/s (Budnikov et al., 1983; Tokarev 1983). This activity continued for 56 hours, during which Cone I grew to a basal diameter of 700 m and relief of 135 m, roughly the size of Lathrop Wells. This eruptive phase was followed by a dramatic increase in eruption intensity. As a result of this change in intensity, the convective ash column height increased to 8 to 10 km and occasionally reached 13 to 15 km (Fedotov, 1983). During this period, the eruption column was incandescent to an altitude of 1 to 2 km above Cone I during daylight hours (Tokarev, 1983). This

Table 12-1. Leachate concentrations (ppm) in three eruptions of Cerro Negro

	Cl	F	SO <sub>4</sub>	Na	K	Ca	Mg	S/Cl
<b>1992, 71 Samples</b>								
avg	88	8	457	17	2	148	175	1.7
max	703	221	3583	271	35	1138	1292	
<b>1971, 53 Samples</b>								
avg	777	14	541	146	20	257	23	0.2
max	1150	20	1240	230	180	510	48	
<b>1968, 41 Samples</b>								
avg	409	8	725	187	22	156	17	0.6
max	1200	22	2400	1500	86	650	54	

activity continued in a near steady-state through July 23, a period of 14 days (Budnikov et al., 1983). Explosive activity then gradually decreased through the end of July. Cones II and III were formed by comparatively low-energy strombolian and vulcanian activity during August. Following these eruptions, the locus of activity shifted south. During September 18, the Southern Breakout eruption began with fire fountaining over a 200 m long zone that gradually lengthened to 600 m. This eruption was entirely effusive, with fountain heights never exceeding 100 m. Effusion rates during the Southern Breakout were estimated to average  $25 \text{ m}^3 \text{ s}^{-1}$  between September and November of 1975.

Cone I and Cone II deposits of the Northern Breakout contain abundant Neogene sedimentary and volcanoclastic xenoliths (Shanster, 1983). These xenoliths effectively sample the stratigraphic section beneath the volcano between 1.8 km and the surface. Although the stratigraphic control is not good immediately beneath the volcano, it is known that the average thickness of Quaternary basalt at the volcano is approximately 500 m (Shanster, 1983). Therefore, it is very likely that all sedimentary crustal xenoliths at Cones I and II represent wall rock carried from greater than repository (300 m) depths. Size distributions and concentrations of xenoliths have not been determined, and the presence or absence of basalt xenoliths from shallow depths ( $< 500 \text{ m}$ ) has not yet been documented.

### 12.2.3 Cinder Cone Eruption Energetics

Wilson et al. (1978) describe a method for estimating thermal energy release of Plinian eruptions, based on ash column height. Assuming that density of basaltic magma is about  $2800 \text{ kg m}^{-3}$  and integrating over the isopach map (Figure 12-3) indicates that the April 1992 Cerro Negro eruption rate during the initial phase of activity was on the order of  $300 \text{ to } 500 \text{ m}^3 \text{ s}^{-1}$ . The steady release of thermal energy during Plinian eruption is given by Wilson et al. (1978):

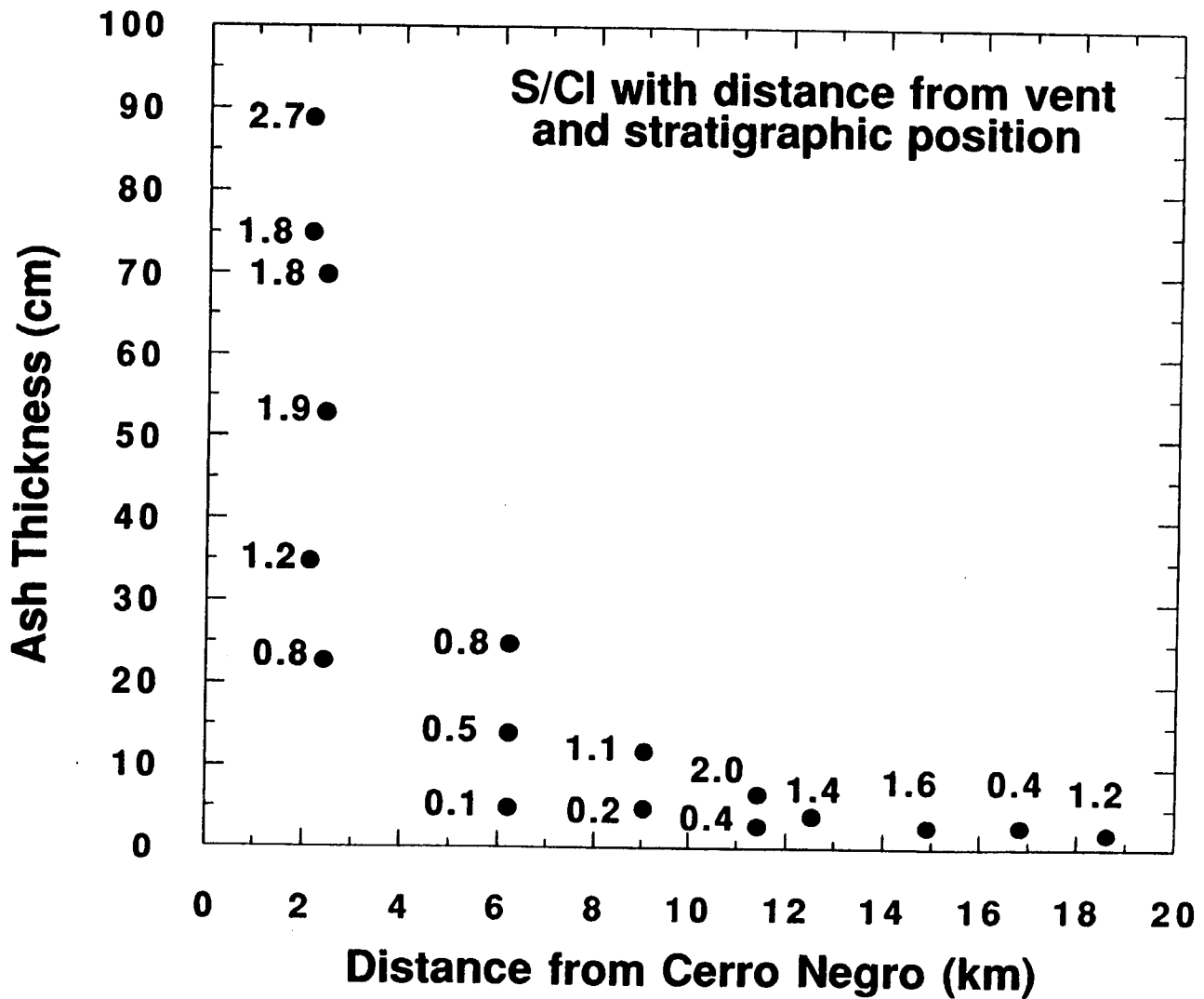


Figure 12-5. The thickness of the ash deposit varies exponentially with distance from Cerro Negro. Ash samples were collected during and immediately following the eruption at several stratigraphic positions along the major axis of dispersion of the deposit, and leachate S/Cl ratios were determined. A sample collected at 16.8 km is believed to have been altered prior to collection.

$$Q = rvs(T_m - T_a) F \quad (12-1)$$

where  $Q$  is the thermal energy in Watts,  $r$  is the magma density ( $2800 \text{ kg m}^{-3}$ ),  $v$  is the average eruption rate (in this case  $300$  to  $500 \text{ m}^3 \text{ s}^{-1}$ ),  $s$  is the specific heat of the magma ( $1.1 \times 10^3 \text{ J kg}^{-1} \text{ }^\circ\text{K}^{-1}$ ),  $T_m$  is the magma temperature,  $T_a$  is ambient air temperature ( $T_m - T_a = 1050 \text{ }^\circ\text{K}$ ), and  $F$  is a factor describing the efficiency of heat transfer to the atmosphere as the magma cools (assumed to be between  $0.7$  and  $1.0$ ). Using this range of values, the average rate of thermal energy release during the initial phase of the eruption was  $6.7 \times 10^{11}$  to  $1.6 \times 10^{12} \text{ W}$ , and total energy release was between  $4.3 \times 10^{16}$  and  $1.0 \times 10^{17} \text{ J}$ . The expected ash column height, given the range of estimated thermal energy release, can then be calculated using the empirical relation of Wilson et al. (1978):

$$H = 8.2Q^{1/4} \quad (12-2)$$

where  $H$  is the column height in meters. Substituting in the calculated values for steady thermal energy release,  $Q$ , the expected column height is between  $7.4 \text{ km}$  and  $9 \text{ km}$  above the volcano. These calculations agree well with observed column heights for the April, 1992 eruption of Cerro Negro (Global Volcanism Network, 1992; Connor et al., 1993). During the second episode of activity at Cerro Negro, column heights were observed to be on the order of  $3.5 \text{ km}$  and relatively sustained (Connor et al., 1993). Based on total accumulation and observed rates of accumulation, average eruption rate during this period was approximately  $25$  to  $30 \text{ m}^3 \text{ s}^{-1}$ . Calculated column heights for this eruption rate are  $4.0$  to  $4.5 \text{ km}$ , again in reasonable agreement with the observed maximum ash column height.

In comparison, ash column heights were between  $150$  and  $1500 \text{ m}$  during activity at Cerro Negro between October 24 and December 10, 1968. Lower column heights are consistent with the less dispersive nature of the 1968 airfall deposit. Rearranging Eq. (12-2), the steady thermal energy release during the 1968 explosive activity was on the order of  $1.1 \times 10^5 \text{ W}$  to  $1.1 \times 10^9 \text{ W}$ , low compared to the 1992 energy release.

Observations and empirical estimates of energy release indicate that the April 1992 eruption of Cerro Negro was more nearly Plinian than strombolian or vulcanian, styles of eruption that are characterized by instantaneous explosions. The two phases of activity during the 1992 eruption maintained convecting ash column heights of  $7.0$  to  $8.0 \text{ km}$  and  $3.5$  to  $4.0 \text{ km}$ , respectively, that resulted in ash accumulation rates and dispersion expected from Plinian-style activity. Based on seismic data from the second, less vigorous eruption, energy release was essentially steady during the eruption, again consistent with a Plinian model. Ash leachate data also suggest that there may have been a change in magma chemistry during the eruption, also consistent with Plinian style activity. Using the volcano explosivity index (Newhall and Self, 1982), the 1992 eruption is classified as VEI 3, although the durations of both phases of the eruption were longer than expected for VEI 3 eruption.

Energy calculations may also be made for the initial phases of the 1975-1976 Tolbachik fissure eruption. The initial, less explosive phase of activity at Cone I (column heights sustained at  $5 \text{ km}$ ) resulted in a rate of thermal energy release of approximately  $1.38 \times 10^{11} \text{ W}$  [Eq. (12-2)]. By using the mass flow from the cone during this period, estimated by Tobarev (1983) to be  $1.25 \times 10^5 \text{ kg s}^{-1}$ , the rate of thermal energy release was  $1.4 \times 10^{11} \text{ W}$  [Eq. (12-1)]. Using a  $10\text{-km}$  average column height, the rate of energy release during subsequent Plinian phase activity was  $2.2 \times 10^{12} \text{ W}$  [Eq. (12-2)].

Given the duration of the eruption, total thermal energy release during Cone I explosive activity was  $2.7 \times 10^{18}$  J. This energy is about one-third the thermal energy release due to the 1883 eruption of Krakatau (Simkin and Fiske, 1983), which is one of the most explosive historical eruptions known.

#### **12.2.4 Implications for Volcanism in the YMR**

Volcanic eruptions are often classified on the basis of dispersion and fragmentation of ash. All three Cerro Negro eruptions for which detailed information of this type is available (1968, 1971, and 1992) and the Cone I eruption at Tolbachik are classified as phreato-Plinian according to these criteria. Based on the dispersion and fragmentation within the ash blanket alone, it could seem that these eruptions would have had a significant phreatic (or hydromagmatic) component, although this is clearly not the case. Walker (1993) has observed a similar pattern of highly fragmented and widely dispersed ash blankets at Parícutin, Jorullo, and Xitle volcanoes, Mexico. At least at Parícutin and Jorullo, a significant hydromagmatic component can be ruled out. Walker (1993) has suggested that the dispersive and fragmented character of the deposits may be related to a high yield strength in the magmas. Yield strength does not so much suppress bubble nucleation as suppress bubble coalescence in the magma (Sparks, 1978), which is necessary to achieve fragmentation. Variation in magma properties may have important implications for the depth of fragmentation and the ability of the magma to erode wall rock at varying stratigraphic levels. For example, the Tolbachik eruption entrained abundant shallow crustal xenoliths (Shanster, 1983) and, although not searched for in a systematic way, shallow crustal xenoliths do occur in Cerro Negro eruption products from the 1968 (Viramonte and Di Scala, 1970) and 1992 eruptions. Comparable entrainment of xenoliths may have occurred at Lathrop Wells, as abundant crustal xenoliths are present in near vent deposits at that cone (Crowe et al., 1983; Connor and Hill, 1993).

Monitoring of active cinder cones indicates that eruptions at these volcanoes can be explosive, highly energetic, and of long duration. Both the 1992 eruption of Cerro Negro and the 1975 eruption of Tolbachik were considerably more energetic than suggested by the terms strombolian or vulcanian (Blackburn et al., 1976). Although these eruptions were small volume and not Plinian in the strictest sense (Simkin et al., 1981), they did have many of the characteristics of Plinian eruptions. For example, eruption columns were sustained over a long period of time, during which significant changes in magma chemistry occurred and total thermal energy release was large, comparable to some Plinian eruptions. Furthermore, muzzle velocities for the Cerro Negro and Tolbachik eruptions were approximately twice those reported for hydromagmatic eruptions (Self et al., 1980). Similar explosive activity may be a common characteristic of cinder cone volcanism in the southwestern United States (Amos et al., 1983). The extent to which this style of activity occurred during eruptions at Lathrop Wells, where strata of a highly fragmented character are common (Crowe et al., 1983), and other Quaternary cones in the western Great Basin will be addressed by the Field Volcanism project as research progresses. In particular, characterization of volcanological features of near-vent deposits, including sorting, grain size, vesicularity, and xenolith concentrations, at Quaternary and historically active cinder cones will provide considerably more confidence in models of YMR volcanism than is otherwise possible.

### **12.3 ASSESSMENT OF PROGRESS**

The Field Volcanism project is in its earliest stages. Currently, work is focused on the initiation of research activities in various aspects of the project. These activities include the following:

- Site selection for the study of near-surface basaltic dikes
- Selection of western Great Basin cinder cones for detailed petrogenetic and physical volcanological studies, as analogs to volcanoes of the YMR
- Initiation of geophysical modeling of dike geometries and study of the resolution of geophysical methods in varying field conditions
- Review of the literature and data collected by the CNWRA staff on historically active and monitored cinder cone eruptions, as discussed previously.

The Field Volcanism project utilizes a dual approach to the evaluation of the consequences of potential volcanic activity in the YMR. Clearly, the range of volcanic activity in the western Great Basin, the duration of this activity, and geology of near-surface structures must be evaluated using detailed field studies of specific sites in the region. Much can also be learned from the study of historically active cinder cones, especially those where eruptions have been rigorously monitored. As described previously, recent work indicates that many physical and conceptual models of cinder cone volcanism do not encompass the range of activity in modern cinder cones. Therefore the dynamics of cinder cone eruptions in the western Great Basin can not be truly assessed without thorough comparison to monitored cinder cone eruptions. One simple approach adopted in the Field Volcanism project is to compare near vent deposits at YMR volcanoes with those at Parícutin, Tolbachik, and Cerro Negro, volcanoes with well known eruption histories. Furthermore, processes such as diffuse degassing and thermal loading operate on geologically limited time scales, but could have important impact on repository performance. These processes can be studied most directly at recently active cinder cones. This integrated approach, the study of western Great Basin cinder cones and recently active cones, will provide the most comprehensive and defensible basis for evaluation of compliance with 40 CFR Part 191 and 10 CFR Part 60.122(c)(15). As such, results of the Field Volcanism project will directly support the LARP. Without this type of integration, consequence studies and their utility in probability model development will become unnecessarily tenuous.

#### **12.4 PLANNED PROGRESS IN THE NEXT SIX MONTHS**

Field work and related data-gathering activities will be the focus of Field Volcanism research during the next 6 months. Specifically, field work will continue at the Cima, Pisgah-Amboy and Fortification Hills sites, and initial work will be done at the Black Hills, California site. Field work in these areas has the primary purpose of: (i) characterizing the volcanological features of near-vent facies to better determine eruption style and energy; (ii) determining the chronology and petrogenetic evolution of these areas to better understand temporal variations in magma flux and the duration of activity in volcanic areas of the western Great Basin; and (iii) mapping dike geometries and investigating dike properties at and near repository depths.

An Intermediate Milestone will be submitted to the NRC in July 1993, reiterating the utility of field studies at recently active cinder cones. During the next 6 months, field work is planned at Cerro Negro and Parícutin volcanoes. The purpose of this field work is to: (i) characterize near vent facies deposited by eruptions of known style and magnitude; (ii) collect samples for grain size, vesicularity, and volatile studies; and (iii) sample gases from active fumaroles on these volcanoes and measure soil radon and mercury gas flux to estimate the vigor and extent of degassing. In addition, Dr. Yuri Doubik,

Institute of Volcanology, Kamchatka, will visit the CNWRA and NRC offices to exchange data and coordinate future field work at Tolbachik.

Geophysical studies also will begin to provide meaningful results during the next 6 months. These studies include characterization of potential field anomalies associated with cinder cones and dikes. Under this program, ground and aeromagnetic, gravity, and electrical anomalies will be modeled in two and one half and three dimensions. A key element of this program will be to incorporate field data on dike geometries into models of expected geophysical anomalies in the YMR. In addition, a systematic review of seismic tomographic methods and their application to study of the structure and activity of volcanic fields will be undertaken in the next 6 months. These activities will culminate in a meeting on research issues related to the geophysical setting of volcanism at the NRC in October in anticipation of a major milestone to be delivered to the NRC early in 1994.

All these activities will be important contributions to the LARP and to CDS development. In addition, these activities will be coordinated with Volcanic Systems of the Basin and Range research in order to refine probability models on a continuing basis.

## 12.5 REFERENCES

- Amos, R.C., S. Self, and B.M. Crowe. 1983. Pyroclastic activity at Sunset Crater: evidence of a large magnitude, high dispersal strombolian eruption. *EOS, Transactions of the American Geophysical Union* 62: 1085.
- Barnard, R.W., M.L. Wilson, H.A. Dockery, J.H. Gauthier, P.G. Kaplan, R.R. Eaton, F.W. Bingham, and T.H. Robey. 1991. *TSPA 1991: An Initial Total-System Performance Assessment for Yucca Mountain*. Sandia National Laboratories Report SAND91-2795. Albuquerque, NM: Sandia National Laboratories.
- Blackburn, E.A., L. Wilson, and R.S.J. Sparks. 1976. Mechanisms and dynamics of strombolian activity. *Journal of the Geological Society of London* 132: 429-440.
- Braytseva, O.A., I.V. Melekestsev, and V.V. Ponomareva. 1983. Age divisions of the Holocene volcanic formations of the Tolbachik valley. *The Great Tolbachik Fissure Eruption, Geological and Geophysical Data 1975-1976*. S.A. Fedotov and Ye. K. Markhinin, eds. Cambridge: Cambridge University Press: 83-95.
- Budnikov, V.A., Ye. K. Markhinin, and A.A. Ovsyannikov. 1983. The quantity, distribution and petrochemical features of pyroclastics of the Great Tolbachik fissure eruption. *The Great Tolbachik Fissure Eruption, Geological and Geophysical Data 1975-1976*. S.A. Fedotov and Ye. K. Markhinin, eds. Cambridge: Cambridge University Press: 41-56.
- Carr, M.J. and J.A. Walker. 1987. Intra-eruption changes in composition of some mafic to intermediate tephra in Central America. *Journal of Volcanology and Geothermal Research* 33: 147-159.
- Connor, C.B., and B.E. Hill. 1993. *NRC High-Level Radioactive Waste Research at CNWRA, July 1 Through December 31, 1992. Chapter 10: Volcanism Research*. NRC-02-88-005. Washington, DC.: Nuclear Regulatory Commission (NRC):10-1-10-31.

- Connor, C.B., L. Powell, J. Thomas, M. Navarro, and W. Strauch. 1993. Comparison of volatile concentrations in three Cerro Negro, Nicaragua, eruptions. *50 Años Del Volcán Parícutin, Reunión Internacional Conmemorativa, Programa y Resúmenes*, Uruapan, Michoacán: Mexico City: Instituto de Geofísica.
- Crowe, B.M., S. Self, D. Vaniman, R. Amos, and F. Perry. 1983. Aspects of potential magmatic disruption of a high-level waste repository in southern Nevada. *Journal of Geology* 91: 259-276.
- Dillard, R. 1968. Cerro Negro volcanic eruption. *Smithsonian Institution Center for the Study of Short-Lived Phenomena*. Event Information Report, October 30, 1968, card no. 197. Washington, DC: Smithsonian Institution.
- Fedotov, S.A., 1983. Chronology and features of the southern breakout of the Great Tolbachik fissure eruption, 1975-1976. *The Great Tolbachik Fissure Eruption, Geological and Geophysical Data 1975-1976*. S.A. Fedotov and Ye. K. Markhinin, eds. Cambridge: Cambridge University Press: 11-26.
- Goldsmith, L.H. 1968. Cerro Negro volcanic eruption. *Smithsonian Institution Center for the Study of Short-Lived Phenomena*. Event Information Report, November 20, 1968, card no. 247. Washington DC: Smithsonian Institution.
- Global Volcanism Network (GVN). 1992. Violent strombolian activity at Cerro Negro. *Bulletin of the Global Volcanism Network* 17(3): 2-4.
- Maleyev, Ye. F., and Yu. V. Vande-Kirkov. 1983. Features of pyroclastics of the northern breakthrough of the Great Tolbachik fissure eruption and the origin of its pale-grey ash. *The Great Tolbachik Fissure Eruption, Geological and Geophysical Data 1975-1976*. S.A. Fedotov and Ye. K. Markhinin, eds. Cambridge: Cambridge University Press: 57-71.
- Margulies, T., L. Lancaster, N. Eisenberg, and L. Abramson. 1992. Probabilistic analysis of magma scenarios for assessing geologic waste repository performance. *American Society of Mechanical Engineers, Winter Annual Meeting*, Anaheim, CA: American Society of Mechanical Engineers.
- Menyailov, I.A. 1977. Prediction of eruptions using changes in composition of volcanic gases. *Bulletin Volcanologique* 37: 122-125.
- Murray, T.L., and E.T. Endo. 1989. *The Real-Time Seismic Amplitude Measurement System (RSAM)*. U.S. Geological Survey Open-File Report 89-684:12.
- Nehring, N.L., and D.A. Johnston. 1981. Using ash leachates to monitor gas emissions in: P.W. Lipman and D.R. Mullineaux, eds., *The 1980 Eruptions of Mount St. Helens, Washington*. U.S. Geological Survey Professional Paper 1250: 251-254.
- Newhall, C.G., and S. Self. 1982. The volcanic explosivity index (VEI): An estimate of the explosive magnitude of historical volcanism. *Journal of Geophysical Research* 87: 1231-1238.

- Rose, W.I. 1977. Scavenging of volcanic aerosols by ash: atmospheric and volcanologic implications. *Geology* 5: 621-624.
- Rose, W.I., Jr., S. Bonis, R.E. Stoiber, M. Keller, and T. Bickford. 1973. Studies of volcanic ash from two recent Central American eruptions. *Bulletin Volcanologique* 37: 338-364.
- Rowland, S.K., Z. Juardo, and G.P.L. Walker. 1991. El Jorullo, Mexico: The nature of "violent" strombolian eruptions is determined by the yield strength of magma? *EOS, Transactions of the American Geophysical Union* 72: 568.
- Self, S., J. Kienle, and J.-P. Huot. 1980. Ukinrek Maars, Alaska, II. Deposits and formation of the 1977 craters. *Journal of Volcanology and Geothermal Research* 7: 39-65.
- Shanster, A. Ye. 1983. Basement xenoliths in the eruption products of the new Tolbachik volcanoes and the problem of the formation of magma conduits in the upper crust. *The Great Tolbachik Fissure Eruption, Geological and Geophysical Data 1975-1976*. S.A. Fedotov and Ye. K. Markhinin, eds. Cambridge: Cambridge University Press: 72-82.
- Simkin, T., and R.S. Fiske. 1983. *Krakatau 1883, The Volcanic Eruption and Its Effects*. Washington, DC: Smithsonian Institution Press: 464.
- Simkin, T., L. Seibert, L. McClelland, D. Bridge, C. Newhall, and J.H. Latter. 1981. *Volcanoes of the World*. Stroudsburg, PA: Hutchinson Ross: 232.
- Smith, E.I., T.R. Feuerbach, and J.E. Faulds. 1990. The area of most recent volcanism near Yucca Mountain, Nevada: Implications for volcanic risk assessment. *High-Level Radioactive Waste Meeting. Proceedings of the Third Topical Meeting*. LaGrange Park, IL. American Nuclear Society 1:81-90.
- Sparks, R.S.J. 1978. The dynamics of bubble formation and growth in magmas: A review and analysis. *Journal of Volcanology and Geothermal Research* 3:1-37.
- Taylor P.S., and R.E. Stoiber. 1973. Soluble material on ash from active Central America volcanoes. *Geological Society of America Bulletin* 84: 1031-1042.
- Tokarev, P.I. 1983. Calculation of magma discharge, growth in the height of the cone and dimensions of the feeder channel of Crater I in the Great Tolbachik fissure eruption, July, 1975. *The Great Tolbachik Fissure Eruption, Geological and Geophysical Data 1975-1976*. S.A. Fedotov and Ye. K. Markhinin, eds. Cambridge: Cambridge University Press: 27-35.
- Valentine, G.A., B.M. Crowe, and F.V. Perry. 1992. Physical processes and effects of magmatism in the Yucca Mountain Region. *Proceedings of the Third International Conference of High-Level Radioactive Waste Management*. Las Vegas, NV: American Nuclear Society and American Society of Civil Engineers: 2014-2024.
- Viramonte, J.G. and L. Di Scala. 1970. Summary of the 1968 eruption of Cerro Negro. *Bulletin Volcanologique* 34: 347-351.

- Viramonte, J.G., E. Ubela, and M. Martinez. 1971. The 1971 eruption of Cerro Negro volcano, Nicaragua. *Smithsonian Institution Center for the Study of Short-Lived Phenomena*. Event Information Report, December 30, 1971, card no. 468. Washington, DC: Smithsonian Institution.
- Walker, G.P.L. 1993. The pyroclastic deposits of El Parícutin. *50 Años Del Volcán Parícutin, Reunión Internacional Conmemorativa, Programa y Resúmenes*, Uruapan, Michoacán: Mexico City: Instituto de Geofísica.
- Walker, G.P.L. 1991. Origin of vesicle types and distribution patterns in the Xitle pahoehoe basalt, in Mexico City. *EOS, Transactions of the American Geophysical Union* 72: 766.
- Wilson, L. 1980. Relationships between pressure, volatile content, and ejecta velocity in three types of volcanic explosion. *Journal of Volcanology and Geothermal Research* 8: 297-313.
- Wilson, L., and J.W. Head III. 1981. Ascent and eruption of basaltic magma on the Earth and Moon. *Journal of Geophysical Research* 86: 2971-3001.
- Wilson, L., R.S.J. Sparks, T.C. Huang, and N.D. Watkins. 1978. The control of volcanic column heights by eruption energetics and dynamics. *Journal of Geophysical Research* 83: 1829-1836.